

Experimental and numerical study of three-dimensional flows generated by ultrasounds

Bjarne Vincent

▶ **To cite this version:**

Bjarne Vincent. Experimental and numerical study of three-dimensional flows generated by ultrasounds. Fluids mechanics [physics.class-ph]. INSA de Lyon; Coventry University (1992-..), 2024. English. ⟨NNT : 2024ISAL0101⟩. ⟨tel-04995640⟩

HAL Id: tel-04995640

https://theses.hal.science/tel-04995640v1

Submitted on 18 Mar 2025

HAL is a multi-disciplinary open access archive for the deposit and dissemination of scientific research documents, whether they are published or not. The documents may come from teaching and research institutions in France or abroad, or from public or private research centers.

L'archive ouverte pluridisciplinaire **HAL**, est destinée au dépôt et à la diffusion de documents scientifiques de niveau recherche, publiés ou non, émanant des établissements d'enseignement et de recherche français ou étrangers, des laboratoires publics ou privés.



HAL Authorization

N° d'ordre NNT : 2024ISAL0101

THESE de DOCTORAT DE L'INSA LYON, membre de l'Université de Lyon

délivré en partenariat international avec
Coventry University, Coventry, UK

Ecole Doctorale N° 162
Mécanique, Energétique, Génie civil et Acoustique (MEGA)

Spécialité/ discipline de doctorat : Mécanique des Fluides

Soutenue publiquement le 29/11/2024, par :

Bjarne VINCENT

Experimental and numerical study of three-dimensional flows generated by ultrasounds

---

Devant le jury composé de :

BARKLEY	Dwight	Professeur	University of Warwick	Examinateur
MARCHIANO	Régis	Professeur	Sorbonne Université	Président / Rapporteur
JUEL	Anne	Professeure	University of Manchester	Rapporteure
BOTTON	Valéry	Professeur	INSA Lyon	Directeur de thèse
POTHÉRAT	Alban	Professeur	Coventry University	Co-directeur de thèse
MIRALLES	Sophie	Maître de Conférences	INSA Lyon	Co-encadrante de thèse
KUMAR	Abhishek	Maître de Conférences	Coventry University	Invité

Thèse accessible à l'adresse : https://theses.insa-lyon.fr/publication/2024ISAL0101/these.pdf © [B. Vincent], [2024], INSA Lyon, tous droits réservés

INSTITUT NATIONAL DES SCIENCES APPLIQUÉES LYON

Département de la Formation par la Recherche et des Études Doctorales (**FEDORA**)

Bâtiment INSA direction, 1er étage
37, av. J. Capelle
69621 Villeurbanne Cédex
fedora@insa-lyon.fr

Référence : TH1130_VINCENT Bjarne

L'INSA Lyon a mis en place une procédure de contrôle systématique via un outil de détection de similitudes (logiciel Compilatio). Après le dépôt du manuscrit de thèse, celui-ci est analysé par l'outil. Pour tout taux de similarité supérieur à 10%, le manuscrit est vérifié par l'équipe de FEDORA. Il s'agit notamment d'exclure les auto-citations, à condition qu'elles soient correctement référencées avec citation expresse dans le manuscrit.

Par ce document, il est attesté que ce manuscrit, dans la forme communiquée par la personne doctorante à l'INSA Lyon, satisfait aux exigences de l'Etablissement concernant le taux maximal de similitude admissible.

INSA LYON
Campus LyonTech La Doua
20, avenue Albert Einstein - 69621 Villeurbanne cedex - France
Tél. +33 (0)4 72 43 83 83 - Fax +33 (0)4 72 43 85 00
www.insa-lyon.fr

membre de UNIVERSITÉ DE LYON

Thèse accessible à l'adresse : https://theses.insa-lyon.fr/publication/2024ISAL0101/these.pdf © [B. Vincent], [2024], INSA Lyon, tous droits réservés

Département FEDORA – INSA Lyon - Ecoles Doctorales

SIGLE	ECOLE DOCTORALE	NOM ET COORDONNEES DU RESPONSABLE
ED 206 CHIMIE	**CHIMIE DE LYON** **https ://www.edchimie-lyon.fr** Sec. : Renée EL MELHEM Bât. Blaise PASCAL, 3e étage **secretariat@edchimie-lyon.fr**	**M. Stéphane DANIELE** C2P2-CPE LYON-UMR 5265 Bâtiment F308, BP 2077 43 Boulevard du 11 novembre 1918 69616 Villeurbanne **directeur@edchimie-lyon.fr**
ED 341 E2M2	**ÉVOLUTION, ÉCOSYSTÈME, MICROBIOLOGIE, MODÉLISATION** **http ://e2m2.universite-lyon.fr** Sec. : Bénédicte LANZA Bât. Atrium, UCB Lyon 1 Tél : 04.72.44.83.62 **secretariat.e2m2@univ-lyon1.fr**	**Mme Sandrine CHARLES** Université Claude Bernard Lyon 1 UFR Biosciences Bâtiment Mendel 43, boulevard du 11 Novembre 1918 69622 Villeurbanne CEDEX **e2m2.codir@listes.univ-lyon1.fr**
ED 205 EDISS	**INTERDISCIPLINAIRE SCIENCES-SANTÉ** **http ://ediss.universite-lyon.fr** Sec. : Bénédicte LANZA Bât. Atrium, UCB Lyon 1 Tél : 04.72.44.83.62 **secretariat.ediss@univ-lyon1.fr**	**Mme Sylvie RICARD-BLUM** Laboratoire ICBMS - UMR 5246 CNRS - Université Lyon 1 Bâtiment Raulin - 2ème étage Nord 43 Boulevard du 11 novembre 1918 69622 Villeurbanne Cedex Tél : +33(0)4 72 44 82 32 **sylvie.ricard-blum@univ-lyon1.fr**
ED 34 EDML	**MATÉRIAUX DE LYON** **http ://ed34.universite-lyon.fr** Sec. : Yann DE ORDENANA Tél : 04.72.18.62.44 **yann.de-ordenana@ec-lyon.fr**	**M. Stéphane BENAYOUN** Ecole Centrale de Lyon Laboratoire LTDS 36 avenue Guy de Collongue 69134 Ecully CEDEX Tél : 04.72.18.64.37 **stephane.benayoun@ec-lyon.fr**
ED 160 EEA	**ÉLECTRONIQUE, ÉLECTROTECHNIQUE, AUTOMATIQUE** **https ://edeea.universite-lyon.fr** Sec. : Philomène TRECOURT Bâtiment Direction INSA Lyon Tél : 04.72.43.71.70 **secretariat.edeea@insa-lyon.fr**	**M. Philippe DELACHARTRE** INSA LYON Laboratoire CREATIS Bâtiment Blaise Pascal, 7 avenue Jean Capelle 69621 Villeurbanne CEDEX Tél : 04.72.43.88.63 **philippe.delachartre@insa-lyon.fr**
ED 512 INFOMATHS	**INFORMATIQUE ET MATHÉMATIQUES** **http ://edinfomaths.universite-lyon.fr** Sec. : Renée EL MELHEM Bât. Blaise PASCAL, 3e étage Tél : 04.72.43.80.46 **infomaths@univ-lyon1.fr**	**M. Hamamache KHEDDOUCI** Université Claude Bernard Lyon 1 Bât. Nautibus 43, Boulevard du 11 novembre 1918 69 622 Villeurbanne Cedex France Tél : 04.72.44.83.69 **direction.infomaths@listes.univ-lyon1.fr**
ED 162 MEGA	**MÉCANIQUE, ÉNERGÉTIQUE, GÉNIE CIVIL, ACOUSTIQUE** **http ://edmega.universite-lyon.fr** Sec. : Philomène TRECOURT Tél : 04.72.43.71.70 Bâtiment Direction INSA Lyon **mega@insa-lyon.fr**	**M. Etienne PARIZET** INSA Lyon Laboratoire LVA Bâtiment St. Exupéry 25 bis av. Jean Capelle 69621 Villeurbanne CEDEX **etienne.parizet@insa-lyon.fr**
ED 483 ScSo	**ScSo**[1] **https ://edsciencessociales.universite-lyon.fr** Sec. : Mélina FAVETON Tél : 04.78.69.77.79 **melina.faveton@univ-lyon2.fr**	**M. Bruno MILLY** (INSA : J.Y. TOUSSAINT) Univ. Lyon 2 Campus Berges du Rhône 18, quai Claude Bernard 69365 LYON CEDEX 07 Bureau BEL 319 **bruno.milly@univ-lyon2.fr**

1. ScSo : Histoire, Géographie, Aménagement, Urbanisme, Archéologie, Science politique, Sociologie, Anthropologie

Thèse accessible à l'adresse : https://theses.insa-lyon.fr/publication/2024ISAL0101/these.pdf © [B. Vincent], [2024], INSA Lyon, tous droits réservés

Thèse accessible à l'adresse : https://theses.insa-lyon.fr/publication/2024ISAL0101/these.pdf © [B. Vincent], [2024], INSA Lyon, tous droits réservés

Acknowledgement

Although this thesis results from an individual research work, finally getting my PhD in fluid mechanics would not have been possible without the support of many people to whom I am extremely grateful.

First of all, I would like to express my deepest gratitude to Valéry BOTTON, Sophie MIRALLES, Alban POTHÉRAT and Abhishek KUMAR. Thank you for your kindness and your continuous support throughout the thesis. I would also like to thank Daniel HENRY: thank you for your availability and for the time you spent answering my questions on hydrodynamic stability and on numerical methods.

I would also like to thank Anne JUEL, Régis MARCHIANO, Dwight BARKLEY and Junho PARK for having accepted to review and assess my thesis. The interest you have shown in my work, your feedback and your questions paved the way to new perspectives for future work on acoustic streaming within the team.

I am extremely grateful to Séverine MILLET, Simon DAGOIS-BOHY and Susanne HORN. Thank you for your interest in my work. My thesis benefited greatly from the numerous comments you made and questions you asked during our meetings. I also wish to thank the members of my French progress review panel, Étienne PARIZET and Jean-Christophe BÉRA, whose comments led to interesting new interpretations of some of my results.

During my thesis, I had the chance to use state-of-the-art experimental and numerical methods. Mastering these tools would not have been possible without the help of several people. I would particularly like to thank Nathalie GROSJEAN for sharing her expertise on particle-based velocity field measurements. I would also like to thank Cédric MARMOUNIER for his help on the test bench development. I am also extremely grateful to Laurent POUILLOUX, Anne CADIOU, Mattéo CAMIER and Alex PEDCENKO who enabled me to carry out my numerical simulations on the high-performance computing clusters in Lyon and Coventry under the best possible conditions. Finally, I thank Hugh M. BLACKBURN for his support on the use of the spectral-element code *Semtex*.

At both the Fluid Mechanics and Acoustics Laboratory (LMFA) in Lyon and the Centre for Fluid and Complex Systems (FCS) in Coventry, I have met and discussed with many people whom I would like to thank for their kindness: Mahmoud EL HAJEM, Cyril MAUGER, Claude INSERRA, Louis GOSTIAUX, Lionel SOULHAC, Nicolas RIVIÈRE, Emmanuel MIGNOT, Diego LOPEZ, Benjamin MIQUEL, Serge SIMOËNS, Benjamin BORGNIC, Guillaume ARHANT, Christophe BAILLY, Laurent MARTIN WITKOWSKI, Benoît PIER, Florence RAYNAL, Chris PRINGLE, Martin HOLDSWORTH, Sascha WALD and Thierry PLATINI. I would like to express my deep gratitude to Nadira MATAR, Zoe GIBBS and Lorna EVERALL who have all helped me enormously when I had to deal with the (sometimes obscure) French and British administrations. I would also like to thank Virginie DARU and Michaël BAUDOIN, with whom I have had the great pleasure of working; I hope that we will have the opportunity to work

Thèse accessible à l'adresse : https://theses.insa-lyon.fr/publication/2024ISAL0101/these.pdf © [B. Vincent], [2024], INSA Lyon, tous droits réservés

together again in the future. Finally, I would like to warmly thank Slim KADDECHE, who came to Lyon several times and with whom I discussed and worked a lot at the end of my thesis: thank you for your kindness and your enthusiasm.

This thesis would not have been the same experience without the many PhD students and post-docs who have accompanied me along the way: Samy LALLOZ, Okba MOSTEFAOUI, Estelle MEZIANI, Clément FAGOUR, Étienne DUREUIL, Elio GUILLON, Antoine LOTTON, Thomas MICOL, Gabriel REGNAULT, Léo GUIOT DE LA ROCHÈRE, Djibrilla MOUNKAILA NOMA, Fabien DEPOILLY, Wesley AGOUA, Nelson POUMAËRE, Ruiyao ZHU, Kouami SESSOU, Camille LOZET, César PLANTEVIN, Declan KEOGH, Rishav RAJ, Will BLOOMER, Sam BOOTH, Shahzad SARWAR, Jacopo GIANFRANI, Heng Jie CHOONG, Abhiram THIRUTHUMMAL and Dimitrios MICHAIL KYRIAKOU. I would like to thank you all for turning this thesis into an unforgettable experience. I would also like to thank the Master's and Engineering students I enjoyed meeting, discussing and working with: Antonin BOBEAU, Lucie LAMPRECHT, Florence LEMANT, Félix SCHWARZENBACH and Florence BRUNOX. I would also like to warmly thank Jaouad BENHAMOU, with whom I had the pleasure of sharing my office when he still was a PhD student, and Abdessamed MEDELFEF for our discussions on stability.

Amongst those who have greatly contributed to the success of this thesis, even though they may not realise it, are my close friends outside the laboratories. They knew how to pull me out of my work when necessary. Thank you very much Seb, Elsa, Coco, Marion, Ludivine, Edern, Anatole, Perrine, Camille and Agathe !

Finally, I would like to thank my family: my parents, my brother, my aunts and uncles. Thank you for your continuous support.

Thèse accessible à l'adresse : https://theses.insa-lyon.fr/publication/2024ISAL0101/these.pdf © [B. Vincent], [2024], INSA Lyon, tous droits réservés

Abstract

The contactless nature of acoustic streaming (i.e., flows driven by the attenuation of progressive sound waves) makes it an attractive flow actuation solution whenever the access to the fluid is difficult. This situation commonly arises when solidifying semiconductors, for instance. In such cases, streaming flows can be beneficial to either control hydrodynamic instabilities or stir the melt in order to improve the properties of the solidified ingot. This study aims precisely to gain a better understanding of streaming jets, and thus to pave the way for the design of complex streaming flows to optimise solidification processes. This thesis is divided into three main studies.

First, I investigated the scaling of streaming jets using numerical simulations. The considered setup is a closed cylindrical cavity, inside which the streaming jet flows over distances larger than the sound attenuation length L_α. As such, this study covers regions in which the acoustic forcing is driving the flow (at distances $x < L_\alpha$ from the source) or nearly ineffective ($> L_\alpha$). I derived scaling laws for the jet velocity in each of these regions, allowing to draw a complete phenomenological picture of a streaming jet.

Second, I studied numerically the stability of that flow for different longitudinal and radial cavity sizes. For each case, destabilisation is rooted in the downstream cavity end, near the jet impingement. Nevertheless, confining the flow greatly affects the nature of the primary instability: whilst non-oscillatory perturbations become unstable in weakly-confined settings, reducing the cavity radius causes the flow to become unstable through either supercritical or subcritical Hopf bifurcations. The change of the unstable perturbation topology as the cavity radius is reduced is explained using critical point theory.

Third, I investigated experimentally a novel three-dimensional (3D) streaming flow for stirring purposes. I relied on a high-end Particle Tracking Velocimetry (PTV) method to capture the flow structures, their leading velocities, and to determine how these velocities scale with the forcing magnitude. The flow was driven by a helix-shaped forcing obtained from multiple reflections of a single sound beam in a closed water cavity. The resulting flow is made of impinging jets creating large vortices at the cavity walls. The main velocity levels are sustained by the jets, followed by the horizontal and vertical velocities. Besides of providing leading frequencies estimates as the forcing magnitude is increased, I showed that the scaling laws derived for a single jet can be used to design this 3D streaming flow.

Keywords: acoustic streaming, stability, Particle Tracking Velocimetry.

Thèse accessible à l'adresse : https://theses.insa-lyon.fr/publication/2024ISAL0101/these.pdf © [B. Vincent], [2024], INSA Lyon, tous droits réservés

Thèse accessible à l'adresse : https://theses.insa-lyon.fr/publication/2024ISAL0101/these.pdf © [B. Vincent], [2024], INSA Lyon, tous droits réservés

Résumé long en français

Le développement des énergies renouvelables et de leurs usages sont des enjeux majeurs de la société d'aujourd'hui. Quelle que soit la nature de cette énergie (solaire, éolienne, etc.), sa conversion sous une autre forme (électrique, par exemple) doit être réalisée avec le meilleur rendement possible pour permettre son utilisation à grande échelle. Dans le cas de l'énergie solaire, cette conversion est réalisée par des cellules photovoltaïques. Ces cellules sont obtenues à partir de la solidification dirigée de silicium photovoltaïque liquide, au cours de laquelle la ségrégation d'impuretés à l'interface solide/liquide et les écoulements résultant d'instabilitiés hydrodynamiques dans la phase liquide agissent directement sur la qualité du lingot solidifié. Afin d'optimiser la qualité de ce dernier, il est donc nécessaire de mettre en œuvre des stratégies de mélange et de contrôle d'écoulement dans le bain fondu.

En raison de fortes contraintes d'isolation thermique des procédés de solidification, il est difficile d'accéder au liquide fondu. Agir sur celui-ci nécessite donc des méthodes peu intrusives. L'équipe du LMFA (Laboratoire de Mécanique des Fluides et d'Acoustique) travaille depuis plusieurs années maintenant sur la possibilité de générer des écoulements dans le bain fondu à l'aide d'ultrasons: l'*acoustic streaming*. Le *streaming* est un phénomène non-linéaire au cours duquel l'atténuation d'ondes acoustiques génère un écoulement. Le champ d'intensité acoustique émis par une source constitue ainsi directement un champ de forçage qui met en mouvement le fluide. Pour agir efficacement sur le bain fondu, il est donc nécessaire de parfaitement comprendre la relation entre le champ de forçage acoustique (son amplitude et sa structure spatiale) et l'écoulement de *streaming* résultant (niveaux de vitesse et structure).

Cette thèse porte tout particulièrement sur l'utilisation de faisceaux d'ultrasons générant des jets de *streaming*, et se positionne en amont d'une mise en œuvre industrielle. Les travaux présentés dans ce manuscrit peuvent être divisés en deux grands pans. Dans un premier temps, je m'intéresse tout particulièrement au jet de *streaming* stationnaire laminaire forcé par un seul faisceau d'ondes ultrasonores progressives atténuées. Ce faisceau est rayonné par une source circulaire plane, et est axisymétrique. L'accent est mis sur les jets de *streaming* s'écoulant sur des distances comparables ou supérieures à la longueur d'atténuation des ondes acoustiques afin de maximiser la quantité de mouvement créée à l'aide d'un seul faisceau. Un paramètre important est donc le nombre adimensionnel N défini comme le rapport entre la longueur d'observation du jet et la longueur d'atténuation des ondes acoustiques. Des simulations numériques sont réalisées pour $N \geq 1$ afin de remplir deux objectifs: (i) obtenir des lois d'échelles reliant les paramètres du forçage acoustique (amplitude du forçage, diffraction du faisceau) aux niveaux de vitesse sur toute la longueur du jet, notamment en vue de prédimensionner des installations industrielles et/ou expérimentales impliquant du *streaming*, et (ii) déterminer quels sont les mécanismes physiques derrière la déstabilisation d'un jet de *streaming*. Bien que d'un intérêt fondamental certain, cette configuration "jet simple axisymétrique" n'est

Thèse accessible à l'adresse : https://theses.insa-lyon.fr/publication/2024ISAL0101/these.pdf © [B. Vincent], [2024], INSA Lyon, tous droits réservés

en revanche pas idéale pour des applications de mélange. Le second pan de cette thèse porte donc sur l'utilisation de plusieurs réflexions acoustiques d'un seul faisceau pour générer un champ de forçage (et donc un écoulement) inédit fortement tridimensionnel. Ce type d'écoulement permettrait d'assurer un meilleur brassage du silicium liquide, tout en n'utilisant qu'une seule source acoustique afin de conserver le caractère peu intrusif de la méthode. Cette étude est quant à elle entièrement expérimentale.

J'effectue tout d'abord dans le chapitre 1 un état des lieux de la littérature sur l'*acoustic streaming*: sa modélisation, et les principaux résultats concernant sa caractérisation et sa stabilité. La modélisation du *streaming* adoptée dans cette thèse repose sur la grande disparité entre les échelles acoustiques et celles de l'écoulement. Ainsi, chaque variable (vitesse, pression et masse volumique) peut être exprimée à l'aide d'une décomposition de Reynolds: la partie moyenne (variations temporelles lentes devant la période acoustique) étant associée au *streaming*, et la partie fluctuante de moyenne nulle correspondant à l'acoustique. De cette manière, on montre que le *streaming* peut-être modélisé par les équations de Navier-Stokes incompressibles avec un terme source correspondant au forçage acoustique. Les précédents travaux de Moudjed *et al.* (2014*a*) ont montré que ce terme source peut être correctement modélisé à partir de l'intégrale de Rayleigh, qui décrit le champ linéaire de pression acoustique rayonné par une source circulaire plane. En revanche, ce modèle intégral doit être adapté pour tenir compte de l'atténuation afin de modéliser des écoulements de *streaming* pour lesquels $N \geq 1$. De manière générale, très peu d'études portent sur une telle configuration, et les seules lois d'échelles existantes décrivent l'accélération du jet proche de la source. En particulier, la décélération du jet plus loin en aval n'a jamais été caractérisée. Il y a donc un vrai manque dans la compréhension d'un jet de *streaming* que ce travail de thèse vise à combler. Enfin, les différentes études de stabilité de la littérature confirment la capacité du *streaming* à stabiliser des écoulements soumis à d'autres phénomènes (chauffage extérieur, par exemple). Néanmoins, ces études reposent sur une modélisation assez grossière du champ de forçage acoustique (pas de diffraction ni d'atténuation du forçage), résultant en un écoulement qui diffère grandement de ceux observés en pratique. Il convient donc d'étudier plus en détails la stabilité d'un jet de *streaming* modélisé à l'aide d'un forçage plus réaliste tenant compte à la fois de l'atténuation et de la diffraction.

Le chapitre 2 est dédié aux développements analytiques effectués au cours de ma thèse. Dans un premier temps, je propose une modification de l'intégrale de Rayleigh. L'idée est d'introduire les effets d'atténuation acoustique, afin d'obtenir un modèle de forçage acoustique valable pour l'étude de jets de *streaming* caractérisés par $N \geq 1$. Le modèle obtenu comporte deux intégrales de Rayleigh atténuées: une pour la fluctuation acoustique de pression p_{ac}, et une autre pour la fluctuation acoustique de vitesse $\boldsymbol{u_{ac}}$; le forçage axisymétrique est ensuite obtenu à partir du produit des deux. Ce nouveau modèle permet également de calculer la divergence du forçage causé par la diffraction du faisceau acoustique: pour des faisceaux fortement diffractés, le forçage radial peut représenter jusqu'à 10 % du forçage axial maximum et n'est donc pas négligeable. Dans un second temps, je m'intéresse aux transferts d'énergie entre les échelles acoustiques et celles de l'écoulement. Modéliser le *streaming* à l'aide de décompositions de Reynolds permet d'établir un lien direct avec les travaux de modélisation de turbulence à masse volumique variable; je m'appuie donc fortement sur les travaux de turbulence de Dupuy *et al.* (2018) pour décrire les transferts entre l'énergie cinétique acoustique moyenne $\left\langle \frac{1}{2}\rho \boldsymbol{u_{ac}} \cdot \boldsymbol{u_{ac}} \right\rangle$ et celle de l'écoulement de *streaming* $\left\langle \frac{1}{2}\rho \boldsymbol{u_s} \cdot \boldsymbol{u_s} \right\rangle$ (ici, ρ est la masse volumique totale et $\boldsymbol{u_s}$ est la vitesse de l'écoulement de *streaming*). En raison des fluctuations de masse

Thèse accessible à l'adresse : https://theses.insa-lyon.fr/publication/2024ISAL0101/these.pdf © [B. Vincent], [2024], INSA Lyon, tous droits réservés

volumique, ces transferts s'effectuent nécessairement par l'intermédiaire de l'énergie mixte moyenne $\langle \rho \boldsymbol{u_s} \cdot \boldsymbol{u_{ac}} \rangle$. Je montre par la suite que le modèle de Dupuy *et al.* (2018) peut être simplifié davantage en estimant l'ordre de grandeur de chaque terme impliqué dans les bilans d'énergie. Le caractère périodique des fluctuations acoustiques joue un rôle majeur sur l'amplitude de ces termes: si on ne tient pas compte de la phase des fluctuations, on peut se tromper de plusieurs ordres de grandeur.

Dans le chapitre 3, je me concentre sur l'établissement de lois d'échelles pour la vitesse de *streaming* le long de l'axe du jet. Ce travail repose sur des simulations numériques dans une cavité cylindrique fermée définie par $N = 4, 5$. La source circulaire plane est placée à une extrémité, et le faisceau d'ondes atténuées force un jet laminaire axisymétrique et stationnaire. Ce jet impacte frontalement la paroi opposée à la source. Grâce à des analyses en ordres de grandeur, j'obtiens des lois d'échelles pour décrire l'évolution de $\boldsymbol{u_s}$ le long de l'axe du jet, depuis la source jusqu'à des distances où le faisceau est entièrement atténué. Dans la zone d'accélération proche de la source, initialement décrite par un équilibre entre les efforts inertiels et le forçage acoustique par Moudjed *et al.* (2014*a*), une nouvelle loi d'échelle tenant compte des forces visqueuses est proposée. Cette nouvelle loi améliore de 50 % la prédiction de la vitesse de jet dans cette zone. Plus loin de la source, en raison de la diffraction du faisceau, le forçage local de l'écoulement devient localement moins important, créant ainsi un pic de vitesse du jet sur son axe. Des lois d'échelles sont proposées pour la position et l'amplitude du pic. Plus loin en aval, la décélération du jet obéit à un équilibre entre les forces visqueuses et le forçage acoustique. Enfin, à des distances supérieures à la longueur d'atténuation, le forçage est quasiment inexistant: le jet obéit donc à un équilibre entre les forces inertielle et visqueuse, et l'évolution de sa vitesse sur son axe est en bon accord avec la loi auto-similaire de Schlichting & Gersten (2000). On obtient ainsi une vue d'ensemble des différentes zones d'écoulement le long du jet, avec de bonnes prédictions des amplitudes et évolutions de vitesse dans chacune de ces zones.

Le chapitre 4 est quant à lui dédié à l'étude de stabilité d'un jet de *streaming*. Cette étude est également entièrement numérique, et la configuration d'écoulement est similaire à celle du chapitre précédent. En particulier, j'étudie l'effet de la taille de cavité (modifiée soit en changeant N, soit en changeant le rapport K_R entre le rayon de cavité et le rayon maximal du faisceau diffracté) sur les propriétés de stabilité de l'écoulement. Dans un premier temps, une analyse de stabilité linéaire est réalisée pour chaque cavité afin de (i) déterminer l'amplitude critique du forçage au-delà de laquelle l'écoulement devient instable, et (ii) identifier les causes d'instabilité à partir de la structure de la perturbation (c'est-à-dire le mode) instable. Pour des configurations à faible confinement radial, l'instabilité est non-oscillatoire et naît à l'impact du jet. Confiner radialement l'écoulement (en réduisant K_R) a non seulement un effet stabilisant, mais aussi change le type et la topologie de la perturbation déstabilisatrice qui devient oscillatoire. Pour ces cas-là, l'instabilité naît du cisaillement entre le jet et les cellules de recirculations résultant de l'impact. J'explique le changement de topologie du mode instable en étudiant ses points critiques (c'est-à-dire ses zéros de vitesse ou de frottement pariétal). Plus précisément, confiner radialement l'écoulement force une réorganisation des points critiques pour que le mode reste valide d'un point de vue purement topologique. Cette "validité topologique" est vérifiée à l'aide de la règle de Hunt *et al.* (1978) et Foss (2004) reliant les différents types de points critiques à la topologie de la surface dans laquelle ils sont observés. Par ailleurs, la nature axisymétrique de l'écoulement de base donne naissance à des points critiques "non standards", ou d'ordre élevé, sur l'axe du mode. Afin de tenir compte de

Thèse accessible à l'adresse : https://theses.insa-lyon.fr/publication/2024ISAL0101/these.pdf © [B. Vincent], [2024], INSA Lyon, tous droits réservés

tels points dans le bilan topologique, je propose une modification de la règle topologique qui est vérifiée avec succès. Dans un second temps, je réalise une étude non-linéaire à l'aide de DNS ("Direct Numerical Simulations", ou "Simulations Numériques Directes") réalisées à des forçages légèrement supercritiques. En étudiant la croissance et saturation de perturbations injectées sous forme de bruit blanc, j'obtiens un panorama complet de la criticalité (ou nature) des bifurcations identifiées lors de l'étude linéaire: pour un faible confinement ($K_R = 6$), la bifurcation primaire est de type fourche supercritique, et est remplacée par une bifurcation de Hopf supercritique dans la géométrie la plus confinée ($K_R = 1$). Pour des confinements intermédiaires, des bifurcations primaires de types fourche sous-critique ($K_R = 3$) et Hopf sous-critique ($K_R = 2$) sont également observées. Pour ces deux derniers cas, la saturation de la perturbation initiale est suivie d'une transition vers un état fortement instationnaire, voire chaotique. Ce dernier régime nécessiterait des études supplémentaires pour être caractérisé. Pour conclure, le travail présenté dans ce chapitre montre qu'une très grande variété de bifurcations primaires peut être obtenue simplement en changeant la géométrie la cavité d'étude, et ce sans modifier la structure du forçage acoustique.

Enfin, le chapitre 5 est dédié à l'étude d'un écoulement de *streaming* fortement tridimensionnel pour des applications de mélange. Cette étude est entièrement expérimentale et est réalisée en eau. Dans un premier temps, je détermine le diamètre actif de la source acoustique utilisée pour générer le *streaming* à l'aide de mesures acoustiques réalisées à l'hydrophone. Dans un second temps, j'utilise cette source pour créer du *streaming* dans une cavité en verre de 183 mm × 183 mm × 160 mm (longueur × largeur × hauteur) remplie d'eau. L'idée est d'introduire un faisceau acoustique dans la partie supérieure de la cavité, et d'orienter le faisceau de telle sorte qu'il se réfléchisse sur les parois verticales tout en suivant un chemin descendant. Le faisceau réfléchi est ensuite entièrement atténué à la paroi inférieure de la cavité. J'obtiens ainsi un forçage acoustique en forme d'hélice descendante faite de cinq réflexions. Les champs de vitesse 3D-3C (trois dimensions, trois composantes) du *streaming* obtenus pour différentes amplitudes de forçage sont ensuite mesurés à l'aide d'une méthode PTV ("Particle Tracking Velocimetry") qui n'avait pas encore été utilisée au laboratoire. Les champs de vitesse moyennés en temps montrent cinq jets de *streaming* suivant globalement le forçage hélicoïdal et impactant les parois verticales. Ces jets créent une rotation globale du fluide autour de l'axe vertical central de la cavité, et cette rotation étire les rouleaux résultant des impacts de jets. La taille de ces rouleaux dépend grandement de la présence de la paroi horizontale inférieure ou d'un autre impact de jet à proximité. Les mouvements descendants, quant à eux, suivent globalement les jets, tandis que les mouvements fluides ascendants sont observés à proximité des parois ainsi que dans une "cheminée" verticale au centre de la cavité. De façon générale, on peut diviser cet écoulement en trois grands éléments en fonction de leurs niveaux de vitesse: (i) les vitesses les plus élevées sont observées dans les jets forcés et impactant les parois, (ii) les niveaux de vitesse intermédiaires sont associés à la rotation globale entraînée par les jets, et (iii) les vitesses les plus basses sont associées aux mouvements verticaux ascendants et descendants; en particulier, la cheminée centrale présente les vitesses verticales les plus faibles. Des mesures PTV complémentaires réalisées autour d'un impact de jet ont mis en lumière le développement d'instationnarités lorsque l'amplitude du forçage est augmentée, avec potentiellement des interactions fortes entre les impacts de jets situés sur une même paroi.

Pour conclure, les travaux analytiques, numériques et expérimentaux de cette thèse ont permis de dresser un tableau assez complet du *streaming* forcé par un faisceau d'ondes

Thèse accessible à l'adresse : https://theses.insa-lyon.fr/publication/2024ISAL0101/these.pdf © [B. Vincent], [2024], INSA Lyon, tous droits réservés

ultrasonores progressives, avec et sans réflexions du faisceau. En particulier, l'étude expérimentale réalisée dans le chapitre 5 a montré que ces lois obtenues pour un seul jet de *streaming* restent valables pour des écoulements tridimensionnels à plusieurs jets impactant des parois solides. On peut donc imaginer utiliser ces lois pour "accorder" la position de l'impact avec la position présumée du maximum de vitesse sur l'axe du jet de manière à maximiser les niveaux de vitesse à une amplitude de forçage donnée, et donc optimiser le mélange. Par ailleurs, l'étude de stabilité d'un jet droit (chapitre 4) a permis de montrer que la déstabilisation de l'écoulement est intimement liée à l'impact du jet et aux recirculations qui en résultent. Pour un usage dans un bain fondu en cours de solidification, maîtriser les instabilités impliquerait de pouvoir suivre l'évolution de la vitesse proche de la zone impactée par le jet. Par ailleurs, la réduction du volume liquide au cours du procédé aurait un effet stabilisant sur le jet, permettant ainsi d'augmenter l'amplitude du forçage tout en gardant un écoulement stable. Pour que ces conclusions restent valables, il faudrait néanmoins que la dynamique ne soit pas affectée par d'autres phénomènes, tels que des gradients de température. Enfin, l'écoulement 3D étudié expérimentalement ayant plusieurs jets, il est légitime de penser que les instationnarités mesurées résultent elles également d'une déstabilisation des impacts de jets et/ou des recirculations associées. Cela nécessiterait néanmoins des études complémentaires (stabilité linéaire, par exemple) spécifiques à cette configuration afin de confirmer ou infirmer cette hypothèse.

Thèse accessible à l'adresse : https://theses.insa-lyon.fr/publication/2024ISAL0101/these.pdf © [B. Vincent], [2024], INSA Lyon, tous droits réservés

Thèse accessible à l'adresse : https://theses.insa-lyon.fr/publication/2024ISAL0101/these.pdf © [B. Vincent], [2024], INSA Lyon, tous droits réservés

Contents

Abstract III

Résumé long en français V

List of Figures XV

List of Tables XXXVII

Introduction 1

1 Elements of acoustics and review of acoustic streaming 3
- 1.1 Introduction to acoustic streaming and position of this thesis relative to former studies made in the laboratory . . . 3
- 1.2 Fundamentals of acoustic wave propagation . . . 6
  - 1.2.1 General equations of fluid mechanics . . . 6
  - 1.2.2 Main assumptions in acoustics, linearisation and attenuation . . . 7
  - 1.2.3 Specific acoustic impedance, acoustic intensity and power . . . 9
    - 1.2.3.1 Specific acoustic impedance . . . 9
    - 1.2.3.2 Acoustic intensity and power . . . 9
  - 1.2.4 Reflection of linear sound waves on a smooth interface . . . 10
- 1.3 Theoretical description of acoustic streaming . . . 11
  - 1.3.1 Modelling acoustic streaming . . . 11
    - 1.3.1.1 First approach: small perturbation expansion of the flow variables . . . 11
    - 1.3.1.2 Second approach: time scales separation . . . 13
    - 1.3.1.3 Current trends in the modelling of Eckart streaming . . . 16
  - 1.3.2 Momentum flux for a streaming jet forced by an attenuated beam . 16
- 1.4 Modelling the acoustic forcing field: the Rayleigh integral . . . 17
  - 1.4.1 Formulation of the unattenuated Rayleigh integral . . . 17
  - 1.4.2 Analytical solution on the acoustic axis and definition of the near- and far- acoustic fields . . . 18
  - 1.4.3 Far-field approximation . . . 20
  - 1.4.4 Numerical computation of the Rayleigh integral . . . 21
- 1.5 Dimensionless numbers and scaling of acoustic streaming flows . . . 23
  - 1.5.1 Dimensionless groups governing the acoustics and streaming problems 23
  - 1.5.2 Scaling of acoustic streaming jet flows . . . 24
    - 1.5.2.1 Acoustic force balanced by either inertia or viscous forces along the jet . . . 24
    - 1.5.2.2 Jet formation at the origin . . . 26

Thèse accessible à l'adresse : https://theses.insa-lyon.fr/publication/2024ISAL0101/these.pdf © [B. Vincent], [2024], INSA Lyon, tous droits réservés

1.5.2.3 Velocity maximum on the streaming jet axis 26
1.6 Stability and dynamics of acoustic streaming jets 28
1.7 Conclusion 33

2 Analytical developments: attenuated Rayleigh integral and energy transfer in acoustic streaming 35
2.1 Introduction 35
2.2 The Rayleigh integral in a viscous medium 35
2.2.1 Assumptions 36
2.2.2 Integral relations for the acoustic intensity field radiated by a plane circular transducer 36
2.2.3 Analytical expressions of the acoustic fields on the transducer axis . 37
2.2.4 Nondimensionalisation of the acoustic forcing equations 39
2.2.5 Numerical integration and effects of diffraction on the forcing structure 40
2.2.5.1 Numerical integration, mesh convergence and comparison with the unattenuated models 40
2.2.5.2 Effects of diffraction on the forcing structure 42
2.3 Energy transfer in acoustic streaming 44
2.3.1 Overview of the energy exchanges in acoustic streaming 44
2.3.2 Further developments to be made 45
2.4 Conclusion 47

3 Scaling of a steady laminar and axisymmetric acoustic streaming jet 49
3.1 Introduction 49
3.2 Problem definition and governing equations 50
3.3 Numerical methods and mesh design 51
3.3.1 Temporal discretisation of the hydrodynamics problem 51
3.3.2 Spatial discretisation of the hydrodynamics problem 52
3.3.3 Mesh design 54
3.4 Grid sensitivity and validation of the numerical model for long-range ($N > 1$) streaming calculations 55
3.4.1 Grid sensitivity analysis 55
3.4.2 Validation of the forcing model for the simulation of long-range ($N > 1$) streaming jets 57
3.5 Characterisation of an acoustic streaming jet 60
3.5.1 Inertia-dominated flow regime close to the transducer 61
3.5.2 Position and magnitude of the on-axis jet velocity peak 62
3.5.3 Viscosity-dominated flow regime beyond the velocity peak 66
3.5.4 Summary of the derived scalings along the jet axis 68
3.6 Conclusion 69

4 Stability analysis of a steady laminar and axisymmetric acoustic streaming jet 71
4.1 Introduction 71
4.2 Investigated parameter range, governing equations and introduction to critical point theory 72
4.2.1 Investigated parameter range 72
4.2.2 Governing equations for the linear stability problem 72
4.2.3 Critical point theory for flow analysis and topological rule 74

Thèse accessible à l'adresse : https://theses.insa-lyon.fr/publication/2024ISAL0101/these.pdf © [B. Vincent], [2024], INSA Lyon, tous droits réservés

4.3 Computational methods and grid sensitivity analysis . . . 76
4.3.1 Numerical methods for linear stability analysis and Direct Numerical Simulations (DNS) . . . 76
4.3.2 Critical point detection method . . . 77
4.3.3 Grid sensitivity analysis . . . 78
4.4 Confinement-induced alteration of the base flow structure and velocity levels 79
4.5 Stability analysis . . . 81
4.5.1 Non-oscillatory instabilities in weakly-confined streaming jet flows . 81
4.5.2 Rise of oscillatory instabilities in confined settings . . . 85
4.5.3 Adapting the topological rule for non-standard critical points on the axis . . . 89
4.6 Bifurcation characterisation . . . 93
4.6.1 Modelling the growth and saturation of finite-amplitude perturbations 94
4.6.2 Nature of the bifurcations . . . 96
4.6.3 Saturated states and secondary instabilities . . . 99
4.7 Conclusion . . . 100

5 Driving an experimental 3D-3C streaming flow using multiple reflections of a single sound beam 103
5.1 Introduction . . . 103
5.2 Experimental estimation of the acoustic source active diameter . . . 104
5.2.1 Test rig, equipment and signal chain for mapping the acoustic pressure and intensity fields . . . 104
5.2.2 Hydrophone measurements . . . 107
5.2.3 Evaluation of the active diameter D_s of the transducer . . . 109
5.3 Working principles of Particle Tracking Velocimetry (PTV), required equipment and validation . . . 111
5.3.1 Working principles of PTV and the Shake-The-Box algorithm . . . 111
5.3.2 Equipment for PTV measurements . . . 113
5.3.2.1 Choice of seeding particles . . . 113
5.3.2.2 Light sources . . . 113
5.3.2.3 Cameras . . . 114
5.3.3 Validation of the PTV methodology against a previously-studied acoustic streaming flow . . . 115
5.3.3.1 Adapting the test rig for PTV measurements of a square acoustic streaming flow . . . 115
5.3.3.2 Processing of the recorded images and particle track detection . . . 117
5.3.3.3 Comparison of the Eulerian velocity fields measured by PIV with those reconstructed from PTV measurements . . . 120
5.4 Experimental setup for the helical streaming flow measurements, control parameter and convergence of the time-averaged flows . . . 123
5.4.1 Modifications applied to the test right for helical flow measurements and recording parameters . . . 123
5.4.2 Effects of the operating temperature on the control parameter magnitude . . . 126
5.4.3 Convergence of the time-averaged flows . . . 126
5.5 Structure of the time-averaged helical flow . . . 127

Thèse accessible à l'adresse : https://theses.insa-lyon.fr/publication/2024ISAL0101/these.pdf © [B. Vincent], [2024], INSA Lyon, tous droits réservés

5.5.1 Impinging jets driven by the sound beam . . . 127
5.5.2 Creation of large-scale vortical structures and helicity generation . . 132
5.6 Characterisation of the 3D-3C nature of the helical acoustic streaming flow 135
5.6.1 Enhancement and scaling of the rotating (or swirling) flow strength with the forcing magnitude . . . 135
5.6.1.1 Development of the swirling velocity with the forcing magnitude . . . 135
5.6.1.2 Nonlinear scaling of the swirling velocity with the forcing magnitude . . . 136
5.6.2 Multiple velocity scales in the vertical streams . . . 137
5.6.2.1 Evaluation and scaling of the downward flow velocity . . . 137
5.6.2.2 Predominant upward flow along the walls and in the corners of the cavity . . . 140
5.6.3 Summary of the streams magnitudes observed in the helical acoustic streaming flow . . . 142
5.7 Flow near a jet impingement: time-averaged topology and development of unsteadiness . . . 143
5.7.1 Vortical topology of the time-averaged flow at the impingement wall 143
5.7.2 Development of flow unsteadiness with increasing forcing magnitude and leading frequencies . . . 147
5.8 Conclusion . . . 151

Conclusion and outlook **153**

Bibliography **155**

A Streaming experiments from the literature: experimental conditions and corresponding dimensionless numbers **165**

B Equations governing the energy exchanges in acoustic streaming **168**

C Preliminary simulations: validation of the spectral-element code *Semtex* **172**

D Grid sensitivity studies for the stability analysis of streaming flows **176**

E Image processing for PTV measurements and Shake-The-Box parameters **178**

Thèse accessible à l'adresse : https://theses.insa-lyon.fr/publication/2024ISAL0101/these.pdf © [B. Vincent], [2024], INSA Lyon, tous droits réservés

List of Figures

1.1 Representation of the two streaming types: (a) Rayleigh-Schlichting streaming (figure taken and adapted from Luo *et al.* (2018)) and (b) Eckart streaming (taken and adapted from Moudjed (2013), who did his Ph.D thesis at the LMFA laboratory). In (b), the black arrows represent an Eckart streaming velocity field measured by PIV in water and averaged over 25 minutes. The thick red arrow indicates the sound wave propagation direction. 4

1.2 (a) Sketch of the square streaming flow configuration studied in a nearly-cubic cavity filled with water (figure taken from Launay *et al.* (2019)). The beam is fired by a plane circular transducer (yellow) outside the cavity and immersed in the same fluid. The beam enters the cavity through a circular aperture covered by a plastic film and, after three reflections, exits the cavity at the same location. (b) PIV measurement of the steady velocity magnitude $\|\boldsymbol{u_s}\|$ in the horizontal mid-height plane for $P_{ac,0} = 1$ W (Cambonie *et al.*, 2017). 6

1.3 Sketch of an incident acoustic wave (red) being transmitted (blue) and reflected (green) at a liquid-solid interface. 10

1.4 Sketch of the plane circular transducer of diameter D_s (grey), modelled as a plane disc vibrating at a uniform velocity u_0 and at an angular frequency ω. The transducer is modelled as an infinite number of point sources, each centred on an elementary surface $\mathrm{d}S$ and contributing to the net acoustic pressure and velocity (hence intensity) levels at M in the fluid domain. As the problem is axisymmetric, M is taken in the (e_x, e_y). 18

1.5 Analytical profiles of the unattenuated on-axis acoustic intensity $I_{ac,x}(x, r = 0)$ normalised by the maximum intensity $I_{ac,\max}$ (equation (1.48)). Three profiles are displayed: the intensity profile obtained assuming plane acoustic waves (solid black curve), the "real wave" formula (1.50) of Greenspan (1979) (solid red curve), and the far-field approximation (1.52) (dashed black curve). The vertical purple line locates the Fresnel distance L_F. All the curves are plotted for $D_s = 28.5$ mm and $\lambda = 0.74$ mm (experimental parameters of Moudjed *et al.* (2014*a*)). 19

1.6 (a) Transverse profiles of $\|\boldsymbol{I_{ac}}\|/I_{ac,\max}$ at different distances x/L_F from the source (a). The amplitudes are normalised by the maximum intensity $I_{ac,\max}$ (equation (1.48)), and the radial coordinates r are normalised by the transducer diameter D_s. The profiles are plotted for $D_s = 0.0285$ mm and $\lambda = 0.74$ mm (experimental parameters of Moudjed *et al.* (2014*a*)). (b) Ratio between the acoustic power $P_{ac,tr}$ flowing through a disk of radius R and the total power $P_{ac,0}$, as a function of R. The values of R are normalised by the central lobe radius $1.22\lambda x/D_s$. 21

Thèse accessible à l'adresse : https://theses.insa-lyon.fr/publication/2024ISAL0101/these.pdf © [B. Vincent], [2024], INSA Lyon, tous droits réservés

1.7 Numerical map of the normalised unattenuated acoustic intensity field $\|\boldsymbol{I_{ac}}\|/I_{ac,\max}$ radiated by a plane circular source at $x = 0$. The map is obtained from the numerical integration of the Rayleigh integral (1.56) for a transducer diameter $D_s = 28.5$ mm and a wavelength $\lambda = 0.74$ mm (experimental parameters of Moudjed *et al.* (2014*a*)). The transducer is discretised with $N_s = 250$ grid points in both the radial and azimuthal directions. The diffraction cone is represented by the green dashed line; the cone angle θ_c is also reported (equation (1.53)). The white arrow at the bottom left-hand corner illustrates how Moudjed *et al.* (2014*a*) defined the forcing field from $\|\boldsymbol{I_{ac}}\|$. The x-and r-coordinates are normalised by the Fresnel length L_F (equation (1.49)) and by D_s, respectively. 22

1.8 Profiles of the time-averaged (over 4.2 minutes) streaming velocity magnitude $\|\overline{\boldsymbol{u_s}}\|$ on the jet axis for different forcing magnitudes Gr_{ac}. The data is taken from the PIV (Particle Image Velocimetry) measurements of Moudjed (2013) (same dimensionless numbers as Moudjed *et al.* (2014*a*) in table A.2) made over three jet sections for each Gr_{ac}, from the jet origin ($x = 0$) to the downstream wall ($x = 16.8$). The transducer is placed at $x = -L_F \approx -9.6$ so that only the far acoustic field drives the flow. All the data is made dimensionless using D_s^2/ν, D_s and $\rho_0 D_s^3$ as time, length and mass scales, respectively. 26

1.9 Comparison of the centreline streaming velocity magnitude $\|\boldsymbol{u_s}\|$ with the scaling laws derived by Moudjed *et al.* (2014*a*): (a) inertial regime (equation (1.61)) and (b) viscous regime (equation (1.62)). The data is taken from Kamakura *et al.* (1996); Mitome (1998); Frenkel *et al.* (2001); Moudjed *et al.* (2014*a*) (corresponding experimental conditions and dimensionless numbers in tables A.1 and A.2, respectively). All quantities are made dimensionless using D_s, $\rho_0 D_s^3$ and D_s^2/ν as length, mass and time scales, respectively, and $x = 0$ corresponds to the jet origin. 27

1.10 Scaling of the jet velocity $\|\boldsymbol{u_s}\|$ on the axis and near the jet origin ($x = 0$). (a) Sketch taken from Moudjed *et al.* (2015) to illustrate how the scaling law (1.63) was derived. The authors applied a mass balance in a cylindrical volume enclosing the origin of an axisymmetric streaming jet. (b) Comparison between the scaling law (1.63) and the numerical simulations of Moudjed *et al.* (2015) and Kamakura *et al.* (1996) (the corresponding dimensionless parameters are given in table A.2) near the jet origin. All quantities are made dimensionless using D_s, $\rho_0 D_s^3$ and D_s^2/ν as length, mass and time scales, respectively. 28

1.11 Experiments of Dentry *et al.* (2014) on the effect of sound frequency f on the streaming velocity $\|\boldsymbol{u_s}\|$. The streaming jet is forced by the transmission of Surface Acoustic Waves (SAW) from a solid substrate into a water cavity (the flow direction is shown by the white arrow in (c)). Different cases are displayed: (a) $N = 0.63$, $Gr_{ac} = 0.3 \times 10^4$, (b) $N = 4.7$, $Gr_{ac} = 0.5 \times 10^4$, (c) $N = 24.2$, $Gr_{ac} = 0.6 \times 10^4$, (d) $N = 93.8$, $Gr_{ac} = 1.3 \times 10^4$, (e) $N = 394.7$, $Gr_{ac} = 6.5 \times 10^4$ and (f) $N = 1442.3$, $Gr_{ac} = 1.2 \times 10^4$. Velocities are normalised by their maximum values: (a) $U = 41.6$, $U = 49.6$, (c) $U = 45.4$, (d) $U = 12.71$, (e) $U = 10.1$ and (f) $U = 3.2$. For all displayed figures, $S \approx 0.015$. 29

Thèse accessible à l'adresse : https://theses.insa-lyon.fr/publication/2024ISAL0101/these.pdf © [B. Vincent], [2024], INSA Lyon, tous droits réservés

1.12 DNS streaming velocity profiles on the jet axis for different forcing magnitudes Gr_{ac} and N (data taken from Daru *et al.* (2024)). The simulations are made for $S = 0.305$, $L = 25$ and $P/F = 1083.3$; the jet is forced by a plane circular transducer at $x = 0$ and flows in a cylindrical cavity with an outflow boundary condition at $x = L$. The solid black line locates the Fresnel distance L_F, and the dashed vertical lines locate the attenuation distance L/N. All quantities are made dimensionless using D_s, $\rho_0 D_s^3$ and D_s^2/ν as length, mass and time scales, respectively. 30

1.13 Evaluation of the scaling law (1.64) proposed by Orosco & Friend (2022) for the position x_p of the velocity peak on the axis of a streaming jet. The scaling law is compared to the experimental data of Dentry *et al.* (2014) (see table A.2 for the corresponding dimensionless numbers), and to the recent numerical simulations data of Daru *et al.* (2024), for which $S \in [0.08, 0.6]$, $F \in [1.6, 460.8] \times 10^4$, $N \in [0.2, 6.6]$, $L \in [6.3, 50]$ and $Gr_{ac} \in [0.04, 1.2] \times 10^4$. 30

1.14 PIV snapshots of the streamwise streaming velocity $u_{s,x}$ near the downstream wall ($x = 16.5$) for $Gr_{ac} = 11.6 \times 10^4$. The figure is taken from Moudjed *et al.* (2014*b*) and made dimensionless using D_s and D_s^2/ν as length and time scales, respectively (the dimensionless parameters are those of Moudjed *et al.* (2014*a*) in table A.2). The jet origin is at $x = 0$ and the transducer is placed at $x = -L_F \approx -9.6$ (with L_F the Fresnel distance). Snapshots (ordered from top to bottom) are separated by $\Delta t = 3.3 \times 10^{-4}$ (0.27 s in dimensional units). 31

1.15 Setup and main results of the Eckart streaming linear stability analyses from the literature. (a) Sketch of the setup, with the definition of the geometrical dimensionless numbers. The forcing is constant along x and y inside the beam (red), and is zero outside (blue). Due to the planar geometry, Gr_{ac} (equation (1.60)) is based on h_b. For $\Lambda \to \infty$, the base flow is an analytical 1D-1C velocity profile (Nyborg, 1953). (b) Leading oscillatory velocity perturbation $\boldsymbol{u'}$ at the instability onset $Gr_{ac}^c = 1089.1$ (Henry *et al.*, 2022), here represented as contours of $\boldsymbol{u'} \cdot \boldsymbol{e_y}$ (red is positive, blue is negative). (c) Evolution of the instability onsets Gr_{ac}^c as a function of $H = h_c/h_b$ for an analytical 1D-1C (Dridi *et al.*, 2010) or a numerically-computed 2D (Ben Hadid *et al.*, 2012) base flow (setup shown in (a)). In both cases, the unstable perturbation is oscillatory. (d) Effect of streaming on the stability of a Rayleigh-Bénard flow (heating from below) for $\Lambda \to \infty$ (figure adapted from Ben Hadid *et al.* (2012)). The critical Rayleigh number Ra_c is normalised by $Ra_0 = 1707.8$ (critical Rayleigh number for $Gr_{ac} = 0$). The horizontal solid and dashed black lines represent pure streaming ($Ra = 0$) and pure convection ($Gr_{ac} = 0$) instability onsets, respectively. 32

Thèse accessible à l'adresse : https://theses.insa-lyon.fr/publication/2024ISAL0101/these.pdf © [B. Vincent], [2024], INSA Lyon, tous droits réservés

2.1 Grid sensitivity for the circular source discretisation. The grid is made of N_s points in both the radial and azimuthal directions. The grid sensitivity is analysed for $S = 0.03$ and $N/L = 0.003$ (acoustic parameters of Moudjed *et al.* (2014*a*)). (a) Evolution with N_s of the relative error e between the analytical (2.17) and numerically-evaluated $\widetilde{I}_{ac,x}$ (equations (2.9) and (2.15)) at different points x on the axis. (b) On-axis profiles of $\widetilde{I}_{ac,x}$ for different assumptions: unattenuated plane-wave approximation (brown, analytical, equation (1.47)), unattenuated "real wave" model of Greenspan (1979) (blue, analytical, equation (2.13) with $N/L = 0$), attenuated "real wave" (black, analytical, equation (2.13) with $N/L = 0.003$) and numerical integration of the attenuated Rayleigh integrals (2.15) (red symbols). . . . 41

2.2 Map of the axial normalised intensity $\widetilde{I}_{ac,x}$ for $N/L = 0.003$ (value of Moudjed *et al.* (2014*a*)). Two values of the diffraction parameter S are displayed: (a) $S = 0.03$ (same value as Moudjed *et al.* (2014*a*)) and (b) $S = 0.2$. In both plot, the Fresnel distance $L_F = \frac{1}{4}\left(\frac{1.22}{S} - \frac{S}{1.22}\right)$ is shown in purple and delimits the near ($x \leq L_F$) from the far ($x \geq L_F$) acoustic fields. The green lines represent the approximate beam edge defined by equation (2.19)). Both plots share the same colour levels. 42

2.3 Map of the radial normalised intensity magnitude $|\widetilde{I}_{ac,r}|$ for $N/L = 0.003$ (value of Moudjed *et al.* (2014*a*)). Two values of the diffraction parameter S are displayed: (a) $S = 0.03$ (same value as Moudjed *et al.* (2014*a*)) and (b) $S = 0.2$. In both plot, the Fresnel distance $L_F = \frac{1}{4}\left(\frac{1.22}{S} - \frac{S}{1.22}\right)$ is shown in purple and delimits the near ($x \leq L_F$) from the far ($x \geq L_F$) acoustic fields. The green lines represent the approximate beam edge defined by equation (2.19)). Both plots share the same colour levels. 43

2.4 Sketch of the energy exchanges between the acoustic and streaming scales. The figure is adapted from Dupuy *et al.* (2018) and Chassaing *et al.* (2002). 46

3.1 Sketch of the computational domain. Being axisymmetric and free of any azimuthal velocity, the streaming flow is studied in the (x, r) plane, where x and r are the axial and radial coordinates, respectively. All indicated quantities are made dimensionless using D_s, $\rho_0 D_s^3$ and D_s^2/ν as length, mass and time scales, respectively (D_s: transducer diameter, ρ_0: fluid density and ν: kinematic viscosity). 50

3.2 (a) Lagrange interpolating polynomials of degree $N_p = 5$ (equation (3.7)). These polynomials are defined on the $(N_p + 1)$ Gauss-Lobatto-Legendre (GLL) points (coloured dots). (b) Sketch of the procedure generating a mesh refined at both ends of the $[0, L]$ interval: evenly-distributed points in $[0, 1]$ are mapped to $[0, 1]$ with the transform (3.8). 53

3.3 Discretisation of the fluid domain with 880 quadrilateral elements. The main lobe of the acoustic beam is represented by the green-shaded area; the corresponding approximate beam radius R_{beam} is given by equation (2.19). The red dots at $(x, r) = (400, 15)$, $(1000, 70)$ and $(1400, 20)$ locate the points where the time series of $\boldsymbol{u}$ and p are recorded to monitor the convergence towards a steady state. 55

Thèse accessible à l'adresse : https://theses.insa-lyon.fr/publication/2024ISAL0101/these.pdf © [B. Vincent], [2024], INSA Lyon, tous droits réservés

3.4 On-axis profile of the normalised axial intensity $\widetilde{I}_{ac,x}$: analytical profile (equation (2.17), black) and numerical integration of the attenuated Rayleigh integral (2.15) at the grid points (red). The grid is made of $N_{e,x} = 44$ elements in the x-direction, with a stretching factor $\gamma_x = 1.35$ (equation (3.9)) and $N_p = 8$. The magenta vertical line locates the Fresnel distance L_F. 56

3.5 Effect of the radial mesh density on the on-axis velocity $u_x(x, r = 0)$ at different positions: (a) $x = 10$, (b) $x = 100$, (c) $x = 500$ and (d) $x = 1000$. The degree N_p of the polynomial expansion basis is also varied. The displayed data is obtained using either $N_{e,r} = 20$ elements in the r-direction (blue curves) or $N_{e,r} = 23$ (red curve). In both cases, the elements sizes increase by a factor 1.3 in the r-direction (i.e., equation (3.10) with $\gamma_r = 1.3$), yielding either 1 or 2 elements in the transducer radius ($0 \leq r \leq 0.5$). The remaining mesh parameters are $N_{e,x} = 44$ and $\gamma_x = 1.35$. 57

3.6 Evolution of the numerically-evaluated momentum flux M_f with the distance x from the transducer. The displayed quantities are obtained for $Gr_{ac} = 10^3$, with either an attenuated $\widetilde{\boldsymbol{I}}_{\boldsymbol{ac}}$ ($N/L = 0.003$, filled symbols) or unattenuated $\widetilde{\boldsymbol{I}}_{\boldsymbol{ac}}$ ($N/L = 0$, empty symbols). The numerical profiles are compared to the theoretical prediction (3.11) for $N/L = 0.003$ (blue solid line) and $N/L \to 0$ (blue dashed line). The horizontal black dashed line indicates the maximum theoretical momentum flux $M = \pi L Gr_{ac}/(32N)$. A detailed view of the momentum profiles near $x = 0$ is shown in the inset. 58

3.7 Effects of acoustic force attenuation on steady flows for $Gr_{ac} = 10^3$ when the attenuation is accounted for ($N/L = 0.003$, see table 3.1, solid) or neglected ($N/L = 0$, dashed line) in $\widetilde{\boldsymbol{I}}_{\boldsymbol{ac}}$ (equation (2.15)). (a) Longitudinal profiles of the on-axis velocity $u_x(x, r = 0)$, with a detailed view close to the transducer shown in the inset. (b) Longitudinal profiles of the jet radius R_{jet} defined as $u_x(x, R_{jet}) = 0.5\, u_x(x, 0)$. The approximate beam radius (equation (2.19)) is shown as a black dotted curve. The magenta vertical line locates the Fresnel distance L_F, and the red vertical line positions the attenuation distance L_α. The blue vertical line indicates the position x_p of the on-axis velocity peak in the attenuated $\widetilde{\boldsymbol{I}}_{\boldsymbol{ac}}$ case. 59

3.8 Typical steady velocity field obtained for $Gr_{ac} = 5 \times 10^3$. Top: velocity magnitude $\|\boldsymbol{u}\|$ together with streamlines. The approximate beam radius R_{beam} (equation (2.19)) is shown in blue, and the inset on the right focuses on the flow region close to the transducer. Bottom: longitudinal profile of u_x on the jet axis on which the Fresnel distance $L_F \approx 1.22/(4\,S)$, the on-axis velocity peak position x_p and the acoustic force attenuation distance $L_\alpha = L/N$ are reported. The right plot focuses on the region framed in black in the left plot. 60

Thèse accessible à l'adresse : https://theses.insa-lyon.fr/publication/2024ISAL0101/these.pdf © [B. Vincent], [2024], INSA Lyon, tous droits réservés

3.9 Longitudinal profiles of the on-axis jet velocity u_x normalised by different scaling laws. The profiles are plotted from the source ($x = 0$) up to the velocity peak position x_p (black points) for different Gr_{ac}. (a) On-axis velocity normalised by the scaling law (1.61), originally derived by Moudjed *et al.* (2014*a*) by balancing the inertial and acoustic forces, and by discarding the viscous forces. (b) On-axis velocity normalised by the scaling law (3.16) incorporating the viscous forces. A perfect scaling law would collapse all the profiles on a single horizontal master curve centred around the horizontal black line. 61

3.10 Momentum balance on a control volume V_c encompassing the jet, as defined by equation (3.13). (a) Map of the velocity magnitude $\|\boldsymbol{u}\|$ for $Gr_{ac} = 1 \times 10^3$; V_c is delimited by the black solid lines. The length and radius of V_c are denoted by L_{CV} and R_{jet}, respectively, and R_{jet} is defined such that $u_x(x, R_{jet}) = 0.5u_x(x, 0)$. (b) Magnitude of the forces acting along $\boldsymbol{e_x}$ and integrated on V_c (see equation (3.13)) defined in (a) for $Gr_{ac} = 1 \times 10^3$ (smallest forcing). (c) Same as (b), but for $Gr_{ac} = 5 \times 10^4$ (largest forcing). In (b) and (c), the insets show the forces along $\boldsymbol{e_x}$ for $0 \leq L_{CV} \leq L$, without taking their absolute values. The red and blue vertical lines locate the attenuation distance $L_\alpha = L/N$ and the on-axis velocity peak x_p, respectively. All computed forces are normalised by $M = \pi L Gr_{ac}/(32N)$. . 63

3.11 Comparison between the scaling laws and data taken from the literature (Kamakura *et al.*, 1996; Mitome, 1998; Frenkel *et al.*, 2001; Moudjed *et al.*, 2014*a*). (a) Comparison with the inertial scaling law (1.61) of Moudjed *et al.* (2014*a*), in which the viscous forces are discarded. (b) Comparison with the scaling law (3.16) derived in this thesis and accounting for the viscous forces. The dimensionless numbers for the literature data are listed in table A.2. Except for Kamakura *et al.* (1996), all the data points are from experiments. 64

3.12 Evolution of the on-axis velocity peak position x_p and amplitude $u_{x,p}$ with Gr_{ac}. (a) Comparison between the peak positions observed in the numerical simulations (black filled symbols), and the predictions when neglecting ($x_{p,i}$, blue line, equation (3.20a)) and considering ($x_{p,v}$, red line, equation (3.21)) viscous forces in the region upstream x_p. The quantity represented on the x-axis is chosen to assess the validity of equation (3.20a). (b) Comparison between the peak amplitudes observed in the numerical simulations (black filled symbols), the experiments from Dentry *et al.* (2014) (empty symbols) and the theoretical predictions (solid lines) when viscous forces upstream x_p are neglected (U_{x,p_i}, blue, equation (3.20b)) and taken into account (U_{x,p_v}, red, equations (3.21) and (3.19)). The quantity plotted on the x-axis is chosen to assess the validity of equation (3.20b). In (b), the data of Dentry *et al.* (2014) are for an Eckart streaming jet driven by the transmission of Surface Acoustic Waves from a rectangular substrate to the bulk of the fluid. The equivalent acoustic source is rectangular, with a height H_s varying with the frequency. The parameters Gr_{ac} and S are thus based on H_s for the experimental points (instead of D_s for the numerical simulations). 65

Thèse accessible à l'adresse : https://theses.insa-lyon.fr/publication/2024ISAL0101/these.pdf © [B. Vincent], [2024], INSA Lyon, tous droits réservés

3.13 Evolution along x of the jet radius R_{jet}, defined as $u_x(x, R_{jet}) = 0.5u_x(x, 0)$. The simulations for all Gr_{ac} are displayed. On each curve, the velocity peak position x_p is located by a filled symbol. The vertical red and purple line locate the attenuation distance $L_\alpha = L/N$ and the Fresnel distance $L_F \approx 1.22/(4S)$, respectively. 66

3.14 On-axis velocity profiles downstream the velocity peak x_p, obtained for different Gr_{ac}. The quantity plotted on the x-axis includes the longitudinal variations of the acoustic force caused by both diffraction and attenuation of the beam (right-hand side of equation (3.23)). The order of magnitude $U_{x,d}$ of the on-axis velocity downstream x_p (equation (3.23)), is shown in black. The coloured solid lines correspond to the numerical data. The dashed lines represent the self-similar jet solution $U_{x,S}$ of Schlichting & Gersten (2000) given by equation (3.25) and based on the maximum axial momentum flux $\pi LGr_{ac}/(32N)$ to be acquired by the jet. The red vertical line locates the attenuation length $L_\alpha = L/N$. 67

3.15 Longitudinal profile of the on-axis axial velocity u_x computed for $Gr_{ac} = 5 \times 10^3$ (solid black line), together with the scaling laws (dashed lines) and the force balance in each jet region. The scaling law in the yellow region is taken from Moudjed *et al.* (2015) (see section 1.5.2.2). The predicted peak position x_{p_v} (equation (3.21)) and amplitude U_{x,p_v} (from equation (3.19) with x_{p_v}) are represented by the dash-dotted blue vertical line and the black star, respectively. The solid blue and red vertical lines locate the actual on-axis velocity peak x_p and the attenuation distance $L_\alpha = L/N$, respectively. 69

4.1 Illustration of critical point theory. (a) Critical point classification for a 2D vector field $\boldsymbol{v}$, based on the eigenvalues $\lambda_{1,2}$ of $\boldsymbol{\nabla v}$ at the critical point. (b) Half saddle and half node appearing at the boundaries of a fluid domain, and caused by zero skin friction at the wall. 75

4.2 Velocity magnitude $\|\boldsymbol{U}\|$ maps of the steady axisymmetric base flows for (a) case 2 and (b) case 3 for $Gr_{ac} = 6400$. The streamlines are displayed along with the critical points: S_i' are half-saddles (zero friction, red squares), N_i are nodes ($\boldsymbol{U} = \boldsymbol{0}$, purple discs) and S_i are saddles ($\boldsymbol{U} = \boldsymbol{0}$, purple squares). The green line represents the approximate beam radius R_{beam} (2.19). Both figures share the same colour levels. 80

4.3 Effect of flow confinement on the jet velocity for $N = 0.25$ and $Gr_{ac} = 6400$. The profiles were obtained for $1 \leq K_R \leq 6$, corresponding to cases 2 to 6 (table 4.1). Background plot: profiles of the on-axis velocity $U_x(x, r = 0)$ along the jet. The dashed vertical represents the Fresnel distance L_F locating the transition between the near ($x < L_F$) and the far ($x > L_F$) acoustic fields. Inset: effect of K_R on the streamwise pressure gradient $\langle dP/dx \rangle_{r,\theta}$ of the base flow taken at the mid cavity length $L/2$ and averaged over the cross-sectional area. 81

Thèse accessible à l'adresse : https://theses.insa-lyon.fr/publication/2024ISAL0101/these.pdf © [B. Vincent], [2024], INSA Lyon, tous droits réservés

4.4 Growth rate σ of the leading eigenmode as a function of the azimuthal wavenumber m for cases 1 to 4. Oscillatory and non-oscillatory modes are represented by filled circles and triangles, respectively. The insets show the evolution of σ with Gr_{ac} for the indicated value of m. The critical Grashof number Gr_{ac}^c, obtained through spline interpolation of σ, is reported in red. The filled black symbols in the inset of (b) are additional eigenvalue computations made to improve the interpolation accuracy near $\sigma = 0$. . . . 82

4.5 Leading mode for case 3 for $Gr_{ac} = 6400$. The mode is non-oscillatory ($\omega = 0$) and unstable ($\sigma = 1.59\times10^{-2} > 0$). (a) Axial velocity perturbation u'_x in the (x, r) plane, along with the streamlines and critical points of the base velocity $\boldsymbol{U}$. (b): velocity perturbation $\boldsymbol{u'}$, with the background color corresponding to its azimuthal component u'_θ. (c) to (h): Slices of $\boldsymbol{u'}$ in constant-x planes located by the blue vertical lines in (a) and (b), with either u'_x or the streamwise vorticity perturbation ω'_x as background colour (negative in blue, positive in red). The purple circles locate the points where $U_x = 0$. In all figures, the green solid line represents the approximate beam radius (2.19), and the blue solid line locates the radius where U_x is 50 % of its on-axis value. All the figures on a given row share the same colour levels. 83

4.6 Lines of the skin friction perturbation stresses on the downstream wall, with the background color corresponding to the azimuthal component of the stress vector (positive in red, negative in blue). These lines are shown along with the critical points (blue symbols) at supercritical Gr_{ac} for (a) case 2, (b) case 3 and (c) case 4. The approximate beam radius (equation (2.19)) is represented by the green circle. The base flow half saddle S'_7 on the downstream wall is located by the solid red circle. The solid blue circle approximates the separation line going through the saddles found at a same distance from the origin. 84

4.7 Growth rate σ of the leading eigenmode as a function of the azimuthal wavenumber m for (a) case 5 and (b) case 6. Oscillatory and non-oscillatory modes are represented by filled circles and triangles, respectively. The insets show the evolution of σ with Gr_{ac} for the indicated value of m. The critical Grashof number Gr_{ac}^c, obtained through spline interpolation of σ, is reported in red. The filled black symbols in the inset of (b) are additional eigenvalue computations made to improve the interpolation accuracy near $\sigma = 0$. 86

4.8 Caption on next page. 87

Thèse accessible à l'adresse : https://theses.insa-lyon.fr/publication/2024ISAL0101/these.pdf © [B. Vincent], [2024], INSA Lyon, tous droits réservés

4.8 Leading mode of case 5 for $Gr_{ac} = 10600$. The mode is oscillatory ($\omega \neq 0$) and unstable ($\sigma = 2.54 \times 10^{-2} > 0$). (a) Azimuthal velocity perturbation u'_θ in the (x, r) plane, along with the critical points of the base velocity $\boldsymbol{U}$. (b) Detailed view near the impingement (region framed in red in (a)) of the axial velocity perturbation u'_x together with the base flow streamlines. (c) Details $\boldsymbol{u'}$ near the impingement, with u'_θ taken as background colour. (d) to (g): Slices of $\boldsymbol{u'}$ in constant-x planes located by the blue vertical lines in (a)-(c), with either u'_x or the streamwise vorticity perturbation ω'_x as background colour (negative in blue, positive in red). The purple circles locate the points where $U_x = 0$. In all figures, the green solid line represents the approximate beam radius (2.19), and the blue solid line locates the radius where U_x is 50 % of its on-axis value. All the figures on a given row share the same colour levels. 88

4.9 Lines of skin friction perturbation stresses on the downstream wall for (a) case 5 and (b) case 6. In each plot, the background colour represents the azimuthal component of the stress vector (positive in red, negative in blue). The lines are shown along with the critical points (blue symbols) and the approximate beam size (green circle, as defined by equation (2.19)). The base flow half saddle S'_7 is also reported in red. 89

4.10 Caption on next page. 90

4.10 Leading mode of case 6 for $Gr_{ac} = 15500$. The mode is oscillatory ($\omega \neq 0$) and unstable ($\sigma = 1.701 \times 10^{-1} > 0$). (a) Azimuthal velocity perturbation u'_θ in the (x, r) plane, along with the critical points of the base velocity $\boldsymbol{U}$. (b) Detailed view near the impingement (region framed in red in (a)) of the axial velocity perturbation u'_x together with the base flow streamlines. (c) Details $\boldsymbol{u'}$ near the impingement, with u'_θ taken as background colour. (d) to (g): Slices of $\boldsymbol{u'}$ in constant-x planes located by the blue vertical lines in (a)-(c), with either u'_x or the streamwise vorticity perturbation ω'_x as background colour (negative in blue, positive in red). The purple circles locate the points where $U_x = 0$. In all figures, the green solid line represents the approximate beam radius (2.19), and the blue solid line locates the radius where U_x is 50 % of its on-axis value. All the figures on a given row share the same colour levels. 91

4.11 Comparison between the leading velocity perturbation $\boldsymbol{u'}$ obtained with LSA (left) and the perturbation obtained with DNS (right). The displayed data corresponds to case 5 at supercritical Gr_{ac} and is plotted at the base flow saddle S_1 ($x = 77.52$, slice 2 in figure 4.8). The indicated σ and ω are those of LSA. The DNS results are extracted from the early exponential growth of the perturbation. Features of the steady base velocity $\boldsymbol{U}$ are reported in both plots: the points where the sign of the streamwise velocity U_x changes (purple circles), and the points where U_x is equal to 50 % of its on-axis value (blue circle). The green circle represents the approximate edge of the beam defined by equation (2.19). 92

Thèse accessible à l'adresse : https://theses.insa-lyon.fr/publication/2024ISAL0101/these.pdf © [B. Vincent], [2024], INSA Lyon, tous droits réservés

4.12 Comparison between the leading velocity perturbation $\boldsymbol{u'}$ obtained with LSA (left) and the perturbation obtained with DNS (right). The displayed data corresponds to case 5 at supercritical Gr_{ac} and is plotted at the base flow saddle S_1 ($x = 80.15$, slice 2 in figure 4.10). The indicated σ and ω are those of LSA. The DNS results are extracted from the early exponential growth of the perturbation. Features of the steady base velocity $\boldsymbol{U}$ are reported in both plots: points where the sign of the streamwise velocity U_x changes (purple circles), and points where U_x is equal to 50 % of its on-axis value (blue circle). 93

4.13 Sketch of a continuous 2D vector field $\boldsymbol{v}$ (red) a p-branch star saddle critical point S_* (blue, here shown for $p = 6$). A circular contour $\mathcal{C}$ (dashed green line) encloses S_*, and φ is the local angle between $\boldsymbol{v}$ and a vector $\boldsymbol{dl}$ tangent to $\mathcal{C}$. 93

4.14 Process for adapting the topological rule (4.13) to star saddles. Mapping the initial TIS (disc, right) to an annular TIS of inner radius R_{int} (left) splits the $2m$-branch star saddle into $2m$ half saddles, without affecting the other critical points. The process is illustrated for case 4, with the friction lines exerted by the leading mode on the downstream wall. The colour represents the azimuthal friction component (positive in red, negative in blue). The χ defining each TIS is also reported. 94

4.15 Caption on next page 96

4.15 Stuart-Landau analyses for all the cases listed in table 4.1. The corresponding Gr_{ac} and r_c (equation (4.26)) are given in table 4.4. Left: growth and saturation of a white-noise-triggered perturbation injected at $t = 0$. The perturbation evolution is monitored by the time series of the azimuthal velocity perturbation u'_θ. Right: evolution of $\mathrm{d}\left(\log|A|\right)/\mathrm{d}t$ as a function of $|A|^2$, with $|A| = |u'_\theta|$ (for cases 5 and 6, the envelope of u'_θ is considered). The dashed black line is obtained by fitting equation (4.23a) to the red curve over the red-shaded range (the corresponding time interval in highlighted in red in the left plots). For all cases, the uncertainty on σ is less than 0.01 % and is thus not reported. 97

4.16 Summary of the instability onsets Gr^c_{ac} for the different cases listed in table 4.1. The stable (green) and unstable (red) regions are represented for $N = 0.25$ (cases 2 to 6). The vertical dashed lines represent the change of bifurcation type; their K_R locations are arbitrarily placed in between the investigated K_R. 98

4.17 Frequencies obtained from the DNS time-series of the azimuthal velocity perturbation $u'_\theta(t)$ for (a) cases 5 and (b) 6. The corresponding time-series are those displayed in figure 4.15 (i) and (j), respectively. The frequencies are computed from FFTs made in the linear regime (ω, blue) and in the saturated regime (ω_{sat}, red). 99

4.18 Time-series of the azimuthal velocity perturbation u'_θ for case 5 and $Gr_{ac} = 10600$ ($r_c = 0.0083$). The time series is recorded at $(x, r, \theta) = (81, 1.3, 0)$. . 100

Thèse accessible à l'adresse : https://theses.insa-lyon.fr/publication/2024ISAL0101/these.pdf © [B. Vincent], [2024], INSA Lyon, tous droits réservés

4.19 Stuart-Landau analysis for case 4, for $Gr_{ac} = 8000$ ($r_c = 0.0320$). (a) Temporal evolution of the azimuthal velocity perturbation u'_θ obtained from DNS and recorded at $(x, r, \theta) = (80, 2, 0)$. The perturbation originates from white noise injected at $t = 0$. (b) Evolution of $\mathrm{d}\left(\log|A|\right)/\mathrm{d}t$ with $|A|^2$ (red curve), where $|A| = |u'_\theta|$ and is extracted from (a). The black dashed line is obtained by fitting the Stuart-Landau equation (4.23a) to the red curve over the range highlighted in red. The positive slope indicates a subcritical transition. 101

5.1 Sketch of the configuration studied experimentally. The flow is driven by a sound beam undergoing multiple reflections (represented as green crosses) on the walls of a water-filled cavity. The beam is obtained from the attenuated Rayleigh integral, and reflections are treated with the method of images (Kinsler *et al.*, 2000). The beam entry point is located by the purple star, and the purple arrows indicate the wave propagation (hence, the forcing) direction. The sound waves are completely attenuated at the bottom wall (deep grey). 104

5.2 Sketch of the test rig used to measure the acoustic field radiated by the transducer. Distances are given in mm. 105

5.3 Picture (a) and sketch (b) of the plane circular acoustic transducer used to create a sound field. 105

5.4 Pictures of the devices used to position the transducer. (a) Mechanical system to carry and position the transducer. (b) Detailed view of the laser guiding device, as initially designed by El Ghani (2020). The discontinuous line represents the laser beam emitted by the diode. The mounting arm shown in (a) features a key, yielding a slip joint between the mounting arm and the laser guiding device. 106

5.5 Signal chain used to generate and record ultrasounds. (a) Picture of the electronic setup. (b) Sketch detailing how the different electronic components are connected to each other. 108

5.6 Comparison between the experimental $\widetilde{I}_{ac,exp}$ and numerical $\widetilde{I}_{ac,num}$ acoustic intensity fields. The numerical field is obtained by computing the Rayleigh integral (2.7) with $D_s = 30$ mm and with the water properties listed in table 1.1. Top: 2D map of $\widetilde{I}_{ac,exp}$ measured in a constant-y plane containing the acoustic axis (white mixed line). The vertical green lines indicate where the transverse profiles of figure 5.7 are made. Bottom: comparison between the numerical (black) and experimental (blue) profiles of the normalised intensities on the acoustic axis, with the associated relative difference. The blue-shaded area represents the uncertainty of the hydrophone measurements (26 %). In all plots, the origin is taken at the centre of the transducer vibrating membrane, and the x and z coordinates are normalised by the Fresnel length $L_F = D_s^2/(4\lambda)$ and by D_s, respectively. The intensities are normalised by their on-axis values at $x = L_F$. 109

Thèse accessible à l'adresse : https://theses.insa-lyon.fr/publication/2024ISAL0101/these.pdf © [B. Vincent], [2024], INSA Lyon, tous droits réservés

5.7 Comparison between the numerical (black) and experimental (blue) transverse profiles of the normalised acoustic intensity $\widetilde{I}_{ac}$ at different distances x from the transducer (see the green lines in the upper plot of figure 5.6): (a) $x = 0.75L_F$, (b) $x = L_F$ and (c) $x = 1.25L_F$, where L_F is the Fresnel distance. The numerical profiles are obtained by computing the Rayleigh integral (2.7) for $D_s = 30$ mm and with the water properties listed in table 1.1. In all plots, the blue-shaded area represents the uncertainty of the intensity measured with the hydrophone (26 %). The relative difference between the black and blue profiles is also reported. The z-coordinates are normalised by D_s, and the intensity profiles are normalised by their on-axis values at $x = L_F$. 110

5.8 Sketch of a *Shake-The-Box* iteration at the time step t_{i+1} (figure taken and adapted from Schröder & Schanz (2023)). The algorithm can be divided into five major steps: (i) new particle positions are predicted by extrapolating the previous tracks, (ii) each particle is then 'shaken" about its predicted position to match a nearby particle in the t_{i+1} frame. If no match is found, the particle is "lost" (e.g., it left the measurement volume) and its track is interrupted. After that, (iii) residual images are computed by subtracting the particles obtained at step (ii) from the t_{i+1} frame, thus (iv) allowing for the detection of new particles. Finally, new tracks are created for these particles and are added to the tracks obtained at the previous time steps. 112

5.9 Light sources used for the PTV measurements: (a) *LaVision GmbH* Flashlight 300 LED panel and (b) a Nd:YAG laser source (*Litron Lasers Ltd* Bernoulli PIV 200-15) emitting a 532 nm beam expanded into a volume by the *LaVision GmbH* Compact Volume Optics fitted with a cylindrical lens (see the inset). The beam is carried to the volume expander through a jointed arm (the green lines and arrows indicate the path followed by the laser beam from the source to the volume expander). Dimensions are given in mm. 114

5.10 Pictures of (a) the *LaVision GmbH MiniShaker* device featuring four cameras (*Basler* acA1920-150um) tracking the seeding particles, and (b) the volumetric plate used to calibrate the *MiniShaker*. Dimensions are given in mm. 115

5.11 Sketch of the test rig used to reproduce the square water streaming flow of Cambonie *et al.* (2017) and Launay *et al.* (2019): (a) side and (b) top views. The green line and arrows represent the axis of the beam emitted by the transducer (grey rectangle) and its direction of travel, respectively. Reflection points of the beam in the VOI are located by the green crosses and are labelled from A to C. The origin of the coordinate system is placed at the centre of the VOI. 116

5.12 Caption on next page 118

Thèse accessible à l'adresse : https://theses.insa-lyon.fr/publication/2024ISAL0101/these.pdf © [B. Vincent], [2024], INSA Lyon, tous droits réservés

5.12 Processing of the frames recorded for the square flow. The first frame of the recording in taken as illustrative example: (a) raw frame, (b) processed frame and (c) parameters of the "Image preprocessing" module of the *LaVision* DaVis 10 software used to generate (b) from (a). The blue square in (a) represents the size of the window over which light intensity is normalised ("normalize with local average" section in (c)). The size of the sliding window (used in the "subtract sliding minimum" section in (c)) is represented by the magnified red squares in (a) and (b). All dimensions are given in pixels. 119

5.13 Snapshot of particles detected by *Shake-The-Box* and their associated tracks for the $Gr_{ac} \approx 1.6 \times 10^4$ ($P_{elec} = 1$ W) square flow: (a) isometric and (b) top views. For clarity, only the tracks in $-0.17 \leq y \leq 0.17$ are displayed. The tracks are coloured by the instantaneous particle velocity magnitude $\|\dot{\boldsymbol{x}}\|$ made dimensionless using $D_s = 30$ mm and $D_s^2/\nu = 916.8$ s as length and time scales, respectively. In both plots, the spatial coordinates are normalised by the cavity sizes in the corresponding direction (183 mm for x and z, and 180 mm for y). The purple star and arrow locate the entry point of the beam and indicate its orientation, respectively. . . . 120

5.14 Comparison of the time-averaged square acoustic streaming flow measured for $Gr_{ac} \approx 1.6 \times 10^4$ ($P_{elec} = 1$ W), along with the jet numbering. The represented flow quantity is a Reynolds number $Re = \|\overline{\boldsymbol{u}}\| D_s/\nu$. Left: reference Eulerian velocity field obtained by PIV (grid resolution: 0.023, or 0.69 mm in dimensional units), as measured by Cambonie *et al.* (2017). The region framed in black illustrates the jet axis location procedure described in the text, and from which the jet origin $x' = 0$ (black cross) is inferred. Right: Eulerian velocity field reconstructed from PTV measurements (grid resolution: 0.031, or 0.94 mm in dimensional units). In both plots, the purple star and arrow locate the entry point of the beam in the VOI and its orientation, respectively. The same colour levels are used in both plots, and the spatial coordinates are normalised by the VOI size in the corresponding directions (183 mm). 121

5.15 Three-dimensional structure of the Eulerian square acoustic streaming flow reconstructed from PTV measurements made for $Gr_{ac} \approx 1.6 \times 10^4$ ($P_{elec} = 1$ W). The displayed quantity is an isocontour of the Reynolds number Re based on the velocity magnitude and on D_s; it is here plotted for $Re = 73.3$ (2.4 mm/s in dimensional units). The velocity field in the mid-height $y = 0$ plane is also shown. The purple star and arrow locate the entry point of the beam in the VOI and its orientation, respectively. The spatial coordinates are normalised by the VOI size in the corresponding directions (183 mm in the horizontal directions, and 160 mm in the vertical one). 121

5.16 Longitudinal profiles of the Reynolds number $Re = \|\overline{\boldsymbol{u}}\| D_s/\nu$ along the axis of each jet, for $Gr_{ac} \approx 1.6 \times 10^4$ ($P_{elec} = 1$ W). The PIV profiles of Cambonie *et al.* (2017) and those obtained from the binning of PTV measurements are displayed. These profiles are normalised by the straight jet scaling law (5.3) originally derived in chapter 3. A perfectly-matching scaling law would collapse the experimental profiles on the black dashed line. Here, x' is made dimensionless by D_s. 123

Thèse accessible à l'adresse : https://theses.insa-lyon.fr/publication/2024ISAL0101/these.pdf © [B. Vincent], [2024], INSA Lyon, tous droits réservés

5.17 Sketch of test rig used to generate and investigate three-dimensional acoustic streaming flows. The green line and arrows represent the axis of the acoustic beam radiated by the transducer (grey rectangle with its mounting arm in black) and its direction of travel. Reflection points of the beam on the vertical walls of the VOI (Volume Of Investigation) are identified by green crosses and labelled from A to E. The origin of the coordinate system is located at the centre of the VOI. The green-shaded area represents the expanded laser beam defining the measurement domain for the time-resolved measurements (section 5.7). The figure is taken from Vincent *et al.* (2024). 124

5.18 Effect of the number of frames used to evaluate local time-averaged velocity magnitudes $Re = \|\overline{\boldsymbol{u}}\| D_s/\nu$ (left panel) and their associated root mean square Re_{RMS} (right panel) for all forcing magnitudes Gr_{ac}. The coloured horizontal bands are defined for each Gr_{ac} and correspond to a ± 2 % confidence interval around the estimate obtained using the entire (100 %) recording duration. The x, y and z coordinates where the velocities are measured are reported directly in the plots, and are normalised by the cavity sizes in the corresponding directions (183 mm for x and z, and 160 mm for y). 128

5.19 Isocontours of the Reynolds number $Re = \|\overline{\boldsymbol{u}}\| D_s/\nu$ coloured by $Re_v = \overline{u_y} D_s/\nu$, with $\overline{u_y}$ the time-averaged vertical velocity. Different Gr_{ac} are displayed, together with the corresponding jet numbering. The isocontours are plotted for (a) $Re = 87.11$ ($\|\boldsymbol{u}\| = 2.5$ mm/s), (b) 111.51 (3.2 mm/s), (c) 163.77 (4.7 mm/s) and (d) 216.04 (6.2 mm/s). The entry point of the sound beam in the VOI is located by the purple star at $(x, y, z) = (0.5, 0.13, 0)$. The spatial coordinates are normalised by the size of the VOI in the corresponding direction (183 mm in the x and z directions, and 160 mm in the y direction). 129

5.20 Time-averaged flow structure for $Gr_{ac} = 15.12 \times 10^4$ ($P_{elec} = 8$ W). (a) Isocontour of the velocity magnitude ($Re = \|\overline{\boldsymbol{u}}\| D_s/\nu = 268.3$, with $\|\overline{\boldsymbol{u}}\| = 7.7$ mm/s), coloured by the Reynolds number Re_v based on the vertical velocity component. The entry point of the beam is located by the purple star at $(x, y, z) = (0.5, 0.13, 0)$. (b) (b) Velocity slice in the plane represented by the blue frame in (a): the map of the Reynolds number Re_n based on the normal velocity component illustrates the large-scale swirling motion sustained by the jets. The in-plane horizontal coordinate is defined as X. In both plots, the axes are normalised by the cavity dimensions in the corresponding directions. 130

5.21 Longitudinal profiles of $Re = \|\overline{\boldsymbol{u}}\| D_s/\nu$ along the axis of jets 1, 3 and 4, for all the forcing magnitudes Gr_{ac}. The profiles are normalised by the jet scaling law (5.3) originally derived in chapter 3. If perfect, the normalised profiles would collapse on the horizontal black dashed line. The distance x' from the estimated jet origin is normalised by D_s. 131

Thèse accessible à l'adresse : https://theses.insa-lyon.fr/publication/2024ISAL0101/these.pdf © [B. Vincent], [2024], INSA Lyon, tous droits réservés

5.22 Profiles of $Re = \|\overline{\boldsymbol{u}}\| D_s/\nu$ along the axes of jets 1, 3 and 4 for all Gr_{ac}. The origin of each jet is at $x' = 0$. The black profile is taken from chapter 3: it is obtained from the simulation of a single steady axisymmetric jet for $0 \leq x' \leq L$, $L = 1500.7$, $Gr_{ac} = 2 \times 10^4$, $S = 0.03$ and $N = 4.5$ (same values of S and N as in the experiment). In the numerical simulation, the transducer is placed at $x' = 0$. In the experiment, the transducer is at $x' = -8.8$, -17.5 and -21.9 for jets 1, 3 and 4, respectively. 132

5.23 Vortical structures of the time-averaged flows, represented as isocontours of the Q-criterion (Hunt *et al.*, 1988; Chakraborty *et al.*, 2005) measured for the three lowest Gr_{ac}. The isocontours are coloured by the normalised helicity $\widetilde{h}$ (equation (5.7)); the jet numbering is also displayed. The isocontours are plotted for (a) $Q = 1.80 \times 10^3$, (b) 3.18×10^3 and (c) 7.49×10^3. The entry point of the sound beam in the VOI is located by the purple star at $(x, y, z) = (0.5, 0.13, 0)$. The spatial coordinates are normalised by the size of the VOI in the corresponding direction (183 mm in the x- and z-directions, and 160 mm in the y-direction). All plots share the same colour levels. 133

5.24 Vortical structures of the time-averaged flows, illustrated by isocontours of the Q-criterion for the two largest Gr_{ac}. The isocontours are coloured by the normalised helicity $\widetilde{h}$ (equation (5.7)) and are plotted for (a) $Q = 11.89 \times 10^3$ and (b) 18.58×10^3. See the caption of figure 5.23 for further details. 134

5.25 Evolution with Gr_{ac} of the net helicity $\mathcal{H}$ (equation (5.8)), made dimensionless using D_s and D_s^2/ν as length as time scales, respectively. 135

5.26 Effect of the forcing magnitude Gr_{ac} on the overall fluid rotation about the vertical axis. (a) Radial profiles of the Reynolds number Re_θ based on D_s and on the time-averaged azimuthal velocity $\langle \overline{u_\theta} \rangle_{\theta,y}$ obtained for different Gr_{ac}: $Gr_{ac} = 1.78 \times 10^4$ ($P_{elec} = 1$ W) in blue, $Gr_{ac} = 3.64 \times 10^4$ (2 W) in orange, $Gr_{ac} = 7.50 \times 10^4$ (4 W) in yellow, $Gr_{ac} = 11.28 \times 10^4$ (6 W) in purple and $Gr_{ac} = 15.12 \times 10^4$ (8 W) in green. Each of these profiles is obtained from equation (5.9), and δ is the mean distance between the maximum velocity and the outer vertical walls. (b) Evolution of Re_h with Gr_{ac}, where Re_h is obtained from the ensemble average of Re_θ over the radial coordinates for each Gr_{ac}: experimental points (squares) and prediction (red curve and area). The prediction is obtained from equations (5.13) and (5.3) for $\beta = 0.5$, $\delta = 15$ mm, $L = 183$ mm and $x' = 2.2$ (i.e., the half-jet length). The envelope (red area) is plotted for the same parameter values but for $\beta = 0.6$ (lower bound) and $\beta = 0.4$ (upper bound). 136

Thèse accessible à l'adresse : https://theses.insa-lyon.fr/publication/2024ISAL0101/these.pdf © [B. Vincent], [2024], INSA Lyon, tous droits réservés

5.27 Vertical velocity component of the time-averaged flow shown in the horizontal $y = 0$ plane (left) and in the vertical $x = 0$ plane (right), together with the streamlines. The two lowest Gr_{ac} are displayed: (a) $Gr_{ac} = 1.78 \times 10^4$ ($P_{elec} = 1$ W) and (b) 3.64×10^4 (2 W). Similar plots at higher Gr_{ac} are given in figure 5.28). The i-th jet impingement is located by a red cross and is labelled as I_i. The entry point of the beam and its orientation are given by the purple star and arrow, respectively. The figures on a same row share the same colour levels, and the grey rectangles cover regions dominated by measurement noise. Finally, the spatial coordinates are normalised by the size of the VOI in the corresponding direction (183 mm in the x and z directions, and 160 mm in the y direction). 138
5.28 Vertical velocity component of the time-averaged flow shown in the horizontal $y = 0$ plane (left) and in the vertical $x = 0$ plane (right), together with the streamlines. The three largest Gr_{ac} are displayed: (a) $Gr_{ac} = 7.50 \times 10^4$ ($P_{elec} = 4$ W), (b) 11.28×10^4 (6 W) and (c) 15.12×10^4 (8 W). See the caption of figure 5.27 for further details. 139
5.29 (a) Profiles along the cavity height of the ratio between the downward and horizontal flow rates Q_{down} and Q_{horiz}, with Q_{horiz} obtained from $Q_{\text{horiz}} = \langle \overline{u_\theta} \rangle_{r,\theta,y} HL/2$. The profiles are given for different forcing magnitudes Gr_{ac}. The x-axis is reversed, as $Q_{\text{down}} < 0$. (b) Vertical profiles of the dimensionless cross-sectional area A_{down} of downward-flowing fluid. In both plots, the height at which the i-th jet impinges a wall is located by dots labelled as I_i. In both plots, the y coordinates are normalised by the VOI height (160 mm). 140
5.30 (a) Profiles along the VOI height of the rate of fluid Q_{chimney} flowing through the chimney, normalized by the horizontal flow rate $Q_{\text{horiz}} = \langle \overline{u_\theta} \rangle_{r,\theta,y} HL/2$. (b) Vertical profile of the dimensionless chimney radius $R_{\text{chimney}} \approx \frac{\sqrt{A_{\text{chimney}}/\pi}}{L}$. In each plot, the height at which the i-th jet impingement occurs is located by a dot labelled as I_i. The y-coordinates are normalised by the VOI height (160 mm). 141
5.31 (a) Profiles along the cavity height of the ratio between the upward and horizontal flow rates Q_{up} and Q_{horiz}, with Q_{horiz} obtained from $Q_{\text{horiz}} = \langle \overline{u_\theta} \rangle_{r,\theta,y} HL$. The profiles are here displayed for different forcing magnitudes Gr_{ac}. (b) Vertical profiles of the dimensionless cross-sectional area $A_{\text{up}} = L^2 - A_{\text{down}} - A_{\text{chimney}}$ of upward-flowing fluid. In both plots, the height at which the i-th jet impinges a wall is located by a dot labelled as I_i. The y-coordinates are normalised by the VOI height (160 mm). 142
5.32 Evolution of the Reynolds numbers Re based on D_s and related to the different motions observed in the time-averaged helical acoustic streaming flow, as a function of the forcing magnitude Gr_{ac}. For jets 1, 3, and 4, Re is evaluated at $x' = L_{\text{jet}}/(2D_s)$, where L_{jet} refers to the distance between two consecutive acoustic reflection points. The upper and lower bounds correspond to Re evaluated at $L_{\text{jet}}/(4D_s)$ and $x' = 3L_{\text{jet}}/(4D_s)$, respectively. The blue envelope is obtained from equation (5.3) with $x' = 2.2$ (i.e., the half-jet length). The red curve is given by equation (5.13) for $H = 160$ mm, $L = 183$ mm, $\delta = 15$ mm and $x' = 2.2$. The values of Re associated with the vertical motions are obtained from the ensemble average of the corresponding velocities over the cavity height. 143

Thèse accessible à l'adresse : https://theses.insa-lyon.fr/publication/2024ISAL0101/these.pdf © [B. Vincent], [2024], INSA Lyon, tous droits réservés

5.33 Time-averaged flow structure near the first jet impingement I_1 and for $Gr_{ac} = 13.80 \times 10^4$ ($P_{elec} = 8$ W): isometric (left) and top (right) views. Slices of the Reynolds number Re_v based on the vertical velocity and on D_s are shown together with the streamlines in the $x = -0.035$ (blue rectangle), $y = 0.115$ (red rectangle) and $z = 0.470$ (black rectangle) planes. Focii detected in constant-x (blue), y (red) and z (black) planes are also displayed. The green square locates the point where the local time series of $\boldsymbol{u}$ are studied (see figure 5.36). Both figures share the same colour levels, and the spatial coordinates are normalised by the VOI size in the corresponding direction (183 mm for x and z, and 160 mm for y). 144

5.34 Caption on next page 145

5.34 Time-averaged flow structure near the first jet impingement I_1, together with slices of the Reynolds number Re_v (based on the vertical velocity component and on D_s) and the in-plane streamlines. Isometric (left) and top (right) views are shown for $1.65 \times 10^4 \leq Gr_{ac} \leq 10.29 \times 10^4$ (see figure 5.33 for the largest Gr_{ac}). A positive Re_v refers to an upward fluid flow. Focii in constant-x, y and z planes are represented by blue, red and black spheres, respectively. The green square at $(x, y, z) = (-0.233, 0.053, 0.470)$ locates the point where the local dynamics are studied (see figure 5.36). All figures share the same color levels. 146

5.35 Temporal evolution of the kinetic energy associated with the velocity perturbations (equation (5.15)) for all forcing magnitudes Gr_{ac}. The displayed quantities are made dimensionless using D_s and D_s^2/ν as length and time scales, respectively. 147

5.36 Local measures of the flow unsteadiness for the two extreme forcing magnitudes: $Gr_{ac} = 1.65 \times 10^4$ ($P_{elec} = 1$ W, left) and $Gr_{ac} = 13.80 \times 10^4$ ($P_{elec} = 8$ W, right). Top row: time series of the angle θ between the instantaneous and time-averaged velocity vector (equation (5.16)) at $(x, y, z) = (-0.233, 0.053, 0.470)$. In both plots, θ is normalised by its RMS value calculated over the recording duration (20 minutes) and t is normalised by D_s^2/ν (only half of the time series is shown for $Gr_{ac} = 13.80 \times 10^4$). Centre and bottom rows: instantaneous streamlines in the $z = 0.470$ plane, for the time stamps given by the labelled vertical lines in the time series. The green square indicates where θ is measured, together with the time-averaged (red) and instantaneous (blue) local velocity directions. The y and z coordinates are normalised by the VOI height (160 mm) and width (183 mm), respectively. 149

5.37 Statistics of the vortices revolving positively about the z-axis and in the vicinity of the jet impingement I_1 (black filament in figures 5.33 and 5.34), as a function of the forcing magnitude Gr_{ac}. The statistics are evaluated over the recording duration (20 minutes for each Gr_{ac}). (a) Number of vortices tracked in the VOI. (b) Mean emergence rate $\langle f \rangle$ of the vortices, as defined by equation (5.17), and bounded by equation (5.19). (c) Mean residence time $\langle t_r \rangle$ of the tracked vortices in the VOI (equation (5.17)), bounded by the standard deviation calculated for each Gr_{ac}. Both $\langle f \rangle$ and $\langle t_r \rangle$ are made dimensionless using the viscous diffusion time at the scale of D_s. 150

Thèse accessible à l'adresse : https://theses.insa-lyon.fr/publication/2024ISAL0101/these.pdf © [B. Vincent], [2024], INSA Lyon, tous droits réservés

C.1 Mesh used for the validation of *Semtex* (Blackburn *et al.*, 2019), with the approximate beam size (of radius $R_{beam} = 0.5 + Sx$) represented by the green-shaded area. The mesh is made of 180 elements, with 20 and 9 elements in the x- and r-directions, respectively. To be refined near the $x = 0$ and $x = L$ end walls, and around the $r = 0$ axis, the mesh was generated with stretching factors $\gamma_x = 1.35$ and $\gamma_r = 1.20$ (equations (3.9) and (3.10)). The red dots at $(x, r) = (2, 1)$, $(6, 2)$ and $(8, 3)$ locate the points were the convergence of $\boldsymbol{u}$ and p towards a steady state is monitored. 173

C.2 Maps of the steady axisymmetric velocity magnitude $\|\boldsymbol{u}\|$ computed with *Semtex* (Blackburn *et al.*, 2019) for (a) $Gr_{ac} = 1.68 \times 10^4$, (b) $Gr_{ac} = 3.47 \times 10^4$ and (c) $Gr_{ac} = 6.71 \times 10^4$. See table C.1 for the remaining computational parameters. All figures share the same colour levels. . . 174

C.3 On-axis profiles of the normalised axial intensity $\widetilde{I}_{ac,x}$ and the normalised axial velocity $\widetilde{u}_x$ for different forcing magnitudes: (a) $Gr_{ac} = 1.68 \times 10^4$, (b) $Gr_{ac} = 3.47 \times 10^4$ and (c) $Gr_{ac} = 6.71 \times 10^4$. The source is placed at $x = -0.35$. For each Gr_{ac}, $\widetilde{u}_x(x, r = 0)$ is normalised by the maximum velocity measured by Moudjed *et al.* (2015) using PIV (solid black curve). The intensity profiles are normalised by the maximum unattenuated intensity on the axis (dashed blue curve). For each Gr_{ac}, I reported the difference between the $\widetilde{u}_x(x, r = 0)$ profile obtained with Semtex and those of Moudjed *et al.* (2015). 175

D.1 Caption on next page. 176

D.1 Grid sensitivity for the stability analysis work in chapter 4: growth rate σ of the leading mode as a function of the polynomial expansion basis degree N_p. For each plot, the corresponding case (table 4.1) is reported along with the forcing magnitude Gr_{ac} and the azimuthal wavenumber m. The green-shaded area represents the ± 0.5 % interval about the σ obtained with the most refined grid ($N_p = 14$). For each case, the retained N_p is shown in red. 177

E.1 Processing of the images recorded in the entire cavity for $Gr_{ac} = 1.78 \times 10^4$ ($P_{elec} = 1$ W): (a) raw image, (b) processed image and (c) parameters of the "Image preprocessing" module of *LaVision GmbH* DaVis 10 to obtain (b) from (a). In (a) and (b), the purple star locates the entry point of the beam. 179

E.2 Processing of the images recorded in the entire cavity for $Gr_{ac} = 3.64 \times 10^4$ ($P_{elec} = 2$ W): (a) raw image, (b) processed image and (c) parameters of the "Image preprocessing" module of *LaVision GmbH* DaVis 10 to obtain (b) from (a). In (a) and (b), the purple star locates the entry point of the beam. 180

E.3 Processing of the images recorded in the entire cavity for $Gr_{ac} = 7.50 \times 10^4$ ($P_{elec} = 4$ W): (a) raw image, (b) processed image and (c) parameters of the "Image preprocessing" module of *LaVision GmbH* DaVis 10 to obtain (b) from (a). In (a) and (b), the purple star locates the entry point of the beam. 181

Thèse accessible à l'adresse : https://theses.insa-lyon.fr/publication/2024ISAL0101/these.pdf © [B. Vincent], [2024], INSA Lyon, tous droits réservés

E.4 Processing of the images recorded in the entire cavity for $Gr_{ac} = 11.28 \times 10^4$ ($P_{elec} = 6$ W): (a) raw image, (b) processed image and (c) parameters of the "Image preprocessing" module of *LaVision GmbH* DaVis 10 to obtain (b) from (a). In (a) and (b), the purple star locates the entry point of the beam. 182

E.5 Processing of the images recorded in the entire cavity for $Gr_{ac} = 15.12 \times 10^4$ ($P_{elec} = 8$ W): (a) raw image, (b) processed image and (c) parameters of the "Image preprocessing" module of *LaVision GmbH* DaVis 10 to obtain (b) from (a). In (a) and (b), the purple star locates the entry point of the beam. 183

E.6 Caption on next page. 184

E.6 Particle track detection by *Shake-The-Box* for $Gr_{ac} = 1.78 \times 10^4$ ($P_{elec} = 1$ W). (a) Snapshot of filtered tracks obtained by *Shake-The-Box* (the purple cross locates the entry point of the beam), (b) parameters of *Shake-The-Box*, as prescribed in the *LaVision GmbH* DaVis 10 software. (c) Parameters of the "Range filter" used to remove spurious tracks: particles whose velocities or acceleration do not fit in the indicated bounds are removed. After filtering, 1 650 301 tracks are obtained, with a mean track length of 3.75 s (the maximum track length is 67.8 s for a particle track at the free surface). The mean number of tracks per time step is 8549. 185

E.7 Caption on next page. 186

E.7 Particle track detection by *Shake-The-Box* for $Gr_{ac} = 3.64 \times 10^4$ ($P_{elec} = 2$ W). (a) Snapshot of filtered tracks obtained by *Shake-The-Box* (the purple cross locates the entry point of the beam), (b) parameters of *Shake-The-Box*, as prescribed in the *LaVision GmbH* DaVis 10 software. (c) Parameters of the "Range filter" used to remove spurious tracks: particles whose velocities or acceleration do not fit in the indicated bounds are removed. After filtering, 1 459 046 tracks are obtained, with a mean track length of 2.0 s (the maximum track length is 74.0 s for a particle track at the free surface). The mean number of tracks per time step is 2444. 187

E.8 Caption on next page. 188

E.8 Particle track detection by *Shake-The-Box* for $Gr_{ac} = 7.50 \times 10^4$ ($P_{elec} = 4$ W). (a) Snapshot of filtered tracks obtained by *Shake-The-Box* (the purple cross locates the entry point of the beam), (b) parameters of *Shake-The-Box*, as prescribed in the *LaVision GmbH* DaVis 10 software. (c) Parameters of the "Range filter" used to remove spurious tracks: particles whose velocities or acceleration do not fit in the indicated bounds are removed. After filtering, 1 174 568 tracks are obtained, with a mean track length of 2.13 s (the maximum track length is 87.6 s for a particle track at the free surface). The mean number of tracks per time step is 2015. 189

E.9 Caption on next page. 190

Thèse accessible à l'adresse : https://theses.insa-lyon.fr/publication/2024ISAL0101/these.pdf © [B. Vincent], [2024], INSA Lyon, tous droits réservés

E.9 Particle track detection by *Shake-The-Box* for $Gr_{ac} = 11.28 \times 10^4$ ($P_{elec} =$ 6 W). (a) Snapshot of filtered tracks obtained by *Shake-The-Box* (the purple cross locates the entry point of the beam), (b) parameters of *Shake-The-Box*, as prescribed in the *LaVision GmbH* DaVis 10 software. (c) Parameters of the "Range filter" used to remove spurious tracks: particles whose velocities or acceleration do not fit in the indicated bounds are removed. After filtering, 2 466 914 tracks are obtained, with a mean track length of 1.0 s (the maximum track length is 46.5 s for a particle track at the free surface). The mean number of tracks per time step is 2060. 191

E.10 Caption on next page. 192

E.10 Particle track detection by *Shake-The-Box* for $Gr_{ac} = 15.12 \times 10^4$ ($P_{elec} =$ 8 W). (a) Snapshot of filtered tracks obtained by *Shake-The-Box* (the purple cross locates the entry point of the beam), (b) parameters of *Shake-The-Box*, as prescribed in the *LaVision GmbH* DaVis 10 software. (c) Parameters of the "Range filter" used to remove spurious tracks: particles whose velocities or acceleration do not fit in the indicated bounds are removed. After filtering, 2 196 447 tracks are obtained, with a mean track length of 0.94 s (the maximum track length is 51 s for a particle track at the free surface). The mean number of tracks per time step is 1744. 193

E.11 Processing of the images recorded near the wall impinged by the first jet for $Gr_{ac} = 1.65 \times 10^4$ ($P_{elec} = 1$ W): (a) raw image, (b) processed image and (c) parameters of the "Image preprocessing" module of *LaVision GmbH* DaVis 10 to obtain (b) from (a). 194

E.12 Processing of the images recorded near the wall impinged by the first jet for $Gr_{ac} = 3.37 \times 10^4$ ($P_{elec} = 2$ W): (a) raw image, (b) processed image and (c) parameters of the "Image preprocessing" module of *LaVision GmbH* DaVis 10 to obtain (b) from (a). 195

E.13 Processing of the images recorded near the wall impinged by the first jet for $Gr_{ac} = 6.82 \times 10^4$ ($P_{elec} = 4$ W): (a) raw image, (b) processed image and (c) parameters of the "Image preprocessing" module of *LaVision GmbH* DaVis 10 to obtain (b) from (a). 196

E.14 Processing of the images recorded near the wall impinged by the first jet for $Gr_{ac} = 10.29 \times 10^4$ ($P_{elec} = 6$ W): (a) raw image, (b) processed image and (c) parameters of the "Image preprocessing" module of *LaVision GmbH* DaVis 10 to obtain (b) from (a). 197

E.15 Processing of the images recorded near the wall impinged by the first jet for $Gr_{ac} = 13.80 \times 10^4$ ($P_{elec} = 8$ W): (a) raw image, (b) processed image and (c) parameters of the "Image preprocessing" module of *LaVision GmbH* DaVis 10 to obtain (b) from (a). 198

E.16 See caption on the next page 199

Thèse accessible à l'adresse : https://theses.insa-lyon.fr/publication/2024ISAL0101/these.pdf © [B. Vincent], [2024], INSA Lyon, tous droits réservés

E.17 Particle track detection by *Shake-The-Box* near the first jet impingement I_1. The case $Gr_{ac} = 1.65 \times 10^4$ ($P_{elec} = 1$ W) is shown. (a) Snapshot of filtered tracks obtained by *Shake-The-Box* (the red cross locates the first jet impingement I_1), (b) parameters of *Shake-The-Box*, as prescribed in the *LaVision GmbH* DaVis 10 software. (c) Parameters of the "Median filter", which removes spurious tracks after three main steps: (i) the neighbours of a given particle are looked for, then (ii) the median velocity of the particle group is computed together with the velocity deviation of each particle. Finally, (iii) the algorithm removes the particles for which the velocity deviation exceeds the prescribed threshold. After filtering, 1 528 214 tracks are obtained over the recording duration (29 minutes), with a mean track length of 4.8 s (the maximum track length is 45.33 s). The mean number of tracks per time step is 6 719. 200

E.18 See caption on the next page 201

E.19 Particle track detection by *Shake-The-Box* near the first jet impingement I_1. The case $Gr_{ac} = 3.37 \times 10^4$ ($P_{elec} = 2$ W) is shown. (a) Snapshot of filtered tracks obtained by *Shake-The-Box* (the red cross locates the first jet impingement I_1), (b) parameters of *Shake-The-Box*, as prescribed in the *LaVision GmbH* DaVis 10 software. (c) Parameters of the "Median filter", which removes spurious tracks after three main steps: (i) the neighbours of a given particle are looked for, then (ii) the median velocity of the particle group is computed together with the velocity deviation of each particle. Finally, (iii) the algorithm removes the particles for which the velocity deviation exceeds the prescribed threshold. After filtering, 3 525 753 tracks are obtained over the recording duration (20 minutes), with a mean track length of 3.6 s (the maximum track length is 39.6 s). The mean number of tracks per time step is 11 123. 202

E.20 Particle track detection by *Shake-The-Box* near the first jet impingement I_1. The case $Gr_{ac} = 6.82 \times 10^4$ ($P_{elec} = 4$ W) is shown. (a) Snapshot of filtered tracks obtained by *Shake-The-Box* (the red cross locates the first jet impingement I_1) and (b) parameters of *Shake-The-Box*, as prescribed in the *LaVision GmbH* DaVis 10 software. The obtained tracks did not require to be filtered. In total, 5 502 200 tracks are obtained over the recording duration (20 minutes), with a mean track length of 2.2 s (the maximum track length is 24 s). The mean number of tracks per time step is 10 551. 203

E.21 See caption on the next page 204

Thèse accessible à l'adresse : https://theses.insa-lyon.fr/publication/2024ISAL0101/these.pdf © [B. Vincent], [2024], INSA Lyon, tous droits réservés

E.22 Particle track detection by *Shake-The-Box* near the first jet impingement I_1. The case $Gr_{ac} = 10.29 \times 10^4$ ($P_{elec} = 6$ W) is shown. (a) Snapshot of filtered tracks obtained by *Shake-The-Box* (the red cross locates the first jet impingement I_1), (b) parameters of *Shake-The-Box*, as prescribed in the *LaVision GmbH* DaVis 10 software. (c) Parameters of the "Median filter", which removes spurious tracks after three main steps: (i) the neighbours of a given particle are looked for, then (ii) the median velocity of the particle group is computed together with the velocity deviation of each particle. Finally, (iii) the algorithm removes the particles for which the velocity deviation exceeds the prescribed threshold. After filtering, 3 837 350 tracks are obtained over the recording duration (20 minutes), with a mean track length of 1.8 s (the maximum track length is 18 s). The mean number of tracks per time step is 5 919. 205
E.23 See caption on the next page 206
E.24 Particle track detection by *Shake-The-Box* near the first jet impingement I_1. The case $Gr_{ac} = 13.80 \times 10^4$ ($P_{elec} = 8$ W) is shown. (a) Snapshot of filtered tracks obtained by *Shake-The-Box* (the red cross locates the first jet impingement I_1), (b) parameters of *Shake-The-Box*, as prescribed in the *LaVision GmbH* DaVis 10 software. (c) Parameters of the "Median filter", which removes spurious tracks after three main steps: (i) the neighbours of a given particle are looked for, then (ii) the median velocity of the particle group is computed together with the velocity deviation of each particle. Finally, (iii) the algorithm removes the particles for which the velocity deviation exceeds the prescribed threshold. After filtering, 3 892 465 tracks are obtained over the recording duration (20 minutes), with a mean track length of 1.6 s (the maximum track length is 20 s). The mean number of tracks per time step is 5 752. 207

Thèse accessible à l'adresse : https://theses.insa-lyon.fr/publication/2024ISAL0101/these.pdf © [B. Vincent], [2024], INSA Lyon, tous droits réservés

List of Tables

1.1 List of material properties and values of α for water (Dinçer & Zamfirescu, 2015), galinstan and liquid silicon (El Ghani, 2020). For water, the bulk and dynamic viscosities η and μ are related to each other through $\eta \approx 3\mu$ (Moudjed *et al.*, 2014*a*). 9

1.2 Properties of the fluid (water, taken from Dinçer & Zamfirescu (2015) at 20 °C) and cavity material (Pyrex glass, taken from Blackstock (2000)) used in the experimental study of a three-dimensional flow driving by reflected waves (chapter 5). In a fluid, sound waves are longitudinal waves so that $c_l = c$. 11

1.3 List of dimensionless numbers from the Eckart streaming and acoustics literature, together with their expression in terms of the dimensionless numbers (1.58) derived by Moudjed *et al.* (2014*a*). The dimensionless numbers of Rudenko & Soluyan (1977) and Orosco & Friend (2022) are based on a streaming length scale L_s; it is assumed that $L_c \sim L_s$. A regularly-encountered number is the Strouhal number $\mathcal{S} = M_{ac}^{-1}$ (Riley, 2001; Michel & Chini, 2019; Dubrovski *et al.*, 2023); as M_{ac} is already listed below, $\mathcal{S}$ is not included. 25

3.1 Values of the dimensionless parameters (1.58) considered in the present study. The values of the parameters S and N/L correspond to the water experiments of Moudjed *et al.* (2014*a*), for which $f = 2 \times 10^6$ Hz, $\alpha \approx 0.1$ m^{-1}, $D_s = 2.85 \times 10^{-2}$ m and $c = 1480$ m.s^{-1}. 51

3.2 Coefficients of the Kth-order splitting scheme (3.3) used for the temporal discretisation of the streaming problem (table reproduced from Karniadakis *et al.* (1991)). 52

3.3 Dependence of the steady on-axis velocity peak position x_p and amplitude $u_{x,p}$ with the polynomial degree N_p of the expansion basis (the mesh is defined by $N_{e,x} = 44$, $N_{e,r} = 20$, $\gamma_x = 1.35$ and $\gamma_r = 1.3$). The calculations are made for $Gr_{ac} = 5 \times 10^4$ (highest forcing magnitude), and the errors are computed relatively to the results obtained for $N_p = 12$. The values of x_p are obtained by finding the point where $\partial u_x/\partial x$ vanishes on the axis, using the Lagrange polynomials (3.7) of the expansion basis as interpolation functions. 56

Thèse accessible à l'adresse : https://theses.insa-lyon.fr/publication/2024ISAL0101/these.pdf © [B. Vincent], [2024], INSA Lyon, tous droits réservés

4.1 Values of the parameters for all the geometries considered in the stability analysis. The parameter K_R is defined as the ratio between the cavity radius $D/2$ and the approximate beam radius evaluated at $x = L$ (equation (4.1)). For all cases, $S = 0.03$ and $N/L = 0.003$. The structure of the forcing field is thus the same as in chapter 3 and in the 2 MHz water experiments of Moudjed *et al.* (2014*a*). 72

4.2 Evolution of the growth rate σ of the leading (i.e., least stable) mode, as a function of the expansion basis polynomial degree N_p. The growth rates are obtained for case 3 (table 4.1) with $Gr_{ac} = 7000$ and $m = 2$. The error is relative to the value of σ obtained for $N_p = 14$. 79

4.3 Characteristics of the meshes used for each case (table 4.1). All meshes were created with axial and radial stretching factors $\gamma_x = 1.35$ and $\gamma_r = 1.30$, respectively (equations (3.9) and (3.10)). 79

4.4 Comparison of the growth rates σ and frequencies ω obtained by linear stability analysis (LSA) and by running direct numerical simulations (DNS) at slightly supercritical forcing magnitudes ($r_c > 0$). The relative errors between the values of σ and ω obtained by LSA and DNS are given by ε_σ and ε_ω, respectively. 98

5.1 Summary of the hardware and recording parameters for the PTV measurements of the square acoustic streaming flow. 117

5.2 Hardware and recording parameters used for PTV flow measurements in the entire fluid domain (first setup, left column) and near the first jet impingement (second setup, right column). The indicated power values are those of P_{elec}. 125

5.3 Conversion table between the electrical power P_{elec} and acoustic Grashof number Gr_{ac}. The transducer efficiency ε_t is obtained through linear interpolation of tabulated data provided by the transducer manufacturer *IMASONIC* (IMASONIC SAS, 2011). Temperatures are given at the start and the end of each recording. Values of Gr_{ac} are bounded using Eq. (5.6), where ΔT is estimated as the sum of twice the thermometer resolution (0.25 °C) and the temperature difference between the beginning and the end of each recording. The derivatives in Eq. (5.6) have been estimated by fitting cubic curves to the reference tables of Dinçer & Zamfirescu (2015). . 127

A.1 List of different streaming experiments, including the operating conditions and observed flow velocities. All the experiments were made in water using a plane circular transducer, except Dentry *et al.* (2014) who investigated a streaming jet forced by a SAW (Surface Acoustic Wave) device (source of rectangular cross section, with its height varying with the frequency f). . . 166

A.2 Experimental conditions of the works listed in table A.1 expressed using the dimensionless numbers introduced by Moudjed *et al.* (2015), who initially considered an experiment of square cross section. To ease the comparison with other experiments, I considered the hydraulic diameter instead. For Dentry *et al.* (2014), the source height varies with the frequency; that height is taken as characteristic length scale. 167

Thèse accessible à l'adresse : https://theses.insa-lyon.fr/publication/2024ISAL0101/these.pdf © [B. Vincent], [2024], INSA Lyon, tous droits réservés

C.1 Dimensionless parameters corresponding to the experimental and numerical benchmark setups of Moudjed *et al.* (2015), with Δx the distance (normalised by the transducer diameter D_s) between the transducer and the upstream cavity wall. The original experiments were made in a $265 \times 180 \times 160$ (length $\times$ width $\times$ height) water cavity of rectangular cross-section. The flow was actuated by a $D_s = 28.5$ mm plane circular transducer emitting 2 MHz acoustic sine waves. 172

E.1 Statistics of the *Shake-The-Box* results obtained for the measurements in the entire cavity (left column) and for the near-impingement measurements (right column). The corresponding values of P_{elec} are given in the brackets. For the entire-cavity-measurements, the longest track lengths are found at the free-surface. 178

Thèse accessible à l'adresse : https://theses.insa-lyon.fr/publication/2024ISAL0101/these.pdf © [B. Vincent], [2024], INSA Lyon, tous droits réservés

Thèse accessible à l'adresse : https://theses.insa-lyon.fr/publication/2024ISAL0101/these.pdf © [B. Vincent], [2024], INSA Lyon, tous droits réservés

Introduction

The development of renewable energies is accelerated by the current environmental challenges. For solar energy in particular, maximising the efficiency of the devices converting sunlight into electricity (i.e., photovoltaic cells) is key.

Photovoltaic cells are mainly obtained from the so-called directional solidification of liquid silicon. The melt is contained by a crucible placed in a furnace. Solidification is then initiated by cooling down the bottom end of the crucible, allowing for a liquid-solid interface to be formed. Once entirely solidified, the silicon ingot is cut into thin slices (wafers), on which photovoltaic cells are based. The performance of these cells greatly depend on the quality of the manufactured ingot, especially on its impurities concentration. These impurities are formed at the liquid-solid interface during the solidification process, and their concentration in both the liquid and solid phase shall be well controlled during the process to ensure a high wafer quality (Trumbore, 1960).

To match the increasing demand on solar cells, manufacturers grow silicon ingots using crucibles of increasing size: whilst these crucible could be 40 cm $\times$ 40 cm $\times$ 40 cm (width $\times$ length $\times$ height) in size a few years ago, ingots of 90 cm $\times$ 90 cm cross-sectional area are now commonly manufactured. In the smaller crucibles, natural convection was sufficient to stir the melt and obtain satisfactory impurities concentration gradients. However, in larger crucibles, higher convection levels are required and thus call for effective stirring methods. Several strategies are possible. First, the melt may be stirred using a mechanical device, such as a propeller (Chatelain *et al.*, 2018). Because it is intrusive, this method however raises the question of the actuator material to be used to prevent melt contamination. A second possibility is to remotely actuate the melt using electromagnetic fields for instance (Delannoy, 2012; Pätzold *et al.*, 2013; Cablea *et al.*, 2014, 2015). However, such approach requires cumbersome magnets that are barely compatible with the tight packaging and thermal constraints of solidification processes. Our research group in France focuses on a third approach, that is ultrasound-generated melt flow. The idea is to create localised flows by radiating ultrasounds into the melt. With a dedicated cylindrical waveguide, our research group recently managed to track the liquid-solid interface during silicon solidification (Miralles *et al.*, 2023); using ultrasounds to further promote melt flow is thus technically feasible.

Ultrasound-driven flows are referred to as *acoustic streaming*; they are forced by a nonlinear process involving the attenuation of travelling sound waves. Acoustic streaming recently received a renewed interest in applications for which flow actuation by other means is more difficult. In microfluidics for instance, sound waves are a popular tool to manipulate small (sub-millimetric) fluid volumes in droplets (Riaud *et al.*, 2017; Baudoin & Thomas, 2019), microchannels/cavities (Hagsäter *et al.*, 2007; Friend & Yeo, 2011; Muller & Bruus, 2015) or around oscillating bubbles (Cleve *et al.*, 2019; Fauconnier *et al.*, 2022; Doinikov *et al.*, 2022), for instance. At larger scales and for industrial applications, acoustic streaming is commonly based on high-power and low-frequency ultrasounds (typically

Thèse accessible à l'adresse : https://theses.insa-lyon.fr/publication/2024ISAL0101/these.pdf © [B. Vincent], [2024], INSA Lyon, tous droits réservés

hundreds of Watts and kilohertz) (Absar *et al.*, 2017; Lebon *et al.*, 2019). In solidification processes, several studies have shown that both the microscopic and macroscopic properties of the solid phase can be enhanced using such sound waves (Jian *et al.*, 2006; Liu *et al.*, 2008; Gao *et al.*, 2009). In particular, acoustic streaming is able to suppress inhomogeneities in the grown solid (Kozhemyakin, 2003). As these inhomogeneities may result from flow instabilities developing in the melt, acoustic streaming is thus an interesting candidate for stirring as well as flow control.

For the streaming examples mentioned above, sound waves are mostly attenuated by cavitation bubbles created near the acoustic source and resulting from the high acoustic levels. Although this leads to strong jets, the coherence of the sound beam is lost at small distances from the source, preventing a controlled flow actuation further away. Instead, our research group focuses on streaming jets forced by high-frequency (MHz range) and low-power (a few Watts) sound waves. The sound beam thus remains coherent, and sound attenuation drives a slender cavitation-free streaming jet. The flow can thus be forced over large distances (decimetric, or even metric); typically up to distances where the sound waves are fully attenuated and thus can no longer force a flow. This long range forcing capability is key for designing geometrically-complex forcing fields needed to stir a silicon melt e.g., using multiple reflections of a single beam on the crucible side walls.

In this thesis, I focus on long-range streaming jets, and how more intricate streaming flows can be used and designed for stirring purposes. In particular, this thesis aims to answer the following questions:

(i) What are the different regimes along a streaming jet, from the source and up to forcing-free regions where the beam is fully attenuated ?

(ii) Does that streaming flow become unstable ? If so, what are the destabilisation mechanisms ?

(iii) Can a highly 3D streaming flow be achieved with multiple reflections of a single sound beam ? What are the main flow features, and how do they scale with the acoustic forcing magnitude ?

Questions (i) and (ii) are addressed using analytical and numerical approaches. The numerical simulations are made in a simple geometry, that is a closed cylindrical vessel in which a laminar streaming jet is forced by an attenuated axisymmetric beam. Question (iii) is answered experimentally; the flow is mapped using high-end PTV (Particle Tracking Velocimetry) equipment and methods that had never been used in the laboratory before my arrival.

The thesis is organised as follows: the acoustic streaming phenomenon is introduced in chapter 1. I shall summarise the streaming literature, with a focus on the modelling strategies and the existing studies on the scaling and stability of streaming flows. Chapter 2 is devoted to the analytical developments I made during the thesis. In particular, a linear acoustics model from the literature is adapted to correctly incorporate the attenuation of sound waves emitted by a plane circular source. The question of energy transfer between the acoustic and streaming scales is also discussed. Chapter 3 focuses on the scaling of long range streaming jets, and their stability is then studied in chapter 4. The experimental study of a highly 3D helical streaming flow is finally presented in chapter 5.

Thèse accessible à l'adresse : https://theses.insa-lyon.fr/publication/2024ISAL0101/these.pdf © [B. Vincent], [2024], INSA Lyon, tous droits réservés

Chapter 1

Elements of acoustics and review of acoustic streaming

1.1 Introduction to acoustic streaming and position of this thesis relative to former studies made in the laboratory

The first experimental evidence of acoustic streaming traces back to the observations of Faraday (1831). Whilst sand on a vibrating plate clusters at the nodal lines (Chladni, 1787), Faraday noticed that very light powders would instead gather at locations of high vibration amplitudes. He attributed this effect to an air stream above the plate, without however providing any mathematical description of this flow.

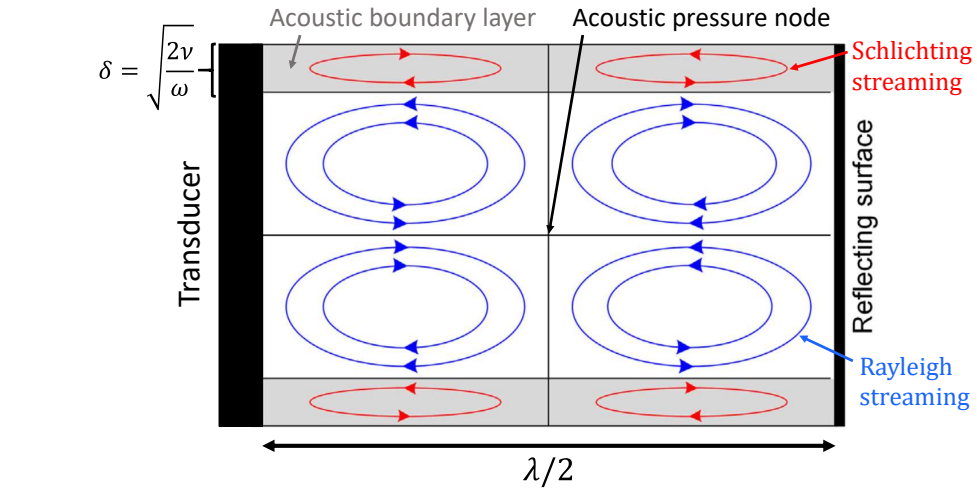
Since the seminal theoretical work of Rayleigh (1884), sound attenuation has been identified as the key ingredient for acoustic streaming to occur. Two main acoustic streaming settings are identified based on (i) the sound attenuation mechanism driving the flow, and (ii) the characteristic streaming length scale L_s compared to the wavelength λ of the sound wave:

1. The first type of streaming is driven by standing waves in a closed resonator. These waves are essentially attenuated close to the solid boundaries within the Stokes layer (I shall refer to it as acoustic boundary layer, or ABL), generating a flow *inside* that layer (figure 1.1 (a)). Such streaming is termed *Schlichting streaming* (Schlichting, 1932), for which L_s is similar to the ABL thickness $\delta = \sqrt{2\nu/\omega}$ (with ν the kinematic viscosity and ω the angular frequency of the sound wave). Sound attenuation within the ABL also drives the so-called *Rayleigh streaming* (Rayleigh, 1884), which features vortices *outside* the ABL. In this Rayleigh-Schlichting setting, the cavity length is typically $L_c = \lambda/2$, and $L_s \sim \lambda/4$ outside the ABL (figure 1.1 (a)).

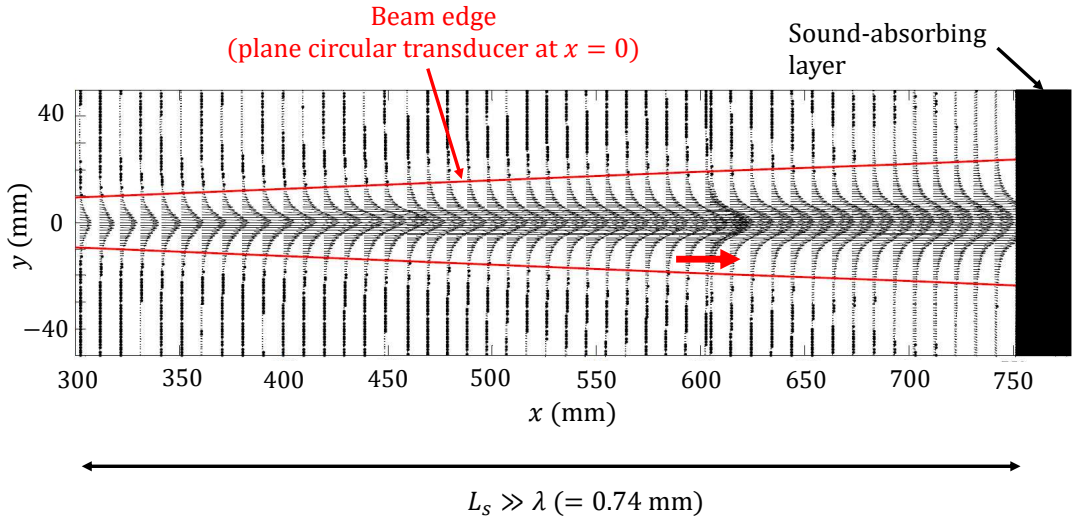
2. The second type of streaming results from sound waves travelling in the bulk of the fluid, away from solid boundaries. Attenuation of these waves drives a jet-like flow in the wave propagation direction (figure 1.1 (b)). This streaming type is called *Eckart streaming* (Eckart, 1948), and is usually studied for $L_c \gg \lambda$ and $L_s \gg \lambda$.

This thesis focuses exclusively on acoustic streaming of the Eckart type; from now, all mentions of acoustic streaming refer to Eckart streaming unless specified otherwise. As we shall see later in this chapter, streaming flows can be modelled

Thèse accessible à l'adresse : https://theses.insa-lyon.fr/publication/2024ISAL0101/these.pdf © [B. Vincent], [2024], INSA Lyon, tous droits réservés



(a)



(b)

Figure 1.1: Representation of the two streaming types: (a) Rayleigh-Schlichting streaming (figure taken and adapted from Luo *et al.* (2018)) and (b) Eckart streaming (taken and adapted from Moudjed (2013), who did his Ph.D thesis at the LMFA laboratory). In (b), the black arrows represent an Eckart streaming velocity field measured by PIV in water and averaged over 25 minutes. The thick red arrow indicates the sound wave propagation direction.

by the incompressible continuity and Navier-Stokes together with a body force:

$$\rho_0 \left[\frac{\partial \boldsymbol{u_s}}{\partial t} + (\boldsymbol{u_s} \cdot \boldsymbol{\nabla})\, \boldsymbol{u_s} \right] = -\boldsymbol{\nabla} p_s + \mu \boldsymbol{\nabla}^2 \boldsymbol{u_s} + \frac{2\alpha}{c} \boldsymbol{I_{ac}}\,, \tag{1.1a}$$

$$\boldsymbol{\nabla} \cdot \boldsymbol{u_s} = \boldsymbol{0}\,, \tag{1.1b}$$

where ρ_0 is the fluid density, $\boldsymbol{u_s}$ and p_s respectively are the streaming velocity and pressure

Thèse accessible à l'adresse : https://theses.insa-lyon.fr/publication/2024ISAL0101/these.pdf © [B. Vincent], [2024], INSA Lyon, tous droits réservés

fields, and t refers to time. The forcing term driving the flow involves three acoustic quantities:

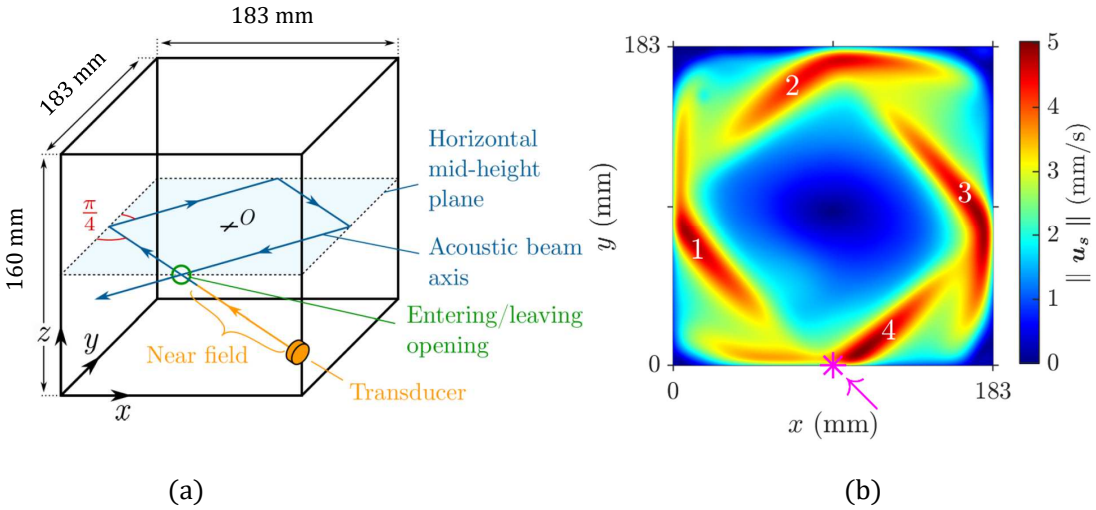
- the speed of sound c (m.s^{-1}), which is specific to the fluid.
- the time-averaged (over an acoustic period) acoustic intensity field $\boldsymbol{I_{ac}}$ (W.m^{-2}), which corresponds to a power per unit area. The orientation of $\boldsymbol{I_{ac}}$ sets the direction along which acoustic energy travels. Therefore, $\boldsymbol{I_{ac}}$ sets the structure, the orientation and the magnitude of the forcing field driving the flow.
- the sound attenuation coefficient α (m^{-1}), which defines the spatial rate at which the amplitude of the acoustic pressure waves decays. For instance, the amplitude of a plane pressure wave p_{ac} travelling in the positive x-direction is: $|p_{ac}| = p_0 e^{-\alpha x}$, with p_0 the wave amplitude at the source. The coefficient α scales as f^2 (with f the sound wave frequency) and involves different material properties, depending on the mechanisms responsible for sound attenuation (e.g., thermal conduction or viscosity). Besides of acting on the forcing magnitude in equation (1.1a), α also affects the spatial structure of $\boldsymbol{I_{ac}}$, hence of the forcing.

The streaming velocity field displayed in figure 1.1 (b) illustrates the streaming jet scales commonly studied by our group. The velocity field is taken from a former Ph.D work carried out at the laboratory (Moudjed, 2013); it corresponds to water experiments ($c = 1480$ m.s^{-1}) made in a 750 mm $\times$ 183 mm $\times$ 160 mm (length $\times$ width $\times$ height) cavity. The flow is forced by a beam of 2 MHz sine sound waves radiated by a plane circular transducer of active diameter $D_s = 28.5$ mm. In this setup, $\lambda = 0.74$ mm and $\alpha \approx 0.1$ m^{-1}, yielding a characteristic sound attenuation distance $1/\alpha \approx 10$ m. The forcing magnitude is changed by tuning the acoustic power $P_{ac,0}$ radiated by the source, with typically 0.5 W $\leq P_{ac,0} \leq 8$ W. For this setting, the maximum streaming velocities on the jet axis range from 1 cm.s^{-1} to 7 cm.s^{-1}. **This configuration is the reference setup on which my numerical single-jet studies are based**. Although I shall describe streaming problems using dimensionless parameters, the latters are chosen to be consistent with the values of D_s, λ and α of Moudjed *et al.* (2014*a*) and Moudjed (2013).

More recently, our research group investigated the use of beam reflections to design more complex forcing fields, hence streaming flows. The idea is illustrated by figure 1.2 (a): the beam enters a cuboid water cavity of square horizontal cross section and, due to its prescribed orientation, undergoes three successive reflections on the sidewalls before exiting the cavity. The beam axis remains in a horizontal plane and drives a square-shaped flow made of four impinging jets (figure 1.2 (b)). **The experimental study presented in chapter 5 directly follows the works of Cambonie *et al.* (2017) and Launay *et al.* (2019) on that square flow**: the idea is to add a vertical tilt to the beam, so that its axis no longer remains horizontal but instead follows a three-dimensional path.

This first chapter aims at (i) providing the building blocks required to model acoustic streaming, and (ii) reviewing the current knowledge on streaming jets. The chapter is organised as follows: section 1.2 is devoted to acoustics; the equations of linear acoustics are provided, and key quantities such as $\boldsymbol{I_{ac}}$ and α are mathematically defined. Section 1.3 focuses on the modelling of acoustic streaming, and shows how the streaming equations (1.1) are derived, and under which assumptions. Then, the model used for $\boldsymbol{I_{ac}}$ is presented in section 1.4. Section 1.5 introduces the set of dimensionless parameters used in this thesis; scaling laws from the literature are then written with these parame-

Thèse accessible à l'adresse : https://theses.insa-lyon.fr/publication/2024ISAL0101/these.pdf © [B. Vincent], [2024], INSA Lyon, tous droits réservés



(a) (b)

Figure 1.2: (a) Sketch of the square streaming flow configuration studied in a nearly-cubic cavity filled with water (figure taken from Launay *et al.* (2019)). The beam is fired by a plane circular transducer (yellow) outside the cavity and immersed in the same fluid. The beam enters the cavity through a circular aperture covered by a plastic film and, after three reflections, exits the cavity at the same location. (b) PIV measurement of the steady velocity magnitude $\|\boldsymbol{u_s}\|$ in the horizontal mid-height plane for $P_{ac,0} = 1$ W (Cambonie *et al.*, 2017).

ters and are reviewed. Finally, the main results on the stability and dynamics of acoustic streaming flows are summarised in section 1.6.

1.2 Fundamentals of acoustic wave propagation

As acoustic streaming denotes flows driven by the propagation of attenuated sound waves, I shall begin this chapter by providing basic elements of acoustics. After introducing the general equations of fluid mechanics and having shown how these equations can describe the propagation of linear sound waves, the fundamental acoustic quantities (attenuation, impedance, intensity and power) involved in both the acoustics and streaming problems are defined. Finally, the reflection of sound waves on a smooth interface is discussed.

1.2.1 General equations of fluid mechanics

Acoustics refers to a class of mechanical waves propagating in a continuum: sound waves. The propagation of such waves is governed by the compressible continuity (1.2) and Navier-Stokes (1.3) equations, along with the conservation of energy (1.4). In the absence of external sources of mass, momentum and energy, these equations are (Giovannini &

Thèse accessible à l'adresse : https://theses.insa-lyon.fr/publication/2024ISAL0101/these.pdf © [B. Vincent], [2024], INSA Lyon, tous droits réservés

Airiau, 2016):

$$\frac{\partial \rho}{\partial t} + \boldsymbol{\nabla} \cdot (\rho \boldsymbol{u}) = 0\,, \tag{1.2}$$

$$\rho \left[\frac{\partial \boldsymbol{u}}{\partial t} + (\boldsymbol{u} \cdot \boldsymbol{\nabla})\, \boldsymbol{u} \right] = -\boldsymbol{\nabla} p + \boldsymbol{\nabla} \cdot \boldsymbol{\sigma}\,, \tag{1.3}$$

$$\rho \left(\frac{\partial e}{\partial t} + \boldsymbol{u} \cdot \boldsymbol{\nabla} e \right) = \boldsymbol{\nabla} \cdot (\kappa \boldsymbol{\nabla} T) - p\,(\boldsymbol{\nabla} \cdot \boldsymbol{u}) + \boldsymbol{\sigma} : \boldsymbol{\nabla} \boldsymbol{u}\,, \tag{1.4}$$

with ρ the density, p the pressure, $\boldsymbol{u}$ the velocity, $\boldsymbol{\sigma}$ the viscous stress tensor, T the temperature, κ the thermal conductivity, and e the specific internal energy. In acoustics, it is often convenient to consider the specific entropy s instead of e. Since $\mathrm{d}e = T\mathrm{d}s + (p/\rho^2)\,\mathrm{d}\rho$, the energy equation (1.4) can be equivalently rewritten as (Giovannini & Airiau, 2016):

$$\rho T \left(\frac{\partial s}{\partial t} + \boldsymbol{u} \cdot \boldsymbol{\nabla} s \right) = \boldsymbol{\nabla} \cdot (\kappa \boldsymbol{\nabla} T) + \boldsymbol{\sigma} : \boldsymbol{\nabla} \boldsymbol{u}\,. \tag{1.5}$$

Furthermore, I shall consider only Newtonian fluids in this thesis, for which:

$$\boldsymbol{\sigma} = \mu \left[\boldsymbol{\nabla} \boldsymbol{u} + (\boldsymbol{\nabla} \boldsymbol{u})^t \right] + \left(\eta - \frac{2}{3}\mu \right) (\boldsymbol{\nabla} \cdot \boldsymbol{u})\, \mathbf{I}\,, \tag{1.6}$$

with μ and η the dynamic and bulk viscosities, respectively, and $\mathbf{I}$ is the identity tensor.

Finally, two equations of state shall be prescribed to close the problem:

$$p = p\,(\rho, s)\ , \tag{1.7a}$$

$$T = T\,(\rho, s)\ . \tag{1.7b}$$

1.2.2 Main assumptions in acoustics, linearisation and attenuation

In acoustics, one deals with small fluctuations travelling at a speed c within the medium. The classical equations of acoustics are obtained by considering small fluctuations (subscript "ac") from a homogeneous resting fluid (subscript "0"):

$$\rho = \rho_0 + \rho_{ac} \tag{1.8}$$

$$\boldsymbol{u} = \mathbf{0} + \boldsymbol{u_{ac}} \tag{1.9}$$

$$p = p_0 + p_{ac} \tag{1.10}$$

$$T = T_0 + T_{ac} \tag{1.11}$$

$$s = s_0 + s_{ac}\,. \tag{1.12}$$

Furthermore, acoustic waves are also defined by $\boldsymbol{\nabla} \times \boldsymbol{u_{ac}} = \mathbf{0}$ (Rudenko & Soluyan, 1977; Blackstock, 2000); this property holds outside the acoustic boundary layer (Kinsler *et al.*, 2000).

The equations governing linear acoustic are then obtained by inserting the decomposition (1.8) into equations (1.2)-(1.5). Assuming constant μ, η and κ, keeping only the

Thèse accessible à l'adresse : https://theses.insa-lyon.fr/publication/2024ISAL0101/these.pdf © [B. Vincent], [2024], INSA Lyon, tous droits réservés

linear terms gives:

$$\frac{\partial \rho_{ac}}{\partial t} + \rho_0 \boldsymbol{\nabla} \cdot \boldsymbol{u_{ac}} = 0\,, \tag{1.13a}$$

$$\rho_0 \frac{\partial \boldsymbol{u_{ac}}}{\partial t} = -\boldsymbol{\nabla} p_{ac} + \left(\frac{4}{3}\mu + \eta\right) \boldsymbol{\nabla} \left(\boldsymbol{\nabla} \cdot \boldsymbol{u_{ac}}\right)\,, \tag{1.13b}$$

$$\rho_0 T_0 \frac{\partial s_{ac}}{\partial t} = \kappa \nabla^2 T_{ac}\,. \tag{1.13c}$$

As a result of linearisation, the effects of viscosity only appear in the acoustic momentum equation (1.13b). Similarly, expanding the equations of state (1.7) up to first order gives:

$$p_{ac} = \left.\frac{\partial p}{\partial \rho}\right|_s \rho_{ac} + \left.\frac{\partial p}{\partial s}\right|_\rho s_{ac} = c^2 \rho_{ac} + \left.\frac{\partial p}{\partial s}\right|_\rho s_{ac}\,, \tag{1.14a}$$

$$T_{ac} = \left.\frac{\partial T}{\partial \rho}\right|_s \rho_{ac} + \left.\frac{\partial T}{\partial s}\right|_\rho s_{ac}\,, \tag{1.14b}$$

since $c^2 = \left.\frac{\partial p}{\partial \rho}\right|_s$. Finally, a wave equation for $\boldsymbol{u_{ac}}$ can be obtained by (i) taking the time derivative of equation (1.13b), (ii) taking the gradient of the linearised continuity equation (1.13a), (iii) combining the two equations together and (iv) assuming weak wave attenuation over a wavelength λ (Coulouvrat, 1992). Assuming a time-periodic monochromatic wave of angular frequency ω (i.e., $\boldsymbol{u_{ac}} = \widehat{\boldsymbol{u}}_{\boldsymbol{ac}} e^{j\omega t}$), the wave propagation problem is described by a complex Helmholtz equation (Blackstock, 2000):

$$\boldsymbol{\nabla}^2 \widehat{\boldsymbol{u}}_{\boldsymbol{ac}} + k_c^2 \widehat{\boldsymbol{u}}_{\boldsymbol{ac}} = 0\,, \tag{1.15}$$

where $k_c = k - j\alpha$ is a complex wavenumber, with $k = \omega/c$ and α is the sound attenuation coefficient.

The sound attenuation coefficient appearing in the imaginary part of k_c defines the exponential decay rate of $\|\boldsymbol{u_{ac}}\|$ (and also $|p_{ac}|$, $|\rho_{ac}|$, etc.) along the propagation path. The expression of α is:

$$\alpha = \frac{\omega^2}{2\rho_0 c^3}\left[\frac{4}{3}\mu + \eta + \frac{(\gamma - 1)}{Pr}\mu\right]\,, \tag{1.16}$$

where γ is the ratio of specific heats and $Pr = \mu c_p/\kappa$ is the Prandtl number, with c_p the specific heat capacity at constant p. Sound attenuation thus results from (i) viscosity (term proportional to $4\mu/3+\eta$) and (ii) thermal conduction (term proportional to $(\gamma - 1)$). Values of α for 2 MHz sound waves in water, galinstan and liquid silicon are provided in table 1.1.

Equation (1.16) has been obtained considering acoustic fluctuations of entropy; however, situations for which $s_{ac} \approx 0$ are rather common. Indeed, Coulouvrat (1992) showed that $s_{ac} \propto (\gamma - 1)$, i.e., s_{ac} vanishes for fluids for which $\gamma \approx 1$ such as water (table 1.1). For such fluids, the linear acoustics problem thus becomes isentropic: the thermal contribution to α can be neglected in equation (1.16), and the linearised equation of state (1.14) reduces to:

$$p_{ac} = c^2 \rho_{ac}\,. \tag{1.17}$$

I stress that although this assumption is convenient, it is however not always satisfied: in liquid galinstan and silicon for instance, $\gamma \neq 1$ (table 1.1) and the thermal contribution to α may even be larger than the viscous contribution $(4\mu/3 + \eta)$.

Thèse accessible à l'adresse : https://theses.insa-lyon.fr/publication/2024ISAL0101/these.pdf © [B. Vincent], [2024], INSA Lyon, tous droits réservés

1.2.3 Specific acoustic impedance, acoustic intensity and power

1.2.3.1 Specific acoustic impedance

Any solution $\boldsymbol{u_{ac}}$ (I shall omit $\widehat{\ }$ for simplicity) of the wave equation (1.15) can be rewritten in terms of ρ_{ac}, p_{ac}, etc. using the linear acoustics equations (1.13) and (1.14). A useful quantity in acoustics is the specific acoustic impedance $Z = p_{ac}/u_{ac}$ which, for an unattenuated ($\alpha = 0$) monochromatic plane wave reads:

$$Z = \frac{p_{ac}}{u_{ac}} = \pm \rho_0 c \,, \tag{1.18}$$

in which the sign depends on the wave propagation direction.

1.2.3.2 Acoustic intensity and power

The time-averaged acoustic intensity $\boldsymbol{I_{ac}}$ (W/m^2) is a nonlinear acoustic quantity defining the acoustic power flowing through a unit surface; it is defined as:

$$\boldsymbol{I_{ac}} = \langle p_{ac} \boldsymbol{u_{ac}} \rangle \ , \tag{1.19}$$

where $\langle\,\rangle$ denotes a time-average over an acoustic period. In an unattenuating medium and for monochromatic linear waves, $\boldsymbol{\nabla \cdot I_{ac}} = 0$ (Pierce, 1981). The instantaneous counterpart of (1.19) will never be used in this thesis; therefore, I will from now omit the "time-averaged" terminology when referring to $\boldsymbol{I_{ac}}$.

Finally, $\boldsymbol{I_{ac}}$ being a power per unit area, the acoustic power P_{ac} flowing through a surface S can thus be obtained from:

$$P_{ac} = \iint_S \boldsymbol{I_{ac}} \cdot \boldsymbol{n} \, \mathrm{d}S \,, \tag{1.20}$$

Table 1.1: List of material properties and values of α for water (Dinçer & Zamfirescu, 2015), galinstan and liquid silicon (El Ghani, 2020). For water, the bulk and dynamic viscosities η and μ are related to each other through $\eta \approx 3\mu$ (Moudjed *et al.*, 2014*a*).

	Water ($T = 293$ K)	Galinstan ($T = 303$ K)	Liquid silicon ($T = 1773$ K)
Density ρ_0 (kg.m^{-3})	998.2	6363.2	2500
Speed of sound c (m.s^{-1})	1483	2747	3900
Dynamic viscosity μ (Pa.s)	1.002×10^{-3}	2.159×10^{-3}	8.000×10^{-3}
Kinematic viscosity ν (m^2.s^{-1})	1.004×10^{-6}	3.393×10^{-7}	3.200×10^{-7}
Bulk viscosity η (Pa.s)	3.006×10^{-3}	1.295×10^{-3}	4.800×10^{-4}
Thermal conductivity κ (W.m^{-1}.K^{-1})	0.61	24	60
Ratio of specific heats γ	1.01	1.11	1.33
Prandtl number Pr	6.87	0.03	0.01
Attenuation coeff. α (m^{-1}, for $f = 2$ MHz)	0.105	0.007	0.011
Attenuation length $1/\alpha$ (m, for $f = 2$ MHz)	9.49	147.58	88.91
α/f^2 (s^2.m^{-1})	2.63×10^{-14}	1.69×10^{-15}	2.81×10^{-15}
Viscous contribution $\left(\frac{4}{3}\mu + \eta\right)$ to α (Pa.s)	4.34×10^{-3}	4.17×10^{-3}	1.55×10^{-3}
Thermal contribution $\left(\frac{\gamma - 1}{Pr}\mu\right)$ to α (Pa.s)	9.64×10^{-7}	7.15×10^{-3}	1.96×10^{-2}

Thèse accessible à l'adresse : https://theses.insa-lyon.fr/publication/2024ISAL0101/these.pdf © [B. Vincent], [2024], INSA Lyon, tous droits réservés

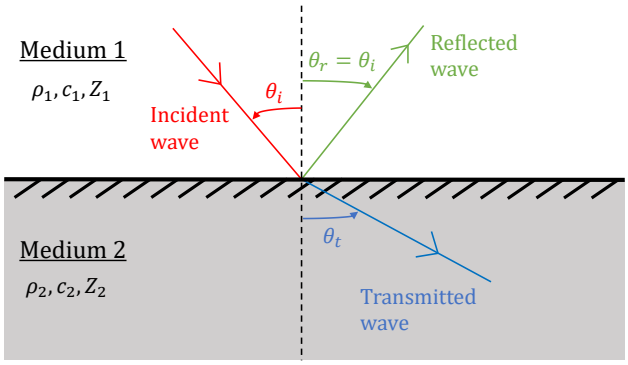


Figure 1.3: Sketch of an incident acoustic wave (red) being transmitted (blue) and reflected (green) at a liquid-solid interface.

where $\boldsymbol{n}$ is the unit vector normal to S. In an unattenuating medium, P_{ac} remains constant. However, sound attenuation causes P_{ac} to decrease along the wave propagation direction. For a wave emitted at $x = 0$ and travelling in the x direction, (1.20) yields:

$$P_{ac}(x) = P_{ac,0}\, e^{-2\alpha x}\,, \tag{1.21}$$

where $P_{ac,0}$ is the acoustic power radiated by the source.

1.2.4 Reflection of linear sound waves on a smooth interface

At the interface between two media 1 and 2, an incident sound wave can either be reflected, transmitted, or both (figure 1.3). The transmission angles θ_i and θ_t (with respect to the direction normal to the interface), respectively, verify the Snell-Descartes law:

$$\frac{\sin(\theta_i)}{c_1} = \frac{\sin(\theta_t)}{c_2}\,, \tag{1.22}$$

where c_1 and c_2 are the wave velocities in media 1 and 2, respectively. In a solid, transmitted waves can either travel as longitudinal waves (phase speed c_l) or transverse waves (phase speed c_{tr}).

Equation (1.22) shows that an increase of θ_i translates into an increase of θ_t, up to a critical incident angle $\theta_{i,cr}$ beyond which waves can no longer be transmitted ($\theta_t = \pi/2$), i.e., incident waves are perfectly reflected:

$$\theta_{i,cr} = \operatorname{asin}\left(\frac{c_1}{c_2}\right)\,. \tag{1.23}$$

The value of $\theta_{i,cr}$ depends on whether an incident sound wave is transmitted as a longitudinal or transverse wave to the solid. Using the material properties of water and glass listed in table 1.2:

- For longitudinal waves: $\theta_{i,cr} = 15.4°$.
- For transverse waves: $\theta_{i,cr} = 26.7°$.

Finally, a wave reaching a surface at an angle $\theta_i < \theta_{i,cr}$ creates both reflected and transmitted waves. The amount of acoustic power being transmitted or reflected is given

Thèse accessible à l'adresse : https://theses.insa-lyon.fr/publication/2024ISAL0101/these.pdf © [B. Vincent], [2024], INSA Lyon, tous droits réservés

Table 1.2: Properties of the fluid (water, taken from Dinçer & Zamfirescu (2015) at 20 °C) and cavity material (Pyrex glass, taken from Blackstock (2000)) used in the experimental study of a three-dimensional flow driving by reflected waves (chapter 5). In a fluid, sound waves are longitudinal waves so that $c_l = c$.

Material	Density ρ_0 (kg/m^3)	Longitudinal speed of sound c_l(m/s)	Transverse speed of sound c_{tr} (Pa.s)	Specific acoustic impedance $Z = \rho_0 c_l$ (Pa.s/m)
Water	998.2	1483	–	1.48×10^6
Glass (Pyrex)	2300	5600	3300	1.29×10^7

by the power transmission and reflection coefficients R and $T = 1 - R$ defined as:

$$R = \left[\frac{Z_2 \cos(\theta_i) - Z_1 \cos(\theta_t)}{Z_2 \cos(\theta_i) + Z_1 \cos(\theta_t)}\right]^2 ,$$

$$T = \frac{4 Z_1 Z_2 \cos(\theta_i) \cos(\theta_t)}{\left[Z_2 \cos(\theta_i) + Z_1 \cos(\theta_t)\right]^2} .$$

In the experimental work presented in chapter 5, $\theta_i = 45°$ and the fluid is water, hence $R \approx 1$ and $T \approx 0$.

1.3 Theoretical description of acoustic streaming

1.3.1 Modelling acoustic streaming

Models of Eckart streaming can be divided into two main categories: those based on the small perturbation expansion of the flow variables about a given state, and those relying on the discrepancy between the acoustic (fast) and streaming (slow) time scales.

1.3.1.1 First approach: small perturbation expansion of the flow variables

The first attempts to model Eckart streaming go back to Eckart (1948), Nyborg (1953) and Westervelt (1953), who relied on a small perturbation expansion of the flow variables.

I shall consider the derivation of Nyborg (1953) and Riaud *et al.* (2017) to show how the streaming equations are obtained. To do so, the authors assumed that:

(i) The thermodynamic processes are isentropic so that the problem is fully described by:

$$\rho\left[\frac{\partial \boldsymbol{u}}{\partial t} + (\boldsymbol{u}\cdot\boldsymbol{\nabla})\,\boldsymbol{u}\right] = -\boldsymbol{\nabla} p + \mu \boldsymbol{\nabla}^2 \boldsymbol{u} + \left(\frac{\mu}{3} + \eta\right)\boldsymbol{\nabla}\left(\boldsymbol{\nabla}\cdot\boldsymbol{u}\right) , \tag{1.25a}$$

$$\frac{\partial \rho}{\partial t} + \boldsymbol{\nabla}\cdot(\rho \boldsymbol{u}) = 0 , \tag{1.25b}$$

$$p = p(\rho) . \tag{1.25c}$$

(ii) The flow variables can be expressed as a small perturbation expansion around an homogeneous medium at rest:

$$\boldsymbol{u} = \boldsymbol{0} + M_{ac}\boldsymbol{u_{ac}} + M_{ac}^2 \boldsymbol{u_s} + \mathcal{O}\left(M_{ac}^3\right) \tag{1.26a}$$

$$p = p_0 + M_{ac} p_{ac} + M_{ac}^2 p_s + \mathcal{O}\left(M_{ac}^3\right) \tag{1.26b}$$

$$\rho = \rho_0 + M_{ac}\rho_{ac} + M_{ac}^2 \rho_s + \mathcal{O}\left(M_{ac}^3\right) \tag{1.26c}$$

Thèse accessible à l'adresse : https://theses.insa-lyon.fr/publication/2024ISAL0101/these.pdf © [B. Vincent], [2024], INSA Lyon, tous droits réservés

with $M_{ac} = u_0/c \ll 1$ the acoustic Mach number, and $u_0 \sim \|\boldsymbol{u_{ac}}\|$. In equation (1.26), the $\mathcal{O}(M_{ac})$ terms correspond to acoustic quantities, meaning that (i) these terms are periodic with a zero time average, and (ii) $\boldsymbol{\nabla} \times \boldsymbol{u_{ac}} = \boldsymbol{0}$. In contrast, the $\mathcal{O}(M_{ac}^2)$ terms are associated with the streaming flow and have a non-zero time average.

(iii) The streaming flow is steady: $\partial \rho_s/\partial t = 0$ and $\partial \boldsymbol{u_s}/\partial t = \boldsymbol{0}$.

Introducing the perturbation expansion (1.26) in the flow equations (1.25) and keeping only the $\mathcal{O}(M_{ac})$ terms, one recovers the equations of attenuated linear acoustics (1.13) in their isentropic form, i.e., with $s_{ac} = 0$ (and T_{ac} is decoupled from the problem). Attenuation is thus solely due to viscosity.

To obtain the streaming equations, Nyborg (1953) and Riaud *et al.* (2017) kept higher-order terms. Up to $\mathcal{O}(M_{ac}^2)$, the time-averaged continuity equation (1.25b) becomes:

$$\boldsymbol{\nabla} \cdot \boldsymbol{u_s} = -\frac{1}{\rho_0} \boldsymbol{\nabla} \cdot \langle \rho_{ac} \boldsymbol{u_{ac}} \rangle \ .$$

As explained by Riaud *et al.* (2017), the magnitude of right-hand side of the equation above is related to sound attenuation. In particular, when the attenuation length is significantly larger than λ (i.e., $\alpha\lambda \ll 1$), $\boldsymbol{\nabla} \cdot \langle \rho_{ac} \boldsymbol{u_{ac}} \rangle$ becomes negligibly small, so that:

$$\boldsymbol{\nabla} \cdot \boldsymbol{u_s} = 0 \, . \tag{1.27}$$

Collecting the $\mathcal{O}(M_{ac}^2)$ in the momentum equation (1.25a) gives, after time-averaging:

$$\left\langle \rho_{ac} \frac{\partial \boldsymbol{u_{ac}}}{\partial t} \right\rangle + \rho_0 \left\langle (\boldsymbol{u_{ac}} \cdot \boldsymbol{\nabla}) \, \boldsymbol{u_{ac}} \right\rangle = -\boldsymbol{\nabla} p_s + \mu \boldsymbol{\nabla}^2 \boldsymbol{u_s}$$

$$\leftrightarrow \boldsymbol{0} = -\boldsymbol{\nabla} p_s + \mu \boldsymbol{\nabla}^2 \boldsymbol{u_s} + \boldsymbol{F} \, , \tag{1.28}$$

in which equations (1.27) and (1.13a) have been used. In equation (1.28), $\boldsymbol{F}$ is a forcing term defined as[1]:

$$\boldsymbol{F} = -\rho_0 \boldsymbol{\nabla} \cdot \langle \boldsymbol{u_{ac}} \otimes \boldsymbol{u_{ac}} \rangle = -\rho_0 \left\langle (\boldsymbol{u_{ac}} \cdot \boldsymbol{\nabla}) \, \boldsymbol{u_{ac}} \right\rangle - \rho_0 \left\langle \boldsymbol{u_{ac}} \boldsymbol{\nabla} \cdot \boldsymbol{u_{ac}} \right\rangle \ . \tag{1.29}$$

The streaming flow is thus forced by Reynolds stresses arising from the propagation of sound waves. Nyborg (1953) further developed $\boldsymbol{F}$ for attenuated plane waves; however, this approach is restrictive as it is limited to a specific wave type. More recently, Riaud *et al.* (2017) extended the result of Nyborg and showed that:

$$\boldsymbol{F} = -\boldsymbol{\nabla} \mathcal{L}_{ac} + \frac{2\alpha}{c} \boldsymbol{I_{ac}}, \tag{1.30}$$

where $\mathcal{L}_{ac} = E_{c,ac} - E_{p,ac}$ is the acoustic Lagrangian, with $E_{c,ac}$ and $E_{p,ac}$ the acoustic kinetic and potential energies respectively defined as:

$$E_{c,ac} = \left\langle \frac{1}{2} \rho_0 \|\boldsymbol{u_{ac}}\|^2 \right\rangle \ , \quad E_{p,ac} = \left\langle \frac{p_{ac}^2}{2\rho_0 c^2} \right\rangle \ . \tag{1.31}$$

The first term in $\boldsymbol{F}$ being a gradient of a scalar potential, it is balanced by a change of hydrostatic pressure and thus cannot drive the streaming flow (Lighthill, 1978; Batchelor, 2000). The streaming momentum equation (1.28) can thus be written as:

$$\boldsymbol{0} = -\boldsymbol{\nabla} p_s' + \mu \boldsymbol{\nabla}^2 \boldsymbol{u_s} + \frac{2\alpha}{c} \boldsymbol{I_{ac}} \, , \tag{1.32}$$

[1] As both ρ_{ac} and $\boldsymbol{u_{ac}}$ are periodic, $\left\langle \frac{\partial (\rho_{ac} \boldsymbol{u_{ac}})}{\partial t} \right\rangle = \boldsymbol{0}$.

Thèse accessible à l'adresse : https://theses.insa-lyon.fr/publication/2024ISAL0101/these.pdf © [B. Vincent], [2024], INSA Lyon, tous droits réservés

with $p_s' = p_s + \mathcal{L}_{ac}$. Equations (1.32) and (1.27) show that, whilst the propagation of sound is a compressible process, acoustic streaming is an incompressible flow driven by an acoustic body force. This forcing vanishes when $\alpha = 0$, confirming that attenuation is a key ingredient for acoustic streaming to occur.

Although being widely used, especially in the field of microfluidics, the model (1.32) suffers from two major problems: first, streaming velocities are assumed to be second-order quantities. For streaming flows over decimetric distances, this is rarely the case: several experiments made in water showed that the streaming velocity can be comparable to the acoustic velocity at the source (see table A.1).

The second issue is a consequence of the first one: assuming second-order streaming velocities results in an inertia-free momentum equation (1.32). As pointed out by Lighthill (1978), that equation is thus valid when $Re_s = \rho_0 U_s L_s/\nu < 1$ (where U_s is a streaming velocity scale), i.e., when inertia forces are negligible. To alleviate this issue, Lighthill (1978) suggested to simply add the inertia terms to the streaming momentum equation (1.32), without however providing a rigorous derivation to support this modification.

1.3.1.2 Second approach: time scales separation

Non-weighted time average description of the streaming flow velocity

The first theoretical developments to include the effects of inertia in the streaming equations go back to the work of Statnikov (1967), which has then been translated to English by Zarembo (1971). The idea of these authors is to split $\boldsymbol{u}$, ρ and p into a mean part associated with the streaming flow (subscript "s") and varying over large time scales (compared to the acoustic period), and a zero-mean periodic contribution (subscript "ac") corresponding to the acoustic signal:

$$\boldsymbol{u} = \boldsymbol{u_s} + \boldsymbol{u_{ac}}\,, \tag{1.33a}$$

$$\rho = \rho_s + \rho_{ac} \tag{1.33b}$$

$$p = p_s + p_{ac}\,. \tag{1.33c}$$

This decomposition is thus analogous to the Reynolds decomposition in turbulence (Chassaing *et al.*, 2002). Besides this decomposition, Statnikov (1967) and Zarembo (1971) further assume that:

(i) The density fluctuations are small: $\rho_{ac} \ll \rho_s$.[2]
(ii) The streaming flow is steady: $\partial\rho_s/\partial t = 0$ and $\partial\boldsymbol{u_s}/\partial t = \boldsymbol{0}$.
(iii) The streaming flow is slow compared to the speed of sound, i.e., $\|\boldsymbol{u_s}\| \ll c$.

In contrast to Nyborg (1953), no assumption is made on the order of $\boldsymbol{u_s}$ relative to $\boldsymbol{u_{ac}}$.

Inserting the decomposition (1.33) in the compressible continuity (1.2) equation and averaging over an acoustic period gives:

$$\boldsymbol{\nabla}\cdot\left[\rho_0\left(\boldsymbol{u_s} + \frac{\langle\rho_{ac}\boldsymbol{u_{ac}}\rangle}{\rho_0}\right)\right] = 0\,. \tag{1.34}$$

Because of assumption (iii), Statnikov (1967) took $\rho_s \approx \rho_0$. Combined with $\rho_{ac} \ll \rho_s$, Statnikov (1967) then simplified equation (1.34) to finally obtain

$$\boldsymbol{\nabla}\cdot\boldsymbol{u_s} \approx \boldsymbol{0}\,. \tag{1.35}$$

[2] This is equivalent to assuming $M_{ac} \ll 1$. Taking $\rho_s \sim \rho_0$ and using the linear equation of state (1.17) together with the specific acoustic impedance (1.18) gives: $\rho_{ac}/\rho_0 \sim p_{ac}/\left(\rho_0 c^2\right) \sim u_{ac}/c \ll 1$.

Thèse accessible à l'adresse : https://theses.insa-lyon.fr/publication/2024ISAL0101/these.pdf © [B. Vincent], [2024], INSA Lyon, tous droits réservés

For the momentum equation, Statnikov (1967) first divided equation (1.25a) by ρ before introducing the time-scale decomposition (1.33). After time-averaging, the right-hand side of the resulting equation features only terms proportional to $1/\rho$. As $\rho_{ac} \ll \rho_s$, Statnikov (1967) applied a Taylor's expansion to each of these terms and obtained:

$$(\boldsymbol{u_s} \cdot \boldsymbol{\nabla})\, \boldsymbol{u_s} = -\frac{1}{\rho_0}\boldsymbol{\nabla} p_s + \frac{\mu}{\rho_0}\boldsymbol{\nabla}^2 \boldsymbol{u_s} + \frac{\boldsymbol{F}}{\rho_0}\,, \tag{1.36}$$

with $\boldsymbol{F}$ an external forcing defined as:

$$\begin{aligned}\boldsymbol{F} = &\left\langle \frac{\rho_{ac}}{\rho_0}\boldsymbol{\nabla} p_{ac} \right\rangle - \mu \left\langle \frac{\rho_{ac}}{\rho_0}\boldsymbol{\nabla}^2 \boldsymbol{u_{ac}} \right\rangle - \left(\frac{\mu}{3} + \eta\right) \left\langle \frac{\rho_{ac}}{\rho_0}\boldsymbol{\nabla}\left(\boldsymbol{\nabla} \cdot \boldsymbol{u_{ac}}\right) \right\rangle \\ &- \rho_0 \left\langle (\boldsymbol{u_{ac}} \cdot \boldsymbol{\nabla})\, \boldsymbol{u_{ac}} \right\rangle .\end{aligned} \tag{1.37}$$

This ends the derivation of Statnikov (1967) and Zarembo (1971).

The forcing term (1.37) looks rather complicated; I shall develop it further for the sake of comparison with the small-perturbation-expansion approach. As $\boldsymbol{\nabla} \times \boldsymbol{u_{ac}} = 0$, $\boldsymbol{\nabla}\left(\boldsymbol{\nabla} \cdot \boldsymbol{u_{ac}}\right) = \boldsymbol{\nabla}^2 \boldsymbol{u_{ac}}$. Then, the isentropic equation of state (1.17) can be used to rewrite equation (1.37) as:

$$\boldsymbol{F} = -\boldsymbol{\nabla}\mathcal{L}_{ac} - \left(\frac{4}{3}\mu + \eta\right) \left\langle \frac{\rho_{ac}}{\rho_0}\boldsymbol{\nabla}^2 \boldsymbol{u_{ac}} \right\rangle , \tag{1.38}$$

Then, using the unattenuated (i.e., for $\alpha = 0$) Helmholtz equation (1.15) together with the equation of state (1.17) gives[3]:

$$\left\langle \frac{\rho_{ac}}{\rho_0}\boldsymbol{\nabla}^2 \boldsymbol{u_{ac}} \right\rangle \approx -\frac{k^2}{\rho_0 c^2}\boldsymbol{I_{ac}}\,.$$

Therefore, the streaming momentum equation (1.36) finally becomes:

$$\rho_0\, (\boldsymbol{u_s} \cdot \boldsymbol{\nabla})\, \boldsymbol{u_s} = -\boldsymbol{\nabla} p_s' + \mu \boldsymbol{\nabla}^2 \boldsymbol{u_s} + \frac{2\alpha}{c}\boldsymbol{I_{ac}}\,. \tag{1.39}$$

The acoustic forcing term is *exactly* the same as in equation (1.32); the only difference is that inertia forces are correctly accounted for in equation (1.39).

Unaware of the work of Statnikov (1967) and Zarembo (1971), Moudjed *et al.* (2014*a*) re-derived equation (1.39) using the same approach but for an unsteady flow; the corresponding streaming equations are those given in the introduction (equation (1.1)). The excellent agreement between their simulations and water experiments proved that including inertia forces is essential to correctly model decimetric Eckart streaming flows. This confirms the superiority of the time-scale discrepancy approach over the traditional small-perturbation method to derive the streaming equations.

[3] One may question the choice of using the unattenuated form of the Helmholtz equation. The underlying idea is that the effects of attenuation on sound propagation are small (although these effects are cumulative). Since the term of interest in (1.38) is already multiplied by an attenuation-related quantity, substituting the *attenuated* Helmholtz equation for $\boldsymbol{\nabla}^2 \boldsymbol{u_{ac}}$ would result in additional terms of negligible magnitudes. In the case of purely viscous attenuation, we can actually show that using the *attenuated* Helmholtz equation gives $\left\langle \frac{\rho_{ac}}{\rho_0}\boldsymbol{\nabla}^2 \boldsymbol{u_{ac}} \right\rangle = -\frac{\omega^2}{\rho_0 c^4}\boldsymbol{I_{ac}} - \frac{2\alpha}{\rho_0 c}\boldsymbol{\nabla} E_{p,ac}$ (the derivation requires the exact expressions (2.3) of the real and imaginary parts of k_c), so that equation (1.38) becomes $\boldsymbol{F} = -\boldsymbol{\nabla}\mathcal{L}_{ac} + \frac{2\alpha}{c}\boldsymbol{I_{ac}} + \left(\frac{2\alpha c}{\omega}\right)^2 \boldsymbol{\nabla} E_{p,ac}$. The additional term not only has a small magnitude when sound attenuation is weak (as that term is multiplied by the squared ratio between the wavelength and the attenuation length), but it is also a potential term that cannot drive the flow. Thus, evaluating $\boldsymbol{\nabla}^2 \boldsymbol{u_{ac}}$ using the unattenuated Helmholtz equation instead of its attenuated counterpart does not affect the expression of the forcing term responsible for acoustic streaming.

Thèse accessible à l'adresse : https://theses.insa-lyon.fr/publication/2024ISAL0101/these.pdf © [B. Vincent], [2024], INSA Lyon, tous droits réservés

Density-weighted time-average description of the streaming flow velocity

The time-scale discrepancy exposed in the previous section relied on the Reynolds decomposition of the flow variables; this is however not the only choice possible.

As we saw, the Reynolds decomposition for $\boldsymbol{u}$ and ρ leads to a source term $\boldsymbol{\nabla \cdot} \langle \rho_{ac} \boldsymbol{u_{ac}} \rangle$ in the time-averaged continuity equation (1.34). To provide a mass-source-free description of Eckart streaming, Rudenko & Soluyan (1977) suggested to instead write $\boldsymbol{u}$ as:

$$\boldsymbol{u} = \widetilde{\boldsymbol{u}} + \boldsymbol{u'}\,, \tag{1.40}$$

with a new definition of the mean (hence, streaming) velocity $\widetilde{\boldsymbol{u}}$ based on a density-weighted time average:

$$\widetilde{\boldsymbol{u}} = \frac{\langle \rho \boldsymbol{u} \rangle}{\langle \rho \rangle} = \boldsymbol{u_s} + \frac{\langle \rho_{ac} \boldsymbol{u_{ac}} \rangle}{\rho_s}\,. \tag{1.41}$$

Although not mentioned as such by the authors, $\widetilde{\boldsymbol{u}}$ is called *Favre-averaged* velocity (Favre, 1958) and is commonly encountered in variable-density turbulence modelling (Chassaing *et al.*, 2002)[4]. The main advantage of $\widetilde{\boldsymbol{u}}$ over $\boldsymbol{u_s}$ is that equation (1.34) reduces to $\boldsymbol{\nabla \cdot} \widetilde{\boldsymbol{u}} = \boldsymbol{0}$ without further assumptions. Rudenko & Soluyan (1977) then derived a streaming momentum equation based on $\widetilde{\boldsymbol{u}}$ instead of $\boldsymbol{u_s}$ and obtained the same acoustic forcing expression as in equation (1.39) (Kamakura *et al.*, 1995; Mitome, 1998).

The coexistence of two streaming velocity definitions raises the question of which time average should be preferred: a Reynolds or Favre average ? This modelling decision can be made based on experimental and theoretical considerations. From the standpoint of an experimentalist, it is easier to measure $\boldsymbol{u_s}$ than $\widetilde{\boldsymbol{u}}$, as the later requires the knowledge of $\langle \rho_{ac} \boldsymbol{u_{ac}} \rangle$; however, the order of magnitude of the latter is usually small. For a plane attenuated wave of amplitude u_0, equation (1.41) gives:

$$\frac{\|\widetilde{\boldsymbol{u}} - \boldsymbol{u_s}\|}{\|\boldsymbol{u_s}\|} = \frac{\| \langle \rho_{ac} \boldsymbol{u_{ac}} \rangle \|}{\rho_s \|\boldsymbol{u_s}\|} \sim \frac{u_0^2}{2cU_s}\,,$$

with U_s the order of magnitude of the streaming velocity[5]. In the case of Mitome (1998), who compared experimentally-measured $\boldsymbol{u_s}$ to numerically-simulated $\widetilde{\boldsymbol{u}}$ without noticing their different mathematical definitions, $u_0^2/(2cU_s) \sim 10^{-4}$ (table A.1). The difference between the streaming velocity defined using either a Reynolds or Favre average is thus marginal.

The main difference between the Reynolds and Favre decompositions relates to the fluctuations. Again, sound waves are defined as zero-mean signals, with a curl-free velocity fluctuation. However, it is easy to prove that none of these properties are verified by $\boldsymbol{u'}$, as:

$$\boldsymbol{u'} = \boldsymbol{u_{ac}} - \frac{\langle \rho_{ac} \boldsymbol{u_{ac}} \rangle}{\rho_s} = \boldsymbol{u_{ac}} - \frac{\boldsymbol{I_{ac}}}{\rho_s c^2}\,, \quad \rightarrow \langle \boldsymbol{u'} \rangle = -\frac{\boldsymbol{I_{ac}}}{\rho_s c^2} \neq \boldsymbol{0}\,.$$

Furthermore, since $\boldsymbol{I_{ac}}$ shapes the acoustic forcing field driving the flow, $\boldsymbol{\nabla} \times \boldsymbol{I_{ac}} \neq \boldsymbol{0}$; hence, $\boldsymbol{\nabla} \times \boldsymbol{u'} \neq \boldsymbol{0}$. Therefore, $\boldsymbol{u'}$ **does not** describe the velocity fluctuation caused by sound.

[4] In turbulence, only $\boldsymbol{u}$ is Favre-averaged; all the other quantities are averaged using the Reynolds (i.e., non-weighted) time average.

[5] Consider the plane attenuated wave travelling in the $+x$-direction $\boldsymbol{u_{ac}} = u_0 e^{j(\omega t - kx)}\, \boldsymbol{e_x}$. Using the linearised continuity equation (1.13a), one obtains: $\| \langle \rho_{ac} \boldsymbol{u_{ac}} \rangle \| = \rho_0 u_0^2 / (2c)$. Finally, taking $U_s \sim \|\boldsymbol{u_s}\|$ yields $\| \langle \rho_{ac} \boldsymbol{u_{ac}} \rangle \| / (\rho_0 \|\boldsymbol{u_s}\|) = u_0^2 / (2cU_s)$.

Thèse accessible à l'adresse : https://theses.insa-lyon.fr/publication/2024ISAL0101/these.pdf © [B. Vincent], [2024], INSA Lyon, tous droits réservés

The inappropriateness of $\boldsymbol{u'}$ for modelling acoustic velocities means that, whenever the streaming velocity is taken as a Favre-averaged (density-weighted time average) $\boldsymbol{u}$, acoustic signals shall still be modelled as deviations from a Reynolds-averaged (i.e, non-weighted time-average) $\boldsymbol{u}$. The coexistence of these two definitions makes theoretical developments clumsy; especially when working on the equations for the acoustic fluctuations. **From now, all the velocities (acoustic and streaming) are based on the Reynolds decomposition** (1.33a)**.**

1.3.1.3 Current trends in the modelling of Eckart streaming

There is a continuous effort on developing new Eckart and Rayleigh-Schlichting streaming models accounting for more complex phenomena such as stratification (Michel & Chini, 2019) or thermally-induced viscosity gradients (Joergensen & Bruus, 2023), for instance. Besides of the time scales separation, these models may also rely on the length scales discrepancy between the streaming flow and the sound field (Orosco & Friend, 2022).

So far, streaming models assume that the development of an Eckart streaming flow does not affect the acoustic field. Is it always the case ? Recently, Dubrovski *et al.* (2023) derived equations for both $\boldsymbol{u_s}$ and $\boldsymbol{u_{ac}}$ based on the time-scales separation approach, and investigated numerically the effect of streaming on sound propagation. For this feedback mechanism to be significant, the authors needed to force the flow with large amplitude waves (up to $M_{ac} \sim 0.1$, which is largely above usual sound amplitudes even in strongly nonlinear acoustics (Coulouvrat, 1992)). Although these simulations showed that a two-way coupling between the acoustic and streaming problems is possible, the conditions under which it occurs still need to be clarified.

Generally speaking, the ability of the streaming flow to affect the sound field raises the questions of what are the mechanisms of energy transfer between the acoustic and streaming scales. The streaming flow arising from the attenuation of sound waves may be intuitively thought as acoustic energy being converted into flow kinetic energy along the sound travelling path. Are there other streaming mechanisms ? Under which conditions ? And following the work of Dubrovski *et al.* (2023), how may the flow alter the sound field ? **In this thesis, I shall lay down the budget equations for the streaming and acoustic kinetic energies**, a first milestone towards understanding energy transfer in acoustic streaming.

1.3.2 Momentum flux for a streaming jet forced by an attenuated beam

Lighthill (1978) was the first one to clearly identify the role of P_{ac} and α on the momentum acquired by the streaming flow. He considered the case of an axisymmetric beam driving a steady axisymmetric jet along $\boldsymbol{e_x}$ without pressure forces. The streaming equations (1.1) thus reduce to the incompressible continuity and boundary-layer equations together with an axial acoustic force:

$$\frac{\partial u_{s,x}}{\partial x} + \frac{1}{r}\frac{\partial \left(r u_{s,r}\right)}{\partial r} = 0\,, \tag{1.42a}$$

$$\rho_0 \left(u_{s,x}\frac{\partial u_{s,x}}{\partial x} + u_{s,r}\frac{\partial u_{s,x}}{\partial r} \right) = \frac{\mu}{r}\frac{\partial}{\partial r}\left(r\frac{\partial u_{s,x}}{\partial r} \right) + \frac{2\alpha}{c} I_{ac,x}\,, \tag{1.42b}$$

where $u_{s,x}$ and $u_{s,r}$ are the axial and radial streaming velocity components, respectively, and $I_{ac,x} = \boldsymbol{I_{ac}} \cdot \boldsymbol{e_x}$. Lighthill (1978) then integrated the boundary layer equation (1.42b)

Thèse accessible à l'adresse : https://theses.insa-lyon.fr/publication/2024ISAL0101/these.pdf © [B. Vincent], [2024], INSA Lyon, tous droits réservés

over a disc of infinite radius. After some manipulation involving the continuity equation (1.42a) and the definition P_{ac} (1.20), he finally obtained a theoretical expression for the momentum flux M_{th} of the streaming flow:

$$M_{th} = \rho_0 \int_{\theta=0}^{2\pi} \int_{r=0}^{\infty} u_{s,x}^2 \, r \, \mathrm{d}r \, \mathrm{d}\theta = \frac{P_{ac,0}}{c} \left(1 - e^{-2\alpha x}\right) , \tag{1.43}$$

with θ the azimuthal coordinate. Equation (1.43) is of primary importance, as it illustrates two fundamental properties of Eckart streaming:

(i) The decay of P_{ac} along the beam drives a build-up of M_{th} with x. The length scale over which M_{th} is created is set by $1/(2\alpha)$, i.e., half the attenuation distance.

(ii) As $x \to \infty$, M_{th} does not grow indefinitely, but instead saturates towards $M_{th,\max} = P_{ac,0}/c$. Although α sets the magnitude of the acoustic forcing (equation (1.39)), $M_{th,\max}$ does not involve attenuation but c. Besides, equation (1.43) also shows that only a fraction of $P_{ac,0}$ is used to create momentum.

From a design perspective, these features have a very practical implication: to make the most out of the sound beam, the flow shall be forced over a distance at least comparable to $1/\alpha$; this choice guarantees that 86.5 % of $M_{th,\max}$ is achieved.

1.4 Modelling the acoustic forcing field: the Rayleigh integral

Acoustic intensity sets the shape, the orientation and magnitude of the force driving the streaming flow. In practice, $\boldsymbol{I_{ac}}$ is emitted by an electronic device converting electric energy into acoustic energy: a transducer. Many transducer types exist and can be classified according to their geometry (e.g. circular or rectangular, plane or concave) and sound-generation mechanism (e.g. vibrating membrane, or transmission of surface waves from a solid immersed in a fluid). I shall focus here exclusively on plane circular transducers; such devices have already been used by our group and are known to radiate axisymmetric sound fields. The corresponding unattenuated acoustic pressure field is modelled by the Rayleigh integral.

1.4.1 Formulation of the unattenuated Rayleigh integral

Let (O, x, y, z) be an orthogonal Cartesian coordinate system, with $(\boldsymbol{e_x}, \boldsymbol{e_y}, \boldsymbol{e_z})$ the associated unit vector basis. The vibrating surface S_t of the transducer is a plane disc of diameter D_s centred on $O = (0, 0, 0)$, so that $\boldsymbol{e_x}$ is the acoustic axis (figure 1.4).

As S_t vibrates uniformly at a velocity u_0 with an angular frequency ω, the transducer radiates a time-periodic acoustic pressure field in the $x \geq 0$ semi-infinite fluid volume. Let M be a point of coordinates (x, r) in the fluid domain, and M' a point on S_t. Since the problem is axisymmetric, M is taken in the $(\boldsymbol{e_x}, \boldsymbol{e_y})$ plane. Besides, I shall use a set of polar coordinates (r', θ') to locate M' on S_t (figure 1.4), so that:

$$\begin{aligned} \boldsymbol{OM} &= x\,\boldsymbol{e_x} + r\,\boldsymbol{e_y} = l\cos(\theta)\,\boldsymbol{e_x} + l\sin(\theta)\,\boldsymbol{e_y} , \\ \boldsymbol{OM'} &= r'\cos(\theta')\,\boldsymbol{e_y} + r'\sin(\theta')\,\boldsymbol{e_y} , \end{aligned}$$

with $l = \sqrt{x^2 + r^2}$ and θ the deviation of $\boldsymbol{OM}$ from the acoustic axis. Then, the complex

Thèse accessible à l'adresse : https://theses.insa-lyon.fr/publication/2024ISAL0101/these.pdf © [B. Vincent], [2024], INSA Lyon, tous droits réservés

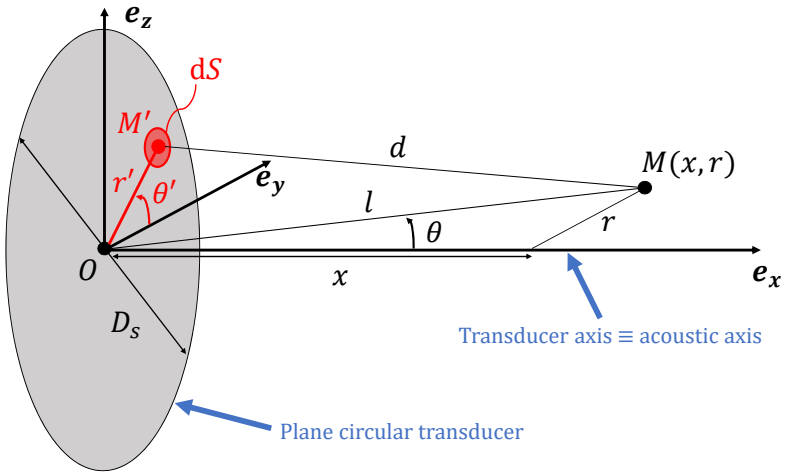


Figure 1.4: Sketch of the plane circular transducer of diameter D_s (grey), modelled as a plane disc vibrating at a uniform velocity u_0 and at an angular frequency ω. The transducer is modelled as an infinite number of point sources, each centred on an elementary surface $\mathrm{d}S$ and contributing to the net acoustic pressure and velocity (hence intensity) levels at M in the fluid domain. As the problem is axisymmetric, M is taken in the (e_x, e_y).

acoustic pressure pressure at M is given by (Kinsler *et al.*, 2000; Blackstock, 2000):

$$p_{ac}\left(t,x,r,\theta\right) = j\frac{\rho_0 c u_0}{\lambda}\iint_{S_t}\frac{e^{j(\omega t-kd)}}{d}\mathrm{d}S\,, \tag{1.44}$$

where d is defined as:

$$\begin{aligned}&\boldsymbol{d} = \boldsymbol{M'M} = x\,\boldsymbol{e_x} + \left[r - r'\cos\left(\theta'\right)\right]\,\boldsymbol{e_y} - r'\sin\left(\theta'\right)\,\boldsymbol{e_z}\,,\\ &\rightarrow d = \|\boldsymbol{d}\| = \sqrt{x^2 + r^2 + r'^2 - 2rr'\cos\left(\theta'\right)} = \sqrt{l^2 + r'^2 - 2lr'\sin\left(\theta\right)\cos\left(\theta'\right)}\,.\end{aligned} \tag{1.45}$$

Equation (1.44) is known as the "Rayleigh integral". It can be seen as an infinite sum of point sources; each of these sources is centred on an elementary surface $\mathrm{d}S$ and radiates a spherical wave contributing to p_{ac} at M.

1.4.2 Analytical solution on the acoustic axis and definition of the near- and far- acoustic fields

The Rayleigh integral (1.44) can be computed analytically for a few specific cases. One of such cases is on the acoustic axis ($r = 0$), where the unattenuated acoustic pressure amplitude $|p_{ac}|$ is given by (Kinsler *et al.*, 2000):

$$|p_{ac}(x, r=0)| = 2\rho_0 c u_0\left|\sin\left[\frac{k}{2}\left(x - \sqrt{x^2 + \frac{D_s^2}{4}}\right)\right]\right|\,. \tag{1.46}$$

The expression of the on-axis acoustic intensity $I_{ac,x}(x, r=0)$ can then be obtained using the specific acoustic impedance (1.18):

$$I_{ac,x}\left(x, r=0\right) = \frac{|p_{ac}\left(x, r=0\right)|^2}{2\rho_0 c} = I_{ac,\max}\sin^2\left[\frac{k}{2}\left(x - \sqrt{x^2 + \frac{D_s^2}{4}}\right)\right]\,, \tag{1.47}$$

Thèse accessible à l'adresse : https://theses.insa-lyon.fr/publication/2024ISAL0101/these.pdf © [B. Vincent], [2024], INSA Lyon, tous droits réservés

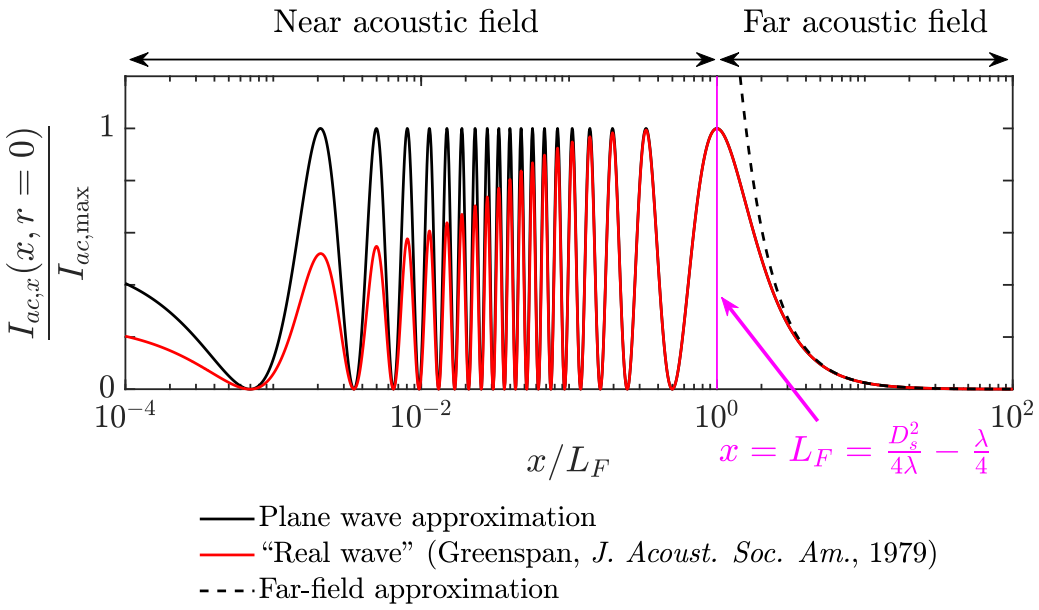


Figure 1.5: Analytical profiles of the unattenuated on-axis acoustic intensity $I_{ac,x}(x, r = 0)$ normalised by the maximum intensity $I_{ac,\max}$ (equation (1.48)). Three profiles are displayed: the intensity profile obtained assuming plane acoustic waves (solid black curve), the "real wave" formula (1.50) of Greenspan (1979) (solid red curve), and the far-field approximation (1.52) (dashed black curve). The vertical purple line locates the Fresnel distance L_F. All the curves are plotted for $D_s = 28.5$ mm and $\lambda = 0.74$ mm (experimental parameters of Moudjed *et al.* (2014*a*)).

where:

$$I_{ac,\max} = 2\rho_0 c u_0^2 \tag{1.48}$$

is the maximum of $I_{ac,x}(x, r = 0)$ for $\alpha = 0$.

The on-axis intensity features successive peaks and zeros, which are followed by a smooth decay (figure 1.5). Each peak position can be determined analytically from the sine term in equation (1.47); in particular, the last intensity peak occurs at the Fresnel distance L_F defined as:

$$L_F = \frac{D_s^2}{4\lambda} - \frac{\lambda}{4} \underset{\lambda \ll D_s}{\approx} \frac{D_s^2}{4\lambda}\,. \tag{1.49}$$

The Fresnel distance is a key quantity defining the structure of $\boldsymbol{I_{ac}}$: it separates the near ($x \leq L_F$) from the far ($x \geq L_F$) acoustic acoustic fields. In addition to $1/\alpha$, L_F thus also sets the "depth" of the acoustic field radiated by a plane circular transducer.

Finally, equation (1.47) is obtained assuming plane acoustic waves. For $x < L_F$ however, the wavefronts are slightly curved; p_{ac} and $\boldsymbol{u_{ac}}$ are not exactly in phase (Moudjed *et al.*, 2015), thus affecting $I_{ac,x}(x, r = 0)$. To obtain a better description of $I_{ac,x}(x, r = 0)$ in the near acoustic field, Greenspan (1979) first derived an expression for $u_{ac,x}(x, r = 0)$ using equation (1.46) and the inviscid form of the linearised Navier-Stokes equation (1.13b). Then, from the definition (1.19) of $\boldsymbol{I_{ac}}$, he obtained:

$$I_{ac}\,(x, r = 0) = \frac{I_{ac,\max}}{2}\left(1 + \frac{x}{\sqrt{x^2 + \frac{D_s^2}{4}}}\right)\sin^2\left[\frac{k}{2}\left(x - \sqrt{x^2 + \frac{D_s^2}{4}}\right)\right]\,. \tag{1.50}$$

Thèse accessible à l'adresse : https://theses.insa-lyon.fr/publication/2024ISAL0101/these.pdf © [B. Vincent], [2024], INSA Lyon, tous droits réservés

Equation (1.50) only differs from its plane-wave counterpart by a factor

$$\frac{1}{2}\left(1+\frac{x}{\sqrt{x^2+\frac{D_s^2}{4}}}\right),$$

which is equal to 0.5 in the near acoustic field ($x < L_F$). In the far acoustic field ($x > L_F$), the plane-wave (1.47) and "real wave" (1.50) expressions of $I_{ac,x}(x, r = 0)$ differ by less than 0.1 % (figure 1.5) and are thus equivalent.

1.4.3 Far-field approximation

In the far acoustic field, $r' \ll l$, so that the Rayleigh integral (1.44) can be simplified to give (Blackstock, 2000):

$$p_{ac}(l,\theta,t) = 2j\rho_0 c u_0 \left(\frac{\pi D_s^2}{8\lambda l}\right)\left[\frac{2J_1\left(k\frac{D_s}{2}\sin\theta\right)}{k\frac{D_s}{2}\sin\theta}\right]e^{j(\omega t-kl)}. \tag{1.51}$$

where J_1 is the first-order Bessel function of the first kind. A far-field approximation of $\|\boldsymbol{I_{ac}}\|$ can then be derived using (1.51) together with the the specific acoustic impedance (1.18). Since $x \gg r$, $l \approx x$ and $\sin\theta \approx r/x$, one finally obtains:

$$\|\boldsymbol{I_{ac}}(x,r)\| = 2\rho_0 c u_0^2 \left(\frac{\pi^2 D_s^4}{64\lambda^2 x^2}\right)\left[\frac{2J_1\left(\frac{kD_s}{2x}r\right)}{\frac{kD_s}{2x}r}\right]^2. \tag{1.52}$$

The far-field $\|\boldsymbol{I_{ac}}\|$ displays a beam-shaped structure made of several lobes (figure 1.6 (a)). The $1/x^2$ decay of the central lobe amplitude is accompanied by a radial enlargement due to the conservation of power along a diffracting beam. The width of the central lobe is set by the first root $R_1 \approx 3.8317$ of J_1 (Abramowitz & Stegun, 1972) which, once equated with the argument of J_1 in equation (1.51), yields:

$$\sin(\theta_c) \approx 1.22\frac{\lambda}{D_s}. \tag{1.53}$$

In equation (1.53), $\sin(\theta_c)$ defines the rate at which the central lobe expands radially as x increases, with θ_c the half diffraction cone angle. The latter is thus a key quantity defining the structure of the acoustic field.

Finally, the question of how to define an effective beam radius can be answered by looking at the acoustic power carried by the central region of the beam. More specifically, I shall define a "truncated power" $P_{ac,tr}$ obtained by integrating $\|\boldsymbol{I_{ac}}\|$ over a disk of radius R and centred on the acoustic axis:

$$P_{ac,tr} = \frac{\rho_0 c u_0^2}{2}\left(\frac{\pi D_s^2}{4}\right)\left[1 - J_0\left(\frac{kD_s R}{2x}\right)^2 - J_1\left(\frac{kD_s R}{2x}\right)^2\right], \tag{1.54}$$

which gives, for $R \to \infty$:

$$P_{ac,tr} = P_{ac,0} = \frac{\rho_0 c u_0^2}{2}\left(\frac{\pi D_s^2}{4}\right). \tag{1.55}$$

Thèse accessible à l'adresse : https://theses.insa-lyon.fr/publication/2024ISAL0101/these.pdf © [B. Vincent], [2024], INSA Lyon, tous droits réservés

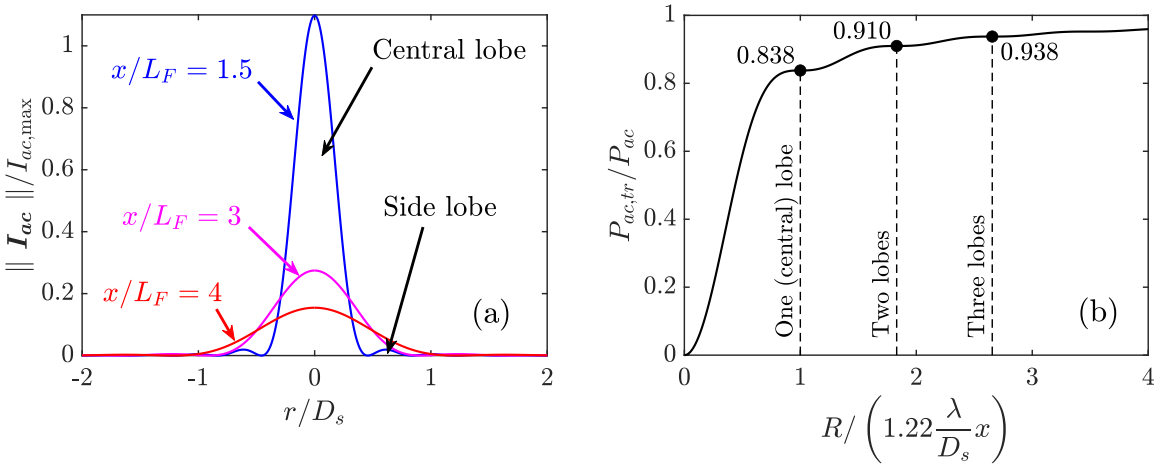


Figure 1.6: (a) Transverse profiles of $\|\boldsymbol{I_{ac}}\|/I_{ac,\max}$ at different distances x/L_F from the source (a). The amplitudes are normalised by the maximum intensity $I_{ac,\max}$ (equation (1.48)), and the radial coordinates r are normalised by the transducer diameter D_s. The profiles are plotted for $D_s = 0.0285$ mm and $\lambda = 0.74$ mm (experimental parameters of Moudjed *et al.* (2014*a*)). (b) Ratio between the acoustic power $P_{ac,tr}$ flowing through a disk of radius R and the total power $P_{ac,0}$, as a function of R. The values of R are normalised by the central lobe radius $1.22\lambda x/D_s$.

Comparing $P_{ac,tr}$ to $P_{ac,0}$ then indicates how much of the total acoustic power flows through a disk of radius R. The evolution of $P_{ac,tr}/P_{ac}$ with R is shown in figure 1.6 (b). The central lobe (the radius of which being $R = 1.22\frac{\lambda}{D_s}x$) contains 83.8 % of $P_{ac,0}$: the radius of the central lobe is thus a representative measure of the beam radius. **Therefore, unless specified otherwise, all mentions of the beam radius refer to the central lobe**.

1.4.4 Numerical computation of the Rayleigh integral

The acoustic axis and the far acoustic field are the rare cases for which analytical expressions of the acoustic intensity can be obtained. In the general case, the Rayleigh integral (1.44) shall be evaluated numerically.

The numerical procedure is the same as Moudjed (2013). The idea is to discretise the transducer surface S_t with an homogeneous grid made of N_s points in both the radial and azimuthal directions. Calling r'_n and θ'_m the radial and azimuthal coordinates of one grid point, the discrete form of (1.44) is:

$$p_{ac} = j\frac{\rho_0 c u_0}{\lambda} e^{j\omega t} \sum_{m=1}^{N_s}\sum_{n=1}^{N_s} \frac{e^{-jk\sqrt{x^2+r^2+{r'_n}^2-2rr'_n\cos(\theta'_m)}}}{\sqrt{x^2+r^2+{r'_n}^2-2rr'_n\cos(\theta'_m)}} r'_n \Delta r' \Delta\theta' \,, \tag{1.56}$$

with $\Delta r'$ and $\Delta\theta'$ the radial and azimuthal grid spacings, respectively. The acoustic intensity magnitude is then obtained by taking the module of (1.56) and using the specific acoustic impedance (1.18):

$$\|\boldsymbol{I_{ac}}\| \approx \frac{|p_{ac}|^2}{2\rho_0 c} \,. \tag{1.57}$$

A two-dimensional map of $\|\boldsymbol{I_{ac}}\|/I_{ac,\max}$ computed for the acoustic parameters of Moudjed *et al.* (2014*a*) (table A.1) and with $N_s = 250$ is shown in figure 1.7. In the

Thèse accessible à l'adresse : https://theses.insa-lyon.fr/publication/2024ISAL0101/these.pdf © [B. Vincent], [2024], INSA Lyon, tous droits réservés

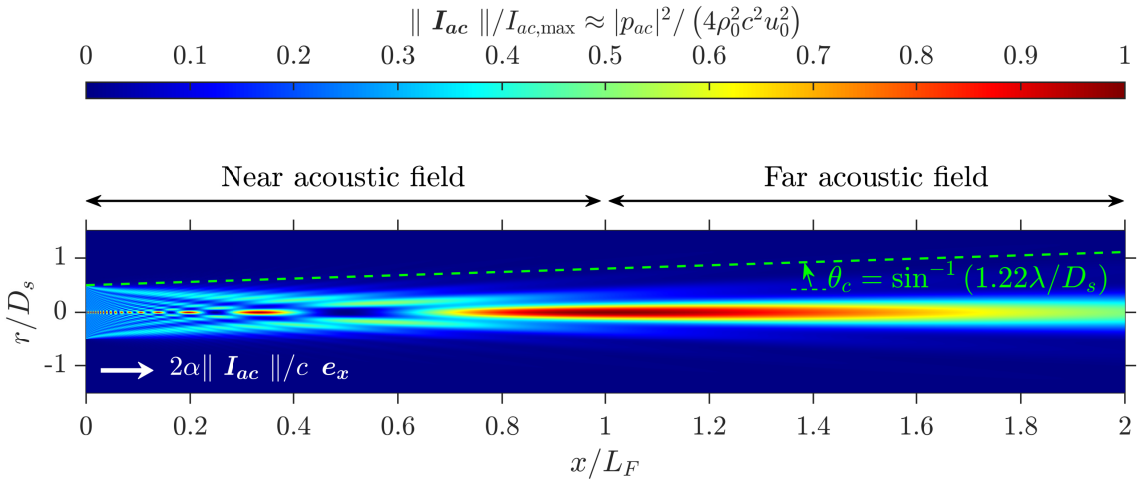


Figure 1.7: Numerical map of the normalised unattenuated acoustic intensity field $\|\boldsymbol{I_{ac}}\|/I_{ac,\max}$ radiated by a plane circular source at $x = 0$. The map is obtained from the numerical integration of the Rayleigh integral (1.56) for a transducer diameter $D_s = 28.5$ mm and a wavelength $\lambda = 0.74$ mm (experimental parameters of Moudjed *et al.* (2014*a*)). The transducer is discretised with $N_s = 250$ grid points in both the radial and azimuthal directions. The diffraction cone is represented by the green dashed line; the cone angle θ_c is also reported (equation (1.53)). The white arrow at the bottom left-hand corner illustrates how Moudjed *et al.* (2014*a*) defined the forcing field from $\|\boldsymbol{I_{ac}}\|$. The x-and r-coordinates are normalised by the Fresnel length L_F (equation (1.49)) and by D_s, respectively.

near acoustic field, the beam radius is approximately $D_s/2$, and regions of high $\|\boldsymbol{I_{ac}}\|$ are only found on the acoustic axis. Diffraction effects become significant in the far acoustic field, where the longitudinal and radial gradients of $\|\boldsymbol{I_{ac}}\|$ are smoother. There, the beam is shaped as a cone of half apex angle θ_c defined by equation (1.53).

The intensity field obtained from equations (1.56) and (1.57) is a scalar field; however, the forcing field driving the streaming flow is also defined by a direction. Our research group essentially considered weak diffraction ($\theta_c \ll 1$) so far and thus followed Moudjed (2013) by taking $\boldsymbol{I_{ac}} \approx \|\boldsymbol{I_{ac}}\|\ \boldsymbol{e_x}$ for a transducer pointing in the $\boldsymbol{e_x}$-direction (see the white arrow in the bottom left-hand corner of figure 1.7). This approximation may however break down when θ_c is no longer small.

To conclude, analytical results of the Rayleigh integral (1.44) are limited to few specific cases; a numerical approach is thus necessary to model the acoustic field driving the streaming flow. Although it does not model sound attenuation, the formulation (1.44) has been used in previous studies of our group; attenuation was only accounted through the prefactor $2\alpha/c$ in the forcing term of the streaming equations (1.1). In this thesis however, I shall investigate streaming jets flowing over distances comparable or greater than $1/\alpha$; effects of attenuation on the *spatial structure* of $\boldsymbol{I_{ac}}$ (hence, of the forcing field) are thus expected to be significant. **Therefore, I shall adapt the Rayleigh integral to account for attenuation**.

Thèse accessible à l'adresse : https://theses.insa-lyon.fr/publication/2024ISAL0101/these.pdf © [B. Vincent], [2024], INSA Lyon, tous droits réservés

1.5 Dimensionless numbers and scaling of acoustic streaming flows

In fluid mechanics, a flow configuration is commonly described by a set of dimensionless parameters, allowing for similarity experiments to be made. I shall first introduce a set of dimensionless numbers describing a streaming configuration, and show how these numbers relate to other commonly-encountered dimensionless quantities. Then, I shall use these dimensionless numbers to review the existing laws for the scaling of streaming jets.

1.5.1 Dimensionless groups governing the acoustics and streaming problems

Acoustic streaming is a complex phenomenon involving different length and time scales. For the case of a streaming jet driven by a single plane baffled transducer, Moudjed *et al.* (2014*a*) identified ten dimensional parameters defining both the streaming and acoustics problems:

- The cavity length L_c and width W_c, together with the transducer (i.e., source) diameter D_s, are the geometrical parameters defining the streaming problem. To ease the comparison with experiments and numerical simulations from the literature, I shall consider the hydraulic diameter D_h of the cavity instead of W_c.
- The fluid parameters are given by ρ_0 and ν.
- The parameters defining the acoustics problem are $P_{ac,0}$, λ, f and α.
- The streaming flow is characterised by the velocity scale U_s.

Taking D_s, $\rho_0 D_s^3$ and D_s^2/ν as length, mass and time scales, respectively, Moudjed *et al.* (2014*a*) applied the Buckingham-Π theorem to derive seven dimensionless groups:

$$N = \chi f^2 L_c\,, \quad S = 1.22\frac{\lambda}{D_s}\,, \quad P = \frac{P_{ac,0} D_s}{\rho_0 \nu^3}\,, \quad F = \frac{f D_s^2}{\nu}\,, \quad L = \frac{L_c}{D_s}\,, \quad D = \frac{D_h}{D_s}\,, \quad U = \frac{U_s D_s}{\nu}\,, \tag{1.58}$$

where $\chi = \alpha/f^2$ involves only the material properties responsible for sound attenuation.

I shall briefly explain the dimensionless numbers (1.58). First, as it compares L_c to the acoustic attenuation length $1/\alpha$, N is a key parameter: following the discussion in section 1.3.2, $N > 1$ ensures that most of the acoustic energy injected into the fluid is used to create streaming kinetic energy. However, the $N > 1$ condition is rarely met in practice (table A.2); **there is thus a crucial need to further explore the $N > 1$ range**. Second, one recognises S as the beam diffraction rate; that parameter thus directly shapes the acoustic forcing field. Third, F compares the viscous diffusion time at the scale of D_s to the acoustic period $1/f$. Fourth, U corresponds to a Reynolds number based on U_s and D_s. Finally, the dimensionless form (based on D_s) of α is N/L.

Using the same length, mass and time scales, the dimensionless forms of the streaming equations (1.1) are:

$$\boldsymbol{\nabla \cdot u_s} = 0\,, \tag{1.59a}$$

$$\frac{\partial \boldsymbol{u_s}}{\partial t} + (\boldsymbol{u_s \cdot \nabla})\,\boldsymbol{u_s} = -\boldsymbol{\nabla} p_s + \boldsymbol{\nabla}^2 \boldsymbol{u_s} + Gr_{ac}\widetilde{\boldsymbol{I}}_{\boldsymbol{ac}}\,. \tag{1.59b}$$

Thèse accessible à l'adresse : https://theses.insa-lyon.fr/publication/2024ISAL0101/these.pdf © [B. Vincent], [2024], INSA Lyon, tous droits réservés

In equation (1.59b), the spatial structure of the acoustic forcing field is prescribed by the normalised intensity $\widetilde{\boldsymbol{I}}_{\boldsymbol{ac}} = \boldsymbol{I}_{\boldsymbol{ac}}/I_{ac,\max}$. The forcing magnitude is set by the acoustic Grashof number Gr_{ac} defined as:

$$Gr_{ac} = \frac{4\alpha u_0^2 D_s^3}{\nu^2} = \frac{32\alpha P_{ac,0} D_s}{\pi \rho_0 c \nu^2} = \frac{32 \times 1.22}{\pi} \frac{NP}{SFL}\,, \tag{1.60}$$

which compares the acoustic forcing magnitude to the viscous forces at the scale of D_s (El Ghani *et al.*, 2021).

I shall mention that the parameters (1.58) and Gr_{ac} are by no means "standard" parameters in the acoustic streaming community. Inspection of the literature indeed shows that different authors may use different dimensionless numbers (table 1.3). A same parameter name may even refer to different quantities depending on the authors (see e.g. the "acoustic Reynolds numbers" in table 1.3). However, to my knowledge, the set of parameters (1.58) is the only one defining all the geometrical, acoustic and flow parameters of a given streaming setup. **In this thesis, the different streaming setups shall be defined using the dimensionless numbers** (1.58)**, and** Gr_{ac} **will be the main control parameter in all my experimental and numerical studies**.

1.5.2 Scaling of acoustic streaming jet flows

1.5.2.1 Acoustic force balanced by either inertia or viscous forces along the jet

Streaming flows forced by a sound beam are shaped as jets (Moudjed *et al.*, 2014*a*), with a strong acceleration near the jet origin ($x = 0$) followed by a region of nearly constant velocity (figure 1.8). Moudjed *et al.* (2014*a*) proposed scaling laws to describe each of these regions:

1. The strong acceleration near the origin suggests that the flow obeys a balance between the acoustic and inertial forces. Assuming that over this jet region (i) the diffraction is weak (i.e., the beam radius is $\approx D_s/2$), and that (ii) attenuation of P_{ac} is negligible, Moudjed *et al.* (2014*a*) showed that:

$$\|\boldsymbol{u_s}\| \sim \frac{1}{2}\sqrt{Gr_{ac}\, x}\,. \tag{1.61}$$

   I shall refer to this regime as the *inertial regime*. The scaling law (1.61) has also been observed in the experiments of Mitome *et al.* (1995) and the numerical simulations of Orosco & Friend (2022).
2. Further downstream, the flatter velocity profile suggests that the flow obeys a balance between acoustic and viscous forces. By taking a similar radial enlargement rate for the beam and for the jet, Moudjed *et al.* (2014*a*) obtained:

$$\|\boldsymbol{u_s}\| \sim \frac{Gr_{ac}}{16}\,. \tag{1.62}$$

   I shall refer to this regime as the *viscous regime*.

The scaling laws proposed by Moudjed *et al.* (2014*a*) correctly estimate the order of magnitude of $\|\boldsymbol{u_s}\|$ in both the inertial and viscous regimes (figure 1.9). In the inertial regime, the scaling law (1.61) differs from streaming measurements by at most a factor 2 (figure 1.9 (a)). However, comparison with the data at constant Gr_{ac} of Kamakura *et al.* (1996) and at constant-x of Mitome (1998) shows that equation (1.61) slightly underestimates the dependency on both x and Gr_{ac}. **Equation** (1.61) **shall thus be improved to better describe the build-up of** $\|\boldsymbol{u_s}\|$ **along** x**.**

Thèse accessible à l'adresse : https://theses.insa-lyon.fr/publication/2024ISAL0101/these.pdf © [B. Vincent], [2024], INSA Lyon, tous droits réservés

Table 1.3: List of dimensionless numbers from the Eckart streaming and acoustics literature, together with their expression in terms of the dimensionless numbers (1.58) derived by Moudjed *et al.* (2014*a*). The dimensionless numbers of Rudenko & Soluyan (1977) and Orosco & Friend (2022) are based on a streaming length scale L_s; it is assumed that $L_c \sim L_s$. A regularly-encountered number is the Strouhal number $\mathcal{S} = M_{ac}^{-1}$ (Riley, 2001; Michel & Chini, 2019; Dubrovski *et al.*, 2023); as M_{ac} is already listed below, $\mathcal{S}$ is not included.

Dimensionless number	Physical interpretation	Original expression	Equivalent expression
Acoustic Mach number M_{ac} (Coulouvrat, 1992)	Ratio of the acoustic velocity amplitude to the speed of sound (measure of acoustic nonlinearity)	$\frac{u_0}{c}$	$\sqrt{\frac{8\times(1.22^3)}{\pi}\frac{P}{(FS)^3}}$
Acoustic Reynolds number $Re_{ac,1}$ (Coulouvrat, 1992)	Ratio between linear propagation effects and viscous forces (measure of sound attenuation)	$\frac{\rho_0 c^2}{\mu\omega}$	$\frac{FS}{2\pi\times(1.22^2)}$
Acoustic Reynolds number $Re_{ac,2}$ (Riaud *et al.*, 2017)	Ratio between the wavelength λ and the (viscous) attenuation distance $1/\alpha$ (measure of sound attenuation)	$\frac{\rho_0 c^2}{\omega\left(\frac{4}{3}\mu+\eta\right)}$	$1.22\pi\frac{L}{NS}$
Acoustic Reynolds number $Re_{ac,3}$ (Rudenko & Soluyan, 1977)	Ratio between nonlinear propagation effects and attenuation effects	$\frac{u_0\omega}{2\alpha c^2}$	$\sqrt{8\pi\times(1.22^5)\times\frac{L^2P}{N^2F^3S^5}}$
Streaming Reynolds number Re_s (Rudenko & Soluyan, 1977; Orosco & Friend, 2022)	Ratio between inertia and viscous forces at the streaming scales	$\frac{U_s L_s}{\nu}$	UL
Froude number Fr (Rudenko & Soluyan, 1977)	Ratio between the streaming kinetic energy and the work of the acoustic force over L_s	$\frac{\rho_0 c U_s^2}{2\alpha I_{ac,\max} L_s}$	$=\frac{\pi}{32\times1.22}\frac{SFU}{NP}=\frac{U}{LGr_{ac}}$
Length scale separation parameter q_λ (Orosco & Friend, 2022)	Ratio between the wavelength λ and a streaming characteristic length scale L_s	$\frac{1}{kL_s}$	$\frac{S}{2.44\pi L}$
Time scale separation parameter q_t (originally called S by Orosco & Friend (2022))	Ratio between the streaming and acoustic time scales	$\frac{\omega L_s}{U_s}$	$\frac{2\pi LF}{U}$

Thèse accessible à l'adresse : https://theses.insa-lyon.fr/publication/2024ISAL0101/these.pdf © [B. Vincent], [2024], INSA Lyon, tous droits réservés

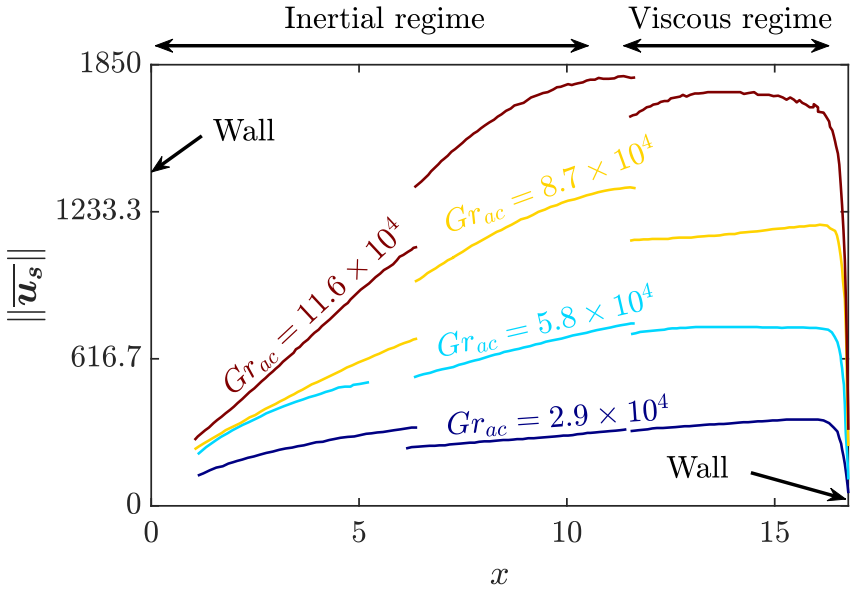


Figure 1.8: Profiles of the time-averaged (over 4.2 minutes) streaming velocity magnitude $\|\overline{\boldsymbol{u_s}}\|$ on the jet axis for different forcing magnitudes Gr_{ac}. The data is taken from the PIV (Particle Image Velocimetry) measurements of Moudjed (2013) (same dimensionless numbers as Moudjed *et al.* (2014*a*) in table A.2) made over three jet sections for each Gr_{ac}, from the jet origin ($x = 0$) to the downstream wall ($x = 16.8$). The transducer is placed at $x = -L_F \approx -9.6$ so that only the far acoustic field drives the flow. All the data is made dimensionless using D_s^2/ν, D_s and $\rho_0 D_s^3$ as time, length and mass scales, respectively.

1.5.2.2 Jet formation at the origin

At distances from the jet origin that are comparable to the transducer diameter, Moudjed *et al.* (2015) noticed that $\boldsymbol{u_s}$ increases more steeply with x than what predicts the inertial scaling law (1.61). By applying a mass balance to a cylindrical control volume near the jet origin (figure 1.10 (a)), the authors showed that:

$$\|\boldsymbol{u_s}\| \sim \sqrt{8Gr_{ac}}\, x^2 \,. \tag{1.63}$$

As shown in figure 1.10 (b), the scaling (1.63) agrees with the numerical simulations of Moudjed *et al.* (2015) and of Kamakura *et al.* (1996) near the source. I stress that equation (1.63) is valid at very close distances from the jet origin only: for $x \geq 0.5$, the jet enters the inertial regime described by equation (1.61).

1.5.2.3 Velocity maximum on the streaming jet axis

The studies of Moudjed *et al.* (2014*a*) focused on straight streaming jets that either kept accelerating over the investigation domain, or reached a velocity plateau near the downstream wall (figure 1.9). However, for larger investigation domains (and more precisely, larger N), different on-axis profiles of $\|\boldsymbol{u_s}\|$ can be observed.

Dentry *et al.* (2014) carried out experiments to study the influence of the acoustic frequency f on the streaming flow. Varying f modifies attenuation (parameters N and N/L) and diffraction (parameter S), and thus affects both the shape and magnitude of the acoustic forcing field. By increasing f up to the GHz range, Dentry *et al.* (2014)

Thèse accessible à l'adresse : https://theses.insa-lyon.fr/publication/2024ISAL0101/these.pdf © [B. Vincent], [2024], INSA Lyon, tous droits réservés

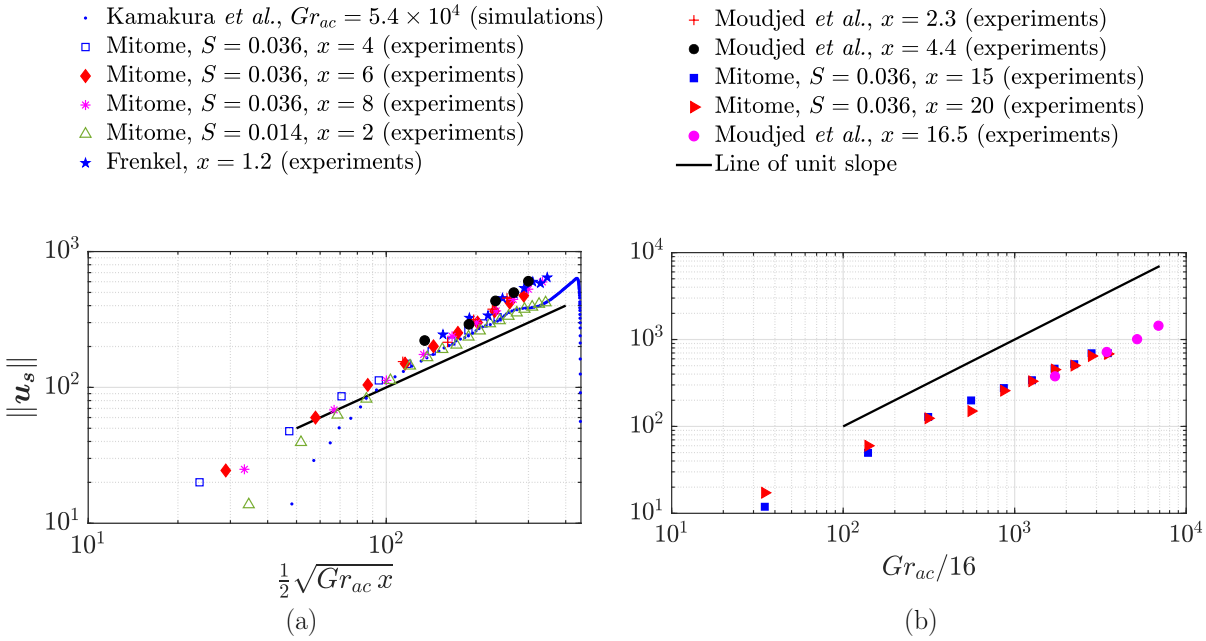


Figure 1.9: Comparison of the centreline streaming velocity magnitude $\|\boldsymbol{u_s}\|$ with the scaling laws derived by Moudjed *et al.* (2014*a*): (a) inertial regime (equation (1.61)) and (b) viscous regime (equation (1.62)). The data is taken from Kamakura *et al.* (1996); Mitome (1998); Frenkel *et al.* (2001); Moudjed *et al.* (2014*a*) (corresponding experimental conditions and dimensionless numbers in tables A.1 and A.2, respectively). All quantities are made dimensionless using D_s, $\rho_0 D_s^3$ and D_s^2/ν as length, mass and time scales, respectively, and $x = 0$ corresponds to the jet origin.

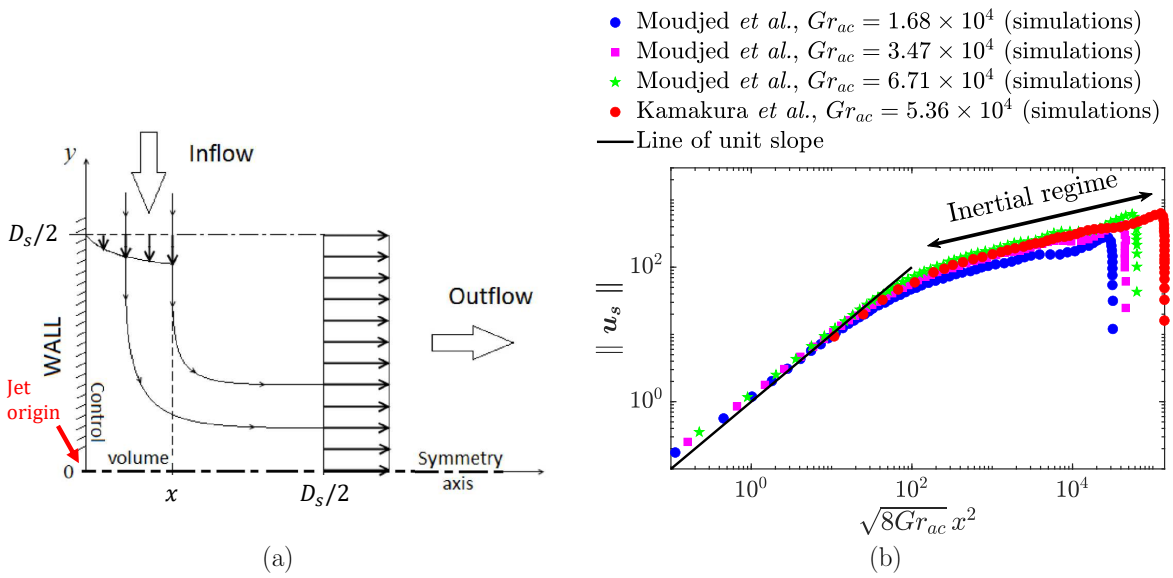
created short jets concentrated near the source (figure 1.11): the streaming velocity thus reaches a maximum before decreasing further downstream. The presence of velocity peak on the jet axis has also been observed in the recent DNS (Direct Numerical Simulations) of Daru *et al.* (2024). Their simulations made at constant S show negligible changes of the peak position x_p with Gr_{ac} (figure 1.12). This suggests that x_p is more closely related to the forcing structure rather than to Gr_{ac}.

Knowing $\boldsymbol{u_s}$ along the entire jet is important to e.g. ensure specific velocity levels at precise locations within the fluid volume. Orosco & Friend (2022) recently proposed a scaling law for x_p based on dimensional analysis. The authors considered f, α, ρ_0 and $P_{ac,0}$ as the most important parameters defining x_p. Using the dimensionless numbers (1.58), the scaling law of Orosco & Friend (2022) reads:

$$x_p \approx 26.4 \left(\frac{Gr_{ac}\, S}{F^2}\right)^{0.1} \left(\frac{L}{N}\right)^{0.6}, \tag{1.64}$$

in which the constant and exponents were obtained by fitting the experimental data of Dentry *et al.* (2014). The error between the predicted and measured x_p remains below 20 % for the data of Dentry *et al.* (2014) (figure 1.13). However, a strong discrepancy is observed between (1.64) and the numerical data of Daru *et al.* (2024), both in terms of the actual x_p values (≥ 50 % error) and on how x_p scales with the control parameters. A valid scaling of x_p thus still needs to be determined. Besides, the jet region downstream x_p has not been investigated in detail yet, meaning that a complete understanding of the different regimes along a streaming jet is still lacking.

Thèse accessible à l'adresse : https://theses.insa-lyon.fr/publication/2024ISAL0101/these.pdf © [B. Vincent], [2024], INSA Lyon, tous droits réservés



(a) (b)

Figure 1.10: Scaling of the jet velocity $\|\boldsymbol{u_s}\|$ on the axis and near the jet origin ($x = 0$). (a) Sketch taken from Moudjed *et al.* (2015) to illustrate how the scaling law (1.63) was derived. The authors applied a mass balance in a cylindrical volume enclosing the origin of an axisymmetric streaming jet. (b) Comparison between the scaling law (1.63) and the numerical simulations of Moudjed *et al.* (2015) and Kamakura *et al.* (1996) (the corresponding dimensionless parameters are given in table A.2) near the jet origin. All quantities are made dimensionless using D_s, $\rho_0 D_s^3$ and D_s^2/ν as length, mass and time scales, respectively.

The evidence of a velocity peak on the jet axis raises the question of why Moudjed *et al.* (2014*a*) did not observe a similar feature. Does the viscous regime identified by Moudjed *et al.* (2014*a*) really exist, or did the authors measure velocity in the vicinity of x_p ? This thesis shall aim to answer these questions.

To conclude, the knowledge on the scaling of streaming jets remains scarce: so far, results of the literature focus on the accelerating region upstream the on-axis $\|\boldsymbol{u_s}\|$ peak, and ignore what happens beyond. **An objective of this thesis is to characterise the streaming jet from its origin and up to distances where the sound beam is fully attenuated, allowing to draw a complete picture of the different regimes along the jet.**

1.6 Stability and dynamics of acoustic streaming jets

Eckart streaming flows are regularly presented as steady (or quasi-steady) flows (Nyborg, 1953; Zarembo, 1971; Riaud *et al.*, 2017). However, such flows may become unsteady for sufficiently high forcing magnitudes.

Destabilisation of Eckart streaming jets has been reported in several experiments. Green *et al.* (2016) studied the Eckart streaming flow in a vertical cylindrical cavity filled with a mixture of diethyl phtalate and ethanol. The circular transducer, placed at the top endwall of the cavity, fired bursts of ultrasonic waves towards the opposite end of the fluid volume, where a layer of sound-absorbing material prevented the backward reflection of the incident sound waves. This setting created a steady streaming flow, which however

Thèse accessible à l'adresse : https://theses.insa-lyon.fr/publication/2024ISAL0101/these.pdf © [B. Vincent], [2024], INSA Lyon, tous droits réservés

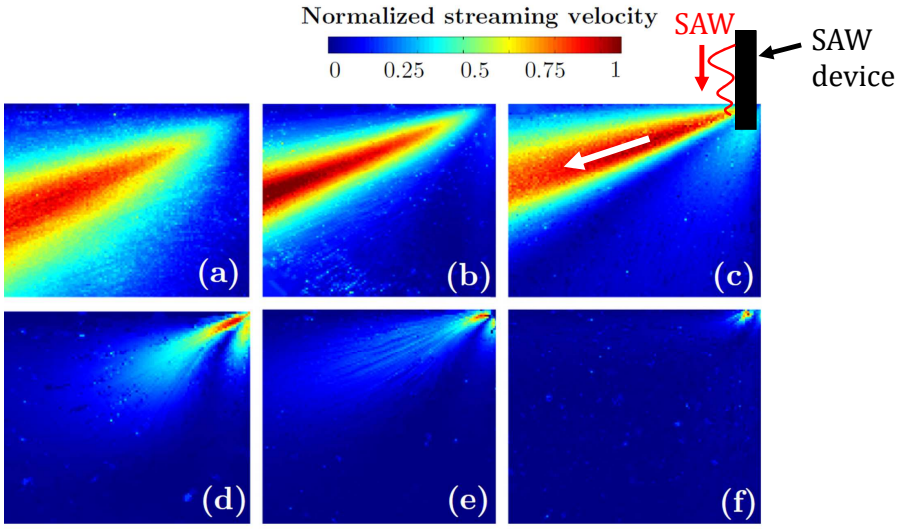


Figure 1.11: Experiments of Dentry *et al.* (2014) on the effect of sound frequency f on the streaming velocity $\|\boldsymbol{u_s}\|$. The streaming jet is forced by the transmission of Surface Acoustic Waves (SAW) from a solid substrate into a water cavity (the flow direction is shown by the white arrow in (c)). Different cases are displayed: (a) $N = 0.63$, $Gr_{ac} = 0.3 \times 10^4$, (b) $N = 4.7$, $Gr_{ac} = 0.5 \times 10^4$, (c) $N = 24.2$, $Gr_{ac} = 0.6 \times 10^4$, (d) $N = 93.8$, $Gr_{ac} = 1.3 \times 10^4$, (e) $N = 394.7$, $Gr_{ac} = 6.5 \times 10^4$ and (f) $N = 1442.3$, $Gr_{ac} = 1.2 \times 10^4$. Velocities are normalised by their maximum values: (a) $U = 41.6$, $U = 49.6$, (c) $U = 45.4$, (d) $U = 12.71$, (e) $U = 10.1$ and (f) $U = 3.2$. For all displayed figures, $S \approx 0.015$.

transitioned towards another state after some time. Green *et al.* (2016) attributed this transition to a thermal instability arising from the sound-absorbing plate progressively heating up. Moudjed (2013) also reported streaming jet oscillations. The oscillation periods were sufficiently long so that different sections of the on-axis $\boldsymbol{u_s}$, even after being time-averaged over 4 minutes, could not form a single continuous profile (figure 1.8). For $Gr_{ac} \geq 11 \times 10^4$, Moudjed *et al.* (2014*b*) even reported severe and intermittent oscillations of the jet near the wall facing the transducer (figure 1.14), suggesting that flow destabilisation is triggered by the jet impingement. Finally, streaming unsteadiness was also reported in the square-flow configuration of Cambonie *et al.* (2017) (figure 1.2). As the authors increased Gr_{ac}, the flow transitioned from a steady to an oscillatory state; the leading frequency ranged from 0.006 Hz to 0.05 Hz for $P_{ac,0} \in [0.8, 6.2]$ W (4.9 and 40.6 for $Gr_{ac} \in [1.6, 12.7] \times 10^4$ in dimensionless units based on $\rho_0 D_s^3$, D_s^2/ν and D_s and mass, time and length scales, respectively). Launay *et al.* (2019) showed that this setting can sustain chaotic states through successions of period doublings and Hopf (i.e., oscillatory) bifurcations; the associated flow symmetry breakings are particularly desirable for stirring (Qu *et al.*, 2022). However, because of the particular nature of that configuration, it remains unclear whether chaos is a common feature shared by streaming flows.

The experimental evidence of single streaming jet unsteadiness motivated stability analyses to understand the destabilisation mechanisms. The first linear stability analyses

Thèse accessible à l'adresse : https://theses.insa-lyon.fr/publication/2024ISAL0101/these.pdf © [B. Vincent], [2024], INSA Lyon, tous droits réservés

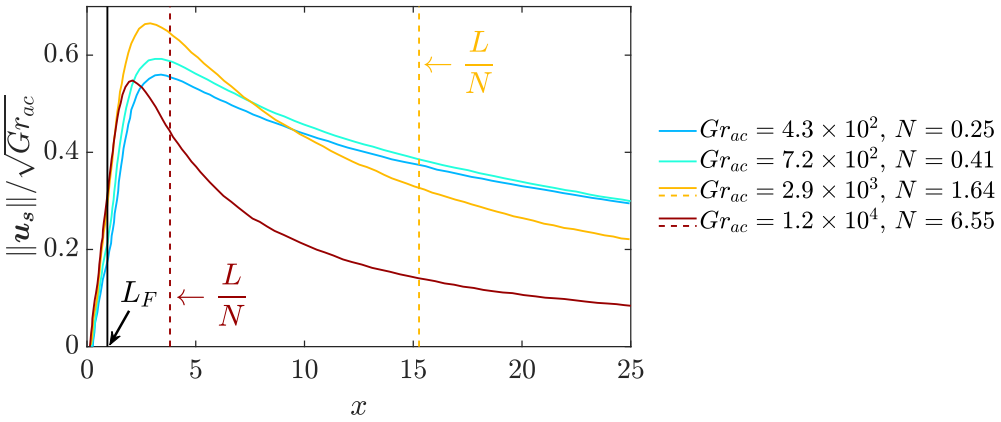


Figure 1.12: DNS streaming velocity profiles on the jet axis for different forcing magnitudes Gr_{ac} and N (data taken from Daru *et al.* (2024)). The simulations are made for $S = 0.305$, $L = 25$ and $P/F = 1083.3$; the jet is forced by a plane circular transducer at $x = 0$ and flows in a cylindrical cavity with an outflow boundary condition at $x = L$. The solid black line locates the Fresnel distance L_F, and the dashed vertical lines locate the attenuation distance L/N. All quantities are made dimensionless using D_s, $\rho_0 D_s^3$ and D_s^2/ν as length, mass and time scales, respectively.

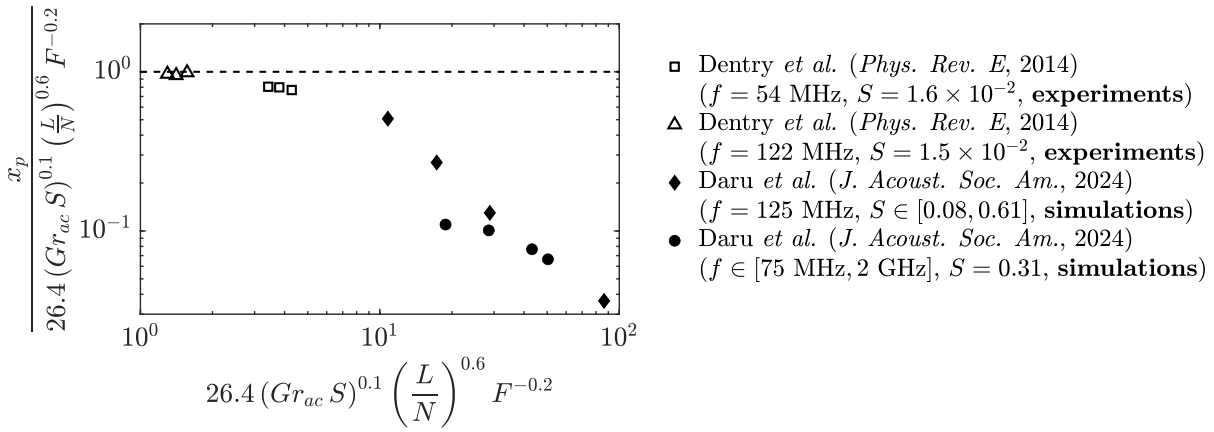


Figure 1.13: Evaluation of the scaling law (1.64) proposed by Orosco & Friend (2022) for the position x_p of the velocity peak on the axis of a streaming jet. The scaling law is compared to the experimental data of Dentry *et al.* (2014) (see table A.2 for the corresponding dimensionless numbers), and to the recent numerical simulations data of Daru *et al.* (2024), for which $S \in [0.08, 0.6]$, $F \in [1.6, 460.8] \times 10^4$, $N \in [0.2, 6.6]$, $L \in [6.3, 50]$ and $Gr_{ac} \in [0.04, 1.2] \times 10^4$.

of Eckart streaming flows go back to Dridi *et al.* (2007, 2008*b*). The authors considered a plane flow in a rectangular cavity of height h_c and length L_c (figure 1.15 (a)). The beam has a constant width h_b along x, creating a constant non-zero forcing inside the beam. The effects of both diffraction and attenuation on the structure of the forcing were thus discarded by Dridi *et al.* (2007, 2008*b*). For $\Lambda = L_c/h_c \to \infty$, the geometry becomes an infinite layer, so that the base flow reduces to an analytical 1D-1C (one-dimensional, one component) velocity profile (Nyborg, 1953; Rudenko & Sukhorukov, 1998).

For various $H = h_c/h_b$, Dridi *et al.* (2007, 2010) showed that the 1D-1C streaming is destabilised by oscillatory perturbations, and that reducing H has a stabilising effect (figure 1.15 (c)). Later multidimensional numerical simulations showed that, in a finite-size

Thèse accessible à l'adresse : https://theses.insa-lyon.fr/publication/2024ISAL0101/these.pdf © [B. Vincent], [2024], INSA Lyon, tous droits réservés

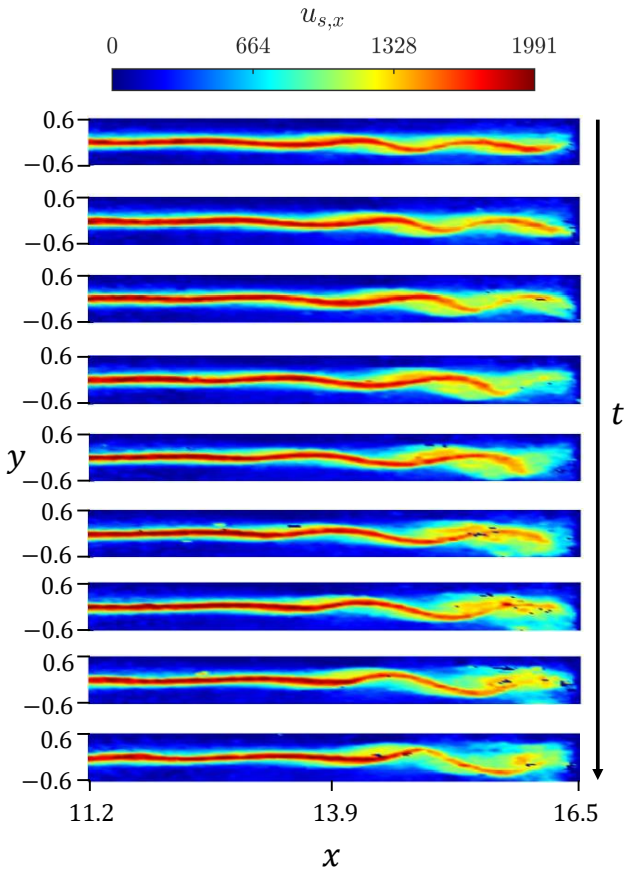
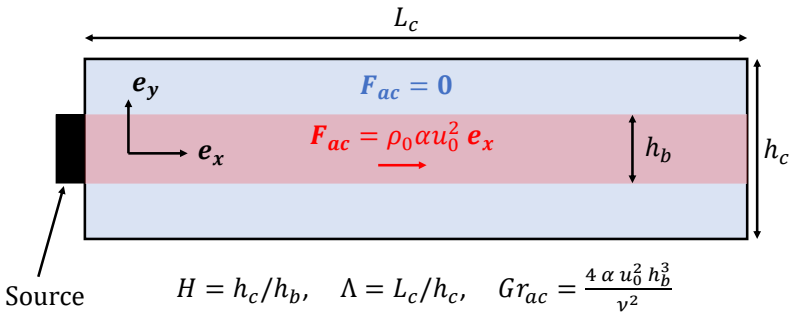


Figure 1.14: PIV snapshots of the streamwise streaming velocity $u_{s,x}$ near the downstream wall ($x = 16.5$) for $Gr_{ac} = 11.6 \times 10^4$. The figure is taken from Moudjed *et al.* (2014*b*) and made dimensionless using D_s and D_s^2/ν as length and time scales, respectively (the dimensionless parameters are those of Moudjed *et al.* (2014*a*) in table A.2). The jet origin is at $x = 0$ and the transducer is placed at $x = -L_F \approx -9.6$ (with L_F the Fresnel distance). Snapshots (ordered from top to bottom) are separated by $\Delta t = 3.3 \times 10^{-4}$ (0.27 s in dimensional units).

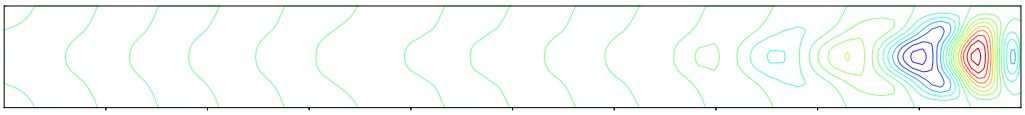
cavity, the leading perturbation remains oscillatory and is concentrated near the impingement wall (figure 1.15 (b)), indicative of an impingement-driven instability. However, the precise destabilisation mechanism remains unclear: is the jet itself that becomes unstable ? Or is the destabilisation rooted in the recirculations at the impingement ? Nevertheless, both the 1D-1C an 2D planar models have been used to study the interaction of Eckart streaming with other flow-driving mechanisms such as thermodiffusion (Charrier-Mojtabi *et al.*, 2012, 2019), species concentration gradients (Lyubimova & Skuridin, 2019), and lateral (Dridi *et al.*, 2008*a*) and vertical (i.e., Rayleigh-Bénard) heating (Ben Hadid *et al.*, 2012; Henry *et al.*, 2022). Regarding that latter configuration, streaming can have a significant stabilising effect: Ben Hadid *et al.* (2012) showed that the critical Rayleigh number Ra_c could be increased by a factor 10 (figure 1.15), highlighting the ability of acoustic streaming to control flows subjected to other destabilising mechanisms.

All the aforementioned stability analyses of single Eckart streaming jet-like flows suffer from a crude modelling of the forcing field. First, beam diffraction was not accounted for. Besides of prescribing a lateral size to the streaming jet (Moudjed *et al.*, 2014*a*), diffraction causes the local forcing magnitude to decrease along the beam. Combining these two effects together yields longitudinal gradients of the streamwise velocity along

Thèse accessible à l'adresse : https://theses.insa-lyon.fr/publication/2024ISAL0101/these.pdf © [B. Vincent], [2024], INSA Lyon, tous droits réservés



(a)



(b) $H = 2.96$, $\Lambda = 10$, $Gr_{ac} = Gr_{ac}^c = 1089.1$

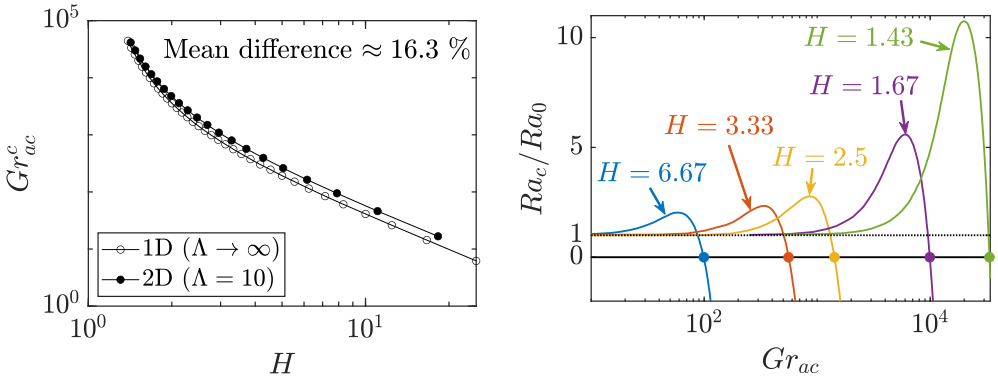


Figure 1.15: Setup and main results of the Eckart streaming linear stability analyses from the literature. (a) Sketch of the setup, with the definition of the geometrical dimensionless numbers. The forcing is constant along x and y inside the beam (red), and is zero outside (blue). Due to the planar geometry, Gr_{ac} (equation (1.60)) is based on h_b. For $\Lambda \to \infty$, the base flow is an analytical 1D-1C velocity profile (Nyborg, 1953). (b) Leading oscillatory velocity perturbation $\boldsymbol{u'}$ at the instability onset $Gr_{ac}^c = 1089.1$ (Henry *et al.*, 2022), here represented as contours of $\boldsymbol{u'} \cdot \boldsymbol{e_y}$ (red is positive, blue is negative). (c) Evolution of the instability onsets Gr_{ac}^c as a function of $H = h_c/h_b$ for an analytical 1D-1C (Dridi *et al.*, 2010) or a numerically-computed 2D (Ben Hadid *et al.*, 2012) base flow (setup shown in (a)). In both cases, the unstable perturbation is oscillatory. (d) Effect of streaming on the stability of a Rayleigh-Bénard flow (heating from below) for $\Lambda \to \infty$ (figure adapted from Ben Hadid *et al.* (2012)). The critical Rayleigh number Ra_c is normalised by $Ra_0 = 1707.8$ (critical Rayleigh number for $Gr_{ac} = 0$). The horizontal solid and dashed black lines represent pure streaming ($Ra = 0$) and pure convection ($Gr_{ac} = 0$) instability onsets, respectively.

the entire cavity length (figures 1.8 and 1.12); such gradients are not recovered with the non-diffracting beam modelling used by Dridi *et al.* (2010) and co-authors. Second, these former works also ignored the attenuation-induced decay of the forcing magnitude along

Thèse accessible à l'adresse : https://theses.insa-lyon.fr/publication/2024ISAL0101/these.pdf © [B. Vincent], [2024], INSA Lyon, tous droits réservés

the beam. This approximation actually violates the fundamental properties of Eckart streaming (section 1.3.2), since attenuation (a) causes the streamwise momentum flux of the jet to remain bounded and to saturate at infinite distances from the source, and (b) attenuation prescribes a length scale over which the jet accumulates momentum. Discarding attenuation of the beam is thus unrealistic. In this thesis, **I shall investigate the stability of a streaming jet forced by a diffracting and attenuated sound beam. In particular, I shall clarify the flow destabilisation mechanism, and characterise the primary flow bifurcation (i.e., whether it is sub- or supercritical).**

1.7 Conclusion

As they propagate within a fluid, sound waves are attenuated due to e.g., thermal or viscous effects. Because of acoustic nonlinearities, this sound attenuation can drive a mean flow called acoustic streaming. Therefore, streaming may intuitively be seen as acoustic kinetic energy being converted into flow kinetic energy; however, a strict energy balance applied to acoustic streaming still lacks in the literature.

Based on the discrepancy between the acoustic and streaming time scales, the streaming flow can be modelled by the incompressible Navier-Stokes equations together with a an acoustic body force. The acoustics and streaming problems are thus weakly-coupled: to simulate streaming flows, the acoustic field can be computed separately and then be used to define the forcing field driving the flow. I shall consider the linear sound field radiated by a plane circular transducer. This acoustic field is shaped as an axisymmetric diffracting beam and is modelled by the Rayleigh integral, which however needs to be adapted to account for sound attenuation.

Attenuation is indeed a key element of acoustic streaming: the attenuation distance $1/\alpha$ of the sound pressure waves defines the length scale over which the streaming flow accumulates momentum. An important parameter is thus $N = \alpha L_c$, which compares the cavity length L_c to $1/\alpha$. In particular, $N > 1$ ensures that most of the acoustic power is used to drive the flow, and should therefore be aimed for in practical streaming applications. However, $N < 1$ in most of the existing streaming experiments; the $N > 1$ range thus calls for a better characterisation. In particular, I shall identify the different regimes and derive associated scaling laws all along a $N > 1$ streaming jet.

Linear stability analyses showed that a laminar streaming jet becomes unstable through a Hopf bifurcation. However, besides of considering a planar geometry inconsistent with the axisymmetric nature of the sound field emitted by a circular transducer, all the stability analyses discarded (i) diffraction, (ii) attenuation along the beam and (iii) realistic transverse gradients of the forcing. These approximations lead to nearly invariant flows that are inconsistent with measurements of the streaming velocity along the jet axis. How do the stability properties evolve when a realistic forcing model (obtained from the attenuated Rayleigh integral) is adopted ? In that case, what are the destabilisation mechanisms ? Is the bifurcation supercritical or subcritical ? These are questions that this thesis shall aim to answer.

Finally, complex streaming flows can be achieved by making use of multiple reflections of a single sound beam. An example is the square flow of Cambonie *et al.* (2017) driven by three beam reflections, yielding a forcing field with an up/down symmetry. The development of unsteadiness and loss of symmetry were found to be key for stirring. This raises the question of whether a more effective stirring configuration can be obtained with an acoustic forcing field free of any symmetry. A final objective of this thesis is thus to

Thèse accessible à l'adresse : https://theses.insa-lyon.fr/publication/2024ISAL0101/these.pdf © [B. Vincent], [2024], INSA Lyon, tous droits réservés

experimentally investigate the flow resulting from such forcing field. In particular, I shall assess to what extent the knowledge I gained for single jets can be used to design a highly 3D streaming flow involving multiple reflections of a single beam.

Thèse accessible à l'adresse : https://theses.insa-lyon.fr/publication/2024ISAL0101/these.pdf © [B. Vincent], [2024], INSA Lyon, tous droits réservés

Chapter 2

Analytical developments: attenuated Rayleigh integral and energy transfer in acoustic streaming

2.1 Introduction

Streaming jets for which $N > 1$ flow over distances comparable (or greater than) the acoustic pressure attenuation length $1/\alpha$. These flows thus experience regions of strong ($x \ll 1/\alpha$) and marginal (because nearly entirely attenuated) acoustic forcing ($x > 1/\alpha$). Therefore, the model used for the acoustic forcing term in the incompressible Navier-Stokes equations (1.39) shall account for the attenuation of acoustic intensity $\boldsymbol{I_{ac}}$ along the beam. **My first aim is to adapt the Rayleigh integral** (1.44) **to attenuated cases, so that accurate** $N > 1$ **jets can be simulated with a forcing field based on linear acoustics**.

On a more general note, the build-up of jet velocity along an attenuated beam implies a transfer of energy from the acoustic scales to the scales of the flow. Separating the streaming and acoustic flow quantities using a Reynolds decomposition (1.33) draws a direct parallel with turbulence modelling (Chassaing *et al.*, 2002; Giovannini & Airiau, 2016), in which energy exchanges between the turbulent fluctuations and the mean flow are commonly studied. **The second aim of this chapter is to lay down the energy balance equations for acoustic streaming**. In particular, I shall discuss how the model of Dupuy *et al.* (2018) for variable-density turbulence can be further developed for acoustic streaming.

This chapter is organised as follows: in section 2.2, I adapt the Rayleigh integral to account for attenuation in the spatial structure of $\boldsymbol{I_{ac}}$ (hence, of the forcing field). The derived integral relations are then made dimensionless using the dimensionless groups of Moudjed *et al.* (2014*a*); the effects of diffraction on the forcing field structure are also discussed. Section 2.3 then focuses on the energy exchanges between the streaming and acoustics scales. Finally, concluding remarks are given in section 2.4.

2.2 The Rayleigh integral in a viscous medium

In this section, I shall derive the equations governing the attenuated acoustic field radiated by a plane circular transducer. For the sake of clarity, the derivation is carried

Thèse accessible à l'adresse : https://theses.insa-lyon.fr/publication/2024ISAL0101/these.pdf © [B. Vincent], [2024], INSA Lyon, tous droits réservés

out using dimensional equations and the coordinate system (and notations) of figure 1.4.

2.2.1 Assumptions

Besides the classical assumptions for linear acoustics outlined in section 1.2.2, I shall further assume that $\gamma \approx 1$; hence, sound propagation can be seen as an isentropic process in which attenuation is solely due to viscous effects (see the discussion in section 1.2.2). In that case, the complex wavenumber k_c in the linear wave equation (1.15) can be exactly expressed as (Kinsler *et al.*, 2000):

$$k_c = k - j\alpha = \frac{\omega}{c\sqrt{1+j\Gamma}}\,, \tag{2.1}$$

in which

$$\Gamma = \frac{\omega}{\rho_0 c^2}\left(\frac{4}{3}\mu + \eta\right) = \frac{NS}{1.22L} \tag{2.2}$$

is a dimensionless number comparing the wavelength to the sound attenuation length. Then, k and α are given by (Kinsler *et al.*, 2000):

$$\begin{aligned} k &= \frac{\omega}{c\sqrt{2}}\left[\frac{\sqrt{1+\Gamma^2}+1}{1+\Gamma^2}\right]^{\frac{1}{2}} & \alpha &= \frac{\omega}{c\sqrt{2}}\left[\frac{\sqrt{1+\Gamma^2}-1}{1+\Gamma^2}\right]^{\frac{1}{2}} \\ &\underset{\Gamma\ll 1}{\sim} \frac{\omega}{c}\,, & &\underset{\Gamma\ll 1}{\sim} \frac{\omega\Gamma}{2c} = \frac{\omega^2}{2\rho_0 c^3}\left(\frac{4}{3}\mu+\eta\right)\,. \end{aligned} \tag{2.3}$$

Finally, using the definition of k_c (2.1), the linearised momentum equation (1.13b) can be rewritten as

$$j\frac{\rho_0 c^2 k_c^2}{\omega}\boldsymbol{u_{ac}} = -\nabla p_{ac} \tag{2.4}$$

for a monochromatic wave. Equation (2.4) can be seen as a generalised acoustic impedance; it will be needed e.g. to obtain $\boldsymbol{u_{ac}}$ from an expression of p_{ac}.

2.2.2 Integral relations for the acoustic intensity field radiated by a plane circular transducer

As for the unattenuated case, the vibrating surface S_t of the transducer is modelled as a plane disc made of an infinite number of point sources (Kinsler *et al.*, 2000; Blackstock, 2000), each centred on an elementary surface dS and creating a flow rate Q_0 through each dS (figure 1.4). The starting point of the derivation is thus to consider the wave emitted by a point source.

A point source may be seen as a special case of a pulsating sphere of vanishing mean radius R_S. By vibrating at a velocity $U_{R_S}e^{j\omega t}\boldsymbol{e_{d'}}$ (with $\boldsymbol{e_{d'}}$ the unit radial vector), the sphere surface produces spherical acoustic pressure waves defined as:

$$p_{ac} = \frac{A}{d'}e^{j[\omega t - k_c(d'-R_S)]}\,, \tag{2.5}$$

with d' the distance from the sphere centre and A the wave amplitude parameter. The sphere thus drives a volumetric flow rate $Q_{R_S} = 4\pi R_S^2 U_{R_S}$ through its surface which, from equations (2.5) and (2.4), reads:

$$Q_{R_S} = -j\frac{4\pi A\omega\,(1+jk_cR_S)}{\rho_0 c^2 k^2}\,.$$

Thèse accessible à l'adresse : https://theses.insa-lyon.fr/publication/2024ISAL0101/these.pdf © [B. Vincent], [2024], INSA Lyon, tous droits réservés

Taking the limit of Q_{R_S} as $R_S \to 0$ yields the strength Q_0 of a point source, allowing to express A in terms of Q_0. Equation (2.5) can then be rewritten as:

$$p_{ac} = j\frac{\rho_0 c^2 k_c^2 Q_0}{4\pi\omega d'} e^{j(\omega t - k_c d')} \tag{2.6}$$

Because of linearity, p_{ac} in the fluid domain is the sum of all pressure waves emitted by each point source on S_t. Since $Q_0 = u_0 \mathrm{d}S$ on S_t (with u_0 the vibrating velocity of the transducer), integrating (2.6) over S_t gives:

$$p_{ac} = j\frac{\rho_0 c^2 k_c^2 u_0}{2\pi\omega} \iint_{S_t} \frac{e^{j(\omega t - k_c d)}}{d} dS\,, \tag{2.7}$$

in which Q_0 has been doubled, since each point source radiates waves in the $x > 0$ semi-infinite domain only. As for the unattenuated case, d is the distance between a point source on S_t and the point in the fluid domain where p_{ac} is evaluated (equation (1.45)). Note that for $\alpha = 0$ and $k_c = k$, equation (2.7) reduces to the unattenuated Rayleigh integral (1.44), as expected.

The integral expression for $\boldsymbol{u_{ac}}$ is obtained with a similar approach. Inserting equation (2.6) into the generalised acoustic impedance (2.4) yields:

$$\boldsymbol{u_{ac}} = \frac{Q_0}{4\pi d'^2}\left(1 + jk_c d'\right) e^{j(\omega t - k_c d')}\, \boldsymbol{e_{d'}}\,,$$

which once integrated over S_t gives:

$$\boldsymbol{u_{ac}} = \frac{u_0}{2\pi} \iint_{S_t} \frac{(1 + jk_c d)}{d^2} \frac{\boldsymbol{d}}{d} e^{j(\omega t - k_c d)} dS\,, \tag{2.8}$$

In equation (2.8), Q_0 has been doubled for the same reason as in (2.7).

Finally, $\boldsymbol{I_{ac}}$ can be calculated everywhere in the fluid domain using equation (1.19) which, using complex notations, reads:

$$\boldsymbol{I_{ac}} = \frac{1}{2}\,\mathrm{Re}\left\{p_{ac}\boldsymbol{u}_{\boldsymbol{ac}}^*\right\}\,, \tag{2.9}$$

with $*$ referring to the complex conjugate.

2.2.3 Analytical expressions of the acoustic fields on the transducer axis

Similarly to the unattenuated case, calculating analytically the Rayleigh integrals (2.7) and (2.8) is limited to few situations only. In this section, I shall derive the analytical expressions of both p_{ac} and $\boldsymbol{u_{ac}}$ on the acoustic axis. These results prove extremely useful when checking the numerical computations of equations (2.7) and (2.8).

I shall first consider p_{ac}. On the axis ($r = 0$), the Rayleigh integral (2.7) reads:

$$p_{ac} = j\frac{\rho_0 c^2 k_c^2 u_0}{2\pi\omega} e^{j\omega t} \iint_{S_t} \frac{e^{-jk_c\sqrt{x^2 + r'^2}}}{\sqrt{x^2 + r'^2}}\, dS\,.$$

Thèse accessible à l'adresse : https://theses.insa-lyon.fr/publication/2024ISAL0101/these.pdf © [B. Vincent], [2024], INSA Lyon, tous droits réservés

By setting $X = \sqrt{x^2 + r'^2}$, the above integral can be calculated analytically to give:

$$\begin{aligned} p_{ac}(x, r=0) &= \frac{\rho_0 c^2 k_c u_0}{\omega} e^{j\omega t} \left(e^{-jk_c x} - e^{-jk_c\sqrt{x^2+\frac{D_s^2}{4}}} \right) \\ &= \frac{\rho_0 c^2 k_c u_0}{\omega} e^{j\omega t} e^{-j\frac{k_c}{2}\left(\sqrt{x^2+\frac{D_s^2}{4}}+x\right)} \left[e^{j\frac{k_c}{2}\left(\sqrt{x^2+\frac{D_s^2}{4}}-x\right)} - e^{-j\frac{k_c}{2}\left(\sqrt{x^2+\frac{D_s^2}{4}}-x\right)} \right] \\ &= j\frac{2\rho_0 c^2 k_c u_0}{\omega} e^{j\omega t} e^{-j\frac{k_c}{2}\left(\sqrt{x^2+\frac{D_s^2}{4}}+x\right)} \sin\left[\frac{k_c}{2}\left(\sqrt{x^2+\frac{D_s^2}{4}} - x \right) \right]. \end{aligned} \tag{2.10}$$

Then, substituting the first equality of equation (2.1) for k_c in equation (2.10) finally gives:

$$\begin{aligned} p_{ac}(x, r=0) =& \frac{2\rho_0 c^2 \left(k - j\alpha\right) u_0}{\omega} e^{-\frac{\alpha}{2}\left(\sqrt{x^2+\frac{D_s^2}{4}}+x\right)} e^{j\left[\omega t - \frac{k}{2}\left(\sqrt{x^2+\frac{D_s^2}{4}}+x\right)\right]} \\ &\times \left(\sinh\left[\frac{\alpha}{2}\left(\sqrt{x^2+\frac{D_s^2}{4}} - x \right) \right] \cos\left[\frac{k}{2}\left(\sqrt{x^2+\frac{D_s^2}{4}} - x \right) \right] \right. \\ &\left. + j \sin\left[\frac{k}{2}\left(\sqrt{x^2+\frac{D_s^2}{4}} - x \right) \right] \cosh\left[\frac{\alpha}{2}\left(\sqrt{x^2+\frac{D_s^2}{4}} - x \right) \right] \right). \end{aligned} \tag{2.11}$$

In contrast to p_{ac}, the Rayleigh integral for $\boldsymbol{u_{ac}}$ (2.8) cannot be calculated analytically for $r = 0$. However, $\boldsymbol{u_{ac}}(x, r=0) = u_{ac,x}(x, r=0)\boldsymbol{e_x}$ can be derived by inserting (2.11) into the generalised acoustic impedance (2.4):

$$\begin{aligned} u_{ac,x}(x, r=0) =& U_1\, e^{-\frac{\alpha}{2}\left(\sqrt{x^2+\frac{D_s^2}{4}}+x\right)} e^{j\left[\omega t - \frac{k}{2}\left(\sqrt{x^2+\frac{D_s^2}{4}}-x\right)\right]} \\ &+ U_2\, e^{-\frac{\alpha}{2}\left(\sqrt{x^2+\frac{D_s^2}{4}}+x\right)} e^{j\left[\omega t - \frac{k}{2}\left(\sqrt{x^2+\frac{D_s^2}{4}}-x\right)+\frac{\pi}{2}\right]}, \end{aligned} \tag{2.12}$$

with:

$$\begin{aligned} U_1 =& u_0 \left(1 - \frac{x}{\sqrt{x^2+\frac{D_s^2}{4}}} \right) \cos\left[\frac{k}{2}\left(\sqrt{x^2+\frac{D_s^2}{4}} - x \right) \right] \cosh\left[\frac{\alpha}{2}\left(\sqrt{x^2+\frac{D_s^2}{4}} - x \right) \right] \\ &+ u_0 \left(1 + \frac{x}{\sqrt{x^2+\frac{D_s^2}{4}}} \right) \sinh\left[\frac{\alpha}{2}\left(\sqrt{x^2+\frac{D_s^2}{4}} - x \right) \right] \cos\left[\frac{k}{2}\left(\sqrt{x^2+\frac{D_s^2}{4}} - x \right) \right], \end{aligned}$$

$$\begin{aligned} U_2 =& u_0 \left(1 - \frac{x}{\sqrt{x^2+\frac{D_s^2}{4}}} \right) \sin\left[\frac{k}{2}\left(\sqrt{x^2+\frac{D_s^2}{4}} - x \right) \right] \sinh\left[\frac{\alpha}{2}\left(\sqrt{x^2+\frac{D_s^2}{4}} - x \right) \right] \\ &+ u_0 \left(1 + \frac{x}{\sqrt{x^2+\frac{D_s^2}{4}}} \right) \sin\left[\frac{k}{2}\left(\sqrt{x^2+\frac{D_s^2}{4}} - x \right) \right] \cosh\left[\frac{\alpha}{2}\left(\sqrt{x^2+\frac{D_s^2}{4}} - x \right) \right]. \end{aligned}$$

Finally, the on-axis intensity $I_{ac,x}(x, r=0)$ is obtained by inserting the analytical

Thèse accessible à l'adresse : https://theses.insa-lyon.fr/publication/2024ISAL0101/these.pdf © [B. Vincent], [2024], INSA Lyon, tous droits réservés

expression of p_{ac} (2.11) and $u_{ac,x}$ (2.12) into equation (2.9):

$$\begin{aligned} I_{ac,x}(x, r=0) = \frac{\rho_0 c^2 u_0^2 k}{2\omega} e^{-\alpha\left(\sqrt{x^2+\frac{D_s^2}{4}}+x\right)} \Bigg(& \left[1 - \frac{x}{\sqrt{x^2+\frac{D_s^2}{4}}}\right] \sinh\left[\alpha\left(\sqrt{x^2+\frac{D_s^2}{4}} - x\right)\right] \\ & + \left[\frac{x}{\sqrt{x^2+\frac{D_s^2}{4}}} + 1\right] \Bigg(\cosh\left[\alpha\left(\sqrt{x^2+\frac{D_s^2}{4}} - x\right)\right] \\ & - \cos\left[k\left(\sqrt{x^2+\frac{D_s^2}{4}} - x\right)\right]\Bigg) \\ & + \frac{\alpha}{k}\left(1 - \frac{x}{\sqrt{x^2+\frac{D_s^2}{4}}}\right) \sin\left[k\left(\sqrt{x^2+\frac{D_s^2}{4}} - x\right)\right]\Bigg) . \end{aligned} \tag{2.13}$$

In the unattenuated case ($\alpha = 0$), equation (2.13) reduces **exactly** to the analytical intensity profile of Greenspan (1979) (equation (1.50)). This perfect agreement adds confidence to the developments made in this section.

2.2.4 Nondimensionalisation of the acoustic forcing equations

To simulate streaming flows using the dimensionless incompressible Navier-Stokes and continuity equations (1.59), $\boldsymbol{I_{ac}}$, $\boldsymbol{u_{ac}}$ and p_{ac} shall now be made dimensionless and be normalised by their respective maximum magnitude. As discussed in section 1.4.2, p_{ac} and $\|\boldsymbol{I_{ac}}\|$ are respectively bounded by $p_{ac,\max} = 2\rho_0 c u_0$ and $I_{ac,\max} = 2\rho_0 c u_0^2$ in the unattenuated limit. Using the plane wave impedance (1.18), this also implies that the maximum on-axis acoustic velocity is $u_{ac,\max} = 2u_0$. Denoting normalised quantities by $\widetilde{\ }$, equation (2.9) can then be rewritten as:

$$\begin{aligned} 2\rho_0 c u_0^2 \widetilde{\boldsymbol{I}}_{\boldsymbol{ac}} &= (2\rho_0 c u_0)\,(2u_0)\,\frac{1}{2}\,\mathrm{Re}\left\{\widetilde{p}_{ac}\widetilde{\boldsymbol{u}}^*_{\boldsymbol{ac}}\right\} \\ \leftrightarrow \widetilde{\boldsymbol{I}}_{\boldsymbol{ac}} &= \mathrm{Re}\left\{\widetilde{p}_{ac}\widetilde{\boldsymbol{u}}^*_{\boldsymbol{ac}}\right\} . \end{aligned} \tag{2.14}$$

Following Moudjed *et al.* (2014*a*), $\widetilde{p}_{ac}$ and $\widetilde{\boldsymbol{u}}_{\boldsymbol{ac}}$ are finally made dimensionless using D_s, $\rho_0 D_s^3$ and D_s^2/ν as length, mass and time scales, respectively:

$$\widetilde{p}_{ac} = j\frac{k_c^2 S}{8 \times 1.22\pi^2}\int_0^{1/2}\int_0^{2\pi} \frac{e^{-jk_c d}}{d} r' dr' d\theta' , \tag{2.15a}$$

$$\widetilde{\boldsymbol{u}}_{\boldsymbol{ac}} = \frac{1}{4\pi}\int_0^{1/2}\int_0^{2\pi} (1 + jk_c d)\,\frac{e^{-jk_c d}}{d^2}\frac{\boldsymbol{d}}{d} r' dr' d\theta' , \tag{2.15b}$$

with:

$$k_c = \frac{2.44\pi}{S} - j\frac{N}{L} . \tag{2.16}$$

The expression of $\boldsymbol{d}$ is recalled below for convenience:

$$\boldsymbol{d} = \boldsymbol{M'M} = x\,\boldsymbol{e_x} + [r - r'\cos(\theta')]\;\boldsymbol{e_y} - r'\sin(\theta')\;\boldsymbol{e_z} , \quad \rightarrow d = \|\boldsymbol{d}\| .$$

Thèse accessible à l'adresse : https://theses.insa-lyon.fr/publication/2024ISAL0101/these.pdf © [B. Vincent], [2024], INSA Lyon, tous droits réservés

An important remark is that, due to the time-average when calculating $\widetilde{\boldsymbol{I}}_{\boldsymbol{ac}}$, the $e^{j\omega t}$ terms in both the acoustic pressure and velocity cancel each other out; the harmonic time dependence is thus dropped in equations (2.15). As a consequence, $\widetilde{p}_{ac}$ and $\widetilde{\boldsymbol{u}}_{\boldsymbol{ac}}$ (hence $\widetilde{\boldsymbol{I}}_{\boldsymbol{ac}}$) are only defined by the diffraction parameter S and the dimensionless sound attenuation coefficient N/L (equation (1.58)). Contrarily to what suggested Moudjed *et al.* (2014*a*), the frequency parameter F is not needed to compute $\widetilde{\boldsymbol{I}}_{\boldsymbol{ac}}$.

Finally, similar normalisation and nondimensionalisation procedures applied to $I_{ac,x}(x, r=0)$ (2.13) give:

$$\begin{aligned}\widetilde{I}_{ac,x}(x,r=0) = \frac{1}{4}e^{-\frac{N}{L}\left(\sqrt{x^2+\frac{1}{4}}+x\right)}\Bigg(&\left[1-\frac{x}{\sqrt{x^2+\frac{1}{4}}}\right]\sinh\left[\frac{N}{L}\left(\sqrt{x^2+\frac{1}{4}}-x\right)\right]\\&+\left[\frac{x}{\sqrt{x^2+\frac{1}{4}}}+1\right]\Bigg(\cosh\left[\frac{N}{L}\left(\sqrt{x^2+\frac{1}{4}}-x\right)\right]\\&-\cos\left[\frac{2.44\pi}{S}\left(\sqrt{x^2+\frac{1}{4}}-x\right)\right]\Bigg)\\&+\frac{NS}{2.44\pi L}\left(1-\frac{x}{\sqrt{x^2+\frac{1}{4}}}\right)\sin\left[\frac{2.44\pi}{S}\left(\sqrt{x^2+\frac{1}{4}}-x\right)\right]\Bigg).\end{aligned} \tag{2.17}$$

from which the far-field approximation is obtained by taking $1/(4x^2) \ll 1$:

$$\widetilde{I}_{ac,x}(x,r=0) \sim \left(\frac{1.22\pi}{8\,S}\right)^2 \frac{e^{-2N\frac{x}{L}}}{x^2}. \tag{2.18}$$

2.2.5 Numerical integration and effects of diffraction on the forcing structure

2.2.5.1 Numerical integration, mesh convergence and comparison with the unattenuated models

The attenuated Rayleigh integrals (2.15) are evaluated numerically in the fluid domain using the same approach as for the unattenuated case (section 1.4.4): the transducer is discretised with an homogeneous grid of N_s points in both the radial and azimuthal directions. To determine the mesh density requirements for the source, I compared the numerically-obtained $\widetilde{I}_{ac,x}(x, r=0)$ to its analytical expression (2.17) for various N_s (figure 2.1 (a)). Whether it is in the near or far acoustic fields, the error e on the numerically-computed $\widetilde{I}_{ac,x}$ falls below 1 % for $N_s \geq 250$. The error keeps decreasing at larger N_s, however for a larger computational time. **Therefore, all numerical computations of $\widetilde{\boldsymbol{I}}_{\boldsymbol{ac}}$ in the remaining of the thesis are made with $N_s = 300$ to ensure accuracy whilst keeping reasonable computational times**.

Finally, both the analytical (2.17) and numerically-obtained $\widetilde{I}_{ac,x}(x, r=0)$ are compared in figure 2.1 (b) to the unattenuated on-axis profiles of $\widetilde{I}_{ac,x}$ introduced in chapter 1. As in the unattenuated case ($N/L = 0$, blue curve), the model derived in this chapter correctly captures the growth of the $\widetilde{I}_{ac,x}(x, r=0)$ envelope up to the Fresnel length L_F (black curve and red symbols). Because of attenuation, the last peak of the attenuated

Thèse accessible à l'adresse : https://theses.insa-lyon.fr/publication/2024ISAL0101/these.pdf © [B. Vincent], [2024], INSA Lyon, tous droits réservés

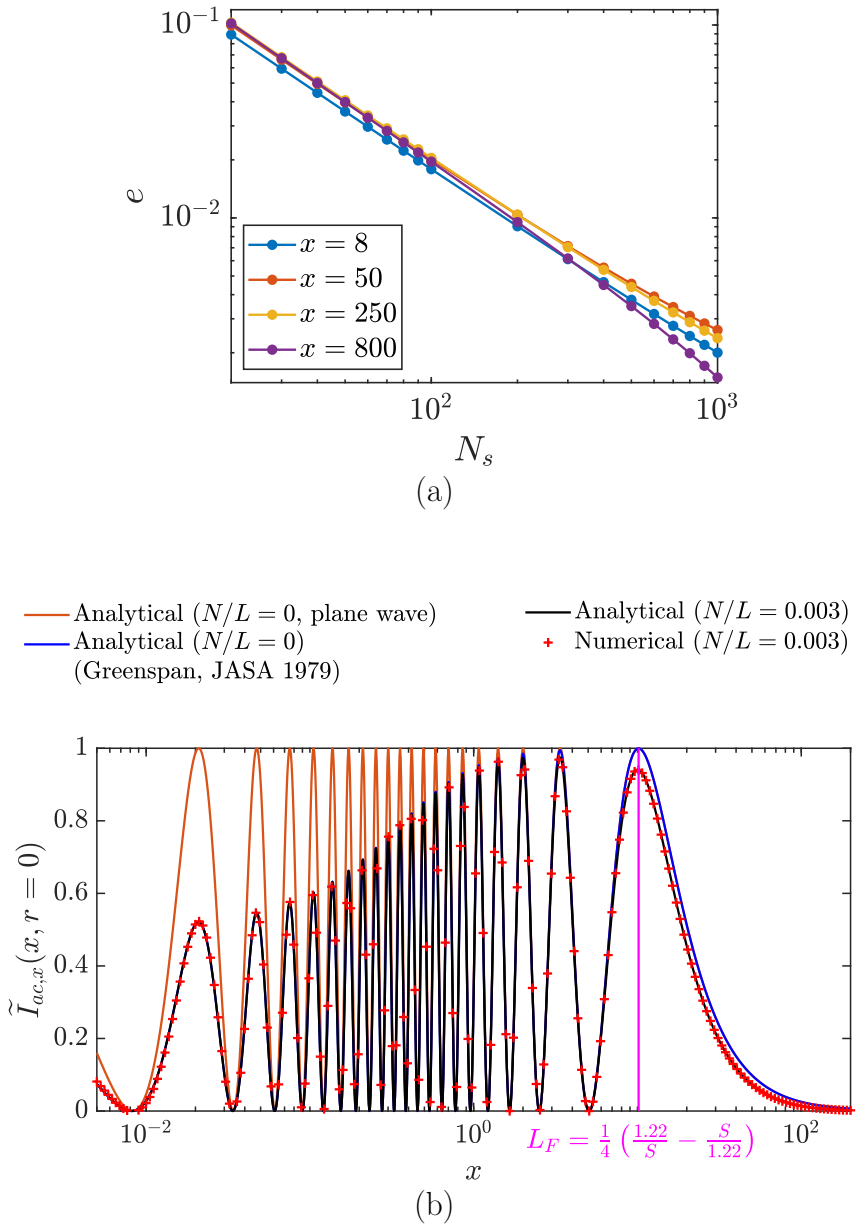


Figure 2.1: Grid sensitivity for the circular source discretisation. The grid is made of N_s points in both the radial and azimuthal directions. The grid sensitivity is analysed for $S = 0.03$ and $N/L = 0.003$ (acoustic parameters of Moudjed *et al.* (2014*a*)). (a) Evolution with N_s of the relative error e between the analytical (2.17) and numerically-evaluated $\widetilde{I}_{ac,x}$ (equations (2.9) and (2.15)) at different points x on the axis. (b) On-axis profiles of $\widetilde{I}_{ac,x}$ for different assumptions: unattenuated plane-wave approximation (brown, analytical, equation (1.47)), unattenuated "real wave" model of Greenspan (1979) (blue, analytical, equation (2.13) with $N/L = 0$), attenuated "real wave" (black, analytical, equation (2.13) with $N/L = 0.003$) and numerical integration of the attenuated Rayleigh integrals (2.15) (red symbols).

$\widetilde{I}_{ac,x}(x, r = 0)$ is no longer unity but ≈ 0.95. By "cutting down" $\widetilde{I}_{ac,x}$, increasing N/L would further decrease that last peak amplitude, and also shift its position towards smaller x[1]. Since $N/L \ll 1$, the attenuated model barely differs from the non-attenuated ones for

[1]For the position of the last $\widetilde{I}_{ac,x}$ peak to be shifted by attenuation, the attenuation distance L/N

Thèse accessible à l'adresse : https://theses.insa-lyon.fr/publication/2024ISAL0101/these.pdf © [B. Vincent], [2024], INSA Lyon, tous droits réservés

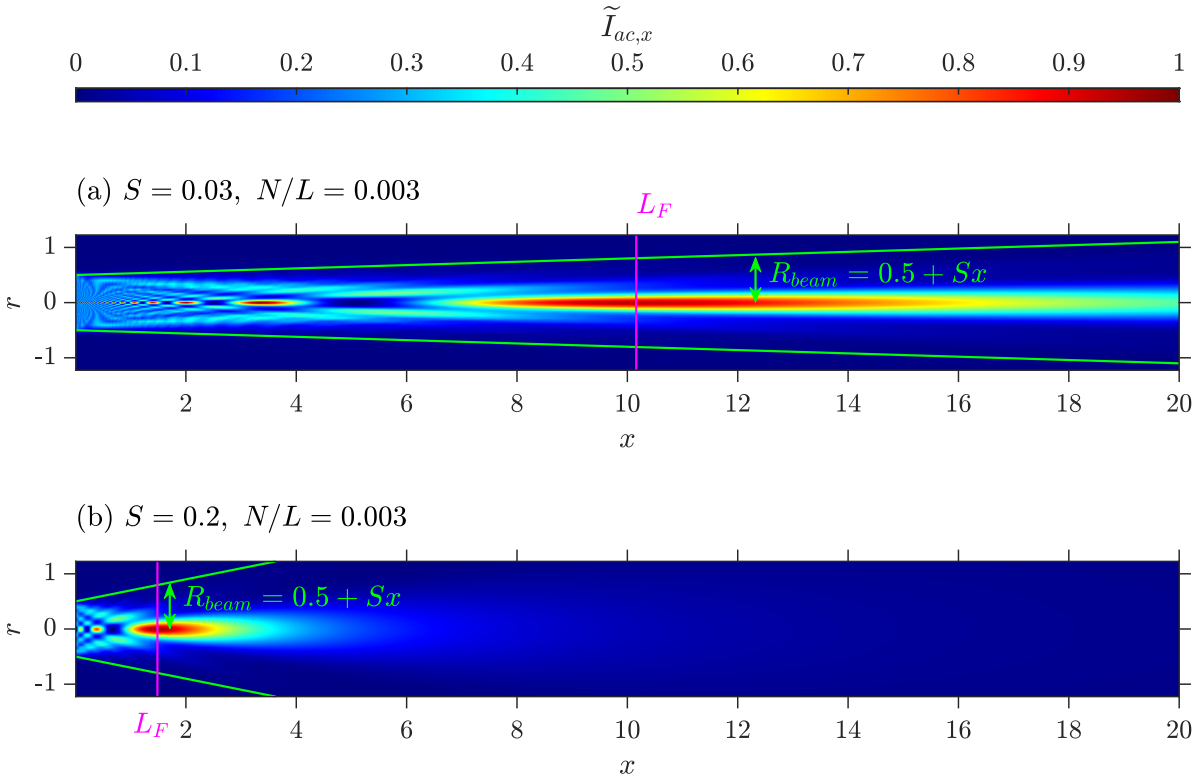


Figure 2.2: Map of the axial normalised intensity $\widetilde{I}_{ac,x}$ for $N/L = 0.003$ (value of Moudjed *et al.* (2014*a*)). Two values of the diffraction parameter S are displayed: (a) $S = 0.03$ (same value as Moudjed *et al.* (2014*a*)) and (b) $S = 0.2$. In both plot, the Fresnel distance $L_F = \frac{1}{4}\left(\frac{1.22}{S} - \frac{S}{1.22}\right)$ is shown in purple and delimits the near ($x \leq L_F$) from the far ($x \geq L_F$) acoustic fields. The green lines represent the approximate beam edge defined by equation (2.19)). Both plots share the same colour levels.

$x \geq L_F$: the local estimates of $\widetilde{I}_{ac,x}(x, r = 0)$ typically differ by ≈ 7 %. Although they are small, these differences are nevertheless key to accurately simulate $N > 1$ streaming flows (chapter 3).

2.2.5.2 Effects of diffraction on the forcing structure

Besides of accounting for attenuation and providing a more realistic description of the near acoustic field, the Rayleigh integrals (2.15a) and (2.15b) also allow for the radial component of $Gr_{ac}\widetilde{\boldsymbol{I}}_{\boldsymbol{ac}}$ to be determined. This differs from the former model used by Moudjed *et al.* (2014*a*), in which the forcing field was arbitrarily set to the direction normal to S_t. I shall now discuss how diffraction affects $\widetilde{\boldsymbol{I}}_{\boldsymbol{ac}}$; hence, the forcing field.

First, changing S affects the radial spreading of the beam, as expected (figure 2.2). As S is increased, the acoustic power is spread over larger surface areas, causing the beam to become wider and "shorter" (figure 2.2 (b)). As the beam radius matches approximately the source radius at $x = 0$ and increases with x at a rate S, the beam edge is thus approximately given by

$$R_{beam} = 0.5 + Sx\,, \tag{2.19}$$

shall be comparable to the expression of L_F indicated in figure 2.1 (b). For the acoustic parameters of Moudjed *et al.* (2014*a*), on which this thesis is based, this is however not the case.

Thèse accessible à l'adresse : https://theses.insa-lyon.fr/publication/2024ISAL0101/these.pdf © [B. Vincent], [2024], INSA Lyon, tous droits réservés

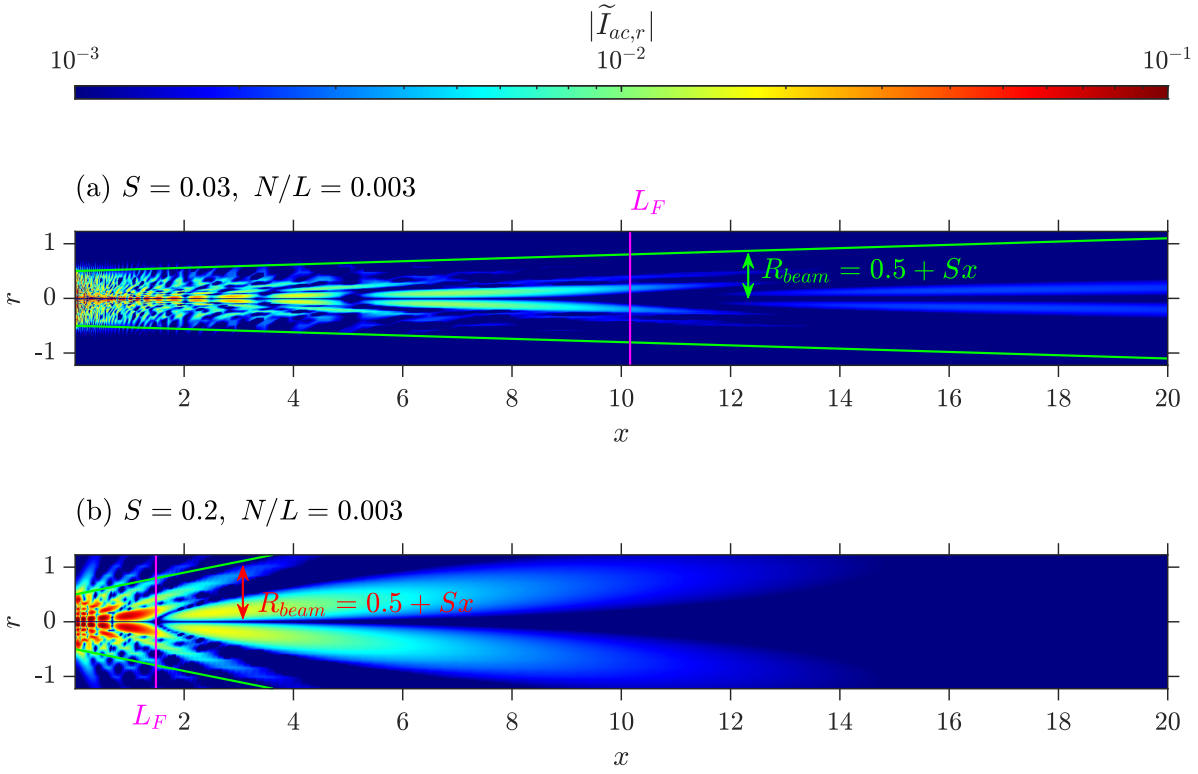


Figure 2.3: Map of the radial normalised intensity magnitude $|\widetilde{I}_{ac,r}|$ for $N/L = 0.003$ (value of Moudjed *et al.* (2014*a*)). Two values of the diffraction parameter S are displayed: (a) $S = 0.03$ (same value as Moudjed *et al.* (2014*a*)) and (b) $S = 0.2$. In both plot, the Fresnel distance $L_F = \frac{1}{4}\left(\frac{1.22}{S} - \frac{S}{1.22}\right)$ is shown in purple and delimits the near ($x \leq L_F$) from the far ($x \geq L_F$) acoustic fields. The green lines represent the approximate beam edge defined by equation (2.19)). Both plots share the same colour levels.

which is represented by the green lines in figure 2.2. Furthermore, increasing S also reduces the number of $\widetilde{I}_{ac,x}$ peaks on the axis ($r = 0$).

Second, as S affects the radial beam size, it is of interest to know whether increasing S yields a significant radial component of $\widetilde{\boldsymbol{I}}_{\boldsymbol{ac}}$. In other words: can $\widetilde{\boldsymbol{I}}_{\boldsymbol{ac}}$ be supposed to be purely axial, as assumed by Moudjed *et al.* (2014*a*) ? For their S, very small regions of high $|\widetilde{I}_{ac,r}|$ (≈ 10 % of the maximum $\widetilde{I}_{ac,x}$) are found near the $r = 0$ axis and for $x \leq L_F$ (figure 2.3 (a)). These regions are located in between the on-axis peaks of $\widetilde{I}_{ac,x}$. For $x \geq L_F$, however, $|\widetilde{I}_{ac,r}|$ is marginal: its magnitude is at most ≈ 0.1 % of the maximum $\widetilde{I}_{ac,x}$. Therefore, discarding the radial forcing is reasonable for the configuration of Moudjed *et al.* (2014*a*). This approximation may however not be valid at higher S. For $S = 0.2$ for instance, the region of large $\widetilde{I}_{ac,r}$ (up to 10 % of the maximum $\widetilde{I}_{ac,x}$) covers the entire near acoustic field (figure 2.3 (b)). The size of this region is comparable to the x-range of significant $\widetilde{I}_{ac,x}$, indicating that neglecting $\widetilde{I}_{ac,r}$ may not be acceptable to simulate streaming in the near field of a highly-diffracted beam. The magnitude of $\widetilde{I}_{ac,r}$ nevertheless significantly decreases beyond L_F, where it is at most 1 % of the maximum $\widetilde{I}_{ac,x}$.

To conclude, I adapted the Rayleigh integral to account for attenuation of the intensity (hence forcing) field. Contrarily to the forcing model used by Moudjed *et al.* (2014*a*), the new formulation (equations (2.15) and (2.9)) also provides the radial forcing. Whilst $\widetilde{I}_{ac,r}$ is negligible in the case of Moudjed *et al.* (2014*a*), it reaches up to 10 % of the maximum

Thèse accessible à l'adresse : https://theses.insa-lyon.fr/publication/2024ISAL0101/these.pdf © [B. Vincent], [2024], INSA Lyon, tous droits réservés

$\widetilde{I}_{ac,x}$ in more diffracted settings.

2.3 Energy transfer in acoustic streaming

I shall now discuss the transfer of energy between the acoustic and streaming scales. As explained by Dupuy *et al.* (2018), the Reynolds decomposition of $\boldsymbol{u}$ (1.33) divides the time-averaged total energy $\langle \mathcal{E} \rangle = \left\langle \rho e + \frac{1}{2}\rho \boldsymbol{u}\cdot\boldsymbol{u} \right\rangle$ into four main contributions:

$$\langle \mathcal{E} \rangle = \overbrace{\langle \rho e \rangle}^{\substack{\text{Time-averaged}\\ \text{internal energy}}} + \underbrace{\left\langle \frac{1}{2}\rho \boldsymbol{u_s}\cdot\boldsymbol{u_s} \right\rangle}_{\substack{\text{Time-averaged}\\ \text{streaming}\\ \text{kinetic energy}}} + \overbrace{\langle \rho \boldsymbol{u_s}\cdot\boldsymbol{u_{ac}} \rangle}^{\substack{\text{Time-averaged}\\ \text{mixed kinetic}\\ \text{energy}}} + \underbrace{\left\langle \frac{1}{2}\rho \boldsymbol{u_{ac}}\cdot\boldsymbol{u_{ac}} \right\rangle}_{\substack{\text{Time-averaged}\\ \text{acoustic}\\ \text{kinetic energy}}} . \tag{2.20}$$

Since $\rho = \rho_s + \rho_{ac}$, none of the terms in the right-hand side of equation (2.20) vanish. To draw the entire picture of all energy transfers at play, transport equations for $\left\langle \frac{1}{2}\rho \boldsymbol{u_s}\cdot\boldsymbol{u_s} \right\rangle$, $\left\langle \frac{1}{2}\rho \boldsymbol{u_s}\cdot\boldsymbol{u_{ac}} \right\rangle$, $\left\langle \frac{1}{2}\rho \boldsymbol{u_{ac}}\cdot\boldsymbol{u_{ac}} \right\rangle$ and $\langle \rho e \rangle$ shall thus be derived. **In this section, these energy equations are provided for dimensional variables and in a generic Cartesian coordinate system using Einstein notation**.

2.3.1 Overview of the energy exchanges in acoustic streaming

The approach to derive the time-averaged energy equations is very similar to the one of Dupuy *et al.* (2018): in addition to $\boldsymbol{u}$, Reynolds decompositions are also applied to p, ρ and to the viscous stresses $\boldsymbol{\sigma}$. Features specific to acoustic streaming are that:

(i) $\boldsymbol{\nabla} \times \boldsymbol{u_{ac}} = \boldsymbol{0}$,

(ii) The acoustic signals are time-periodic.

Despite these two features, the derivation of the time-averaged energy equations is very similar to what Dupuy *et al.* (2018) did. Therefore, I only provide the results here (the derivations are detailed in appendix B):

$$\frac{\partial \left\langle \frac{1}{2}\rho u_{s,i}^2 \right\rangle}{\partial t} + \frac{\partial \left\langle \frac{1}{2}\rho u_{s,i}^2 u_j \right\rangle}{\partial x_j} = \Phi_{p_s} + \Phi_{\sigma_s} + \mathcal{P}_s - \Upsilon_s - \varepsilon_s \,, \tag{2.21a}$$

$$\frac{\partial \left\langle \frac{1}{2}\rho u_{ac,i}^2 \right\rangle}{\partial t} + \frac{\partial \left\langle \frac{1}{2}\rho u_{ac,i}^2 u_j \right\rangle}{\partial x_j} = \Phi_{p_{ac}} + \Phi_{\sigma_{ac}} + \mathcal{P}_{ac} - \Upsilon_{ac} - \varepsilon_{ac} \,, \tag{2.21b}$$

$$\frac{\partial \left\langle \rho u_{ac,i} u_{s,i} \right\rangle}{\partial t} + \frac{\partial \left\langle \rho u_{ac,i} u_{s,i} u_j \right\rangle}{\partial x_j} = -\mathcal{P}_s - \mathcal{P}_{ac} \,, \tag{2.21c}$$

$$\frac{\partial \left\langle \rho e \right\rangle}{\partial t} + \frac{\partial \left\langle \rho e u_j \right\rangle}{\partial x_j} = \Phi_T + \Upsilon_s + \Upsilon_{ac} + \varepsilon_s + \varepsilon_{ac} \,, \tag{2.21d}$$

in which:

- $\Phi_{p_s} = -\frac{\partial (p_s u_{s,j})}{\partial x_j}$ and $\Phi_{p_{ac}} = -\left\langle \frac{\partial (p_{ac} u_{ac,j})}{\partial x_j} \right\rangle$ are the power of the external pressure forces for the streaming flow and the acoustic fluctuations, respectively. They are conserved quantities.
- $\Phi_{\sigma_s} = \frac{\partial (\sigma_{s,ij}\, u_{s,i})}{\partial x_j}$ and $\Phi_{\sigma_{ac}} = \left\langle \frac{\partial (\sigma_{ac,ij} u_{ac,i})}{\partial x_j} \right\rangle$ are the powers of the external viscous forces for the streaming flow and the acoustic waves, respectively. As Φ_{p_s} and $\Phi_{p_{ac}}$, Φ_{σ_s} and $\Phi_{\sigma_{ac}}$ are conserved quantities.

Thèse accessible à l'adresse : https://theses.insa-lyon.fr/publication/2024ISAL0101/these.pdf © [B. Vincent], [2024], INSA Lyon, tous droits réservés

- $\Upsilon_s = -p_s \frac{\partial u_{s,j}}{\partial x_j}$ and $\Upsilon_{ac} = -\left\langle p_{ac} \frac{\partial u_{ac,j}}{\partial x_j} \right\rangle$ are the powers of pressure-dilatation forces at the streaming and acoustic scales, respectively. These contributions are specific to flows for which $\boldsymbol{\nabla \cdot u} \neq \mathbf{0}$ (Chassaing *et al.*, 2002).
- $\varepsilon_s = \sigma_{s,ij} \frac{\partial u_{s,i}}{\partial x_j}$ and $\varepsilon_{ac} = \left\langle \sigma_{ac,ij} \frac{\partial u_{ac,i}}{\partial x_j} \right\rangle$ respectively correspond to the dissipation of the streaming and acoustic kinetic energies due to viscous forces at their respective scales.
- $\Phi_T = \left\langle \frac{\partial}{\partial x_j} \left(\kappa \frac{\partial T}{\partial x_j} \right) \right\rangle$ is a source of internal energy due to thermal conduction.
- $\mathcal{P}_s$ is a production term for the time-averaged streaming kinetic energy; it is defined as:

$$\begin{aligned} \mathcal{P}_s = \langle \rho_{ac} u_{ac,j} \rangle \frac{\partial \left(\frac{1}{2} u_{s,i}^2 \right)}{\partial x_j} - \rho_s u_{s,j} \frac{\partial \left\langle \frac{1}{2} u_{ac,i}^2 \right\rangle}{\partial x_j} + u_{s,i} \left\langle \frac{\rho_{ac}}{\rho} \frac{\partial p_s}{\partial x_i} \right\rangle - u_{s,i} \left\langle \frac{\rho_{ac}}{\rho} \frac{\partial \sigma_{s,ij}}{\partial x_j} \right\rangle \\ + u_{s,i} \left\langle \frac{\rho_{ac}}{\rho} \frac{\partial p_{ac}}{\partial x_i} \right\rangle - u_{s,i} \left\langle \frac{\rho_{ac}}{\rho} \frac{\partial \sigma_{ac,ij}}{\partial x_j} \right\rangle . \end{aligned} \tag{2.22}$$

  In particular, using the equations of linear acoustics (1.13) and for $\rho_{ac}/\rho \ll 1$, the last term of $\mathcal{P}_s$ can be rewritten as:

$$-\boldsymbol{u_s} \left\langle \frac{\rho_{ac}}{\rho} \frac{\partial \sigma_{ac,ij}}{\partial x_j} \right\rangle \approx \frac{2\alpha}{c} \boldsymbol{I_{ac} \cdot u_s} ,$$

  with α representing viscous attenuation only. The power of the acoustic forcing is thus correctly accounted for in the energy balance.
- $\mathcal{P}_{ac}$ is a production term for $\left\langle \frac{1}{2} \rho \boldsymbol{u_{ac} \cdot u_{ac}} \right\rangle$:

$$\begin{aligned} \mathcal{P}_{ac} = -\left\langle \rho u_{ac,i} u_{ac,j} \frac{\partial u_{s,i}}{\partial x_j} \right\rangle + \langle \rho_{ac} u_{ac,j} \rangle \frac{\partial \left\langle \frac{1}{2} u_{ac,i}^2 \right\rangle}{\partial x_j} + \langle \rho_{ac} u_{ac,i} \rangle \left\langle \frac{1}{\rho} \frac{\partial p_s}{\partial x_i} \right\rangle \\ - \langle \rho_{ac} u_{ac,i} \rangle \left\langle \frac{1}{\rho} \frac{\partial \sigma_{s,ij}}{\partial x_j} \right\rangle + \langle \rho_{ac} u_{ac,i} \rangle \left\langle \frac{1}{\rho} \frac{\partial p_{ac}}{\partial x_i} \right\rangle - \langle \rho_{ac} u_{ac,i} \rangle \left\langle \frac{1}{\rho} \frac{\partial \sigma_{ac,ij}}{\partial x_j} \right\rangle \end{aligned} \tag{2.23}$$

  The first term of P_{ac} represents the production of acoustic kinetic energy by the shear of the streaming flow; it is analogous to the turbulent kinetic production term in incompressible turbulence (Giovannini & Airiau, 2016).

The different energy exchanges are sketched in figure 2.4. The production terms $\mathcal{P}_s$ and $\mathcal{P}_{ac}$ represent energy exchanges between $\left\langle \frac{1}{2} \rho \boldsymbol{u_s \cdot u_s} \right\rangle$ and $\langle \rho \boldsymbol{u_s \cdot u_{ac}} \rangle$, and between $\left\langle \frac{1}{2} \rho \boldsymbol{u_{ac} \cdot u_{ac}} \right\rangle$ and $\langle \rho \boldsymbol{u_s \cdot u_{ac}} \rangle$, respectively. In particular, no energy is directly exchanged between $\left\langle \frac{1}{2} \rho \boldsymbol{u_s \cdot u_s} \right\rangle$ and $\left\langle \frac{1}{2} \rho \boldsymbol{u_{ac} \cdot u_{ac}} \right\rangle$. Exchanges between the time-averaged acoustic kinetic energy and $\langle \rho e \rangle$ occur through viscous dissipation ε_{ac}, and through the power of pressure-dilatation forces Υ_{ac}. Same remarks apply for the energy exchanges between $\left\langle \frac{1}{2} \rho \boldsymbol{u_s \cdot u_s} \right\rangle$ and $\langle \rho e \rangle$.

2.3.2 Further developments to be made

The kinetic energy production terms $\mathcal{P}_s$ (equation (2.22)) and $\mathcal{P}_{ac}$ (equation (2.23)) look rather complicated and call for simplification. Indeed, these equations were obtained without making any assumption regarding $\boldsymbol{\nabla \cdot u_s}$ or the variations of ρ_s. In particular, the fact that $\rho_{ac}/\rho_s \ll 1$ can be used to expand all terms involving $1/\rho$. However, to which order shall the expansion be truncated for the energy equations to remain consistent ? In

Thèse accessible à l'adresse : https://theses.insa-lyon.fr/publication/2024ISAL0101/these.pdf © [B. Vincent], [2024], INSA Lyon, tous droits réservés

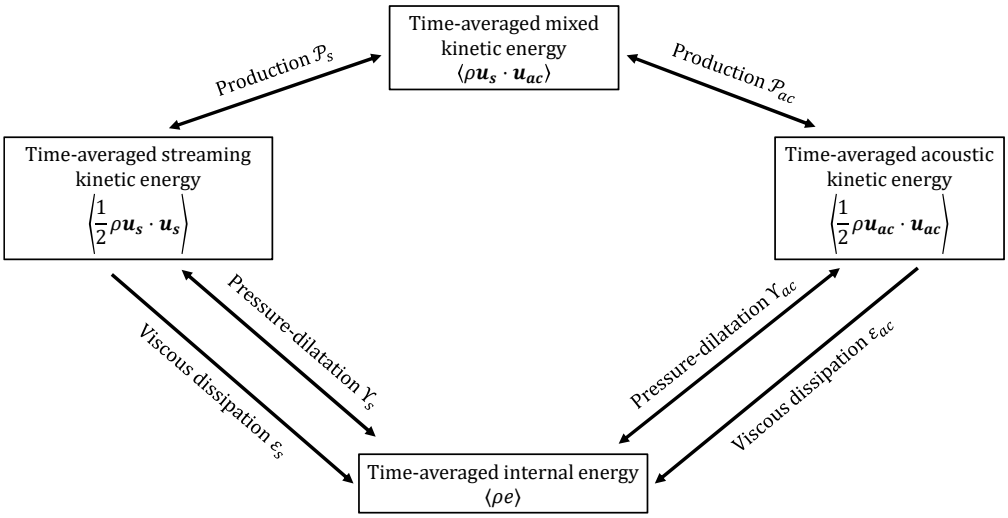


Figure 2.4: Sketch of the energy exchanges between the acoustic and streaming scales. The figure is adapted from Dupuy *et al.* (2018) and Chassaing *et al.* (2002).

the remaining terms, which ones are dominant ? For which values of N, S, etc. ? Furthermore, is there any combination of these dimensionless numbers for which $\boldsymbol{\nabla \cdot u_s} \neq \mathbf{0}$, yielding a non-zero Υ_s ? All these questions can only be answered by carefully evaluating the order of magnitude of each term.

A major difference with turbulence is that the fluctuations in streaming are time-periodic signals. This property has a strong influence on the magnitude of time-averaged fluctuation products, as we shall see with the following example. Consider for instance the product:

$$u_{ac,x} \frac{\partial u_{ac,x}}{\partial x} \,, \tag{2.24}$$

with $u_{ac,x}$ an attenuated plane travelling in the positive x-direction:

$$u_{ac,x} = u_0 e^{-\alpha x} e^{j(\omega t - kx)} \,.$$

Then:

$$u_{ac,x} \frac{\partial u_{ac,x}}{\partial x} = \left[u_0 e^{-\alpha x} e^{j(\omega t - kx)} \right] \left[-u_0 k \left(\frac{\alpha}{k} + j \right) e^{-\alpha x} e^{j(\omega t - kx)} \right] . \tag{2.25}$$

By further assuming that $\alpha/k \ll 1$ (i.e., the attenuation length is large compared to the wavelength[2]), the order of magnitude of the *instantaneous* product (2.25) is thus $\left| u_{ac,x} \frac{\partial u_{ac,x}}{\partial x} \right| \sim (k u_0^2)$. This is typically how the leading acoustic terms are identified when deriving the equations of linear and nonlinear acoustics involving only instantaneous quantities (Coulouvrat, 1992). Now, one may consider that time-averaged quantities have the same order of magnitude than their instantaneous counterparts. However, it can easily be shown from (2.25) that:

$$\left\langle u_{ac,x} \frac{\partial u_{ac,x}}{\partial x} \right\rangle = -\frac{\alpha}{2} u_0^2 e^{-2\alpha x} \sim \alpha u_0^2 \,, \tag{2.26}$$

[2]This assumption is usually verified. For the 2 MHz water experiments of Moudjed *et al.* (2014*a*), $\alpha/k \approx 10^{-5}$ (table A.1). In water, $\alpha \sim k$ for $f \approx 100$ GHz.

Thèse accessible à l'adresse : https://theses.insa-lyon.fr/publication/2024ISAL0101/these.pdf © [B. Vincent], [2024], INSA Lyon, tous droits réservés

i.e., the magnitudes of the instantaneous (2.25) and time-averaged (2.26) products differ by a factor $\alpha/k \ll 1$! This difference arises from the periodic nature of the acoustic fluctuations: if two signals are in quadrature, their product has a zero time average, regardless of the magnitude of each signal. **Therefore, knowing precisely the phase difference between acoustic signals is key to identify the dominant terms in the energy equations** (2.21). That phase difference is directly imposed by the equations governing wave propagation and by the wave shape e.g. a plane wave, a spherical wave, a beam with a slowly-varying envelope, or something else. Therefore, finding the leading energy transfer terms is restricted to a specific wave shape.

Unfortunately, I did not have enough time to estimate the order of the different terms in the energy equations (2.21). We recently started a collaboration with Michaël Baudoin (professor at Université de Lille, France); the idea is to use orders of magnitudes to rigorously justify which terms can be neglected (and under which circumstances) when deriving the continuity (1.35) and momentum (1.39) equations for the streaming flow. This collaboration will therefore also help for the study of energy exchanges between the acoustic and streaming scales.

2.4 Conclusion

In this chapter dedicated to my analytical work, (i) I adapted the model for the acoustic fields radiated by a plane circular baffled piston to account for attenuation, and (ii) I layed down the equations governing the energy exchanges between the acoustics and streaming scales.

The derived acoustic forcing model consists of two integral relations: one for the acoustic pressure p_{ac}, seen as an attenuated version of the Rayleigh integral (1.44) available in acoustics textbooks (Kinsler *et al.*, 2000; Blackstock, 2000), and one for the acoustic velocity fluctuations $\boldsymbol{u_{ac}}$. Based on linear acoustics, this model correctly accounts for the decay of the normalised acoustic intensity $\widetilde{\boldsymbol{I}}_{\boldsymbol{ac}}$ (hence, the forcing driving the streaming flow) due to attenuation. The proposed model is thus suitable for simulating streaming flows over distances larger than the characteristic sound attenuation distance, whilst keeping the low computational effort associated with linear acoustics. Contrarily to the approach of Moudjed *et al.* (2014*a*), the forcing direction is not set arbitrarily to the direction at which the source is pointing, but instead results from the computed forcing structure. In particular, the proposed attenuated model calculates the radial forcing component induced by the beam diffraction. Whilst this enhancement is negligible for weak diffraction, it nevertheless becomes important for highly-diffracted beams: in the near acoustic field, the magnitude of that radial forcing may reach up to 10 % of the maximum axial forcing. In such case, imposing arbitrarily the direction of $\widetilde{\boldsymbol{I}}_{\boldsymbol{ac}}$ may thus have significant impact of the structure and velocity levels of the simulated streaming jet.

In a second section, I provided the equations governing the energy exchanges between the streaming and acoustic scales; these equations are based on the work of Dupuy *et al.* (2018) on variable-density turbulence. The energy balance equations show that any energy transfer between the time-averaged streaming kinetic energy $\left\langle \frac{1}{2}\rho \boldsymbol{u_s}\cdot\boldsymbol{u_s}\right\rangle$ and acoustic kinetic energy $\left\langle \frac{1}{2}\rho \boldsymbol{u_s}\cdot\boldsymbol{u_{ac}}\right\rangle$ occurs through the mixed energy $\left\langle \rho \boldsymbol{u_s}\cdot\boldsymbol{u_{ac}}\right\rangle$. That energy transfer mechanism is specific to flows with density fluctuations, as it is the case in acoustics. The energy transfer model of Dupuy *et al.* (2018) may be further simplified by estimating the magnitude of each correlation (i.e., the time-averaged product of acoustic signals), allowing to identify the leading energy transfer terms. These simplifications

Thèse accessible à l'adresse : https://theses.insa-lyon.fr/publication/2024ISAL0101/these.pdf © [B. Vincent], [2024], INSA Lyon, tous droits réservés

would exploit the fact that (i) the (acoustic) density fluctuations are weak compared to the mean density, (ii) the (acoustic) velocity fluctuations are irrotational, and (iii) all acoustic signals are periodic. This last property, in particular, plays a major role on the magnitude of a given correlation: depending on whether the acoustic signals are in phase or in quadrature, the correlation can differ from its instantaneous (i.e., non time-averaged) counterpart by several orders of magnitudes, or even completely vanish. The phase differences between acoustic signals result from the wave propagation equations (e.g., the equations (1.13) of linear acoustics), and depend on the shape of the sound waves. Identifying the leading energy transfer terms is thus only possible by assuming a certain acoustic wave shape, to the expense of a reduced generality of the energy transfer analysis.

Thèse accessible à l'adresse : https://theses.insa-lyon.fr/publication/2024ISAL0101/these.pdf © [B. Vincent], [2024], INSA Lyon, tous droits réservés

Chapter 3

Scaling of a steady laminar and axisymmetric acoustic streaming jet

3.1 Introduction

Most existing Eckart streaming works from the literature focus on cases for which the attenuation distance L_α is greater than the size of the investigation domain, i.e., on $N < 1$ jets (table A.2). However, these settings are not optimum situations, since the jet shall be forced over distances at least L_α in order to maximise the jet momentum flux (see the discussion in section 1.3.2).

The few experimental and numerical $N > 1$ studies of Dentry *et al.* (2014) and Daru *et al.* (2024) showed that the streaming jet may reach a velocity peak on its axis, before decelerating further downstream. This result contrasts significantly with previous $N < 1$ experiments (Kamakura *et al.*, 1995; Mitome, 1998; Moudjed *et al.*, 2014*a*; Frenkel *et al.*, 2001), in which the short investigation domains prevented observing a velocity maximum on the jet axis. Being able to predict the velocity peak position x_p proves important in several situations, as for the design of impinging streaming jets e.g., to clean a surface (Busnaina & Elsawy, 1998) or enhance heat or mass transfers at a wall (El Ghani *et al.*, 2021).

Nevertheless, the physical mechanism responsible for this velocity peak remains unclear, and the scaling proposed by Orosco & Friend (2022) for the peak position x_p remains unsatisfactory (figure 1.13). Besides, the decelerating flow region downstream x_p is yet to be investigated. **This work aims to identify and characterise the different regimes along the jet, from the transducer and up to distances where the forcing vanishes due to attenuation. In particular, I shall provide scaling laws for each of these regimes**. The accuracy of the obtained scaling laws is assessed with numerical simulations of a steady laminar axisymmetric streaming jet. The flow is forced by an attenuated diffracting beam modelled by the attenuated Rayleigh integrals derived in chapter 2.

This chapter is organised as follows: the problem is first defined in section 3.2. The numerical methods are then detailed in section 3.3, and the numerical model is validated in section 3.4. The streaming flow is then analysed in section 3.5 before giving the concluding remarks in section 3.6.

Thèse accessible à l'adresse : https://theses.insa-lyon.fr/publication/2024ISAL0101/these.pdf © [B. Vincent], [2024], INSA Lyon, tous droits réservés

3.2 Problem definition and governing equations

The configuration is entirely defined using the dimensionless numbers (1.58) of (Moudjed *et al.*, 2014*a*). I consider the case of an axisymmetric streaming flow of velocity $\boldsymbol{u}$ (the subscript "s" is dropped for clarity) in a cylindrical cavity entirely filled with a Newtonian fluid (figure 3.1). The cavity length and diameter are denoted by L and D, respectively. I shall adopt a cylindrical coordinate system, in which $\boldsymbol{e_x}$ and $\boldsymbol{e_r}$ are the normal unit vectors in the axial and radial directions, respectively. The associated coordinates are denoted by x and r. The plane circular transducer, of unit diameter, is placed at $x = 0$ and fires an axisymmetric beam-shaped sound field centred on the $r = 0$ axis. Because of diffraction, the beam grows radially at a rate S. Furthermore, attenuation causes the pressure waves amplitude to decay exponentially at a rate N/L, allowing to define an acoustic pressure attenuation length $L_\alpha = L/N$.

The flow model is based on the discrepancy between the time scales of the acoustics and streaming problems (chapter 1, section 1.3.1.2). As such, the streaming flow is described by the incompressible Navier-Stokes and continuity equations together with a body force (equations (1.39) and (1.35)); these equations are reminded below for convenience:

$$\frac{\partial \boldsymbol{u}}{\partial t} + (\boldsymbol{u}\cdot\boldsymbol{\nabla})\,\boldsymbol{u} = -\boldsymbol{\nabla} p + \boldsymbol{\nabla}^2\boldsymbol{u} + Gr_{ac}\widetilde{\boldsymbol{I}}_{\boldsymbol{ac}}\,, \tag{3.1a}$$

$$\boldsymbol{\nabla}\cdot\boldsymbol{u} = 0\,. \tag{3.1b}$$

The cavity walls at $x = 0$, $x = L$ and $r = D/2$ are perfectly sound-absorbing and impermeable. Incident sound waves thus cannot be reflected, and $\boldsymbol{u} = \boldsymbol{0}$ at the walls. To enforce axisymmetry, the following conditions are prescribed at $r = 0$:

$$u_r(x, r = 0) = \frac{\partial u_x}{\partial r}(x, r = 0) = \frac{\partial p}{\partial r}(x, r = 0) = 0\,, \tag{3.2}$$

with $u_x = \boldsymbol{u}\cdot\boldsymbol{e_x}$ and $u_r = \boldsymbol{u}\cdot\boldsymbol{e_r}$.

The values adopted for the dimensionless parameters describing the problem are listed in table 3.1. The parameters S and N/L defining the beam geometry match those of

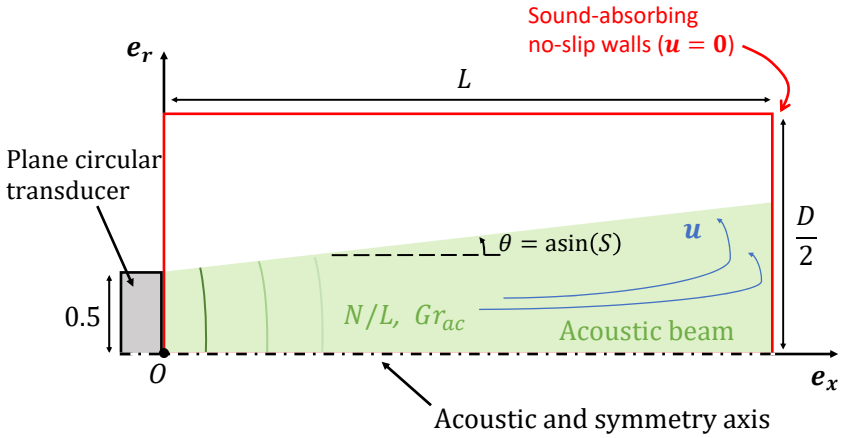


Figure 3.1: Sketch of the computational domain. Being axisymmetric and free of any azimuthal velocity, the streaming flow is studied in the (x, r) plane, where x and r are the axial and radial coordinates, respectively. All indicated quantities are made dimensionless using D_s, $\rho_0 D_s^3$ and D_s^2/ν as length, mass and time scales, respectively (D_s: transducer diameter, ρ_0: fluid density and ν: kinematic viscosity).

Thèse accessible à l'adresse : https://theses.insa-lyon.fr/publication/2024ISAL0101/these.pdf © [B. Vincent], [2024], INSA Lyon, tous droits réservés

Table 3.1: Values of the dimensionless parameters (1.58) considered in the present study. The values of the parameters S and N/L correspond to the water experiments of Moudjed *et al.* (2014*a*), for which $f = 2 \times 10^6$ Hz, $\alpha \approx 0.1$ m^{-1}, $D_s = 2.85 \times 10^{-2}$ m and $c = 1480$ m.s^{-1}.

S	N	L	D	Gr_{ac}
0.03	4.5	1500.7	548.3	Varied between 10^3 and 5×10^4

Moudjed *et al.* (2014*a*); Moudjed (2013); Moudjed *et al.* (2015), meaning that the structure of $\widetilde{\boldsymbol{I}}_{\boldsymbol{ac}}$ is thus representative of existing experiments. I stress that an important aspect of this work is the moderately large value of N, i.e., far regions where the beam is nearly entirely attenuated always exist. Typically, at $x = L$, the remaining acoustic power is about 0.01 % of the power radiated by the transducer. Finally, as this work is concerned with the scaling of a single straight streaming jet, interactions with the cavity walls shall be avoided. Therefore, the cavity diameter is taken such that $D = 12\, R_{beam}|_{x=L}$, with $R_{beam}|_{x=L}$ the approximate beam radius (equation (2.19)) at the downstream wall.

3.3 Numerical methods and mesh design

The scaling analysis is tackled with numerical simulations. I shall describe here the temporal and spatial discretisation strategies to compute the axisymmetric streaming flows.

3.3.1 Temporal discretisation of the hydrodynamics problem

To obtain steady axisymmetric streaming flows, the streaming equations (3.1) are marched forward in time until a steady state is reached. The temporal discretisation relies on the splitting scheme of Karniadakis *et al.* (1991), which integrates explicitly the nonlinear terms of equation (3.1a), whilst the linear terms are integrated implicitly. The velocity $\boldsymbol{u}^{(n+1)}$ at time step $(n+1)$ is obtained from the following semi-discrete form:

$$\frac{\gamma_0 \boldsymbol{u}^{(n+1)} - \sum_{q=0}^{K-1} c_q \boldsymbol{u}^{(n-q)}}{\Delta t} = -\boldsymbol{\nabla} p^{(n+1)} - \sum_{q=0}^{K-1} \beta_q \left[\boldsymbol{N}(\boldsymbol{u}^{(n-q)}) - Gr_{ac} \widetilde{\boldsymbol{I}}_{\boldsymbol{ac}}^{(n-q)} \right] + \boldsymbol{L}(\boldsymbol{u}^{(n+1)}), \tag{3.3}$$

where Δt is the time step, K is the order of the scheme, $\boldsymbol{N}(\boldsymbol{u}) = (\boldsymbol{u} \cdot \boldsymbol{\nabla})\, \boldsymbol{u}$ and $\boldsymbol{L}(\boldsymbol{u}) = \boldsymbol{\nabla}^2 \boldsymbol{u}$. The coefficients for the backwards-differencing approximation of $\partial \boldsymbol{u}^{(n+1)}/\partial t$ are denoted by c_q, and β_q are the coefficients for polynomial extrapolation from time steps $(n-q)$ to $(n+1)$. Values of c_q and β_q for $K \in \{1, 2, 3\}$ are listed in table 3.2. For the steady axisymmetric flow computations, I took only $K = 1$. Higher-order formulations shall be used in chapter 4 for non-axisymmetric DNS and linear stability analysis.

Thèse accessible à l'adresse : https://theses.insa-lyon.fr/publication/2024ISAL0101/these.pdf © [B. Vincent], [2024], INSA Lyon, tous droits réservés

Table 3.2: Coefficients of the Kth-order splitting scheme (3.3) used for the temporal discretisation of the streaming problem (table reproduced from Karniadakis *et al.* (1991)).

Order K	1	2	3
γ_0	1	3/2	11/6
c_0	1	2	3
c_1	0	−1/2	−3/2
c_2	0	0	1/3
β_0	1	2	3
β_1	0	−1	−3
β_2	0	0	1

One time step of equation (3.3) is divided into four intermediate stages:

$$\frac{\boldsymbol{u}_1 - \sum_{q=0}^{K-1} c_q \boldsymbol{u}^{(n-q)}}{\Delta t} = -\sum_{q=0}^{K-1} \beta_q \left[\boldsymbol{N}(\boldsymbol{u}^{(n-q)}) - Gr_{ac} \widetilde{\boldsymbol{I}}_{\boldsymbol{ac}}^{(n-q)} \right] , \tag{3.4a}$$

$$\nabla^2 p^{(n+1)} = \frac{1}{\Delta t} \boldsymbol{\nabla} \cdot \boldsymbol{u}_1 , \tag{3.4b}$$

$$\frac{\boldsymbol{u}_2 - \boldsymbol{u}_1}{\Delta t} = -\boldsymbol{\nabla} p^{(n+1)} , \tag{3.4c}$$

$$\frac{\gamma_0 \boldsymbol{u}^{(n+1)} - \boldsymbol{u}_2}{\Delta t} = \boldsymbol{L}(\boldsymbol{u}^{(n+1)}) , \tag{3.4d}$$

where $\boldsymbol{u}_1$ and $\boldsymbol{u}_2$ are intermediate velocities. At each time step, p is updated by solving the Poisson equation (3.4b), which is obtained by taking the divergence of (3.4c) and by setting $\boldsymbol{\nabla} \cdot \boldsymbol{u_2} = \boldsymbol{0}$. For that Poisson equation to be solved, consistent Neumann pressure conditions are derived from the semi-discrete Navier-Stokes equations (3.3). Noting that $\boldsymbol{\nabla}^2 \boldsymbol{u} = -\boldsymbol{\nabla} \times \boldsymbol{\nabla} \times \boldsymbol{u}$ because of the incompressibility constraint (3.1b), the boundary condition for $p^{(n+1)}$ at the walls is:

$$\frac{\partial p^{(n+1)}}{\partial n} = -\boldsymbol{n} \cdot \left(\sum_{q=0}^{K-1} \beta_q \left[\boldsymbol{N}(\boldsymbol{u}^{(n-q)}) + \boldsymbol{\nabla} \times \boldsymbol{\nabla} \times \boldsymbol{u}^{(n-q)} - Gr_{ac} \widetilde{\boldsymbol{I}}_{\boldsymbol{ac}}^{(n-q)} \right] \right) , \tag{3.5}$$

where $\boldsymbol{n}$ is the wall-normal unit vector.

As the time scheme involves the explicit integration of $\boldsymbol{N}(\boldsymbol{u})$, Δt was adapted for each Gr_{ac} so that the maximum CFL (Courant-Friedrichs-Lewy) number remained below unity to ensure numerical stability. For instance, for $Gr_{ac} = 1 \times 10^3$, I set $\Delta t = 10^{-3}$, yielding a maximum CFL number of 0.68.

Finally, the first axisymmetric steady flow was computed for $Gr_{ac} = 1 \times 10^3$ and was initiated with $\boldsymbol{u} = \boldsymbol{0}$ and $p = 0$. To accelerate the convergence towards a steady state at larger Gr_{ac}, I initiated the calculations with steady flows computed previously at smaller Gr_{ac}.

3.3.2 Spatial discretisation of the hydrodynamics problem

The spatial discretisation method shall be able to handle regions of strong forcing and velocity gradients (e.g., near acoustic field and the region of jet acceleration up to the on-axis velocity peak x_p), as well as regions of smooth $\widetilde{\boldsymbol{I}}_{\boldsymbol{ac}}$ and $\boldsymbol{u}$ (far acoustic field

Thèse accessible à l'adresse : https://theses.insa-lyon.fr/publication/2024ISAL0101/these.pdf © [B. Vincent], [2024], INSA Lyon, tous droits réservés

and jet deceleration beyond x_p). For these reasons, equations (3.1) are discretised in space using the spectral element method (SEM), which allows for local mesh refinements whilst keeping the exponential ("spectral") convergence properties of traditional spectral methods (Blackburn *et al.*, 2019).

In the SEM, the (x, r) plane is partitioned into non-overlapping elements Ω^e, which are quadrilaterals in this work. Each of these elements can be mapped to a reference quadrilateral $\Omega^e_{\text{std}} = [-1, 1] \times [-1, 1]$ (Blackburn & Sherwin, 2004; Karniadakis & Sherwin, 2005), in which both $\boldsymbol{u}$ and p are decomposed using a set of polynomial basis functions ψ_{ij}. These functions are tensor products of equal-degree Lagrange interpolating polynomials l_i and l_j:

$$\psi_{ij}(\xi, \iota) = l_i(\xi) l_j(\iota)\,, \tag{3.6}$$

where $(\xi, \iota) \in \Omega^e_{\text{std}}$ are the local coordinates attached to the standard element, and:

$$l_i(\xi) = \frac{1}{N_p\,(N_p+1)} \frac{(1-\xi^2)}{(\xi_i - r)\,L_{N_p}(\xi_i)} \frac{\mathrm{d}L_{N_p}}{\mathrm{d}\xi}(\xi)\,. \tag{3.7}$$

with L_{N_p} the N_p-th degree Legendre polynomial. The Lagrange polynomials are defined on the $(N_p + 1)$ Gauss-Lobatto-Legendre (GLL) quadrature points ξ_i (with $0 \leq i \leq N_p$). As a consequence, $l_k(\xi_i) = \delta_{ik}$, where δ_{ik} is the Kronecker delta symbol (figure 3.2 (a)). The spatial resolution is then enhanced by increasing N_p.

The different operations (3.4) to compute one time step are of two types. First, equations (3.4a) and (3.4c) are updating operations, and are thus carried out on an element-by-element basis. Second, equations (3.4b) and (3.4d) require the solution of elliptic equations (Poisson or Helmholtz). Note that since the streaming flow is axisymmetric and swirl-free ($u_\theta = 0$), $\boldsymbol{\nabla}^2\boldsymbol{u}$ does not couple the different components of $\boldsymbol{u}$. Equation (3.4d) is thus treated as two uncoupled scalar Helmholtz problems. To solve these equations, the SEM relies on the method of weighted residuals, in which the discrete problem is derived from the weak form of the continuous problem (Canuto *et al.*, 2006). Thorough details on how the matrix system is formed from the weak form are given in Karniadakis & Sherwin (2005); Canuto *et al.* (2006); Blackburn *et al.* (2019).

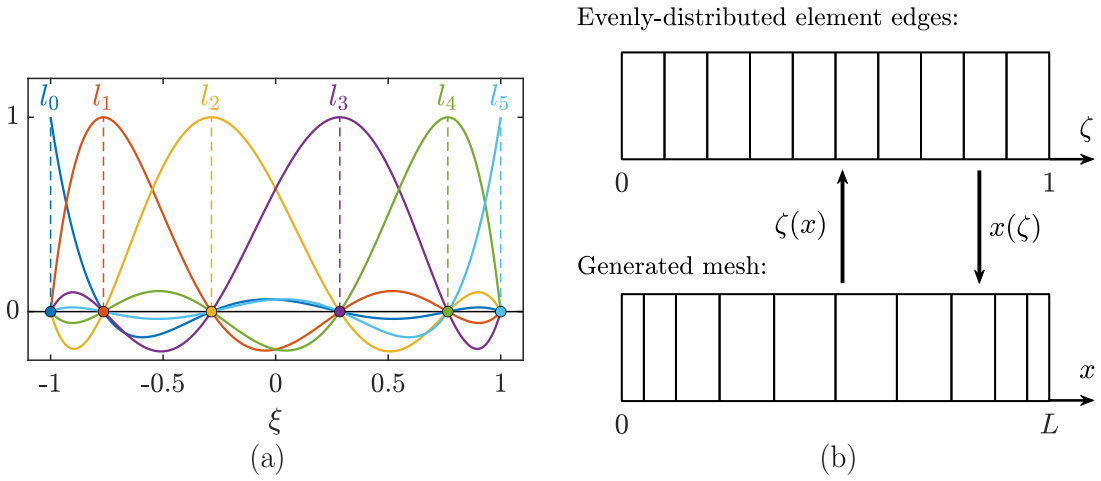


Figure 3.2: (a) Lagrange interpolating polynomials of degree $N_p = 5$ (equation (3.7)). These polynomials are defined on the $(N_p + 1)$ Gauss-Lobatto-Legendre (GLL) points (coloured dots). (b) Sketch of the procedure generating a mesh refined at both ends of the $[0, L]$ interval: evenly-distributed points in $[0, 1]$ are mapped to $[0, 1]$ with the transform (3.8).

Thèse accessible à l'adresse : https://theses.insa-lyon.fr/publication/2024ISAL0101/these.pdf © [B. Vincent], [2024], INSA Lyon, tous droits réservés

3.3.3 Mesh design

The (x, r) plane is discretised with a structured mesh refined in regions where strong gradients of $\boldsymbol{u}$ and/or $\widetilde{\boldsymbol{I}}_{\boldsymbol{ac}}$ occur, namely near $x = 0$, $x = L$ and $r = 0$.

In the x-direction, the elements sizes were prescribed through a stretching transformation. I defined the positions of the edges of $N_{e,x}$ elements with $(N_{e,x} + 1)$ evenly-distributed points $\zeta \in [0, 1]$ (see figure 3.2 (b)). The corresponding x-coordinates in $[0, L]$ of the element edges are then related to ζ through the following transformation (see § 4.4 in Farrashkhalvat & Miles (2003)):

$$\zeta(x) = \frac{L}{2\left[1 + \left(\frac{\beta+1}{\beta-1}\right)^{2x-1}\right]} \left(\beta \left[\left(\frac{\beta+1}{\beta-1} \right)^{2x-1} - 1 \right] + 1 + \left(\frac{\beta+1}{\beta-1} \right)^{2x-1} \right) , \tag{3.8}$$

where $\beta > 1$ is a tuning parameter defining the grid density near the $x = 0$ and $x = L$ walls: the closer β is to unity, the stronger is the stretching between two neighbouring elements. To quantify the mesh density, I shall define the "axial stretching factor" γ_x as the maximum lengths ratio between two neighbouring elements:

$$\gamma_x = \max_{0 \leq n \leq (N_{e,x}-2)} \left(\frac{\Delta x_{n+1}}{\Delta x_n} \right) , \tag{3.9}$$

where Δx_n is the size in x-direction of the n-th element.

To obtain the mesh from given values of ζ, the transform (3.8) needed to be inverted. In practice, this was done with the Newton-Raphson algorithm, with β being the adjusted variable. For a given $N_{e,x}$, β was corrected at each Newton iteration until the difference between the desired and actual values of γ_x fell below 10^{-10}. As an illustrative example, for $L = 1500.7$ and $N_{e,x} = 44$, $\gamma_x = 1.35$ is achieved with $\beta = 1.0027$.

In the r-direction, the domain is discretised using $N_{e,r}$ elements. Their radial size is constantly increased from $r = 0$ up to $r = D/2$ according to the geometric progression:

$$\Delta r_{(p+1)} = \gamma_r \Delta r_p \, , \quad \text{with } 0 \leq p \leq (N_{e,r} - 2) \, , \tag{3.10}$$

where Δr_p is the radial size of the p-th element discretising the radial direction and γ_r is a constant radial stretching factor.

To summarise, the numerical procedure to simulate steady axisymmetric streaming flows can be divided into three major steps:

(i) The computational domain Ω is discretised with quadrangles (figure 3.3). The element sizes in the x- and r-directions are defined by the numbers of elements $N_{e,x}$ and $N_{e,r}$ and by the stretching factors γ_x and γ_r (equations (3.9) and (3.10)).

(ii) The acoustic forcing $Gr_{ac}\widetilde{\boldsymbol{I}}_{\boldsymbol{ac}}$ is computed at the grid points (i.e., the GLL points of each element) through the numerical evaluation of the attenuated Rayleigh integrals (2.15).

(iii) The streaming problem is marched forward in time using the splitting-scheme (3.3) with $K = 1$. A steady state is assumed to be reached when the time-series of $\boldsymbol{u}$ and p, recorded at different locations in the fluid domain (red dots in figure 3.3), do not vary with a precision of five significant figures over 100 consecutive time steps.

The steps (i) and (ii) were carried out with MATLAB codes I developed for these purposes. The steady axisymmetric flow fields (step (iii)) were computed with the open-source code *Semtex* (Blackburn *et al.*, 2019; Blackburn & Sherwin, 2004), in which both

Thèse accessible à l'adresse : https://theses.insa-lyon.fr/publication/2024ISAL0101/these.pdf © [B. Vincent], [2024], INSA Lyon, tous droits réservés

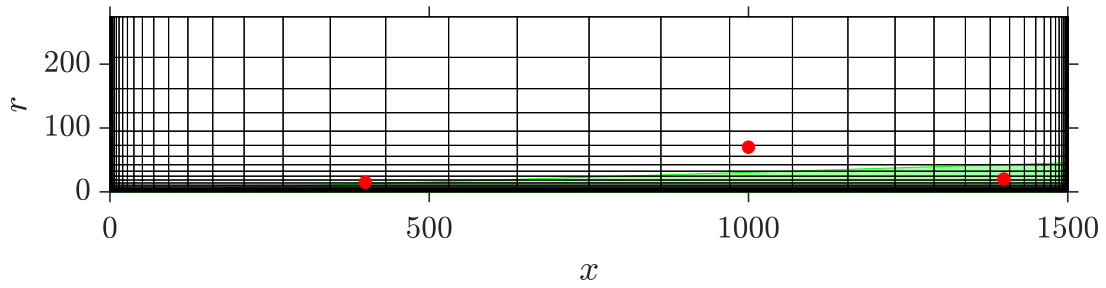


Figure 3.3: Discretisation of the fluid domain with 880 quadrilateral elements. The main lobe of the acoustic beam is represented by the green-shaded area; the corresponding approximate beam radius R_{beam} is given by equation (2.19). The red dots at $(x, r) = (400, 15)$, $(1000, 70)$ and $(1400, 20)$ locate the points where the time series of $\boldsymbol{u}$ and p are recorded to monitor the convergence towards a steady state.

the SEM and the time-splitting scheme were already implemented. In the code, the linear matrix systems for the discrete Poisson (3.4b) and Helmholtz (3.4d) equations are solved with a direct method together with static condensation.

3.4 Grid sensitivity and validation of the numerical model for long-range ($N > 1$) streaming calculations

Prior to be used for the scaling of streaming jets, the numerical model first needs be validated. After having assessed the ability of *Semtex* to simulate streaming flows from former experimental and numerical studies in appendix C, I shall determine the mesh density required for the simulations to be grid-independent. Then, I shall validate the forcing field obtained from the attenuated Rayleigh integral (2.15). In particular, I give here an example of the errors made on the simulated flow if attenuation is not modelled in $\widetilde{\boldsymbol{I}}_{\boldsymbol{ac}}$.

3.4.1 Grid sensitivity analysis

In spectral-element methods, convergence is achieved by increasing the degree N_p of the expansion basis, i.e., through p-refinement (Blackburn *et al.*, 2019). In the present case, the near acoustic forcing field features strong gradients that are undersampled to keep the calculations tractable (figure 3.4). Therefore, increasing the mesh density (either through N_p or through the number of elements) does not only act on the quality of the computed flow structures, but also affects the amount of acoustic power radiated by the source; hence, the momentum that shall be acquired by the jet.

To assess the radial density requirements, I considered either $N_{e,r} = 20$ or $N_{e,x} = 23$ elements in the r-direction. As the elements are were stretched with a factor $\gamma_r = 1.3$, the two meshes featured either 1 or 2 elements in $0 \leq r \leq 0.5$, i.e., in a cylindrical region of same radius as the transducer. I ran simulations using both meshes and then measured the on-axis velocity $u_x(x, r = 0)$ at different x-positions (figure 3.5). Whether it is in the near (figure 3.5 (a)) or far (figure 3.5 (b) to (c)) acoustic field, the two meshes provide similar velocity estimates for sufficiently high N_p: with $N_p \geq 7$, the obtained velocities

Thèse accessible à l'adresse : https://theses.insa-lyon.fr/publication/2024ISAL0101/these.pdf © [B. Vincent], [2024], INSA Lyon, tous droits réservés

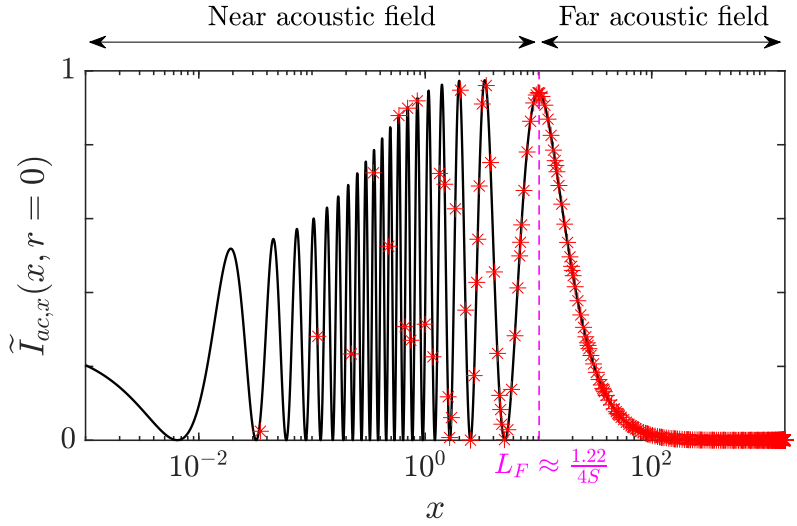


Figure 3.4: On-axis profile of the normalised axial intensity $\widetilde{I}_{ac,x}$: analytical profile (equation (2.17), black) and numerical integration of the attenuated Rayleigh integral (2.15) at the grid points (red). The grid is made of $N_{e,x} = 44$ elements in the x-direction, with a stretching factor $\gamma_x = 1.35$ (equation (3.9)) and $N_p = 8$. The magenta vertical line locates the Fresnel distance L_F.

Table 3.3: Dependence of the steady on-axis velocity peak position x_p and amplitude $u_{x,p}$ with the polynomial degree N_p of the expansion basis (the mesh is defined by $N_{e,x} = 44$, $N_{e,r} = 20$, $\gamma_x = 1.35$ and $\gamma_r = 1.3$). The calculations are made for $Gr_{ac} = 5 \times 10^4$ (highest forcing magnitude), and the errors are computed relatively to the results obtained for $N_p = 12$. The values of x_p are obtained by finding the point where $\partial u_x/\partial x$ vanishes on the axis, using the Lagrange polynomials (3.7) of the expansion basis as interpolation functions.

N_p	x_p	$u_{x,p}$	Relative error on x_p (%)	Relative error on $u_{x,p}$ (%)
4	23.187	736.05	2.2787	0.4412
5	23.702	732.68	0.1123	0.0186
6	23.748	732.45	0.0823	0.0505
7	23.732	732.79	0.0145	0.0047
8	23.729	732.76	0.0023	0.0088
9	23.731	732.70	0.0133	0.0172
10	23.735	732.57	0.0278	0.0345
11	23.733	732.62	0.0219	0.0271
12	23.728	732.82	–	–

simulated with either meshes differ by at most 0.05 %. Therefore, using only 1 element in $0 \leq r \leq 0.5$ is sufficient if $N_p \geq 7$.

I then assessed the effect of p-refinement on the position x_p and amplitude $U_{x,p}$ of the on-axis velocity peak (table 3.3). The errors on both x_p and $u_{x,p}$ were found to saturate towards $\approx 10^{-1}$ % for $N_p \geq 7$. The non-monotonic evolution of these errors with N_p is attributed to the near acoustic field being undersampled.

From this grid sensitivity analysis, I thus considered a mesh defined by $N_{e,x} = 44$, $N_{e,r} = 20$, $\gamma_x = 1.35$, $\gamma_r = 1.3$ and $N_p = 8$ for the scaling study. Such mesh was proven to be sufficiently refined for the effects of the near acoustic field undersampling to be

Thèse accessible à l'adresse : https://theses.insa-lyon.fr/publication/2024ISAL0101/these.pdf © [B. Vincent], [2024], INSA Lyon, tous droits réservés

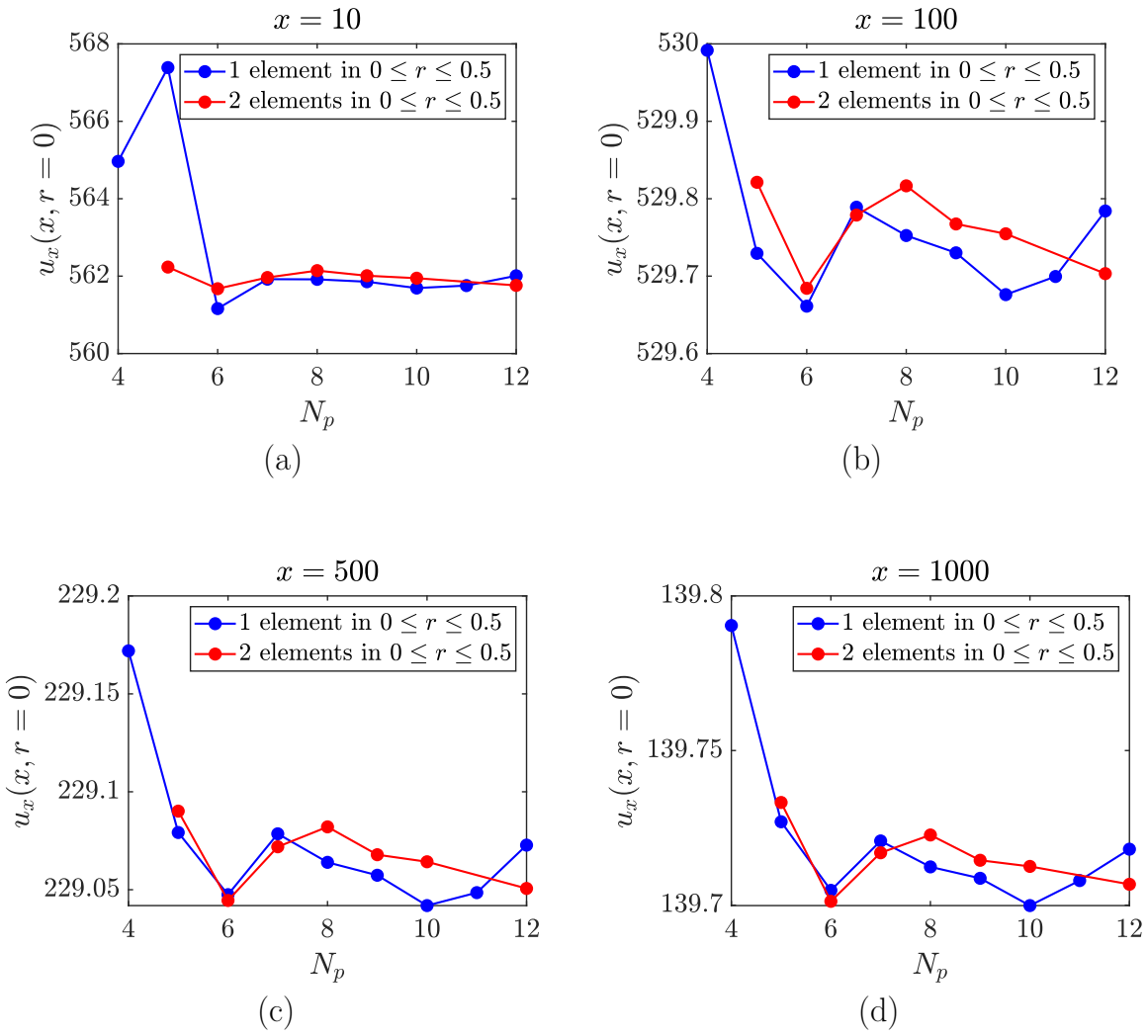


Figure 3.5: Effect of the radial mesh density on the on-axis velocity $u_x(x, r = 0)$ at different positions: (a) $x = 10$, (b) $x = 100$, (c) $x = 500$ and (d) $x = 1000$. The degree N_p of the polynomial expansion basis is also varied. The displayed data is obtained using either $N_{e,r} = 20$ elements in the r-direction (blue curves) or $N_{e,r} = 23$ (red curve). In both cases, the elements sizes increase by a factor 1.3 in the r-direction (i.e., equation (3.10) with $\gamma_r = 1.3$), yielding either 1 or 2 elements in the transducer radius ($0 \leq r \leq 0.5$). The remaining mesh parameters are $N_{e,x} = 44$ and $\gamma_x = 1.35$.

negligible.

3.4.2 Validation of the forcing model for the simulation of long-range ($N > 1$) streaming jets

I shall now proceed with the assessment of the forcing field, and also illustrate the error made if the Rayleigh integral had not been adapted to account for attenuation.

My analysis relies on the analytical result of Lighthill (1978) for the theoretical momentum flux M_{th} along a streaming jet forced by an attenuated beam (equation (1.43)). Once made dimensionless using D_s, $\rho_0 D_s^3$ and D_s^2/ν as length, mass and time scales,

Thèse accessible à l'adresse : https://theses.insa-lyon.fr/publication/2024ISAL0101/these.pdf © [B. Vincent], [2024], INSA Lyon, tous droits réservés

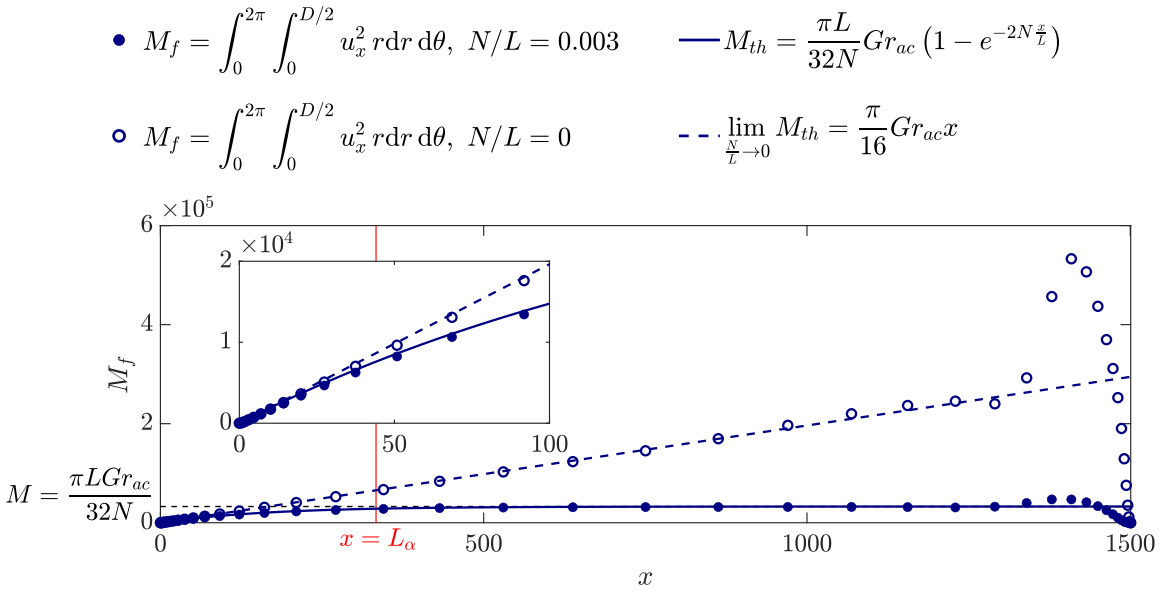


Figure 3.6: Evolution of the numerically-evaluated momentum flux M_f with the distance x from the transducer. The displayed quantities are obtained for $Gr_{ac} = 10^3$, with either an attenuated $\widetilde{\boldsymbol{I}}_{\boldsymbol{ac}}$ ($N/L = 0.003$, filled symbols) or unattenuated $\widetilde{\boldsymbol{I}}_{\boldsymbol{ac}}$ ($N/L = 0$, empty symbols). The numerical profiles are compared to the theoretical prediction (3.11) for $N/L = 0.003$ (blue solid line) and $N/L \to 0$ (blue dashed line). The horizontal black dashed line indicates the maximum theoretical momentum flux $M = \pi L Gr_{ac}/(32N)$. A detailed view of the momentum profiles near $x = 0$ is shown in the inset.

respectively, Lighthill's result becomes:

$$M_{th} = \int_0^{2\pi}\int_0^{\infty} u_x^2 r dr d\theta = M\left(1 - e^{-2N\frac{x}{L}}\right), \tag{3.11}$$

with $M = \pi L Gr_{ac}/(32N)$ the maximum theoretical momentum flux. As the sole role of attenuation is to set the length scale over which M_{th} grows (see the discussion in section 1.3.2), equation (3.11) is expected to break down if the forcing field is modelled as an unattenuated beam. Indeed, applying a Taylor's expansion to M_{th} in the limit of vanishing attenuation (i.e., $2Nx/L \ll 1$) yields $M_{th} = \pi Gr_{ac} x/16$. In other words, ignoring attenuation in the forcing field structure leads to an unimpeded build-up of M_{th}, which is in total contradiction with the bounded growth predicted by equation (3.11) ! From these two expressions of M_{th}, the relative error ε made on the jet momentum injected up to x when discarding attenuation is:

$$\varepsilon = \frac{\frac{2x}{L_\alpha}}{1 - e^{-\frac{2x}{L_\alpha}}} - 1\,. \tag{3.12}$$

That error increases rapidly with x: for instance, $\varepsilon \approx 0.1$ for $x = 0.1 L_\alpha$ and $\varepsilon \approx 1.3$ for $x = L_\alpha$. Hence, modelling acoustic streaming with an unattenuated $\widetilde{\boldsymbol{I}}_{\boldsymbol{ac}}$ is expected to greatly affect the flow even at $x \ll L_\alpha$.

To support my theoretical arguments, I simulated two $Gr_{ac} = 1 \times 10^3$ streaming jets: one forced by an attenuated $\widetilde{\boldsymbol{I}}_{\boldsymbol{ac}}$ ($N/L = 0.003$, as listed in table 3.1), and one for which $\widetilde{\boldsymbol{I}}_{\boldsymbol{ac}}$ is computed with $N/L = 0$ (i.e., with an unattenuated Rayleigh integral). For both cases, I calculated the numerical momentum flux M_f by integrating u_x^2 over a cross

Thèse accessible à l'adresse : https://theses.insa-lyon.fr/publication/2024ISAL0101/these.pdf © [B. Vincent], [2024], INSA Lyon, tous droits réservés

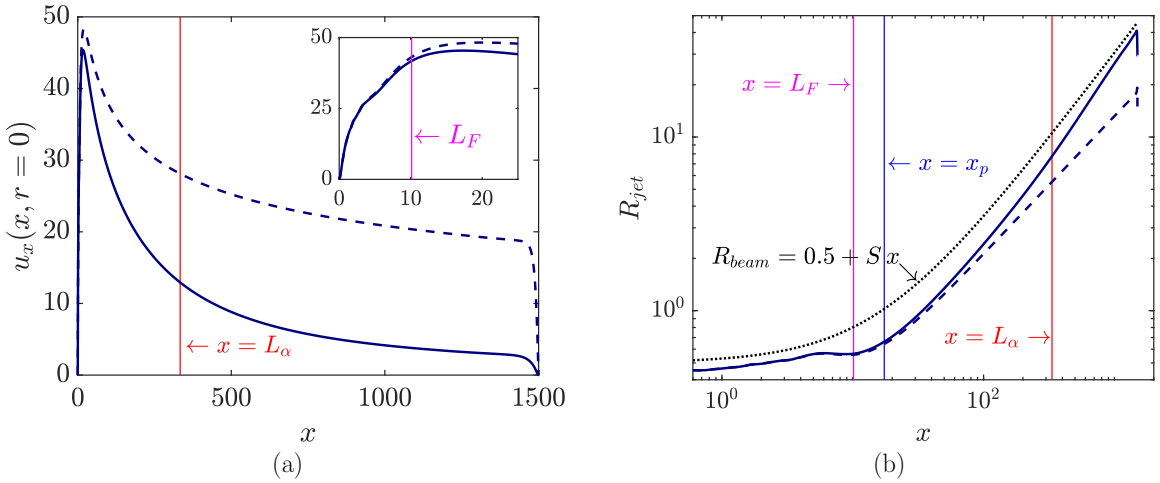


Figure 3.7: Effects of acoustic force attenuation on steady flows for $Gr_{ac} = 10^3$ when the attenuation is accounted for ($N/L = 0.003$, see table 3.1, solid) or neglected ($N/L = 0$, dashed line) in $\widetilde{\boldsymbol{I}}_{\boldsymbol{ac}}$ (equation (2.15)). (a) Longitudinal profiles of the on-axis velocity $u_x(x, r = 0)$, with a detailed view close to the transducer shown in the inset. (b) Longitudinal profiles of the jet radius R_{jet} defined as $u_x\,(x, R_{jet}) = 0.5\,u_x\,(x, 0)$. The approximate beam radius (equation (2.19)) is shown as a black dotted curve. The magenta vertical line locates the Fresnel distance L_F, and the red vertical line positions the attenuation distance L_α. The blue vertical line indicates the position x_p of the on-axis velocity peak in the attenuated $\widetilde{\boldsymbol{I}}_{\boldsymbol{ac}}$ case.

section of the cavity, and compared the numerical results to the theoretical predictions (figure 3.6). For an attenuated $\widetilde{\boldsymbol{I}}_{ac}$, M_f indeed saturates towards M and up to $x = 1300$. On the contrary, setting $N/L = 0$ leads to the expected linear increase of M_f with x. For $x > 1300$, the discrepancy between M_f and M_{th} for both the attenuated and unattenuated cases is caused by the flow recirculation imposed by the $x = L$ wall; such recirculation is absent in the free-jet setting from which equation (3.11) was derived (Lighthill, 1978).

As attenuation directly defines how momentum is created along the jet, neglecting the effects of attenuation in $\widetilde{\boldsymbol{I}}_{\boldsymbol{ac}}$ naturally greatly affects $\boldsymbol{u}$ on the axis (figure 3.7 (a)). For $x < 8$ (i.e., $x/L_\alpha < 5 \times 10^{-2}$), no significant difference between the two profiles is observed. However, the discrepancy builds up further downstream, as does ε. For an unattenuated $\widetilde{\boldsymbol{I}}_{\boldsymbol{ac}}$, u_x reaches a maximum at a greater distance x_p from the transducer, and with a larger magnitude. The velocity drop downstream x_p is also greatly affected, as u_x decays at a significantly slower rate with x. At $x \approx L$, the on-axis u_x differs by nearly a factor 10 between the attenuated and non-attenuated cases.

The large discrepancy observed between the $u_x(x, 0)$ profiles is accompanied by a different radial spreading rate of the jet (figure 3.7 (b)). In the near-acoustic field region ($x \leq L_F$), the jet radius R_{jet} (based on 50 % of $u_x(x, 0)$) remains nearly constant for both the attenuated and unattenuated cases. Beyond L_F, R_{jet} increases similarly to R_{beam} and up to $x \approx 2 \times 10^2$ for an unattenuated $\widetilde{\boldsymbol{I}}_{\boldsymbol{ac}}$, whereas R_{jet} experiences a larger increase in the attenuated case. This is related to the jet velocity: when high (as for the unattenuated $\widetilde{\boldsymbol{I}}_{\boldsymbol{ac}}$), viscous diffusion weakly affects the radial spread of the jet. Thus, the shape of the jet tends to follow more closely the shape of the beam, which is, in turn, dictated by acoustic diffraction. By contrast, low velocities (as for an attenuated $\widetilde{\boldsymbol{I}}_{\boldsymbol{ac}}$), increase the role of viscous diffusion. This leads to a greater radial enlargement of the jet as x

Thèse accessible à l'adresse : https://theses.insa-lyon.fr/publication/2024ISAL0101/these.pdf © [B. Vincent], [2024], INSA Lyon, tous droits réservés

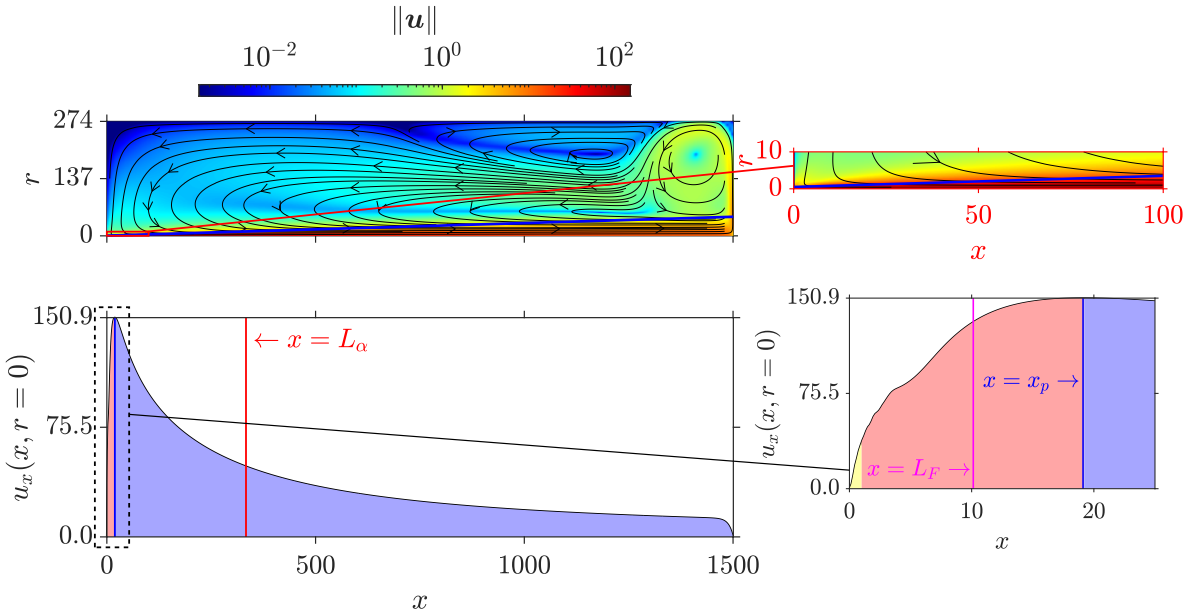


Figure 3.8: Typical steady velocity field obtained for $Gr_{ac} = 5 \times 10^3$. Top: velocity magnitude $\|\boldsymbol{u}\|$ together with streamlines. The approximate beam radius R_{beam} (equation (2.19)) is shown in blue, and the inset on the right focuses on the flow region close to the transducer. Bottom: longitudinal profile of u_x on the jet axis on which the Fresnel distance $L_F \approx 1.22/(4\,S)$, the on-axis velocity peak position x_p and the acoustic force attenuation distance $L_\alpha = L/N$ are reported. The right plot focuses on the region framed in black in the left plot.

increases, as observed in figure 3.7 (b).

To conclude, the strong agreement between M_f and M_{th} for an attenuated $\widetilde{\boldsymbol{I}}_{\boldsymbol{ac}}$ validates the forcing model based on the attenuated Rayleigh integral. If the latter had not been modified to account for attenuation, large errors would have been obtained on both the jet velocity $\boldsymbol{u}$ and the jet structure. For instance, neglecting attenuation of the forcing field structure typically overestimates $u_x(x, 0)$ by up to a factor 10 for $Gr_{ac} = 1 \times 10^3$. **From now, all the results to be presented were obtained with an attenuated $\widetilde{\boldsymbol{I}}_{\boldsymbol{ac}}$.**

3.5 Characterisation of an acoustic streaming jet

A typical illustration of the studied velocity fields is shown in figure 3.8. The flow is steady, axisymmetric and laminar, and is shaped as a jet centred on the $r = 0$ axis. The jet strongly accelerates near the transducer (yellow and red regions in the bottom plot of figure 3.8). There, the on-axis velocity $u_x(x, r = 0)$ builds up and displays irregularities caused by the large longitudinal forcing gradients in the acoustic near field (figure C.3). Then, $u_x(x, r = 0)$ eventually reaches a maximum of 150.9 for $Gr_{ac} = 5 \times 10^3$ at a distance x_p from the source; x_p does not coincide with either L_F or L_α. Finally, $u_x(x, r = 0)$ further downstream (blue region in the bottom plot of figure 3.8). Despite $N = 4.5$, the jet impinges the downstream wall with a velocity of nearly 10 % of its peak value. The jet impingement creates a large vortex of weak $\|\boldsymbol{u}\|$. In this section, I shall only consider the jet itself. I shall characterise each of the flow features identified on the $u_x(x, r = 0)$

Thèse accessible à l'adresse : https://theses.insa-lyon.fr/publication/2024ISAL0101/these.pdf © [B. Vincent], [2024], INSA Lyon, tous droits réservés

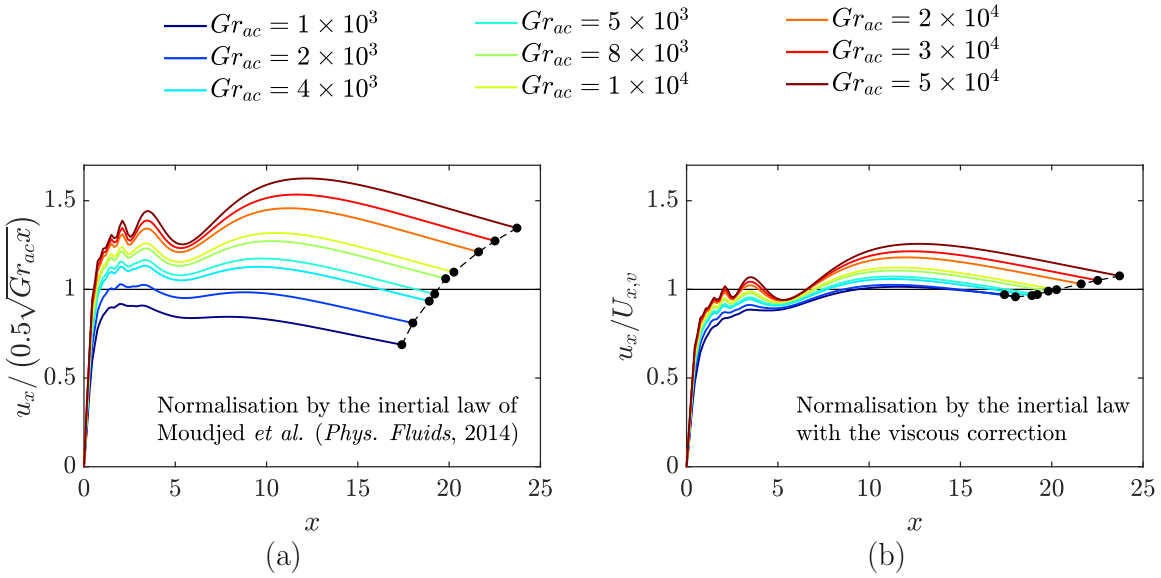


Figure 3.9: Longitudinal profiles of the on-axis jet velocity u_x normalised by different scaling laws. The profiles are plotted from the source ($x = 0$) up to the velocity peak position x_p (black points) for different Gr_{ac}. (a) On-axis velocity normalised by the scaling law (1.61), originally derived by Moudjed *et al.* (2014*a*) by balancing the inertial and acoustic forces, and by discarding the viscous forces. (b) On-axis velocity normalised by the scaling law (3.16) incorporating the viscous forces. A perfect scaling law would collapse all the profiles on a single horizontal master curve centred around the horizontal black line.

profile, from the fluid region close to the transducer up to the downstream wall.

3.5.1 Inertia-dominated flow regime close to the transducer

The on-axis jet velocity profile can be divided into several regions (bottom plot of figure 3.8); I shall first focus on the $0.5 \leq x \leq x_p$ region over which the jet accelerates. I deliberately leave the $x \leq 0.5$ region out of the analysis (shown in yellow in the inset of the bottom plot in figure 3.8), as (i) it is extremely small compared to L, and (ii) that region was already studied by Moudjed *et al.* (2015) (see section 1.5.2.2).

For $0.5 \leq x \leq x_p$, Moudjed *et al.* (2014*a*) proposed a scaling obtained from a balance between the acoustic and inertia forces (equation (1.61)). As shown in figure 3.9 (a), that scaling law correctly recovers the increase of u_x on $0.5 \leq x \leq x_p$. However, the scaling either overestimates u_x by nearly 30 % for $Gr_{ac} = 1 \times 10^3$, or instead underestimates it by 55 % for $Gr_{ac} = 5 \times 10^4$.

The discrepancy between the inertial scaling (1.61) and the numerical profiles may be attributed to the viscous forces neglected by Moudjed *et al.* (2014*a*). The magnitude of the viscous forces, compared to the other forces, can be determined from a momentum balance. Integrating the conservative form of the steady incompressible Navier-Stokes equations (3.1a) over a control volume V_c yields:

$$\overbrace{\oiint_{\partial V_c} \boldsymbol{u}\,(\boldsymbol{u}\cdot\boldsymbol{n})\,\mathrm{d}S}^{\text{Inertia forces}} = \overbrace{-\oiint_{\partial V_c} p\boldsymbol{n}\,\mathrm{d}S}^{\text{Pressure forces}} + \overbrace{\oiint_{\partial V_c} \boldsymbol{\sigma}\cdot\boldsymbol{n}\,\mathrm{d}S}^{\text{Viscous forces}} + \overbrace{\iiint_{V_c} Gr_{ac}\widetilde{\boldsymbol{I}}_{\boldsymbol{ac}}\,\mathrm{d}V}^{\text{Acoustic force}}, \tag{3.13}$$

Thèse accessible à l'adresse : https://theses.insa-lyon.fr/publication/2024ISAL0101/these.pdf © [B. Vincent], [2024], INSA Lyon, tous droits réservés

where ∂V_c is the outer surface of V_c, $\boldsymbol{n}$ is the outward unit vector normal to ∂V_c, and $\boldsymbol{\sigma}$ is the tensor of axisymmetric viscous stresses defined as:

$$\boldsymbol{\sigma} = 2\frac{\partial u_x}{\partial x}\,\boldsymbol{e_x}\otimes\boldsymbol{e_x} + \left(\frac{\partial u_x}{\partial r}+\frac{\partial u_r}{\partial x}\right)\boldsymbol{e_x}\otimes\boldsymbol{e_r} + \left(\frac{\partial u_r}{\partial x}+\frac{\partial u_x}{\partial r}\right)\boldsymbol{e_r}\otimes\boldsymbol{e_x} + 2\frac{\partial u_r}{\partial r}\,\boldsymbol{e_r}\otimes\boldsymbol{e_r} + 2\frac{u_r}{r}\,\boldsymbol{e_\theta}\otimes\boldsymbol{e_\theta}\,.$$

The chosen V_c encompasses the jet; the length of V_c is denoted by $L_{CV}\in[0,L]$, and its radius matches the jet radius R_{jet} defined as the point of 50 % of $u_x(x,0)$ (figure 3.10 (a)). Evaluating the integrals of equation (3.13) shows that, for $0\leq L_{CV}\leq x_p$ and $Gr_{ac}=1\times10^3$, the viscous forces are far from being negligible (figure 3.10 (b)). In contrast, increasing Gr_{ac} decreases the ratio between the viscous and inertia forces (figure 3.10 (c)). In other words, the balance between the acoustic and inertia forces assumed by Moudjed *et al.* (2014*a*) is only satisfied in the high Gr_{ac} limit.

To improve the scaling of the on-axis u_x in the accelerating region of the jet, I shall thus modify the inertial scaling (1.61) to account for the viscous forces. From an order of magnitude perspective, the steady dimensionless Navier-Stokes equations (3.1a) give:

$$\frac{1}{2}\frac{\partial\left(U_{x,v}^2\right)}{\partial x}\sim-\frac{U_{x,v}}{R_{jet}^2}+Gr_{ac}\widetilde{I}_{ac,x}\,, \tag{3.14}$$

where $U_{x,v}$ (subscript "v" stands for "viscous") is an order of magnitude of $u_x\,(x,r=0)$. From the definition of acoustic power (1.20):

$$\widetilde{I}_{ac,x}\sim\frac{e^{-2N\frac{x}{L}}}{16R_{beam}^2}\,. \tag{3.15}$$

Since the scaling law for $U_{x,v}$ is sought for $x\ll L_\alpha$, and because the diffraction-caused beam enlargement is small in that region, $R_{beam}\sim0.5$, which is also the order of R_{jet} (figures 3.7 (b) and 3.10 (a)). Then, by further taking $\partial\left(U_{x,v}^2\right)/\partial x\sim U_{x,v}^2/x$, equation (3.14) reduces to a quadratic polynomial, for which the positive root is

$$U_{x,v}=-4x+\frac{\sqrt{2}}{2}\sqrt{32x^2+Gr_{ac}x}\,. \tag{3.16}$$

The new scaling law (3.16) clearly improves the description of the jet acceleration on $0\leq x\leq x_p$ (figure 3.9 (b)): the discrepancy between $U_{x,v}$ and u_x is reduced to at most 25 %, confirming that the viscous forces play a non-negligible role in the $0.5\leq x\leq x_p$ jet region. This new scaling law also compares better to data from the literature (figure 3.11). Whilst the scaling of Moudjed *et al.* (2014*a*) could differ from literature data by a factor 2 (figure 3.11 (a)), the new scaling law (3.16) reduces the discrepancy to at most 50 % (figure 3.11 (b)). This further confirms the superiority of the new scaling law (3.16) over (1.61) to better describe the jet acceleration upstream x_p.

3.5.2 Position and magnitude of the on-axis jet velocity peak

The region of jet acceleration is followed by a velocity peak $u_{x,p}$ at x_p. Both x_p and $u_{x,p}$ display a dependency on Gr_{ac} that I shall now further investigate.

Thèse accessible à l'adresse : https://theses.insa-lyon.fr/publication/2024ISAL0101/these.pdf © [B. Vincent], [2024], INSA Lyon, tous droits réservés

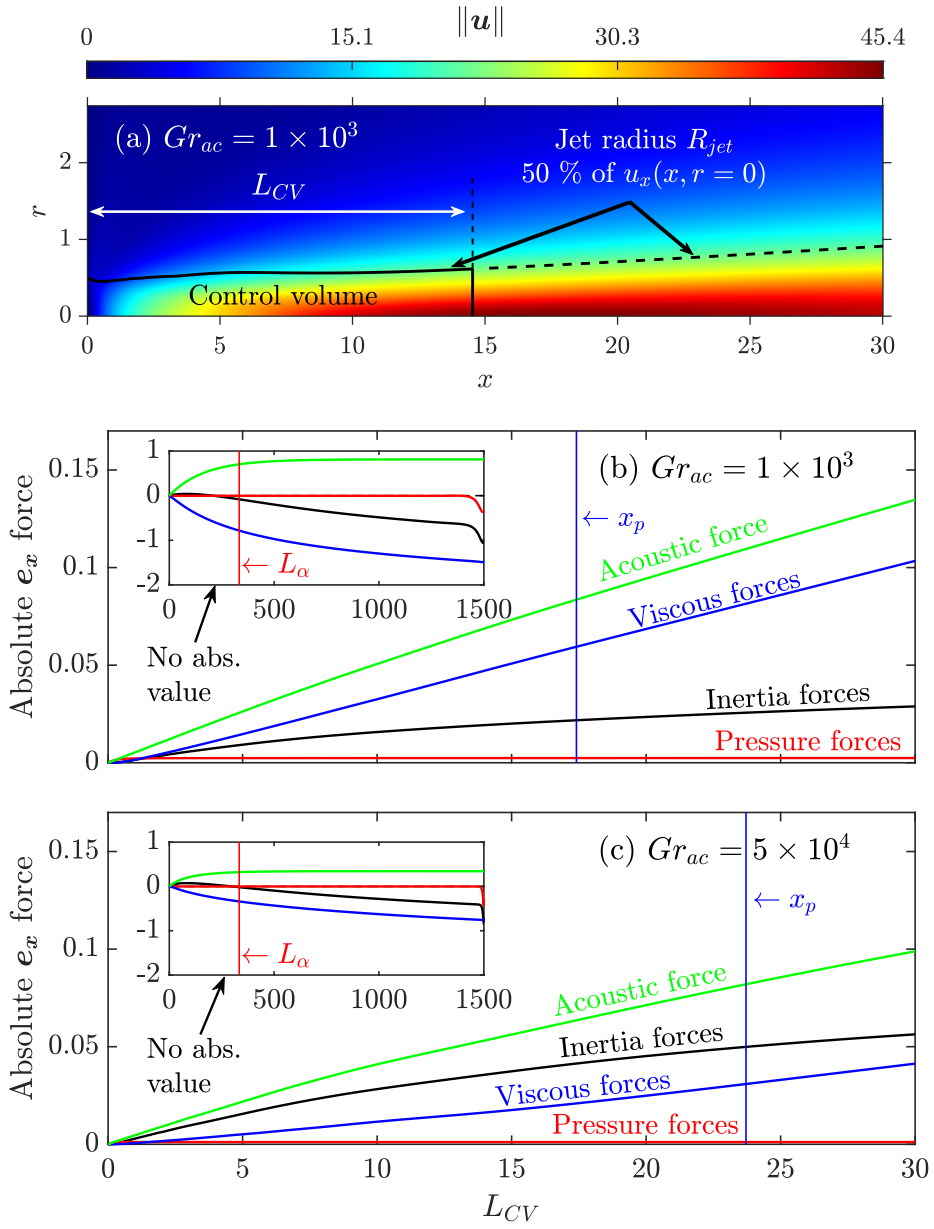


Figure 3.10: Momentum balance on a control volume V_c encompassing the jet, as defined by equation (3.13). (a) Map of the velocity magnitude $\|\boldsymbol{u}\|$ for $Gr_{ac} = 1 \times 10^3$; V_c is delimited by the black solid lines. The length and radius of V_c are denoted by L_{CV} and R_{jet}, respectively, and R_{jet} is defined such that $u_x(x, R_{jet}) = 0.5u_x(x, 0)$. (b) Magnitude of the forces acting along $\boldsymbol{e_x}$ and integrated on V_c (see equation (3.13)) defined in (a) for $Gr_{ac} = 1 \times 10^3$ (smallest forcing). (c) Same as (b), but for $Gr_{ac} = 5 \times 10^4$ (largest forcing). In (b) and (c), the insets show the forces along $\boldsymbol{e_x}$ for $0 \leq L_{CV} \leq L$, without taking their absolute values. The red and blue vertical lines locate the attenuation distance $L_\alpha = L/N$ and the on-axis velocity peak x_p, respectively. All computed forces are normalised by $M = \pi L Gr_{ac}/(32N)$.

At x_p and for a steady flow, the inertia term in the dimensionless Navier-Stokes equations (3.1a) vanishes, so that $u_{x,p}$ satisfies a local balance between the acoustic and viscous forces:

$$2\frac{U_{x,p}}{R_{jet,p}^2} \sim Gr_{ac}\widetilde{I}_{axis}\,, \tag{3.17}$$

Thèse accessible à l'adresse : https://theses.insa-lyon.fr/publication/2024ISAL0101/these.pdf © [B. Vincent], [2024], INSA Lyon, tous droits réservés

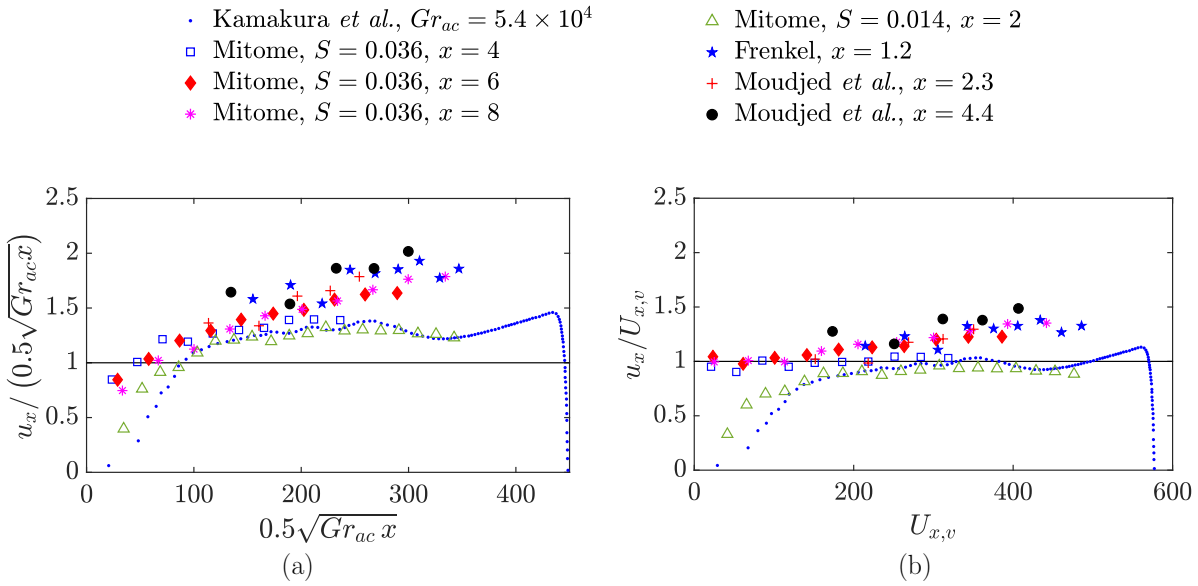


Figure 3.11: Comparison between the scaling laws and data taken from the literature (Kamakura *et al.*, 1996; Mitome, 1998; Frenkel *et al.*, 2001; Moudjed *et al.*, 2014*a*). (a) Comparison with the inertial scaling law (1.61) of Moudjed *et al.* (2014*a*), in which the viscous forces are discarded. (b) Comparison with the scaling law (3.16) derived in this thesis and accounting for the viscous forces. The dimensionless numbers for the literature data are listed in table A.2. Except for Kamakura *et al.* (1996), all the data points are from experiments.

where $U_{x,p}$ and $R_{jet,p}$ are orders of magnitude of the velocity amplitude and jet radius at x_p, respectively. Using equation (3.11) together with $M = \pi L Gr_{ac}/(32N)$, $R_{jet,p}$ can be related to $U_{x,p}$ through:

$$U_{x,p}^2 R_{jet,p}^2 \sim \frac{L}{64N} Gr_{ac} \left(1 - e^{-2N\frac{x_p}{L}}\right) . \tag{3.18}$$

In the present work, the on-axis velocity peak occurs in the acoustic far field. Using the far-field expression of $\widetilde{I}_{ac,x}(x,0)$ (equation (2.18)) together with (3.18) and assuming $2Nx_p/L \ll 1$, equation (3.17) becomes:

$$U_{x,p} \sim \left(\frac{1.22\pi\, Gr_{ac}}{64\, S}\right)^{\frac{2}{3}} x_p^{-\frac{1}{3}} . \tag{3.19}$$

An estimate of $U_{x,p}$ is thus needed to determine a scaling for x_p. Two options are available: using either the inertial scaling of Moudjed *et al.* (2014*a*), which discards the viscous forces for $x < x_p$, or using the corrected scaling law (3.16). In the first case, using equation (1.61) yields the following expressions for the peak position x_{p_i} and amplitude U_{x,p_i} (the subscript "i" stands for "inviscid"):

$$x_{p_i} \sim \left[\left(\frac{1.22\pi}{8\, S}\right)^4 \frac{Gr_{ac}}{64}\right]^{\frac{1}{5}} , \tag{3.20a}$$

$$U_{x,p_i} \sim \frac{1}{2}\left[\frac{1}{64}\left(\frac{1.22\pi}{8\, S}\right)^4\right]^{0.1} Gr_{ac}^{0.6} . \tag{3.20b}$$

Thèse accessible à l'adresse : https://theses.insa-lyon.fr/publication/2024ISAL0101/these.pdf © [B. Vincent], [2024], INSA Lyon, tous droits réservés

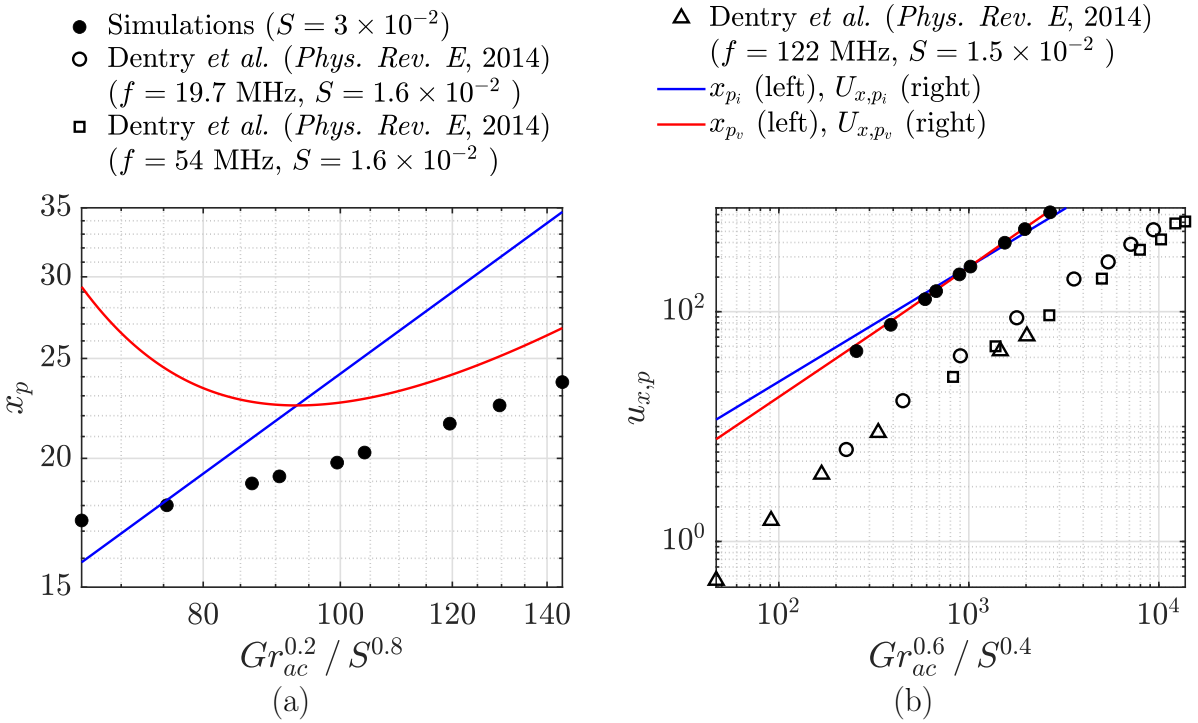


Figure 3.12: Evolution of the on-axis velocity peak position x_p and amplitude $u_{x,p}$ with Gr_{ac}. (a) Comparison between the peak positions observed in the numerical simulations (black filled symbols), and the predictions when neglecting ($x_{p,i}$, blue line, equation (3.20a)) and considering ($x_{p,v}$, red line, equation (3.21)) viscous forces in the region upstream x_p. The quantity represented on the x-axis is chosen to assess the validity of equation (3.20a). (b) Comparison between the peak amplitudes observed in the numerical simulations (black filled symbols), the experiments from Dentry *et al.* (2014) (empty symbols) and the theoretical predictions (solid lines) when viscous forces upstream x_p are neglected (U_{x,p_i}, blue, equation (3.20b)) and taken into account (U_{x,p_v}, red, equations (3.21) and (3.19)). The quantity plotted on the x-axis is chosen to assess the validity of equation (3.20b). In (b), the data of Dentry *et al.* (2014) are for an Eckart streaming jet driven by the transmission of Surface Acoustic Waves from a rectangular substrate to the bulk of the fluid. The equivalent acoustic source is rectangular, with a height H_s varying with the frequency. The parameters Gr_{ac} and S are thus based on H_s for the experimental points (instead of D_s for the numerical simulations).

In the second case, substituting (3.16) for $U_{x,p}$ yields:

$$4x_{p_v}^{\frac{4}{3}} - \frac{\sqrt{2}}{2}\left(32x_{p_v}^{\frac{8}{3}} + Gr_{ac}x_{p_v}^{\frac{5}{3}}\right)^{\frac{1}{2}} + \left(\frac{1.22\pi\, Gr_{ac}}{64\, S}\right)^{\frac{2}{3}} = 0\,, \tag{3.21}$$

which requires to be numerically solved for x_{p_v}. The corresponding velocity magnitude U_{x,p_v} is then recovered from equation (3.16) at x_{p_v}.

These different predictions are compared to the values of x_p observed in the numerical simulations in figure 3.12 (a). Neglecting the effects of the viscous forces in the fluid region upstream the velocity peak overestimates the dependency of x_p on Gr_{ac} (blue curve in figure 3.12 (a)). This leads to an error on x_p ranging from 1 % to 46 % over the Gr_{ac} range. By contrast, x_{p_v} is a better estimate of the peak position: the difference between x_p and x_{p_v} remains between 11 % and 13 % for $Gr_{ac}^{0.2}/S^{0.8} \geq 105$. At lower Gr_{ac}, that

Thèse accessible à l'adresse : https://theses.insa-lyon.fr/publication/2024ISAL0101/these.pdf © [B. Vincent], [2024], INSA Lyon, tous droits réservés

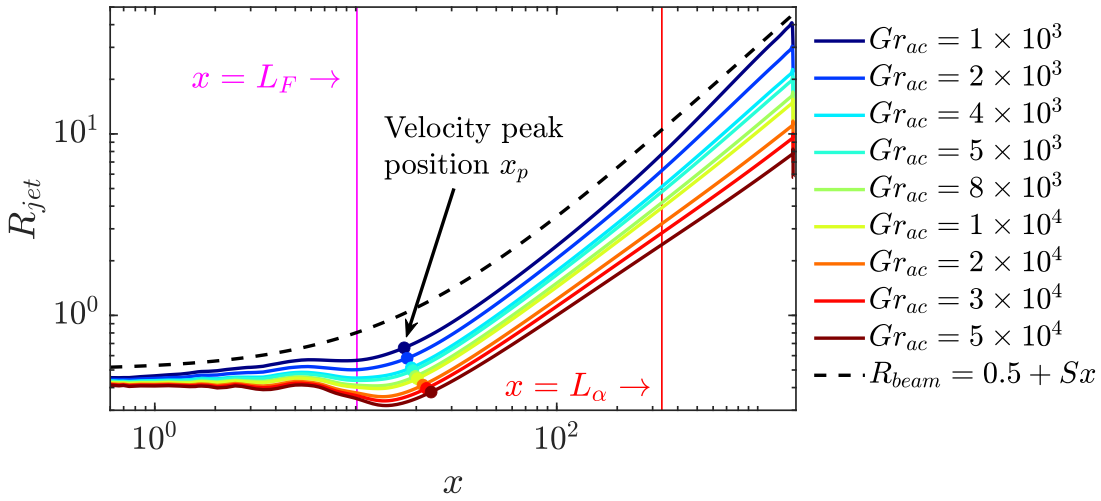


Figure 3.13: Evolution along x of the jet radius R_{jet}, defined as $u_x(x, R_{jet}) = 0.5u_x(x, 0)$. The simulations for all Gr_{ac} are displayed. On each curve, the velocity peak position x_p is located by a filled symbol. The vertical red and purple line locate the attenuation distance $L_\alpha = L/N$ and the Fresnel distance $L_F \approx 1.22/(4S)$, respectively.

discrepancy is however larger. The reason is that for decreasing values of Gr_{ac}, the jet velocity also decreases. As a consequence, the effect of viscous diffusion on the radial enlargement of the jet becomes more important: at L_F, R_{jet} measured for $Gr_{ac} = 10^3$ is 64 % larger than for $Gr_{ac} = 5 \times 10^4$ (figure 3.13). Thus, considering the same R_{jet} for all Gr_{ac} in the scaling law (3.14) leads to an overestimate of the viscous forces at low Gr_{ac}. Using a larger value of R_{jet} in equation (3.14) would also shift the range of Gr_{ac} values over which this equation is valid towards lower Gr_{ac}, as discussed in the previous section.

The same loss of accuracy at low Gr_{ac} is found for U_{x,p_v}, albeit to a lesser extent (figure 3.12 (b)). Although U_{x,p_i} provides an acceptable discrepancy of 8.7 % with the velocity peak magnitudes observed in the numerical simulations, its variation with Gr_{ac} is further improved when viscous forces are taken into account upstream the peak. The difference between U_{x,p_v} and $u_{x,p}$ indeed falls below 3 % for $Gr_{ac}^{0.6}/S^{0.4} \geq 4 \times 10^2$.

3.5.3 Viscosity-dominated flow regime beyond the velocity peak

We shall finally consider the fluid region located downstream x_p, where the on-axis jet velocity decays smoothly before reaching the wall at $x = L$ (blue region in the bottom plot of figure 3.8). Since inertial effects become negligible near x_p, $U_{x,d}$ is driven by the balance between the acoustic and the viscous forces; hence, using equation (3.15) gives:

$$\frac{U_{x,d}}{R_{jet}^2} \sim \frac{Gr_{ac}}{16R_{beam}^2} e^{-2N\frac{x}{L}}. \tag{3.22}$$

To derive the viscous scaling (1.62), Moudjed *et al.* (2014*a*) assumed similar longitudinal rate of change for R_{jet} and R_{beam}, besides of neglecting the variations of forcing along x due to attenuation. As a result, the viscous scaling (1.62) predicted a constant $u_x(x, 0)$. Clearly, this is not observed here (figure 3.13), and beam attenuation is too weak to be the sole responsible for the velocity decay downstream of x_p (figure 3.8). It is thus of primary importance to rely on an accurate estimate of the axial jet profile to assess the

Thèse accessible à l'adresse : https://theses.insa-lyon.fr/publication/2024ISAL0101/these.pdf © [B. Vincent], [2024], INSA Lyon, tous droits réservés

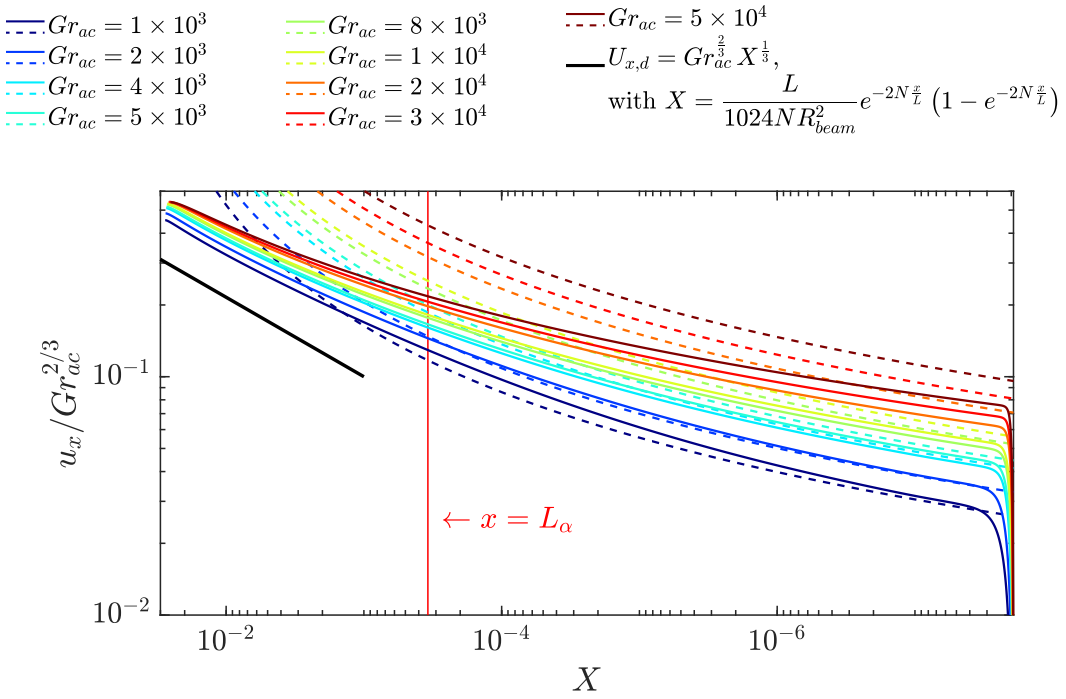


Figure 3.14: On-axis velocity profiles downstream the velocity peak x_p, obtained for different Gr_{ac}. The quantity plotted on the x-axis includes the longitudinal variations of the acoustic force caused by both diffraction and attenuation of the beam (right-hand side of equation (3.23)). The order of magnitude $U_{x,d}$ of the on-axis velocity downstream x_p (equation (3.23)), is shown in black. The coloured solid lines correspond to the numerical data. The dashed lines represent the self-similar jet solution $U_{x,S}$ of Schlichting & Gersten (2000) given by equation (3.25) and based on the maximum axial momentum flux $\pi L Gr_{ac}/(32N)$ to be acquired by the jet. The red vertical line locates the attenuation length $L_\alpha = L/N$.

viscous effects. In equation (3.22), substituting equation (3.18) for R_{jet}^2 yields:

$$U_{x,d} \sim Gr_{ac}^{\frac{2}{3}} X^{\frac{1}{3}}, \quad \text{with } X = \frac{L}{1024 N R_{beam}^2} e^{-2N\frac{x}{L}} \left(1 - e^{-2N\frac{x}{L}}\right). \tag{3.23}$$

As the considered flow region is located downstream L_F, the diffraction of the beam is significant and needs to be taken into account in X. This means that R_{beam} can no longer be considered constant, but should be evaluated using equation (2.19) instead. Thus, from equation (3.23), the longitudinal variations of u_x are caused by both the diffraction and the attenuation.

The scaling law (3.23) describes accurately the longitudinal decrease of u_x observed in the numerical simulations up to $x \approx L_\alpha$ (figure 3.14). At greater x-coordinates, the acoustic force amplitude keeps decreasing due to attenuation. Its magnitude relative to inertia keeps reducing with x, to the point where both become comparable for $x \gg L_\alpha$, a region where equation (3.23) is no more valid.

Another approach is thus required for $x \gg L_\alpha$. There, most of the beam energy has been attenuated, causing the acoustic force to be negligible. The jet thus satisfies a balance between the viscous and inertia forces at $x \gg L_\alpha$, and can therefore be modelled by the incompressible boundary layer and continuity equations (Schlichting & Gersten,

Thèse accessible à l'adresse : https://theses.insa-lyon.fr/publication/2024ISAL0101/these.pdf © [B. Vincent], [2024], INSA Lyon, tous droits réservés

2000):

$$u_x \frac{\partial u_x}{\partial x} + u_r \frac{\partial u_x}{\partial r} = \frac{1}{r} \frac{\partial}{\partial r} \left(r \frac{\partial u_x}{\partial r} \right) , \tag{3.24a}$$

$$\frac{\partial u_x}{\partial x} + \frac{1}{r} \frac{\partial \left(r u_r \right)}{\partial r} = 0 . \tag{3.24b}$$

Besides, the jet momentum flux is $\approx M = \pi L G r_{ac} / \left(32 N \right)$ for $x \gg L_\alpha$ (figure 3.6). Therefore, the situation becomes similar to the case of a straight jet of constant axial momentum M emerging from an orifice, for which a self-similar solution of equations (3.24) exists (Schlichting & Gersten, 2000):

$$u_x = \frac{3}{8\pi} \frac{M}{x} \frac{1}{\left(1 + \upsilon^2 \right)^2} ,$$

where

$$\upsilon = \frac{1}{8} \sqrt{\frac{3M}{\pi}} \frac{r}{x}$$

is the self-similar variable. Therefore, the on-axis streaming velocity at $x \gg L_\alpha$ can be described by:

$$U_{x,S} = \frac{3 L G r_{ac}}{256 N x} . \tag{3.25}$$

Equation (3.25) correctly reproduces the asymptotic behaviour of the on-axis velocity at $x \gg L_\alpha$ (dashed lines in figure 3.14), with a relative difference between $U_{x,S}$ and u_x ranging from 0.6 % to 29 % for $Gr_{ac} = 2 \times 10^3$ and 5×10^4, respectively, just upstream the impingement.

3.5.4 Summary of the derived scalings along the jet axis

All the scaling laws derived in this chapter for a steady and axisymmetric Eckart streaming jet, together with the scaling law of Moudjed *et al.* (2015) to describe the jet formation for $x \leq 0.5$, are summarised in figure 3.15. The acoustic force first causes the fluid to strongly accelerate near the source. In this region of the jet, the acoustic force is balanced by both the inertia and viscous forces (red region in figure 3.15). Though they are not dominant (especially at large Gr_{ac}), accounting for the viscous friction forces leads to an improvement of the scaling law describing this jet region, as discussed in section 3.5.1. The observed oscillations of u_x are directly correlated to the strong longitudinal gradient of the acoustic force in the near-acoustic field (figure C.3).

As x increases, the diffraction of the beam becomes significant enough for the acoustic force to decrease locally. This causes the jet to decelerate, up to the point where inertia completely vanishes, at the velocity peak x_p. Further downstream, as the beam keeps opening up due to diffraction, the on-axis acoustic force becomes locally weaker and it is balanced by the viscous forces (blue region in figure 3.15, for $x < L_\alpha$). This jet region is characterised by a smooth velocity decay on the jet axis.

For $x \gg L_\alpha$, the beam energy is almost entirely dissipated. Thus, the momentum balance reduces to an equilibrium between viscous and inertial forces, the axial momentum of the jet saturates to the constant value $M = \pi L G r_{ac} / \left(32 N \right)$ (equation (3.11)). As a consequence, the scaling law of the jet recovers that of a self-similar axisymmetric jet of constant momentum (3.25), represented by the dashed black line in figure 3.15.

Thèse accessible à l'adresse : https://theses.insa-lyon.fr/publication/2024ISAL0101/these.pdf © [B. Vincent], [2024], INSA Lyon, tous droits réservés

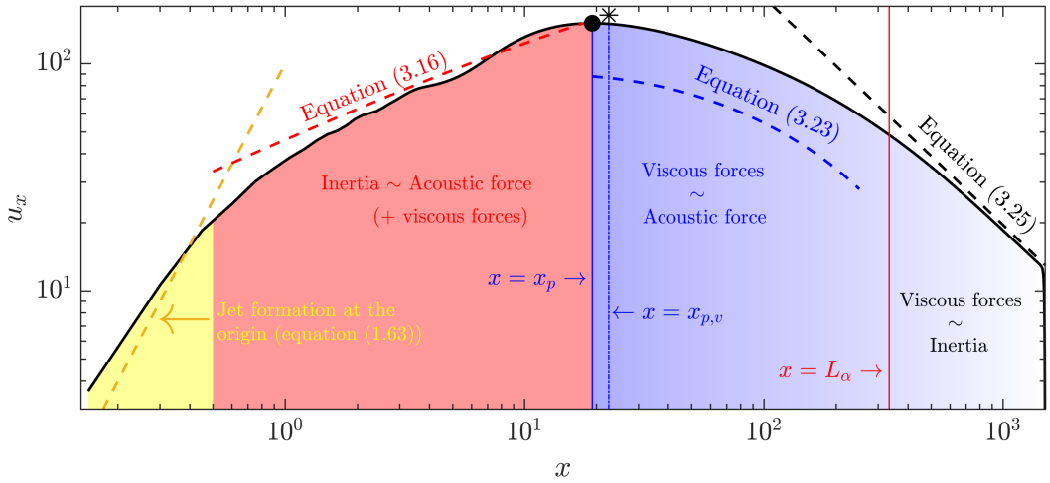


Figure 3.15: Longitudinal profile of the on-axis axial velocity u_x computed for $Gr_{ac} = 5 \times 10^3$ (solid black line), together with the scaling laws (dashed lines) and the force balance in each jet region. The scaling law in the yellow region is taken from Moudjed *et al.* (2015) (see section 1.5.2.2). The predicted peak position x_{p_v} (equation (3.21)) and amplitude U_{x,p_v} (from equation (3.19) with x_{p_v}) are represented by the dash-dotted blue vertical line and the black star, respectively. The solid blue and red vertical lines locate the actual on-axis velocity peak x_p and the attenuation distance $L_\alpha = L/N$, respectively.

3.6 Conclusion

In this chapter, I studied the scaling of a streaming jet based on numerical simulations. The flow develops in a closed and elongated cylindrical cavity entirely filled with a viscous liquid. The acoustic source is a plane circular transducer, of axis aligned with the cylinder axis, placed at one end of the cavity, in direct contact with the fluid. It radiates an axisymmetric beam-shaped acoustic field yielding a body force that drives the flow. An important aspect of this work is that the characteristic attenuation length L_α of the acoustic pressure waves is smaller but comparable to the cavity length (i.e., $N > 1$), so that the jet features both a region close to the source with prominent acoustic force, and regions further away where it is not. The diameter of the cavity is sufficiently large to avoid the influence of the lateral wall on the jet. The range of acoustic forces, measured by the acoustic Grashof number Gr_{ac}, is limited to moderate values, so that the resulting Eckart streaming jet remains axisymmetric, steady and laminar.

I first validated the forcing model based on the attenuated Rayleigh integral (2.15). I showed that, if the Rayleigh integral had not been adapted in chapter 2 to account for attenuation, the momentum flux M_f of the simulated jet would continuously grow along the axial direction x. This is contradictory to the fundamental result of Lighthill (1978), according to which M_f shall saturates towards a constant value instead (see section 1.3.2 in chapter 1). The error incurred on M_f when neglecting attenuation grows quickly along x: it is already 10 % at a distance $0.1L_\alpha$ from the source, and continues to increase further downstream. As a consequence, the unattenuated beam approximation severely overestimates the jet velocity along its axis, which in turn affects the flow structure by reducing the impact of viscous diffusion on the radial spreading of the jet.

The velocity of a jet forced by an attenuated acoustic beam evolves non-monotonically along the jet axis. I identified the different flow regions along the jet, and highlighted the

Thèse accessible à l'adresse : https://theses.insa-lyon.fr/publication/2024ISAL0101/these.pdf © [B. Vincent], [2024], INSA Lyon, tous droits réservés

driving mechanisms in each of them. I derived scaling laws based on physical arguments in each flow region; all these scalings are summarised in figure 3.15:

(i) Close to the transducer, the fluid is strongly accelerated, as a result of jet inertia mostly being balanced by viscous (Mitome *et al.*, 1995; Moudjed *et al.*, 2014*a*; Orosco & Friend, 2022), especially at large Gr_{ac}. However, at low Gr_{ac}, I showed that viscous forces are far from being negligible, causing a discrepancy of nearly 50 % between the simulated profiles and the scaling law of Moudjed *et al.* (2014*a*). I thus proposed a new scaling law that improves the velocity scaling on Gr_{ac} and reduces to 25 % the error on the predicted velocity.

(ii) The acceleration region is followed by a velocity peak on the jet axis. Beam diffraction causes the acoustic force on the axis to significantly drop locally, so that the acceleration vanishes. I obtained a scaling law for the peak position x_p and its magnitude $U_{x,p}$ from a local balance between the acoustic and viscous forces.

(iii) For $x_p \leq x \lesssim L_\alpha$, the longitudinal variation of the velocity obeys a balance between the acoustic and viscous forces. The beam diffraction and attenuation jointly drive for the velocity decay with x.

(iv) Finally, at $x \gg L_\alpha$, the beam attenuation causes the acoustic force to be almost zero and the jet momentum to saturate. The evolution of the velocity recovers that of classical a self-similar jet (Schlichting & Gersten, 2000).

The different results obtained in this chapter thus draw a clear and complete picture of the successive regimes occurring along an acoustic streaming jet that is several times longer than the attenuation length. This paves the way for enlightened designs relying on streaming jets. For instance, the derived scaling may be used to match x_p with a jet impingement in a closed cavity to, e.g., maximise the shear stresses at the impingement for mass transfer enhancement (El Ghani *et al.*, 2021) or for surface cleaning (Busnaina & Elsawy, 1998). On the contrary, if only a large-scale flow is sought while minimising the recirculations strengths at the impingement, one could rely on these scaling laws to design a x_p far upstream the impingement.

Finally, it would be interesting to see whether the different approaches used in the present work could be applied to the study of other flows forced by external beam-shaped fields. Despite obvious differences related to the type of waves driving the fluid flow, Eckart streaming indeed shares common aspects with flows driven by the attenuation of laser light (Savchenko *et al.*, 1997; Shneider & Semak, 2016; Wunenburger *et al.*, 2011) or internal gravity wave beams (Bordes *et al.*, 2012; Grisouard *et al.*, 2013; Dauxois *et al.*, 2018). These similarities may potentially make it possible to transpose some of the derivations from this chapter to such flows.

Thèse accessible à l'adresse : https://theses.insa-lyon.fr/publication/2024ISAL0101/these.pdf © [B. Vincent], [2024], INSA Lyon, tous droits réservés

Chapter 4

Stability analysis of a steady laminar and axisymmetric acoustic streaming jet

4.1 Introduction

The different streaming jet regimes being characterised all along the jet, I shall now study the stability of that flow.

As discussed in chapter 1, all previous Eckart streaming stability studies relied on a crude modelling of the forcing field: a beam of square cross-section inside which the forcing magnitude is constant. In particular, forcing gradients due to diffraction and sound attenuation were ignored; that forcing field is thus very different from the forcing obtained with a plane circular transducer (chapter 2). These approximations greatly affect the simulated streaming flow, both in terms of the jet width and on the streaming velocity levels (chapter 3). Besides, none of the existing studies addressed the question of the bifurcation nature (i.e, criticality). Knowing whether the bifurcation is subcritical or supercritical is important to design control strategies to either prevent or trigger destabilisation.

The aim of this work is precisely to determine how an axisymmetric streaming jet driven by an attenuated and diffracting ultrasound beam becomes unstable. The configuration is the same as in chapter 3: a straight laminar jet in a closed cylindrical cavity. In the present work, I shall also assess the role of longitudinal and radial confinement on the stability of the streaming flow. The problem is addressed by means of numerical simulations, using Linear Stability Analysis (LSA) together with Direct Numerical Simulations (DNS). This chapter aims to answer the following questions:

(i) What is the mechanism responsible for flow destabilisation ?
(ii) What is the type (oscillatory or not) of the unstable perturbation, and how does the perturbation topology change when varying the cavity size ?
(iii) Is the bifurcation supercritical or subcritical ?

This chapter is organised as follows: in section 4.2, I shall define the range of investigated parameters along with the equations governing the stability problem. The fundamentals of critical point theory for flow analysis are also provided. Section 4.3 is devoted to the numerical methods and to grid convergence analyses. I shall then discuss the effect of confinement on the base flow structure and velocity levels in section 4.4. After that, I carry out the LSA for different cavity sizes in section 4.5, and determine the nature of the bifurcations in section 4.6. Concluding remarks are finally given in section 4.7.

Thèse accessible à l'adresse : https://theses.insa-lyon.fr/publication/2024ISAL0101/these.pdf © [B. Vincent], [2024], INSA Lyon, tous droits réservés

4.2 Investigated parameter range, governing equations and introduction to critical point theory

4.2.1 Investigated parameter range

The streaming configuration considered for the stability analysis is the same as in chapter 3, but for different cavity lengths and diameters. The cavity lengths are varied through N, and the cavity radii are parametrised by the ratio K_R between $D/2$ and the beam radius (equation (2.19)) at the downstream wall:

$$K_R = \frac{D/2}{0.5 + SL} \,. \tag{4.1}$$

In total, six different geometries are considered (table 4.1). All cases have the same dimensionless attenuation coefficient N/L and the diffraction parameter S; their values and are the same as in the scaling analysis of chapter 3. Therefore, varying either N or K_R amounts to changing the size of the cavity with respect to the beam size, however without affecting the beam structure. The chosen values of N are smaller than in the scaling study of chapter 3 for two reasons: (i) to be closer to streaming experiments from the literature (table A.2), and (ii) to reduce the number of degrees of freedom for the leading mode calculations to remain tractable (section 4.3.1).

4.2.2 Governing equations for the linear stability problem

As in chapter 3, the base flows are axisymmetric and swirl-free ($u_\theta = 0$); however, they may allow for three-dimensional perturbations to become unstable under certain forcing and/or geometrical conditions. Each flow variable can thus be decomposed into a steady axisymmetric part associated with the base flow, and an infinitesimal time-dependent contribution associated with the perturbation:

$$\boldsymbol{u} = \boldsymbol{U}\,(x,r) + \boldsymbol{u'}\,(x,r,\theta,t) \;, \tag{4.2a}$$
$$p = P\,(x,r) + p'\,(x,r,\theta,t) \;. \tag{4.2b}$$

Table 4.1: Values of the parameters for all the geometries considered in the stability analysis. The parameter K_R is defined as the ratio between the cavity radius $D/2$ and the approximate beam radius evaluated at $x = L$ (equation (4.1)). For all cases, $S = 0.03$ and $N/L = 0.003$. The structure of the forcing field is thus the same as in chapter 3 and in the 2 MHz water experiments of Moudjed *et al.* (2014*a*).

Case number	N	L	D	K_R
1	1	333.5	126.51	6
2	0.25	83.5	36.12	6
3	0.25	83.5	24.08	4
4	0.25	83.5	18.06	3
5	0.25	83.5	12.04	2
6	0.25	83.5	6.02	1

Thèse accessible à l'adresse : https://theses.insa-lyon.fr/publication/2024ISAL0101/these.pdf © [B. Vincent], [2024], INSA Lyon, tous droits réservés

The LSA equations are then obtained by inserting the above decomposition into the Navier-Stokes (3.1a) and continuity (3.1b) equations, and by linearising around $(\boldsymbol{U}, P)$:

$$\frac{\partial \boldsymbol{u'}}{\partial t} + (\boldsymbol{U} \cdot \boldsymbol{\nabla})\, \boldsymbol{u'} + (\boldsymbol{u'} \cdot \boldsymbol{\nabla})\, \boldsymbol{U} = -\boldsymbol{\nabla} p' + \boldsymbol{\nabla}^2 \boldsymbol{u'}\,, \tag{4.3}$$

$$\boldsymbol{\nabla} \cdot \boldsymbol{u'} = 0\,. \tag{4.4}$$

Because of both the invariance of the base flow in the $\boldsymbol{e_\theta}$-direction and 2π periodicity of the domain in the same direction, $\boldsymbol{u'}$ and p' are further expressed using Fourier series:

$$\boldsymbol{u'}\,(x, r, \theta, t) = \sum_{m=-\infty}^{+\infty} \widehat{\boldsymbol{u'}}_m\,(x, r, t)\, e^{jm\theta}\,, \tag{4.5a}$$

$$p'\,(x, r, \theta, t) = \sum_{m=-\infty}^{+\infty} \widehat{p'}_m\,(x, r, t)\, e^{jm\theta}\,, \tag{4.5b}$$

where m is an integer azimuthal wavenumber defining the number of wavelengths in $[0, 2\pi]$. Since equations (4.3)-(4.4) are linear, the LSA is decoupled for each $\widehat{\boldsymbol{u'}}_m$.

As for the base flow, the no-slip boundary condition at the walls imposes $\boldsymbol{u'} = \boldsymbol{0}$ there for any m. On the axis, however, the modal representation of $\widehat{\boldsymbol{u'}}$ and $\widehat{p'}$ requires m-dependent conditions. These conditions are derived (i) from the requirement of $\boldsymbol{u'}$ and p' to be single-valued on the axis (Batchelor & Gill, 1962; Khorrami *et al.*, 1989), and (ii) from parity requirements (Blackburn & Sherwin, 2004):

$$m = 0 : \begin{cases} \dfrac{\partial \widehat{u'}_{x,0}}{\partial r} = 0\,, \\ \widehat{u'}_{r,0} = 0\,, \\ \widehat{u'}_{\theta,0} = 0\,, \\ \dfrac{\partial \widehat{p'}_0}{\partial r} = 0\,, \end{cases} \qquad m = 1 : \begin{cases} \widehat{u'}_{x,1} = 0\,, \\ \widehat{u'}_{r,1} + j\widehat{u'}_{\theta} = 0\,, \\ \dfrac{\partial \left(\widehat{u'}_{r,1} - j\widehat{u'}_{\theta,1}\right)}{\partial r} = 0\,, \\ \widehat{p'}_1 = 0\,, \end{cases} \qquad m > 1 : \begin{cases} \widehat{u'}_{x,m} = 0\,, \\ \widehat{u'}_{r,m} = 0\,, \\ \widehat{u'}_{\theta,m} = 0\,, \\ \widehat{p'}_m = 0\,. \end{cases} \tag{4.6}$$

The stability problem is addressed using a "timestepper approach". From the linearised Navier-Stokes equations (4.3), the perturbation at a time $(t + \tau)$ can be seen as the result of an evolution operator $\mathcal{A}(\tau)$ applied to the same perturbation at a previous time (Barkley *et al.*, 2008):

$$\boldsymbol{u'}\,(t + \tau) = \mathcal{A}\,(\tau)\, \boldsymbol{u'}\,(t)\ . \tag{4.7}$$

The idea is then to access the stability of the flow through $\mathcal{A}(\tau)$. Since eigenmode solutions of (4.3)-(4.4) have the form:

$$\boldsymbol{u'}(t) = e^{(\sigma_k + j\omega_k)t}\, \widetilde{\boldsymbol{u'}}_k\,, \tag{4.8}$$

with $(\sigma_k + j\omega_k)$ the complex eigenvalue associated with the eigenvector $\widetilde{\boldsymbol{u'}}_k$, then equation (4.5) can be recast as:

$$\mathcal{A}(\tau)\widetilde{\boldsymbol{u'}}_k = \zeta_k \widetilde{\boldsymbol{u'}}_k\,, \quad \text{with: } \zeta_k = e^{(\sigma_k + j\omega_k)\tau}\,. \tag{4.9}$$

Studying the flow stability thus consists in solving an eigenvalue problem for $\mathcal{A}(\tau)$. The eigenvectors of the linearised Navier-Stokes and continuity equations (4.3)-(4.4) are those of $\mathcal{A}(\tau)$, and the growth rate σ_k and frequency ω_k are related to ζ_k through:

$$\sigma_k = \frac{\ln\left(|\zeta_k|\right)}{\tau}, \quad \omega_k = \frac{\varphi_k}{\tau} \tag{4.10}$$

Thèse accessible à l'adresse : https://theses.insa-lyon.fr/publication/2024ISAL0101/these.pdf © [B. Vincent], [2024], INSA Lyon, tous droits réservés

where φ_k is the complex argument of ζ_k. A base flow $(\boldsymbol{U}, P)$ is said to be unstable if, for any value of m, there is at least one perturbation $(\boldsymbol{u}'_k, p'_k)$ for which $\sigma_k > 0$. Conversely, the base flow is stable if $\max(\sigma_k) < 0$. The minimum value of Gr_{ac} for which $\max(\sigma_k) = 0$ is called the critical acoustic Grashof number Gr^c_{ac}.

4.2.3 Critical point theory for flow analysis and topological rule

To analyse the structure of the flow and of the modes, I shall rely on critical point theory (Hunt *et al.*, 1978; Foss, 2004) applied to 2D slices of $\boldsymbol{u}$ or to the skin friction $\boldsymbol{\mathcal{T}}$ exerted by $\boldsymbol{u}$ on a solid surface. For simplicity, any of these 2D vector fields is referred to as $\boldsymbol{v}$.

A critical point $\boldsymbol{x}_{CP}$ is a point of zero $\boldsymbol{v}$. Then, at a small distance $\boldsymbol{\delta_x}$:

$$\boldsymbol{v}(\boldsymbol{x}_{CP} + \boldsymbol{\delta_x}) = \boldsymbol{0} + \boldsymbol{\nabla v}(\boldsymbol{x_{CP}})\boldsymbol{\delta x} + \dots \tag{4.11}$$

i.e., the patterns of $\boldsymbol{v}$ near $\boldsymbol{x}_{CP}$ are given by $\boldsymbol{\nabla v}$ at first order. As illustrated in figure 4.1 (a), different types of critical points can thus be identified based on the eigenvalues $\lambda_{1,2}$ of $\boldsymbol{\nabla v}$ (Perry & Fairlie, 1975; Bakker, 1991):

- If $\lambda_{1,2}$ are both real and of opposite sign, the critical point is a *saddle*. The eigenvectors then define the directions along which lines of $\boldsymbol{v}$ diverge from (positive eigenvalue) or converge to (negative eigenvalue) $\boldsymbol{x}_{CP}$.
- If $\lambda_{1,2}$ are both real and have the same sign, the critical point is a *node*. If $\lambda_{1,2} > 0$ (respectively < 0), the node is said *repelling* (respectively *attracting*).
- If $\lambda_{1,2}$ are complex conjugate and $\mathrm{Re}\{\lambda_{1,2}\} \neq 0$, the critical point is a *focus*. Around such point, the lines of $\boldsymbol{v}$ display a spiralling pattern that either converges ($\mathrm{Re}\{\lambda_{1,2}\} < 0$) or diverges ($\mathrm{Re}\{\lambda_{1,2}\} > 0$) from $\boldsymbol{x}_{CP}$.
- Finally, complex conjugate $\lambda_{1,2}$ with zero real parts correspond to a *centre*: the lines around $\boldsymbol{x}_{CP}$ are closed orbits.

At a wall, friction lines patterns provide useful information on the nearby flow. I shall consider the downstream cavity wall at $x = L$, for instance. The flow in a nearby parallel plane can be obtained from a Taylor's expansion (Lighthill, 1988; Hunt *et al.*, 1978; Foss, 2004):

$$\begin{aligned} u_r(L - \delta x, r, \theta) &= 0 + \mathcal{T}_r(L, r, \theta)\delta x + \mathcal{O}\left(\delta x^2\right), \\ u_\theta(x - \delta x, r, \theta) &= 0 + \mathcal{T}_\theta(L, r, \theta)\delta x + \mathcal{O}\left(\delta x^2\right), \end{aligned} \tag{4.12}$$

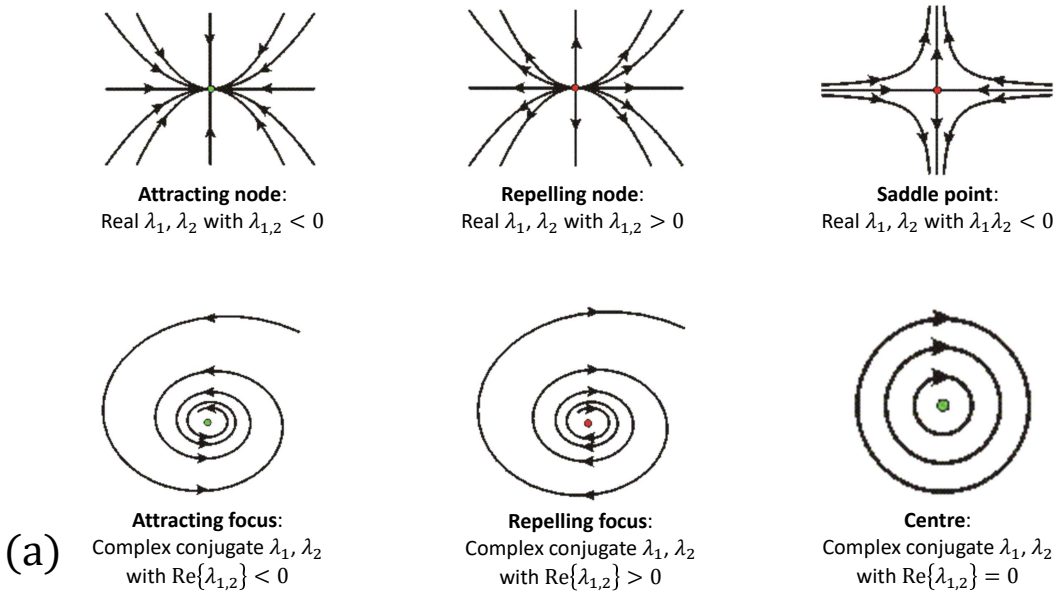
with $\mathcal{T}_r = -\partial u_r/\partial x$ and $\mathcal{T}_\theta = -\partial u_\theta/\partial x$ the radial and azimuthal wall friction components, respectively, and δx is a small distance to the wall. Equation (4.12) thus shows that the friction lines are aligned with the streamlines in a nearby **parallel** wall. Hence, because of mass conservation, critical points of $\boldsymbol{\mathcal{T}}$ are points where the flow either attaches to or detaches from the wall. In a plane **normal** to the wall, these points appear as half-saddles or half-nodes in the streamlines patterns (figure 4.1 (b)).

The distribution and types of critical points in a 2D plane are not arbitrary, but instead verify a strict topological balance. The number of nodes Σ_N, of half-nodes $\Sigma_{N'}$, of saddles Σ_S and of half-saddles $\Sigma_{S'}$ are related to each other through (Hunt *et al.*, 1978; Foss, 2004):

$$2\Sigma_N + \Sigma_{N'} - 2\Sigma_S - \Sigma_{S'} = \chi, \tag{4.13}$$

in which focci and centres are counted as nodes. In equation (4.13), χ is an integer defining the topology of the surface containing the critical points (I shall refer to this surface as the

Thèse accessible à l'adresse : https://theses.insa-lyon.fr/publication/2024ISAL0101/these.pdf © [B. Vincent], [2024], INSA Lyon, tous droits réservés



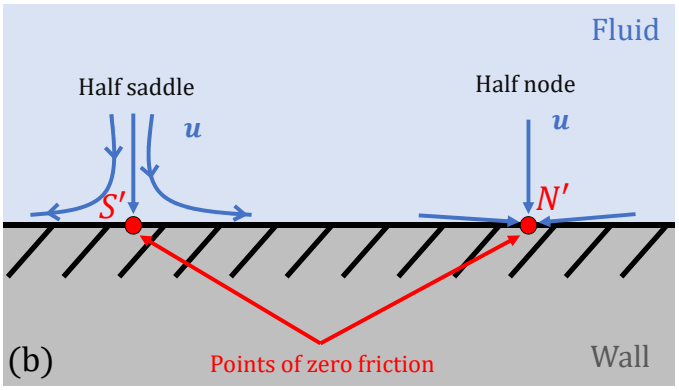


Figure 4.1: Illustration of critical point theory. (a) Critical point classification for a 2D vector field $\boldsymbol{v}$, based on the eigenvalues $\lambda_{1,2}$ of $\boldsymbol{\nabla v}$ at the critical point. (b) Half saddle and half node appearing at the boundaries of a fluid domain, and caused by zero skin friction at the wall.

TIS, for "topology investigation surface"). The value of χ is determined using the concept of "collapsed surface" of Foss (2004). The idea is that any TIS is formed by collapsing a 3D surface on itself; χ is then the Euler characteristic of the collapsed surface. I shall consider three TIS:

- the (x, r) plane, obtained by collapsing a sphere[1] ($\chi = 2$),
- a cavity cross-section at constant-x i.e. a disc, also obtained by collapsing a sphere ($\chi = 2$),
- an annulus at constant-x, obtained by collapsing a torus ($\chi = 0$).

In this chapter, the topological rule (4.13) will be extensively used for two purposes: (i) to validate the computed velocity fields from a topological perspective, and (ii) to analyse the change of leading mode shape when modifying K_R.

[1] A "sphere" refers here to a closed surface that can be arbitrarily deformed without creating any hole or handle. As such, a cube, a cylinder, a pencil or a spoon for instance are spheres.

Thèse accessible à l'adresse : https://theses.insa-lyon.fr/publication/2024ISAL0101/these.pdf © [B. Vincent], [2024], INSA Lyon, tous droits réservés

4.3 Computational methods and grid sensitivity analysis

Different numerical techniques are employed to either compute the leading (i.e., least stable) mode, perform fully 3D Direct Numerical Simulations (DNS) or locate critical points. I shall present these methods here, and also verify that the stability results are grid-independent.

4.3.1 Numerical methods for linear stability analysis and Direct Numerical Simulations (DNS)

In total, the stability work carried out in this chapter involves three different numerical computations. First, the base flow is computed using the same methodology as in chapter 3 (see section 3.3 therein). Second, linear stability analysis (LSA) is carried out for each of the cases listed in table 4.1. The leading eigenmode and eigenvalue are computed by solving the eigenvalue problem (4.9) for $0 \leq m \leq 10$. This allows to determine Gr_{ac}^c and identify the shape of the unstable perturbation for each case. Third, fully three-dimensional DNS are run at slightly supercritical Gr_{ac} for two purposes: (i) to validate the LSA, and (ii) to determine the bifurcation nature (sub- or supercritical). Bifurcation nature is inferred by modelling the growth and saturation of a perturbation near Gr_{ac}^c with a Stuart-Landau equation (Landau & Lifschitz, 1987), the parameters of which being evaluated from time series of the flow variables (Sheard *et al.*, 2004).

For LSA, the leading eigenmode and associated eigenvalue are determined using the iterative method of Barkley *et al.* (2008). The idea is to form a low-dimensional projection of the evolution operator $\mathcal{A}(\tau)$ onto a Krylov subspace, allowing for a direct diagonalisation. This requires to fill a N_K-th order Krylov sequence $\boldsymbol{K}_{N_K}$:

$$\boldsymbol{\mathcal{K}}_{N_K} = [\boldsymbol{u}_0, \boldsymbol{u}_1, \boldsymbol{u}_2, ..., \boldsymbol{u}_{N_K-1}] = \left[\frac{\boldsymbol{u}_0}{a_0}, \frac{\mathcal{A}(\tau)\boldsymbol{u}_0}{a_1}, \frac{\mathcal{A}(\tau)\boldsymbol{u}_1}{a_2}, ..., \frac{\mathcal{A}(\tau)\boldsymbol{u}_{N_K-1}}{a_{N_K}}\right], \tag{4.14}$$

with $a_n = \|\mathcal{A}(\tau)\boldsymbol{u}_{n-1}\|$ for all n. The vectors in $\boldsymbol{\mathcal{K}}_{N_K}$ are obtained by repeated applications of $\mathcal{A}(\tau)$, which is obtained from a time-stepping code. I shall refer to each application of $\mathcal{A}(\tau)$ as a "Krylov iteration". This algorithm is best at converging the eigenvalues ζ_k of $\mathcal{A}(t)$ of largest magnitude. From (4.10), these eigenvalues precisely correspond to the eigenvalues of the linearised Navier-Stokes equations (4.3) having the largest growth rate σ_k. This numerical method is thus suitable for finding the leading (i.e., least stable) modes of equations (4.3)-(4.4).

The algorithm of Barkley *et al.* (2008) is readily implemented in *Semtex* through the *DOG* (Direct Optimal Growth) module. The Krylov sequence (4.14) is initialised with a pseudo-random white noise $\boldsymbol{u_0}$. The $\boldsymbol{u_n}$ are then obtained by time-marching over τ the linearised Navier-Stokes equations (4.3) initialised with $\boldsymbol{u_{n-1}}$. Time-integration is done with the second-order splitting scheme of Karniadakis *et al.* (1991) (section 3.3.1), in which the nonlinear advection operator $\boldsymbol{N(U)}$ is replaced by its linearised version:

$$\boldsymbol{N_U(u')} = (\boldsymbol{u'} \cdot \boldsymbol{\nabla})\,\boldsymbol{U} + (\boldsymbol{u'} \cdot \boldsymbol{\nabla})\,\boldsymbol{U}\,,$$

and the time step Δt is the same as for the base flow calculations. Convergence of the leading eigenvalue and eigenvector pair is achieved when the associated residual norm (see the end of section 3.2.2 in Barkley *et al.* (2008)) falls below 10^{-8}. If $\boldsymbol{\mathcal{K}}_{N_K}$ is filled

Thèse accessible à l'adresse : https://theses.insa-lyon.fr/publication/2024ISAL0101/these.pdf © [B. Vincent], [2024], INSA Lyon, tous droits réservés

before reaching convergence, the oldest vector is dropped, and another Krylov iteration is carried out. The process is repeated until convergence is achieved. All LSA results presented in this chapter were obtained with $N_K = 16$; however, I checked that either smaller ($N_K = 10$) or larger (up to $N_K = 32$) values yielded identical results. Finally, the choice of τ is problem-dependent: to allow for the leading perturbation to develop, τ shall not be too small compared to the characteristic growth/decay time $1/|\sigma|$[2]. For instance, for case 3 with $Gr_{ac} = 7000$, the leading perturbation is an unstable $m = 2$ mode, with $1/|\sigma| \approx 13.0$. I converged that mode after 73 Krylov iterations, with $\tau = 0.5$ and 5000 time steps per Krylov iteration.

Finally, I carried out DNS to study the growth and saturation of perturbations near criticality. The DNS were initialised by duplicating along $\boldsymbol{e_\theta}$ the steady axisymmetric base flow, to which I added white noise. The noise was evenly distributed over all m, ensuring that the initial disturbance was not biased towards a preferred mode shape. That perturbation was then evolved in time using the splitting scheme (3.3) in its third-order formulation. The standard deviation of the white noise was set to 1 for the DNS of cases 1 and 2. At smaller K_R, this however yielded too large initial disturbance magnitudes, preventing to observe the early growth of the perturbation. I thus reduced the noise standard deviation to 0.1 for cases 3 and 4, and to 0.01 for cases 5 and 6. These choices correspond to initial perturbation kinetic energies of ≈ 1 % of the base flow kinetic energy for cases 1 to 4, and ≈ 0.1 % for cases 5 and 6.

4.3.2 Critical point detection method

Critical points in a 2D plane are determined numerically with a self-developed MATLAB program. The method is illustrated for the friction perturbation $\boldsymbol{\mathcal{T}'}$ on the downstream wall ($x = L$):

$$\begin{aligned} \mathcal{T}'_r &= \mathrm{Re}\left\{\widehat{\mathcal{T}'}_r e^{jm\theta}\right\}, \quad \text{with } \widehat{\mathcal{T}'}_r = -\frac{\partial \widehat{u'}_r}{\partial x}, \\ \mathcal{T}'_\theta &= \mathrm{Re}\left\{\widehat{\mathcal{T}'}_\theta e^{jm\theta}\right\}, \quad \text{with } \widehat{\mathcal{T}'}_\theta = -\frac{\partial \widehat{u'}_\theta}{\partial x}. \end{aligned} \tag{4.15}$$

Adapting the method for the critical points in the (x, r) plane is straightforward and is thus not detailed here.

The critical points $\boldsymbol{x_{CP}} = (r_{CP}, \theta_{CP})$ of $\boldsymbol{\mathcal{T}'}$ are computed using a Newton algorithm, for which the p-th iteration reads:

$$\begin{aligned} &\begin{bmatrix} \mathrm{Re}\left\{\frac{\partial \widehat{\mathcal{T}'}^{(p)}_{r,m}}{\partial r}\right\} & \mathrm{Re}\left\{\frac{\partial \widehat{\mathcal{T}'}^{(p)}_{r,m}}{\partial \theta}\right\} \\ \mathrm{Re}\left\{\frac{\partial \widehat{\mathcal{T}'}^{(p)}_{\theta,m}}{\partial r}\right\} & \mathrm{Re}\left\{\frac{\partial \widehat{\mathcal{T}'}^{(p)}_{\theta,m}}{\partial \theta}\right\} \end{bmatrix} \begin{bmatrix} \delta r_{CP} \\ \delta \theta_{CP} \end{bmatrix} = - \begin{bmatrix} \mathrm{Re}\left\{\widehat{\mathcal{T}'}^{(p)}_{r,m}\right\} \\ \mathrm{Re}\left\{\widehat{\mathcal{T}'}^{(p)}_{\theta,m}\right\} \end{bmatrix} \\ \rightarrow &\begin{bmatrix} r^{(p+1)}_{CP} \\ \theta^{(p+1)}_{CP} \end{bmatrix} = \begin{bmatrix} r^{(p)}_{CP} + \delta r_{CP} \\ \theta^{(p+1)}_{CP} + \delta \theta_{CP} \end{bmatrix}. \end{aligned} \tag{4.16}$$

Once localised, the critical point is finally classified based on the eigenvalues of $\boldsymbol{\nabla \mathcal{T}'}$

[2] I also noticed that for oscillatory modes, a "too large" τ could lead to a wrong estimate of the mode frequency. In such cases, different values of τ were tested to make sure the obtained results were τ-independent.

Thèse accessible à l'adresse : https://theses.insa-lyon.fr/publication/2024ISAL0101/these.pdf © [B. Vincent], [2024], INSA Lyon, tous droits réservés

(figure 4.1 (a)):

$$\boldsymbol{\nabla \mathcal{T}'} = \begin{bmatrix} \mathrm{Re}\left\{\frac{\partial \widehat{\mathcal{T}'}_{r,m}}{\partial r} e^{jm\theta}\right\} & \mathrm{Re}\left\{\left(jm\frac{\widehat{\mathcal{T}'}_r}{r} - \frac{\widehat{\mathcal{T}'}_\theta}{r}\right) e^{jm\theta}\right\} \\ \mathrm{Re}\left\{\frac{\partial \widehat{\mathcal{T}'}_\theta}{\partial r} e^{jm\theta}\right\} & \mathrm{Re}\left\{\left(jm\frac{\widehat{\mathcal{T}'}_\theta}{r} + \frac{\widehat{\mathcal{T}'}_r}{r}\right) e^{jm\theta}\right\} \end{bmatrix} . \tag{4.17}$$

Whether it is to locate critical points (equation (4.16)) or to determine their type (equation (4.17)), radial gradients of $\boldsymbol{\mathcal{T}'}$ (hence $\boldsymbol{u'}$) need to be evaluated. The first-order derivatives of $\boldsymbol{u'}$ are computed at the grid points by differentiating the Lagrange polynomials from the expansion basis (equation (3.7)). Higher-order derivatives of $\boldsymbol{u'}$ are evaluated with finite differences, e.g.:

$$\begin{aligned} \frac{\partial \widehat{T'}_{r,m}}{\partial r}(r,\theta) &\approx \frac{\widehat{T'}_{r,m}(r+\epsilon_r,\theta) - \widehat{T'}_{r,m}(r-\epsilon_r,\theta)}{2\varepsilon_r} \\ &= \frac{1}{2\varepsilon_r}\left(\frac{\partial \widehat{u'}_{r,m}}{\partial r}(r+\varepsilon_r,\theta) - \frac{\partial \widehat{u'}_{r,m}}{\partial r}(r-\varepsilon_r,\theta)\right) , \end{aligned} \tag{4.18}$$

with ε_r a small numerical increment that does not necessarily correspond to the radial grid spacing. To be evaluated at $(r+\varepsilon_r,\theta)$, $\partial \widehat{u'}_{r,m}/\partial r$ is thus interpolated with cubic splines.

Equation (4.17) involves terms becoming singular at $r = 0$. Since $\boldsymbol{\mathcal{T}'}$ is similar to $\boldsymbol{u'}$ in a nearby plane parallel to the wall (equation (4.12)), $\widehat{\mathcal{T}'}_{r,m}$ and $\widehat{\mathcal{T}'}_{\theta,m}$ verify the same axis conditions (4.6) as $\widehat{u'}_{r,m}$ and $\widehat{u'}_{\theta,m}$, respectively. Therefore, the singular terms in equation (4.17) can be evaluated using l'Hôpital's rule.

The Newton algorithm (4.16) is initialised with each grid point coordinates, and may thus converge several times to the same critical points. A post-processing step is thus applied to remove possible duplicate critical points.

Finally, all critical points presented in this chapter were obtained with $\varepsilon_r = \varepsilon_\theta = 10^{-4}$. Varying these parameters between 10^{-3} and 10^{-6} did not affect the critical point detection and classification.

4.3.3 Grid sensitivity analysis

As in chapter 3, the near acoustic field is undersampled to keep the numerical computations tractable. To assess the minimum spatial resolution required for this local undersampling to be marginal on the stability results, I carried out grid sensitivity analyses through p-refinement. In particular, I identified the minimum N_p above which the variations of the leading eigenvalue remained below 0.5 %.

An example of grid sensitivity analysis for case 3 at $Gr_{ac} = 7000$ (the largest Gr_{ac} for that case) is shown in table 4.2. The leading perturbation is an unstable non-oscillatory $m = 2$ mode. A satisfactory choice is $N_p = 8$, since variations of σ with respect to the most refined grid are at most ≈ 0.1 % for larger N_p. I repeated this p-refinement study for each of the cases (see appendix D; the mesh parameters along with N_p are listed in table 4.3.

For the 3D DNS, the flow variables were expanded along $\boldsymbol{e_\theta}$ according to equation (4.5) using a finite number of Fourier mode N_F. I assessed the effect of N_F by computing the flow kinetic energy over the entire cavity after the perturbation had saturated. For case 6 with $Gr_{ac} = 15500$ for instance, the relative difference between the kinetic energies computed with either $N_F = 32$ or 64 is about 0.03 %. Even smaller differences were obtained for the supercritical cases 1 to 3. The DNS were thus performed with $N_F = 32$.

Thèse accessible à l'adresse : https://theses.insa-lyon.fr/publication/2024ISAL0101/these.pdf © [B. Vincent], [2024], INSA Lyon, tous droits réservés

Table 4.2: Evolution of the growth rate σ of the leading (i.e., least stable) mode, as a function of the expansion basis polynomial degree N_p. The growth rates are obtained for case 3 (table 4.1) with $Gr_{ac} = 7000$ and $m = 2$. The error is relative to the value of σ obtained for $N_p = 14$.

N_p	σ	Relative difference (%)
5	0.10249	33.11
6	0.07379	4.17
7	0.07792	1.20
8	0.07695	0.05
9	0.07710	0.13
10	0.07709	0.12
11	0.07696	0.05
12	0.07702	0.03
13	0.07701	0.02
14	0.07700	–

Table 4.3: Characteristics of the meshes used for each case (table 4.1). All meshes were created with axial and radial stretching factors $\gamma_x = 1.35$ and $\gamma_r = 1.30$, respectively (equations (3.9) and (3.10)).

Case	Number of elements $N_{e,x}$ along $\boldsymbol{e_x}$	Number of elements $N_{e,r}$ along $\boldsymbol{e_r}$	Total number of elements	Polynomial degree N_p of expansion basis
1	34	14	476	8
2	24	10	240	7
3	24	9	216	8
4	24	9	216	9
5	24	7	168	10
6	24	5	120	11

4.4 Confinement-induced alteration of the base flow structure and velocity levels

Prior to studying the stability of the streaming flow for different cavity sizes, I shall first evaluate the effect of confinement on the base flow. This preliminary study shall also be the opportunity to illustrate the use of the topological rule (4.13).

The steady axisymmetric base flow computed for case 2 and $Gr_{ac} = 6400$ is shown in figure 4.2 (a). The TIS is the entire $-D/2 \leq r \leq D/2$ meridional plane, obtained by reflecting the $r \geq 0$ half-plane about the $r = 0$ axis. Besides the large vortex resulting from the impingement at $x = L$ and spreading over nearly $D/2$, a recirculation bubble attached to the lateral wall is formed. Moffatt vortices (Moffatt, 1964) in the corners are also made visible by the streamlines. In total, there are

$$\Sigma_N = 8\,, \quad \Sigma_{N'} = 0\,, \quad \Sigma_S = 0\,, \quad \Sigma_{S'} = 14$$

Thèse accessible à l'adresse : https://theses.insa-lyon.fr/publication/2024ISAL0101/these.pdf © [B. Vincent], [2024], INSA Lyon, tous droits réservés

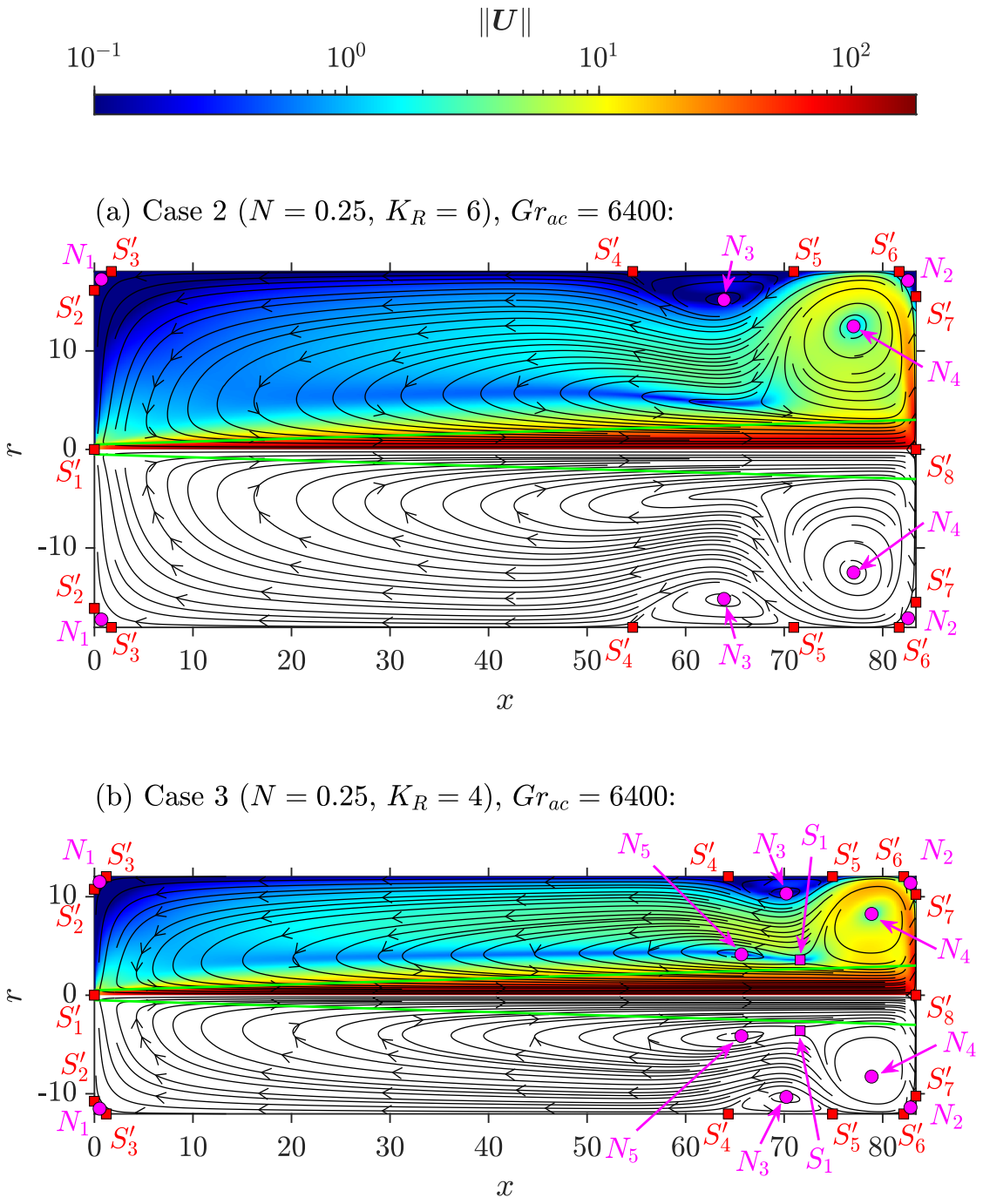


Figure 4.2: Velocity magnitude $\|\boldsymbol{U}\|$ maps of the steady axisymmetric base flows for (a) case 2 and (b) case 3 for $Gr_{ac} = 6400$. The streamlines are displayed along with the critical points: S'_i are half-saddles (zero friction, red squares), N_i are nodes ($\boldsymbol{U} = \boldsymbol{0}$, purple discs) and S_i are saddles ($\boldsymbol{U} = \boldsymbol{0}$, purple squares). The green line represents the approximate beam radius R_{beam} (2.19). Both figures share the same colour levels.

critical points (figure 4.2 (a)), so that the left-hand side of (4.13) is equal to 2. As the TIS is defined by $\chi = 2$, the topological rule is thus satisfied. Therefore, the entire flow topology is captured in figure 4.2 (a).

Confining the low by reducing K_R may alter the base flow structure; however, any topological change shall comply with equation (4.13). For instance, reducing K_R from 4 to 6 yields a node N_5 and a saddle S_1 in the bulk of the flow (figure 4.2 (b)). Despite

Thèse accessible à l'adresse : https://theses.insa-lyon.fr/publication/2024ISAL0101/these.pdf © [B. Vincent], [2024], INSA Lyon, tous droits réservés

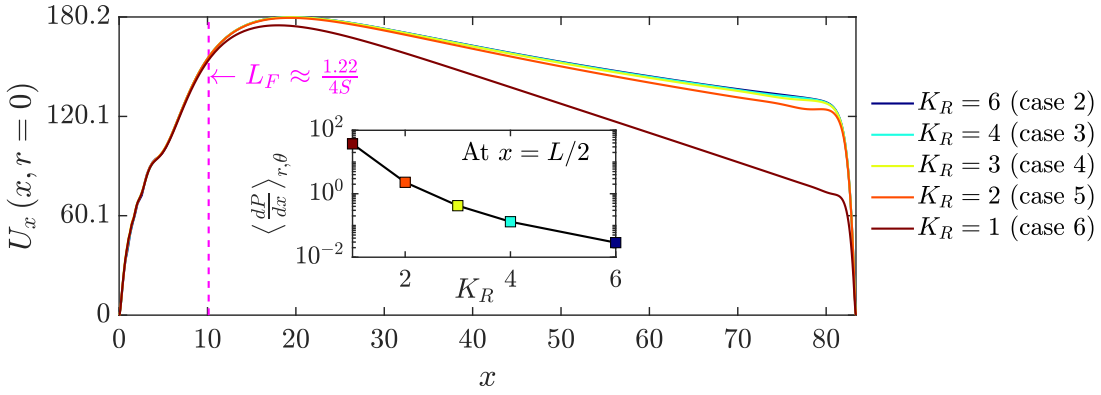


Figure 4.3: Effect of flow confinement on the jet velocity for $N = 0.25$ and $Gr_{ac} = 6400$. The profiles were obtained for $1 \leq K_R \leq 6$, corresponding to cases 2 to 6 (table 4.1). Background plot: profiles of the on-axis velocity $U_x(x, r = 0)$ along the jet. The dashed vertical represents the Fresnel distance L_F locating the transition between the near ($x < L_F$) and the far ($x > L_F$) acoustic fields. Inset: effect of K_R on the streamwise pressure gradient $\langle dP/dx \rangle_{r,\theta}$ of the base flow taken at the mid cavity length $L/2$ and averaged over the cross-sectional area.

these new critical points, the left-hand side of (4.13) is still equal to 2 because the TIS is unchanged. On a more general note, changing K_R does not systematically alter the base flow topology: besides of the cases shown in figure 4.2, I observed confinement-induced topological changes when reducing K_R from 2 (case 5) to 1 (case 6) and for $Gr_{ac} \approx Gr_{ac}^c$. Both these cases satisfy the topological rule (4.13).

Finally, lowering K_R decelerates the jet, especially downstream the on-axis velocity peak. Figure 4.3 shows several profiles of the on-axis base velocity $U_x(x, r = 0)$ computed for $1 \leq K_R \leq 6$ and $Gr_{ac} = 6400$. For $2 \leq K_R \leq 6$, this confinement-induced jet deceleration is marginal: $U_x(x, r = 0)$ differ by at most 5.5 %. However, the jet is significantly decelerated for $K_R = 1$: near the jet impingement, $U_x(x, r = 0)$ for $K_R = 1$ is 50 % of the velocity obtained at the same location in the $K_R \geq 2$ cases. This jet deceleration is caused by the growth, as K_R is reduced, of a streamwise pressure gradient (inset of figure 4.3). This pressure force acts against the acoustic forcing and drives the return flow so that the net mass flux through a cross section is zero (Rudenko & Sukhorukov, 1998).

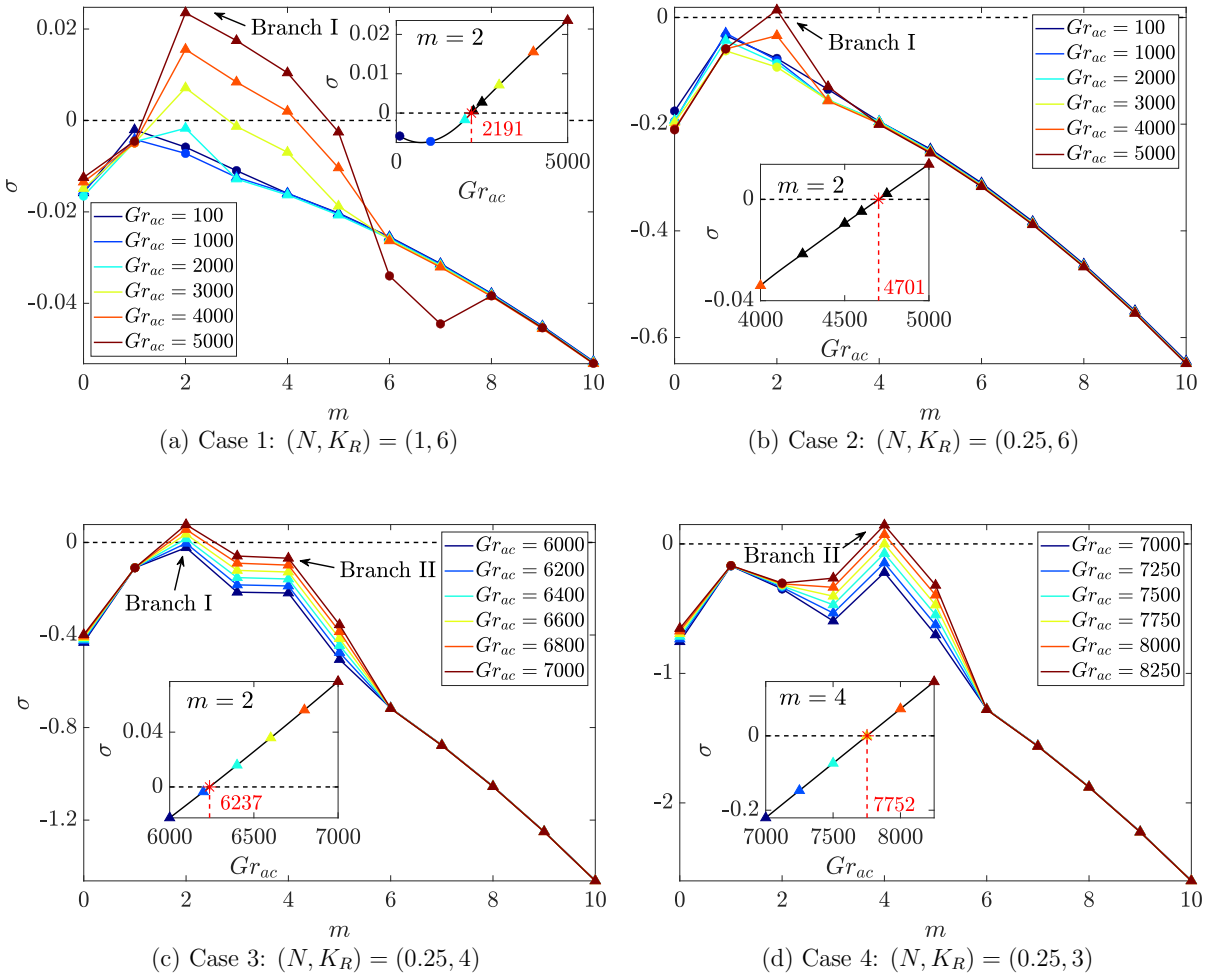
4.5 Stability analysis

I shall now turn to the LSA for the different geometrical setting listed in table 4.1. I first focus on the weakly-confined cases ($K_R \geq 3$) before analysing the $K_R \leq 2$ cases.

4.5.1 Non-oscillatory instabilities in weakly-confined streaming jet flows

For each case, Gr_{ac} is gradually increased until unstable modes are reached. The evolution of the leading mode growth rate σ with Gr_{ac} and m for cases 1 to 4 is shown in figure 4.4. For cases 1 to 3, the same non-oscillatory $m = 2$ mode is found to destabilise the flow; I shall denote the associated mode branch as "Branch I". Despite the unstable mode branch being the same for $4 \leq K_R \leq 6$, reducing K_R nevertheless affects the onset of instability: Gr_{ac}^c indeed increases from 2191 for case 1 to 6237 for case 3. Therefore,

Thèse accessible à l'adresse : https://theses.insa-lyon.fr/publication/2024ISAL0101/these.pdf © [B. Vincent], [2024], INSA Lyon, tous droits réservés



(a) Case 1: $(N, K_R) = (1, 6)$

(b) Case 2: $(N, K_R) = (0.25, 6)$

(c) Case 3: $(N, K_R) = (0.25, 4)$

(d) Case 4: $(N, K_R) = (0.25, 3)$

Figure 4.4: Growth rate σ of the leading eigenmode as a function of the azimuthal wavenumber m for cases 1 to 4. Oscillatory and non-oscillatory modes are represented by filled circles and triangles, respectively. The insets show the evolution of σ with Gr_{ac} for the indicated value of m. The critical Grashof number Gr^c_{ac}, obtained through spline interpolation of σ, is reported in red. The filled black symbols in the inset of (b) are additional eigenvalue computations made to improve the interpolation accuracy near $\sigma = 0$.

confining the streaming jet flow has a stabilising effect, similarly to confined flows past bluff bodies (Mondal & Mahbub Alam, 2023).

To identify the destabilisation mechanism associated with an unstable Branch I mode, I shall analyse the spatial structure of the mode and relate its main features to the base flow structure. The leading mode shape is shown in figure 4.5 for case 3, along with the critical points of the base flow. From the mode shape in the (x, r) plane (figure 4.5 (a) and (b)), $\boldsymbol{u'}$ is clearly concentrated in the downstream half of the cavity. Two regions of large perturbation magnitude can be identified.

First, $|u'_x|$ is large at $x \geq 60$, and more precisely around N_5 and N_4 (figure 4.5 (a)). The N_4-centred vortex of the base flow deviates $\boldsymbol{u'}$ towards the jet and to enter R_{beam} (2.19) (green line in figure 4.5), i.e., a fluid region of effective forcing. Nevertheless, slices of $\boldsymbol{u'}$ in multiple constant-x planes show that u'_x remains outside the jet core (blue solid circle in figure 4.5 (c) to (d)) for all x. In these constant-x planes, $\boldsymbol{u'}$ displays rolls clustered around a circle of zero U_x, i.e., around a shear layer. There, localised spots of streamwise vorticity perturbation ω'_x are created in the return flow (see (f) to (h) in figure 4.5),

Thèse accessible à l'adresse : https://theses.insa-lyon.fr/publication/2024ISAL0101/these.pdf © [B. Vincent], [2024], INSA Lyon, tous droits réservés

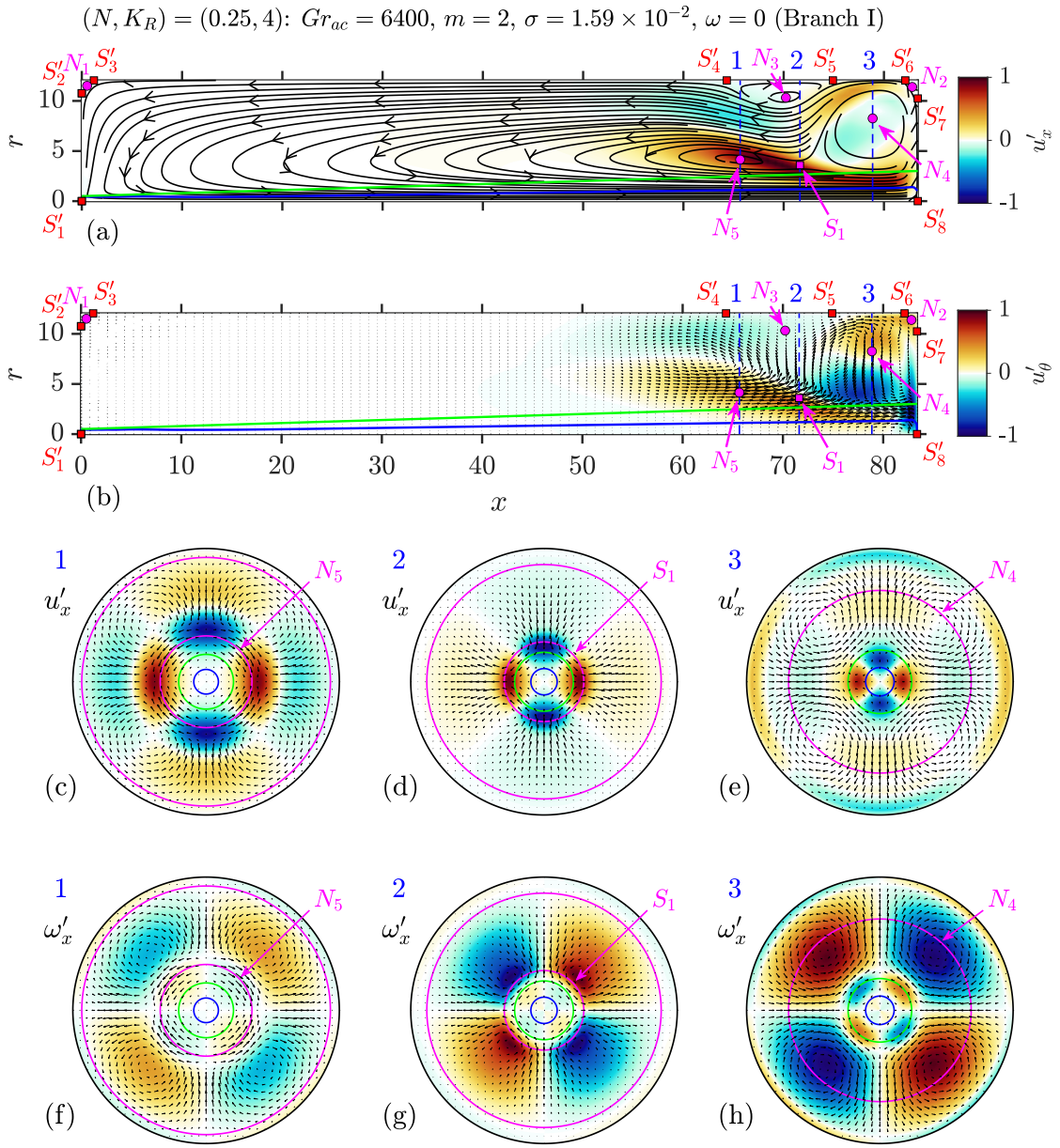


Figure 4.5: Leading mode for case 3 for $Gr_{ac} = 6400$. The mode is non-oscillatory ($\omega = 0$) and unstable ($\sigma = 1.59 \times 10^{-2} > 0$). (a) Axial velocity perturbation u'_x in the (x, r) plane, along with the streamlines and critical points of the base velocity $\boldsymbol{U}$. (b): velocity perturbation $\boldsymbol{u'}$, with the background color corresponding to its azimuthal component u'_θ. (c) to (h): Slices of $\boldsymbol{u'}$ in constant-x planes located by the blue vertical lines in (a) and (b), with either u'_x or the streamwise vorticity perturbation ω'_x as background colour (negative in blue, positive in red). The purple circles locate the points where $U_x = 0$. In all figures, the green solid line represents the approximate beam radius (2.19), and the blue solid line locates the radius where U_x is 50 % of its on-axis value. All the figures on a given row share the same colour levels.

with their maximums in the shear layer. All these features indicate a destabilisation of the recirculations arising from the jet impingement, rather than a destabilisation of the jet itself. This may be attributed to the forcing, which imposes a radial length scale (chapter 3) stabilising the jet.

Second, figure 4.5 (c) shows that $|u'_\theta|$ is maximum at the jet impingement, right above

Thèse accessible à l'adresse : https://theses.insa-lyon.fr/publication/2024ISAL0101/these.pdf © [B. Vincent], [2024], INSA Lyon, tous droits réservés

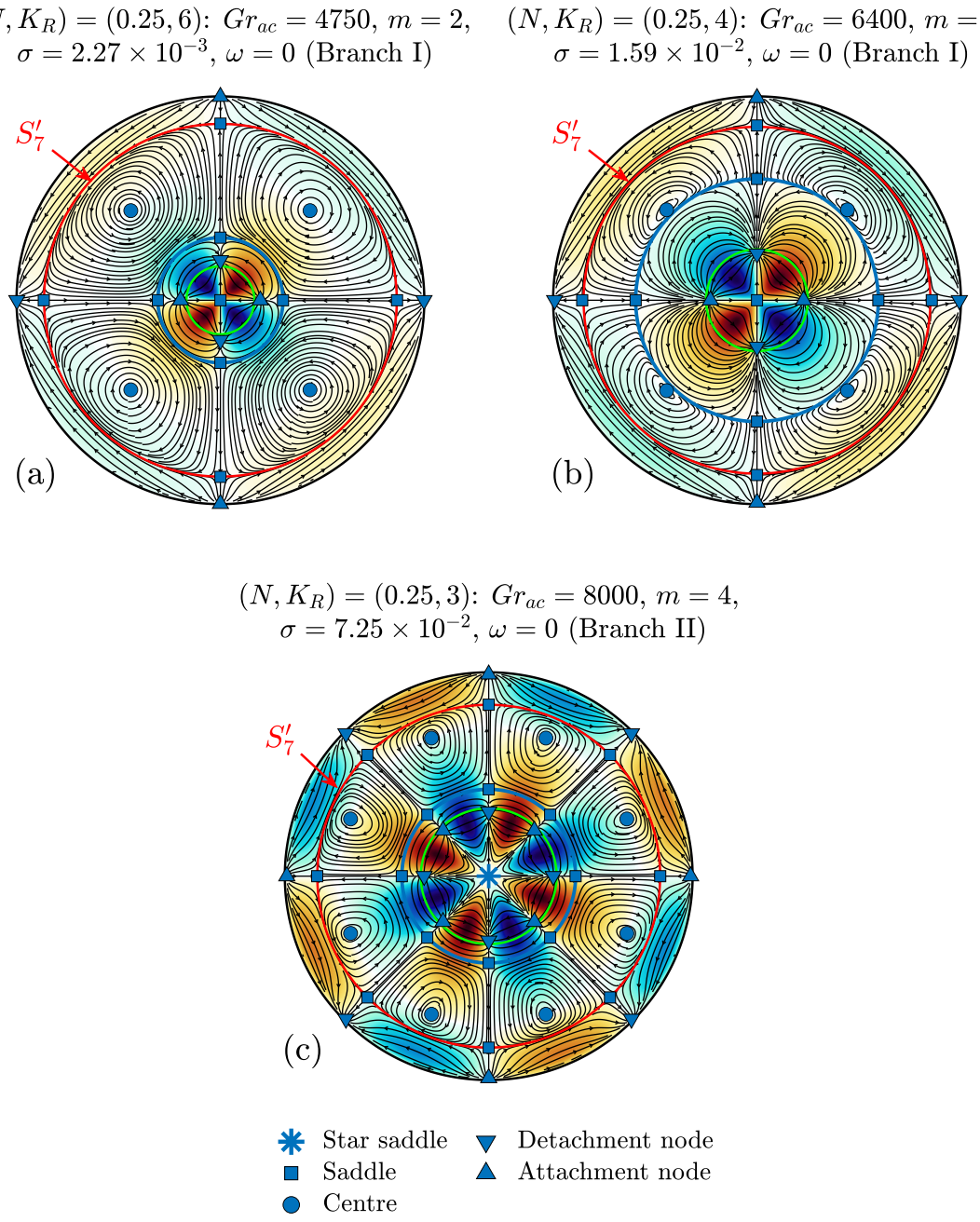


Figure 4.6: Lines of the skin friction perturbation stresses on the downstream wall, with the background color corresponding to the azimuthal component of the stress vector (positive in red, negative in blue). These lines are shown along with the critical points (blue symbols) at supercritical Gr_{ac} for (a) case 2, (b) case 3 and (c) case 4. The approximate beam radius (equation (2.19)) is represented by the green circle. The base flow half saddle S'_7 on the downstream wall is located by the solid red circle. The solid blue circle approximates the separation line going through the saddles found at a same distance from the origin.

the stagnation point S'_8. This indicates an instability driven by an important shear of the nearby wall jet flow. The lines of the skin friction perturbation on the downstream wall provide useful information on the nearby $\boldsymbol{u'}$. In figure 4.6 (b), these lines are shown in a

Thèse accessible à l'adresse : https://theses.insa-lyon.fr/publication/2024ISAL0101/these.pdf © [B. Vincent], [2024], INSA Lyon, tous droits réservés

plain disc TIS ($\chi = 2$) and display:

$$\Sigma_N = 8\,, \quad \Sigma_{N'} = 4\,, \quad \Sigma_S = 9\,, \quad \Sigma_{S'} = 0$$

critical points. The topological rule (4.13) is thus satisfied, validating the mode structure shown in figure 4.6 (b). Interestingly, the mode shape features attachment and detachment nodes near regions of large azimuthal stresses, indicative of a $\boldsymbol{u'}$ causing the flow to respectively attach to and separate from the wall. Finally, the base flow half saddle S'_7 (red line in the left plot of figure 4.6) lies on a separator (i.e., on a line going through a saddle) of the skin friction perturbation field. Such line cannot be crossed; friction lines located on either side of a separator thus necessarily originate from distinct regions (Délery, 2001). There is thus no friction (hence velocity) perturbation flux between the Moffatt vortex and the remaining of the flow at the downstream wall.

For $K_R = 4$, another local maximum of $\sigma(m)$ actually exists (figure 4.4 (c)). The leading modes of this new branch, to which I refer to as "Branch II", correspond to non-oscillatory $m = 4$ perturbations. Although not dominant for case 3, the leading Branch II mode is the first to become unstable at $Gr^c_{ac} = 7752$ for case 4 ($K_R = 3$). This change of destabilising mode branch is the first significant manifestation of confinement on the flow stability, and proves the existence of a minimum radial length scale below which the shape of the leading perturbation is altered.

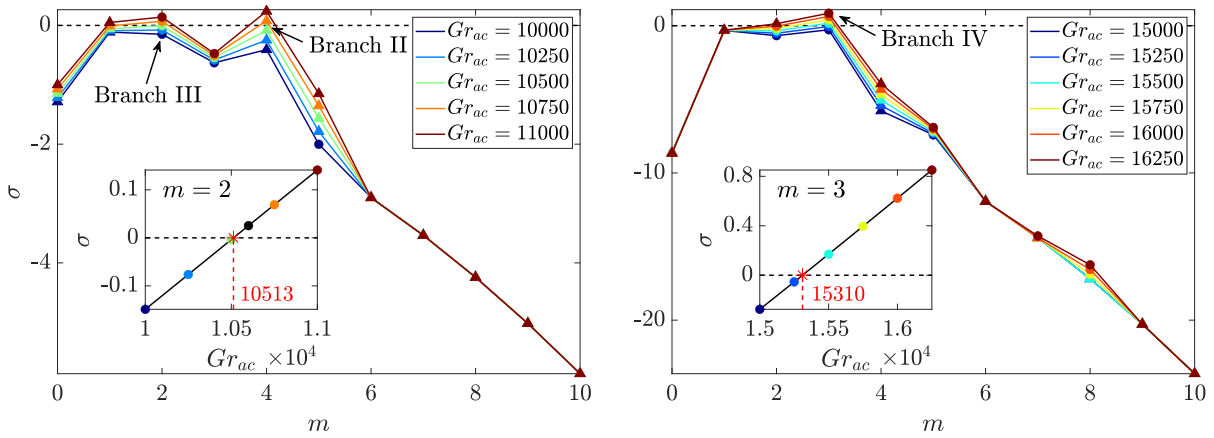
To understand the change of leading mode branch, I shall turn again to the friction lines patterns on the downstream wall. For the sake of explanation, let us first consider a weaker confinement setting, such as case 2 ($K_R = 4$, Branch I). The friction lines feature four centres, i.e., four points around which the lines form closed loops (figure 4.6 (a)). These points are located between two separators; the inner one is represented by the solid blue circle, and the outer separator is overlayed to S'_7 (red circle). For the same Branch I mode, decreasing K_R narrows down the gap between the two separators (figure 4.6 (b)) and thus significantly reduces the space available for the friction lines to form closed loops. A greater flow confinement would eventually collapse the centres on the inner separator (blue circle), making impossible to form closed friction loops around the centres without crossing the separator. In other words, **further reducing K_R necessarily requires the skin friction lines patterns to be rearranged for basic topological rules to not be violated**. This topological rearrangement of the leading mode shape is allowed by a different m, hence a new mode branch.

As shown in figure 4.6 (c), the leading Branch II mode features a new set of saddles and centres. Both the friction vector and its gradient vanish at $r = 0$. That point is thus again a critical point, which however cannot be classified according to the terminology introduced in section 4.2.3. As the friction lines around the centre point display a star-like pattern, I shall refer to this critical point as a "star saddle". I delay to section 4.5.3 further discussion about "star saddles"; the important point to note for the moment is that the topological rule (4.13) needs to be adapted to account for such points.

4.5.2 Rise of oscillatory instabilities in confined settings

As K_R is further decreased, the modes destabilising the flow become oscillatory. For instance, the $K_R = 2$ flow (case 5) is destabilised at $Gr^c_{ac} = 10513$ by the growth of an oscillatory $m = 2$ perturbation (figure 4.7 (a)). This mode is is associated with a new branch that I label as "Branch III". Interestingly, Branch III and Branch II coexist for this K_R, and the leading Branch II mode becomes unstable at $Gr_{ac} \approx 10630 \approx 1.01 Gr^c_{ac}$.

Thèse accessible à l'adresse : https://theses.insa-lyon.fr/publication/2024ISAL0101/these.pdf © [B. Vincent], [2024], INSA Lyon, tous droits réservés



(a) Case 5: $(N, K_R) = (0.25, 2)$ (b) Case 6: $(N, K_R) = (0.25, 1)$

Figure 4.7: Growth rate σ of the leading eigenmode as a function of the azimuthal wavenumber m for (a) case 5 and (b) case 6. Oscillatory and non-oscillatory modes are represented by filled circles and triangles, respectively. The insets show the evolution of σ with Gr_{ac} for the indicated value of m. The critical Grashof number Gr_{ac}^c, obtained through spline interpolation of σ, is reported in red. The filled black symbols in the inset of (b) are additional eigenvalue computations made to improve the interpolation accuracy near $\sigma = 0$.

The σ of the Branch II mode increases more rapidly with Gr_{ac} than the σ of the Branch III mode, so that Branch II becomes dominant for $Gr_{ac} \geq 11000 \approx 1.04 Gr_{ac}^c$.

For case 5, the increased flow confinement and the greater Gr_{ac}^c cause the flow structures resulting from the jet impingement to shrink down and to be further concentrated near the downstream wall (figure 4.8 (a)-(c)). In particular, N_5 and S_1 now lie inside the main forcing region; that was not the case for larger K_R. Therefore, part of the return flow near N_5 and S_1 now faces the acoustic forcing.

The velocity perturbation field displays distinct features compared to the previous $K_R \geq 3$ cases. First, $|u'_\theta|$ is no longer maximum at the impingement, but near S_1 instead (figure 4.8 (c)). The flow is thus no longer destabilised by the jet impingement, but by the shear layer N_5 and S_1 instead. This is confirmed by the shape of $\boldsymbol{u'}$ and ω_x at N_5 and S_1 (figure 4.8 (d)-(g)): as for $K_R \geq 3$, the perturbation is still clustered near a surface of zero U_x, with a slight winding around that surface. Second, u'_θ displays in the x-direction a wave-like structure, the amplitude of which being significantly reduced as the distance from the downstream wall increases. This wave propagates backwards (i.e., along the negative $\boldsymbol{e_x}$-direction). This is consistent with the findings of Henry *et al.* (2022), who reported similar unstable waves for a 2D streaming flow forced by a non-diffracting and non-attenuated beam of square cross section. Finally, for $K_R = 2$, the saddles of the skin friction perturbation on the downstream wall no longer coincide with the base flow half saddle S'_7 (left plot of figure 4.9). In other words, reducing the cavity radius creates a perturbation flux between the Moffatt roll delimited by S'_7 and the remaining of the flow near $x = L$.

For the most confined geometry (case 6, $K_R = 1$), a new mode branch arises (figure 4.7 (b)). This branch, to which I shall refer as "Branch IV", is defined by a leading $m = 3$ oscillatory mode. The associated Hopf bifurcation occurs at $Gr_{ac}^c = 15310$. At $Gr_{ac} \approx Gr_{ac}^c$, both the enhanced confinement and the greater strength of the return flow resulting from the larger Gr_{ac}^c significantly affect the base flow topology near the down-

Thèse accessible à l'adresse : https://theses.insa-lyon.fr/publication/2024ISAL0101/these.pdf © [B. Vincent], [2024], INSA Lyon, tous droits réservés

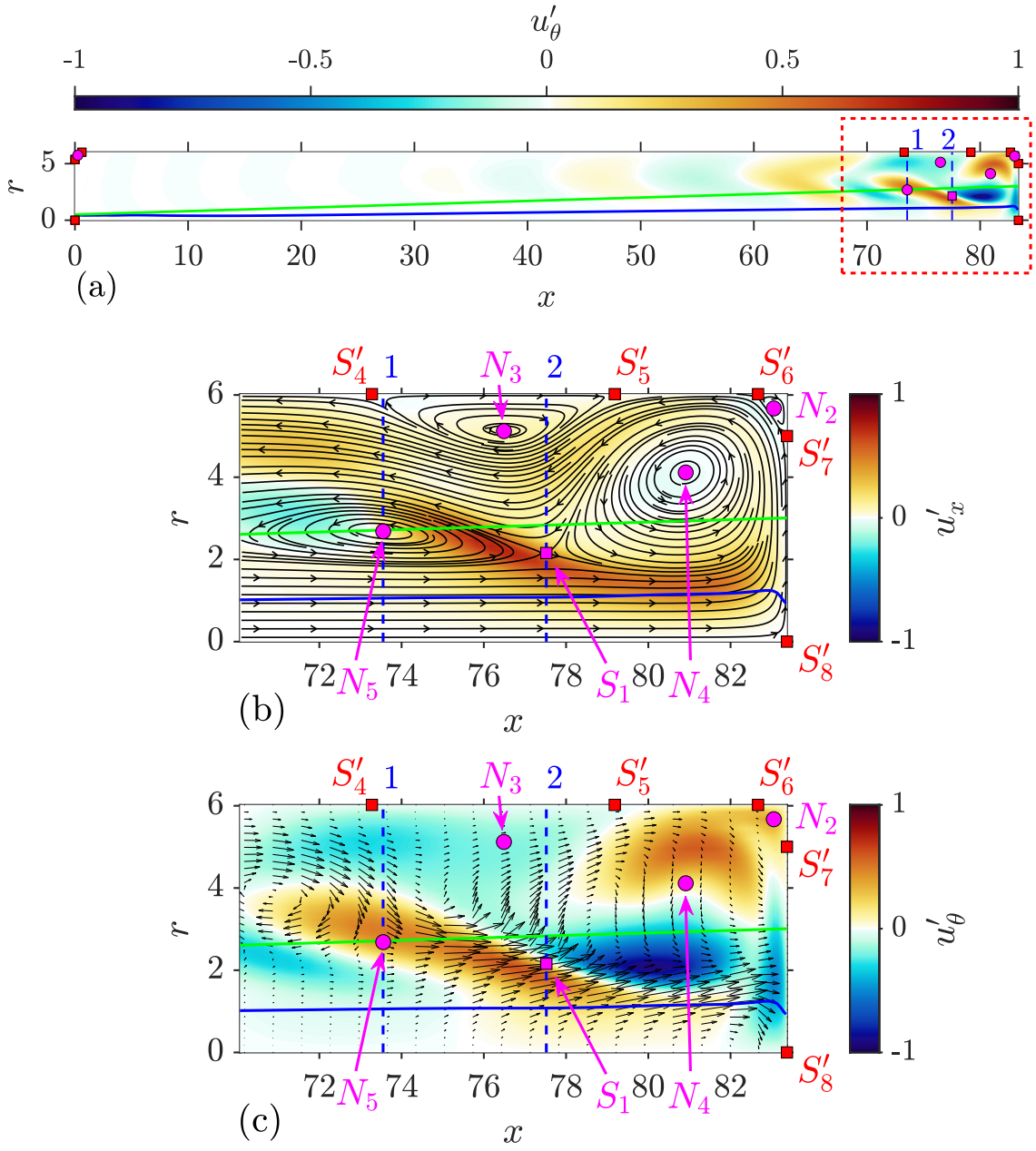


Figure 4.8: Caption on next page.

stream wall (figure 4.10 (a) to (c)). First, the size of the recirculating flow structures is greatly reduced e.g., the recirculation bubble on the lateral wall nearly vanishes. Second, the reduced K_R yields two new critical points N_6 and S_2 in the spatial structure of $\boldsymbol{U}$. These new critical points appear at approximately the same r as N_5 and S_1.

Maps of $\boldsymbol{u'}$ in the (x, r) plane show that $|u'_x|$ and $|u'_\theta|$ are maximums near N_5 and S_1, i.e., at regions of high shear in the bulk of the base flow (figure 4.10 (b) and (c)). This confirms the trend observed for $K_R = 2$: confining the flow shifts the root of the instability from the impingement to the shear layer near N_5 and S_1. This change of instability origin is also favoured by the build-up of an adverse pressure gradient slowing down the jet (inset of figure 4.3). Besides, $\boldsymbol{u'}$ is again marginal in the jet (blue line and circles in figure 4.10) and creates strong ω_x at the $U_x = 0$ interface. Finally, the leading

Thèse accessible à l'adresse : https://theses.insa-lyon.fr/publication/2024ISAL0101/these.pdf © [B. Vincent], [2024], INSA Lyon, tous droits réservés

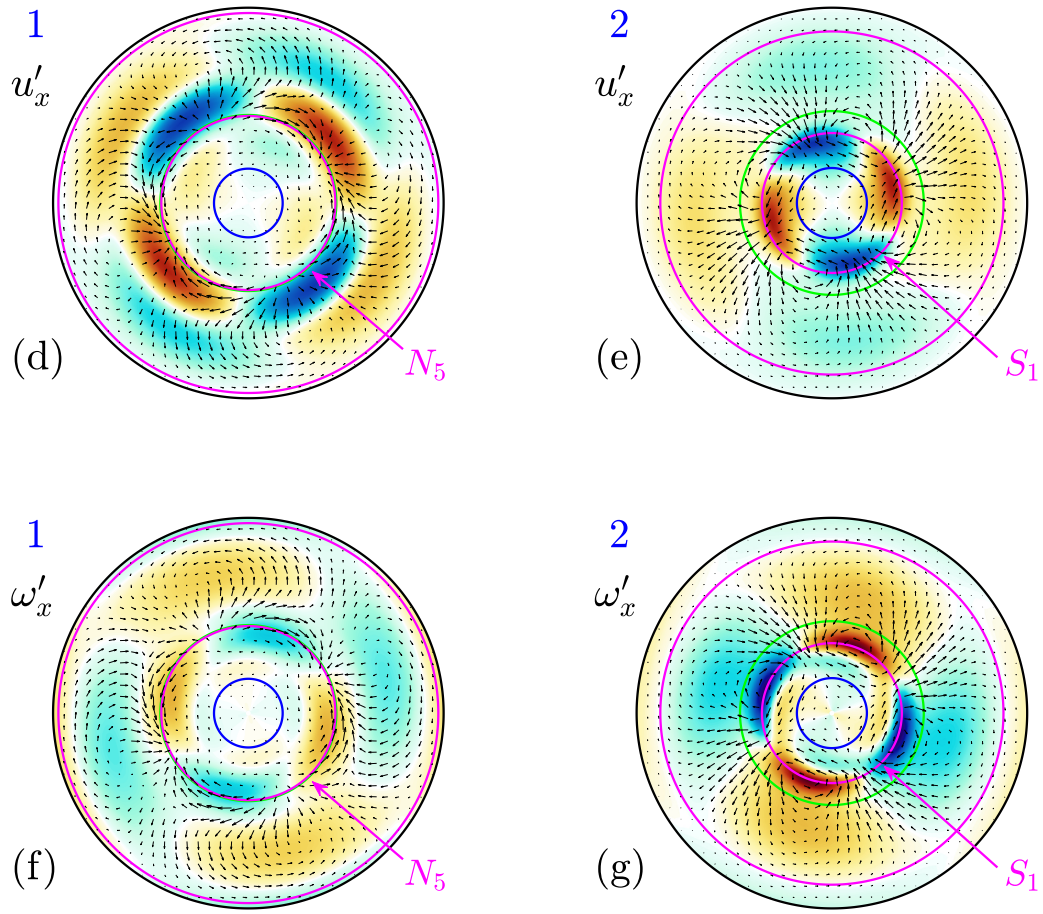


Figure 4.8: Leading mode of case 5 for $Gr_{ac} = 10600$. The mode is oscillatory ($\omega \neq 0$) and unstable ($\sigma = 2.54 \times 10^{-2} > 0$). (a) Azimuthal velocity perturbation u'_θ in the (x, r) plane, along with the critical points of the base velocity $\boldsymbol{U}$. (b) Detailed view near the impingement (region framed in red in (a)) of the axial velocity perturbation u'_x together with the base flow streamlines. (c) Details $\boldsymbol{u'}$ near the impingement, with u'_θ taken as background colour. (d) to (g): Slices of $\boldsymbol{u'}$ in constant-x planes located by the blue vertical lines in (a)-(c), with either u'_x or the streamwise vorticity perturbation ω'_x as background colour (negative in blue, positive in red). The purple circles locate the points where $U_x = 0$. In all figures, the green solid line represents the approximate beam radius (2.19), and the blue solid line locates the radius where U_x is 50 % of its on-axis value. All the figures on a given row share the same colour levels.

Branch IV mode features a "star saddle" critical point at $r = 0$ (figure 4.9 (b)), as does the leading mode for case 4 (Branch II).

As we have seen, the modes the base flows of cases 5 and 6 are destabilised by oscillatory modes. These modes are defined by a pair of complex conjugate eigenvalues corresponding to counter-propagating waves in the $\boldsymbol{e_\theta}$-direction. Depending on the complex amplitudes of these unstable modes, their combination results in either a standing wave or a travelling wave (Clune & Knobloch, 1993). These complex amplitudes cannot be obtained from LSA; however, they do appear in DNS. DNS thus not only allow to validate the mode shape identified by LSA, but also to determine whether that mode develops into a standing or travelling wave along $\boldsymbol{e_\theta}$. The leading LSA mode shapes are compared to DNS snapshots in figures 4.11 and 4.12 for cases 5 and 6, respectively. The DNS snapshots are taken from the early stage of the exponential growth of the pertur-

Thèse accessible à l'adresse : https://theses.insa-lyon.fr/publication/2024ISAL0101/these.pdf © [B. Vincent], [2024], INSA Lyon, tous droits réservés

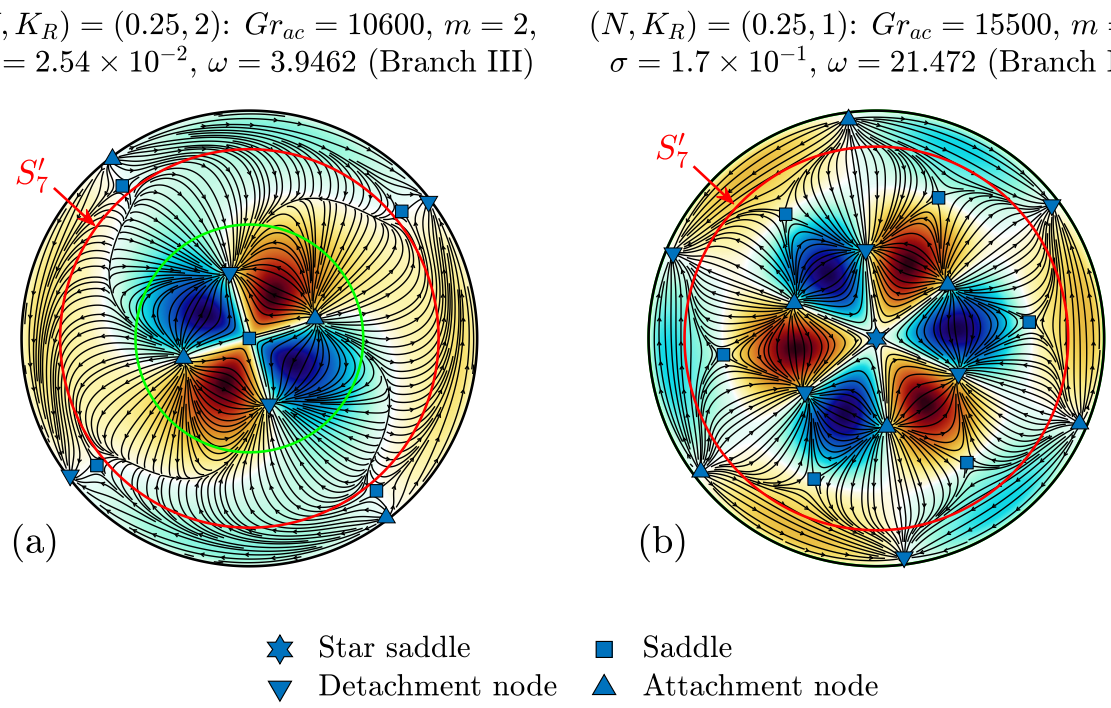


Figure 4.9: Lines of skin friction perturbation stresses on the downstream wall for (a) case 5 and (b) case 6. In each plot, the background colour represents the azimuthal component of the stress vector (positive in red, negative in blue). The lines are shown along with the critical points (blue symbols) and the approximate beam size (green circle, as defined by equation (2.19)). The base flow half saddle S_7' is also reported in red.

bation to avoid nonlinear effects on the perturbation shape. For both cases, a strong agreement in found between the Branches III and IV mode shapes obtained by LSA and DNS. Furthermore, both perturbations correspond to travelling waves.

To conclude, a large variety of instabilities may be achieved by simply considering different cavity sizes without modifying the shape of the forcing field. For the considered values of N, the primary bifurcations are associated with unstable non-oscillatory perturbations in weakly-confined geometries ($3 \leq K_R \leq 6$), and travelling waves for the two most confined geometries ($1 \leq K_R \leq 2$).

4.5.3 Adapting the topological rule for non-standard critical points on the axis

I shall now focus on the star saddles observed on the axis (figures 4.6 (c) and 4.9), and more precisely on how to adapt the topological rule (4.13) to account for such points.

The relationship between m and the number of star saddle branches shall be first clearly established. Consider a generic continuous 2D vector field $\boldsymbol{v}$ having a p-branch star saddle S_* (figure 4.13). Let $\mathcal{C}$ be a closed circular path enclosing S_* only, without any other critical point. Let $\boldsymbol{dl}$ be the unit vector along $\mathcal{C}$, and φ the angle between $\boldsymbol{dl}$ and $\boldsymbol{v}$. Then, for one loop on $\mathcal{C}$,

$$\cos(\varphi) = \frac{\boldsymbol{v} \cdot \boldsymbol{dl}}{\|\boldsymbol{v}\| \, \|\boldsymbol{dl}\|}$$

has exactly p zeros. Since $\boldsymbol{v}$ is continuous and m-periodic along $\mathcal{C}$, so is φ. Therefore,

Thèse accessible à l'adresse : https://theses.insa-lyon.fr/publication/2024ISAL0101/these.pdf © [B. Vincent], [2024], INSA Lyon, tous droits réservés

$(N, K_R) = (0.25, 1)$: $Gr_{ac} = 15500$, $m = 3$, $\sigma = 1.701 \times 10^{-1}$, $\omega = 21.472$ (Branch IV)

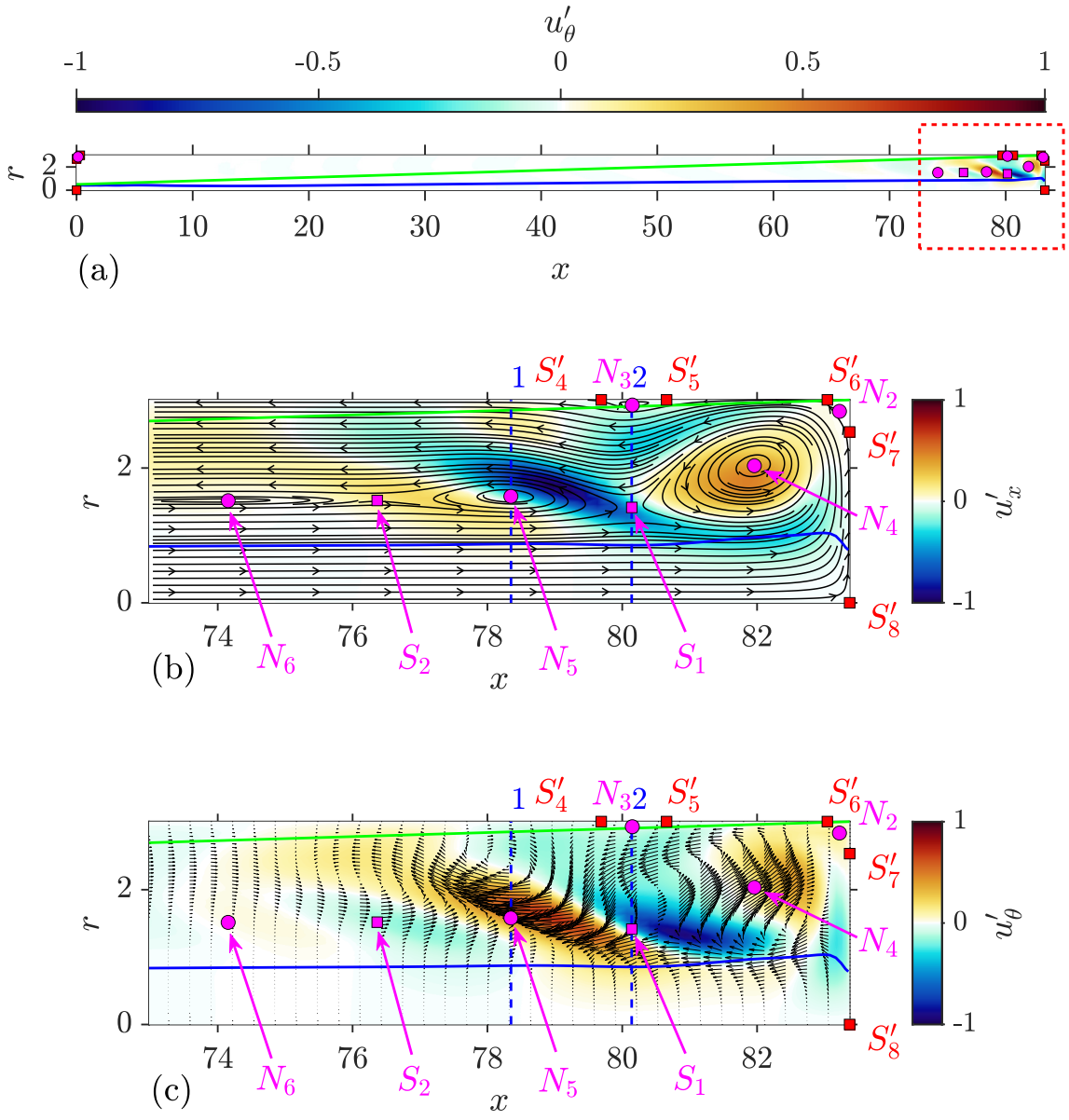


Figure 4.10: Caption on next page.

$\cos(\varphi)$ has two zeros per wavelengths i.e., $p = 2m$. A star saddle in a m-mode thus necessarily has $2m$ branches.

To study the topology of a mode with $2m$-branch star saddles, I suggest to rewrite the topological rule (4.13) as:

$$2\Sigma_N + \Sigma_{N'} - 2\Sigma_S - \Sigma_{S'} + w_{*,2m}\Sigma_{*,2m} = \chi\,, \tag{4.19}$$

where $\Sigma_{*,2m}$ is the number of $2m$-branch star saddles in the TIS, and $w_{*,2m}$ is the associated "topological weight", which I shall now express in terms of m.

The idea is to deform the initial TIS so that the topological rule, in its original form (4.13), can be applied. This is achieved by mapping the TIS to an annulus of inner radius R_{int}. In this new TIS, the star saddle from the original TIS is split into $2m$

Thèse accessible à l'adresse : https://theses.insa-lyon.fr/publication/2024ISAL0101/these.pdf © [B. Vincent], [2024], INSA Lyon, tous droits réservés

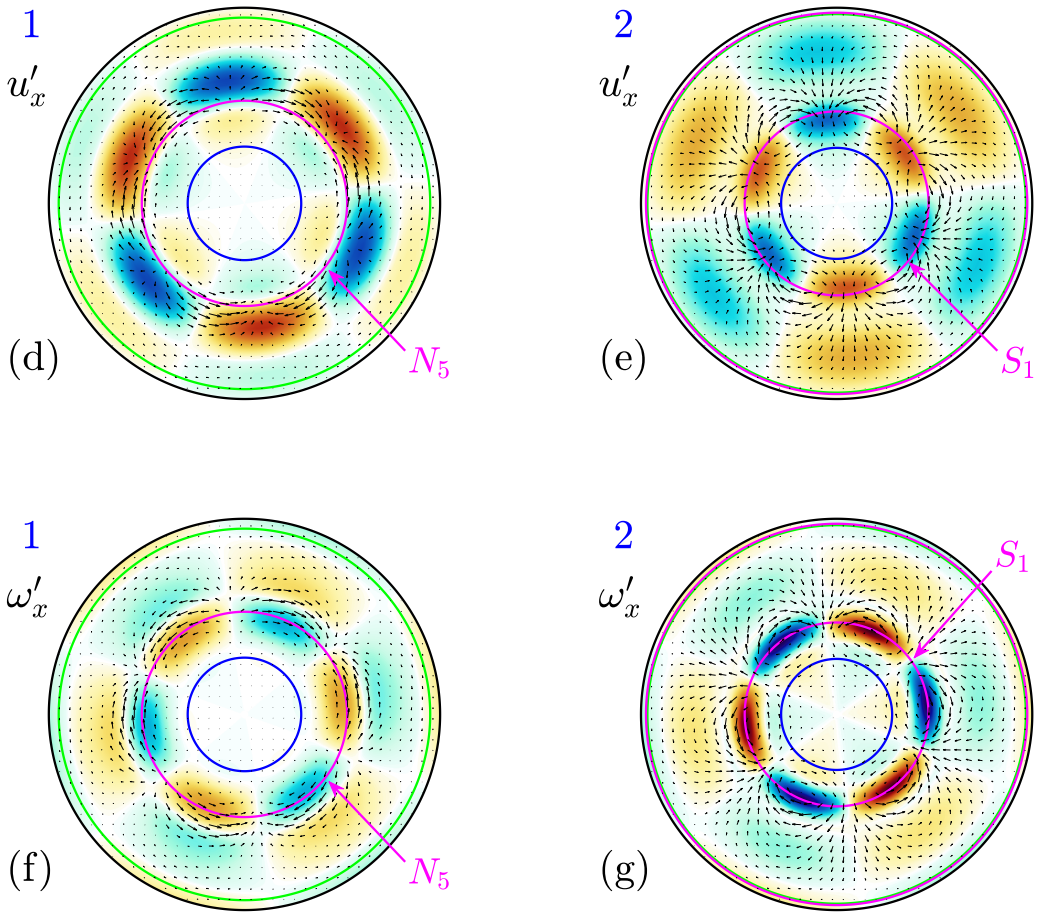


Figure 4.10: Leading mode of case 6 for $Gr_{ac} = 15500$. The mode is oscillatory ($\omega \neq 0$) and unstable ($\sigma = 1.701 \times 10^{-1} > 0$). (a) Azimuthal velocity perturbation u'_θ in the (x, r) plane, along with the critical points of the base velocity $\boldsymbol{U}$. (b) Detailed view near the impingement (region framed in red in (a)) of the axial velocity perturbation u'_x together with the base flow streamlines. (c) Details $\boldsymbol{u'}$ near the impingement, with u'_θ taken as background colour. (d) to (g): Slices of $\boldsymbol{u'}$ in constant-x planes located by the blue vertical lines in (a)-(c), with either u'_x or the streamwise vorticity perturbation ω'_x as background colour (negative in blue, positive in red). The purple circles locate the points where $U_x = 0$. In all figures, the green solid line represents the approximate beam radius (2.19), and the blue solid line locates the radius where U_x is 50 % of its on-axis value. All the figures on a given row share the same colour levels.

half saddles that are evenly distributed over R_{int}, whilst the other critical points remain unchanged. The $2m$ star saddle is then recovered by taking $R_{int} \to 0$ (figure 4.14). For these two TIS, the adapted and original topological rules read:

$$\text{original TIS (disc, } \chi = 2): \quad 2\Sigma_N + \Sigma_{N'} - 2\Sigma_N - \Sigma_{S'} + w_{*,2m} = 2\,, \tag{4.20a}$$

$$\text{deformed TIS (annulus, } \chi = 0): \quad 2\Sigma_N + \Sigma_{N'} - 2\Sigma_S - (\Sigma_{S'} + 2m) = 0\,. \tag{4.20b}$$

The topological balance in the annulus (4.20b) can be equally written as:

$$2\Sigma_N + \Sigma_{N'} - 2\Sigma_S - \Sigma_{S'} - 2\,(m-1) = 2\,,$$

which gives, by direct inspection of (4.20a):

$$w_{*,2m} = -2\,(m-1)\ . \tag{4.21}$$

Thèse accessible à l'adresse : https://theses.insa-lyon.fr/publication/2024ISAL0101/these.pdf © [B. Vincent], [2024], INSA Lyon, tous droits réservés

Case 5: $(N, K_R) = (0.25, 2)$, $Gr_{ac} = 10600$,
$\sigma = 2.54 \times 10^{-2}$, $\omega = 3.9462$ (Branch III)

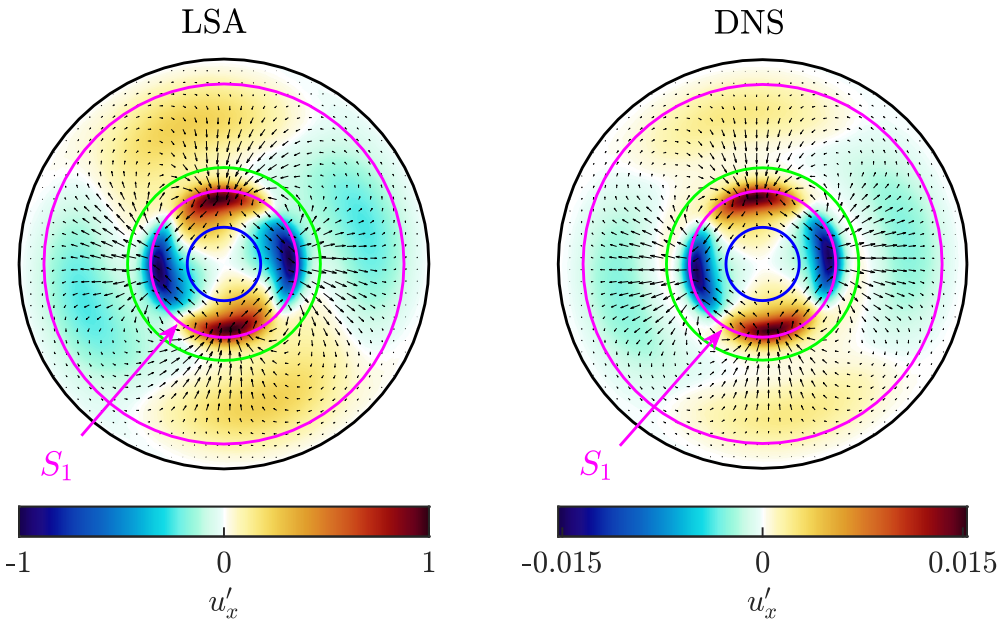


Figure 4.11: Comparison between the leading velocity perturbation $\boldsymbol{u'}$ obtained with LSA (left) and the perturbation obtained with DNS (right). The displayed data corresponds to case 5 at supercritical Gr_{ac} and is plotted at the base flow saddle S_1 ($x = 77.52$, slice 2 in figure 4.8). The indicated σ and ω are those of LSA. The DNS results are extracted from the early exponential growth of the perturbation. Features of the steady base velocity $\boldsymbol{U}$ are reported in both plots: the points where the sign of the streamwise velocity U_x changes (purple circles), and the points where U_x is equal to 50 % of its on-axis value (blue circle). The green circle represents the approximate edge of the beam defined by equation (2.19).

Note that for $m = 2$, the star saddle reduces to a regular saddle, and is counted as such by equation (4.21).

To verify the validity of (4.21), I shall apply the modified topological rule (4.19) to the leading friction perturbations on the downstream wall for cases 4 (figure 4.6 (c)) and 6 (figure 4.9 (b)). For case 4:

$$\begin{aligned} &\Sigma_N = 16\,, \quad \Sigma_{N'} = 8\,, \quad \Sigma_S = 16\,, \quad \Sigma_{S'} = 0\,, \quad \Sigma_{*,2m} = 1\,, \quad m = 4\,, \\ \rightarrow\, &2 \times 16 + 8 - 2 \times 16 - 0 - 2 \times (4 - 1) = 2\,. \end{aligned}$$

and for case 6:

$$\begin{aligned} &\Sigma_N = 6\,, \quad \Sigma_{N'} = 6\,, \quad \Sigma_S = 6\,, \quad \Sigma_{S'} = 0\,, \quad \Sigma_{*,2m} = 1\,, \quad m = 3\,, \\ \rightarrow\, &2 \times 6 + 6 - 2 \times 6 - 0 - 2 \times (3 - 1) = 2\,. \end{aligned}$$

The modified topological rule (4.19) together with the obtained $w_{*,2m}$ (4.21) is thus verified for the leading modes of cases 4 ($m = 4$) and 6 ($m = 3$).

Thèse accessible à l'adresse : https://theses.insa-lyon.fr/publication/2024ISAL0101/these.pdf © [B. Vincent], [2024], INSA Lyon, tous droits réservés

Case 6: $(N, K_R) = (0.25, 1)$, $Gr_{ac} = 15500$,
$\sigma = 1.701 \times 10^{-1}$, $\omega = 21.472$ (Branch IV)

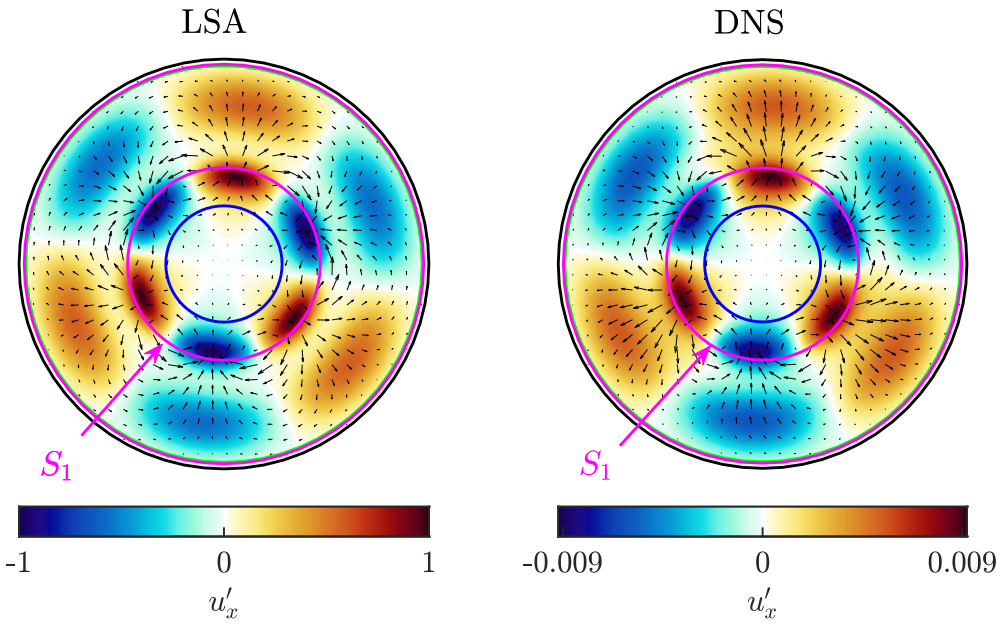


Figure 4.12: Comparison between the leading velocity perturbation $\boldsymbol{u'}$ obtained with LSA (left) and the perturbation obtained with DNS (right). The displayed data corresponds to case 5 at supercritical Gr_{ac} and is plotted at the base flow saddle S_1 ($x = 80.15$, slice 2 in figure 4.10). The indicated σ and ω are those of LSA. The DNS results are extracted from the early exponential growth of the perturbation. Features of the steady base velocity $\boldsymbol{U}$ are reported in both plots: points where the sign of the streamwise velocity U_x changes (purple circles), and points where U_x is equal to 50 % of its on-axis value (blue circle).

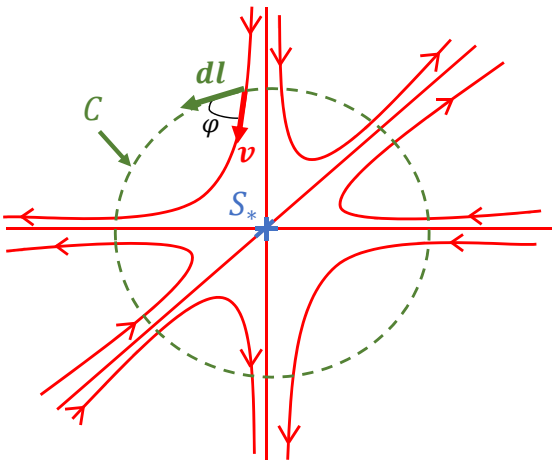


Figure 4.13: Sketch of a continuous 2D vector field $\boldsymbol{v}$ (red) a p-branch star saddle critical point S_* (blue, here shown for $p = 6$). A circular contour $\mathcal{C}$ (dashed green line) encloses S_*, and φ is the local angle between $\boldsymbol{v}$ and a vector $\boldsymbol{dl}$ tangent to $\mathcal{C}$.

4.6 Bifurcation characterisation

To complete the stability analysis, I shall characterise the bifurcations identified with LSA. After having presented my methodology, a Stuart-Landau analysis is made for each

Thèse accessible à l'adresse : https://theses.insa-lyon.fr/publication/2024ISAL0101/these.pdf © [B. Vincent], [2024], INSA Lyon, tous droits réservés

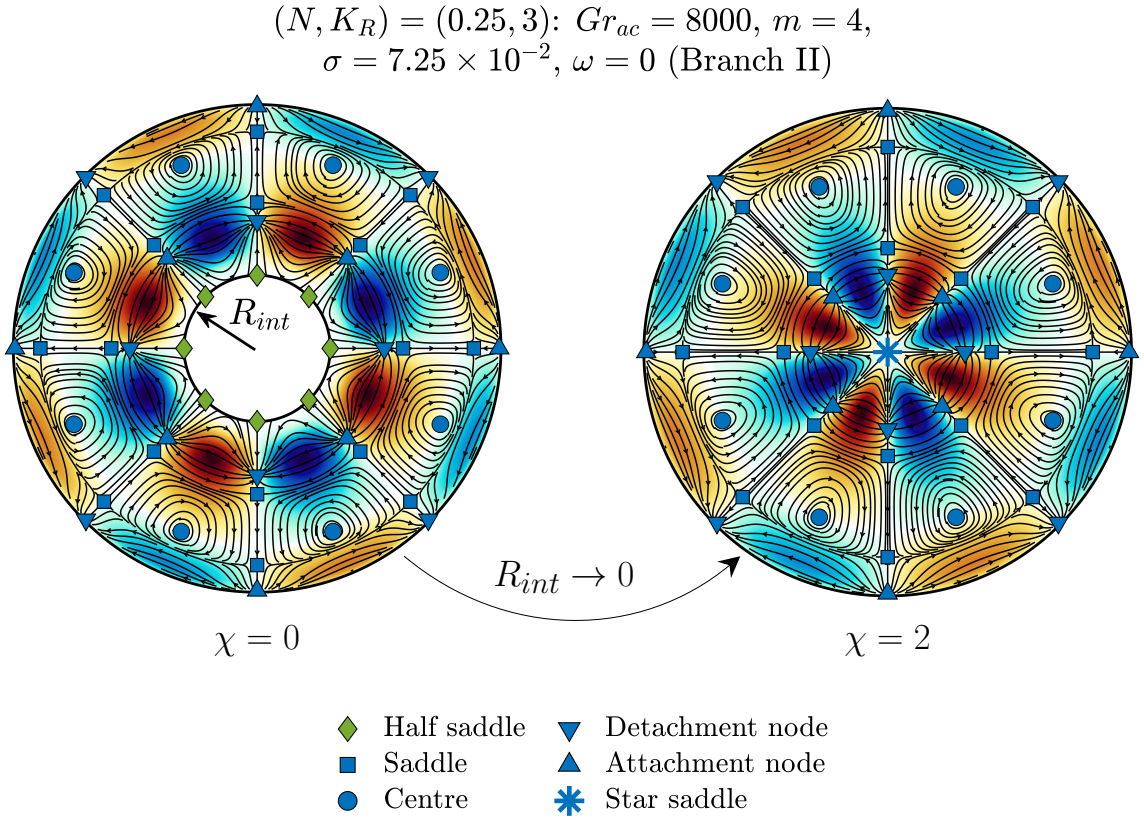


Figure 4.14: Process for adapting the topological rule (4.13) to star saddles. Mapping the initial TIS (disc, right) to an annular TIS of inner radius R_{int} (left) splits the $2m$-branch star saddle into $2m$ half saddles, without affecting the other critical points. The process is illustrated for case 4, with the friction lines exerted by the leading mode on the downstream wall. The colour represents the azimuthal friction component (positive in red, negative in blue). The χ defining each TIS is also reported.

case to determine whether the bifurcation is sub- or supercritical. Finally, I briefly discuss the saturated states following the growth of perturbations, and what may occur beyond these states.

4.6.1 Modelling the growth and saturation of finite-amplitude perturbations

To determine the nature of a bifurcation, I shall rely on the model of Landau & Lifschitz (1987) that describes the growth and saturation of a perturbation near the instability onset. This model has been extensively used to study and classify the bifurcations arising in numerous situations, such as the flow past rings (Sheard *et al.*, 2004), the wake behind a sphere (Thompson *et al.*, 2001) and behind one or multiple cylinders (Henderson & Barkley, 1996; Henderson, 1997; Carmo *et al.*, 2008). The Stuart-Landau model reads:

$$\frac{\mathrm{d}A}{\mathrm{d}t} = (\sigma + j\omega)\, A - l\,(1 + jc_L)\,|A|^2 A + \mathcal{O}(A^5)\,. \tag{4.22}$$

where A is a complex perturbation, and l and c_L are two real constants. The mechanism responsible for the saturation of A is easily understood from the sign of l. If $l > 0$, the cubic term in the right-hand side of equation (4.22) acts against the growth of A and is

Thèse accessible à l'adresse : https://theses.insa-lyon.fr/publication/2024ISAL0101/these.pdf © [B. Vincent], [2024], INSA Lyon, tous droits réservés

sufficient to reach saturation: this situation corresponds to a supercritical bifurcation. On the contrary, for $l < 0$, that cubic term instead further amplifies the growth of A; higher-order terms are thus required for A to saturate. Such case corresponds to a subcritical bifurcation. Thus, only the sign of l is required to infer the nature (sub- or supercritical) of the bifurcation.

As explained by Sheard *et al.* (2004) and Kumar & Pothérat (2020), l may be inferred from a more convenient form of equation (4.22). Plugging $A(t) = |A(t)|e^{j\phi(t)}$ into the Landau model (4.22) gives, after separating the real and imaginary parts:

$$\frac{\mathrm{d}\log|A|}{\mathrm{d}t} = \sigma - l|A|^2 + \mathcal{O}(|A|^4), \tag{4.23a}$$

$$\frac{\mathrm{d}\phi}{\mathrm{d}t} = \omega - lc_L|A|^2 + \mathcal{O}(|A|^4)\,. \tag{4.23b}$$

The bifurcation nature can then be determined by plotting $(\mathrm{d}\log|A|/\mathrm{d}t)$ against $|A|^2$; the slope of the resulting curve is $-l$ for sufficiently small $|A|^2$. Besides, σ can be obtained from the y-intercept, allowing to both confirm the LSA results and assess the accuracy of the l estimate. Note that $\phi(t) = 0$ for a non-oscillatory perturbation, hence only equation (4.23a) is needed in such case.

Information regarding the saturated state can be obtained from the steady-state forms of equations (4.23). For a supercritical ($l > 0$) bifurcation for instance, the first two terms in the right-hand side of the amplitude equation (4.23a) are dominant, so that the saturated perturbation amplitude is:

$$|A_{sat}| = \sqrt{\frac{\sigma}{l}}\,. \tag{4.24}$$

Furthermore, if the saturated state is a time-periodic signal of constant amplitude $|A_{sat}|$, then $\mathrm{d}\phi/\mathrm{d}t$ reduces to the saturated frequency ω_{sat}. Using equation (4.24), the steady-state version of equation (4.23b) gives, for the Landau constant c_L:

$$c_L = \frac{\omega - \omega_{sat}}{\sigma}\,, \tag{4.25}$$

thus allowing for all the quantities in the truncated Stuart-Landau model (4.22) to be characterised.

I shall now define the perturbation A in terms of flow quantities. I decided to follow Kumar & Pothérat (2020) and base $|A|$ on a local value of a flow variable, and more particularly on $u'_\theta(t)$. Other choices are possibles, including global measures of the flow unsteadiness (Thompson *et al.*, 2001; Sheard *et al.*, 2004; Sherwin & Blackburn, 2005; Sapardi *et al.*, 2017). For oscillatory bifurcations, I considered the envelope of $u'_\theta(t)$. Choosing where to record $u'_\theta(t)$ is based on the need to obtain clean signals. To maximise the signal-to-noise ratio, I thus chose points where LSA predicted large $|u'_\theta|$, namely around the N_5 and S_1 and near the impingement.

From a numerical point of view, the fully 3D nonlinear DNS were run for slightly supercritical Gr_{ac}. The relative gap to Gr^c_{ac} is defined by the criticality parameter r_c:

$$r_c = \frac{Gr_{ac}}{Gr^c_{ac}} - 1\,, \tag{4.26}$$

with $r_c > 0$ (respectively $r_c < 0$) corresponding to a supercritical (respectively subcritical) forcing magnitude. Finally, $(\mathrm{d}\log|A|/\mathrm{d}t)$ was computed from the time series using centred finite differences.

Thèse accessible à l'adresse : https://theses.insa-lyon.fr/publication/2024ISAL0101/these.pdf © [B. Vincent], [2024], INSA Lyon, tous droits réservés

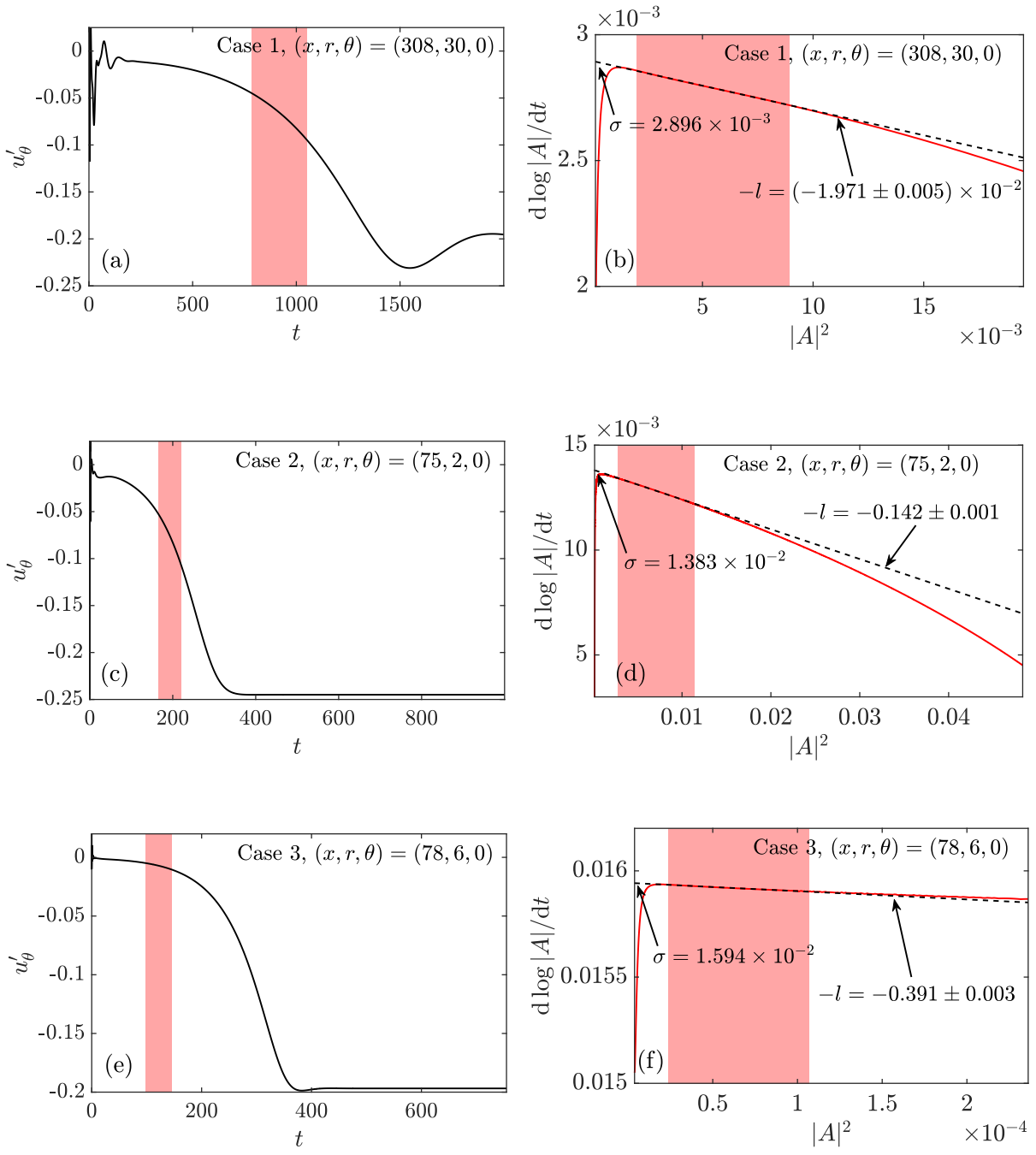


Figure 4.15: Caption on next page

4.6.2 Nature of the bifurcations

I carried out the Stuart-Landau analysis for all the different geometries (figure 4.15). For each case, the initial instants of $u'_\theta(t)$ are dominated by noise, as shown in e.g. figure 4.15 (a). The Stuart-Landau equation for $|A|$ is then fitted over a noise-free linear range; that range depicted in red in each plot of figure 4.15 and the fitting results are given in the right plots of figure 4.15.

For cases 1 ($N = 1$, $K_R = 6$) to 3 ($N = 0.25$, $K_R = 4$), $l > 0$ near the instability onset (figure 4.15 (b), (d) and (f)). The leading Branch I mode thus destabilises the flow through a supercritical circular pitchfork bifurcation. Further decreasing K_R yields $l < 0$ for case 4 (figure 4.15 (h)), indicating that an unstable Branch II mode triggers a

Thèse accessible à l'adresse : https://theses.insa-lyon.fr/publication/2024ISAL0101/these.pdf © [B. Vincent], [2024], INSA Lyon, tous droits réservés

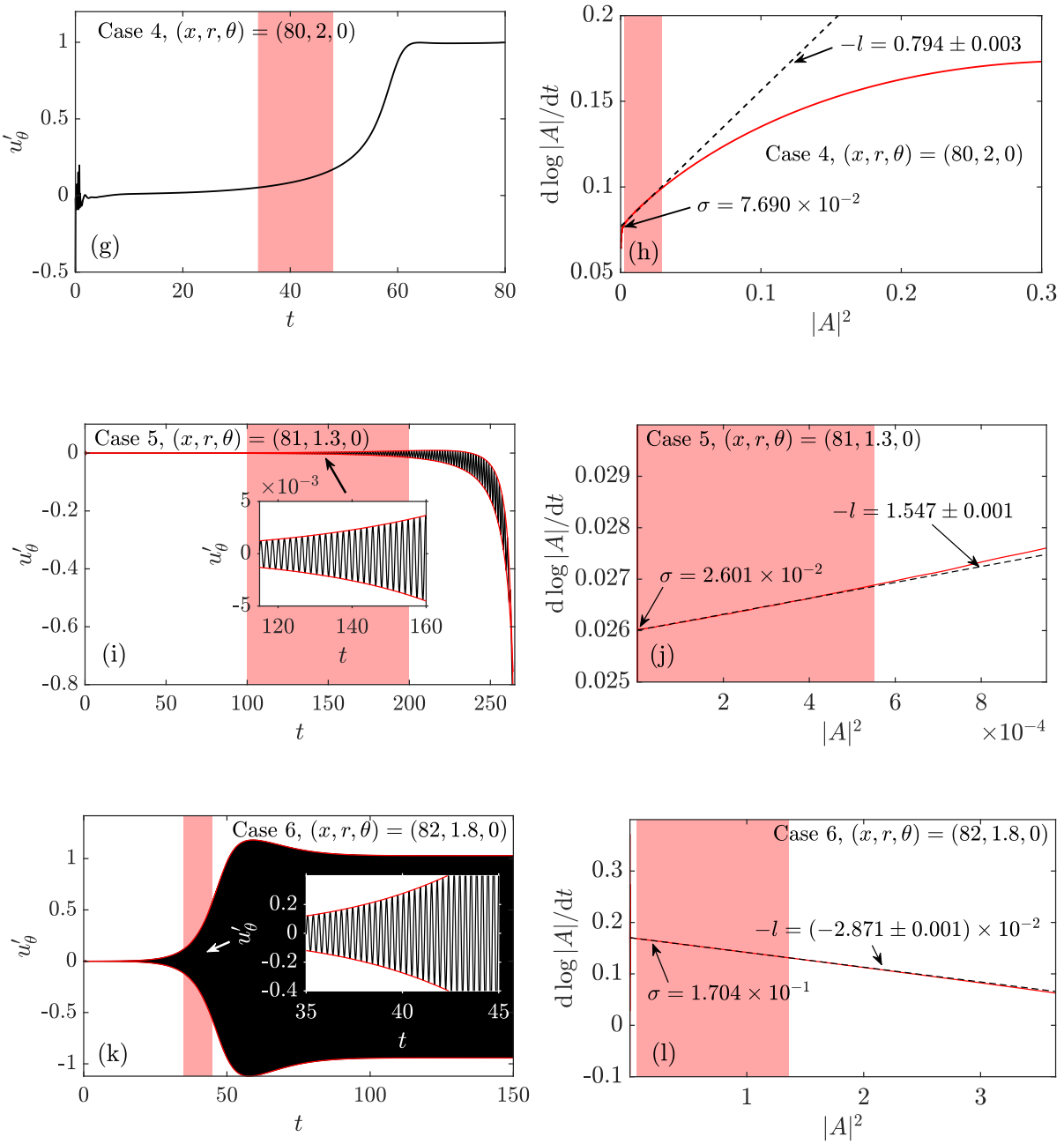


Figure 4.15: Stuart-Landau analyses for all the cases listed in table 4.1. The corresponding Gr_{ac} and r_c (equation (4.26)) are given in table 4.4. Left: growth and saturation of a white-noise-triggered perturbation injected at $t = 0$. The perturbation evolution is monitored by the time series of the azimuthal velocity perturbation u'_θ. Right: evolution of $\mathrm{d}\left(\log|A|\right)/\mathrm{d}t$ as a function of $|A|^2$, with $|A| = |u'_\theta|$ (for cases 5 and 6, the envelope of u'_θ is considered). The dashed black line is obtained by fitting equation (4.23a) to the red curve over the red-shaded range (the corresponding time interval in highlighted in red in the left plots). For all cases, the uncertainty on σ is less than 0.01 % and is thus not reported.

subcritical circular pitchfork bifurcation. Although the leading mode becomes oscillatory for case 5 ($K_R = 2$), l still remains negative: the Hopf bifurcation is thus subcritical. Finally, $l > 0$ for case 6 ($K_R = 1$, see figure 4.15 (l)), hence unstable Branch IV modes are associated with a supercritical Hopf bifurcation. For all cases, the difference between

Thèse accessible à l'adresse : https://theses.insa-lyon.fr/publication/2024ISAL0101/these.pdf © [B. Vincent], [2024], INSA Lyon, tous droits réservés

Table 4.4: Comparison of the growth rates σ and frequencies ω obtained by linear stability analysis (LSA) and by running direct numerical simulations (DNS) at slightly supercritical forcing magnitudes ($r_c > 0$). The relative errors between the values of σ and ω obtained by LSA and DNS are given by ε_σ and ε_ω, respectively.

Case	Gr_{ac}	r_c	σ (LSA)	σ (DNS)	ε_σ (%)	ω (LSA)	ω (DNS)	ε_ω (%)	ω - ω_{sat}
1	2500	0.141	2.755×10^{-3}	2.896×10^{-3}	4.87	0	0	–	–
2	5000	0.064	1.384×10^{-2}	1.383×10^{-2}	0.07	0	0	–	–
3	6400	0.026	1.591×10^{-2}	1.594×10^{-2}	0.19	0	0	–	–
4	8000	0.032	7.245×10^{-2}	7.690×10^{-2}	5.79	0	0	–	–
5	10600	0.008	2.540×10^{-2}	2.601×10^{-2}	2.35	3.946	3.958	0.30	1.166
6	15500	0.012	1.701×10^{-1}	1.704×10^{-1}	0.18	21.472	21.409	0.29	0

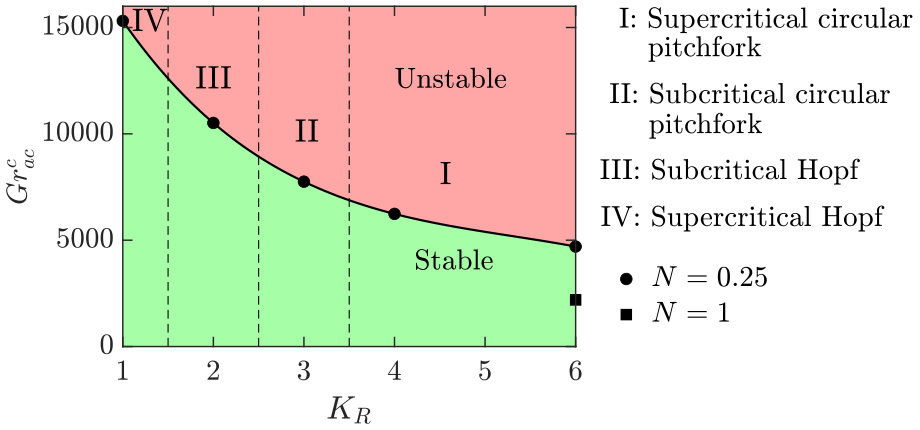


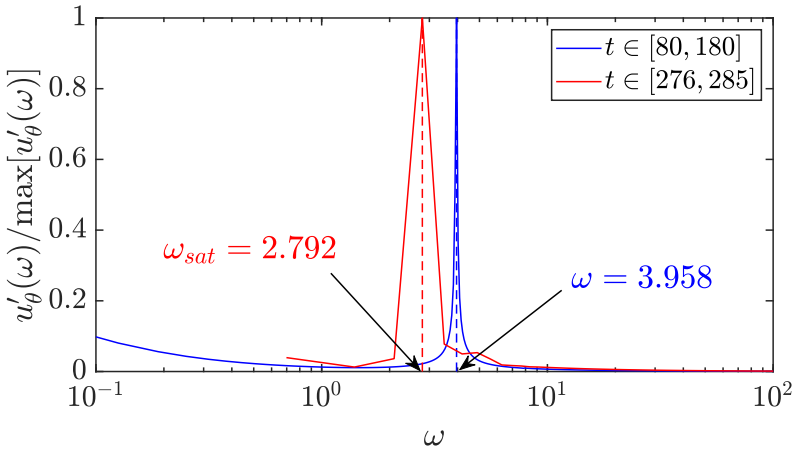
Figure 4.16: Summary of the instability onsets Gr_{ac}^c for the different cases listed in table 4.1. The stable (green) and unstable (red) regions are represented for $N = 0.25$ (cases 2 to 6). The vertical dashed lines represent the change of bifurcation type; their K_R locations are arbitrarily placed in between the investigated K_R.

the σ obtained with DNS and LSA is at most 6 % (table 4.4). This excellent agreement (i) confirms the relevance of LSA to investigate the stability of streaming jets, and (ii) bring further confidence on the validity of the Stuart-Landau analyses.

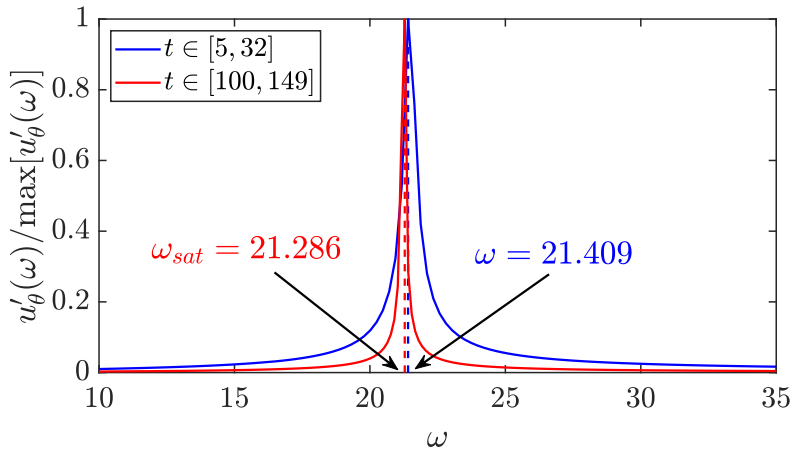
Finding subcritical bifurcations for cases 4 and 5 raises the question of whether these instabilities could be triggered for $r_c < 0$. For both cases, introducing white noise for $-0.05 \leq r_c \leq -0.01$ did not cause the flow to deviate from its axisymmetric base state. Triggering these bifurcations at $Gr_{ac} < Gr_{ac}^c$ would require different tools, e.g. the analysis of the transient growth of non-modal perturbations (Schmid, 2007). This is nevertheless is out of the scope of the present work.

The main outcomes of LSA and the Stuart-Landau analyses are summarised in figure 4.16. Confining the flow axially (by varying N) or axially (by varying K_R) not only has a stabilising effect, but also changes the primary bifurcation. For six (N, K_R) pairs, four different bifurcations were found: circular pitchforks (either supercritical or subcritial) for the least-confined cases ($K_R \geq 3$), and Hopf bifurcations (either subcritical or supercritical) for $K_R \leq 2$. A single-jet streaming flow thus destabilises through a large variety of paths simply by changing the cavity size and without changing the forcing shape.

Thèse accessible à l'adresse : https://theses.insa-lyon.fr/publication/2024ISAL0101/these.pdf © [B. Vincent], [2024], INSA Lyon, tous droits réservés



(a) Case 5 ($N = 0.25$, $K_R = 2$), $Gr_{ac} = 10600$ ($r_c = 0.0083$)



(b) Case 6 ($N = 0.25$, $K_R = 1$), $Gr_{ac} = 15500$ ($r_c = 0.0124$)

Figure 4.17: Frequencies obtained from the DNS time-series of the azimuthal velocity perturbation $u'_\theta(t)$ for (a) cases 5 and (b) 6. The corresponding time-series are those displayed in figure 4.15 (i) and (j), respectively. The frequencies are computed from FFTs made in the linear regime (ω, blue) and in the saturated regime (ω_{sat}, red).

4.6.3 Saturated states and secondary instabilities

The perturbations ultimately end up saturating; I shall finally characterise these saturated states.

For Hopf bifurcations, the frequency ω_{sat} of the saturated perturbation may differ from ω in the linear regime (regime of exponential perturbation growth), yielding a non-zero c_L (equation (4.25)). A change of oscillation frequency can be captured by taking the Fast Fourier Transform (FFT) of $u'_\theta(t)$ both in the linear and saturated regimes (figure 4.17).

For case 5 ($K_R = 1$), a 41.8 % difference is observed between ω and ω_{sat} (figure 4.17 (a)). In that case, $c = 44.83 \pm 14.63$, and the discrepancy between the values of ω predicted by LSA and DNS is 0.30 % (table 4.4). For case 6, the ω and ω_{sat} obtained by DNS in the linear and saturated regimes, respectively, are almost identical (figure 4.17 (b)). They also barely differ from the frequency predicted by LSA: the observed discrepancies are of 0.29 % and 0.87 % in the linear and saturated regimes, respectively (table 4.4). Given these small differences, ω and ω_{sat} are considered to be

Thèse accessible à l'adresse : https://theses.insa-lyon.fr/publication/2024ISAL0101/these.pdf © [B. Vincent], [2024], INSA Lyon, tous droits réservés

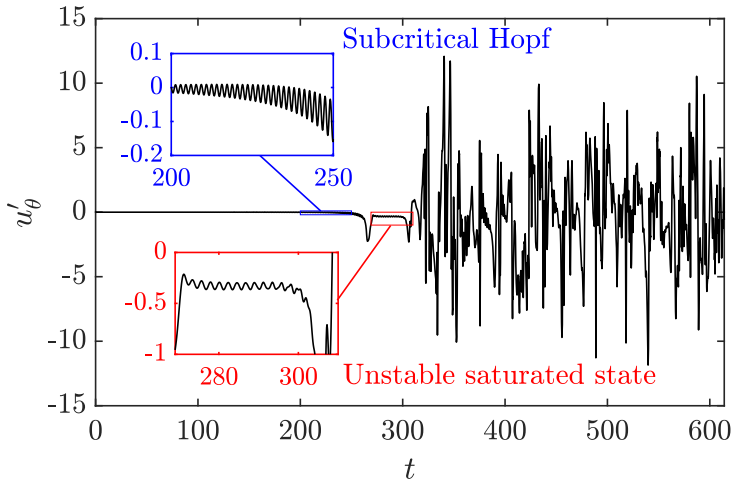


Figure 4.18: Time-series of the azimuthal velocity perturbation u'_θ for case 5 and $Gr_{ac} = 10600$ ($r_c = 0.0083$). The time series is recorded at $(x, r, \theta) = (81, 1.3, 0)$.

equal, hence $c_L = 0$.

The Stuart-Landau analysis for case 5 shows a large uncertainty on c_L. This is due to the rather wide band in the saturated regime spectrum (figure 4.17 (a)), which itself originates from the limited duration of the saturated regime. Indeed, the saturated state lasts about 10 oscillation periods, after which u'_θ changes abruptly (figure 4.18). This indicates that the saturated state is itself unstable. From there, the secondary instability triggers a transition towards a highly unsteady and chaotic flow regime. Unfortunately, the secondary instability develops too abruptly for a Stuart-Landau analysis to be applicable.

The development of a secondary instability has also been observed for case 4 ($K_R = 3$) with $r_c = 0.0320$ (figure 4.19 (a)). For that case, the saturated state is unstable to a non-oscillatory perturbation. Contrarily to case 5, the flow deviates slowly from the saturated state, allowing for a Stuart-Landau analysis to be made (figure 4.19 (b)). As the primary bifurcation, the secondary instability is found to be subcritical. However, it remains unclear whether the temporal variations of u'_θ observed for $t \geq 110$ in that case correspond to a transient regime before reaching a stable steady state, or instead are the beginning of a chaotic regime. Significantly longer simulations would be necessary to address this question.

4.7 Conclusion

In this chapter, I studied the stability of a laminar Eckart streaming jet in a configuration comparable to the one considered in chapter 3. In particular, I assessed the effect of the cavity size on the streaming flow stability. Different flow confinements were obtained by either varying the cavity length with respect to the attenuation length ($N = 1$ and 0.25), and by changing the ratio K_R between the cavity radius and the beam radius at the downstream cavity wall ($K_R \in [1, 6]$). For each case, I determined the critical forcing magnitude Gr^c_{ac} above which the flow is unstable using LSA, and determined the bifurcation nature (subcritical/supercritical) with DNS-based Stuart-Landau analyses. The main outcomes are illustrated by figure 4.16 and summarised below:

(i) For all geometries, recirculations originating from the jet impingement are formed near the downstream wall. The primary bifurcations result from the destabilisation

Thèse accessible à l'adresse : https://theses.insa-lyon.fr/publication/2024ISAL0101/these.pdf © [B. Vincent], [2024], INSA Lyon, tous droits réservés

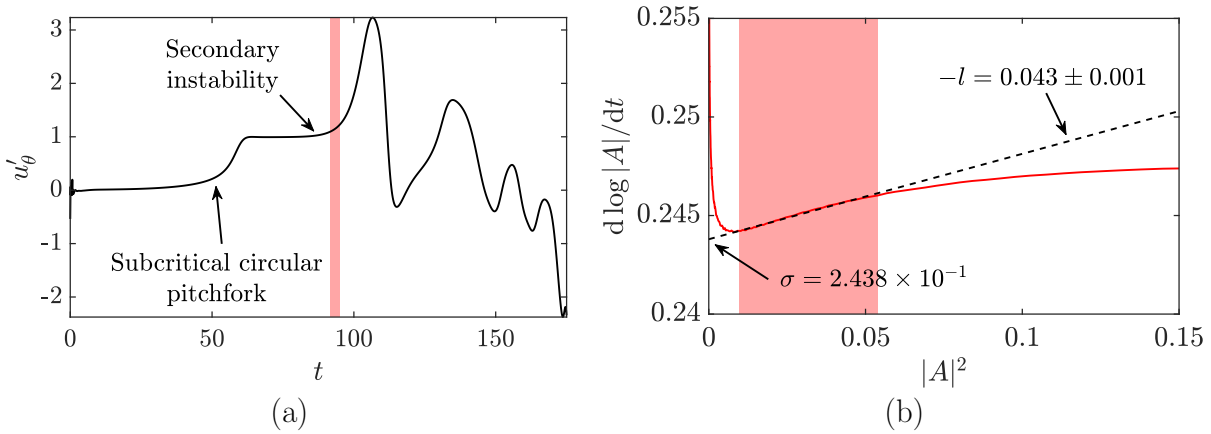


Figure 4.19: Stuart-Landau analysis for case 4, for $Gr_{ac} = 8000$ ($r_c = 0.0320$). (a) Temporal evolution of the azimuthal velocity perturbation u'_θ obtained from DNS and recorded at $(x, r, \theta) = (80, 2, 0)$. The perturbation originates from white noise injected at $t = 0$. (b) Evolution of $\mathrm{d}\left(\log|A|\right)/\mathrm{d}t$ with $|A|^2$ (red curve), where $|A| = |u'_\theta|$ and is extracted from (a). The black dashed line is obtained by fitting the Stuart-Landau equation (4.23a) to the red curve over the range highlighted in red. The positive slope indicates a subcritical transition.

of these recirculations, instead of the streaming jet.

(ii) Reducing the cavity size systematically has a stabilising effect. For weak confinements ($4 \leq K_R \leq 6$), the leading perturbation is non-oscillatory (Branch I). This unstable mode displays large velocity perturbation in the vicinity of the jet impingement, indicating a shear-driven flow destabilisation along the wall. The first significant effect of flow confinement occurs for $K_R = 3$: the leading mode remains non-oscillatory, but its topology changes (Branch II). This change of leading mode shape results from a topological constraint on the critical points (i.e., zeros of friction and velocity) of the perturbation. Flows in further confined settings are destabilised by oscillatory perturbations travelling in the azimuthal direction (Branch IV for $K_R = 1$). For $K_R = 2$, these perturbations also propagate backwards, i.e., towards the source (Branch III). Overall, reducing K_R (a) increases the shear in a layer near counter-rotating structures in the bulk of the flow, and (b) increases an adverse pressure gradient slowing down the jet. As a consequence, reducing K_R moves the root of instability from the jet impingement to the shear layer in the bulk of the flow.

(iii) Finally, changing the flow confinement significantly affects the nature of the primary bifurcations. Whilst the unstable modes of Branches I and IV respectively trigger supercritical pitchfork and Hopf bifurcations, the onsets of Branch II and III modes are subcritical.

A large variety of instabilities thus arises simply by varying the cavity size whilst keeping the forcing structure (e.g., diffraction) unchanged !

Having subcritical bifurcations for the $K_R \in \{2, 3\}$ cases raises the question of whether these bifurcations could be triggered $Gr_{ac} < Gr^c_{ac}$. DNS carried out between $0.95\,Gr^c_{ac}$ and $0.99\,Gr^c_{ac}$ revealed that white-noise-based perturbations could not to ignite subcritical transitions towards another state. The possibility of this scenario to occur, for instance by injecting initial disturbances maximising the energy growth over a finite time range (Schmid, 2007), remains uncertain at this stage.

Thèse accessible à l'adresse : https://theses.insa-lyon.fr/publication/2024ISAL0101/these.pdf © [B. Vincent], [2024], INSA Lyon, tous droits réservés

For $K_R = 2$ and 3, DNS carried out for $Gr_{ac} > Gr_{ac}^c$ showed that the growth and saturation of the initial white-noise perturbation were followed by the development of a secondary instability. For $K_R = 2$ in particular, that secondary instability triggered a transition towards a highly unsteady state. Is this the trace of an "edge state" (Camobreco *et al.*, 2023) i.e, is there a threshold for the initial perturbation energy below which the saturated state returns back to the initial steady axisymmetric state ? Or does the saturated state systematically transition towards a chaotic regime ? Further analysis is needed to elucidate all these questions.

Finally, this study proves the relevance of a numerical approach to study the stability of streaming flows for two reasons. First, the identified Gr_{ac}^c are comparable to (or even lower than) the Gr_{ac} of previous water experiments (see appendix A and table A.2 therein). Low-Gr_{ac} decimetric streaming experiments are particularly difficult to carry out due to the weak velocities involved. Although they were made for slightly different N and K_R than those I considered, these experiments were likely to be conducted beyond their respective Gr_{ac}^c. Second, the unstable oscillatory perturbations oscillate extremely slowly. Using the experimental parameters of Moudjed *et al.* (2014*a*) (table A.1) to convert back the stability results to dimensional units, the oscillation periods of the leading Branch III and Branch IV modes are 21 minutes 33 s and 3 minutes 58 s, respectively ! Accurate measurements of these oscillations would thus require long experiments that are very difficult to implement.

Thèse accessible à l'adresse : https://theses.insa-lyon.fr/publication/2024ISAL0101/these.pdf © [B. Vincent], [2024], INSA Lyon, tous droits réservés

Chapter 5

Driving an experimental 3D-3C streaming flow using multiple reflections of a single sound beam

5.1 Introduction

In this final chapter, I shall characterise both the topology and properties of a streaming flow forced by a reflected sound beam. Part of this work has been published in *Physical Review Fluids* (Vincent *et al.*, 2024).

Taking advantage of controlled sound reflections to tailor a complex forcing field greatly extends the range of flows that can be driven acoustically, and thus also calls for a better understanding. Whatever the targeted application, the question is first to determine the properties of that flow: is it 2D or 3D ? Steady or unsteady ? Predictable or chaotic ? From a practical standpoint, the question arises of whether a single beam can effectively drive a flow in the entire fluid volume after multiple reflections. Each of these questions may require a specific study to be answered, but the basic mechanisms are best discovered in a generic geometry. Hence, I shall consider the simplest setting: a parallelepipedic volume enclosed by solid walls.

The questions set out above are tackled experimentally using water as a working fluid, allowing to map the flow by means of optical methods. More precisely, the three-dimensional Eulerian velocity fields of the streaming flows are reconstructed from Particle Tracking Velocimety (PTV) measurements. The approach relies on successive reflections of the beam on the fluid domain boundaries to drive a flow with effective stirring properties. The flow is studied in a nearly cubic cavity, with a square horizontal cross section of 183×183 mm^2. The beam enters the cavity with a 45° horizontal angle with the side walls together with a small vertical inclination. This beam orientation results in an acoustic forcing pointing downwards and taking a nearly helical shape (figure 5.1). Because of mass conservation, the descending flow promoted by the forcing is necessarily accompanied by ascending streams. It is however difficult to predict beforehand whether these ascending flows occur at the centre of the cavity or at its corners instead. This last point is key from a process standpoint, as regions of stagnant fluid usually reported at the corners are unwanted. Finally, I emphasise that this work aims to check that this original acoustic forcing is able to drive a large-scale flow in the entire fluid volume. The design of an optimised stirring setting for this cavity should be the topic of another study.

This last chapter is organised as follows: section 5.2 is devoted to the characterisation

Thèse accessible à l'adresse : https://theses.insa-lyon.fr/publication/2024ISAL0101/these.pdf © [B. Vincent], [2024], INSA Lyon, tous droits réservés

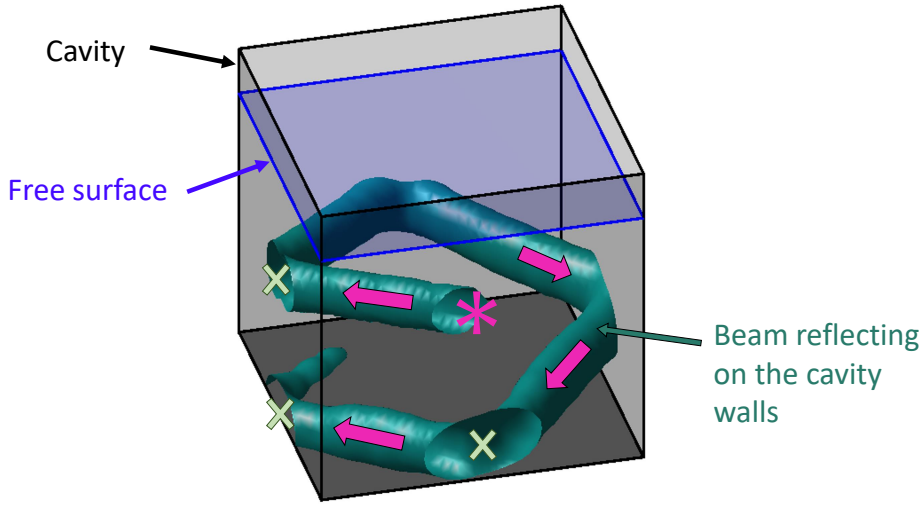


Figure 5.1: Sketch of the configuration studied experimentally. The flow is driven by a sound beam undergoing multiple reflections (represented as green crosses) on the walls of a water-filled cavity. The beam is obtained from the attenuated Rayleigh integral, and reflections are treated with the method of images (Kinsler *et al.*, 2000). The beam entry point is located by the purple star, and the purple arrows indicate the wave propagation (hence, the forcing) direction. The sound waves are completely attenuated at the bottom wall (deep grey).

of the cylindrical transducer used to drive the streaming flow. After exposing the working principles of PTV, I shall assess the ability of this method to recover 3D Eulerian velocity fields of streaming flows in section 5.3. The experimental setup used to investigate the helical flow is then detailed in section 5.4, in which the convergence of the time-averaged flows is also assessed. The following section is devoted to the analysis of the jet-like structures in the time-averaged flows, and to the generation of helicity. Section 5.6 focuses on the large-scale vertical and horizontal streams, and how their strength scales with the forcing magnitude. Finally, I shall focus on the flow structure near the first jet impingement, together with its unsteadiness, in section 5.7.

5.2 Experimental estimation of the acoustic source active diameter

The helical flow to be studied is driven by a complex acoustic field, which is itself radiated by a plane circular source. I shall first characterise this source in water, and more specifically determine its active diameter from measurements of the radiated sound field.

5.2.1 Test rig, equipment and signal chain for mapping the acoustic pressure and intensity fields

The acoustic field measurements were made in an glass aquarium entirely filled with water (figure 5.2). The aquarium was split into two subvolumes: the smallest subvolume

Thèse accessible à l'adresse : https://theses.insa-lyon.fr/publication/2024ISAL0101/these.pdf © [B. Vincent], [2024], INSA Lyon, tous droits réservés

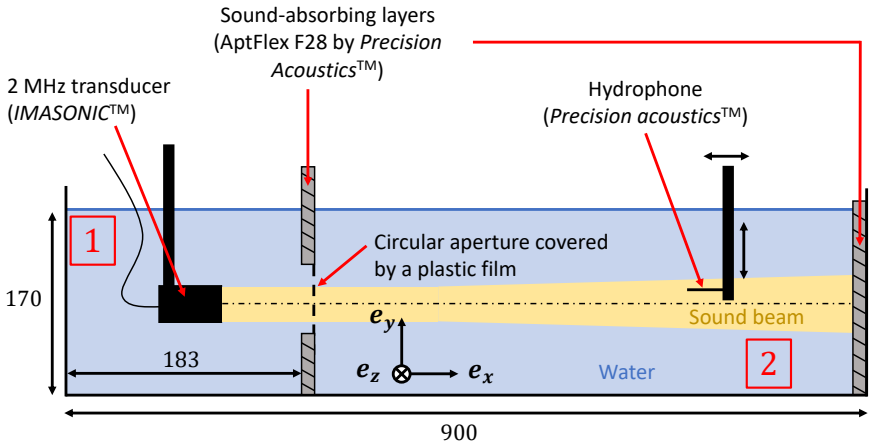
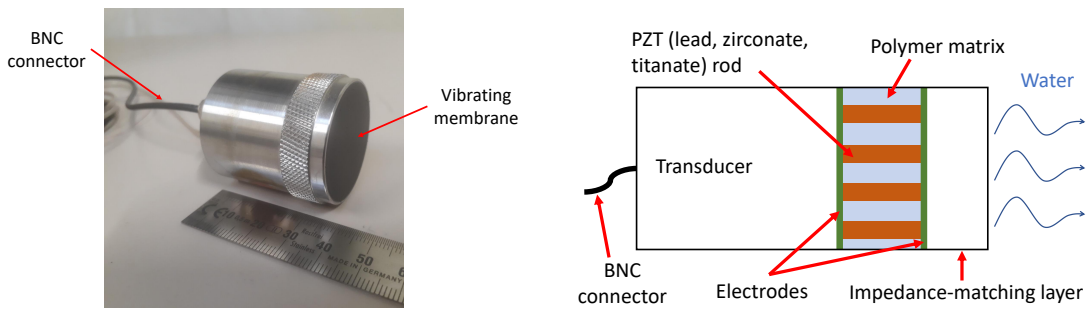


Figure 5.2: Sketch of the test rig used to measure the acoustic field radiated by the transducer. Distances are given in mm.

(labelled as "1" in figure 5.2) featured the acoustic source, which radiated a sound field in the largest subvolume (labelled as "2").

The acoustic source was a plane circular transducer manufactured by *IMASONIC*™ (figure 5.3 (a)). The 34.9 mm-in-diameter external casing of the transducer was made of stainless steel and enclosed a piezocomposite material fitted with electrodes, to which an adapting layer was finally attached (figure 5.3 (b)). The piezocomposite material was made of PZT (lead, zirconate, titanate) rods placed in a polymer matrix. The transducer relied on the piezoelectric effect to convert electrical energy into acoustic energy: as an alternating potential difference is applied to the electrodes, the piezocomposite material is strained, causing the attached layer to oscillate. To maximise the transmission of these oscillations as sound waves to the surrounding fluid, the material of that layer is chosen so that its acoustic impedance $\rho_m c_m$ (with ρ_m and c_m the material density and the associated speed of sound) matches the acoustic impedance of water.

The transducer was mounted on the same mechanical system as the one used by El Ghani (2020) during her thesis. The device featured two protractors (1° resolution), allowing to precisely control the angular positions of the transducer about the y- and z-axes (figure 5.4 (a)). These two protractors were clamped on two plates, each allowing for a longitudinal motion in either the y- (plate A) or z-directions (plate B). Finally,



(a) (b)

Figure 5.3: Picture (a) and sketch (b) of the plane circular acoustic transducer used to create a sound field.

Thèse accessible à l'adresse : https://theses.insa-lyon.fr/publication/2024ISAL0101/these.pdf © [B. Vincent], [2024], INSA Lyon, tous droits réservés

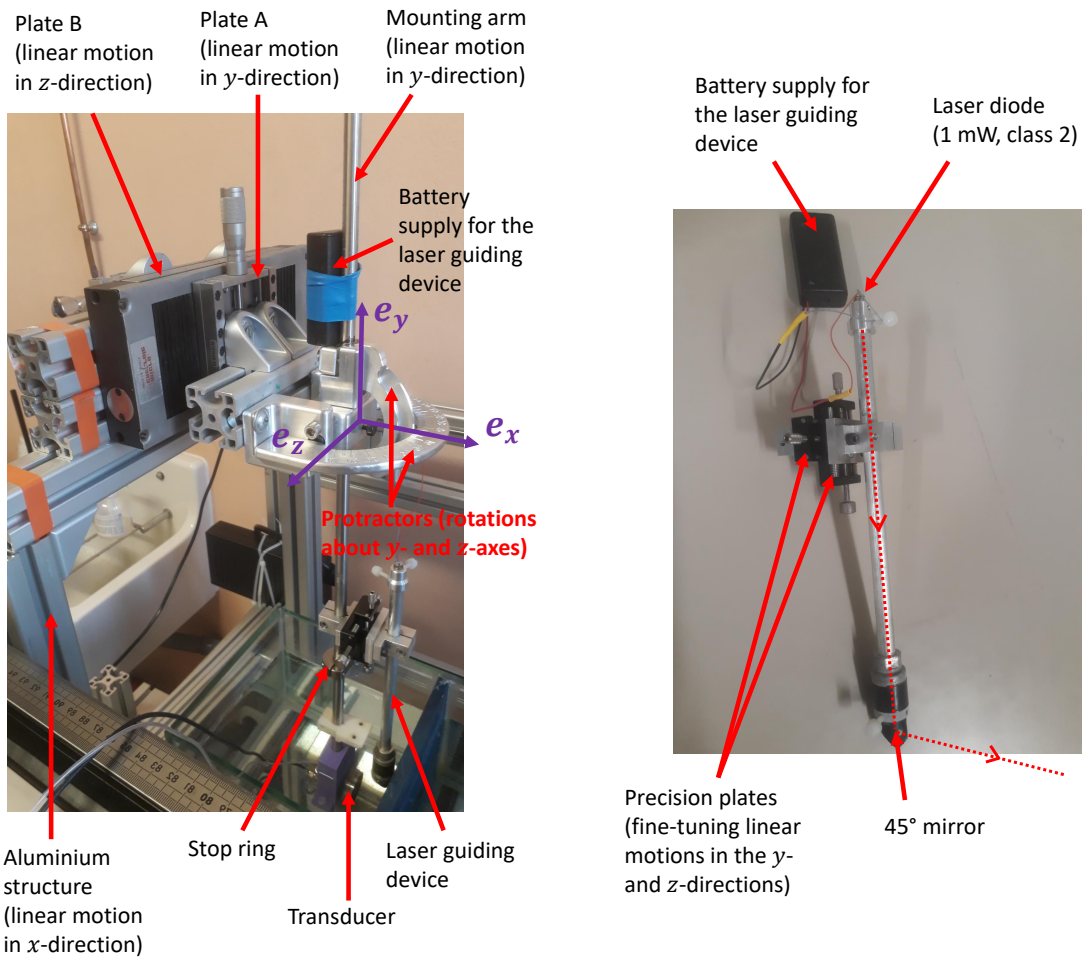


Figure 5.4: Pictures of the devices used to position the transducer. (a) Mechanical system to carry and position the transducer. (b) Detailed view of the laser guiding device, as initially designed by El Ghani (2020). The discontinuous line represents the laser beam emitted by the diode. The mounting arm shown in (a) features a key, yielding a slip joint between the mounting arm and the laser guiding device.

the complete mechanical system holding the transducer was mounted on an aluminium structure, which is itself clamped to the test rig. The fixture between the aluminium structure holding the transducer and the test rig could be loosened to form a slip joint, allowing for the whole mechanical system to be moved in the x-direction. In total, the transducer could be positioned and oriented using five degrees of freedom (two rotations and three linear motions).

To provide an optical representation of the acoustic axis when the transducer is manipulated, the mounting arm to which the transducer was attached was further fitted with a laser guiding device designed by El Ghani (2020) during her thesis. It featured a 2.4 mm-in-diameter laser diode (class 2), which emitted a red laser beam pointing downwards, in a direction parallel to the axis of the mounting arm (figure 5.4 (b)). The bottom end of the laser guiding device was fitted with a 45° mirror that reflected the incident laser beam. The mounting arm carrying the transducer acted as a shaft along which the laser system could move (a key on the mounting arm prevented any rotation of the laser guid-

Thèse accessible à l'adresse : https://theses.insa-lyon.fr/publication/2024ISAL0101/these.pdf © [B. Vincent], [2024], INSA Lyon, tous droits réservés

ing system). To help setting-up the transducer position and orientation, the laser guiding system was loosened and slid downwards until reaching a ring stop (figure 5.4 (a)), so that the red laser beam could be aligned with the acoustic axis. Once the transducer was correctly positioned and ready to operate, the laser was slid back upwards to avoid any obstruction in front of the transducer.

In subvolume 2, the acoustic pressure field $p_{ac,exp}$ radiated by the transducer was measured by a hydrophone manufactured by *Precision Acoustics*^{TM}. The acoustic pressure field was measured with an uncertainty of 13 % (Moudjed, 2013) at the tip of a 1 mm-in-diameter needle immersed in water. The hydrophone was mounted on a plate allowing for displacements along the y-direction. This plate was further mounted on two *Charlyrobot*^{TM} motors, each providing a translational degree of freedom in the x- and z-directions.

A sound-absorbing plate was placed at the end of subvolume 2 to prevent any reflection of an incident sound wave (figure 5.2). The plate was a 10 mm-thick polyurethane layer (AptFlex F28 manufactured by *Precision Acoustics*^{TM}) designed to attenuate 99 % of an incident 2 MHz acoustic pressure wave. This ensured that the sound field measured by the hydrophone indeed corresponded to the sound field radiated by the transducer, and was not contaminated by reflections on the wall facing the source.

Finally, most of the electronic devices were controlled by a main computer (figure 5.5). Dedicated *LabView* programs (i) sent sine signals to the transducer via a PXI 5404 function generator, (ii) recorded the acoustic pressure signal measured by the hydrophone via a PXI oscilloscope (sampling frequency of 100 MHz), (iii) regulated the electrical power P_{elec} prescribed to the transducer and (iv) actuated the *Charlyrobot*^{TM} motors to move the hydrophone horizontally at points prescribed either before or during the experiments. In contrast, the vertical displacements were not automated, but instead prescribed "by hand" using a separate Newport SMC100 controller (figure 5.5 (b)).

5.2.2 Hydrophone measurements

The transducer manufacturer *IMASONIC* provided physical dimensions of the source, including a primary estimation of its active diameter D_s. The latter nevertheless calls for a better evaluation before using the transducer to drive streaming flows. The methodology to evaluate D_s can be divided into three main steps.

First, I calibrated the transducer orientation so that any vertical and horizontal inclinations of the acoustic axis could be precisely read on (or prescribed by) the protractors (figure 5.4 (a)). At this stage, the protractors were set to zero vertical and horizontal inclinations, and the transducer operated at a constant electrical power $P_{elec} = 1$ W. I then looked for points of maximum acoustic pressure, since these maxima lie on the acoustic axis in the far acoustic field. The hydrophone thus initially placed at an approximate distance of $x \approx 27$ cm of the transducer. The hydrophone was then moved in both the y- and z-directions until the point of maximum acoustic pressure is found with a 1 mm resolution. This procedure was then repeated at larger distances x from the source, so that the acoustic axis could be located at six different distances from the transducer, ranging from $x \approx 27$ cm to $x \approx 52$ cm and separated by 5 cm. The transducer position was then adjusted by rotating the mounting arm (figure 5.4 (a)) relative to the protractors. Finally, I repeated the whole procedure until I achieved a maximum deviation of 1 mm between the acoustic axis and the cavity centre line in either the y- and z-directions. Over the x-range, this deviation corresponds to an error of 0.23° on the transducer orientation.

Thèse accessible à l'adresse : https://theses.insa-lyon.fr/publication/2024ISAL0101/these.pdf © [B. Vincent], [2024], INSA Lyon, tous droits réservés

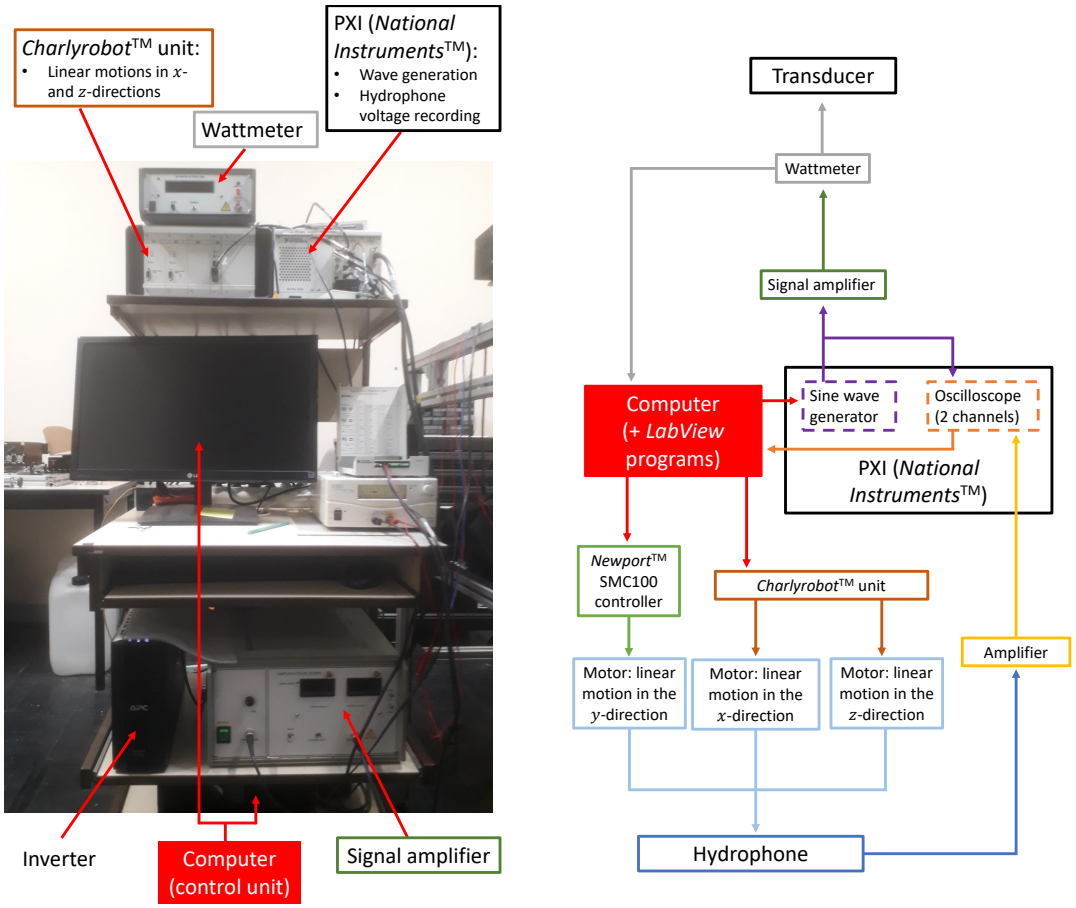


Figure 5.5: Signal chain used to generate and record ultrasounds. (a) Picture of the electronic setup. (b) Sketch detailing how the different electronic components are connected to each other.

Second, I mapped the acoustic fields (pressure and intensity) in a horizontal plane containing the acoustic axis. The probed area was a 380×70 mm^2 plane approximately centred around the last pressure peak, with a resolution of 2 mm in the z-direction. The same resolution was adopted in the x-direction, except beyond the last pressure peak, where measurements were made every 5 mm. In total, $p_{ac,exp}$ was thus measured at 8211 different points. At each of these points, $p_{ac,exp}$ was averaged over five distinct 1.5 s recordings, each separated by 0.1 s. After each displacement, the hydrophone waited 3 s before starting the measurements to avoid any transient effects. In total, the mapping of $p_{ac,exp}$ lasted 26 hours and 21 minutes, during which the electrical power was maintained at $P_{elec} = 1$ W.

Finally, I compared the experimental acoustic intensity map $I_{ac,exp} \approx p_{ac,exp}^2 / (2\rho_0 c)$ to intensity maps $I_{ac,num} \approx p_{ac,num}^2 / (2\rho_0 c)$ generated by computing the attenuated Rayleigh integral (2.7) with the water properties listed in table 1.1. I then assessed the discrepancy between the two normalised fields in a least-squares sense:

$$\mathcal{X} = \sqrt{\frac{1}{N_x N_z} \sum_{i=1}^{N_x} \sum_{j=1}^{N_z} \left[\widetilde{I}_{ac,exp}(x_i, z_j) - \widetilde{I}_{ac,num}(x_i, z_j) \right]^2}, \tag{5.1}$$

where N_x and N_z are the number of measurement points in the x- and z-directions, re-

Thèse accessible à l'adresse : https://theses.insa-lyon.fr/publication/2024ISAL0101/these.pdf © [B. Vincent], [2024], INSA Lyon, tous droits réservés

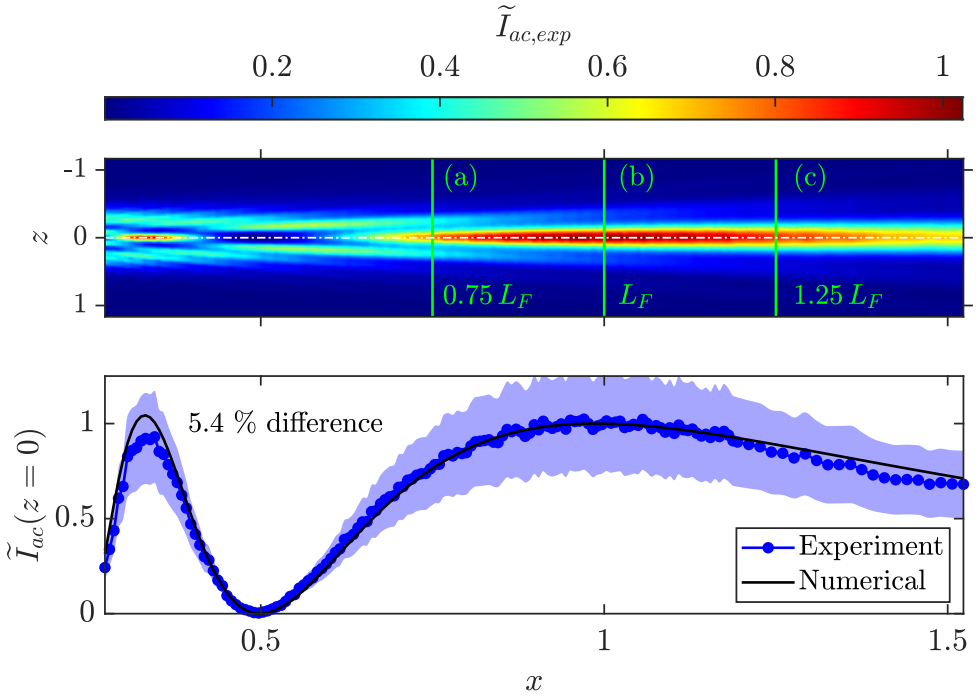


Figure 5.6: Comparison between the experimental $\widetilde{I}_{ac,exp}$ and numerical $\widetilde{I}_{ac,num}$ acoustic intensity fields. The numerical field is obtained by computing the Rayleigh integral (2.7) with $D_s = 30$ mm and with the water properties listed in table 1.1. Top: 2D map of $\widetilde{I}_{ac,exp}$ measured in a constant-y plane containing the acoustic axis (white mixed line). The vertical green lines indicate where the transverse profiles of figure 5.7 are made. Bottom: comparison between the numerical (black) and experimental (blue) profiles of the normalised intensities on the acoustic axis, with the associated relative difference. The blue-shaded area represents the uncertainty of the hydrophone measurements (26 %). In all plots, the origin is taken at the centre of the transducer vibrating membrane, and the x and z coordinates are normalised by the Fresnel length $L_F = D_s^2/(4\lambda)$ and by D_s, respectively. The intensities are normalised by their on-axis values at $x = L_F$.

spectively. In equation (5.1), the $\widetilde{\ }$ symbol means that the intensity field amplitudes are normalised by their on-axis values at the last intensity peak, which is approximately located at the Fresnel distance $L_F \approx D_s^2/(4\lambda)$ from the transducer (with λ the wavelength). In the experimental field, L_F was taken as the last peak of the on-axis intensity profile smoothed using a 38 mm sliding average; this window size was sufficiently large to effectively filter out measurement noise whilst preserving the shape of the on-axis profile. I applied this smoothing step only to locate the last intensity peak; the "raw" experimental intensity is considered in equation 5.1. The best match between $\widetilde{I}_{ac,exp}$ and $\widetilde{I}_{ac,num}$ was then obtained by minimising $\mathcal{X}$ using two degrees of freedom: (i) the value of D_s used to compute the Rayleigh integral, and (ii) the x-position of the transducer.

5.2.3 Evaluation of the active diameter D_s of the transducer

As expected, the measured intensity field is shaped as a diffracting beam (upper plot of figure 5.6). The area covered by the hydrophone comprises the last two intensity peaks on the acoustic axis, and the radial enlargement of the beam caused by diffraction is also captured.

Thèse accessible à l'adresse : https://theses.insa-lyon.fr/publication/2024ISAL0101/these.pdf © [B. Vincent], [2024], INSA Lyon, tous droits réservés

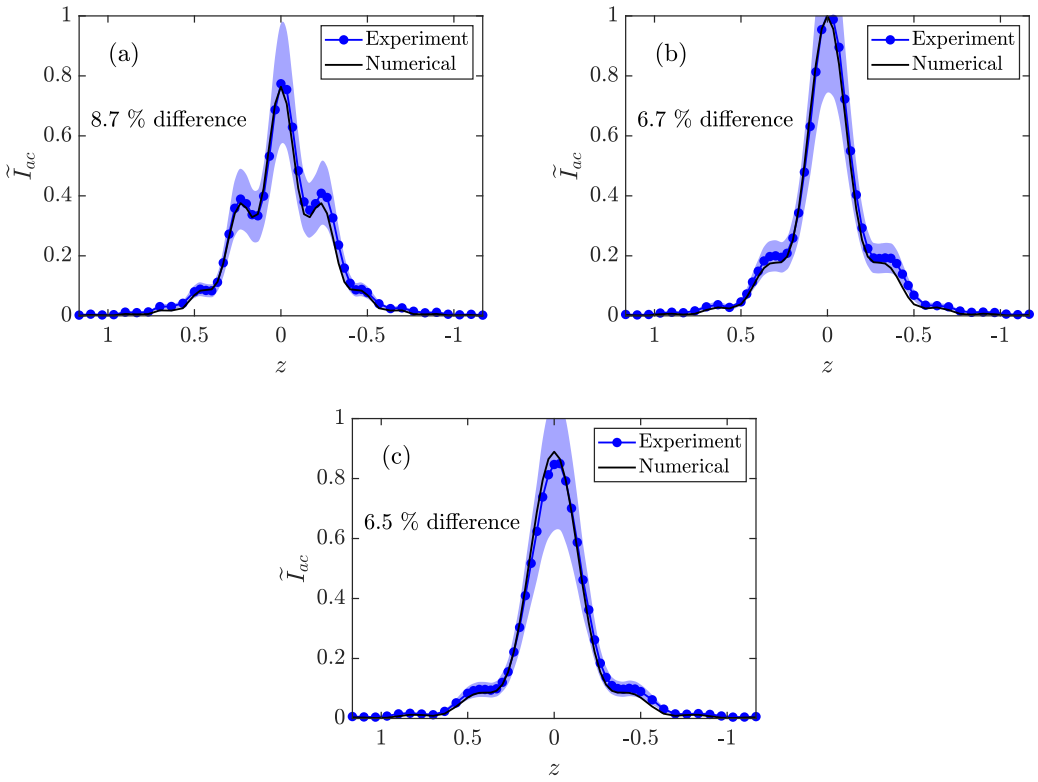


Figure 5.7: Comparison between the numerical (black) and experimental (blue) transverse profiles of the normalised acoustic intensity $\widetilde{I}_{ac}$ at different distances x from the transducer (see the green lines in the upper plot of figure 5.6): (a) $x = 0.75L_F$, (b) $x = L_F$ and (c) $x = 1.25L_F$, where L_F is the Fresnel distance. The numerical profiles are obtained by computing the Rayleigh integral (2.7) for $D_s = 30$ mm and with the water properties listed in table 1.1. In all plots, the blue-shaded area represents the uncertainty of the intensity measured with the hydrophone (26 %). The relative difference between the black and blue profiles is also reported. The z-coordinates are normalised by D_s, and the intensity profiles are normalised by their on-axis values at $x = L_F$.

The minimum $\mathcal{X} = 2.44 \times 10^{-2}$ is obtained for $D_s = 30$ mm. For this D_s, the discrepancy between the on-axis profiles of $\widetilde{I}_{ac,exp}$ and $\widetilde{I}_{ac,num}$ is 5.4 % (bottom plot of figure 5.6). As this difference falls below the uncertainty of the acoustic measurement ($\pm$26 % for 2 MHz waves, as represented by the blue shaded area in figure 5.6), the discrepancy is acceptable. An excellent agreement is also found between transverse profiles of intensity at different distances from the transducer: the discrepancy ranges from 6.5 % at $x = 1.25L_F$ (figure 5.7 (c)) to 8.7 % at $x = 0.75L_F$ (figure 5.7 (a)).

I shall briefly discuss the challenges of measuring acoustic signals in their near field. There, the acoustic field features sharp gradients in both the longitudinal (bottom plot of figure 5.6) and transverse (figure 5.7 (a)) directions. At very close distances from the transducer ($x \ll L_f$), these gradients actually occur over length scales that may become smaller than the hydrophone diameter, hence its spatial resolution (Moudjed *et al.*, 2014*a*). Mapping precisely the very-near acoustic field close to the transducer thus is unrealistic, and should not be considered when characterising the active diameter D_s of the transducer.

To conclude, the active diameter of the transducer is $D_s = 30.0$ mm, i.e., D_s is smaller than the external casing (34.9 mm). This could be expected, though: because the edge of

Thèse accessible à l'adresse : https://theses.insa-lyon.fr/publication/2024ISAL0101/these.pdf © [B. Vincent], [2024], INSA Lyon, tous droits réservés

the vibrating membrane is clamped to the casing, all the membrane surface does not contribute to the radiated acoustic field, thus explaining why D_s is smaller than the diameter of the external casing. Regarding the dimensionless numbers describing the acoustic field radiated by this transducer, the obtained D_s gives $S \approx 0.03$ and $N/L \approx 0.003$ in water. **Therefore, the structure of the acoustic forcing field created by this transducer in water is comparable to the forcing fields considered in the scaling and stability studies of chapters 3 and 4, respectively.**

5.3 Working principles of Particle Tracking Velocimetry (PTV), required equipment and validation

I shall now focus on the generation of a three-dimensional streaming flow using the transducer that has just been characterised. The flow is studied experimentally by means of Particle Tracking Velocimetry (PTV). After having presented the working principle of PTV, and how Eulerian velocity fields can be recovered from PTV data, I shall outline the changes made to the test rig for the flow measurements. I shall finally quantify the effects of temperature variations on the actual acoustic forcing magnitude.

5.3.1 Working principles of PTV and the Shake-The-Box algorithm

Particle Tracking Velocimetry (PTV) is an optical method that tracks moving objects in a flow. Similarly to PIV (Particle Image Velocimetry), which is another popular method to measure fluid flows, PTV thus requires the working fluid to be seeded with particles. These particles are then lit by either a planar or volumetric light source (e.g., laser), and their motion in the measurement volume are recorded by one or multiple cameras at a controlled frame rate. In PIV, each frame is divided into square interrogation windows containing between 10 and 15 particles defining a *particle pattern*. The pattern displacement is then obtained from cross-correlations between the interrogation windows of two consecutive frames, thus yielding Eulerian velocity data. In contrast, PTV directly tracks *individual particles* and reconstructs their trajectories (or tracks) in space. PTV is thus a Lagrangian measurement technique.

Still, Eulerian fields may be retrieved from PTV measurement by applying a *binning* method. In this approach, the measurement volume is divided into cubic cells, or bins. At each time step, one checks whether particles lie within the cell. If so, the instantaneous velocities of all these particles are used to estimate an Eulerian velocity at the cell centroid. This approach is an advantageous alternative to tomographic PIV (i.e, "3D PIV"), as binning does not require computationally-demanding (in terms of CPU time) 3D cross-correlations, which besides may act as filters degrading the spatial resolution (Schneiders & Scarano, 2016). However, the binning robustness and accuracy is directly related to the number of particles (and trajectories) the PTV system is able to detect in successive frames.

In a three-dimensional measurement domain, the Lagrangian nature of PTV naturally affects the maximum seeding density (i.e., particle concentration) to be used, hence the amount of data to be recovered. For individual particles to be detected, the amount of

Thèse accessible à l'adresse : https://theses.insa-lyon.fr/publication/2024ISAL0101/these.pdf © [B. Vincent], [2024], INSA Lyon, tous droits réservés

seeding particles on the optical path of the cameras must be sufficiently low to avoid the masking of particles in the background of the measurement domain. Masking effects are the main reason why seeding densities are lower in PTV than PIV (Schneiders & Scarano, 2016).

The computational advantages of PTV motivated the development of particle tracking algorithms allowing for greater seeding densities. In particular, the recent *Shake-The-Box* algorithm of Schanz *et al.* (2016) showed its ability to track particles with seeding densities comparable to those encountered in tomographic PIV. A time step of *Shake-The-Box* is depicted in figure 5.8 and can be summarised as follows (Schanz *et al.*, 2016; Schröder & Schanz, 2023):

(i) For an already-existing track, the new particle position is estimated by extrapolating its positions at previous times using a Wiener filter.
(ii) The particle is "shaken" around its predicted position to match a nearby particle in the current frame. If no match is found, the particle is assumed to be "lost" (e.g., it left the measurement domain) and the track is broken.
(iii) Residual images are computed by subtracting the particles obtained at step (ii) from the current frame.

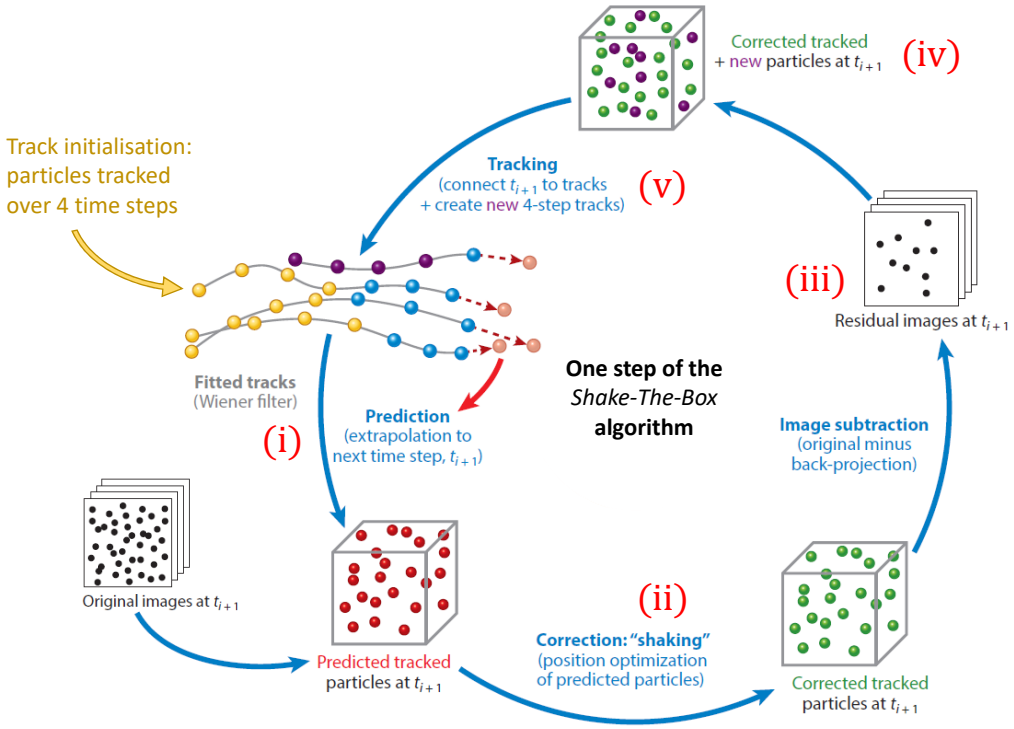


Figure 5.8: Sketch of a *Shake-The-Box* iteration at the time step t_{i+1} (figure taken and adapted from Schröder & Schanz (2023)). The algorithm can be divided into five major steps: (i) new particle positions are predicted by extrapolating the previous tracks, (ii) each particle is then 'shaken" about its predicted position to match a nearby particle in the t_{i+1} frame. If no match is found, the particle is "lost" (e.g., it left the measurement volume) and its track is interrupted. After that, (iii) residual images are computed by subtracting the particles obtained at step (ii) from the t_{i+1} frame, thus (iv) allowing for the detection of new particles. Finally, new tracks are created for these particles and are added to the tracks obtained at the previous time steps.

Thèse accessible à l'adresse : https://theses.insa-lyon.fr/publication/2024ISAL0101/these.pdf © [B. Vincent], [2024], INSA Lyon, tous droits réservés

(iv) New particles are identified and located in the residual images.
(v) Add the updated particle positions to the associated tracks, and generate new tracks for particles that have been correctly followed within four consecutive time steps.

This process is then repeated for all recorded frames.

5.3.2 Equipment for PTV measurements

5.3.2.1 Choice of seeding particles

To accurately measure the velocity fields, the seeding particles must be small enough to faithfully follow the flow, whilst at the same time to be sufficiently large to appear clearly on the frames recorded by the cameras. For the measurement of streaming velocities, two criteria must be fulfilled.

First, the particles shall be sufficiently small to not be affected by the acoustic radiation pressure, which is a force exerted by sound waves on solid bodies (Baudoin & Thomas, 2019). The former study of Ben Haj Slama *et al.* (2017) showed that, for 2 MHz sound waves, particles of diameter $d_p = 5$ μm are sufficiently small to not be "pushed away" by the sound waves.

Second, the seeding particles shall be sufficiently small to correctly follow the flow streamlines. This ability is usually assessed by the Stokes number (Raffel *et al.*, 2018):

$$St = \frac{\tau_p}{\tau_f}\,, \tag{5.2}$$

which compares the viscous response time of the particle $\tau_p = \rho_p d_p^2 / (18\rho_0\nu)$ (with ρ_p and d_p the particle density and diameter, respectively) to a flow time scale τ_f. Seeding particles thus accurately follow the flow if their response time is significantly smaller than τ_f, i.e., if $St \ll 1$ (Tropea *et al.*, 2007). Taking $\rho_p \sim \rho_0$ in water (table 1.1) and $\tau_f \sim U_s \,/\, D_s$ (with $U_s \sim 5$ cm/s a flow velocity scale (Moudjed *et al.*, 2014*a*)) yields $St \sim 10^{-6} \ll 1$. **I thus used $d_p = 5$ μm seeding particles for all streaming velocity measurements**.

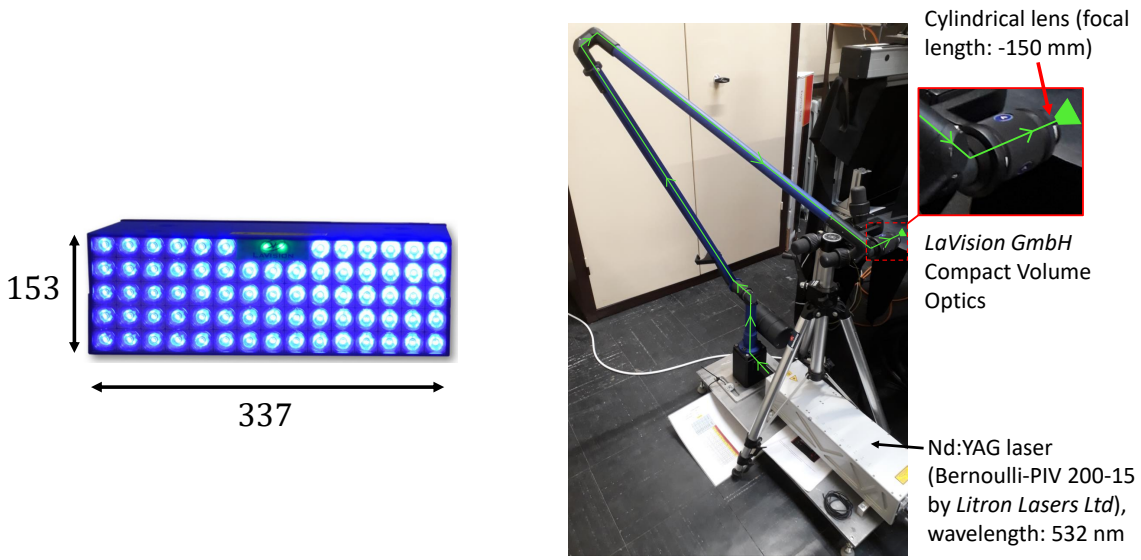
5.3.2.2 Light sources

Once immersed in the fluid volume of interest, the seeding particles need to be lit. I considered two different light sources: a LED panel and a laser, depending on the size of the fluid volume to be probed.

The LED panel (*LaVision GmbH* Flashlight 300) featured a 337×153 mm^2 array of 72 LEDs emitting 450 ± 10 nm light (figure 5.9 (a)). The LED panel has the advantage of creating a large high-power (290 W) volumetric lighting without additional devices. I used the LED panel to light 5 μm PSP particles made by *Dantec Dynamics*. However, the spectrum of the light emitted by the seeding particles may be close to the LED spectrum, thus preventing to filter out the LED light from the recorded frames. This is particularly detrimental near light-reflecting boundaries such as glass walls.

The noise induced by light reflections at the boundaries can be removed by changing both the light source and the seeding particles. I considered a laser source (Nd:YAG Bernoulli-PIV 200-15 by *Litron Lasers Ltd*) emitting a 6.15 mm-in-diameter beam of 532 nm light. The beam was carried to the *LaVision GmbH* Compact Volume Optics

Thèse accessible à l'adresse : https://theses.insa-lyon.fr/publication/2024ISAL0101/these.pdf © [B. Vincent], [2024], INSA Lyon, tous droits réservés



(a) (b)

Figure 5.9: Light sources used for the PTV measurements: (a) *LaVision GmbH* Flashlight 300 LED panel and (b) a Nd:YAG laser source (*Litron Lasers Ltd* Bernoulli PIV 200-15) emitting a 532 nm beam expanded into a volume by the *LaVision GmbH* Compact Volume Optics fitted with a cylindrical lens (see the inset). The beam is carried to the volume expander through a jointed arm (the green lines and arrows indicate the path followed by the laser beam from the source to the volume expander). Dimensions are given in mm.

device by a jointed arm (figure 5.9 (b)), inside which the laser light was reflected by mirrors. The *LaVision GmbH* was fitted with a cylindrical lens of -150 mm focal length, thus expanding the beam into a $170 \times 25 \times 75$ mm^3 (length $\times$ width $\times$ height) volume of elliptical cross-section. The volume-expanded laser lit 5 μm fluorescent polystyrene particles (*microParticles GmbH* PS-FluoRed-5.0) emitting light at a controlled 607 nm wavelength, which was isolated by mounting filters on the cameras. However, the resulting increased signal-to-noise ratio on the recorded frames comes to the expense of reduced overall light levels. Therefore, I used this light source/particles combination for flow measurements in small volumes only, in which I could sufficiently focus the laser light.

5.3.2.3 Cameras

The 3D motions of the seeding particles were recorded using the *LaVision MiniShaker* (figure 5.10 (a)). This device is made of four cameras (*Basler* acA1920-150um), each being separated by 100 mm. Prior to any measurement, I calibrated these cameras using a 100×100 mm^2 plate featuring a distribution of white dots on two planes separated by 2 mm (figure 5.10 (b)), thus allowing for a volumetric calibration of the cameras. When the fluid volume was seeded with laser-lit fluorescent particles, I filtered out the laser light by fitting the cameras with high-pass *Kodak* Wratten 22 filters (cut-off wavelength ≈ 550 nm).

Thèse accessible à l'adresse : https://theses.insa-lyon.fr/publication/2024ISAL0101/these.pdf © [B. Vincent], [2024], INSA Lyon, tous droits réservés

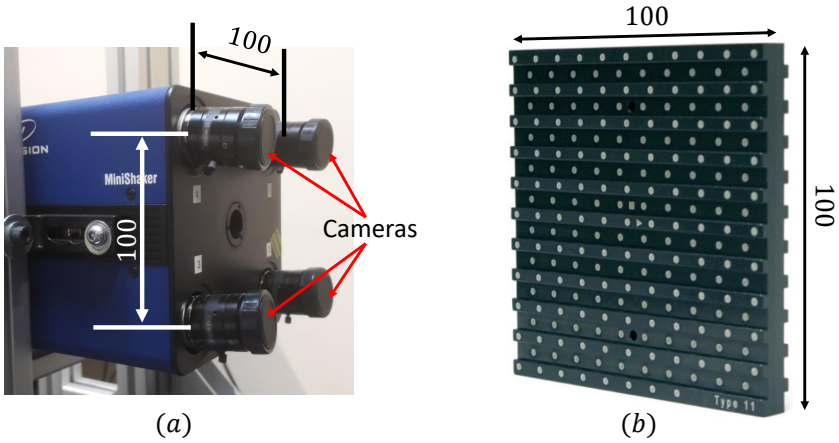


Figure 5.10: Pictures of (a) the *LaVision GmbH MiniShaker* device featuring four cameras (*Basler* acA1920-150um) tracking the seeding particles, and (b) the volumetric plate used to calibrate the *MiniShaker*. Dimensions are given in mm.

5.3.3 Validation of the PTV methodology against a previously-studied acoustic streaming flow

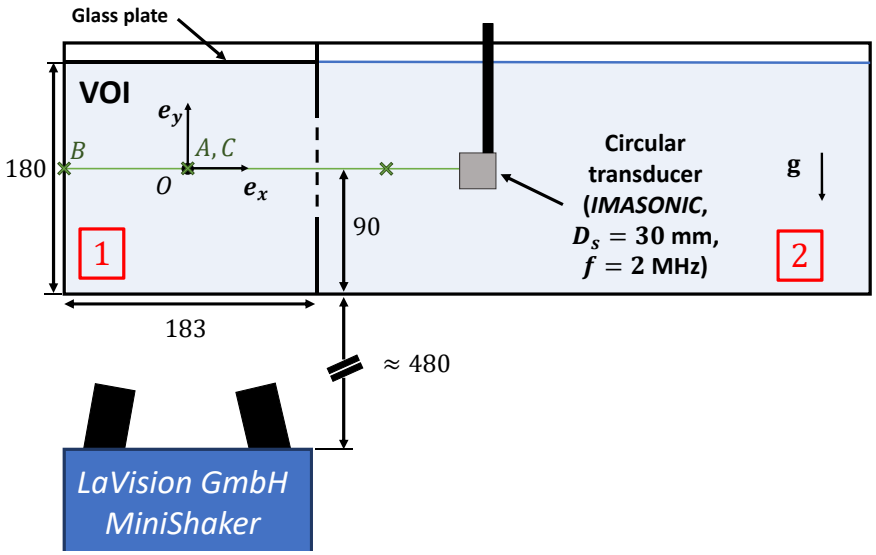
The PTV equipment, and the procedure to recover an Eulerian velocity field from PTV measurements, were first benchmarked against a known acoustic streaming flow. After introducing the benchmark case and the associated setup, I shall provide an example of how I processed the frames recorded by the cameras to obtain particle tracks. I shall then assess the ability of PTV to recover Eulerian streaming velocity fields.

5.3.3.1 Adapting the test rig for PTV measurements of a square acoustic streaming flow

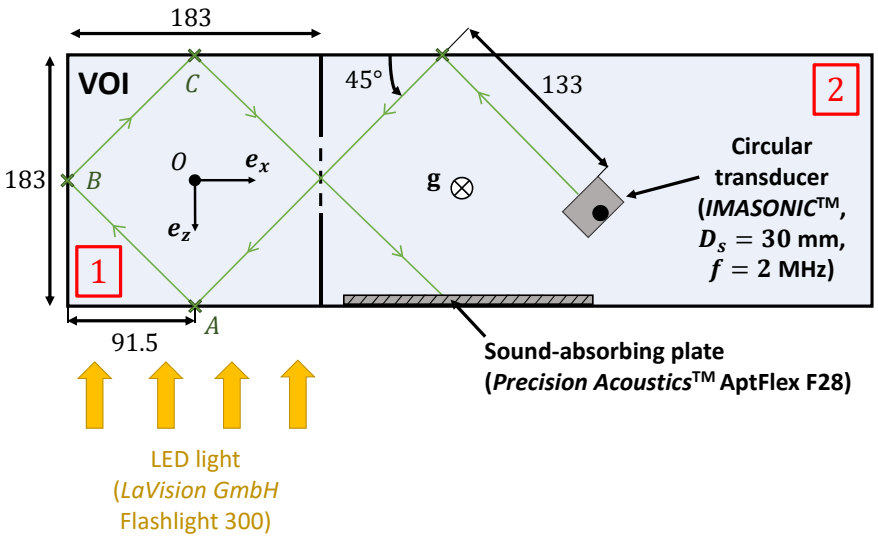
To assess the suitability of PTV for the investigation of streaming flows, I recreated the configuration investigated experimentally by Cambonie *et al.* (2017) using PIV and numerically by Launay *et al.* (2019). The configuration is shown in figure 1.2: a horizontal beam is reflected on the walls of a cubic water cavity and drives a square streaming flow made of four impinging jets. Although the beam axis remains horizontal, the jet impingements create three-dimensional structures near the walls (Launay *et al.*, 2019): these structures could not be measured by PIV; however, they shall be captured by PTV.

After having characterised the transducer, and set up the protractors and laser guiding device, I adjusted the test rig used for the hydrophone measurements to allow for the investigation of the square streaming flow. I did the PTV measurements in subvolume 1 only (figure 5.11). I placed in subvolume 2 the transducer characterised in section 5.2. I gave the transducer an initial inclination of 45° in the horizontal plane, so that the emitted sound beam underwent a first reflection before entering the VOI through a circular plastic-film-covered aperture. I positioned the transducer such that the beam enters the first reflection point in the VOI (labelled as "A" in figure 5.11) lies in the far acoustic field. This choice was also made by Cambonie *et al.* (2017) to avoid the velocity irregularities caused by the strong gradients of $\boldsymbol{I_{ac}}$ in the near acoustic field. In the VOI, the beam underwent three reflections before leaving the VOI through the circular aperture, thus yielding a horizontal square-shaped forcing field. The total distance covered by the beam in the VOI is $L_{\text{beam}} \approx 518$ mm. I finally placed in subvolume 2 a *Precision Acoustics*^{TM}

Thèse accessible à l'adresse : https://theses.insa-lyon.fr/publication/2024ISAL0101/these.pdf © [B. Vincent], [2024], INSA Lyon, tous droits réservés



(a) Side view (distances in mm)



(b) Top view (distances in mm)

Figure 5.11: Sketch of the test rig used to reproduce the square water streaming flow of Cambonie *et al.* (2017) and Launay *et al.* (2019): (a) side and (b) top views. The green line and arrows represent the axis of the beam emitted by the transducer (grey rectangle) and its direction of travel, respectively. Reflection points of the beam in the VOI are located by the green crosses and are labelled from A to C. The origin of the coordinate system is placed at the centre of the VOI.

AptFlex F28 plate to absorb the sound waves leaving the VOI.

Because of the VOI dimensions ($183 \times 183 \times 180$ mm^3), a large lighting volume was required. For this purpose, I used the *LaVision GmbH* Flashlight 300 LED panel (figure 5.9 (a)) and seeded the VOI with the 5 μm PSP particles. The *MiniShaker* cameras tracking the particles were calibrated using a single picture of the volumetric calibration

Thèse accessible à l'adresse : https://theses.insa-lyon.fr/publication/2024ISAL0101/these.pdf © [B. Vincent], [2024], INSA Lyon, tous droits réservés

Table 5.1: Summary of the hardware and recording parameters for the PTV measurements of the square acoustic streaming flow.

Light source	*LaVision GmbH* LED Flashlight 300 (blue), pulsed-overdrive mode, pulse duration: 335 μs. The LED panel is placed at approximately 5 cm from the VOI.
Focal length of the camera lenses	12 mm
Seeding particles	*Dantec Dynamics* Polyamid Seeding Particles (PSP), 5 μm in diameter, density of 1030 kg/m^3.
Frame rate	4 Hz
Exposure	335 μs
Recording duration	16.7 minutes

plate (figure 5.10 (b)) in the horizontal $y = 0$ plane. Further details on the hardware and recording parameters are listed in table 5.1.

The transducer operated at a steady power $P_{elec} = 1$ W, which is related to $P_{ac,0}$ through the transducer efficiency ε_t. The manufacturer *IMASONIC*^{TM} provided a reference table of ε_t measurements for this specific transducer, giving $\varepsilon_t = 75$ % for that P_{elec}. Therefore, $P_{ac,0} = 0.75S$ W and $Gr_{ac} \approx 1.6 \times 10^4$. At this Gr_{ac}, the flow is marginally unsteady (Cambonie *et al.*, 2017); it is thus suitable to assess the reconstruction of time-averaged Eulerian velocity fields from PTV measurements.

Finally, all the experimental flow results were obtained from tracks detected by the *Shake-The-Box* algorithm (figure 5.8) implemented in the commercial *LaVision* DaVis 10 software. I reconstructed the associated Eulerian velocity fields with the binning algorithm from the same software. I then processed the Eulerian velocity fields using self-developed *MATLAB* codes.

5.3.3.2 Processing of the recorded images and particle track detection

To ease the particle track detection by *Shake-The-Box*, I first needed to process the recorded frames. The processing of one frame is shown in figure 5.12 as illustrative example. The beam-shaped light emitted by the LED panel creates gradients of light intensity $\mathcal{I}$ near the solid walls, as well as in the VOI bulk (deep blue in figure 5.12 (a)). These lighting conditions render difficult to distinguish a seeding particle from the frame background (see the magnified plot in figure 5.12 (a)). I alleviated this problem by applying a set of operations to the recorded frames (figure 5.12 (c)):

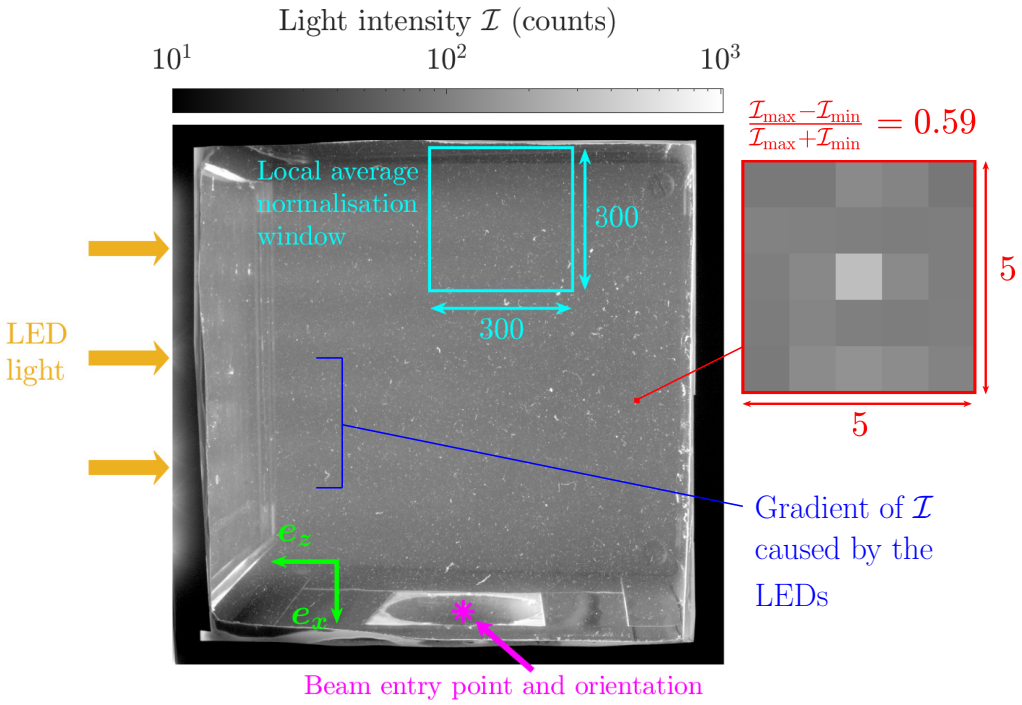
(i) I homogenised the background by subtracting from each pixel its minimum $\mathcal{I}$ measured over five consecutive frames. I then subtracted a minimum obtained in a 5 pixels $\times$ 5 pixels sliding window (red square and inset in figure 5.12).

(ii) To reduce the gradients of $\mathcal{I}$ in the VOI bulk (deep blue in figure 5.12 (a)), each frame was divided into 300 pixels $\times$ 300 pixels windows (light blue square in figure 5.12 (a)). In each window, $\mathcal{I}$ is then normalized by its mean value.

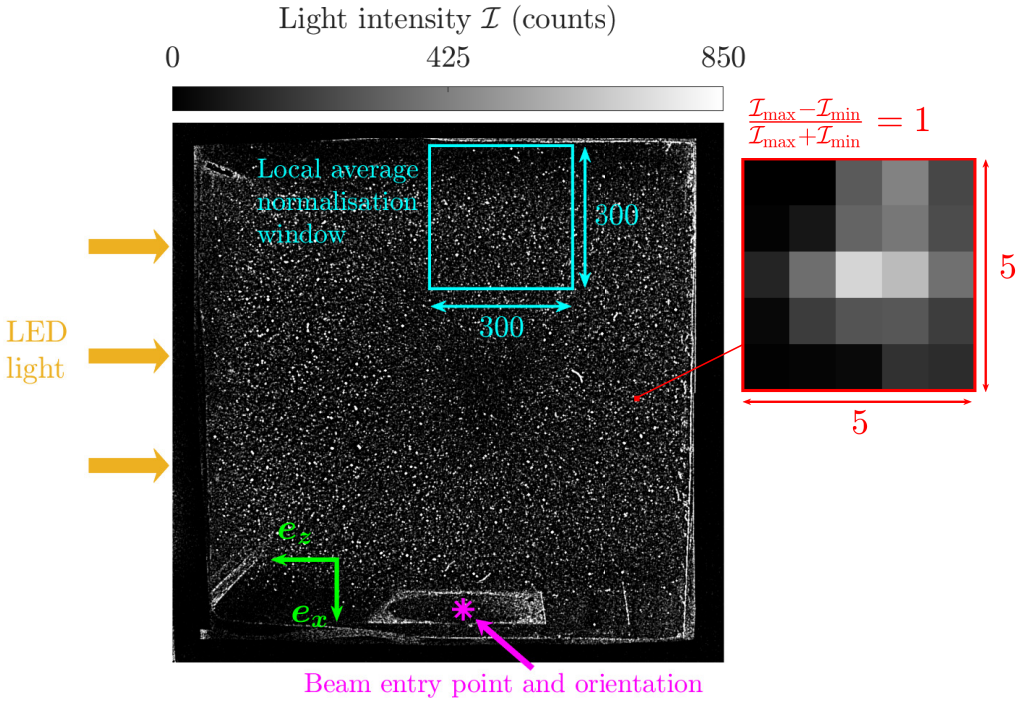
(iii) On a raw image, a seeding particle typically had a size comparable to a pixel (inset of figure 5.12 (a)). The particle is made larger on the frame by applying a 2.6 pixel sliding Gaussian filter.

(iv) Finally, I improved the contrast between the particles and the background by subtracting a constant $\mathcal{I}$ from each pixel, and to multiply the result by 100, i.e., the

Thèse accessible à l'adresse : https://theses.insa-lyon.fr/publication/2024ISAL0101/these.pdf © [B. Vincent], [2024], INSA Lyon, tous droits réservés



(a)



(b)

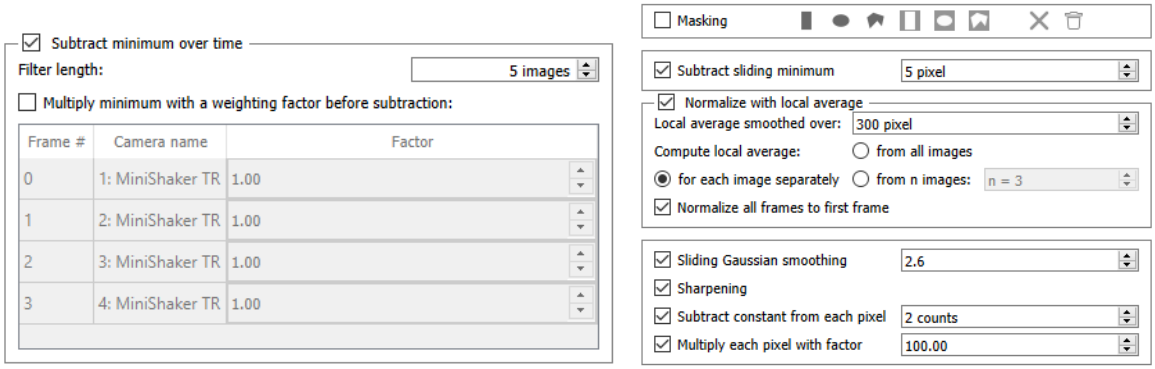
Figure 5.12: Caption on next page

maximum constant allowed by DaVis 10.

As shown in figure 5.12 (b), these operations result in a clearer separation of the seeding particles from the background: the contrast $\mathcal{I}_{max} - \mathcal{I}_{min} / (\mathcal{I}_{max} + \mathcal{I}_{min})$ in a 5×5 window is typically increased by nearly a factor 2 between the raw and processed frames.

Finding an optimum way to process the raw images is case-specific. Although the

Thèse accessible à l'adresse : https://theses.insa-lyon.fr/publication/2024ISAL0101/these.pdf © [B. Vincent], [2024], INSA Lyon, tous droits réservés



(c)

Figure 5.12: Processing of the frames recorded for the square flow. The first frame of the recording in taken as illustrative example: (a) raw frame, (b) processed frame and (c) parameters of the "Image preprocessing" module of the *LaVision* DaVis 10 software used to generate (b) from (a). The blue square in (a) represents the size of the window over which light intensity is normalised ("normalize with local average" section in (c)). The size of the sliding window (used in the "subtract sliding minimum" section in (c)) is represented by the magnified red squares in (a) and (b). All dimensions are given in pixels.

bounds of some parameters value may be inferred intuitively (e.g., to avoid blurred images, the Gaussian filter size shall not be chosen significantly larger than the particle sizes on the raw images), most of the parameter values shown in figure 5.12 (c) were obtained on a trial-and-error basis. To assess the performance of a given set of processing operations, I systematically ran *Shake-The-Box* on the obtained frames. I then retained the case that maximised the total number of tracked particles and the average track length over the recording duration. I stress that this processing stage shall not be overlooked: the number of tracked particles could differ by an order of magnitude between "badly"-processed frames and the optimum ones. For each recording I did in this thesis, I typically spent up to four working days to find the optimum set of image processing parameters.

Particle tracks could then be obtained from the processed frames (figure 5.13). These tracks are observed in a volume centred around the horizontal $y = 0$ plane. The particle tracks of high velocity $\|\dot{\boldsymbol{x}}\|$ depict the four-impinging-jet structure of the flow, including the spreading of the jets downstream their impingements. However, poor track density is observed in the flow regions of small flow velocity, namely in the central region and near the corners. Because the seeding density must be sufficiently small to avoid the masking of particles in the processed frames of the VOI (figure 5.13 (b)), finding tracks in these low-velocity regions is difficult. Besides, the short average track length (4 s, or 4.4×10^{-3} when normalised by the viscous time scale D_s^2/ν) indicates that a given particle is not tracked over the entire recording duration, but instead fractions of its trajectory are actually obtained. As I shall use PTV to reconstruct 3D Eulerian velocity fields but not to carry Lagrangian flow analyses, having short tracks is however not critical. Despite these limitations, the volumetric *Shake-The-Box* results (figure 5.13) proves the ability of the experimental setup and method to measure 3D streaming velocity data.

Thèse accessible à l'adresse : https://theses.insa-lyon.fr/publication/2024ISAL0101/these.pdf © [B. Vincent], [2024], INSA Lyon, tous droits réservés

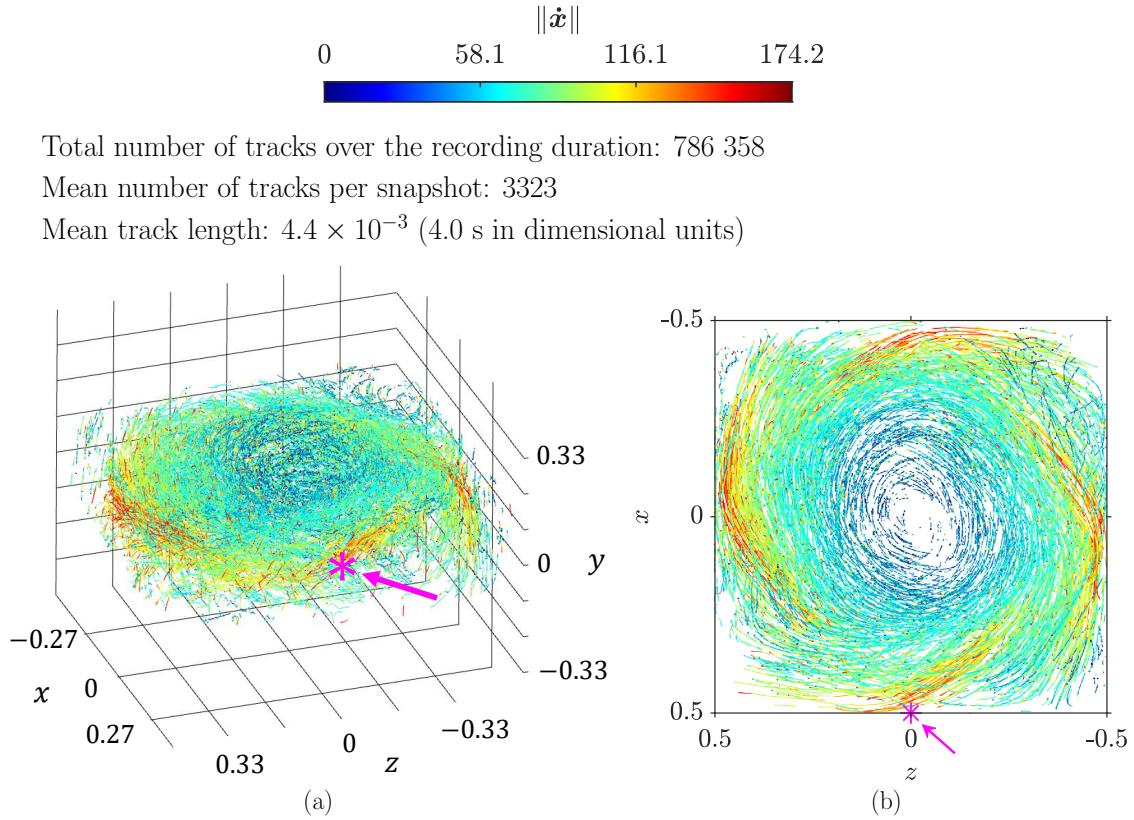


Figure 5.13: Snapshot of particles detected by *Shake-The-Box* and their associated tracks for the $Gr_{ac} \approx 1.6 \times 10^4$ ($P_{elec} = 1$ W) square flow: (a) isometric and (b) top views. For clarity, only the tracks in $-0.17 \leq y \leq 0.17$ are displayed. The tracks are coloured by the instantaneous particle velocity magnitude $\|\dot{\boldsymbol{x}}\|$ made dimensionless using $D_s = 30$ mm and $D_s^2/\nu = 916.8$ s as length and time scales, respectively. In both plots, the spatial coordinates are normalised by the cavity sizes in the corresponding direction (183 mm for x and z, and 180 mm for y). The purple star and arrow locate the entry point of the beam and indicate its orientation, respectively.

5.3.3.3 Comparison of the Eulerian velocity fields measured by PIV with those reconstructed from PTV measurements

Finally, I binned the particle tracks to recover the associated time-averaged Eulerian velocity field $\overline{\boldsymbol{u}}$ (with the $\overline{\ }$ symbol standing for "time-average"). A strong qualitative agreement is found with the PIV measurements of Cambonie *et al.* (2017): in either case, the flow features four jets approximately following the beam and impinging the lateral cavity walls (figure 5.14). Similar levels of Reynolds number Re (based on the velocity magnitude and on D_s) are obtained using either method, with a maximum Re of about 150. Unsurprisingly, PTV-based measurements feature areas of unavailable data at the VOI corners because of the lack of tracks measured there. Nevertheless, the PTV system indeed recovers a three-dimensional Eulerian velocity field (figure 5.15). This field features structures that could not be observed in the previous 2D PIV experiments, such as the vertical recirculations on either side of the jet impingements.

I shall now focus on the jets and first identify their flow regime. The idea is to rely on the simulation results obtained in chapter 3 for similar S and N/L. As we saw in chapter 3, the on-axis velocity peak position x'_p locates the transition from an accelerating

Thèse accessible à l'adresse : https://theses.insa-lyon.fr/publication/2024ISAL0101/these.pdf © [B. Vincent], [2024], INSA Lyon, tous droits réservés

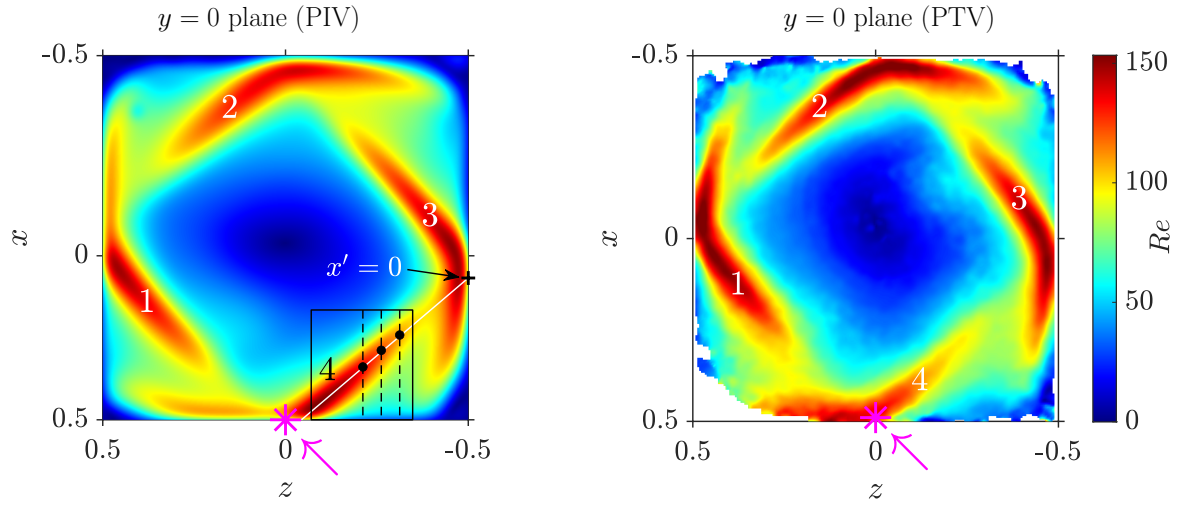


Figure 5.14: Comparison of the time-averaged square acoustic streaming flow measured for $Gr_{ac} \approx 1.6 \times 10^4$ ($P_{elec} = 1$ W), along with the jet numbering. The represented flow quantity is a Reynolds number $Re = \|\overline{\boldsymbol{u}}\| D_s/\nu$. Left: reference Eulerian velocity field obtained by PIV (grid resolution: 0.023, or 0.69 mm in dimensional units), as measured by Cambonie *et al.* (2017). The region framed in black illustrates the jet axis location procedure described in the text, and from which the jet origin $x' = 0$ (black cross) is inferred. Right: Eulerian velocity field reconstructed from PTV measurements (grid resolution: 0.031, or 0.94 mm in dimensional units). In both plots, the purple star and arrow locate the entry point of the beam in the VOI and its orientation, respectively. The same colour levels are used in both plots, and the spatial coordinates are normalised by the VOI size in the corresponding directions (183 mm).

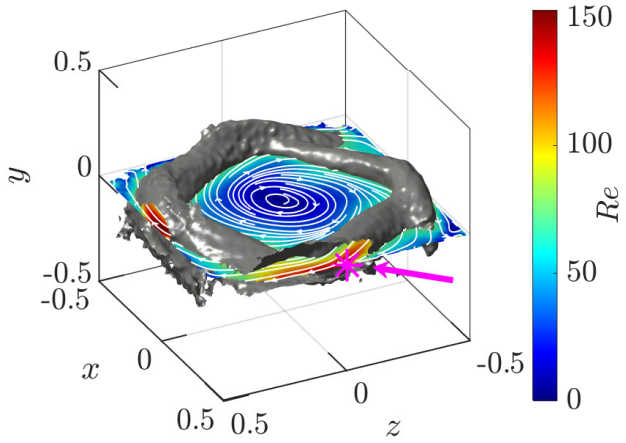


Figure 5.15: Three-dimensional structure of the Eulerian square acoustic streaming flow reconstructed from PTV measurements made for $Gr_{ac} \approx 1.6 \times 10^4$ ($P_{elec} = 1$ W). The displayed quantity is an isocontour of the Reynolds number Re based on the velocity magnitude and on D_s; it is here plotted for $Re = 73.3$ (2.4 mm/s in dimensional units). The velocity field in the mid-height $y = 0$ plane is also shown. The purple star and arrow locate the entry point of the beam in the VOI and its orientation, respectively. The spatial coordinates are normalised by the VOI size in the corresponding directions (183 mm in the horizontal directions, and 160 mm in the vertical one).

Thèse accessible à l'adresse : https://theses.insa-lyon.fr/publication/2024ISAL0101/these.pdf © [B. Vincent], [2024], INSA Lyon, tous droits réservés

jet regime to a decelerating regime in which the acoustic forcing is balanced by the viscous forces. For $Gr_{ac} \sim 10^4$, the on-axis velocity peak occurred at a distance $x'_p \sim 20$ from the jet origin (figure 3.13). However, that x'_p greatly exceeds the distance between two consecutive beam reflections (which is approximately 4.3), hence exceeds the maximum jet length that can be observed. Therefore, each jet of the square streaming flow is expected to be in the accelerating regime.

As shown in chapter 3, the scaling law (3.16) accurately describes the velocity-build along the axis of a single jet; I shall now check whether that corrected law is also verified by the square flow jets. Due to attenuation along the beam, each jet experiences a slightly different forcing magnitude. To account for this effect, the jet scaling law (3.16) is modified to become:

$$Re_{\text{jet}} = -4x + \frac{\sqrt{2}}{2}\sqrt{32x^2 + Gr'_{ac}x}\,, \tag{5.3}$$

where $Re_{\text{jet}} = \|\overline{\boldsymbol{u}}\|D_s/\nu$ and

$$Gr'_{ac} = Gr_{ac}e^{-2N\frac{x'_s}{L_{ac}}} \tag{5.4}$$

is an attenuated Gr_{ac} in which x'_s is the total distance to the transducer normalised by D_s, and $L_{ac} = L_{\text{beam}}/D_s$. The decay rate of Gr'_{ac} is given by $2N = 2\alpha L_{\text{beam}} \approx 0.109$, meaning that $\left(1 - e^{-2N}\right) \approx 10$ % of Gr_{ac} is attenuated between the beam entry and exit points of the VOI.

To compare the jet velocity profiles to equation (5.3), it is first necessary to locate the axis of each jet. The determination of the axis of jet 4 is illustrated in the left plot of figure 5.14. First, a rectangular fluid region encompassing the jet (black rectangle) is defined. It is then sliced by either lines (black dashed lines) or planes, depending on whether the velocity field is 2D (PIV data) or 3D (PTV-based data), respectively. In each slice, the point of maximum velocity is sought (represented as a black dot), and the line fitted to all the successive velocity maxima is finally considered to be the jet axis (white line). In this procedure, the points near the jet impingement are deliberately discarded, as the impingement causes the jet to deviate from its axis there. The jet origin, defined by $x' = 0$ (black cross in the left plot of figure 5.14), is then taken as the intersection between the determined jet axis and the upstream wall.

On each jet axis, the longitudinal profiles of Re obtained from PTV measurements display a similar evolution with x' to those of Cambonie *et al.* (2017) (figure 5.16). The region close to each jet origin ($x' \leq 1$) displays large Re due to the impingement of the upstream jet. As x' increases, the influence of that upstream impingement drops, causing Re to decrease. For $1.5 \leq x' \leq 3.5$, the evolution of Re is extremely well described by the scaling law (5.3): the deviation between the experimental and predicted profiles remains below 15 %. This excellent agreement thus not only confirms that the forcing is indeed mostly balanced by inertia forces in the jets, but also provides an experimental evidence of the accuracy of equation (5.3).

Finally, comparing the PIV and PTV-based jet velocity profiles over a common range of x'-coordinates yields a mean discrepancy of 11.2 %, with a minimum of 4.7 % for jet 3 and a maximum of 17.5 % for jet 2. Given that these two experimental methods were not operated simultaneously, this discrepancy is acceptable. This preliminary study thus confirms the ability of PTV to reconstruct accurate 3D-3C Eulerian streaming velocity fields in a configuration that is close to the helical one (figure 5.1).

Thèse accessible à l'adresse : https://theses.insa-lyon.fr/publication/2024ISAL0101/these.pdf © [B. Vincent], [2024], INSA Lyon, tous droits réservés

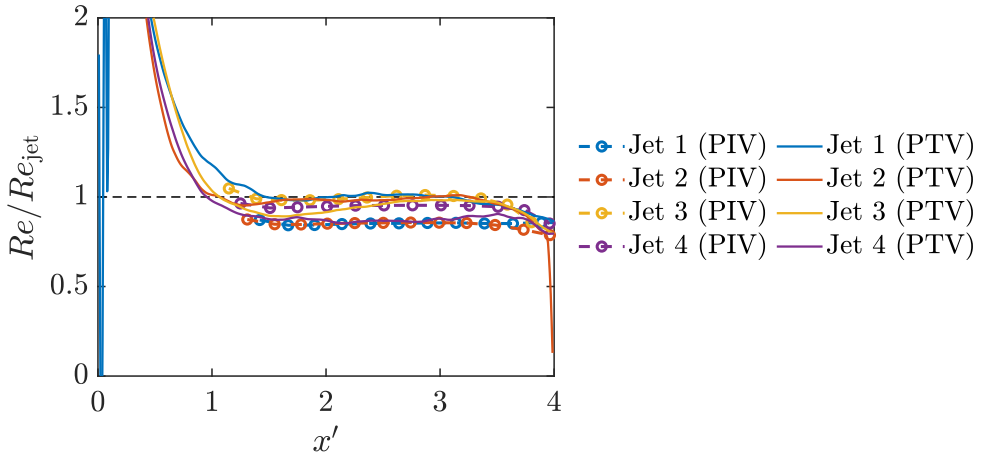


Figure 5.16: Longitudinal profiles of the Reynolds number $Re = \|\overline{\boldsymbol{u}}\|D_s/\nu$ along the axis of each jet, for $Gr_{ac} \approx 1.6 \times 10^4$ ($P_{elec} = 1$ W). The PIV profiles of Cambonie *et al.* (2017) and those obtained from the binning of PTV measurements are displayed. These profiles are normalised by the straight jet scaling law (5.3) originally derived in chapter 3. A perfectly-matching scaling law would collapse the experimental profiles on the black dashed line. Here, x' is made dimensionless by D_s.

5.4 Experimental setup for the helical streaming flow measurements, control parameter and convergence of the time-averaged flows

After detailing the test rig for the helical flow measurements, I shall quantify the uncertainty on the Gr_{ac} values for which the experiments were made. Finally, I shall assess whether the recording durations are large enough to for the time-averaged Eulerian velocity fields to be converged.

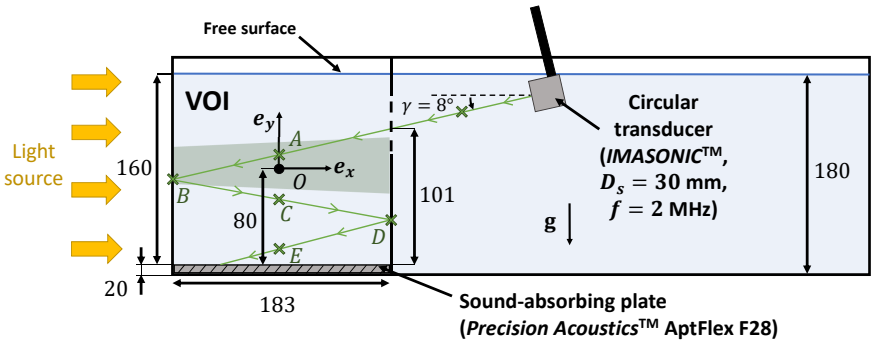
5.4.1 Modifications applied to the test right for helical flow measurements and recording parameters

The test rig mainly differed from the one used for the square flow measurements on three aspects: (i) the upper glass plate bounding the VOI was removed, (ii) the *LaVision GmbH MiniShaker* cameras were moved to the side of the VOI and, most importantly, (iii) a vertical inclination of $\gamma = 8°$ was given to the transducer.

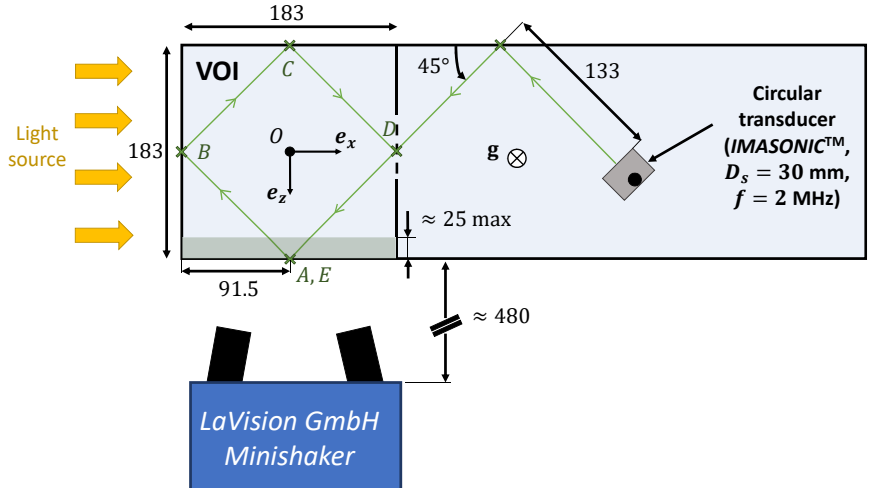
The prescribed transducer orientation forced the sound beam emitted by the transducer to undergo five reflections on the vertical walls of the VOI whilst following a descending path. This setting created a helix-shaped acoustic field and axis (the acoustic axis is represented as green lines in figure 5.17) featuring one reflection on each vertical wall, except on the $z = 91.5$ mm wall were two reflections occurred at points A and E. Finally, I prevented sound reflections at the bottom of the VOI by placing a sound-absorbing plate there. The length of the forcing field in the VOI thus matched the helix length $L_{\text{helix}} \approx 725$ mm. As a result, $2N \approx 0.15$, so that $\left(1 - e^{-2N}\right) \approx 14$ % of $P_{ac,0}$ is attenuated along the beam. For this forcing structure, I carried out two PTV measurement campaigns, each made for $P_{elec} = 1$, 2, 4, 6, and 8 W.

In the first measurement campaign, I measured $\overline{\boldsymbol{u}}$ in the entire VOI. As for the square flow, I used the LED panel (figure 5.9 (a)) to light this large fluid volume

Thèse accessible à l'adresse : https://theses.insa-lyon.fr/publication/2024ISAL0101/these.pdf © [B. Vincent], [2024], INSA Lyon, tous droits réservés



(a) Side view (distances in mm)



(b) Top view (distances in mm)

Figure 5.17: Sketch of test rig used to generate and investigate three-dimensional acoustic streaming flows. The green line and arrows represent the axis of the acoustic beam radiated by the transducer (grey rectangle with its mounting arm in black) and its direction of travel. Reflection points of the beam on the vertical walls of the VOI (Volume Of Investigation) are identified by green crosses and labelled from A to E. The origin of the coordinate system is located at the centre of the VOI. The green-shaded area represents the expanded laser beam defining the measurement domain for the time-resolved measurements (section 5.7). The figure is taken from Vincent *et al.* (2024).

($183 \times 183 \times 160$ mm^3), which was seeded with the *Dantec Dynamics*™ 5 μm PSP particles. However, this setting created important light reflections at the VOI corners, leading to poor measurements there. For this reason, $\overline{\boldsymbol{u}}$ were reconstructed in a domain slightly cropped in both horizontal directions, with x and z ranging from -89.5 to 89.5 mm. In this setting, the cameras were calibrated using pictures of the volumetric calibration plate (figure 5.10 (b)) taken at $x = y = 0$ for 10 different z-positions, each separated by 1 cm. Further details on the recording parameters are listed in table 5.2.

In the second measurement campaign, I investigated the development of unsteadiness as P_{elec} is increased. I focused on a volume encompassing the first jet impingement (green-shaded region in figure 5.17). As the size of this volume was significantly smaller than in the first measurement campaign ($\approx 170 \times 25 \times 75$ mm^3), I could use the volume-expanded

Thèse accessible à l'adresse : https://theses.insa-lyon.fr/publication/2024ISAL0101/these.pdf © [B. Vincent], [2024], INSA Lyon, tous droits réservés

Table 5.2: Hardware and recording parameters used for PTV flow measurements in the entire fluid domain (first setup, left column) and near the first jet impingement (second setup, right column). The indicated power values are those of P_{elec}.

	Measurements in the entire cavity	Near-impingement flow measurements
Size of the measurement domain	$179 \times 179 \times 160$ mm^3 (length × width × height) cuboid.	Elliptic cross section, approximately $170 \times 25 \times 75$ mm^3 (length × width × height).
Light source	Same as for the square flow (table 5.1)	Double cavity Nd:Yag pulsed laser (wavelength: 532 nm). The light beam is expanded using the Compact Volume Optics device by *LaVision GmbH* fitted with a cylindrical lens (focal length of -150 mm) and placed at 32 cm from the VOI.
Focal length of the camera lenses	Same as for the square flow (table 5.1)	25 mm
Optical filters	None	High-pass Kodak Wratten 22 (cutoff wavelength: ≈ 550 nm)
Seeding particles	Same as for the square flow (table 5.1)	*microParticles GmbH* fluorescent polystyrene particles (PS-FluoRed-5.0), 5 μm in diameter, density of 1050 kg/m^3.
Frame rate	4 Hz (1 W), 8 Hz (2 and 4 W) and 16 Hz (6 and 8 W)	1.875 Hz (1 W), 2.5 Hz (2 W) and 5 Hz (4, 6 and 8 W).
Exposure	Same as for the square flow (table 5.1)	105 μs
Recording duration	12.5 minutes (1 W), 20.8 minutes (2, 4, 6 and 8 W).	20.0 minutes (all powers).

laser (figure 5.9 (b)) to light the 5 μm fluorescent particles. I isolated the light emitted by these particles using high-pass filters with a cut-off wavelength of ≈ 550 nm. Due to the small volume depth of these near-wall measurements (25 mm), I calibrated the cameras only a single picture of the calibration plate placed at 1 cm from the cavity wall. More details on the recording parameters for this measurement campaign are given in table 5.2.

All the recordings required to be processed individually. All the image processing, *Shake-The-Box* and track filtering parameters are given in appendix E. These tracks were then binned on homogeneous Cartesian grids of resolutions $\Delta x = 2.2$ mm and 1.4 mm for the time-averaged and near-wall time-resolved measurements, respectively.

Finally, one shall not overlook the amount of storage space when doing such measurements. For these two measurements campaigns, recording the movies, processing their frames, tracking the particles and reconstructing the Eulerian velocity fields) yielded 14 TB of data.

Thèse accessible à l'adresse : https://theses.insa-lyon.fr/publication/2024ISAL0101/these.pdf © [B. Vincent], [2024], INSA Lyon, tous droits réservés

5.4.2 Effects of the operating temperature on the control parameter magnitude

In these experiments, only P_{elec} was changed; all other parameters (e.g. the helix pitch) remained constant. Therefore, the sole dimensionless control parameter is Gr_{ac} (equation (1.60)). In water, the dynamic and bulk viscosities μ and η are related to each other though $\eta \approx 3\nu$ (Kinsler *et al.*, 2000; Moudjed *et al.*, 2014*a*), so that the sound attenuation coefficient (1.16) reads

$$\alpha \approx \frac{26\pi^2 f^2 \nu}{3c^3}\,,$$

hence:

$$Gr_{ac} = \frac{832\pi\varepsilon_t P_{elec} D_s f^2}{3\rho_0 c^4 \nu}\,. \tag{5.5}$$

The acoustic Grashof number thus involves three material properties (ρ_0, c, and ν) that may vary because of temperature departures. In other words, different operating conditions between two experiments may yield different Gr_{ac} values, despite P_{elec} being the same. From equation (5.5), the absolute uncertainty ΔGr_{ac} is:

$$\Delta Gr_{ac} = Gr_{ac}\left(\frac{1}{\rho_0}\left|\frac{\mathrm{d}\rho_0}{\mathrm{d}T}\right| + \frac{1}{\nu}\left|\frac{\mathrm{d}\nu}{\mathrm{d}T}\right| + \frac{4}{c}\left|\frac{\mathrm{d}c}{\mathrm{d}T}\right|\right)\Delta T\,, \tag{5.6}$$

where ΔT is a temperature difference. By looking at the magnitudes of the derivatives in equation (5.6), one is able to determine which material property variation has the largest effect on ΔGr_{ac}. Cubic interpolation of the reference tables of Dinçer & Zamfirescu (2015) gives, for $T = 21$ °C:

$$\frac{1}{\rho_0}\left|\frac{\mathrm{d}\rho_0}{\mathrm{d}T}\right| \approx 2.16\times10^{-4}\,\mathrm{K}^{-1},\quad \frac{1}{\nu}\left|\frac{\mathrm{d}\nu}{\mathrm{d}T}\right| \approx 2.44\times10^{-2}\,\mathrm{K}^{-1},\quad \frac{1}{c}\left|\frac{\mathrm{d}c}{\mathrm{d}T}\right| \approx 2.03\times10^{-3}\,\mathrm{K}^{-1}\,.$$

Therefore, the temperature-caused variations of ν are the largest contribution to ΔGr_{ac}.

For each measurement campaign, I measured the water temperature before and after each recording to obtain a confidence interval on Gr_{ac} (table 5.3). The maximum temperature difference between the start and the end of a recording was 0.5 °C which, added to the temperature reading uncertainty due to the thermometer resolution, yields a maximum uncertainty of 3.3 % on Gr_{ac} for the measurements made near the first jet impingement for $P_{elec} = 4$ W. The sensitivity of Gr_{ac} to temperature was further observed by comparing values obtained at the same electrical power but at different temperatures, for the overall time-averaged flow and near-impingement measurements. For instance, a 6°C variation of T yields a discrepancy of 10 % for $P_{elec} = 4$ W (table 5.3).

From now, all the results to be presented and discussed are made dimensionless using D_s, D_s^2/ν and $\rho_0 D_s^3$ as length, time and mass scales, respectively. I shall also normalise the spatial coordinates by the VOI size in the corresponding direction (183 mm in the x and z directions, and 160 mm in the y direction).

5.4.3 Convergence of the time-averaged flows

Before analysing the time-averaged flow structures and properties, it is first necessary to determine whether the averages are converged. I assessed the convergence by monitoring the variations of $Re = \|\overline{\boldsymbol{u}}\|D_s/\nu$ as the fraction of the total recording duration used

Thèse accessible à l'adresse : https://theses.insa-lyon.fr/publication/2024ISAL0101/these.pdf © [B. Vincent], [2024], INSA Lyon, tous droits réservés

Table 5.3: Conversion table between the electrical power P_{elec} and acoustic Grashof number Gr_{ac}. The transducer efficiency ε_t is obtained through linear interpolation of tabulated data provided by the transducer manufacturer *IMASONIC* (IMASONIC SAS, 2011). Temperatures are given at the start and the end of each recording. Values of Gr_{ac} are bounded using Eq. (5.6), where ΔT is estimated as the sum of twice the thermometer resolution (0.25 °C) and the temperature difference between the beginning and the end of each recording. The derivatives in Eq. (5.6) have been estimated by fitting cubic curves to the reference tables of Dinçer & Zamfirescu (2015).

		Overall mean flow measurements		Near-impingement measurements	
P_{elec} (W)	ε (%)	Temp. (°C)	Gr_{ac}	Temp. (°C)	Gr_{ac}
1	75.0	$[26.0, 26.0]$	$(1.78 \pm 0.03) \times 10^4$	$[21.5, 21.5]$	$(1.65 \pm 0.03) \times 10^4$
2	76.6	$[26.0, 26.0]$	$(3.64 \pm 0.05) \times 10^4$	$[21.0, 21.5]$	$(3.37 \pm 0.11) \times 10^4$
4	78.7	$[26.0, 26.5]$	$(7.50 \pm 0.22) \times 10^4$	$[20.0, 20.5]$	$(6.82 \pm 0.23) \times 10^4$
6	78.6	$[26.5, 26.5]$	$(11.28 \pm 0.17) \times 10^4$	$[20.5, 21.0]$	$(10.29 \pm 0.34) \times 10^4$
8	78.8	$[26.5, 27.0]$	$(15.12 \pm 0.44) \times 10^4$	$[21.0, 21.0]$	$(13.80 \pm 0.23) \times 10^4$

for time-averaging is increased (left panel of figure 5.18). To avoid any bias, this analysis is carried out at different places in the VOI: these points are chosen either close to ($z > 0$) or away from the cameras ($z < 0$), as well as near the LED panel ($x < 0$) or away from it ($x > 0$).

For all Gr_{ac}, using 75 % of the recording duration to time-average the flow (instead of 100 %) leads to discrepancies on Re that are bounded by 2 %, wherever Re is evaluated (left panel of figure 5.18). Since it is a quadratic quantity, the Reynolds number Re_{RMS} based on the root-mean square of $\overline{\boldsymbol{u}}$ converges at a slower rate than Re, as expected (right panel of figure 5.18). Using 75 % of the total recording duration instead of 100 % yields a mean variation of 2 % on Re_{RMS}, with a minimum and maximum of 0.2 % and 6.6 %. Nevertheless, the small discrepancies on both Re and Re_{RMS} confirm that converged time-averaged flows are obtained with the recording durations listed in table 5.2.

5.5 Structure of the time-averaged helical flow

The time-averaged helical flow is highly three-dimensional and displays consistent features. They thus correspond to robust elements illustrating the basic properties of a flow driven by a sound beam undergoing multiple reflections in a cavity. I shall first analyse the jet structures resulting from the acoustic forcing, and compare the jet velocities to relevant scaling laws. Then, the helicity created from the impingements of the jets on the cavity walls is investigated.

5.5.1 Impinging jets driven by the sound beam

The time-averaged flow features multiple descending jets, each following the beam axis and impinging a vertical cavity wall (figures 5.19 and 5.20 (a)). Similarly to the configuration of Moudjed *et al.* (2016) featuring a single jet impingement, or to the benchmark "square flow" configuration, each jet spreads downstream its corresponding impingement, as well as in both vertical directions. For increasing Gr_{ac}, the jets appearing in the isocontours of velocity magnitude in figure 5.19 become straighter and are more sharply defined.

Thèse accessible à l'adresse : https://theses.insa-lyon.fr/publication/2024ISAL0101/these.pdf © [B. Vincent], [2024], INSA Lyon, tous droits réservés

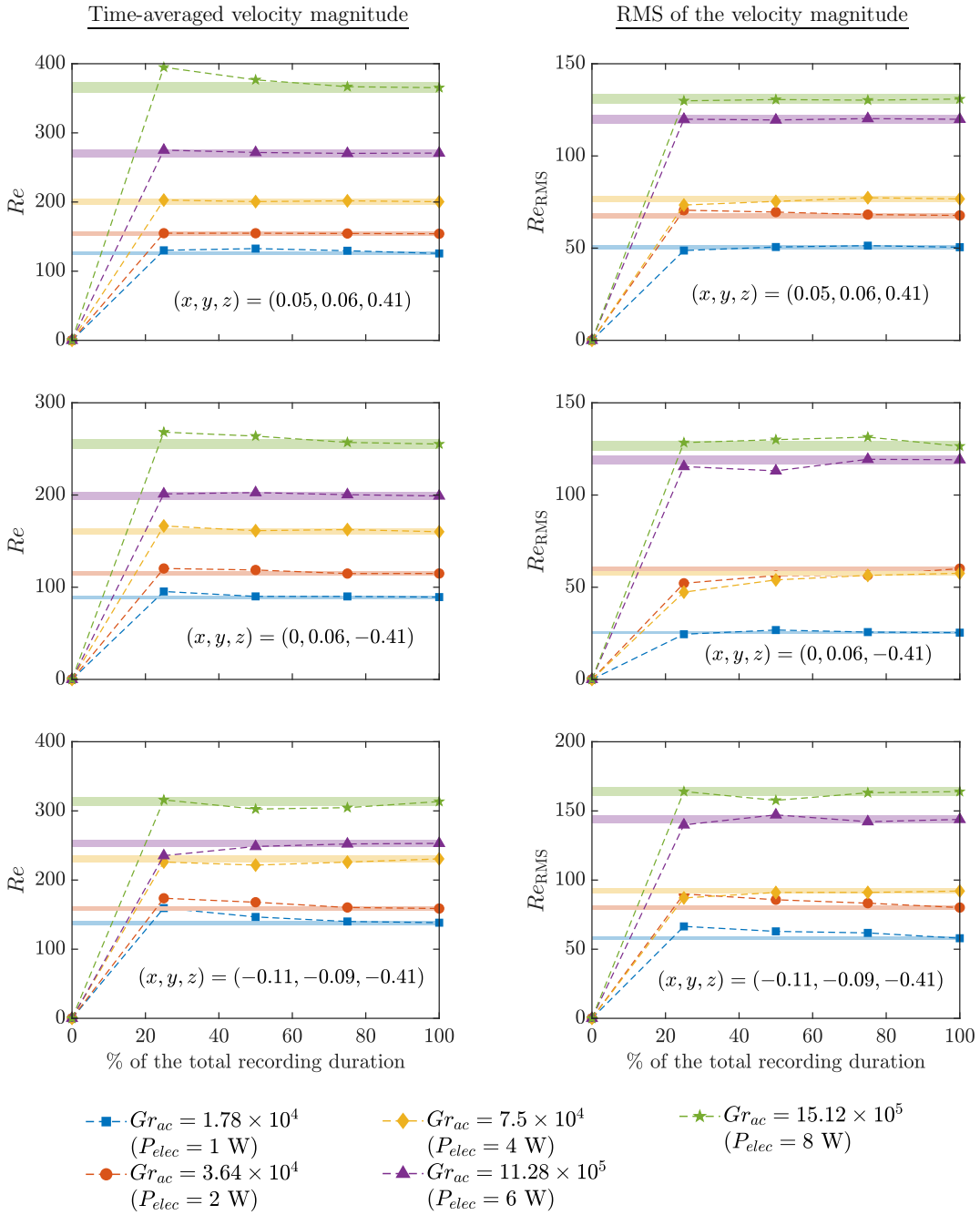
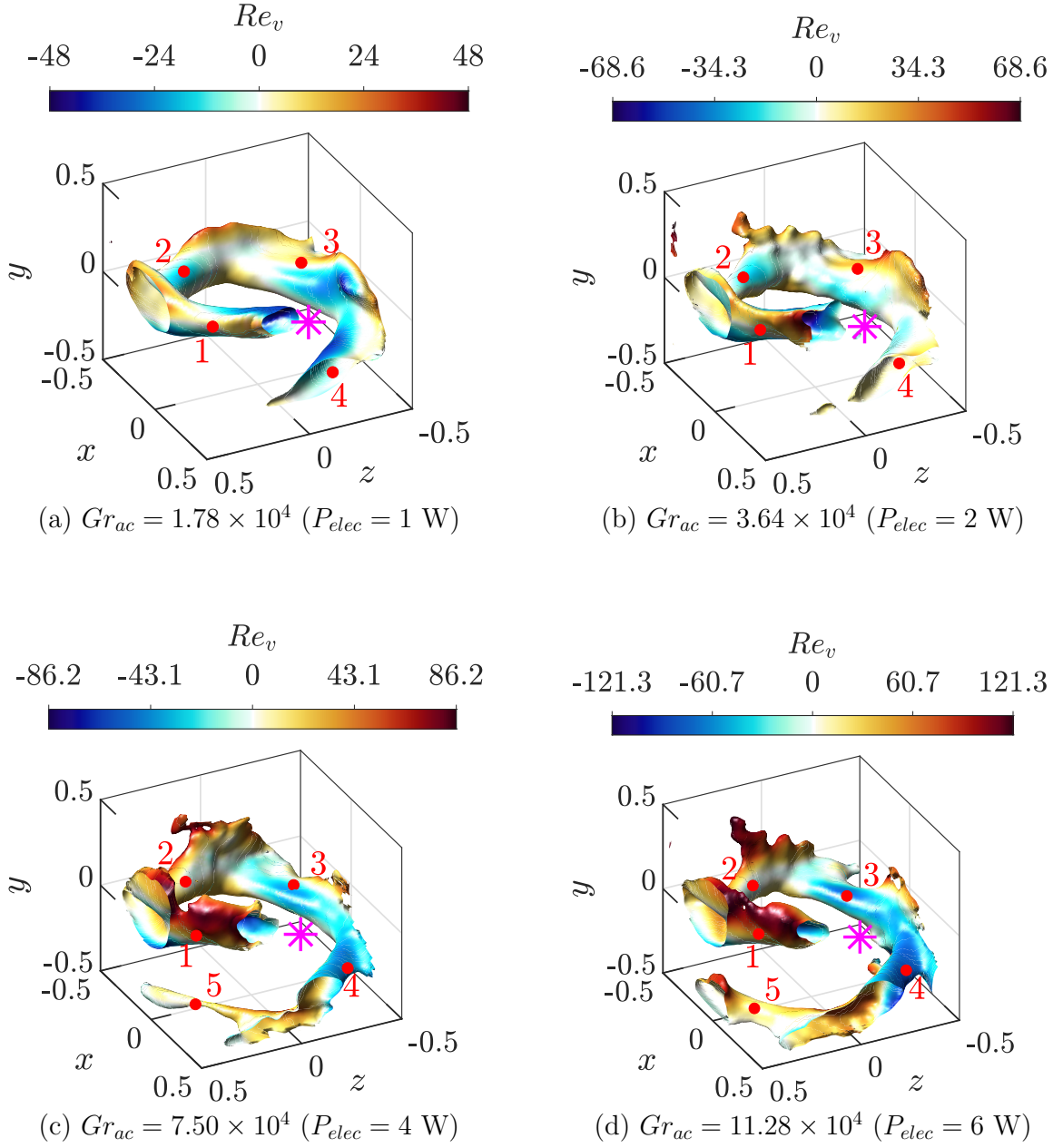


Figure 5.18: Effect of the number of frames used to evaluate local time-averaged velocity magnitudes $Re = \|\overline{\boldsymbol{u}}\| D_s/\nu$ (left panel) and their associated root mean square Re_{RMS} (right panel) for all forcing magnitudes Gr_{ac}. The coloured horizontal bands are defined for each Gr_{ac} and correspond to a ± 2 % confidence interval around the estimate obtained using the entire (100 %) recording duration. The x, y and z coordinates where the velocities are measured are reported directly in the plots, and are normalised by the cavity sizes in the corresponding directions (183 mm for x and z, and 160 mm for y).

This is again consistent with the measurements of Cambonie *et al.* (2017) in the "square flow" configuration.

Four jets are consistently observed for all the considered forcing magnitudes; however, a fifth jet of velocity magnitude comparable to the four other jets is reported in the time-averaged flow measured for $Gr_{ac} \geq 7.50 \times 10^4$. As the shape of the acoustic forcing field

Thèse accessible à l'adresse : https://theses.insa-lyon.fr/publication/2024ISAL0101/these.pdf © [B. Vincent], [2024], INSA Lyon, tous droits réservés



(a) $Gr_{ac} = 1.78 \times 10^4$ ($P_{elec} = 1$ W) (b) $Gr_{ac} = 3.64 \times 10^4$ ($P_{elec} = 2$ W)

(c) $Gr_{ac} = 7.50 \times 10^4$ ($P_{elec} = 4$ W) (d) $Gr_{ac} = 11.28 \times 10^4$ ($P_{elec} = 6$ W)

Figure 5.19: Isocontours of the Reynolds number $Re = \|\overline{\boldsymbol{u}}\| D_s/\nu$ coloured by $Re_v = \overline{u_y} D_s/\nu$, with $\overline{u_y}$ the time-averaged vertical velocity. Different Gr_{ac} are displayed, together with the corresponding jet numbering. The isocontours are plotted for (a) $Re = 87.11$ ($\|\boldsymbol{u}\| = 2.5$ mm/s), (b) 111.51 (3.2 mm/s), (c) 163.77 (4.7 mm/s) and (d) 216.04 (6.2 mm/s). The entry point of the sound beam in the VOI is located by the purple star at $(x, y, z) = (0.5, 0.13, 0)$. The spatial coordinates are normalised by the size of the VOI in the corresponding direction (183 mm in the x and z directions, and 160 mm in the y direction).

remains the same throughout this study (only its magnitude is changed), this indicates a non-negligible influence of the overall rotating fluid motion on the jet structures driven by the acoustic forcing.

The velocity levels of the jets obviously depends on Gr_{ac}. Increasing Gr_{ac} results

Thèse accessible à l'adresse : https://theses.insa-lyon.fr/publication/2024ISAL0101/these.pdf © [B. Vincent], [2024], INSA Lyon, tous droits réservés

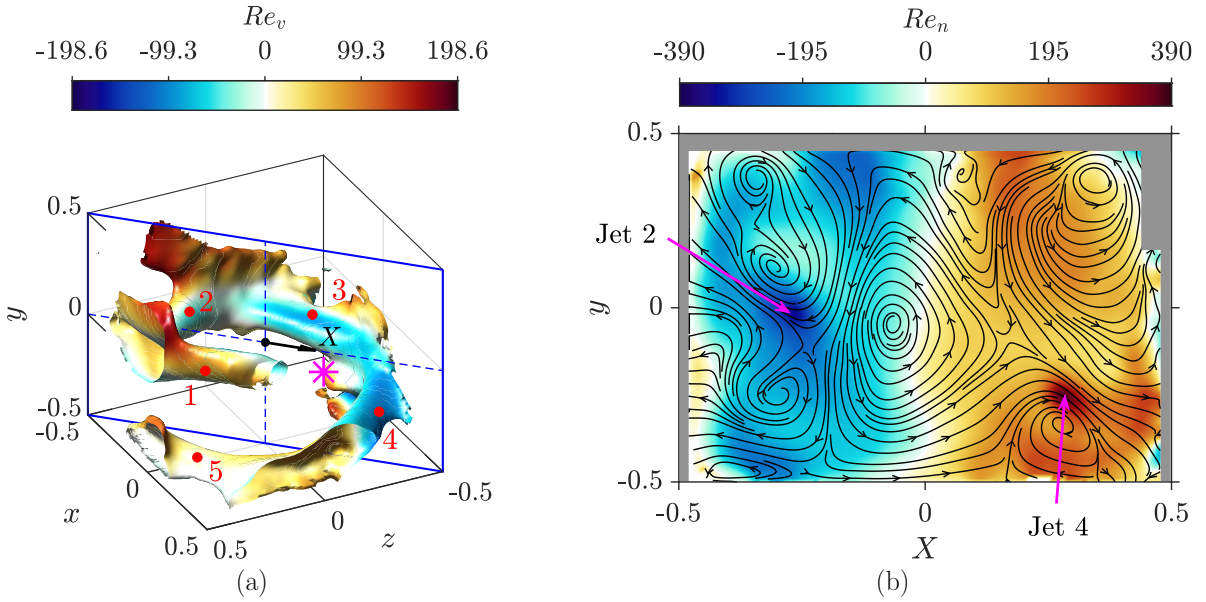


Figure 5.20: Time-averaged flow structure for $Gr_{ac} = 15.12 \times 10^4$ ($P_{elec} = 8$ W). (a) Isocontour of the velocity magnitude ($Re = \|\overline{\boldsymbol{u}}\| D_s/\nu = 268.3$, with $\|\overline{\boldsymbol{u}}\| = 7.7$ mm/s), coloured by the Reynolds number Re_v based on the vertical velocity component. The entry point of the beam is located by the purple star at $(x, y, z) = (0.5, 0.13, 0)$. (b) (b) Velocity slice in the plane represented by the blue frame in (a): the map of the Reynolds number Re_n based on the normal velocity component illustrates the large-scale swirling motion sustained by the jets. The in-plane horizontal coordinate is defined as X. In both plots, the axes are normalised by the cavity dimensions in the corresponding directions.

in higher jet velocities and enhanced inertia, resulting in larger spreadings of the jets at their impingements. These structures are particularly visible for $Gr_{ac} \geq 7.50 \times 10^4$ (figure 5.19 (c) and (d) and figure 5.20 (a)).

As for the "square" streaming flow, profiles of the time-averaged velocity magnitude are extracted on the axis of each jet using the procedure described in section 5.3.3. The axes of all jets but jets 2 and 5 could be successfully located. Besides of being visible only for $Gr_{ac} \geq 7.50 \times 10^4$, jet 5 is also very close to the bottom wall of the cavity, which affects the velocity profile along the axis of that jet. For these reasons, jet 5 is taken out of the analysis. Jet 2 is also deliberately discarded because its axis displays a too strong bending caused by the ascending flow between the jet and the corner of the VOI (figure 5.20 (b)).

Figure 5.21 shows Re profiles along the axes of jets 1, 3 and 4 for all the investigated Gr_{ac}. These profiles are normalised by the predicted jet Reynolds number Re_{jet} obtained from the scaling law (5.3). For $x' < 1$, jet 1 behaves differently from the other jets, in the sense that the Re or jet 1 features a steep increase close to its origin. This feature has already been observed by Moudjed *et al.* (2015) for short streaming jets: it is due to the jet build-up at the entrance point of the sound beam in the VOI. On the contrary, all the other jet origins lie in the impingement zone of an upstream jet, and thus feature larger Re/Re_{jet}, as in the "square flow" (figure 5.14).

For $1.5 \leq x' \leq 3.5$, $Re/Re_{\text{jet}} \sim 1$, with a maximum discrepancy of 30 % between the experimental profiles and Re_{jet} for jet 3. Two key learnings can be inferred from this excellent agreement: first, the scaling law (5.3) correctly predicts the velocity levels of the jets, despite the undeniable three-dimensionality of the helical flow. This means

Thèse accessible à l'adresse : https://theses.insa-lyon.fr/publication/2024ISAL0101/these.pdf © [B. Vincent], [2024], INSA Lyon, tous droits réservés

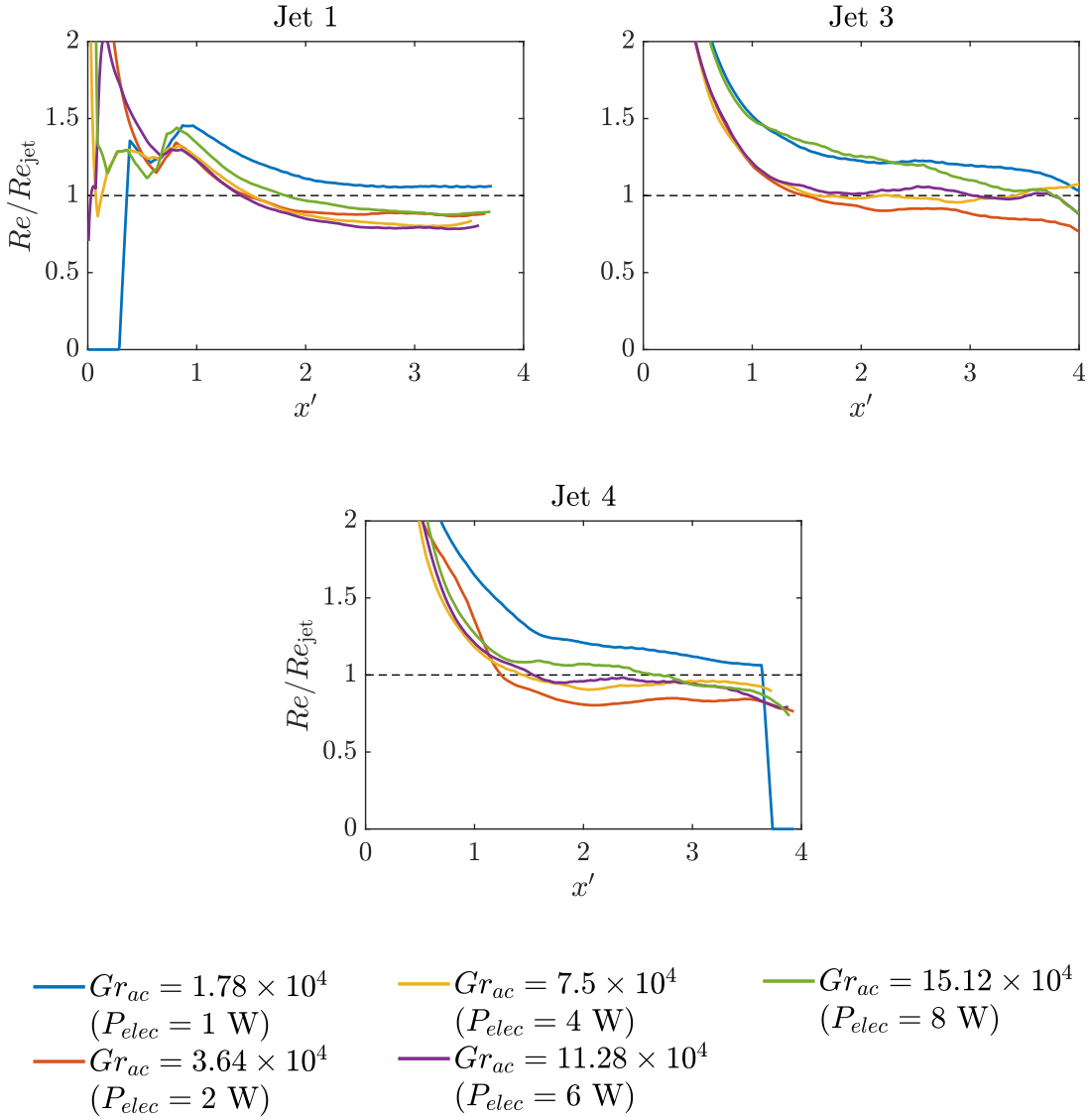


Figure 5.21: Longitudinal profiles of $Re = \|\overline{\boldsymbol{u}}\| D_s/\nu$ along the axis of jets 1, 3 and 4, for all the forcing magnitudes Gr_{ac}. The profiles are normalised by the jet scaling law (5.3) originally derived in chapter 3. If perfect, the normalised profiles would collapse on the horizontal black dashed line. The distance x' from the estimated jet origin is normalised by D_s.

that equation (5.3) can indeed be used for the preliminary design of a helical streaming flow. Second, all jets have similar Re at a given Gr_{ac}. Typical dimensional jet velocity magnitudes are 4, 6 and 8 mm/s for $P_{elec} = 1$, 4 and 8 W (corresponding to $Re = 119$, 239 and 358 for $Gr_{ac} = 1.78 \times 10^4$, 7.50×10^4 and 15.12×10^4, respectively).

To conclude, despite the flow being highly three-dimensional, the observed jets obey to the same scaling law as a single free acoustic streaming jet driven by a straight sound beam (chapter 3). Therefore, the helical flow may be constructed on a jet-by-jet basis. In particular, the different scaling laws obtained in chapter 3 for a single streaming jet may thus be used as design tools. For instance, one could use the scaling law for the on-axis jet velocity peak position x_p (chapter 3) to set the helix pitch so that a jet impingement coincides with x_p. This would maximise the velocities of the jets at their impingement (by a factor 2.5 in the present case, see figure 5.22), hence the overall velocity levels of

Thèse accessible à l'adresse : https://theses.insa-lyon.fr/publication/2024ISAL0101/these.pdf © [B. Vincent], [2024], INSA Lyon, tous droits réservés

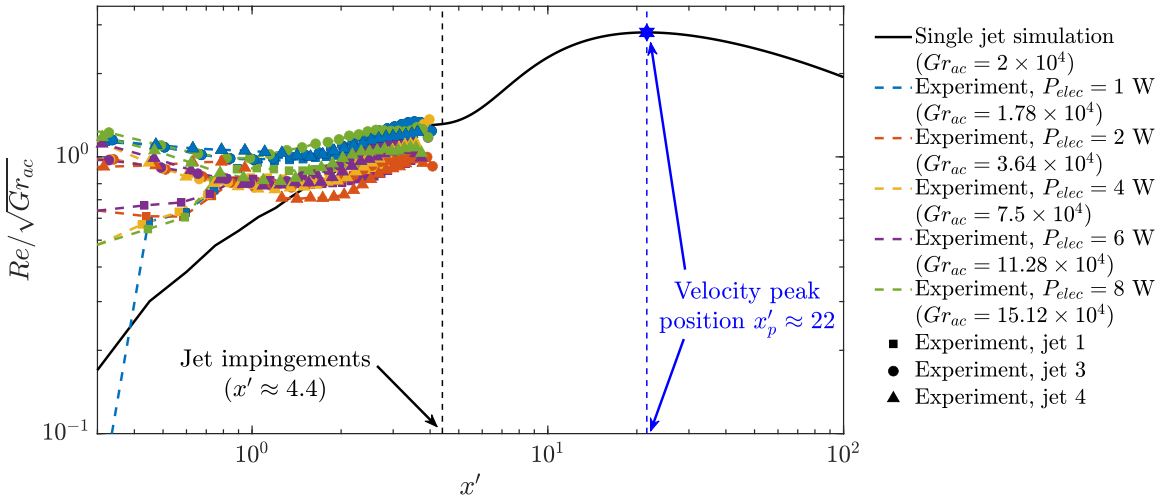


Figure 5.22: Profiles of $Re = \|\overline{\boldsymbol{u}}\| D_s/\nu$ along the axes of jets 1, 3 and 4 for all Gr_{ac}. The origin of each jet is at $x' = 0$. The black profile is taken from chapter 3: it is obtained from the simulation of a single steady axisymmetric jet for $0 \leq x' \leq L$, $L = 1500.7$, $Gr_{ac} = 2 \times 10^4$, $S = 0.03$ and $N = 4.5$ (same values of S and N as in the experiment). In the numerical simulation, the transducer is placed at $x' = 0$. In the experiment, the transducer is at $x' = -8.8$, -17.5 and -21.9 for jets 1, 3 and 4, respectively.

the helical flow.

5.5.2 Creation of large-scale vortical structures and helicity generation

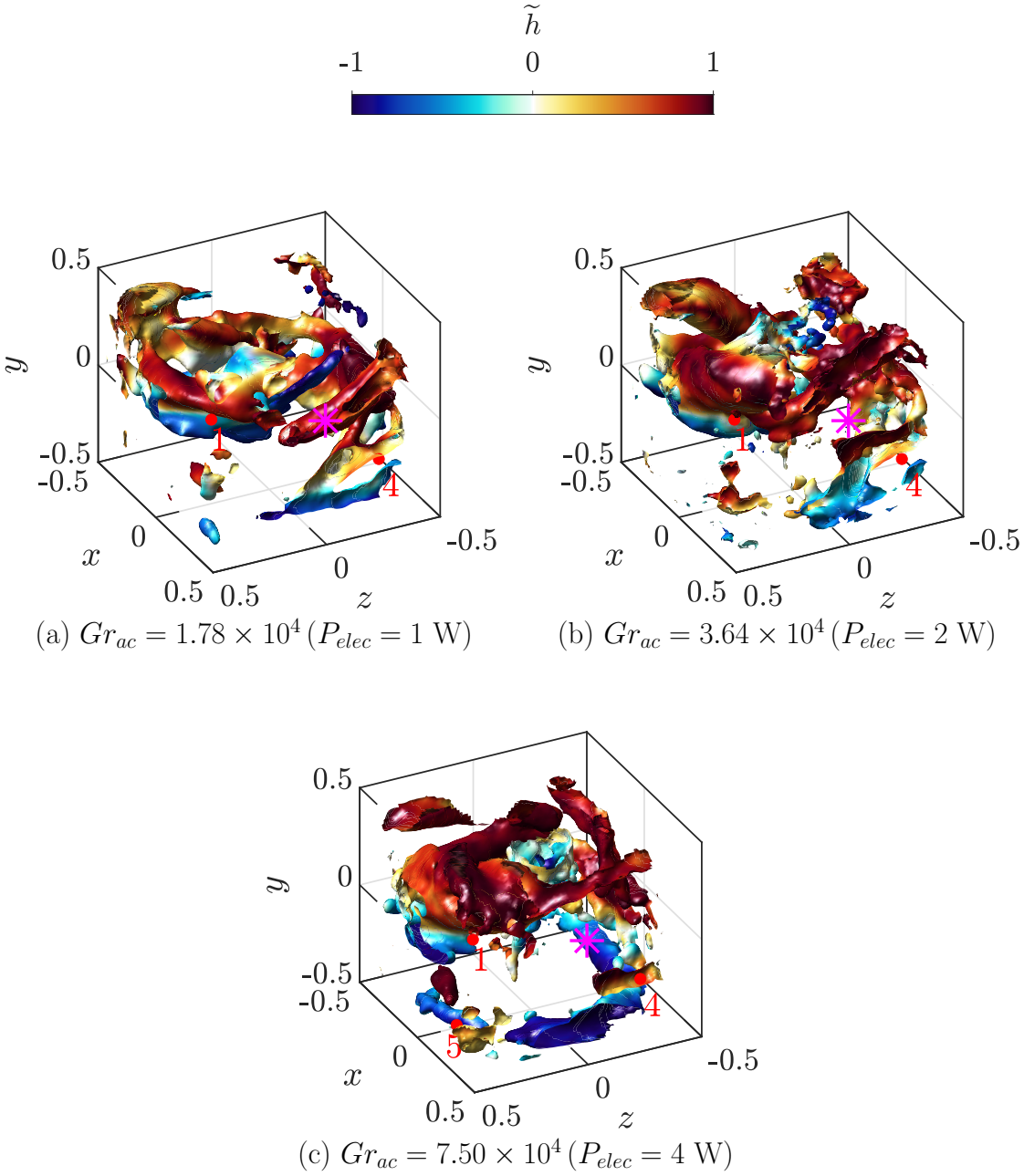
The helical flow is actually more complex than successive straight jets impinging the vertical cavity walls. At an impingement, the vertical spreading of the jet creates recirculations and strong local vorticity on either side of the impingement. The size of the created vortices depends on the "available space" around the impingement, which may be affected by the presence of another jet impinging the same wall, but at a different height. This is for instance the case of jets 1 and 5, which impinge the same wall (figure 5.19), and thus restrict the development of the vortex in between the two jet impingements.

The descending jets drive a large-scale rotation about a vertical axis that stretches the recirculations near the jet impingements, creating large vortical structures (figures 5.23 and 5.24). For $Gr_{ac} \leq 3.64 \times 10^4$, the strongest vortical structures are clustered near the jet impingements (figure 5.23 (a) and (b)). These structures are accompanied by the generation of helicity, which is defined as:

$$\widetilde{h} = \frac{\overline{\boldsymbol{u}} \cdot \overline{\boldsymbol{\omega}}}{\|\overline{\boldsymbol{u}}\| \, \|\overline{\boldsymbol{\omega}}\|}, \tag{5.7}$$

where $\overline{\boldsymbol{\omega}}$ is the time-averaged vorticity vector. From equation (5.7), $\widetilde{h}$ is thus a direct measure of the local alignment between $\overline{\boldsymbol{u}}$ and $\overline{\boldsymbol{\omega}}$: a negative normalised helicity corresponds to the case of opposed velocity and vorticity vectors, whereas $\widetilde{h} > 0$ implies that $\overline{\boldsymbol{u}}$ and $\overline{\boldsymbol{\omega}}$ are approximately pointing in the same direction. The sign of $\widetilde{h}$ in the vortices can actually be predicted beforehand: for instance, in the time-averaged flow measured for $Gr_{ac} = 3.64 \times 10^4$, the spreading of jet 1 above its impingement generates a vortex rotating about the x-axis, leading to the creation of vorticity aligned with the negative

Thèse accessible à l'adresse : https://theses.insa-lyon.fr/publication/2024ISAL0101/these.pdf © [B. Vincent], [2024], INSA Lyon, tous droits réservés



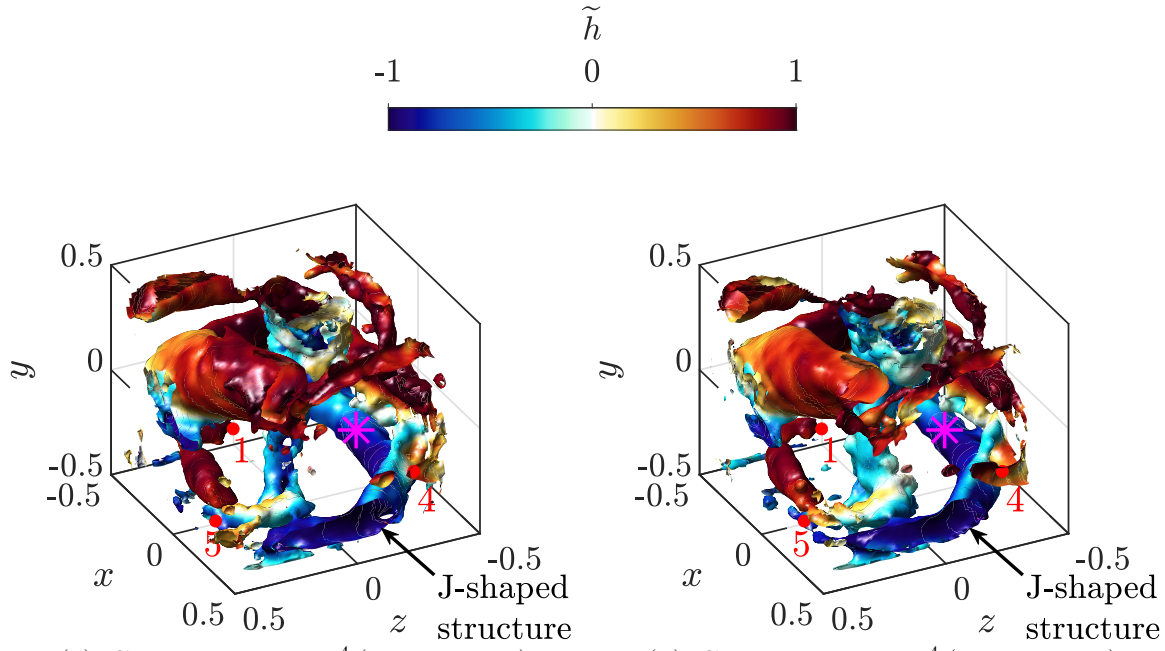
(a) $Gr_{ac} = 1.78 \times 10^4$ ($P_{elec} = 1$ W) (b) $Gr_{ac} = 3.64 \times 10^4$ ($P_{elec} = 2$ W)

(c) $Gr_{ac} = 7.50 \times 10^4$ ($P_{elec} = 4$ W)

Figure 5.23: Vortical structures of the time-averaged flows, represented as isocontours of the Q-criterion (Hunt *et al.*, 1988; Chakraborty *et al.*, 2005) measured for the three lowest Gr_{ac}. The isocontours are coloured by the normalised helicity $\widetilde{h}$ (equation (5.7)); the jet numbering is also displayed. The isocontours are plotted for (a) $Q = 1.80 \times 10^3$, (b) 3.18×10^3 and (c) 7.49×10^3. The entry point of the sound beam in the VOI is located by the purple star at $(x, y, z) = (0.5, 0.13, 0)$. The spatial coordinates are normalised by the size of the VOI in the corresponding direction (183 mm in the x- and z-directions, and 160 mm in the y-direction). All plots share the same colour levels.

x-direction. Besides, the overall fluid rotation also prescribes a mean horizontal velocity that approximately points in the same direction in that fluid region. From equation (5.7), $\widetilde{h}$ is hence expected to be positive in that vortex, which is indeed the case (figure 5.23 (b)). The same reasoning naturally applies to the vortices located below an impingement: in that case, the vortices rotate in the opposite direction, yielding $\widetilde{h} < 0$ there.

Thèse accessible à l'adresse : https://theses.insa-lyon.fr/publication/2024ISAL0101/these.pdf © [B. Vincent], [2024], INSA Lyon, tous droits réservés



(a) $Gr_{ac} = 11.28 \times 10^4$ ($P_{elec} = 6$ W) (b) $Gr_{ac} = 15.12 \times 10^4$ ($P_{elec} = 8$ W)

Figure 5.24: Vortical structures of the time-averaged flows, illustrated by isocontours of the Q-criterion for the two largest Gr_{ac}. The isocontours are coloured by the normalised helicity $\widetilde{h}$ (equation (5.7)) and are plotted for (a) $Q = 11.89 \times 10^3$ and (b) 18.58×10^3. See the caption of figure 5.23 for further details.

Increasing the forcing magnitude promotes the growth (in size) of the vortical structures in the time-averaged flow. Increasing Gr_{ac} not only enhances the inertia of the impinging jets; it also increases the overall fluid rotation (which I shall refer to as the "large-scale swirling motion", see figure 5.20 (b)) about the vertical axis. This, in turn, stretches further the vortices created by the jet impingements. The vortex originating from below the impingement of jet 3 illustrates this effect: this vortex is transported towards the wall at $x = 0.5$, along which it is further stretched. As result, a large J-shaped structure of negative $\widetilde{h}$ is formed close to the bottom wall (figure 5.24).

Besides of yielding larger vortices, increasing Gr_{ac} results in the emergence of another structure at the centre of the time-average flow. This structure appears for $Gr_{ac} > 7.50 \times 10^4$ and corresponds to a vortex rotating about a vertical axis. On its Q-criterion isocontour, this vertical vortex features nearly orthogonal $\overline{\boldsymbol{u}}$ and $\overline{\boldsymbol{\omega}}$, yielding weak $\widetilde{h}$ there. I shall refer to this vertical vortex as the central "chimney" in the following.

The different vortical structures identified in this flow create a net helicity $\mathcal{H}$ within the measurement domain $\widetilde{V}$. This quantity is defined as:

$$\mathcal{H} = \int_{\widetilde{V}} \|\overline{\boldsymbol{u}}\| \, \|\overline{\boldsymbol{\omega}}\| \, \widetilde{h} \, dV \, . \tag{5.8}$$

In the evaluation of $\mathcal{H}$, the noisy data points close to the boundaries and the free surface are removed. As seen in figure 5.25, $\mathcal{H}$ is positive and scales linearly with the forcing magnitude for $Gr_{ac} \leq 11.28 \times 10^4$. This trend is not observed at a higher forcing; however, the discrepancy between the size of the measurement domain and the VOI size may hide a non-negligible amount of $\mathcal{H}$ created near the walls. The value of $\mathcal{H}$ may thus be underestimated at $Gr_{ac} = 15.12 \times 10^4$.

Thèse accessible à l'adresse : https://theses.insa-lyon.fr/publication/2024ISAL0101/these.pdf © [B. Vincent], [2024], INSA Lyon, tous droits réservés

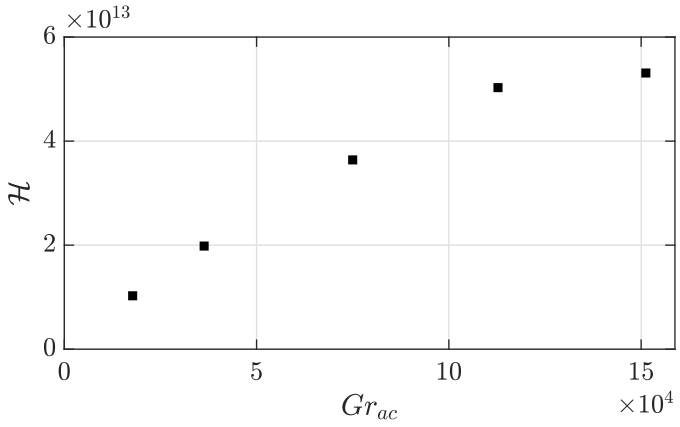


Figure 5.25: Evolution with Gr_{ac} of the net helicity $\mathcal{H}$ (equation (5.8)), made dimensionless using D_s and D_s^2/ν as length as time scales, respectively.

At a given forcing magnitude, $\mathcal{H}$ may be changed by acting on the pitch of the helix (which is kept constant here) or by modifying the cavity height, for instance. Tuning the helicity can be of interest when studying dynamo effects in MHD flows (Moffatt, 2018), or in atmospheric rotating flows like hurricanes.

5.6 Characterisation of the 3D-3C nature of the helical acoustic streaming flow

The jets and their impingements on the cavity walls create complex horizontal and vertical streams, in both ascending and descending directions. Knowing the velocity of each of these streams, and how it scales with Gr_{ac}, is of primary importance when considering a specific application of this streaming flow (e.g., stirring). For this reason, I shall first focus on the large-scale swirling motion, and derive a scaling law to relate its characteristic velocity to Gr_{ac}. Then, the vertical streams shall be characterised, allowing to draw a complete picture of the different velocity scales constituting the helical flow.

5.6.1 Enhancement and scaling of the rotating (or swirling) flow strength with the forcing magnitude

5.6.1.1 Development of the swirling velocity with the forcing magnitude

Just like the multiple jets studied in the previous sections, the swirling motion is one of the key features of the flow obtained by reflection of a single sound beam, that does not occur in straight acoustic streaming jets. The velocity magnitude associated with the swirl may be estimated in each constant-y plane in which the rotating motion occurs. In these planes, a centre of rotation O' can be located to define a local polar coordinate system $(O', \boldsymbol{e_r}, \boldsymbol{e_\theta})$, in which $\boldsymbol{e_r}$ and $\boldsymbol{e_\theta}$ are the unit vectors in the radial and azimuthal directions, respectively. The time-averaged azimuthal velocity at a point M defined as $\boldsymbol{O'M} = r\,\boldsymbol{e_r}$ is then given by $\overline{u_\theta} = \overline{\boldsymbol{u}} \cdot \boldsymbol{e_\theta}$. This quantity can then be averaged over both θ and y-coordinates to yield a single radial profile of $\overline{u_\theta}$ per acoustic forcing:

$$\langle \overline{u_\theta}(r) \rangle_{\theta,y} = \frac{1}{N_\theta N_y} \sum_{j=1}^{N_y} \sum_{i=1}^{N_\theta} \overline{\boldsymbol{u}}\,(r, \theta_i, y_j) \cdot \boldsymbol{e_\theta}\,, \tag{5.9}$$

Thèse accessible à l'adresse : https://theses.insa-lyon.fr/publication/2024ISAL0101/these.pdf © [B. Vincent], [2024], INSA Lyon, tous droits réservés

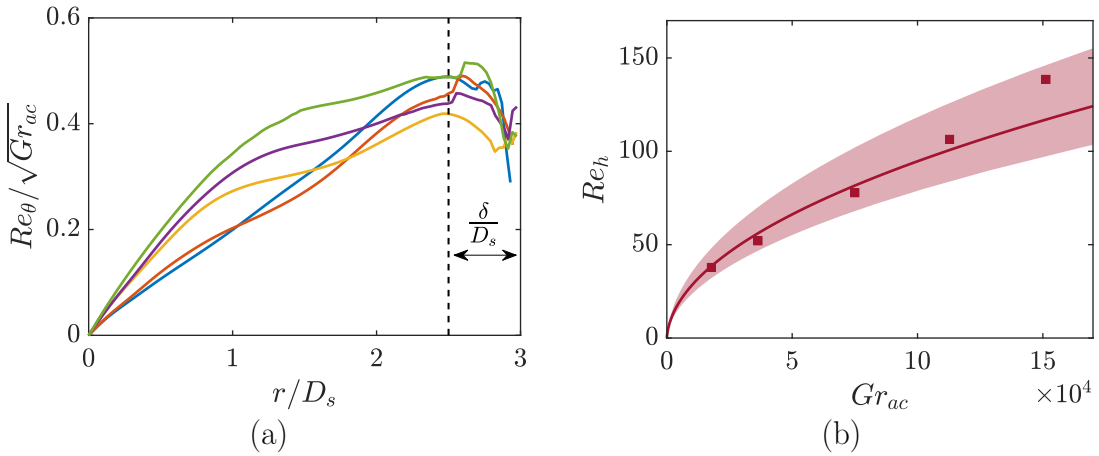


Figure 5.26: Effect of the forcing magnitude Gr_{ac} on the overall fluid rotation about the vertical axis. (a) Radial profiles of the Reynolds number Re_θ based on D_s and on the time-averaged azimuthal velocity $\langle\overline{u_\theta}\rangle_{\theta,y}$ obtained for different Gr_{ac}: $Gr_{ac} = 1.78 \times 10^4$ ($P_{elec} = 1$ W) in blue, $Gr_{ac} = 3.64 \times 10^4$ (2 W) in orange, $Gr_{ac} = 7.50 \times 10^4$ (4 W) in yellow, $Gr_{ac} = 11.28 \times 10^4$ (6 W) in purple and $Gr_{ac} = 15.12 \times 10^4$ (8 W) in green. Each of these profiles is obtained from equation (5.9), and δ is the mean distance between the maximum velocity and the outer vertical walls. (b) Evolution of Re_h with Gr_{ac}, where Re_h is obtained from the ensemble average of Re_θ over the radial coordinates for each Gr_{ac}: experimental points (squares) and prediction (red curve and area). The prediction is obtained from equations (5.13) and (5.3) for $\beta = 0.5$, $\delta = 15$ mm, $L = 183$ mm and $x' = 2.2$ (i.e., the half-jet length). The envelope (red area) is plotted for the same parameter values but for $\beta = 0.6$ (lower bound) and $\beta = 0.4$ (upper bound).

where $\langle\,\rangle_{\theta,y}$ refers to the ensemble averages over the N_θ azimuthal angles and N_y y-coordinates.

The build-up of Re_θ with Gr_{ac} proves an enhancement of the swirling motion (figure 5.26). For $Gr_{ac} = 1.78 \times 10^4$ and 3.64×10^4, the swirl is similar to a solid-body rotation, with a velocity magnitude scaling as $Re_\theta \propto Gr_{ac}^{1/2}$. For $Gr_{ac} \geq 7.50 \times 10^4$, the Re_θ profiles are however different: they display a non-linear evolution with two regions over which Re_θ increases with r/D_s at different rates, and the radial position where that rate changes increases with Gr_{ac}. In contrast, the position of the maximum Re_θ along its profile does not show a significant dependency on Gr_{ac}: its distance δ to the nearest vertical wall remains approximately half of the source diameter, i.e., $\delta/D_s \sim 0.5$. Further averaging the profiles of $\langle\overline{u_\theta}\rangle_{\theta,y}$ over the radial coordinates yields a single velocity estimate $\langle\overline{u_\theta}\rangle_{r,\theta,y}$ quantifying the swirling motion (squares in figure 5.26 (b)). I shall now focus on the scaling of that swirling velocity with Gr_{ac}.

5.6.1.2 Nonlinear scaling of the swirling velocity with the forcing magnitude

The non-linear evolution of $\langle\overline{u_\theta}\rangle_{r,\theta,y}$ quantity with Gr_{ac} can be explained based on orders of magnitudes. On the one hand, N_{jets} jets of velocity magnitude $\|\overline{\boldsymbol{u}}_{\mathbf{jet}}\|$ create a torque by viscous entrainment. This torque drives the swirling motion. On the other hand, friction forces arises at the jet impingement locations and create a torque acting

Thèse accessible à l'adresse : https://theses.insa-lyon.fr/publication/2024ISAL0101/these.pdf © [B. Vincent], [2024], INSA Lyon, tous droits réservés

against the swirl. Balancing these two torques yields:

$$N_{\text{jets}} \overbrace{\sigma_{\text{jet}} S_{\text{jet}}}^{\substack{\text{Friction on}\\ \text{the lateral}\\ \text{jet surface}}} \underbrace{L_a}_{\substack{\text{Lever}\\ \text{arm}}} \sim N_{\text{jets}} \overbrace{\sigma_f S_f}^{\substack{\text{Wall}\\ \text{friction}}} \underbrace{\frac{L}{2}}_{\substack{\text{Lever}\\ \text{arm}}} , \tag{5.10}$$

where L is the cavity width, $L_a = L\sqrt{2}/4$, and σ_{jet} and σ_f are the viscous shear stresses on the lateral jet surface S_{jet} and on the wall friction surface S_f, respectively. Then, by assuming that the jet length L_{jet} is approximately equal to the horizontal distance between two consecutive acoustic reflection points, i.e., $L_{\text{jet}} \sim L/\sqrt{2}$:

$$\sigma_{\text{jet}} S_{\text{jet}} \sim \mu \frac{\|\overline{\boldsymbol{u}}_{\mathbf{jet}}\|}{\frac{D_s}{2}} \pi D_s L_{\text{jet}} \sim \sqrt{2}\mu\pi L \|\overline{\boldsymbol{u}}_{\mathbf{jet}}\| \,. \tag{5.11}$$

As the wall friction surface actually involved in the torque balance is expected to be smaller than the area of a single vertical wall, S_f shall be defined as $S_f \sim \beta H L$, where H is the cavity height and $\beta < 1$ is a tuning parameter. Besides, the velocity gradient length scale at the wall is given by δ (figure 5.26 (a)), so that S_f becomes:

$$\sigma_f S_f \sim \mu \frac{2\left\langle \overline{u_\theta} \right\rangle_{r,\theta,y}}{\delta} \beta H L \,. \tag{5.12}$$

Finally, using equations (5.11) and (5.12), the torque balance gives:

$$Re_h \sim \frac{\pi}{2\beta} \frac{\delta}{H} Re_{\text{jet}} \,, \tag{5.13}$$

where Re_h is the Reynolds number based on $\left\langle \overline{u_\theta} \right\rangle_{r,\theta,y}$. In equation (5.13), Re_{jet} is obtained by evaluating equation (5.3) at the half jet length, i.e., at $x' \approx L_{jet}/\left(2D_s\right)$. This introduces a square-root dependency of Re_h on Gr_{ac}, which is experimentally observed for $Gr_{ac} \leq 7.50 \times 10^4$ (figure 5.26 (b)). The discrepancy between the experimental points and equation (5.13) however builds up at higher forcing. This trend may be attributed to the development of flow unsteadiness as Gr_{ac} is increased, which is discarded in the derivation of equation (5.13). Flow unsteadiness shall be investigated in more details in a later section.

5.6.2 Multiple velocity scales in the vertical streams

In addition to the swirling motion studied above, the jets are also responsible for vertical flows in both the upward and downward directions. I shall now study into more details these vertical flows, and quantify the evolution of their velocity with Gr_{ac}.

5.6.2.1 Evaluation and scaling of the downward flow velocity

The helix-shaped forcing field induces a downward flow. This motion is sustained by the jets, and mainly occurs in the bulk of the flow and marginally beneath each jet impingement (figures 5.27 and 5.28). In constant-y planes, these regions of downward

Thèse accessible à l'adresse : https://theses.insa-lyon.fr/publication/2024ISAL0101/these.pdf © [B. Vincent], [2024], INSA Lyon, tous droits réservés

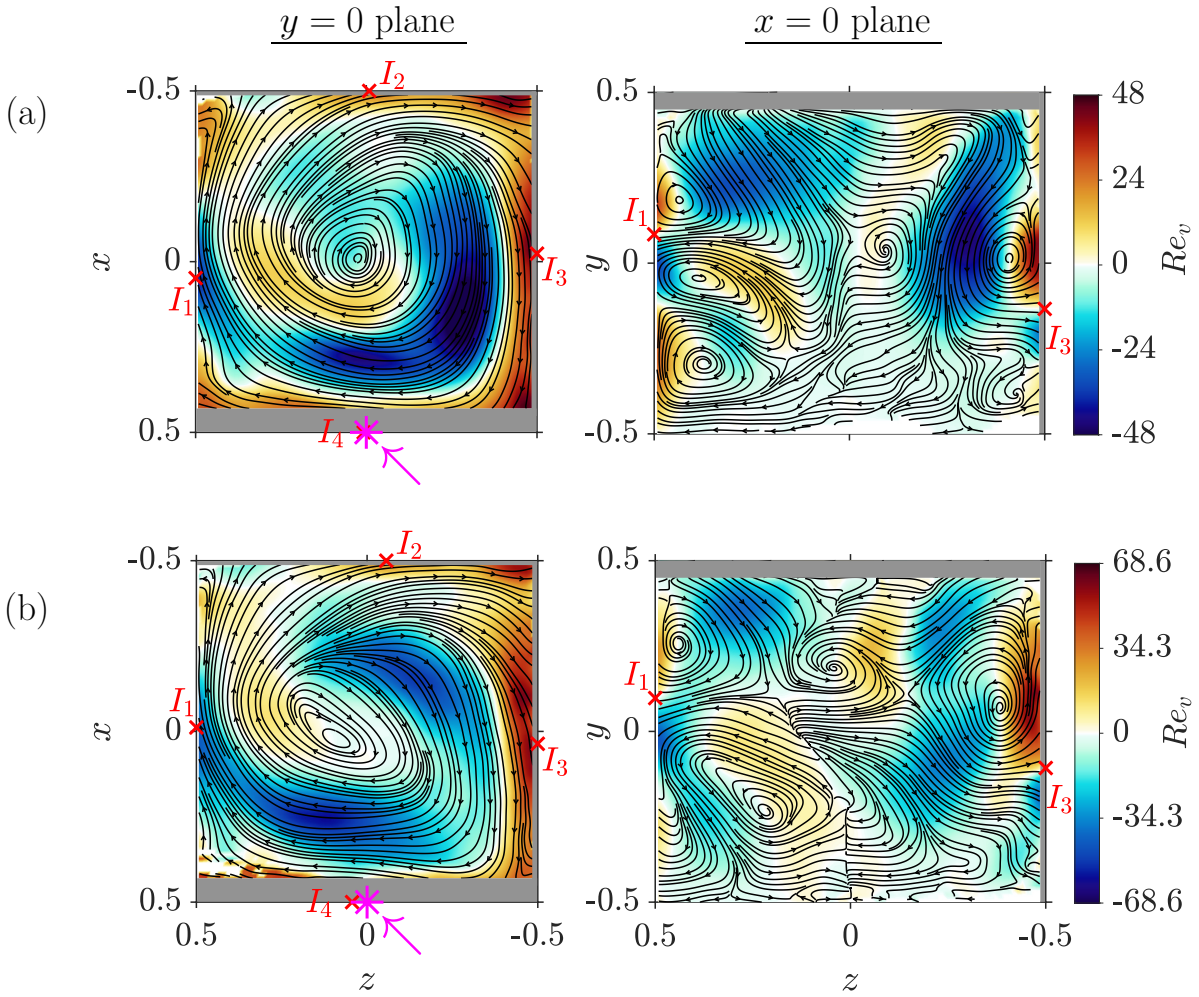


Figure 5.27: Vertical velocity component of the time-averaged flow shown in the horizontal $y = 0$ plane (left) and in the vertical $x = 0$ plane (right), together with the streamlines. The two lowest Gr_{ac} are displayed: (a) $Gr_{ac} = 1.78 \times 10^4$ ($P_{elec} = 1$ W) and (b) 3.64×10^4 (2 W). Similar plots at higher Gr_{ac} are given in figure 5.28). The i-th jet impingement is located by a red cross and is labelled as I_i. The entry point of the beam and its orientation are given by the purple star and arrow, respectively. The figures on a same row share the same colour levels, and the grey rectangles cover regions dominated by measurement noise. Finally, the spatial coordinates are normalised by the size of the VOI in the corresponding direction (183 mm in the x and z directions, and 160 mm in the y direction).

flow appear as large patches of negative vertical velocity. The rate of fluid Q_{down} flowing through these patches, as well as their areas A_{down}, are defined as:

$$Q_{\text{down}}(y) = \sum_{\substack{n=1,\\ \overline{v_n}(y)<0}}^{N_{\text{down}}} \overline{v_n}(y)\Delta x^2 \,, \qquad A_{\text{down}}(y) = N_{\text{down}}\Delta x^2 \,. \tag{5.14}$$

In equation (5.14), the sum applies to the N_{down} points for which $\overline{v_n} = \overline{\boldsymbol{u}} \cdot \boldsymbol{e_y} < 0$ in a constant-y plane. Figure 5.29 (a) shows the vertical distribution of Q_{down} for all forcing magnitudes. These profiles are normalised by the horizontal flow rate Q_{horiz}, which is

Thèse accessible à l'adresse : https://theses.insa-lyon.fr/publication/2024ISAL0101/these.pdf © [B. Vincent], [2024], INSA Lyon, tous droits réservés

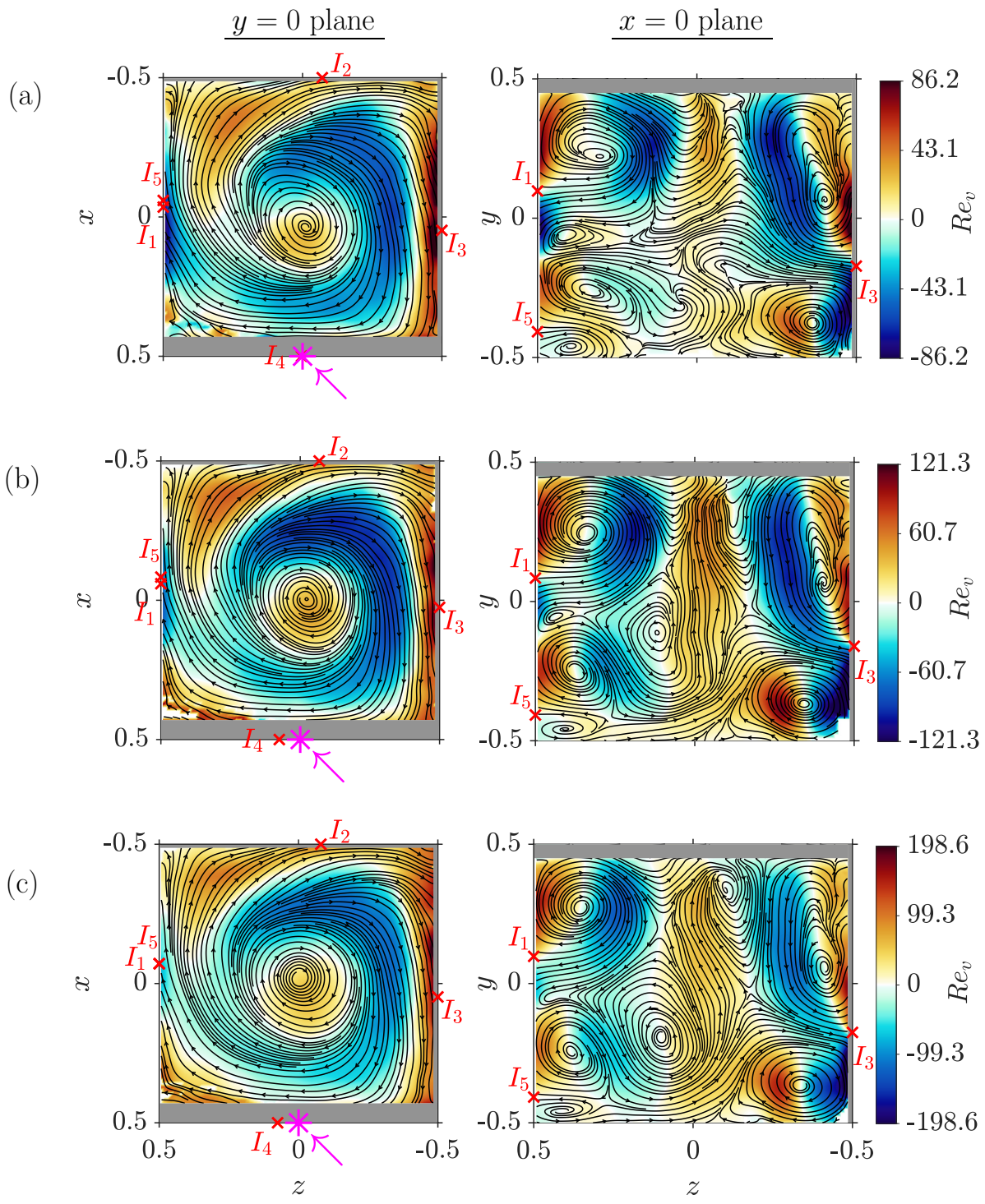


Figure 5.28: Vertical velocity component of the time-averaged flow shown in the horizontal $y = 0$ plane (left) and in the vertical $x = 0$ plane (right), together with the streamlines. The three largest Gr_{ac} are displayed: (a) $Gr_{ac} = 7.50 \times 10^4$ ($P_{elec} = 4$ W), (b) 11.28×10^4 (6 W) and (c) 15.12×10^4 (8 W). See the caption of figure 5.27 for further details.

based on $\langle \overline{u_\theta} \rangle_{r,\theta,y}$ and on the area $A_{\text{horiz}} = HL/2$. The downward flow rate increases from zero at the bottom wall, before starting to decrease at a height that lies slightly above the entrance height of the beam. Interestingly, the maximum of Q_{down} is found in a forcing-free region: the descending jets thus are not the only contributors to the downward flow; the recirculations occurring in the upper part of the VOI and originating from the

Thèse accessible à l'adresse : https://theses.insa-lyon.fr/publication/2024ISAL0101/these.pdf © [B. Vincent], [2024], INSA Lyon, tous droits réservés

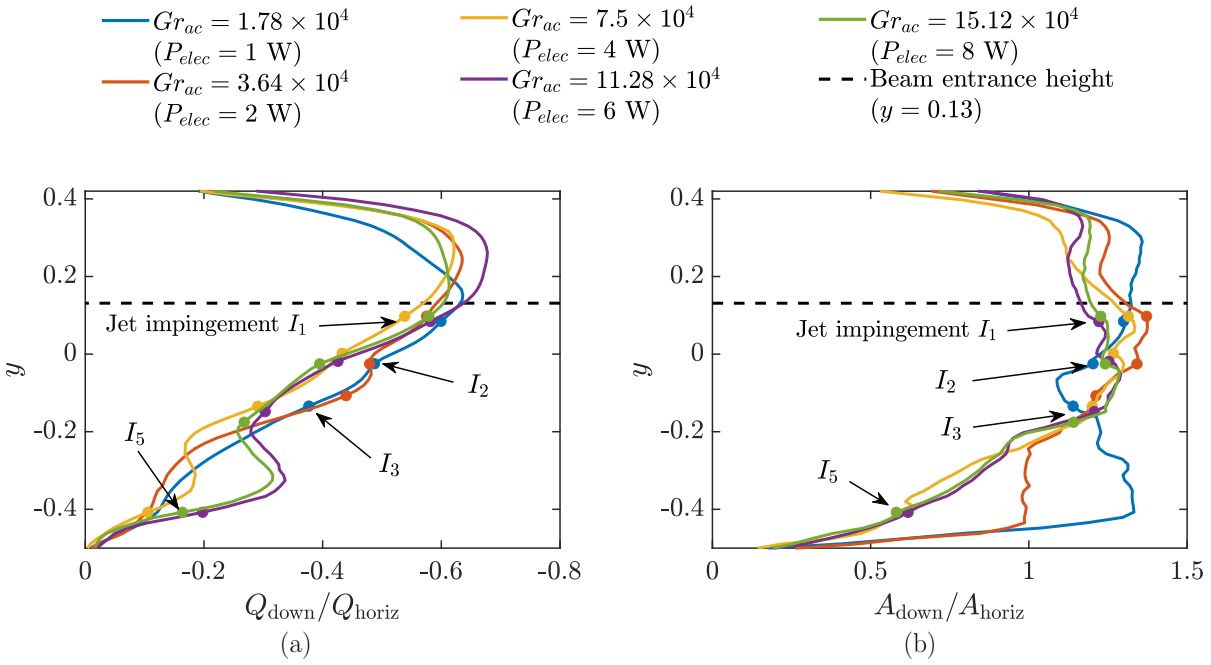


Figure 5.29: (a) Profiles along the cavity height of the ratio between the downward and horizontal flow rates Q_{down} and Q_{horiz}, with Q_{horiz} obtained from $Q_{\text{horiz}} = \langle \overline{u_\theta} \rangle_{r,\theta,y} HL/2$. The profiles are given for different forcing magnitudes Gr_{ac}. The x-axis is reversed, as $Q_{\text{down}} < 0$. (b) Vertical profiles of the dimensionless cross-sectional area A_{down} of downward-flowing fluid. In both plots, the height at which the i-th jet impinges a wall is located by dots labelled as I_i. In both plots, the y coordinates are normalised by the VOI height (160 mm).

jet impingements also greatly contribute to the reported descending flow motions. Large velocities thus are achieved even in forcing-free regions, proving the ability of the helical streaming flow to promote fluid motions in the entire cavity.

All the $Q_{\text{down}}/Q_{\text{horiz}}$ profiles nearly collapse on a single curve. This feature proves a scaling of Q_{down} as $\sqrt{Gr_{ac}}$, since Q_{horiz} is based on a velocity that scales similarly with Gr_{ac} (equation (5.13)). Nevertheless, a "bump" of Q_{down} at $y \approx -0.31$ is visible only for $Gr_{ac} \geq 11.28 \times 10^4$. This feature is clearly not associated with a sudden change of A_{down}, since that area is rather homogeneous over the entire cavity height (figure 5.29 (b)). Instead, this "bump" is caused by the J-shaped vortical structure near the bottom wall. This vortex creates local regions of important velocity, provides a further evidence that the recirculations caused by the jet impingements significantly contribute to the rate of descending fluid.

5.6.2.2 Predominant upward flow along the walls and in the corners of the cavity

Because of mass conservation, any downward flow is necessarily accompanied by ascending motions. These motions occur in two fluid regions. First, along the walls, as well as in the corners of the VOI. The ascending flows developing there are essentially associated with the vortices arising from the vertical spreading of the jets at their impingements (right panel of figures 5.27 and 5.28). Second, in the central chimney visible only $Gr_{ac} > 7.50 \times 10^4$. This structure may span almost the entire cavity height for

Thèse accessible à l'adresse : https://theses.insa-lyon.fr/publication/2024ISAL0101/these.pdf © [B. Vincent], [2024], INSA Lyon, tous droits réservés

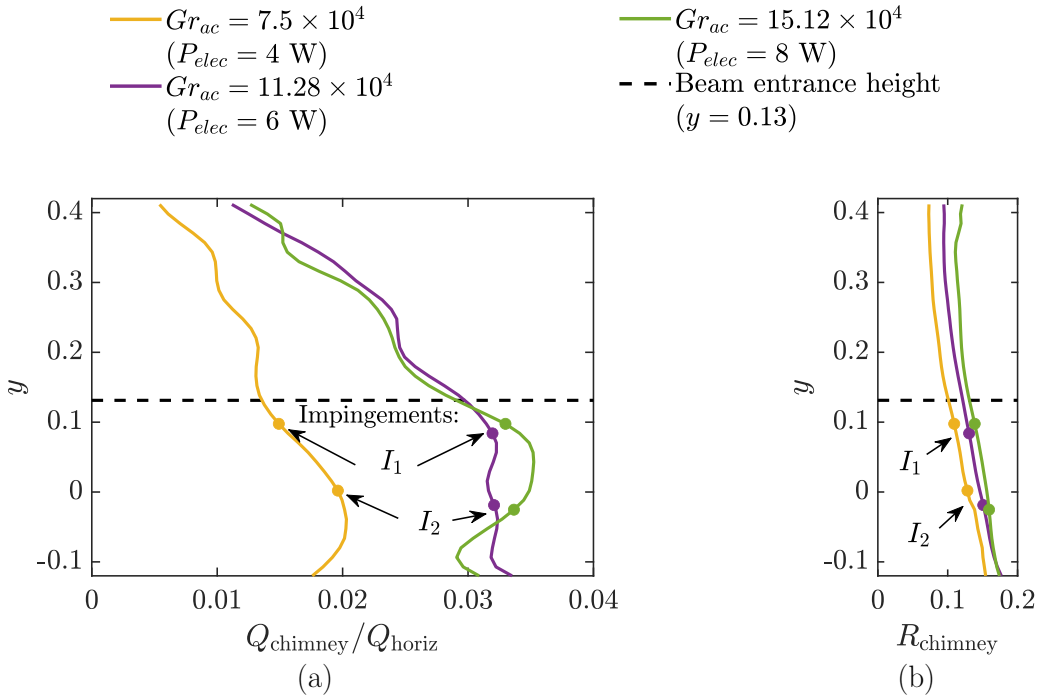


Figure 5.30: (a) Profiles along the VOI height of the rate of fluid Q_{chimney} flowing through the chimney, normalized by the horizontal flow rate $Q_{\text{horiz}} = \langle \overline{u_\theta} \rangle_{r,\theta,y} HL/2$. (b) Vertical profile of the dimensionless chimney radius $R_{\text{chimney}} \approx \frac{\sqrt{A_{\text{chimney}}/\pi}}{L}$. In each plot, the height at which the i-th jet impingement occurs is located by a dot labelled as I_i. The y-coordinates are normalised by the VOI height (160 mm).

$Gr_{ac} \geq 11.28 \times 10^4$, and appears in a constant-y plane as a closed contour of positive vertical velocity at the centre of the plane. The area of that closed contour shall be referred to as A_{chimney}. The rate of fluid Q_{chimney} flowing through A_{chimney} is then computed similarly to Q_{down} (equation (5.14)); the only difference being that only points for which $\overline{v_n}(y) > 0$ in the chimney are of interest.

The rate of fluid flowing vertically through the chimney displays a non-trivial evolution with y (figure 5.30 (a)). From the bottom of the cavity to $y \approx 0.13$, Q_{chimney} oscillates, before steeply decreasing at heights corresponding to the forcing-free region. Just as Q_{down}, the ascending flow rate in the chimney seems to scale approximately as $\sqrt{Gr_{ac}}$ for $Gr_{ac} \geq 11.28 \times 10^4$. Besides, the overall increase of Q_{chimney} with Gr_{ac} forces the chimney structure to become slightly wider (figure. 5.30 (b)): the chimney radius R_{chimney} is greater at the bottom of the VOI where it is fed with fluid, and becomes thinner at higher y (above the dashed line in figures). The slope of each R_{chimney} profiles clearly changes once the force-free part of the VOI is reached, where R_{chimney} is typically one tenth of the cavity size. Nevertheless, at a given Gr_{ac}, the maximum of Q_{chimney} remains more than an order of magnitude below the largest $|Q_{\text{down}}|$. In other words, the flow in the chimney only constitutes a small fraction of the upward flow. This feature could not be predicted beforehand, and thus constitutes a key finding: it shows that the ascending streams essentially occurs near the vertical walls and in the corners of the VOI at a rate $Q_{\text{up}} = -Q_{\text{down}} - Q_{\text{chimney}} \approx -Q_{\text{down}}$ and through a surface area $A_{\text{up}} = L^2 - A_{\text{down}} - A_{\text{chimney}}$. The vertical profile of $Q_{\text{up}}/Q_{\text{horiz}}$ shown in figure 5.31 confirms that $Q_{\text{up}} \gg Q_{\text{chimney}}$.

Thèse accessible à l'adresse : https://theses.insa-lyon.fr/publication/2024ISAL0101/these.pdf © [B. Vincent], [2024], INSA Lyon, tous droits réservés

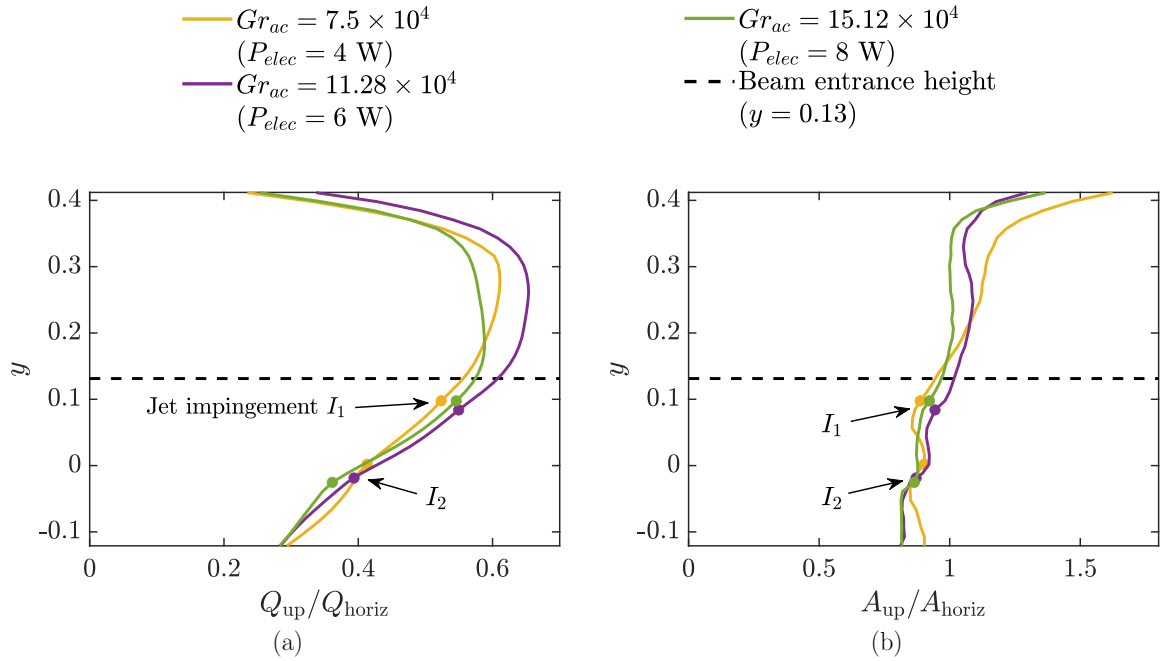


Figure 5.31: (a) Profiles along the cavity height of the ratio between the upward and horizontal flow rates Q_{up} and Q_{horiz}, with Q_{horiz} obtained from $Q_{\mathrm{horiz}} = \langle \overline{u_\theta} \rangle_{r,\theta,y} HL$. The profiles are here displayed for different forcing magnitudes Gr_{ac}. (b) Vertical profiles of the dimensionless cross-sectional area $A_{\mathrm{up}} = L^2 - A_{\mathrm{down}} - A_{\mathrm{chimney}}$ of upward-flowing fluid. In both plots, the height at which the i-th jet impinges a wall is located by a dot labelled as I_i. The y-coordinates are normalised by the VOI height (160 mm).

5.6.3 Summary of the streams magnitudes observed in the helical acoustic streaming flow

I shall now conclude on the analysis of the time-averaged helical flow. Figure 5.32 summarises the velocities associated with the features identified in the previous sections, and how these velocities scale with Gr_{ac}. This plot shows that the helical flow can be split into three distinct contributions. These contributions are listed below, in descending order of their associated Reynolds number Re:

(i) The jets constitute the primary flow. The evolution with Gr_{ac} of Re evaluated at the half jet length (blue, orange and yellow dots in figure 5.32) confirms a scaling as $\sqrt{Gr_{ac}}$, except at the lowest power.

(ii) The swirling motion (or horizontal flow), which is driven by the jets, constitutes a secondary flow. The associated Re differs from the jet Reynolds number by a factor 3. The magnitude of the swirling flow scales as $\sqrt{Gr_{ac}}$ for $Gr_{ac} \leq 7.50 \times 10^4$. At higher forcings, the discrepancy may be attributed to the rise of flow unsteadiness.

(iii) Finally, the vertical flows are characterised by the lowest Re; they thus constitute a tertiary flow. The Re associated with each vertical flow is based on a single mean velocity $\langle U \rangle_y = \frac{1}{h} \int_h \frac{Q(y)}{A(y)} dy$, with h the y-interval of available data. Amongst the vertical flows, the one occurring in the chimney is the slowest one.

Thèse accessible à l'adresse : https://theses.insa-lyon.fr/publication/2024ISAL0101/these.pdf © [B. Vincent], [2024], INSA Lyon, tous droits réservés

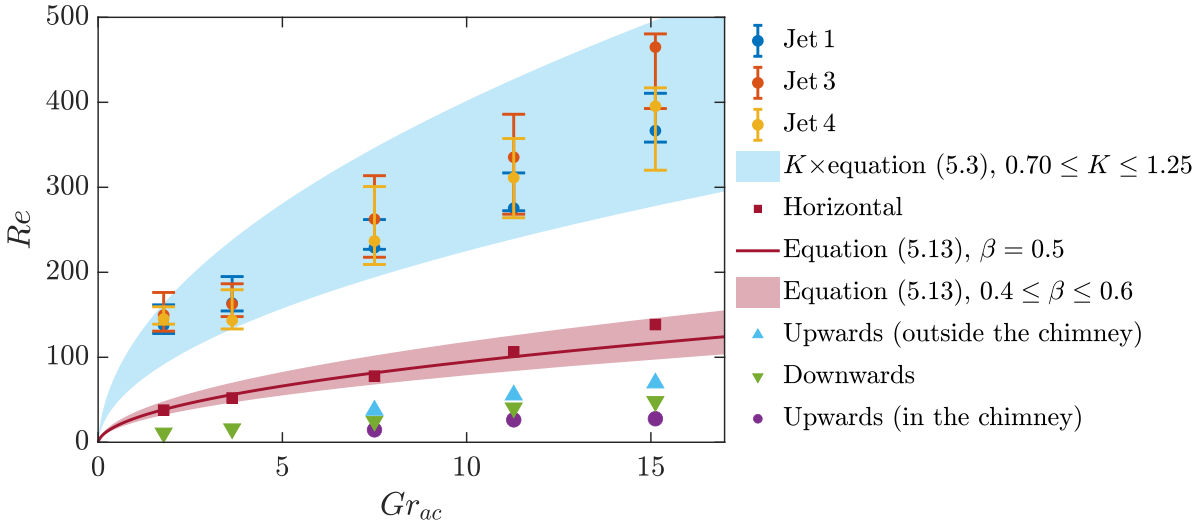


Figure 5.32: Evolution of the Reynolds numbers Re based on D_s and related to the different motions observed in the time-averaged helical acoustic streaming flow, as a function of the forcing magnitude Gr_{ac}. For jets 1, 3, and 4, Re is evaluated at $x' = L_{\text{jet}}/(2D_s)$, where L_{jet} refers to the distance between two consecutive acoustic reflection points. The upper and lower bounds correspond to Re evaluated at $L_{\text{jet}}/(4D_s)$ and $x' = 3L_{\text{jet}}/(4D_s)$, respectively. The blue envelope is obtained from equation (5.3) with $x' = 2.2$ (i.e., the half-jet length). The red curve is given by equation (5.13) for $H = 160$ mm, $L = 183$ mm, $\delta = 15$ mm and $x' = 2.2$. The values of Re associated with the vertical motions are obtained from the ensemble average of the corresponding velocities over the cavity height.

5.7 Flow near a jet impingement: time-averaged topology and development of unsteadiness

As the studied flow configuration relies on successive reflections of a single acoustic beam, the fluid regions close to the cavity walls, on which the jets impinge, are salient features of this flow. Using a second lighting setup (table 5.2), the region where the first jet impingement occurs (green-shaded area in figure 5.17) is studied into more details, both in terms of its time-averaged structure and in terms of the flow unsteadiness taking place there.

5.7.1 Vortical topology of the time-averaged flow at the impingement wall

The time-averaged flow structures, near the first jet impingement I_1, are shown in figures 5.33 and 5.34 for all Gr_{ac}. In these plots, the axes of the vortical structures are located using critical point theory (Chong *et al.* (1990), see chapter 4). More precisely, I sliced the VOI in each direction, and looked for points of zero in-plane velocity around which the streamlines display a spiralling pattern (i.e., focii). For instance, the blue filaments in figure 5.33 are formed by focii in constant-x planes, and thus correspond to the axis of the roll located under below I_1. This roll results from the vertical spreading of the jet impinging at I_1, and is further stretched by the overall fluid rotation about the vertical axis. This structure is observed for all the Gr_{ac}, although the small VOI size in the z-direction prevents the detection of the axis of that roll over the entire cavity length

Thèse accessible à l'adresse : https://theses.insa-lyon.fr/publication/2024ISAL0101/these.pdf © [B. Vincent], [2024], INSA Lyon, tous droits réservés

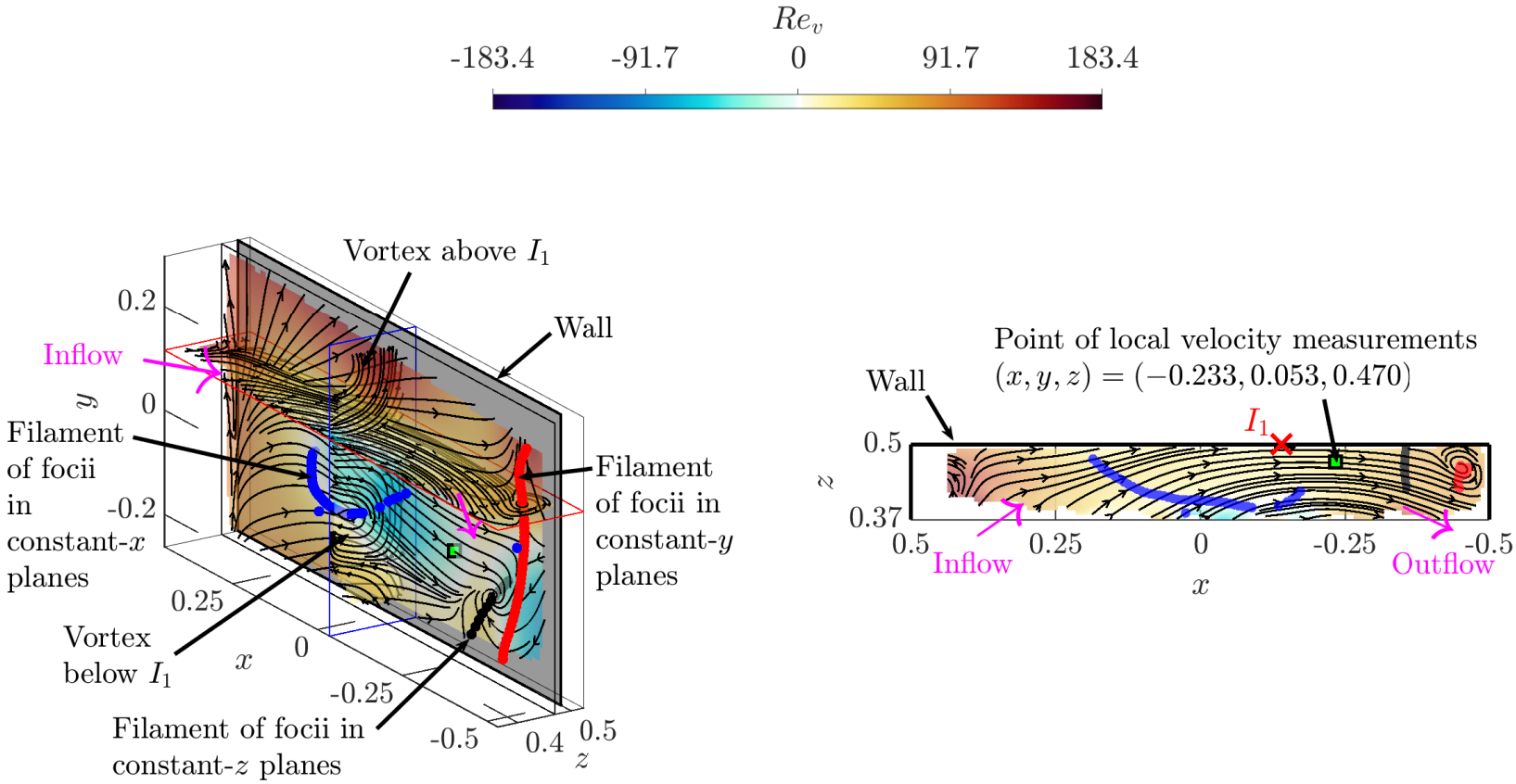


Figure 5.33: Time-averaged flow structure near the first jet impingement I_1 and for $Gr_{ac} = 13.80 \times 10^4$ ($P_{elec} = 8$ W): isometric (left) and top (right) views. Slices of the Reynolds number Re_v based on the vertical velocity and on D_s are shown together with the streamlines in the $x = -0.035$ (blue rectangle), $y = 0.115$ (red rectangle) and $z = 0.470$ (black rectangle) planes. Focii detected in constant-x (blue), y (red) and z (black) planes are also displayed. The green square locates the point where the local time series of $\boldsymbol{u}$ are studied (see figure 5.36). Both figures share the same colour levels, and the spatial coordinates are normalised by the VOI size in the corresponding direction (183 mm for x and z, and 160 mm for y).

Thèse accessible à l'adresse : https://theses.insa-lyon.fr/publication/2024ISAL0101/these.pdf © [B. Vincent], [2024], INSA Lyon, tous droits réservés

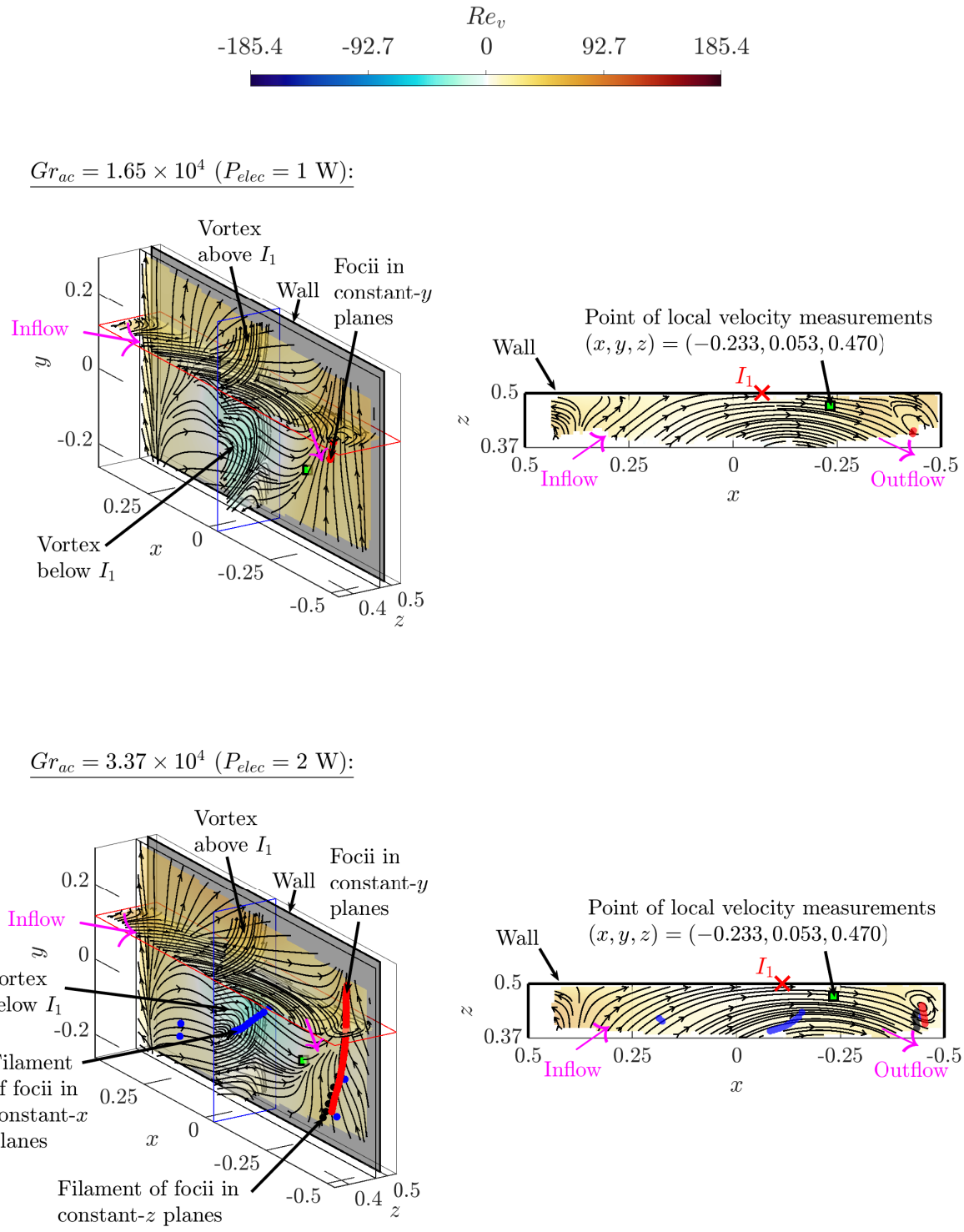


Figure 5.34: Caption on next page

for $Gr_{ac} \leq 10.29 \times 10^4$. Indeed, increasing the forcing magnitude confines that roll towards the wall impinged by the jet. This, in turn, increases the space available at the centre of the fluid volume for the central chimney to develop (figure 5.27). Finally, the limited size of the VOI in the y-direction prevents the observation of the vortex located above I_1 and also resulting from the splitting of the jet there. Its presence can nevertheless be inferred from the streamlines in the vertical $x = 0$ plane around I_1.

Thèse accessible à l'adresse : https://theses.insa-lyon.fr/publication/2024ISAL0101/these.pdf © [B. Vincent], [2024], INSA Lyon, tous droits réservés

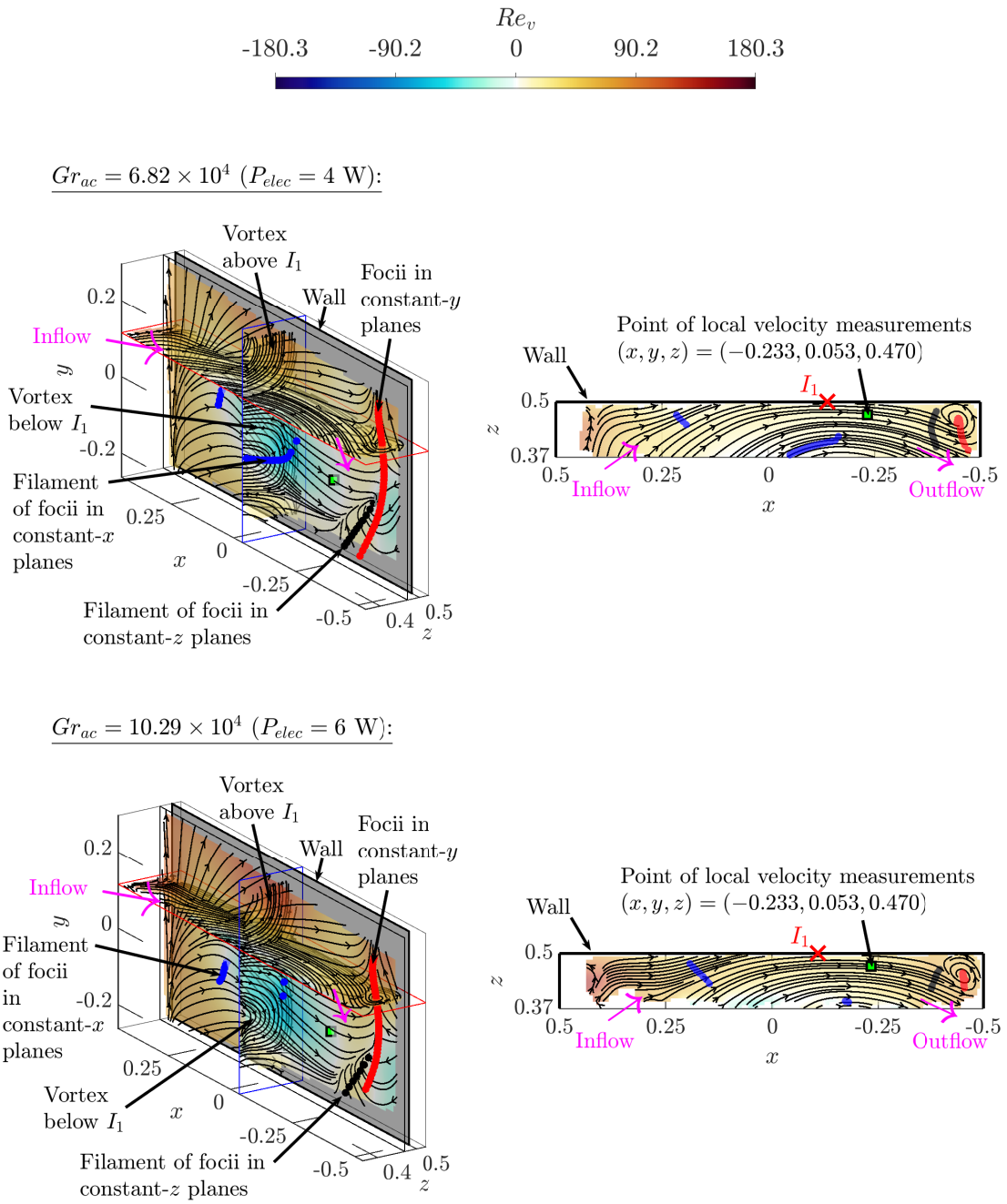


Figure 5.34: Time-averaged flow structure near the first jet impingement I_1, together with slices of the Reynolds number Re_v (based on the vertical velocity component and on D_s) and the in-plane streamlines. Isometric (left) and top (right) views are shown for $1.65 \times 10^4 \leq Gr_{ac} \leq 10.29 \times 10^4$ (see figure 5.33 for the largest Gr_{ac}). A positive Re_v refers to an upward fluid flow. Focii in constant-x, y and z planes are represented by blue, red and black spheres, respectively. The green square at $(x, y, z) = (-0.233, 0.053, 0.470)$ locates the point where the local dynamics are studied (see figure 5.36). All figures share the same color levels.

A roll of nearly vertical axis is observed in the corner of the VOI for $Gr_{ac} \geq 3.37 \times 10^4$ (red filament in figures 5.33 and 5.34). Increasing Gr_{ac} straightens up the axis of this vortex. The latter emerges in the time-averaged flow together with a third vortex, the axis of which being represented by focii in constant-z planes (black filaments in figures 5.33

Thèse accessible à l'adresse : https://theses.insa-lyon.fr/publication/2024ISAL0101/these.pdf © [B. Vincent], [2024], INSA Lyon, tous droits réservés

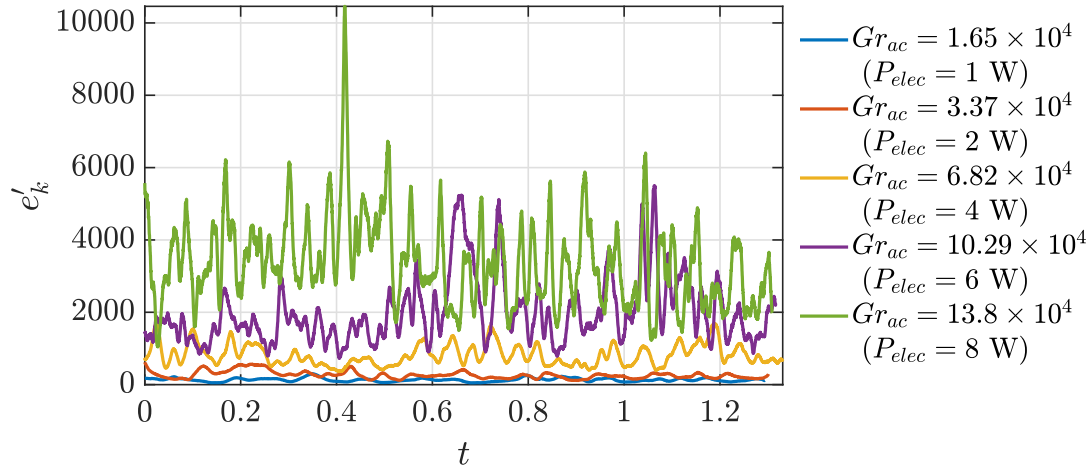


Figure 5.35: Temporal evolution of the kinetic energy associated with the velocity perturbations (equation (5.15)) for all forcing magnitudes Gr_{ac}. The displayed quantities are made dimensionless using D_s and D_s^2/ν as length and time scales, respectively.

and 5.34). Given the rotating direction of this structure, and that its axis points slightly towards the bottom of the fluid volume, this vortex might be related to the vortex located below I_2 and resulting from the spreading of jet 2 there. This structure displayed significant fluctuations over time, making it suitable to characterise the rise of unsteadiness close to I_1 as Gr_{ac} is increased.

5.7.2 Development of flow unsteadiness with increasing forcing magnitude and leading frequencies

First, the development of flow unsteadiness as the forcing magnitude is increased can be witnessed through the total kinetic energy of the fluctuations. At a given time t, it is defined over the entire VOI as:

$$e'_k(t) = \frac{1}{N_p(t)} \sum_{n=1}^{N_p(t)} \frac{1}{2} \boldsymbol{u'}(\boldsymbol{x_n}, t) \cdot \boldsymbol{u'}(\boldsymbol{x_n}, t)\,, \tag{5.15}$$

where the coordinates of the n-th grid point (out of $N_p(t)$ in total) of the discretised measurement domain are given by $\boldsymbol{x_n}$, and $\boldsymbol{u'}(\boldsymbol{x_n}, t) = \boldsymbol{u}(\boldsymbol{x_n}, t) - \overline{\boldsymbol{u}}(\boldsymbol{x_n})$. As Gr_{ac} is increased, the overall level of e'_k increases too, thus indicating a build up of flow unsteadiness (figure 5.35). The time series of e'_k may even features short and high-intensity events during the recording duration; this is especially the case for $Gr_{ac} \geq 6.82 \times 10^4$. These may also be overlayed to slower fluctuations, as it is the case for the time series recorded for $Gr_{ac} = 13.80 \times 10^4$, for instance. Combined with the fact that none of the signals shown in figure 5.35 is actually perfectly periodic, no leading frequency clearly emerges from the frequency spectrum of e'_k. This is also the case for the time series of local velocities extracted at one location in the measurement domain. Longer measurements would thus be required to accurately capture the dynamics of the system (and especially its slow fluctuations) near I_1. Such situation is not unique to the helical flow studied here: it has already been encountered in the resembling "square" streaming flow configuration (Cambonie *et al.*, 2017), for which several hours of observation were actually required to fully

Thèse accessible à l'adresse : https://theses.insa-lyon.fr/publication/2024ISAL0101/these.pdf © [B. Vincent], [2024], INSA Lyon, tous droits réservés

characterise the flow dynamics (Launay *et al.*, 2019). From an experiments perspective, such large recording durations are unfortunately out of reach, due to both equipment (e.g., the sedimentation of the seeding particles over time) and software (i.e., terabytes of disk space would be required for several hours of data acquisition) limitations.

The dynamics of the flow near I_1 may nevertheless be quantitatively estimated by tracking the emergence and disappearance of large-scale flow features (e.g., vortices) within the measurement domain. Such events lead to strong local deformations of the streamlines, which can be evaluated by the instantaneous angle θ between $\boldsymbol{u}(t)$ and $\overline{\boldsymbol{u}}$ at a given point of the measurement domain. This angle, as well as its root-mean square θ_{RMS}, is given by:

$$\begin{aligned} \theta(t) &= \arccos\left[\frac{\overline{\boldsymbol{u}}\cdot\boldsymbol{u}(t)}{\|\overline{\boldsymbol{u}}\|\,\|\boldsymbol{u}(t)\|}\right], \\ \theta_{RMS} &= \sqrt{\frac{1}{N_s}\sum_{n=1}^{N_s}\theta(t_n)^2}, \end{aligned} \tag{5.16}$$

where N_s is the number of snapshots in the dataset. Examples of the temporal evolution of θ at $(x, y, z) = (-0.233, 0.053, 0.470)$ (represented by the green rectangle in figure 5.33) for the two extreme forcing magnitudes are shown in figure 5.36.

For $Gr_{ac} = 1.65 \times 10^4$, the time series of θ features only isolated fluctuations of large amplitude (more than $3 \times \theta_{RMS}$). The orientation of the mean velocity vector (shown as a red arrow in the snapshots (a) and (b) of figure 5.36) indicates that the fluid essentially flows upwards at the probe location. At each of the large variations of θ reported for this case, the fluid suddenly starts to flow towards the bottom of the cavity, before returning back to its mean local direction. From the peak widths observed in the time series of θ, the mean duration of this local flow deviation is 0.024 (or approximately 22 s, in dimensional units) at the lowest Gr_{ac}.

For $Gr_{ac} = 13.80 \times 10^4$ (plots on the right-hand side of figure 5.36), a significantly greater number of peaks, associated with events of shorter durations (typically about 0.0063, i.e., 6 s in dimensional units) is reported in the time series of θ. These peaks however illustrate a different phenomenon from the one observed for the lowest forcing case. Indeed, for $Gr_{ac} = 13.80 \times 10^4$, the time-averaged velocity vector is nearly horizontal at the probe location (snapshots (c) and (d) in figure 5.36), and the fast variations of θ are caused by the emergence of a vortex similar to the one represented by the black filament in the time-averaged velocity field in figure 5.33. This structure enters the measurement volume from below (snapshot (d)), and then moves upwards, causing a strong variation of θ as it passes near the probe (snapshot (c)). This vortical structure then eventually leaves the measurement domain. As this vortex has been observed multiple times in constant-z planes and for different Gr_{ac}, its evolution within the measurement has been chosen as a consistent indicator of the flow dynamics near I_1.

The existence of such roll (which is rotating in the counter-clockwise direction about the z-axis, according to the point of view adopted in the snapshots of figure 5.36) in the measurement domain has been tracked over time by locating focii in constant-z planes for each frame. A "ribbon" of focii could thus be formed at each timestamp to represent the instantaneous core line of the vortex in the measurement domain. The emergence and disappearance of this vortex core line has then been monitored over the entire recording duration. As shown in figure 5.37 (a), the number of vortices N_v appearing in the measurement domain during each recording scales linearly with the forcing magnitude for almost all the Gr_{ac} considered. Only the case of lowest forcing ($Gr_{ac} = 1.65 \times 10^4$) does

Thèse accessible à l'adresse : https://theses.insa-lyon.fr/publication/2024ISAL0101/these.pdf © [B. Vincent], [2024], INSA Lyon, tous droits réservés

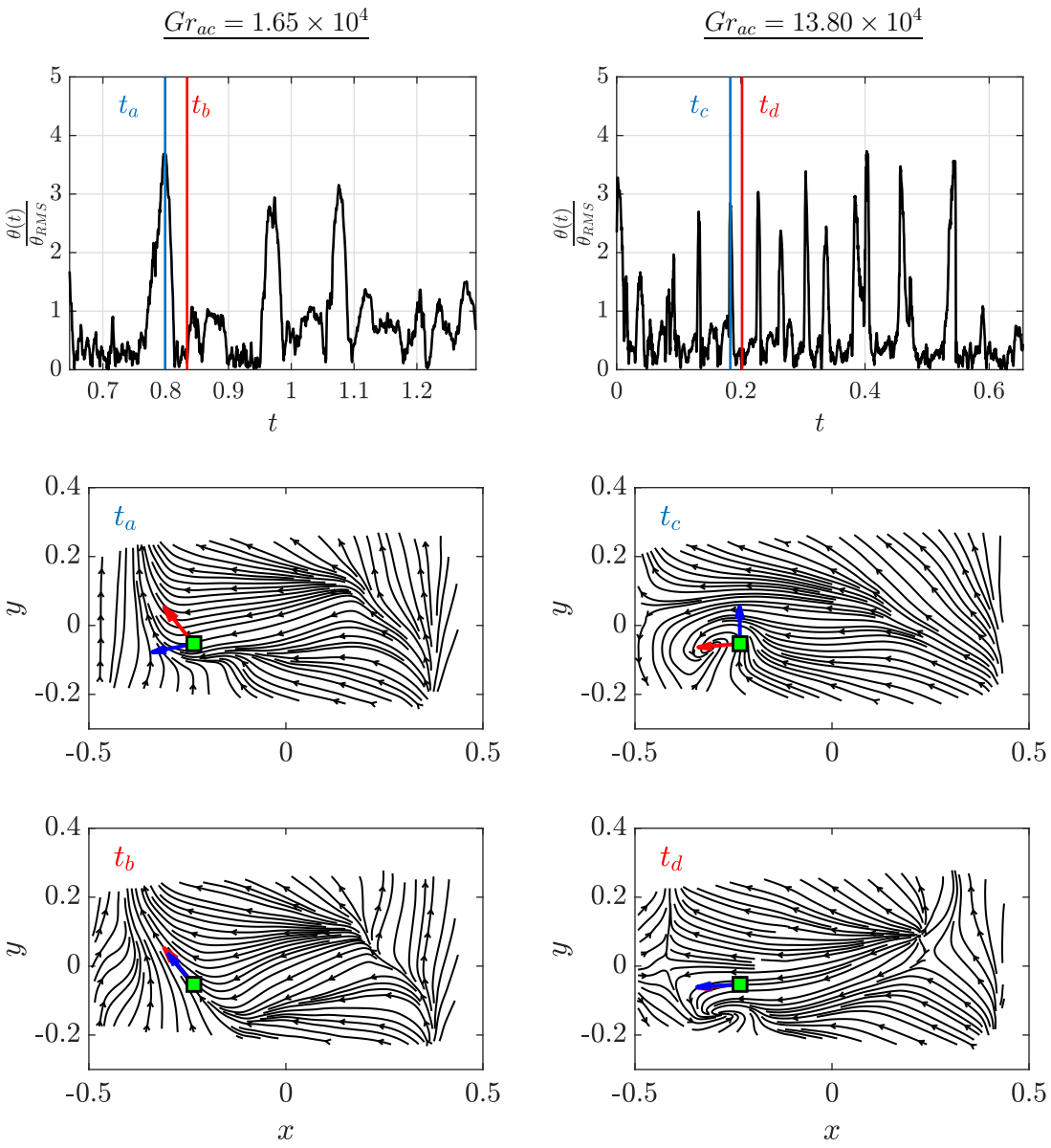


Figure 5.36: Local measures of the flow unsteadiness for the two extreme forcing magnitudes: $Gr_{ac} = 1.65 \times 10^4$ ($P_{elec} = 1$ W, left) and $Gr_{ac} = 13.80 \times 10^4$ ($P_{elec} = 8$ W, right). Top row: time series of the angle θ between the instantaneous and time-averaged velocity vector (equation (5.16)) at $(x, y, z) = (-0.233, 0.053, 0.470)$. In both plots, θ is normalised by its RMS value calculated over the recording duration (20 minutes) and t is normalised by D_s^2/ν (only half of the time series is shown for $Gr_{ac} = 13.80 \times 10^4$). Centre and bottom rows: instantaneous streamlines in the $z = 0.470$ plane, for the time stamps given by the labelled vertical lines in the time series. The green square indicates where θ is measured, together with the time-averaged (red) and instantaneous (blue) local velocity directions. The y and z coordinates are normalised by the VOI height (160 mm) and width (183 mm), respectively.

not follow that trend. This behaviour may be caused by a too short recording duration to be a truthfully representation of the flow dynamics at that forcing magnitude.

By identifying the timestamps at which each vortex core line enters and leaves the measurement domain, I could also estimate a mean residence time $\langle t_r \rangle$ and emergence

Thèse accessible à l'adresse : https://theses.insa-lyon.fr/publication/2024ISAL0101/these.pdf © [B. Vincent], [2024], INSA Lyon, tous droits réservés

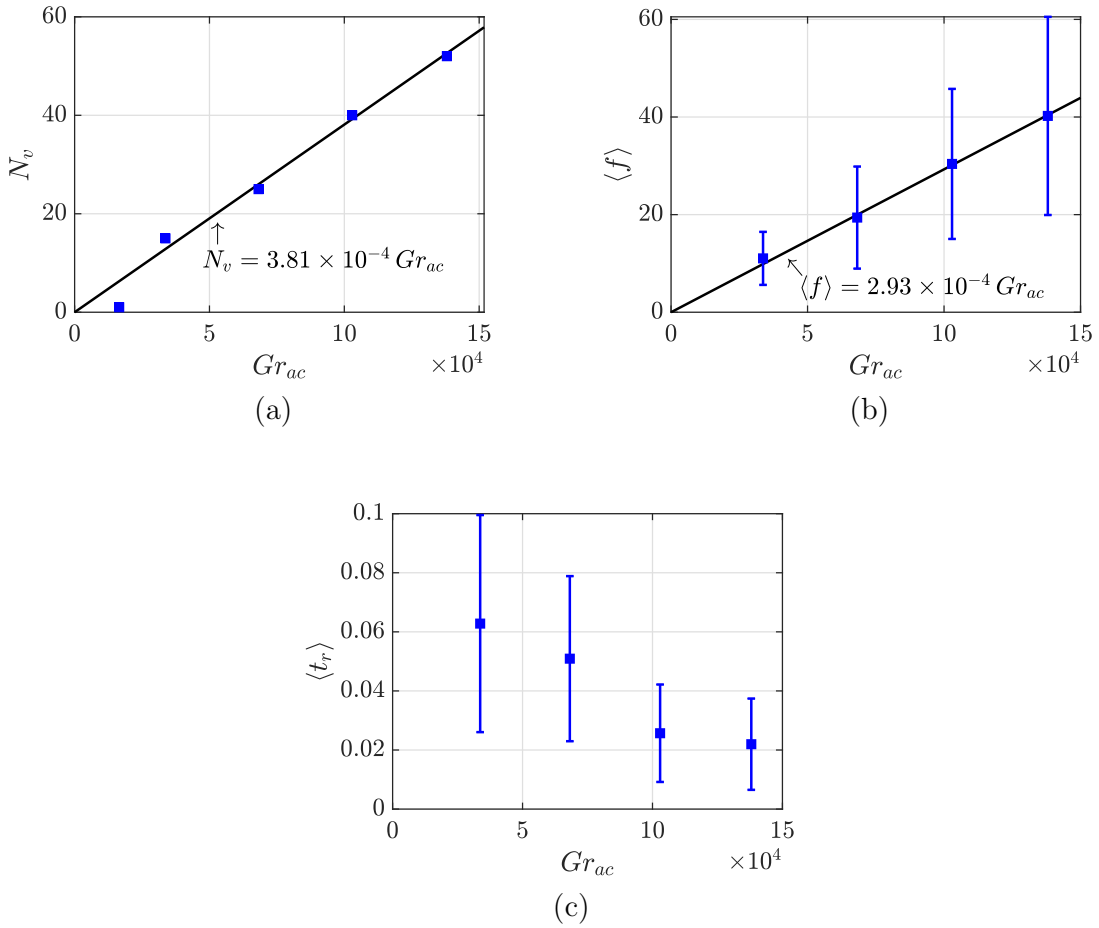


Figure 5.37: Statistics of the vortices revolving positively about the z-axis and in the vicinity of the jet impingement I_1 (black filament in figures 5.33 and 5.34), as a function of the forcing magnitude Gr_{ac}. The statistics are evaluated over the recording duration (20 minutes for each Gr_{ac}). (a) Number of vortices tracked in the VOI. (b) Mean emergence rate $\langle f \rangle$ of the vortices, as defined by equation (5.17), and bounded by equation (5.19). (c) Mean residence time $\langle t_r \rangle$ of the tracked vortices in the VOI (equation (5.17)), bounded by the standard deviation calculated for each Gr_{ac}. Both $\langle f \rangle$ and $\langle t_r \rangle$ are made dimensionless using the viscous diffusion time at the scale of D_s.

rate $\langle f \rangle$ related to these structures. These quantities are defined as:

$$\langle t_r \rangle = \frac{1}{N_v} \sum_{n=1}^{N_v} \left(t_{out}^n - t_{in}^n \right) , \tag{5.17}$$

and:

$$\frac{1}{\langle f \rangle} = \langle T_e \rangle = \frac{1}{N_v - 1} \sum_{n=1}^{N_v - 1} \left(t_{in}^{n+1} - t_{in}^n \right) , \tag{5.18}$$

where t_{in}^n and t_{out}^n are the timestamps at which the n-th vortex core line enters and leaves the measurement volume, respectively. The mean vortex emergence period is given by $\langle T_e \rangle$. An estimate of the uncertainty interval bounding is thus given by:

$$\Delta f = \langle f \rangle \frac{\sigma_{T_e}}{\langle T_e \rangle} , \tag{5.19}$$

Thèse accessible à l'adresse : https://theses.insa-lyon.fr/publication/2024ISAL0101/these.pdf © [B. Vincent], [2024], INSA Lyon, tous droits réservés

where the standard deviation of T_e, determined for each Gr_{ac}, is given by σ_{T_e}. The evolution of the mean vortex emergence rate and its the mean residence time are shown in figure 5.37 (b) and (c), respectively. Both quantities correspond to shorter time scales than the diffusive time at the scale D_s. The vortex emergence rate $\langle f \rangle$ scales linearly with Gr_{ac}, although with a greater dispersion. This indicates that no drastic flow regime seems to occur in the range of Gr_{ac} considered throughout this study. On the other hand, $\langle t_r \rangle$ is seen to decrease with power, however at a higher rate for low ($Gr_{ac} < 10.29 \times 10^4$) than for high ($Gr_{ac} \geq 10.29 \times 10^4$) forcings. The decrease of $\langle t_r \rangle$ with Gr_{ac} indicates that, although the vortices appear at a higher rate, they are more rapidly swept away from the measurement domain as the forcing is enhanced. The helical flow considered here is thus far from being steady, and its unsteadiness clearly builds up when the magnitude of the acoustic forcing is increased.

5.8 Conclusion

In this chapter, I carried out experiments to measure and analyse and highly three-dimensional streaming flows. After having determined the active diameter of a plane circular transducer through hydrophone measurements, I focused on how its radiated sound field can be exploited to drive a novel highly three-dimensional flow in a closed cavity without using any moving part (e.g., a propeller).

I carried out the experiments in a nearly cubic cavity filled with water, and attempted for the very first time to take advantage of multiple sound beam reflections to create a three-dimensional forcing field. The sound beam entered in the upper half of the cavity with horizontal and vertical inclinations, causing the beam to perfectly reflect five times on the vertical cavity walls whilst propagating downwards at the same time. This beam orientation resulted in a helix-shaped forcing field spanning the cavity height, driving a helical flow in the entire cavity that had never been observed before. This work thus proves that highly 3D streaming flows can indeed be achieved using multiple beam reflections, and paves the way to novel 3D streaming designs.

My measurements relied on Particle Tracking Velocimetry (PTV), a method that had never been used in the laboratory before. These measurements allowed me to reconstruct 3D-3C Eulerian streaming velocity fields for different forcing magnitudes, which are quantified by the acoustic Grashof number Gr_{ac}.

Although the time-averaged flows measured in the entire fluid volume (or VOI, for "Volume Of Investigation") display a complex structure in which jets and vortices coexist, I identified three main contributions to the flow (figure 5.32), and classify these contributions based on their characteristic velocity magnitudes:

(i) The streaming jets, directly driven by the beam, feature the largest velocity and can thus be seen the primary flow. Their Reynolds number scales similarly to a single streaming jet, for which $Re_{\text{jet}} = -4x + \frac{\sqrt{2}}{2}\sqrt{32x^2 + Gr_{ac}x}$ (see chapter 3). This scaling law is thus a useful tool to get a preliminary jet velocity estimation when designing a similar helical streaming flow. Furthermore, each jet impinges a vertical wall, forming counter-rotating vortices on either side of the impingement, and contributing to the creation of helicity within the VOI.

(ii) The jets sustain a large-scale rotation about a central vertical axis. Although the associated Reynolds number scales linearly with Re_{jet}; it nevertheless remains significantly smaller, by a factor based on the boundary layer thickness at the walls. This swirling motion thus constitute the secondary flow.

Thèse accessible à l'adresse : https://theses.insa-lyon.fr/publication/2024ISAL0101/these.pdf © [B. Vincent], [2024], INSA Lyon, tous droits réservés

(iii) The downward-pointing forcing drives low-velocity vertical streams, corresponding to the tertiary flow. Whilst the downward flow occurs around the jets, most of return ascending flow develops near the edges and corners of the VOI. This finding is key for mixing applications, in which regions of stagnant fluid are usually undesirable. Another vertical stream, shaped as a chimney, develops for $Gr_{ac} \geq 7.50 \times 10^4$ at the centre of the VOI. The associated velocity levels however remain one order of magnitude smaller than those of the near-wall upward flows.

Still, the time-averaged jet velocities remain small: they are typically about 1 cm/s for the largest Gr_{ac}, i.e., half of the jet velocities observed at a similar forcing magnitude but without a vertical beam inclination (Cambonie *et al.*, 2017). The validation of the experimental setup in section 5.3.3 confirms that this discrepancy is not related to the difference in experimental methods, but is rather due to the forcing and flow characteristics. This observation naturally raises the question of whether the geometry of the helical forcing could be altered to "optimise" the flow. For this purpose, the knowledge gained for single straight jets (chapter 3) can be useful: the pitch of the helix-shaped forcing may be chosen so that the jet impingement coincides with the on-axis jet velocity peak (figure 5.22), thus leading to an increase of the overall velocity levels.

I finally studied the development of flow unsteadiness in a reduced measurement domain encompassing the first jet impingement. Increasing Gr_{ac} is seen to amplify aperiodic velocity fluctuations, leading to short and intense kinetic energy bursts at the largest forcing magnitude. These high-intensity events near the first jet impingement involve fluctuations of vortical structures, whose origins may be closely related to the fifth jet impinging the same wall but at a lower height. Although their fluctuations are aperiodic, their mean emergence frequency scales linearly with Gr_{ac}, showing a smooth evolution of the flow structure instead of an abrupt flow regime change. Simultaneously, the residence time of the vortices in the measurement domain decreases with larger Gr_{ac}, as a consequence of the enhanced of the overall convective motions.

The observed flow unsteadiness proves that the experiments were made beyond the primary flow bifurcation. This could be expected: all the Gr_{ac} considered here were larger than the critical values determined in the stability analysis of a single-jet streaming flow (chapter 4). This raises the question of whether the destabilisation mechanism is the same. Indeed, the recirculations created by the jet impingements are a salient feature of the helical flow, and were found to destabilise a single-jet streaming flow. Therefore, a destabilisation of the helical flow rooted in these recirculations seems to be a plausible scenario that still needs to be confirmed. However, major differences between the two configurations may lead to a different destabilition mechanism. For instance, each jet impinges a wall at an angle, not frontally. Does this orientation affect the stability characteristics ? And if so, how ? Is destabilisation still triggered by the effects of a single impingement, or is it instead driven by interactions between multiple impingements occurring on a same wall ? And finally, is the observed unsteady state a trace of the primary bifurcation, or instead overshadows it ? Although this experimental study does not answer these questions, it still provides a measure of the characteristic frequencies that may be used to fine-tune the flow for a targeted application, or to benchmark a numerical model to study the flow stability.

Thèse accessible à l'adresse : https://theses.insa-lyon.fr/publication/2024ISAL0101/these.pdf © [B. Vincent], [2024], INSA Lyon, tous droits réservés

Conclusion and outlook

In this thesis, I presented several studies devoted to acoustic streaming flows forced by an ultrasonic beam, with or without acoustic reflections. Each of these studies aimed at gaining a better understanding of streaming jets, with the long-term objective of using such flows to improve solidification processes in the semiconductors industry. I relied on complementary and high-end numerical and experimental approaches to answer the three questions set out in the introduction:

(i) The evolution of the streaming jet velocity along its axis can be split into separate regimes. Near the source and for sufficiently large forcing magnitudes, the jet acceleration results from a balance between the acoustic and inertia forces. After reaching a peak velocity, the jet decelerates smoothly as a result of the acoustic forcing being balanced by the viscous forces. At distances from the source large than the acoustic attenuation length of the sound waves, the forcing is marginal and the jet thus obeys a balance between inertia and viscous forces.

(ii) The stability study shed light on the role of the jet impingement on the flow stability. For weakly-confined settings, the destabilisation is rooted in the shear flow along the impinged wall and around the stagnation point of the jet. In that case, the leading unstable mode is non-oscillatory. Besides of stabilising the flow, changing the radial cavity size modifies the topology and type of the unstable mode, which becomes oscillatory for the most confined settings. Furthermore, radially confining the flow shifts the origin of destabilisation from the impinged wall to a shear layer between the jet and the recirculating cells resulting from its impingement. A nonlinear analysis showed that the primary bifurcations identified for each geometry are either sub- or supercritical.

(iii) Finally, I showed that a single ultrasound beam can be reflected several times inside a closed cavity to create a helix-shaped forcing field, hence to drive a 3D streaming flow suitable for stirring purposes. That flow is made of several jets, each forced by the reflected beam and impinging the cavity wall. High-end PTV measurements allowed me to map and characterise the flow, and to identify the leading frequencies associated with the development of flow unsteadiness as the forcing magnitude is increased.

Although these studies focused on different streaming configurations (either a single straight jet forced by a single beam or a 3D flow forced by beam reflections), they nevertheless remain complementary and have direct implications for the use of acoustic streaming in solidification processes.

First, the scaling laws for the on-axis velocity of a single jet were also verified by the jets of the 3D helical streaming flow. Therefore, these scaling laws could be used for instance to match the presumed point of maximum streaming velocity with the jet impingement. Doing so would help maximising the overall velocity levels for a given forcing magnitude. From a process standpoint, this is desirable e.g. to enhance shear at

Thèse accessible à l'adresse : https://theses.insa-lyon.fr/publication/2024ISAL0101/these.pdf © [B. Vincent], [2024], INSA Lyon, tous droits réservés

the walls and the liquid/solid interface, or to promote mixing in the melt.

Second, if a single jet directed towards the liquid/solid interface is used to act on the melt, a possible flow destabilisation could be detected by monitoring flow velocity near the interface. Besides, the reduction of the melt volume during its solidification would have a stabilising effect, allowing to increase the streaming velocity levels whilst keeping the flow stable. For these outcomes to remain valid, the flow destabilisation mechanisms should nevertheless not be overshadowed by other effects such as temperature gradients for instance. On a more general note, these single-jet stability results also help at better understanding more complex streaming flows. For instance, the experimentally-studied 3D flow features multiple jets; their respective impingements may play a key role on the observed unsteadiness development.

The different findings presented in this thesis call for further short-and long-term studies. For example, my stability work on the single-jet setting could be extended using receptivity/sensitivity analysis to design effective control strategies. Another example relates to the 3D streaming flow forced by a helical forcing field. Although my experimental work allowed to draw a clear picture of the flow structure and to identify design guidelines, it also raised several questions: how does the pitch of the helical forcing affect the flow ? Is there an optimum set of design parameters for which the mixing is the most effective ? Regarding the stability of that flow, does the jet impingement angle affect the onset of unsteadiness ? Does the observed unsteady flow result from a primary bifurcation ? A secondary bifurcation ? Besides, is that flow representative of the perturbation that initiated the transition towards that unsteady state ? Dedicated studies should be carried out to answer thoroughly all these questions. Finally, at a more fundamental level, it would be interesting to go deeper in the analysis of the energy exchanges between the acoustic waves and the streaming flow. This would allow to clearly determine the theoretical conditions (in terms of suitable dimensionless numbers) for which a given transfer mechanism is dominant.

Thèse accessible à l'adresse : https://theses.insa-lyon.fr/publication/2024ISAL0101/these.pdf © [B. Vincent], [2024], INSA Lyon, tous droits réservés

Bibliography

Abramowitz, M. & Stegun, I. A. 1972 *Handbook of Mathematical Functions with Formulas, Graphs and Mathematical Tables*. Dover Publications. 20

Absar, S., Pasumarthi, P. & Choi, H. 2017 Numerical and experimental studies about the effect of acoustic streaming on ultrasonic processing of metal matrix nanocomposites (MMNCs). *J. Manuf. Process.* **28**, 515–522. 2

Bakker, P. G. 1991 *Bifurcations in Flow Patterns*, , vol. 2. Springer Netherlands. 74

Barkley, D., Blackburn, H. M. & Sherwin, S. J. 2008 Direct optimal growth analysis for timesteppers. *Intl J. Numer. Meth. Fluids* **57**, 1435–1458. 73, 76

Batchelor, G. K. 2000 *An Introduction to Fluid Dynamics*. Cambridge University Press. 12

Batchelor, G. K. & Gill, A. E. 1962 Analysis of the stability of axisymmetric jets. *J. Fluid Mech.* **14**, 529. 73

Baudoin, M. & Thomas, J.-L. 2019 Acoustic tweezers for particle and fluid micromanipulation. *Annu. Rev. Fluid Mech.* **52**, 10. 1, 113

Ben Hadid, H., Dridi, W., Botton, V., Moudjed, B. & Henry, D. 2012 Instabilities in the Rayleigh-Bénard-Eckart problem. *Phys. Rev. E* **86**, 016312. XVII, 31, 32

Ben Haj Slama, R., Gilles, B., Ben Chiekh, M. & Béra, J.-C. 2017 PIV for the characterization of focused field induced acoustic streaming: seeding particle choice evaluation. *Ultrasonics* **76**, 217–226. 113

Blackburn, H.M., Lee, D., Albrecht, T. & Singh, J. 2019 Semtex: a spectral element–Fourier solver for the incompressible Navier–Stokes equations in cylindrical or cartesian coordinates. *Comput. Phys. Commun.* **245**, 106804. XXXII, 53, 54, 55, 172, 173, 174

Blackburn, H.M. & Sherwin, S.J. 2004 Formulation of a Galerkin spectral element–Fourier method for three-dimensional incompressible flows in cylindrical geometries. *J. Comput. Phys.* **197**, 759–778. 53, 54, 73

Blackstock, D.T. 2000 *Fundamentals of Physical Acoustics*. John Wiley & Sons, Inc. XXXVII, 7, 8, 11, 18, 20, 36, 47

Bordes, G., Venaille, A., Joubaud, S., Odier, P. & Dauxois, T. 2012 Experimental observation of a strong mean flow induced by internal gravity waves. *Phys. Fluids* **24**, 086602. 70

Thèse accessible à l'adresse : https://theses.insa-lyon.fr/publication/2024ISAL0101/these.pdf © [B. Vincent], [2024], INSA Lyon, tous droits réservés

Busnaina, A. A. & Elsawy, T. M. 1998 Post-CMP cleaning using acoustic streaming. *J. Electron. Mat.* **27**, 1095–1098. 49, 70

Cablea, M., Zaidat, K., Gagnoud, A., Nouri, A., Chichignoud, G. & Delannoy, Y. 2015 Multi-crystalline silicon solidification under controlled forced convection. *J. Cryst. Growth* **417**, 44–50. 1

Cablea, M., Zaidat, K., Gagnoud, A., Nouri, A. & Delannoy, Y. 2014 Directional solidification of silicon under the influence of travelling magnetic field. *J. Cryst. Growth* **401**, 883–887. 1

Cambonie, T., Moudjed, B., Botton, V., Henry, D. & Ben Hadid, H. 2017 From flying wheel to square flow: Dynamics of a flow driven by acoustic forcing. *Phys. Rev. Fluids* **2**, 123901. XV, XXVI, XXVII, 5, 6, 29, 33, 115, 116, 117, 120, 121, 122, 123, 128, 147, 152

Camobreco, C. J., Pothérat, A. & Sheard, G. J. 2023 Subcritical transition to turbulence in quasi-two-dimensional shear flows. *J. Fluid Mech.* **963**, R3. 102

Canuto, C., Hussaini, M. Y., Quarteroni, A. & Zang, T. A. 2006 *Spectral Methods: Fundamentals in Single Domains*. Springer Berlin Heidelberg. 53

Carmo, B. S., Sherwin, S. J., Bearman, P. W. & Willden, R. H. J. 2008 Wake transition in the flow around two circular cylinders in staggered arrangements. *J. Fluid Mech.* **597**, 1–29. 94

Chakraborty, P., Balachandar, S. & Adrian, R. J. 2005 On the relationships between local vortex identification schemes. *J. Fluid Mech.* **535**, 189–214. XXIX, 133

Charrier-Mojtabi, M-C., Fontaine, A. & Mojtabi, A. 2012 Influence of acoustic streaming on thermo-diffusion in a binary mixture under microgravity. *Intl. J. Heat Mass Transfer* **55**, 5992–5999. 31

Charrier-Mojtabi, M-C., Jacob, X., Dochy, T. & Mojtabi, A. 2019 Species separation of a binary mixture under acoustic streaming. *Eur. Phys. J. E* **42**, 64. 31

Chassaing, P., Antonia, R. A., Anselmet, F., Joly, L. & Sarkar, S. 2002 *Variable Density Fluid Turbulence*, , vol. 69. Springer Netherlands. XVIII, 13, 15, 35, 45, 46

Chatelain, M., Botton, V., Albaric, M., Pelletier, D., Cariteau, B., Abdo, D. & Borrelli, M. 2018 Mechanical stirring influence on solute segregation during plane front directional solidification. *Intl. J. Therm. Sci.* **126**, 252–262. 1

Chladni, E. 1787 *Entdeckungen ueber die Theorie des Klanges*. Leipzig: Bey Weidmanns Erben und Reich. 3

Chong, M. S., Perry, A. E. & Cantwell, B. J. 1990 A general classification of three-dimensional flow fields. *Phys. Fluids A* **2**, 765–777. 143

Cleve, S., Guédra, M., Mauger, C., Inserra, C. & Blanc-Benon, P. 2019 Microstreaming induced by acoustically trapped, non-spherically oscillating microbubbles. *J. Fluid Mech.* **875**, 597–621. 1

Thèse accessible à l'adresse : https://theses.insa-lyon.fr/publication/2024ISAL0101/these.pdf © [B. Vincent], [2024], INSA Lyon, tous droits réservés

Clune, T. & Knobloch, E. 1993 Pattern selection in rotating convection with experimental boundary conditions. *Phys. Rev. E* **47**, 2536–2550. 88

Coulouvrat, F. 1992 On the equations of nonlinear acoustics. *J. Acoust.* **5**, 321–359. 8, 16, 25, 46

Daru, V., Vincent, B. & Baudoin, M. 2024 High-speed and acceleration micrometric jets induced by GHz streaming: A numerical study with direct numerical simulations. *J. Acoust. Soc. Am.* **155**. XVII, 27, 30, 49

Dauxois, T., Joubaud, S., Odier, P. & Venaille, A. 2018 Instabilities of internal gravity wave beams. *Annu. Rev. Fluid Mech.* **50**, 131–156. 70

Delannoy, Y. 2012 Purification of silicon for photovoltaic applications. *J. Cryst. Growth* **360**, 61–67. 1

Dentry, M. B., Yeo, L. Y. & Friend, J. R. 2014 Frequency effects on the scale and behavior of acoustic streaming. *Phys. Rev. E* **89**, 013203. XVI, XVII, XX, XXXVIII, 26, 27, 29, 30, 49, 65, 166, 167

Dinçer, I. & Zamfirescu, C. 2015 *Drying Phenomena: Theory and Applications*. John Wiley & Sons, Ltd. XXXVII, XXXVIII, 9, 11, 126, 127

Doinikov, A. A., Regnault, G., Mauger, C., Blanc-Benon, P. & Inserra, C. 2022 Acoustic microstreaming produced by two interacting gas bubbles undergoing axisymmetric shape oscillations. *J. Fluid Mech.* **931**, A19. 1

Dridi, W., Henry, D. & Ben Hadid, H. 2007 Influence de l'acoustic streaming sur la stabilité d'une couche de fluide isotherme ou chauffée latéralement. *C. R. - Mec.* **335**, 175–180. 30

Dridi, W., Henry, D. & Ben Hadid, H. 2008*a* Influence of acoustic streaming on the stability of a laterally heated three-dimensional cavity. *Phys. Rev. E* **77**, 046311. 31

Dridi, W., Henry, D. & Ben Hadid, H. 2008*b* Influence of acoustic streaming on the stability of melt flows in horizontal Bridgman configurations. *J. Cryst. Growth* **310**, 1546–1551. 30

Dridi, W., Henry, D. & Hadid, H. Ben 2010 Stability of buoyant convection in a layer submitted to acoustic streaming. *Phys. Rev. E* **81**, 056309. XVII, 30, 32

Dubrovski, O., Friend, J. & Manor, O. 2023 Theory of acoustic streaming for arbitrary Reynolds number flow. *J. Fluid Mech.* **975**, A4. XXXVII, 16, 25

Dupuy, D., Toutant, A. & Bataille, F. 2018 Equations of energy exchanges in variable density turbulent flows. *Phys. Lett. A* **382**, 327–333. VI, VII, XVIII, 35, 44, 46, 47

Délery, J. M. 2001 Robert Legendre and Henri Werlé: Toward the elucidation of three-dimensional separation. *Ann. Rev. Fluid Mech.* **33**, 129–154. 85

Eckart, C. 1948 Vortices and streams caused by sound waves. *Phys. Rev.* **73**, 68–76. 3, 11

Thèse accessible à l'adresse : https://theses.insa-lyon.fr/publication/2024ISAL0101/these.pdf © [B. Vincent], [2024], INSA Lyon, tous droits réservés

El Ghani, N. 2020 Modélisation expérimentale du transfert de masse en croissance cristalline par des méthodes électrochimiques en présence d'ultrasons. PhD thesis, Université de Lyon. XXV, XXXVII, 9, 105, 106

El Ghani, N., Miralles, S., Botton, V., Henry, D., Ben Hadid, H., Ter-Ovanessian, B. & Marcelin, S. 2021 Acoustic streaming enhanced mass transfer at a wall. *Intl. J. Heat Mass Transfer* **172**. 24, 49, 70

Faraday, M. 1831 On a peculiar class of acoustical figures; and on certain forms assumed by groups of particles upon vibrating elastic surfaces. *Philos. Trans. R. Soc. London* **121**, 299–340. 3

Farrashkhalvat, M & Miles, J 2003 *Basic Structured Grid Generation with an introduction to unstructured grid generation*. Butterworth Heinemann. 54

Fauconnier, M., Mauger, C., Béra, J-C. & Inserra, C. 2022 Nonspherical dynamics and microstreaming of a wall-attached microbubble. *J. Fluid Mech.* **935**, A22. 1

Favre, A. J. 1958 Equations statistiques des gaz turbulents. *C.-R. Ac. Sci. Paris* **248**, 2576–3219. 15

Foss, J. F. 2004 Surface selections and topological constraint evaluations for flow field analyses. *Exp. Fluids* **37**, 883–898. VII, 74, 75

Frenkel, V., Gurka, R., Liberzon, A., Shavit, U. & Kimmel, E. 2001 Preliminary investigations of ultrasound induced acoustic streaming using particle image velocimetry. *Ultrasonics* **39**, 153–156. XVI, XX, 27, 49, 64, 166, 167

Friend, J. & Yeo, L. Y. 2011 Microscale acoustofluidics: microfluidics driven via acoustics and ultrasonics. *Rev. Mod. Phys.* **83**, 647–704. 1

Gao, D., Li, Z., Han, Q. & Zhai, Q. 2009 Effect of ultrasonic power on microstructure and mechanical properties of AZ91 alloy. *Mater. Sci. Eng. A* **502** (1), 2–5. 2

Giovannini, A. & Airiau, C. 2016 *Aérodynamique fondamentale*. Cépaduès Editions. 6, 7, 35, 45

Green, A., Marshall, J. S., Ma, D. & Wu, J. 2016 Acoustic streaming and thermal instability of flow generated by ultrasound in a cylindrical container. *Phys. Fluids* **28**, 104105. 28, 29

Greenspan, . 1979 Piston radiator: some extensions of the theory. *J. Acoust. Soc. Am.* **65**, 608–621. XV, XVIII, 19, 39, 41

Grisouard, N., Leclair, M., Gostiaux, L. & Staquet, C. 2013 Large scale energy transfer from an internal gravity wave reflecting on a simple slope. *Procedia IUTAM* **8**, 119–128. 70

Hagsäter, S. M., Glasdam Jensen, T., Bruus, H. & Kutter, J. P. 2007 Acoustic resonances in microfluidic chips: full-image micro-PIV experiments and numerical simulations. *Lab Chip* **7**. 1

Thèse accessible à l'adresse : https://theses.insa-lyon.fr/publication/2024ISAL0101/these.pdf © [B. Vincent], [2024], INSA Lyon, tous droits réservés

Henderson, R. D. 1997 Nonlinear dynamics and pattern formation in turbulent wake transition. *J. Fluid Mech.* **352**, 65–112. 94

Henderson, R. D. & Barkley, D. 1996 Secondary instability in the wake of a circular cylinder. *Phys. Fluids* **8**, 1683–1685. 94

Henry, D., Vincent, B., Miralles, S., Botton, V. & Hadid, H. Ben 2022 Steady and oscillatory flows generated by Eckart streaming in the two-dimensional Rayleigh–Bénard configuration. *J. Fluid Mech.* **952**, A28. XVII, 31, 32, 86

Hunt, J.C.R, Wray, A.A & Moin, P. 1988 Eddies, streams, and convergence zones in turbulent flows. In *Center for Turbulence Research, Proceedings of the Summer Program*, pp. 193–208. XXIX, 133

Hunt, J. C. R., Abell, C. J., Peterka, J. A. & Woo, H. 1978 Kinematical studies of the flows around free or surface-mounted obstacles; applying topology to flow visualization. *J. Fluid Mech.* **86**, 179–200. VII, 74

IMASONIC SAS 2011 *Rapport de mesure: Transducteur monoélément 2 MHz*. XXXVIII, 127

Jian, X., Meek, T.T. & Han, Q. 2006 Refinement of eutectic silicon phase of aluminum A356 alloy using high-intensity ultrasonic vibration. *Scripta Mater.* **54** (5), 893–896. 2

Joergensen, J. H. & Bruus, H. 2023 Theory and modeling of nonperturbative effects in thermoviscous acoustofluidics. *Phys. Rev. E* **107**, 015106. 16

Kamakura, T., Matsuda, K., Kumamoto, Y. & Breazeale, M. A. 1995 Acoustic streaming induced in focused gaussian beams. *J. Acoust. Soc. Am.* **97**, 2740–2746. 15, 49

Kamakura, T., Sudo, T., Matsuda, K. & Kumamoto, Y. 1996 Time evolution of acoustic streaming from a planar ultrasound source. *J. Acoust. Soc. Am.* **100**, 132–138. XVI, XX, 24, 26, 27, 28, 64, 166, 167

Karniadakis, G. E., Israeli, M. & Orszag, S. A. 1991 High-order splitting methods for the incompressible Navier-Stokes equations. *J. Comput. Phys.* **97**, 414–443. XXXVII, 51, 52, 76

Karniadakis, G. E. & Sherwin, S. J. 2005 *Spectral/hp Element Methods for Computational Fluid Dynamics*, 2nd edn. Oxford University Press. 53

Khorrami, M. R., Malik, M. R. & Ash, R. L. 1989 Application of spectral collocation techniques to the stability of swirling flows. *J. Comput. Phys.* **81**, 206–229. 73

Kinsler, L. E., Frey, A. R., Coppens, A. B. & Sanders, J. V. 2000 *Fundamentals of Acoustics*, 4th edn. John Wiley & Sons, Inc. XXV, 7, 18, 36, 47, 104, 126

Kozhemyakin, G.N. 2003 Imaging of convection in a Czochralski crucible under ultrasound waves. *J. Cryst. Growth* **257** (3), 237–244. 2

Kumar, A. & Pothérat, A. 2020 Mixed baroclinic convection in a cavity. *J. Fluid Mech.* **885**, A40. 95

Thèse accessible à l'adresse : https://theses.insa-lyon.fr/publication/2024ISAL0101/these.pdf © [B. Vincent], [2024], INSA Lyon, tous droits réservés

Landau, L. D. & Lifschitz, E. M. 1987 *Fluid Mechanics*, 2nd edn. Pergamon Books Ltd. 76, 94

Launay, G., Cambonie, T., Henry, D., Pothérat, A. & Botton, V. 2019 Transition to chaos in an acoustically driven cavity flow. *Phys. Rev. Fluids* **4**, 044401. XV, XXVI, 5, 6, 29, 115, 116, 148

Lebon, G., Salloum-Abou-Jaoude, G., Eskin, D., Tzanakis, I., Pericleous, K. & Jarry, P. 2019 Numerical modelling of acoustic streaming during the ultrasonic melt treatment of direct-chill (DC) casting. *Ultrason. Sonochem.* **54**, 171–182. 2

Lighthill, J. 1978 Acoustic streaming. *J. Sound Vib.* **61**, 391–418. 12, 13, 16, 57, 59, 69

Lighthill, J. 1988 Boundary layer theory. In *Laminar Boundary Layers* (ed. L. Rosenhead), pp. 72 – 82. Dover Publications, Inc. 74

Liu, X., Osawa, Y., Takamori, S. & Mukai, T. 2008 Microstructure and mechanical properties of AZ91 alloy produced with ultrasonic vibration. *Mater. Sci. Eng. A* **487** (1), 120–123. 2

Luo, X., Cao, J., Gong, H., Yan, H. & He, L. 2018 Phase separation technology based on ultrasonic standing waves: A review. *Ultrason. Sonochem.* **48**, 287–298. XV, 4

Lyubimova, T. P. & Skuridin, R. V. 2019 The effect of acoustic wave on the stability of stationary convective flow of binary fluid in a horizontal layer subjected to horizontal temperature and concentration gradients. *Intl. J. Heat Mass Transfer* **132**, 789–801. 31

Michel, G. & Chini, G. P. 2019 Strong wave–mean-flow coupling in baroclinic acoustic streaming. *J. Fluid Mech.* **858**, 536–564. XXXVII, 16, 25

Miralles, S., Albaric, M., Brizé, V., Guy, P., Vincent, B., Garandet, J.-P, Willemetz, J.-C., Henry, D. & Botton, V. 2023 In situ ultrasonic interface tracking for photovoltaic silicon directional solidification. *J. Cryst. Growth* **621**, 127362. 1

Mitome, H. 1998 The mechanism of generation of acoustic streaming. *Electron. Commun. Japan* **81**. XVI, XX, 15, 24, 27, 49, 64, 166, 167

Mitome, H., Kozuka, T. & Tuziuti, T. Tuziuti Toru 1995 Effects of nonlinearity in development of acoustic streaming. *Jap. J. Appl. Phys.* **34**, 2584. 24, 70

Moffatt, H. K. 1964 Viscous and resistive eddies near a sharp corner. *J. Fluid Mech.* **18**, 1–18. 79

Moffatt, H. K. 2018 Helicity. *C. R. Méca.* **346**, 165–169. 135

Mondal, R. & Mahbub Alam, Md. 2023 Blockage effect on wakes of various bluff bodies: A review of confined flow. *Ocean Eng.* **286**, 115592. 82

Thèse accessible à l'adresse : https://theses.insa-lyon.fr/publication/2024ISAL0101/these.pdf © [B. Vincent], [2024], INSA Lyon, tous droits réservés

Moudjed, B. 2013 Caractérisation expérimentale et théorique des écoulements entraînés par ultrasons. Perspectives d'utilisation dans les procédés de solidification du Silicium Photovoltaïque. PhD thesis, INSA de Lyon. XV, XVI, 4, 5, 21, 22, 26, 29, 51, 107

Moudjed, B., Botton, V., Henry, D., Ben Hadid, H. & Garandet, J.-P. 2014*a* Scaling and dimensional analysis of acoustic streaming jets. *Phys. Fluids* **26**, 093602. VI, VII, XV, XVI, XVII, XVIII, XX, XXXVII, XXXVIII, 5, 9, 14, 19, 21, 22, 23, 24, 25, 26, 27, 28, 31, 35, 39, 40, 41, 42, 43, 46, 47, 49, 50, 51, 61, 62, 64, 66, 70, 72, 102, 110, 113, 126, 166, 167

Moudjed, B., Botton, V., Henry, D., Millet, S. & Ben Hadid, H. 2016 Y-shaped jets driven by an ultrasonic beam reflecting on a wall. *Ultrasonics* **68**, 33–42. 127

Moudjed, B., Botton, V., Henry, D., Millet, S., Garandet, J.-P. & Ben Hadid, H. 2014*b* Oscillating acoustic streaming jet. *Appl. Phys. Lett.* **105**. XVII, 29, 31

Moudjed, B., Botton, V., Henry, D., Millet, S., Garandet, J.-P. & Ben Hadid, H. 2015 Near-field acoustic streaming jet. *Phys. Rev. E* **91**, 033011. XVI, XXI, XXXII, XXXVIII, XXXIX, 19, 26, 28, 51, 61, 68, 69, 130, 167, 172, 173, 174, 175

Muller, P. B. & Bruus, H. 2015 Theoretical study of time-dependent, ultrasound-induced acoustic streaming in microchannels. *Phys. Rev. E* **92**, 063018. 1

Nyborg, W. L. 1953 Acoustic streaming due to attenuated plane waves. *J. Acoust. Soc. Am.* **25**, 68–75. XVII, 11, 12, 13, 28, 30, 32

Orosco, J. & Friend, J. 2022 Modeling fast acoustic streaming: steady-state and transient flow solutions. *Phys. Rev. E* **106**, 045101. XVII, XXXVII, 16, 24, 25, 27, 30, 49, 70

Perry, A.E. & Fairlie, B.D. 1975 *Critical Points in Flow Patterns*, , vol. 18, pp. 299–315. 74

Pierce, A. D. 1981 *Acoustics : an introduction to its physical principles and applications*. McGraw-Hill Book Co. 9

Pätzold, O., Niemietz, K., Lantzsch, R., Galindo, V., Grants, I., Bellmann, M. & Gerbeth, G. 2013 The use of magnetic fields in vertical Bridgman/Gradient Freeze-type crystal growth. *Eur. Phys. J. Spec. Top.* **220**, 243–257. 1

Qu, J., Henry, D., Miralles, S., Botton, V. & Raynal, F. 2022 Chaotic mixing in an acoustically driven cavity flow. *Phys. Rev. Fluids* **7**, 064501. 29

Raffel, M., Willert, C. E., Scarano, F., Kähler, C. J., Wereley, S. T. & Kompenhans, J. 2018 *Particle Image Velocimetry*. Springer International Publishing. 113

Rayleigh, L. 1884 On the circulation of air observed in Kundt's tubes , and on some allied acoustical problems. *Phil. Trans. R. Soc. London* **175**, 1–21. 3

Thèse accessible à l'adresse : https://theses.insa-lyon.fr/publication/2024ISAL0101/these.pdf © [B. Vincent], [2024], INSA Lyon, tous droits réservés

Riaud, A., Baudoin, M., Bou Matar, O., Thomas, J-L. & Brunet, P. 2017 On the influence of viscosity and caustics on acoustic streaming in sessile droplets: an experimental and a numerical study with a cost-effective method. *J. Fluid Mech.* **821**, 384–420. 1, 11, 12, 25, 28

Riley, N. 2001 Steady streaming. *Annu. Rev. Fluid Mech.* **33**, 43–65. XXXVII, 25

Rudenko, O.V & Sukhorukov, A.A. 1998 Nonstationary Eckart Streaming and Pumping of Liquid in an Ultrasonic Field. *Acoust. Phys.* **44**, 565–570. 30, 81

Rudenko, O. V. & Soluyan, S. I. 1977 *Theoretical Foundations of Nonlinear Acoustics*. Springer US. XXXVII, 7, 15, 25

Sapardi, A. M., Hussam, W. K., Pothérat, A. & Sheard, G. J. 2017 Linear stability of confined flow around a 180-degree sharp bend. *J. Fluid Mech.* **822**, 813–847. 95

Savchenko, A. Yu., Tabiryan, N. V. & Zel'dovich, B. Ya. 1997 Transfer of momentum and torque from a light beam to a liquid. *Phys. Rev. E* **56**, 4773–4779. 70

Schanz, D., Gesemann, S. & Schröder, A. 2016 Shake-the-box: Lagrangian particle tracking at high particle image densities. *Exp. Fluids* **57**. 112

Schlichting, H. 1932 Berechnung ebner periodischer Grenzschichtstroemungen. *Phys. Z* **33**, 327–335. 3

Schlichting, H. & Gersten, K. 2000 *Boundary-Layer Theory*, 8th edn. Springer Berlin Heidelberg. VII, XXI, 67, 68, 70

Schmid, P. J. 2007 Nonmodal stability theory. *Ann. Rev. Fluid Mech.* **39**, 129–162. 98, 101

Schneiders, J.F.G. & Scarano, F. 2016 Dense velocity reconstruction from tomographic PTV with material derivatives. *Exp. Fluids* **57**. 111, 112

Schröder, A. & Schanz, D. 2023 3D Lagrangian Particle Tracking in Fluid Mechanics. *Ann. Rev. Fluid Mech.* **55**, 511–540. XXVI, 112

Sheard, G. J., Thompson, M. C. & Hourigan, K. 2004 From spheres to circular cylinders: non-axisymmetric transitions in the flow past rings. *J. Fluid Mech.* **506**, 45–78. 76, 94, 95

Sherwin, S. J. & Blackburn, H. M. 2005 Three-dimensional instabilities and transition of steady and pulsatile axisymmetric stenotic flows. *J. Fluid Mech.* **533**, 297–327. 95

Shneider, M. N. & Semak, V. V. 2016 Ponderomotive convection in water induced by a CW laser. *J. Appl. Phys.* **120**, 244902. 70

Statnikov, Y. G. 1967 Flow currents generated by finite amplitude sound. *Akust. Zh.* **13**, 146–148. 13, 14, 168

Thompson, M.C., Leweke, T. & Provansal, M. 2001 Kinematics and dynamics of sphere wake transition. *J. Fluids Struct.* **15**, 575–585. 94, 95

Thèse accessible à l'adresse : https://theses.insa-lyon.fr/publication/2024ISAL0101/these.pdf © [B. Vincent], [2024], INSA Lyon, tous droits réservés

Tropea, C., Yarin, A. L. & Foss, J. F. 2007 *Springer Handbook of Experimental Fluid Mechanics*. Springer Berlin Heidelberg. 113

Trumbore, F. A. 1960 Solid solubilities of impurity elements in germanium and silicon. *Bell Syst. Tech. J.* **39** (1), 205–233. 1

Vincent, B., Miralles, S., Henry, D., Botton, V. & Pothérat, A. 2024 Experimental study of a helical acoustic streaming flow. *Phys. Rev. Fluids* **9**, 024101. XXVIII, 103, 124

Westervelt, P. 1953 The theory of steady rotational flow generated by a sound field. *J. Acoust. Soc. Am.* **25**, 60–67. 11

Wunenburger, R., Issenmann, B., Brasselet, E., Loussert, C., Hourtane, V. & Delville, J.-P. 2011 Fluid flows driven by light scattering. *J. Fluid Mech.* **666**, 273–307. 70

Zarembo, L. K. 1971 Acoustic streaming. In *High-Intensity Ultrasonic Fields* (ed. L. Rozenberg), chap. 3, pp. 137 – 199. Springer Science. 13, 14, 28, 168

Thèse accessible à l'adresse : https://theses.insa-lyon.fr/publication/2024ISAL0101/these.pdf © [B. Vincent], [2024], INSA Lyon, tous droits réservés

Thèse accessible à l'adresse : https://theses.insa-lyon.fr/publication/2024ISAL0101/these.pdf © [B. Vincent], [2024], INSA Lyon, tous droits réservés

Appendix A

Streaming experiments from the literature: experimental conditions and corresponding dimensionless numbers

Numerous experiments from the literature are mentioned in chapters 1 and 3, especially to illustrate the accuracy of scalng laws for the streaming velocity. The conditions and parameters of these experiments are listed in table A.1, and the corresponding dimensionless numbers (1.58) are given in table A.2.

Thèse accessible à l'adresse : https://theses.insa-lyon.fr/publication/2024ISAL0101/these.pdf © [B. Vincent], [2024], INSA Lyon, tous droits réservés

Table A.1: List of different streaming experiments, including the operating conditions and observed flow velocities. All the experiments were made in water using a plane circular transducer, except Dentry *et al.* (2014) who investigated a streaming jet forced by a SAW (Surface Acoustic Wave) device (source of rectangular cross section, with its height varying with the frequency f).

	Kamakura *et al.* (1996)	Mitome (1998) (two setups)	Frenkel *et al.* (2001)	Moudjed *et al.* (2014*a*)	Dentry *et al.* (2014) (six setups)
Parallelepiped cavity size (length × width × height) (cm)	Cylindrical cavity (length = 27 cm, diameter = 8.6 cm)	$60 \times 30 \times 36$	$14 \times 25 \times 17$	$47 \times 18 \times 16$	$7.5 \times 2.5 \times 2.5$
Transducer diameter D_s (cm)	1.8	1.0 (setup 1), 2.5 (setup 2)	2.5	2.85	Width = 0.33 cm ($f \leq$ 490 MHz) or 0.17 cm (f = 936 MHz), height $\in [0.6, 0.01]$ cm
Density ρ (kg/m^3)	1000	998.2	998.2	998.2	998.0
Dynamic viscosity (Pa.s)	10^{-3}	10^{-3}	10^{-3}	10^{-3}	10^{-3}
Frequency f (MHz)	5	5.05 (setup 1), 5.33 (setup 2)	3	2	$[19.7, 936.0]$
Speed of sound c (m/s)	1491	1480	1480	1480	1498
Fresnel distance L_F (cm)	27.2	8.5 (setup 1), 56.3 (setup 2)	31.7	27.4	$[0.2, 11.7]$
Attenuation coefficient α (m^{-1})	0.65	0.67 (setup 1), 0.75 (setup 2)	0.24	0.11	$[8.3, 1.9 \times 10^4]$
Measurement range from the source (cm)	$[0, 27]$	$[0, 20]$	~ 3	$[27.4, 82.3]$	$[0, 1]$
Acoustic power $P_{ac,0}$ range (W)	0.68	$[0.012, 1.2]$ (setup 1), $[0.0042, 1.7]$ (setup 2)	$[2, 10]$	$[0.7, 5.6]$	$[1.8 \times 10^{-5}, 0.7]$
Acoustic velocity u_0 on the source (cm/s)	6.0	$[1.4, 14.4]$ (setup 1), $[0.34, 6.8]$ (setup 2)	$[7.4, 16.6]$	$[3.9, 10.9]$	$[0.4, 52]$
Maximum streaming velocity U_s (cm/s)	~ 3.5	$\sim$ 7 (setup 1), $\sim$ 2 (setup 2)	~ 2.5	~ 5	Up to 30

Thèse accessible à l'adresse : https://theses.insa-lyon.fr/publication/2024ISAL0101/these.pdf © [B. Vincent], [2024], INSA Lyon, tous droits réservés

Table A.2: Experimental conditions of the works listed in table A.1 expressed using the dimensionless numbers introduced by Moudjed *et al.* (2015), who initially considered an experiment of square cross section. To ease the comparison with other experiments, I considered the hydraulic diameter instead. For Dentry *et al.* (2014), the source height varies with the frequency; that height is taken as characteristic length scale.

	Kamakura *et al.* (1996)	Mitome (1998) (setup 1)	Mitome (1998) (setup 2)	Frenkel *et al.* (2001)	Moudjed *et al.* (2014*a*)	Dentry *et al.* (2014) (six setups)
L	15.0	60	24	5.6	16.5	$[12.6, 656.5]$
D	4.8	45.0	18.0	8.1	8.1	$[4.2, 218.8]$
S	0.020	0.036	0.014	0.024	0.032	$[0.015, 0.017]$
F	16.2×10^8	5.0×10^8	33.3×10^8	18.7×10^8	16.2×10^8	$[0.1, 7.0] \times 10^8$
N	0.17	0.40	0.45	0.033	0.050	$[0.6, 1442.3]$
P	1.2×10^{13}	$[0.01, 1.2] \times 10^{13}$	$[0.010, 4.1] \times 10^{13}$	$[5.0, 24.9] \times 10^{13}$	$[2.0, 15.9] \times 10^{13}$	$[1.7 \times 10^{-6}, 0.5] \times 10^{13}$
Gr_{ac}	5.4×10^4	$[0.056, 5.6] \times 10^4$	$[0.05, 21.4] \times 10^4$	$[8.2, 40.9] \times 10^4$	$[1.4, 11.6] \times 10^4$	$[0.0038, 50.9] \times 10^4$
U	~ 630	~ 700	~ 500	~ 620	~ 1420	Up to ~ 650

Thèse accessible à l'adresse : https://theses.insa-lyon.fr/publication/2024ISAL0101/these.pdf © [B. Vincent], [2024], INSA Lyon, tous droits réservés

Appendix B

Equations governing the energy exchanges in acoustic streaming

In this appendix, I shall derive the energy budget equations given in chapter 2. All derivations are made **in a generic Cartesian coordinate system using Einstein notation, and with dimensional variables**. As in chapter 1, quantities associated to the acoustic fluctuations and the streaming flow are denoted by the subscripts "ac" and "s", respectively.

Obtaining the momentum equations for the streaming flow and the acoustic waves

The first step is to derive the momentum equations for both the streaming flow and the acoustic waves. Following Statnikov (1967) and Zarembo (1971), the compressible Navier-Stokes equations (1.3) are first divided by ρ. The streaming momentum equation (per unit mass) is then obtained by applying the Reynolds decomposition to the flow variables and averaging over an acoustic period:

$$\begin{aligned}\frac{\partial u_{s,i}}{\partial t}+u_{s,j}\frac{\partial u_{s,i}}{\partial x_j}=&-\left\langle\frac{1}{\rho}\frac{\partial p_s}{\partial x_i}\right\rangle-\left\langle\frac{1}{\rho}\frac{\partial p_{ac}}{\partial x_i}\right\rangle+\left\langle\frac{1}{\rho}\frac{\partial \sigma_{s,ij}}{\partial x_j}\right\rangle+\left\langle\frac{1}{\rho}\frac{\partial \sigma_{ac,ij}}{\partial x_j}\right\rangle\\&-\frac{\partial}{\partial x_i}\left\langle\frac{1}{2}u_{ac,j}^2\right\rangle,\end{aligned} \tag{B.1}$$

in which the curl-free property of $\boldsymbol{u_{ac}}$ has been used. Taking the difference between the instantaneous compressible Navier-Stokes equation (1.3) and (B.1) then yields the momentum (per unit mass) equation for the fluctuations:

$$\begin{aligned}\frac{\partial u_{ac,i}}{\partial t}+u_{s,j}\frac{\partial u_{ac,i}}{\partial x_j}+\frac{\partial\left(\frac{1}{2}u_{ac,j}^2\right)}{\partial x_i}+u_{ac,j}\frac{\partial u_{s,i}}{\partial x_j}-\frac{\partial\left\langle\frac{1}{2}u_{ac,j}^2\right\rangle}{\partial x_i}=&-\frac{1}{\rho}\frac{\partial p_s}{\partial x_i}+\left\langle\frac{1}{\rho}\frac{\partial p_s}{\partial x_i}\right\rangle\\&-\frac{1}{\rho}\frac{\partial p_{ac}}{\partial x_i}+\left\langle\frac{1}{\rho}\frac{\partial p_{ac}}{\partial x_i}\right\rangle+\frac{1}{\rho}\frac{\partial \sigma_{s,ij}}{\partial x_j}-\left\langle\frac{1}{\rho}\frac{\partial \sigma_{s,ij}}{\partial x_j}\right\rangle+\frac{1}{\rho}\frac{\partial \sigma_{ac,ij}}{\partial x_j}-\left\langle\frac{1}{\rho}\frac{\partial \sigma_{ac,ij}}{\partial x_j}\right\rangle.\end{aligned} \tag{B.2}$$

Thèse accessible à l'adresse : https://theses.insa-lyon.fr/publication/2024ISAL0101/these.pdf © [B. Vincent], [2024], INSA Lyon, tous droits réservés

Equations for the energy exchanges between the acoustics and streaming scales

As explained in chapter 2, the energy exchanges between the streaming and acoustic scales are fully described by the transport equations for:

- the time-averaged streaming kinetic energy $\left\langle \frac{1}{2}\rho \boldsymbol{u_s}\cdot\boldsymbol{u_s}\right\rangle$,
- the time-averaged acoustic kinetic energy $\left\langle \frac{1}{2}\rho \boldsymbol{u_{ac}}\cdot\boldsymbol{u_{ac}}\right\rangle$,
- the time-averaged mixed kinetic energy $\langle \rho \boldsymbol{u_s}\cdot\boldsymbol{u_{ac}}\rangle$, and
- the time-averaged internal energy $\langle \rho e\rangle$.

In this section, I shall derive each of these equations. The reader shall refer to chapter 2 for the physical interpretation of each term of these equations.

Transport equation for the time-averaged internal energy

The transport equation for $\langle \rho e\rangle$ is obtained by averaging the conservative form of (1.4) over an acoustic period:

$$\begin{aligned}\frac{\partial \langle \rho e\rangle}{\partial t}+\frac{\partial \langle \rho e u_j\rangle}{\partial x_j}=&\overbrace{\frac{\partial}{\partial x_j}\left\langle \kappa\frac{\partial T}{\partial x_j}\right\rangle}^{\Phi_T}\overbrace{-p_s\frac{\partial u_{s,j}}{\partial x_j}}^{\Upsilon_s}\overbrace{-\left\langle p_{ac}\frac{\partial u_{ac,j}}{\partial x_j}\right\rangle}^{\Upsilon_{ac}}\\&+\underbrace{\sigma_{s,ij}\frac{\partial u_{s,i}}{\partial x_j}}_{\varepsilon_s}+\underbrace{\left\langle \sigma_{ac,ij}\frac{\partial u_{ac,i}}{\partial x_j}\right\rangle}_{\varepsilon_{ac}}.\end{aligned}\tag{B.3}$$

Transport equation for the time-averaged streaming kinetic energy

The first step to obtain a transport equation for $\left\langle \frac{1}{2}\rho \boldsymbol{u_s}\cdot\boldsymbol{u_s}\right\rangle$ is to multiply the streaming momentum equation (B.1) by $\rho u_{s,i}$. After some manipulations involving the continuity equation (1.2), one obtains:

$$\begin{aligned}\frac{\partial\left(\frac{1}{2}\rho u_{s,i}^2\right)}{\partial t}+\frac{\partial\left(\frac{1}{2}\rho u_{s,i}^2 u_j\right)}{\partial x_j}=&\rho u_{ac,j}\frac{\partial\left(\frac{1}{2}u_{s,i}^2\right)}{\partial x_j}-\rho u_{s,i}\left\langle\frac{1}{\rho}\frac{\partial p_s}{\partial x_i}\right\rangle-\rho u_{s,i}\left\langle\frac{1}{\rho}\frac{\partial p_{ac}}{\partial x_i}\right\rangle\\&+\rho u_{s,i}\left\langle\frac{1}{\rho}\frac{\partial \sigma_{s,ij}}{\partial x_j}\right\rangle+\rho u_{s,i}\left\langle\frac{1}{\rho}\frac{\partial \sigma_{ac,ij}}{\partial x_j}\right\rangle\\&-\rho u_{s,i}\frac{\partial\left\langle\frac{1}{2}u_{ac,j}^2\right\rangle}{\partial x_i},\end{aligned}$$

which, once averaged over an acoustic period, gives:

$$\begin{aligned}\frac{\partial\left\langle\frac{1}{2}\rho u_{s,i}^2\right\rangle}{\partial t}+\frac{\partial\left\langle\frac{1}{2}\rho u_{s,i}^2 u_j\right\rangle}{\partial x_j}=&\langle\rho_{ac}u_{ac,j}\rangle\frac{\partial\left(\frac{1}{2}u_{s,i}^2\right)}{\partial x_j}-\rho_s u_{s,i}\left\langle\frac{1}{\rho}\frac{\partial p_s}{\partial x_i}\right\rangle-\rho_s u_{s,i}\left\langle\frac{1}{\rho}\frac{\partial p_{ac}}{\partial x_i}\right\rangle\\&+\rho_s u_{s,i}\left\langle\frac{1}{\rho}\frac{\partial \sigma_{s,ij}}{\partial x_j}\right\rangle+\rho_s u_{s,i}\left\langle\frac{1}{\rho}\frac{\partial \sigma_{ac,ij}}{\partial x_j}\right\rangle\\&-\rho_s u_{s,i}\frac{\partial\left\langle\frac{1}{2}u_{ac,j}^2\right\rangle}{\partial x_i}.\end{aligned}\tag{B.4}$$

Thèse accessible à l'adresse : https://theses.insa-lyon.fr/publication/2024ISAL0101/these.pdf © [B. Vincent], [2024], INSA Lyon, tous droits réservés

Then, noting that for pressure for instance (same remarks apply for the viscous stresses):

$$\begin{aligned}
\rho_s u_{s,i} \left\langle \frac{1}{\rho} \frac{\partial p_s}{\partial x_i} \right\rangle &= u_{s,i} \left\langle \frac{\rho_s}{\rho} \frac{\partial p_s}{\partial x_i} \right\rangle \\
&= u_{s,i} \frac{\partial p_s}{\partial x_i} - u_{s,i} \left\langle \frac{\rho_{ac}}{\rho} \frac{\partial p_s}{\partial x_i} \right\rangle \\
&= \frac{\partial \left(p_s u_{s,i} \right)}{\partial x_i} - p_s \frac{\partial u_{s,i}}{\partial x_i} - u_{s,i} \left\langle \frac{\rho_{ac}}{\rho} \frac{\partial \sigma_{ac,ij}}{\partial x_j} \right\rangle \,, \\
\rho_s u_{s,i} \left\langle \frac{1}{\rho} \frac{\partial p_{ac}}{\partial x_i} \right\rangle &= u_{s,i} \left\langle \frac{\rho_s}{\rho} \frac{\partial p_{ac}}{\partial x_i} \right\rangle \\
&= 0 - u_{s,i} \left\langle \frac{\rho_{ac}}{\rho} \frac{\partial p_{ac}}{\partial x_i} \right\rangle \,,
\end{aligned}$$

equation (B.4) can finally be written as:

$$\frac{\partial \left\langle \frac{1}{2} \rho u_{s,i}^2 \right\rangle}{\partial t} + \frac{\partial \left\langle \frac{1}{2} \rho u_{s,i}^2 u_j \right\rangle}{\partial x_j} = \Phi_{p_s} + \Phi_{\sigma_s} + \mathcal{P}_s - \Upsilon_s - \varepsilon_s \,, \tag{B.5}$$

with

$$\Phi_{p_s} = - \frac{\partial \left(p_s u_{s,j} \right)}{\partial x_j} \,, \quad \Phi_{\sigma_s} = \frac{\partial \left(\sigma_{s,ij} \, u_{s,i} \right)}{\partial x_j} \,,$$

and:

$$\begin{aligned}
\mathcal{P}_s = \langle \rho_{ac} u_{ac,j} \rangle \frac{\partial \left(\frac{1}{2} u_{s,i}^2 \right)}{\partial x_j} - \rho_s u_{s,j} \frac{\partial \left\langle \frac{1}{2} u_{ac,i}^2 \right\rangle}{\partial x_j} + u_{s,i} \left\langle \frac{\rho_{ac}}{\rho} \frac{\partial p_s}{\partial x_i} \right\rangle - u_{s,i} \left\langle \frac{\rho_{ac}}{\rho} \frac{\partial \sigma_{s,ij}}{\partial x_j} \right\rangle \\
+ u_{s,i} \left\langle \frac{\rho_{ac}}{\rho} \frac{\partial p_{ac}}{\partial x_i} \right\rangle - u_{s,i} \left\langle \frac{\rho_{ac}}{\rho} \frac{\partial \sigma_{ac,ij}}{\partial x_j} \right\rangle \,.
\end{aligned} \tag{B.6}$$

Besides, the streaming kinetic energy equation (B.5) comprises the terms:

$$\Upsilon_s = - p_s \frac{\partial u_{s,i}}{\partial x_i} \,, \quad \varepsilon_s = \sigma_{s,ij} \frac{\partial u_{s,i}}{\partial x_j}$$

that are also found in the equation (B.3) for $\langle \rho e \rangle$.

Transport equation for the time-averaged acoustic kinetic energy

To obtain a transport equation for $\left\langle \frac{1}{2} \rho \boldsymbol{u_{ac}} \cdot \boldsymbol{u_{ac}} \right\rangle$, the first step is to multiply the acoustic momentum equation (B.2) by $\rho u_{ac,i}$. Using the continuity equation (1.2) to obtain a conservative form yields, after some manipulation:

$$\begin{aligned}
\frac{\partial \left(\frac{1}{2} \rho u_{ac,i}^2 \right)}{\partial t} + \frac{\partial \left(\frac{1}{2} \rho u_{ac,i}^2 u_j \right)}{\partial x_j} = &- \rho u_{ac,i} u_{ac,j} \frac{\partial u_{s,i}}{\partial x_j} + \rho u_{ac,i} \frac{\partial \left\langle \frac{1}{2} u_{ac,j}^2 \right\rangle}{\partial x_j} - u_{ac,i} \frac{\partial p_s}{\partial x_i} - u_{ac,i} \frac{\partial p_{ac}}{\partial x_i} \\
&+ \rho u_{ac,i} \left\langle \frac{1}{\rho} \frac{\partial p_s}{\partial x_i} \right\rangle + \rho u_{ac,i} \left\langle \frac{1}{\rho} \frac{\partial p_{ac}}{\partial x_i} \right\rangle + u_{ac,i} \frac{\partial \sigma_{s,ij}}{\partial x_j} \\
&+ u_{ac,i} \frac{\partial \sigma_{ac,ij}}{\partial x_j} - \rho u_{ac,i} \left\langle \frac{1}{\rho} \frac{\partial \sigma_{s,ij}}{\partial x_j} \right\rangle - \rho u_{ac,i} \left\langle \frac{1}{\rho} \frac{\partial \sigma_{ac,ij}}{\partial_j} \right\rangle \,.
\end{aligned} \tag{B.7}$$

Thèse accessible à l'adresse : https://theses.insa-lyon.fr/publication/2024ISAL0101/these.pdf © [B. Vincent], [2024], INSA Lyon, tous droits réservés

The second and final step is to average equation (B.7) over an acoustic period. Then, after integrating by parts $\left\langle u_{ac,i} \frac{\partial p_{ac}}{\partial x_i} \right\rangle$ and $\left\langle u_{ac,i} \frac{\partial \sigma_{ac,ij}}{\partial x_i} \right\rangle$, one obtains:

$$\frac{\partial \left\langle \frac{1}{2} \rho u_{ac,i}^2 \right\rangle}{\partial t} + \frac{\partial \left\langle \frac{1}{2} \rho u_{ac,i}^2 u_j \right\rangle}{\partial x_j} = \Phi_{p_{ac}} + \Phi_{\sigma_{ac}} + \mathcal{P}_{ac} - \Upsilon_{ac} - \varepsilon_{ac} \,, \tag{B.8}$$

with:

$$\Phi_{p_{ac}} = -\frac{\partial \left\langle p_{ac} u_{ac,j} \right\rangle}{\partial x_j} \,, \quad \Phi_{\sigma_{ac}} = \frac{\partial \left\langle \sigma_{ac,ij} u_{ac,i} \right\rangle}{\partial x_j} \,, \quad \Upsilon_{ac} = -\left\langle p_{ac} \frac{\partial u_{ac,i}}{\partial x_i} \right\rangle \,,$$
$$\varepsilon_{ac} = \left\langle \sigma_{ac,ij} \frac{\partial u_{ac,i}}{\partial x_j} \right\rangle \,,$$

and:

$$\begin{aligned} \mathcal{P}_{ac} = &- \left\langle \rho u_{ac,i} u_{ac,j} \frac{\partial u_{s,i}}{\partial x_j} \right\rangle + \left\langle \rho_{ac} u_{ac,j} \right\rangle \frac{\partial \left(\frac{1}{2} u_{ac,i}^2 \right)}{\partial x_j} + \left\langle \rho_{ac} u_{ac,i} \right\rangle \left\langle \frac{1}{\rho} \frac{\partial p_s}{\partial x_i} \right\rangle \\ &- \left\langle \rho_{ac} u_{ac,i} \right\rangle \left\langle \frac{1}{\rho} \frac{\partial \sigma_{s,ij}}{\partial x_j} \right\rangle + \left\langle \rho_{ac} u_{ac,i} \right\rangle \left\langle \frac{1}{\rho} \frac{\partial p_{ac}}{\partial x_i} \right\rangle - \left\langle \rho_{ac} u_{ac,i} \right\rangle \left\langle \frac{1}{\rho} \frac{\partial \sigma_{ac,ij}}{\partial x_j} \right\rangle \,. \end{aligned} \tag{B.10}$$

Transport equation for the time-averaged mixed kinetic energy

Finally, to obtain the transport equation for $\langle \rho \boldsymbol{u_s} \cdot \boldsymbol{u_{ac}} \rangle$, the streaming (B.1) and acoustic (B.2) momentum equations shall be multiplied by $\rho u_{ac,i}$ and $\rho u_{s,i}$, respectively. Adding the two resulting equations together yields, after time-averaging (the calculations are analogous to those of the previous sections, and are thus not repeated):

$$\frac{\partial \left\langle \rho u_{ac,i} u_{s,i} \right\rangle}{\partial t} + \frac{\partial \left\langle \rho u_{ac,i} u_{s,i} u_j \right\rangle}{\partial x_j} = -\mathcal{P}_s - \mathcal{P}_{ac} \,, \tag{B.11}$$

in which $\mathcal{P}_s$ and $\mathcal{P}_{ac}$ are given by equations (B.6) and (B.10), respectively.

Thèse accessible à l'adresse : https://theses.insa-lyon.fr/publication/2024ISAL0101/these.pdf © [B. Vincent], [2024], INSA Lyon, tous droits réservés

Appendix C

Preliminary simulations: validation of the spectral-element code *Semtex*

Prior to the scaling analysis of streaming jets (chapter 3), I checked that the acoustic forcing was correctly accounted for by *Semtex* (Blackburn *et al.*, 2019) (open-source spectral-element code used to compute the streaming flows).

Test configuration, parameters and mesh

To validate the code, I reproduced the configuration of Moudjed *et al.* (2015), and compared the on-axis jet velocity profiles obtained with *Semtex* to the experimental and numerical simulations of the authors.

Moudjed *et al.* (2015) studied the streaming jet forced by the near acoustic of an axisymmetric beam. The geometry is similar to the one shown in figure 3.1, except that the transducer is placed at a distance Δx from the upstream cavity wall (but still immersed in the same fluid), instead of being fitted to the cavity. The dimensionless numbers defining this reference case are listed in table C.1. The original experiment was made in a water tank with a rectangular cross section and a free surface, which cannot be exactly recreated in *Semtex*. Therefore, I considered a cylindrical cavity whose diameter matches the hydraulic diameter of Moudjed *et al.* (2015). In total, I simulated the flow for three forcing magnitudes: $Gr_{ac} = 1.68 \times 10^4$, 3.47×10^4 and 6.71×10^4.

Besides of PIV measurements, Moudjed *et al.* (2015) also made simulations in the same configuration. As in this thesis, the flow was modelled using the incompressible Navier-Stokes together with an acoustic forcing computed separately. However, the forcing field computed by Moudjed *et al.* (2015) (i) did not account for attenuation ($NL/ = 0$), and (ii) was modelled assuming plane waves which is known to overestimate the acosutic intensity

Table C.1: Dimensionless parameters corresponding to the experimental and numerical benchmark setups of Moudjed *et al.* (2015), with Δx the distance (normalised by the transducer diameter D_s) between the transducer and the upstream cavity wall. The original experiments were made in a $265 \times 180 \times 160$ (length $\times$ width $\times$ height) water cavity of rectangular cross-section. The flow was actuated by a $D_s = 28.5$ mm plane circular transducer emitting 2 MHz acoustic sine waves.

S	N	L	D	Δx	Gr_{ac}
0.032	0.028	0.337	8.08	0.35	1.68×10^4, 3.47×10^4 and 6.71×10^4

Thèse accessible à l'adresse : https://theses.insa-lyon.fr/publication/2024ISAL0101/these.pdf © [B. Vincent], [2024], INSA Lyon, tous droits réservés

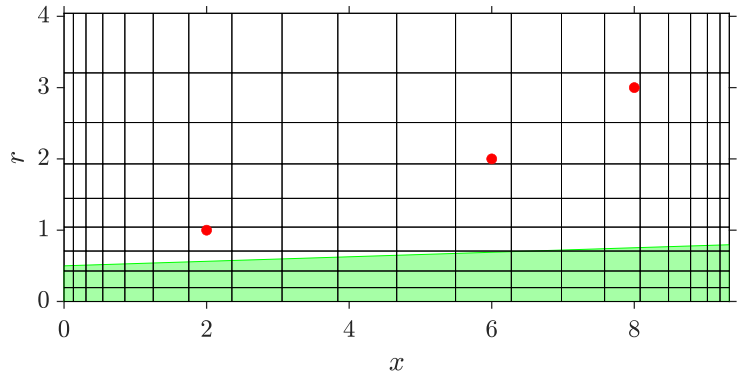


Figure C.1: Mesh used for the validation of *Semtex* (Blackburn *et al.*, 2019), with the approximate beam size (of radius $R_{beam} = 0.5 + Sx$) represented by the green-shaded area. The mesh is made of 180 elements, with 20 and 9 elements in the x- and r-directions, respectively. To be refined near the $x = 0$ and $x = L$ end walls, and around the $r = 0$ axis, the mesh was generated with stretching factors $\gamma_x = 1.35$ and $\gamma_r = 1.20$ (equations (3.9) and (3.10)). The red dots at $(x, r) = (2, 1)$, $(6, 2)$ and $(8, 3)$ locate the points were the convergence of $\boldsymbol{u}$ and p towards a steady state is monitored.

in the near acoustic field (figure 1.5). I shall determine whether these two approximations yield significant difference on the simulated streaming velocities.

The mesh used for the computations features 180 elements in total, with 20 and 9 elements in the x- and r-directions, respectively (figure C.1). These validation simulations were made with expansion polynomials of degree $N_p = 10$ in all elements; for higher N_p, the velocity changes at $r = 0$ remained below 0.2 % on the axis.

Finally, the three simulations were initiated with $\boldsymbol{u} = \boldsymbol{0}$ and $p = 0$, and the splitting-scheme (3.3) was used in its first-order form ($K = 1$). To ensure the CFL < 1 stability condition, the time step was set to $\Delta t = 10^{-5}$ ($Gr_{ac} = 1.68 \times 10^4$), 5×10^{-6} ($Gr_{ac} = 3.47 \times 10^4$) and 4×10^{-6} ($Gr_{ac} = 1.68 \times 10^4$), which yielded maximum CFL numbers of 0.68, 0.55 and 0.66, respectively.

Validation against former experimental (PIV) and numerical work

The streaming flow computed with *Semtex* is shaped as a jet impinging the surface facing the transducer (figure C.2). The jet impingement at $x = L$ creates a large recirculation that spans nearly the entire cavity radius. Increasing Gr_{ac} leads to larger $\|\boldsymbol{u}\|$ and, for $Gr_{ac} \geq 3.47 \times 10^4$, to the emergence of a recirculation bubble along the side wall. For $Gr_{ac} = 6.71 \times 10^4$, the bubble length is greater than $L/2$, and its diameter is $\approx D/4$ (figure C.2 (c)).

The on-axis velocity profiles obtained with Semtex are compared with those of Moudjed *et al.* (2015) in figure C.3. For each Gr_{ac}, the velocity profiles depict variations caused by the strong gradients of $\widetilde{I}_{ac,x}$ in the near acoustic field. Overall, an excellent agreement is found between the *Semtex* simulations and the PIV profiles of Moudjed *et al.* (2015): the discrepancy is at most 7.1 % for $Gr_{ac} = 1.68 \times 10^4$. This difference may be attributed to the uncertainties on the Gr_{ac} estimates. Indeed, material properties variations caused by different working fluid temperatures may yield significant Gr_{ac} changes (e.g., for water,

Thèse accessible à l'adresse : https://theses.insa-lyon.fr/publication/2024ISAL0101/these.pdf © [B. Vincent], [2024], INSA Lyon, tous droits réservés

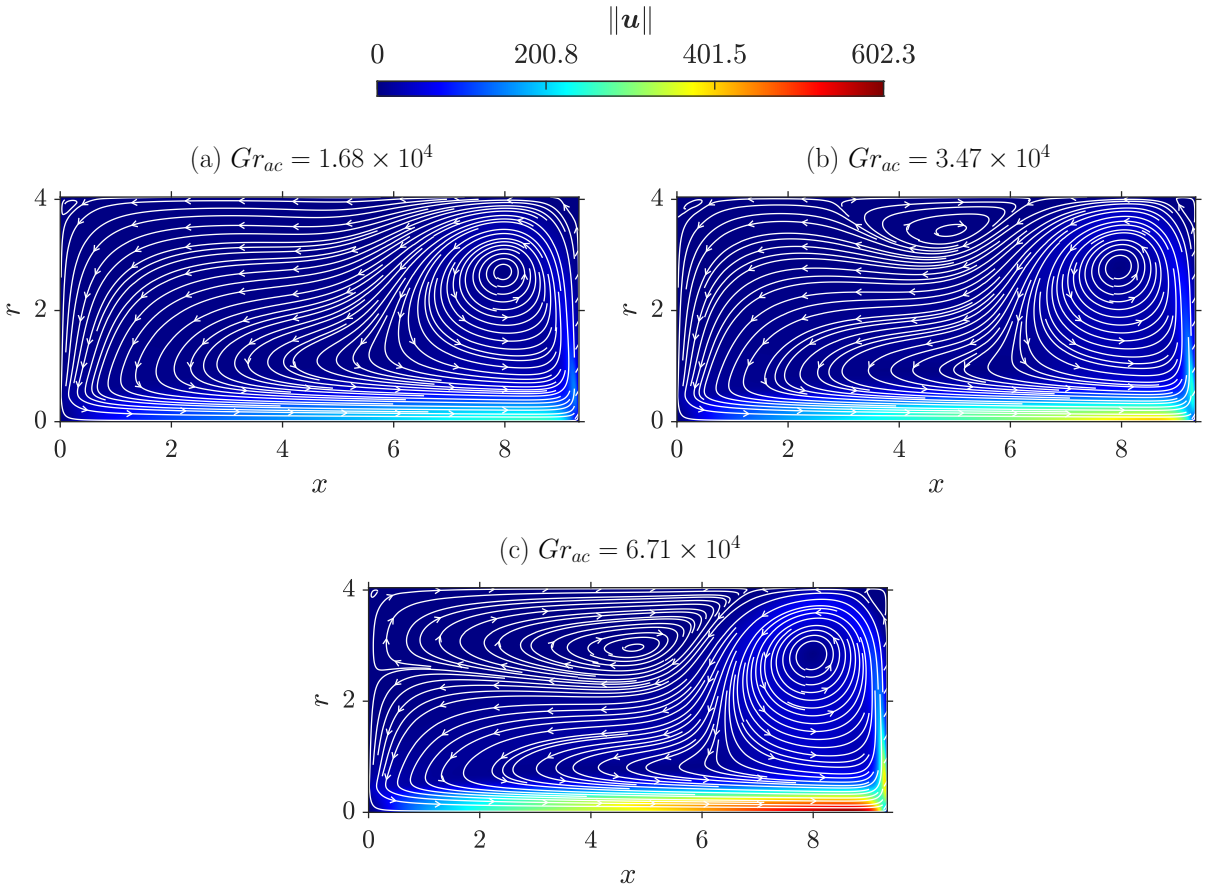


Figure C.2: Maps of the steady axisymmetric velocity magnitude $\|\boldsymbol{u}\|$ computed with *Semtex* (Blackburn *et al.*, 2019) for (a) $Gr_{ac} = 1.68 \times 10^4$, (b) $Gr_{ac} = 3.47 \times 10^4$ and (c) $Gr_{ac} = 6.71 \times 10^4$. See table C.1 for the remaining computational parameters. All figures share the same colour levels.

a variation of 6 °C translates into a 10 % difference on Gr_{ac}, see section 5.4.2).

Besides, an excellent agreement is also found between the $\widetilde{u}_x(x, r = 0)$ profiles obtained with *Semtex* and the numerical profiles of Moudjed *et al.* (2015). Despite the approximations made by Moudjed *et al.* (2015) to model the forcing field, the discrepancy on $\widetilde{u}_x(x, r = 0)$ remains below 3 %. Nevertheless, the overestimation of $\widetilde{I}_{ac,x}(x, r = 0)$ caused by both the plane wave and unattenuated approximations leads to slightly larger maximum $\widetilde{u}_x$ in the numerical profiles of Moudjed *et al.* (2015) (blue solid curves in figure C.3): the discrepancy ranges from 1.7 % for $Gr_{ac} = 6.71 \times 10^4$ to 2.8 % for $Gr_{ac} = 3.47 \times 10^4$.

To conclude, an excellent agreement is found between the velocity profiles obtained between the *Semtex* simulations and the numerical and experimental profiles of Moudjed *et al.* (2015). This confirms the ability of *Semtex* to faithfully simulate streaming flows.

Thèse accessible à l'adresse : https://theses.insa-lyon.fr/publication/2024ISAL0101/these.pdf © [B. Vincent], [2024], INSA Lyon, tous droits réservés

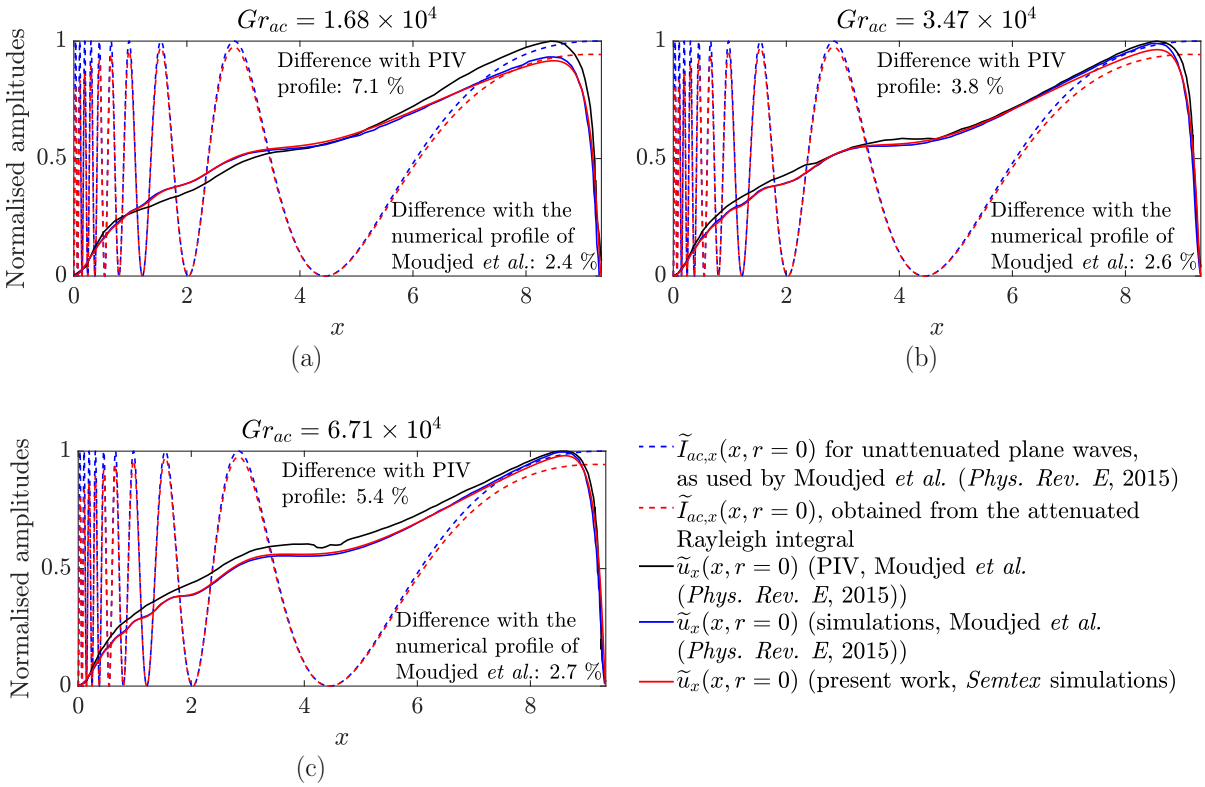


Figure C.3: On-axis profiles of the normalised axial intensity $\widetilde{I}_{ac,x}$ and the normalised axial velocity $\widetilde{u}_x$ for different forcing magnitudes: (a) $Gr_{ac} = 1.68 \times 10^4$, (b) $Gr_{ac} = 3.47 \times 10^4$ and (c) $Gr_{ac} = 6.71 \times 10^4$. The source is placed at $x = -0.35$. For each Gr_{ac}, $\widetilde{u}_x(x, r = 0)$ is normalised by the maximum velocity measured by Moudjed *et al.* (2015) using PIV (solid black curve). The intensity profiles are normalised by the maximum unattenuated intensity on the axis (dashed blue curve). For each Gr_{ac}, I reported the difference between the $\widetilde{u}_x(x, r = 0)$ profile obtained with Semtex and those of Moudjed *et al.* (2015).

Thèse accessible à l'adresse : https://theses.insa-lyon.fr/publication/2024ISAL0101/these.pdf © [B. Vincent], [2024], INSA Lyon, tous droits réservés

Appendix D

Grid sensitivity studies for the stability analysis of streaming flows

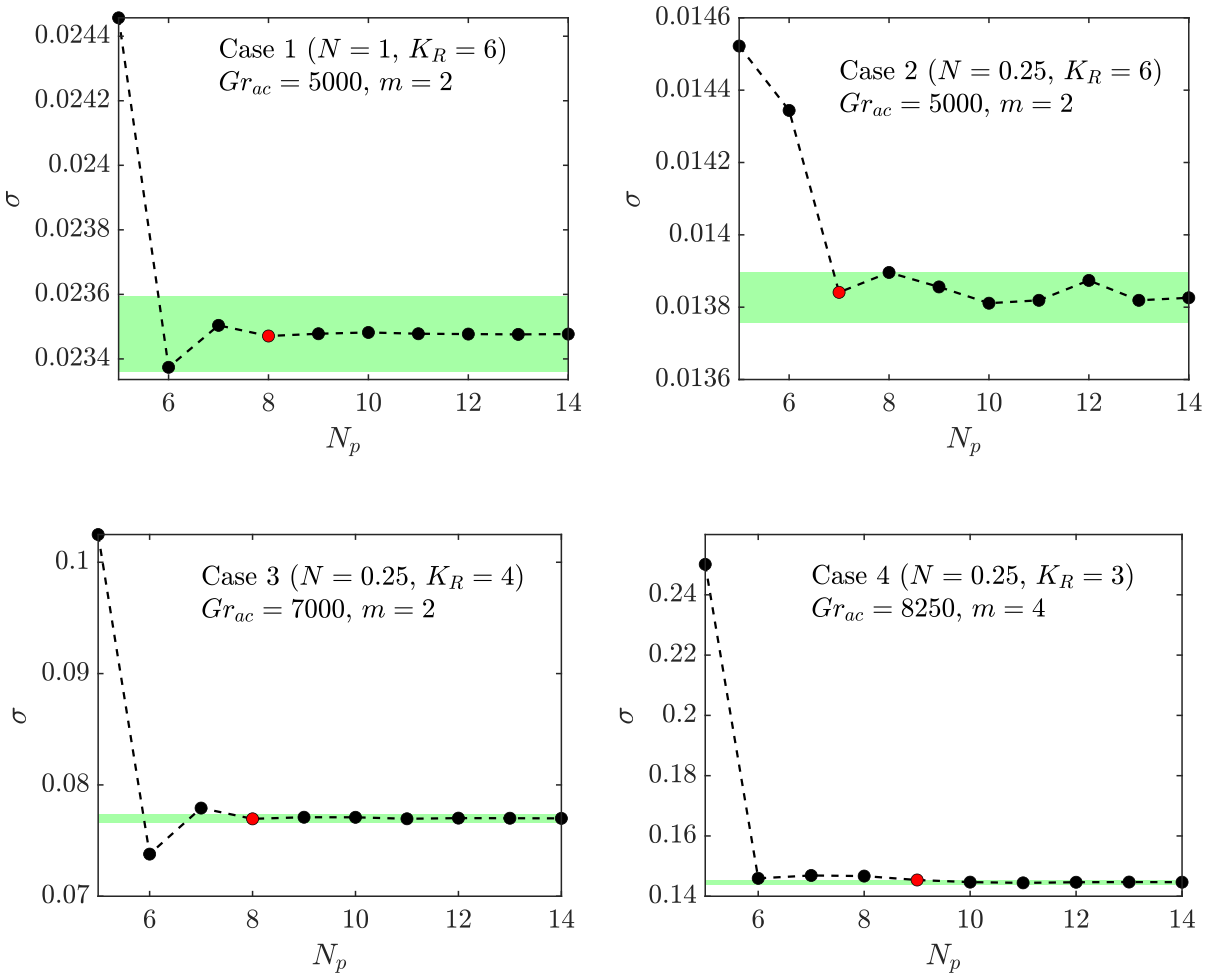


Figure D.1: Caption on next page.

Thèse accessible à l'adresse : https://theses.insa-lyon.fr/publication/2024ISAL0101/these.pdf © [B. Vincent], [2024], INSA Lyon, tous droits réservés

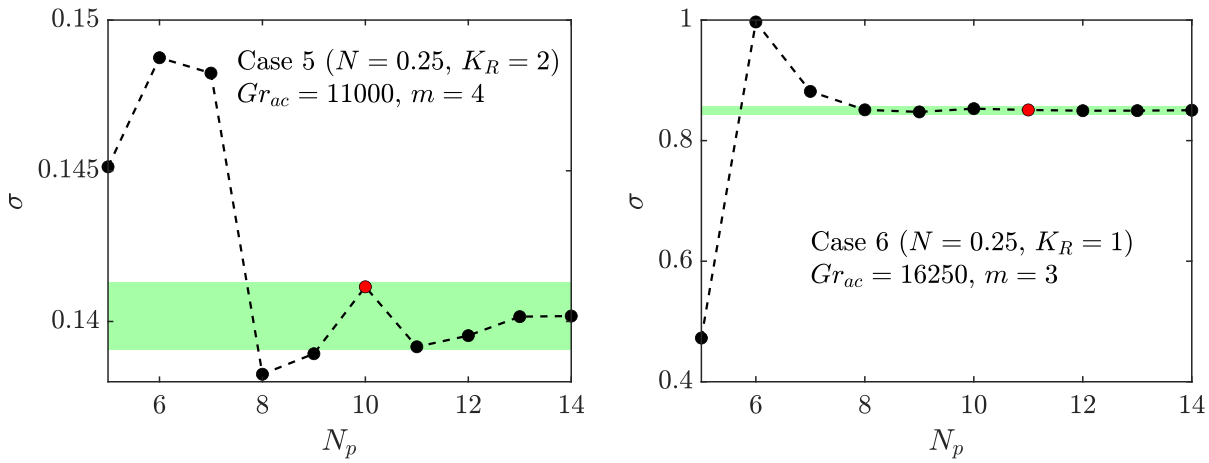


Figure D.1: Grid sensitivity for the stability analysis work in chapter 4: growth rate σ of the leading mode as a function of the polynomial expansion basis degree N_p. For each plot, the corresponding case (table 4.1) is reported along with the forcing magnitude Gr_{ac} and the azimuthal wavenumber m. The green-shaded area represents the ± 0.5 % interval about the σ obtained with the most refined grid ($N_p = 14$). For each case, the retained N_p is shown in red.

Thèse accessible à l'adresse : https://theses.insa-lyon.fr/publication/2024ISAL0101/these.pdf © [B. Vincent], [2024], INSA Lyon, tous droits réservés

Appendix E

Image processing for PTV measurements and Shake-The-Box parameters

All the recordings made when studying the helical flow (chapter 5) required to be first processed before running the tracking algorithm *Shake-The-Box*. I shall provide the parameters I used to process the images and to run *Shake-The-Box* for both the measurements in the entire cavity and for the near-wall measurements. The track statistics obtained for each measurement are summarised in table E.1.

Processing of the images used for the mean flow measurements in the entire cavity

Table E.1: Statistics of the *Shake-The-Box* results obtained for the measurements in the entire cavity (left column) and for the near-impingement measurements (right column). The corresponding values of P_{elec} are given in the brackets. For the entire-cavity-measurements, the longest track lengths are found at the free-surface.

	Measurements in the entire cavity	Near-impingement measurements
Total number of tracks over the recording duration	Between 1 174 568 (4 W) and 2 466 914 (6 W)	Between 1 528 214 (1 W) and 5 502 200 (4 W)
Mean track length over the recording duration	Between 0.94 s (8 W) and 3.75 (1 W)	Between 1.6 s (8 W) and 4.8 s (1 W)
Maximum track length over the recording duration	Between 46.5 s (6 W) and 87.63 s (4 W)	Between 18 s (6 W) and 45.3 s (1 W)
Mean number of tracks per snapshot	Between 1 744 (8 W) and 8 594 (1 W)	Between 5 752 (8 W) and 11 123 (2 W)

Thèse accessible à l'adresse : https://theses.insa-lyon.fr/publication/2024ISAL0101/these.pdf © [B. Vincent], [2024], INSA Lyon, tous droits réservés

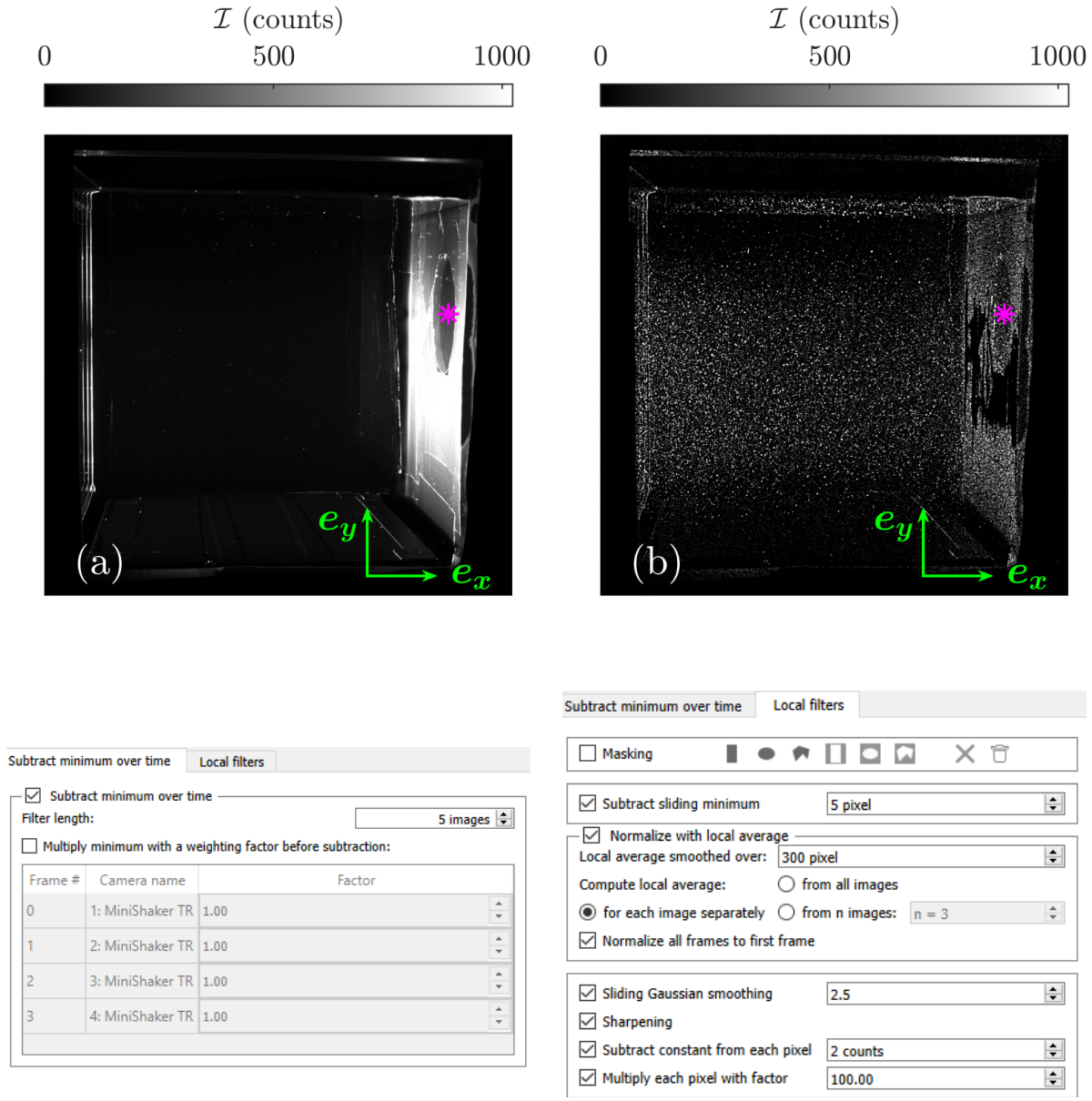


Figure E.1: Processing of the images recorded in the entire cavity for $Gr_{ac} = 1.78 \times 10^4$ ($P_{elec} = 1$ W): (a) raw image, (b) processed image and (c) parameters of the "Image preprocessing" module of *LaVision GmbH* DaVis 10 to obtain (b) from (a). In (a) and (b), the purple star locates the entry point of the beam.

Thèse accessible à l'adresse : https://theses.insa-lyon.fr/publication/2024ISAL0101/these.pdf © [B. Vincent], [2024], INSA Lyon, tous droits réservés

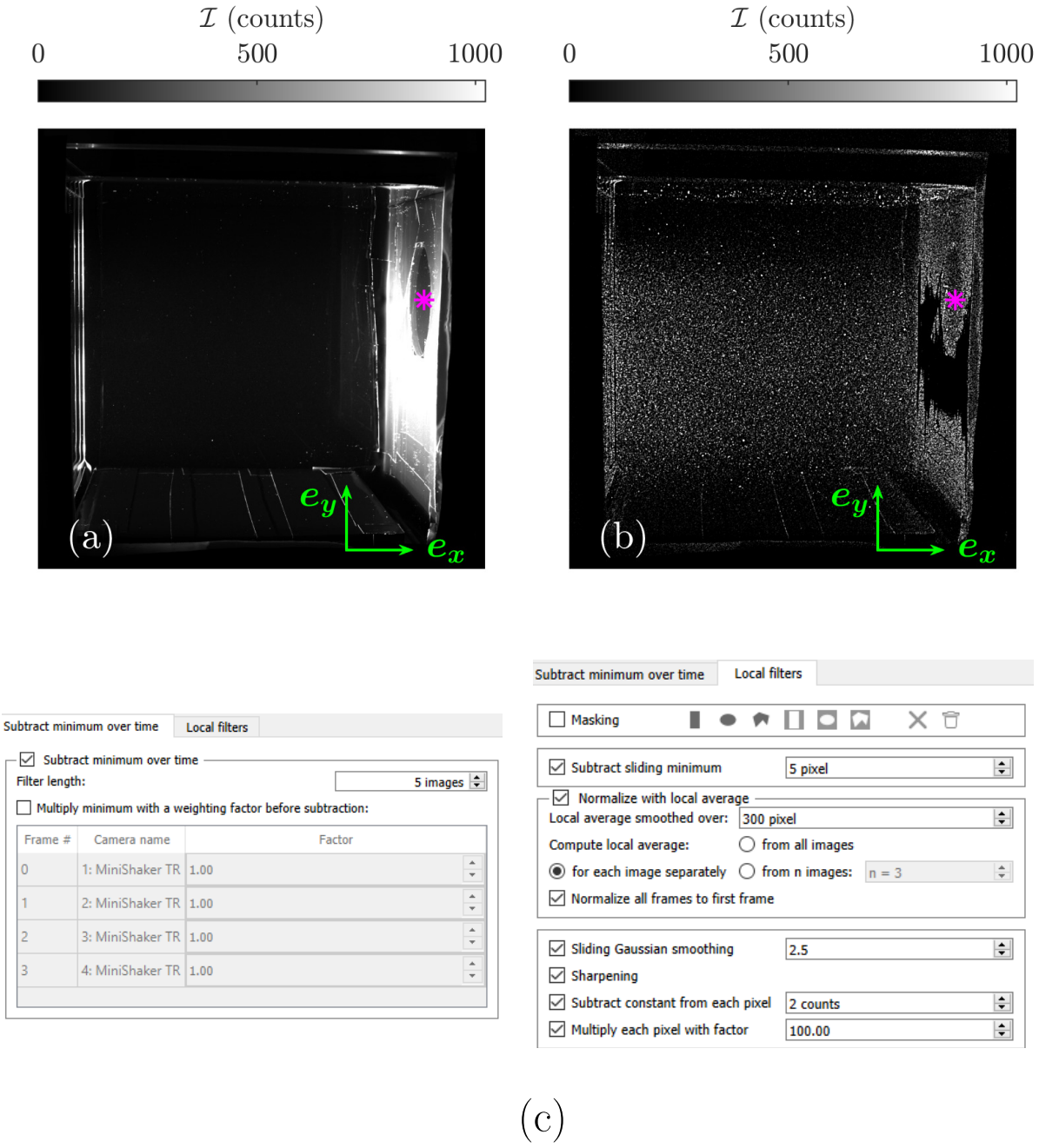


Figure E.2: Processing of the images recorded in the entire cavity for $Gr_{ac} = 3.64 \times 10^4$ ($P_{elec} = 2$ W): (a) raw image, (b) processed image and (c) parameters of the "Image preprocessing" module of *LaVision GmbH* DaVis 10 to obtain (b) from (a). In (a) and (b), the purple star locates the entry point of the beam.

Thèse accessible à l'adresse : https://theses.insa-lyon.fr/publication/2024ISAL0101/these.pdf © [B. Vincent], [2024], INSA Lyon, tous droits réservés

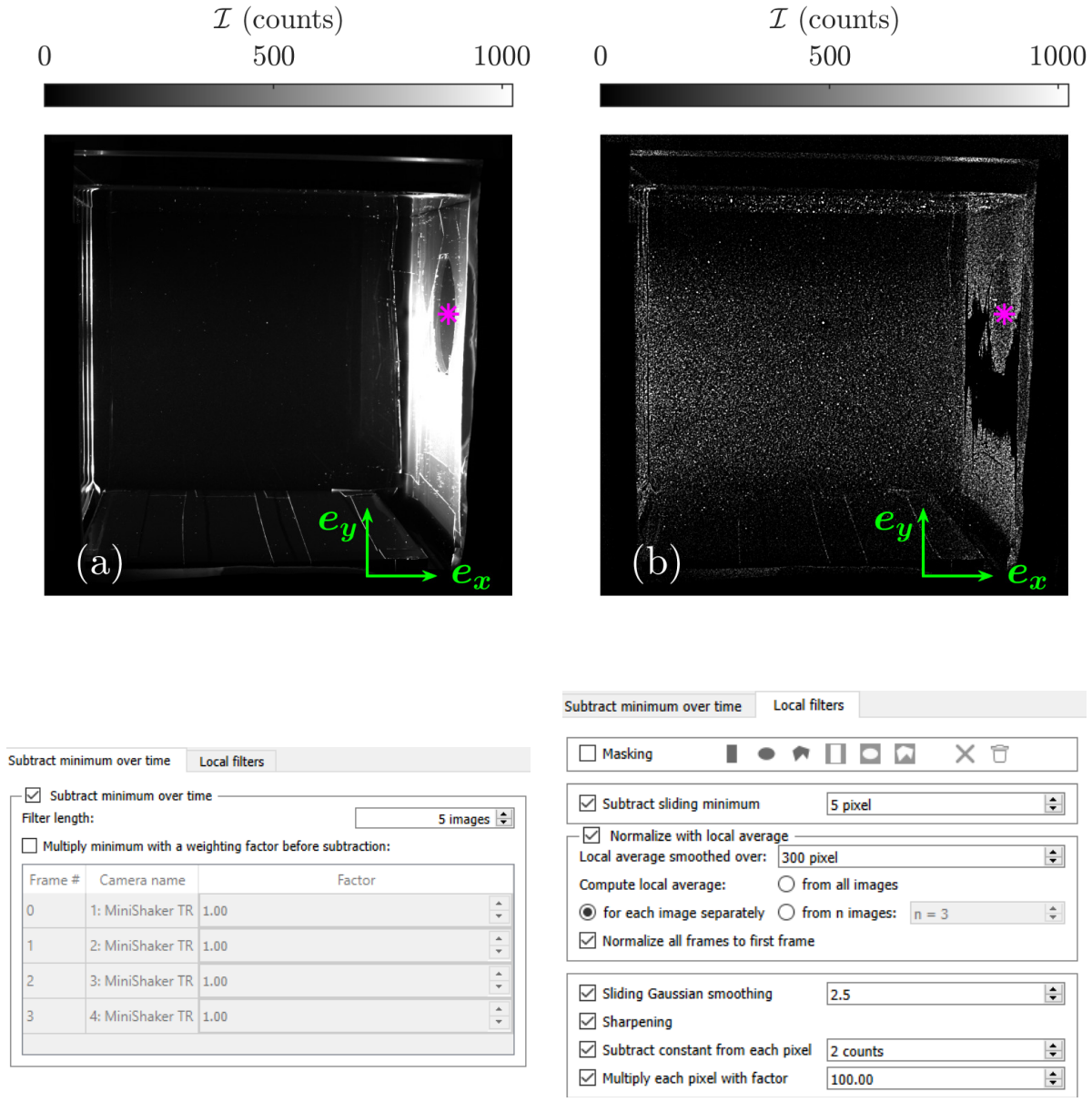


Figure E.3: Processing of the images recorded in the entire cavity for $Gr_{ac} = 7.50 \times 10^4$ ($P_{elec} = 4$ W): (a) raw image, (b) processed image and (c) parameters of the "Image preprocessing" module of *LaVision GmbH* DaVis 10 to obtain (b) from (a). In (a) and (b), the purple star locates the entry point of the beam.

Thèse accessible à l'adresse : https://theses.insa-lyon.fr/publication/2024ISAL0101/these.pdf © [B. Vincent], [2024], INSA Lyon, tous droits réservés

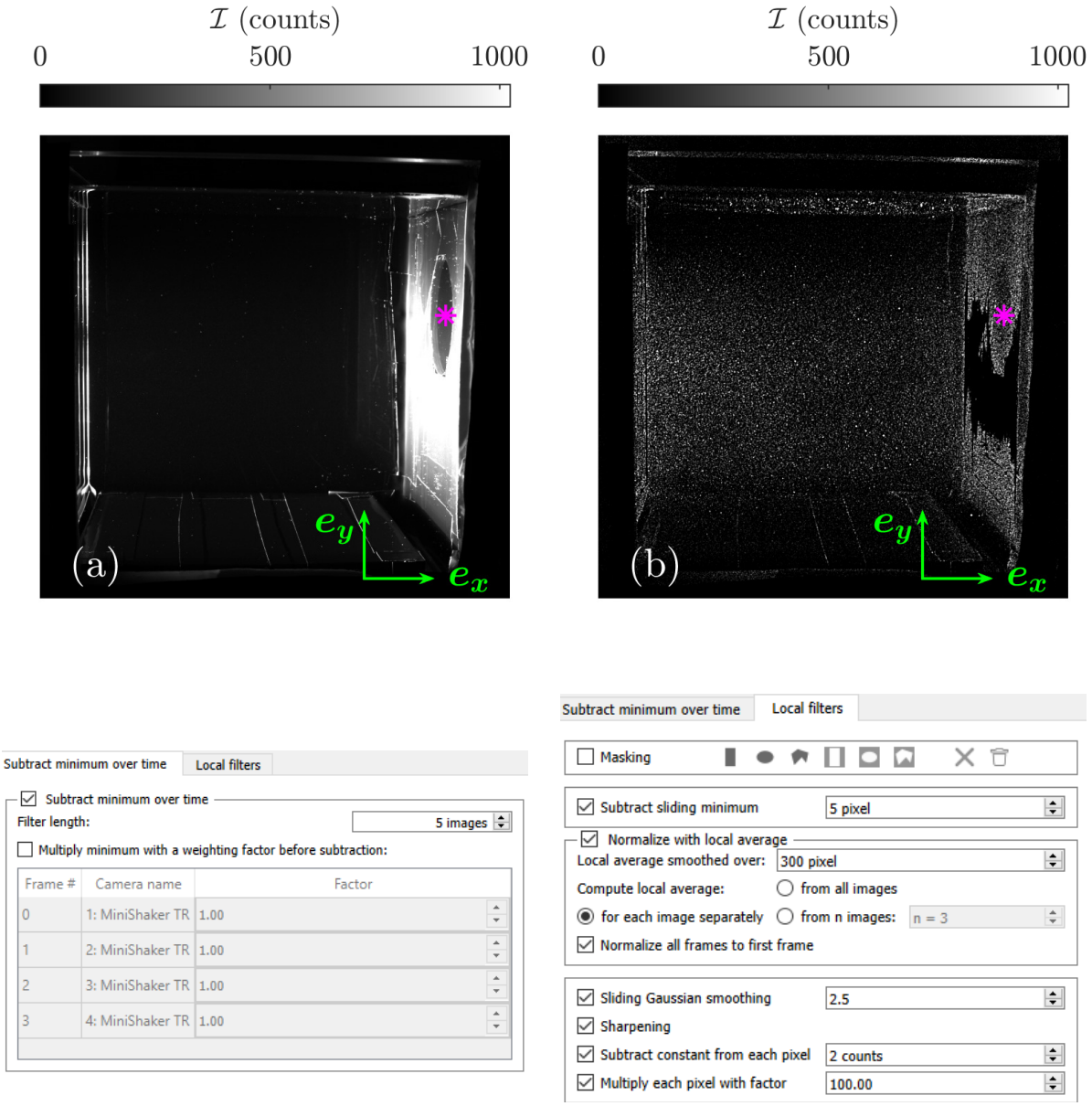


Figure E.4: Processing of the images recorded in the entire cavity for $Gr_{ac} = 11.28 \times 10^4$ ($P_{elec} = 6$ W): (a) raw image, (b) processed image and (c) parameters of the "Image preprocessing" module of *LaVision GmbH* DaVis 10 to obtain (b) from (a). In (a) and (b), the purple star locates the entry point of the beam.

Thèse accessible à l'adresse : https://theses.insa-lyon.fr/publication/2024ISAL0101/these.pdf © [B. Vincent], [2024], INSA Lyon, tous droits réservés

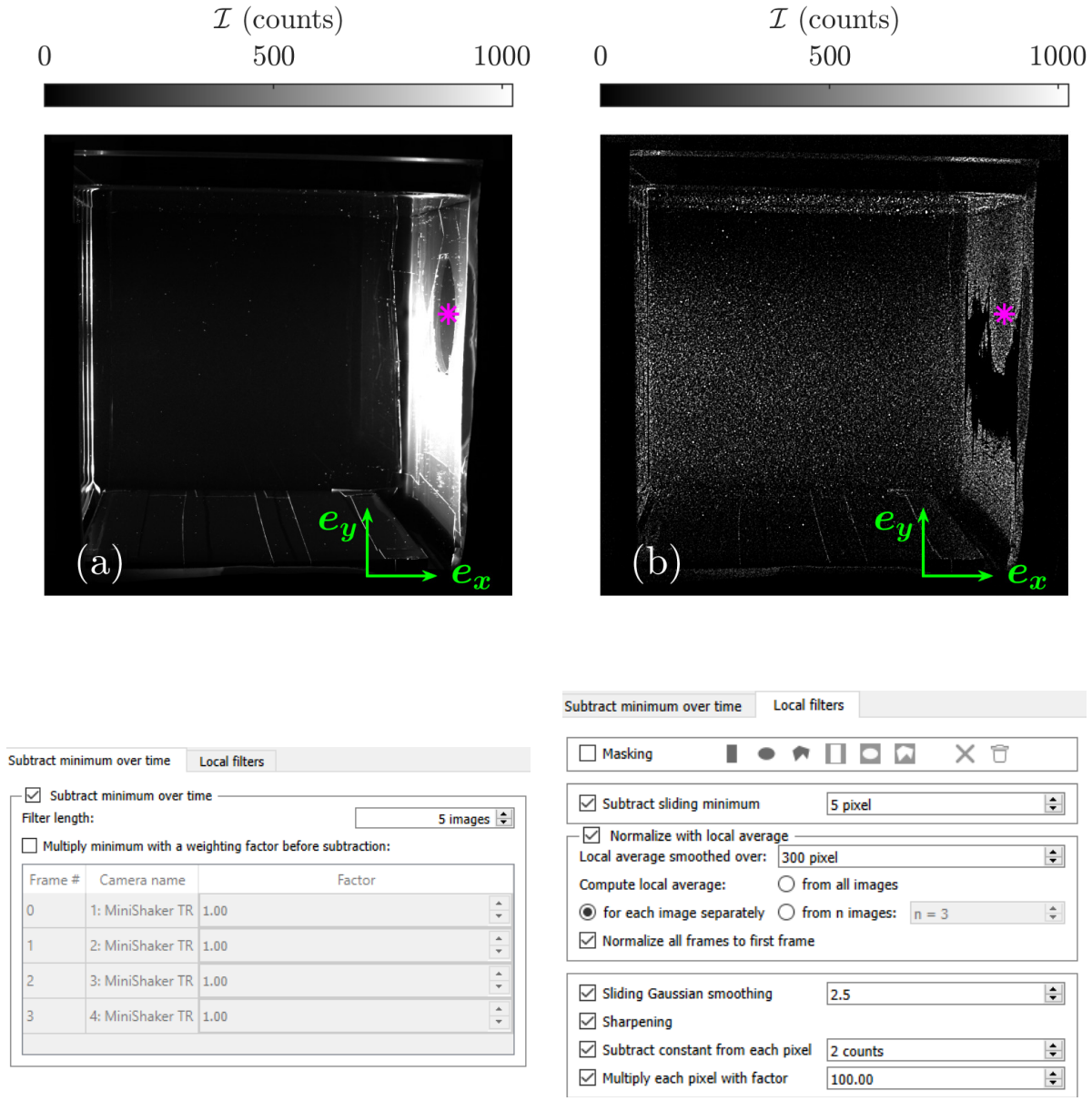


Figure E.5: Processing of the images recorded in the entire cavity for $Gr_{ac} = 15.12 \times 10^4$ ($P_{elec} = 8$ W): (a) raw image, (b) processed image and (c) parameters of the "Image preprocessing" module of *LaVision GmbH* DaVis 10 to obtain (b) from (a). In (a) and (b), the purple star locates the entry point of the beam.

Thèse accessible à l'adresse : https://theses.insa-lyon.fr/publication/2024ISAL0101/these.pdf © [B. Vincent], [2024], INSA Lyon, tous droits réservés

Shake-The-Box parameters and filtering the tracks measured in the entire cavity

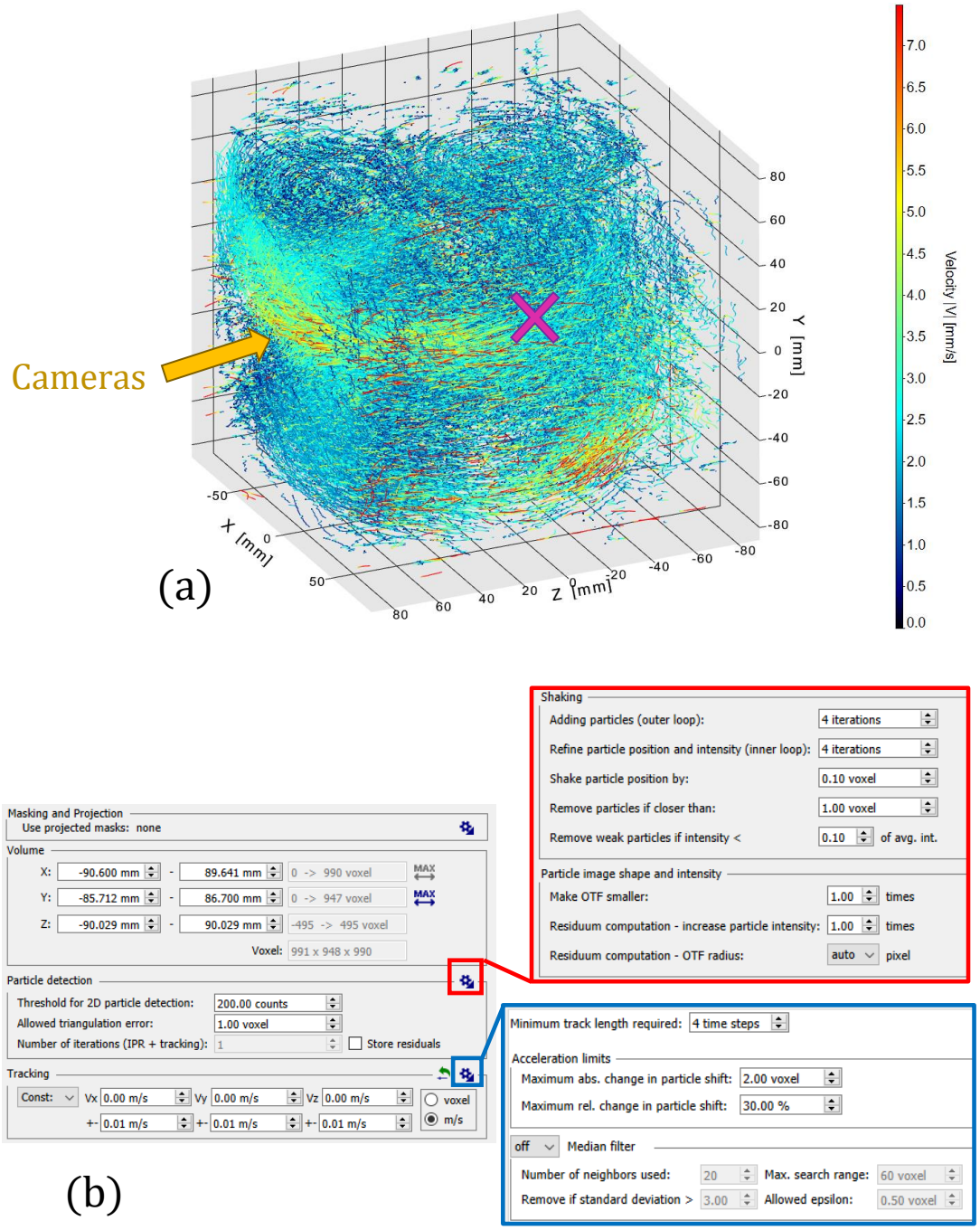


Figure E.6: Caption on next page.

Thèse accessible à l'adresse : https://theses.insa-lyon.fr/publication/2024ISAL0101/these.pdf © [B. Vincent], [2024], INSA Lyon, tous droits réservés

(c)

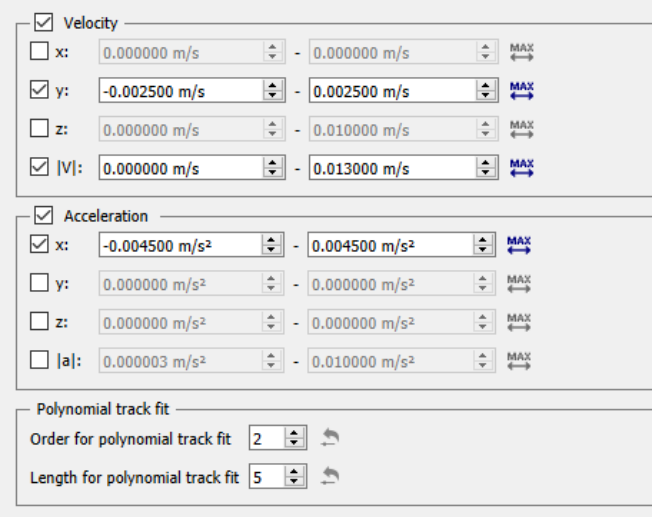


Figure E.6: Particle track detection by *Shake-The-Box* for $Gr_{ac} = 1.78 \times 10^4$ ($P_{elec} = 1$ W). (a) Snapshot of filtered tracks obtained by *Shake-The-Box* (the purple cross locates the entry point of the beam), (b) parameters of *Shake-The-Box*, as prescribed in the *LaVision GmbH* DaVis 10 software. (c) Parameters of the "Range filter" used to remove spurious tracks: particles whose velocities or acceleration do not fit in the indicated bounds are removed. After filtering, 1 650 301 tracks are obtained, with a mean track length of 3.75 s (the maximum track length is 67.8 s for a particle track at the free surface). The mean number of tracks per time step is 8549.

Thèse accessible à l'adresse : https://theses.insa-lyon.fr/publication/2024ISAL0101/these.pdf © [B. Vincent], [2024], INSA Lyon, tous droits réservés

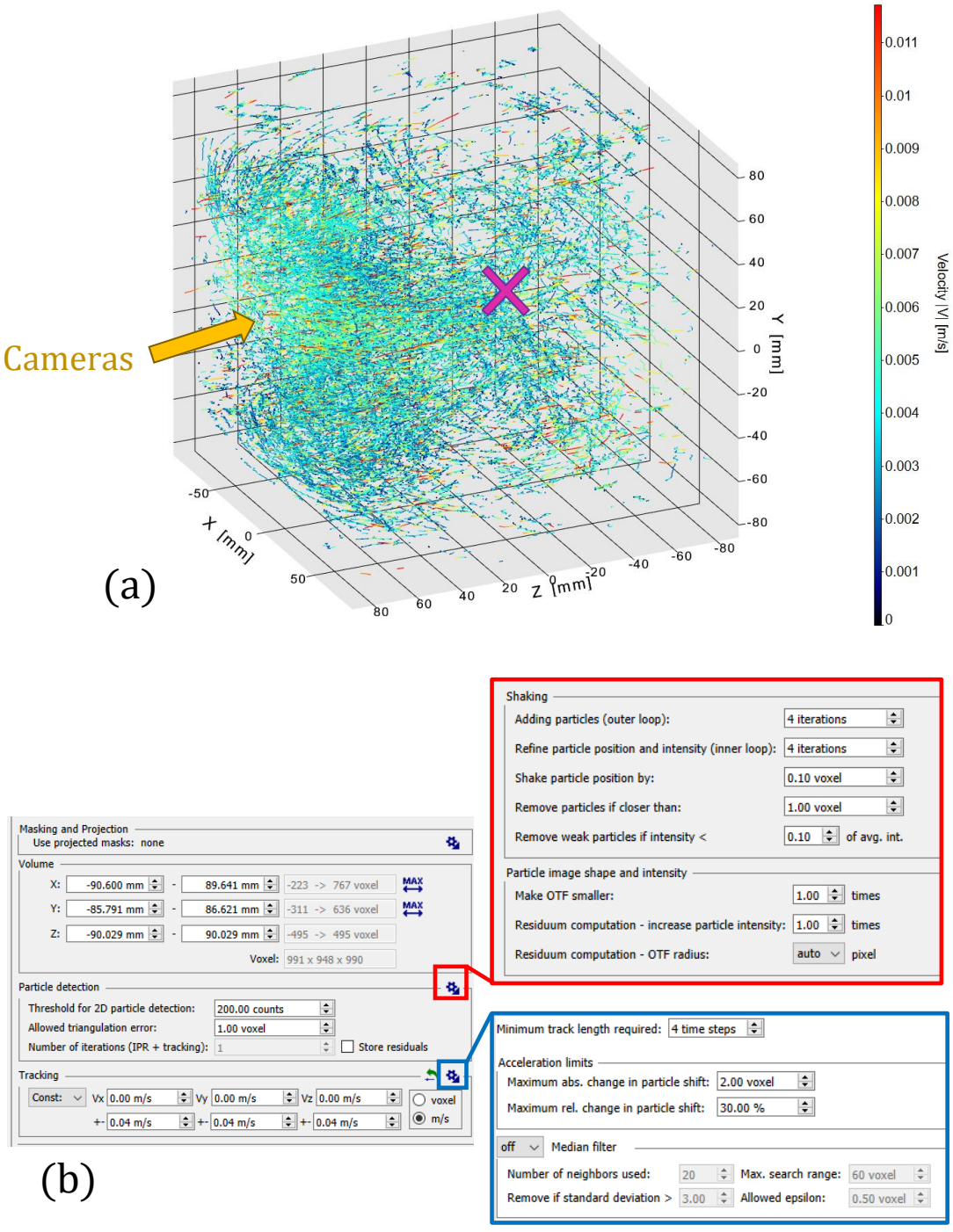


Figure E.7: Caption on next page.

Thèse accessible à l'adresse : https://theses.insa-lyon.fr/publication/2024ISAL0101/these.pdf © [B. Vincent], [2024], INSA Lyon, tous droits réservés

(c)

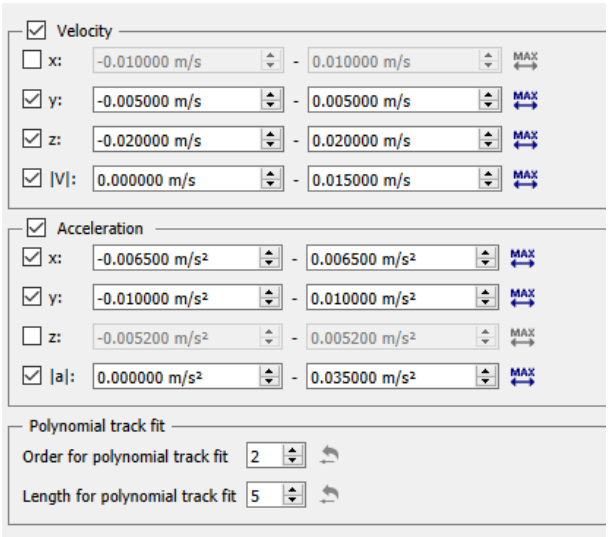


Figure E.7: Particle track detection by *Shake-The-Box* for $Gr_{ac} = 3.64{\times}10^4$ ($P_{elec} = 2$ W). (a) Snapshot of filtered tracks obtained by *Shake-The-Box* (the purple cross locates the entry point of the beam), (b) parameters of *Shake-The-Box*, as prescribed in the *LaVision GmbH* DaVis 10 software. (c) Parameters of the "Range filter" used to remove spurious tracks: particles whose velocities or acceleration do not fit in the indicated bounds are removed. After filtering, 1 459 046 tracks are obtained, with a mean track length of 2.0 s (the maximum track length is 74.0 s for a particle track at the free surface). The mean number of tracks per time step is 2444.

Thèse accessible à l'adresse : https://theses.insa-lyon.fr/publication/2024ISAL0101/these.pdf © [B. Vincent], [2024], INSA Lyon, tous droits réservés

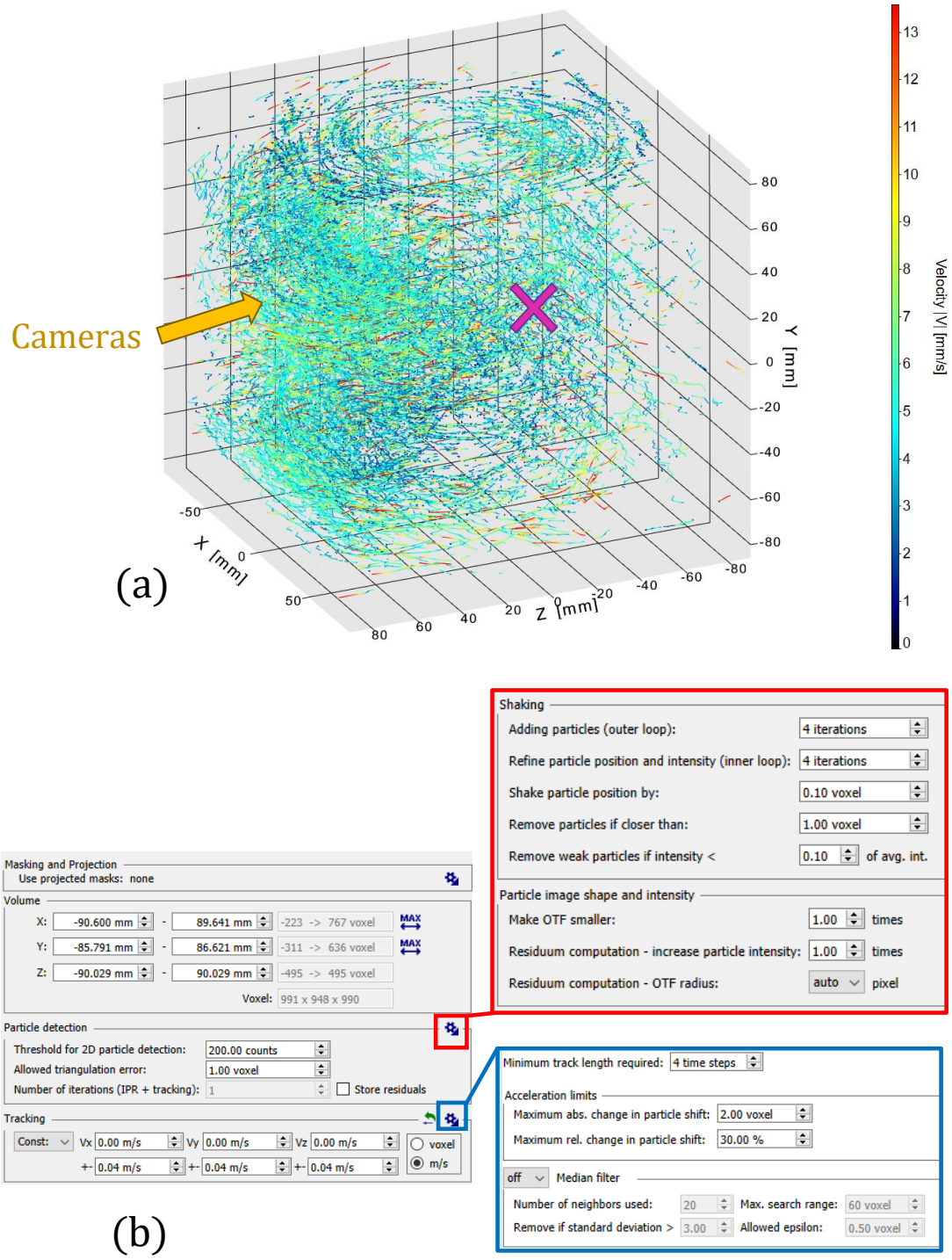


Figure E.8: Caption on next page.

Thèse accessible à l'adresse : https://theses.insa-lyon.fr/publication/2024ISAL0101/these.pdf © [B. Vincent], [2024], INSA Lyon, tous droits réservés

(c)

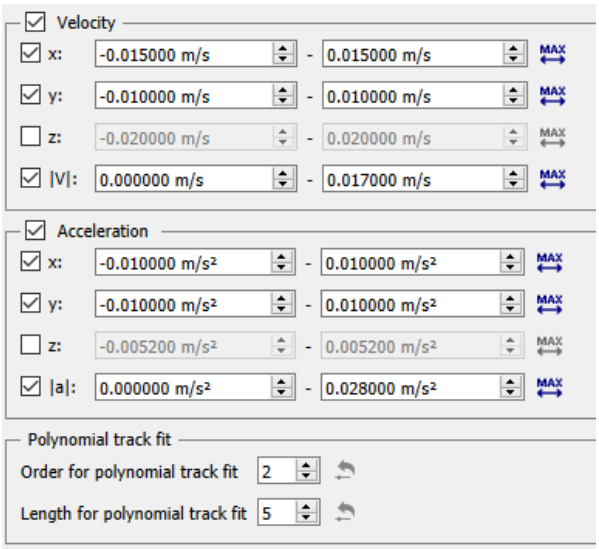


Figure E.8: Particle track detection by *Shake-The-Box* for $Gr_{ac} = 7.50 \times 10^4$ ($P_{elec} = 4$ W). (a) Snapshot of filtered tracks obtained by *Shake-The-Box* (the purple cross locates the entry point of the beam), (b) parameters of *Shake-The-Box*, as prescribed in the *LaVision GmbH* DaVis 10 software. (c) Parameters of the "Range filter" used to remove spurious tracks: particles whose velocities or acceleration do not fit in the indicated bounds are removed. After filtering, 1 174 568 tracks are obtained, with a mean track length of 2.13 s (the maximum track length is 87.6 s for a particle track at the free surface). The mean number of tracks per time step is 2015.

Thèse accessible à l'adresse : https://theses.insa-lyon.fr/publication/2024ISAL0101/these.pdf © [B. Vincent], [2024], INSA Lyon, tous droits réservés

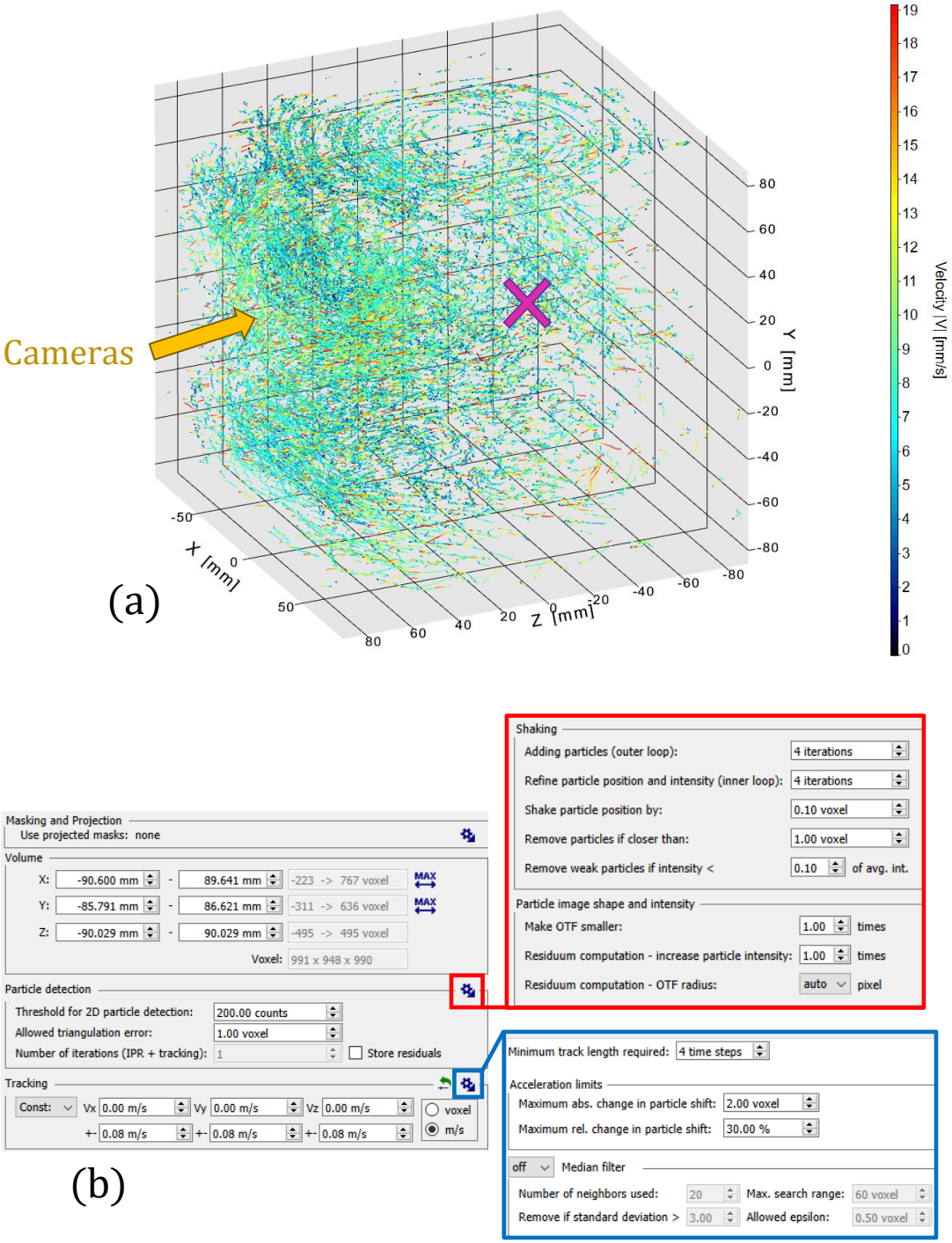


Figure E.9: Caption on next page.

Thèse accessible à l'adresse : https://theses.insa-lyon.fr/publication/2024ISAL0101/these.pdf © [B. Vincent], [2024], INSA Lyon, tous droits réservés

(c)

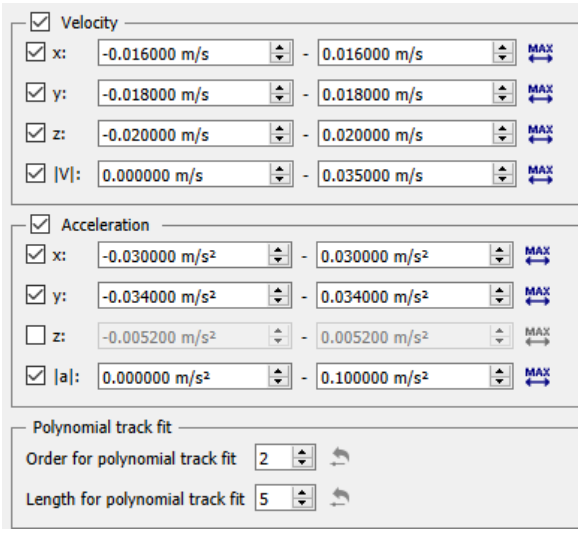


Figure E.9: Particle track detection by *Shake-The-Box* for $Gr_{ac} = 11.28 \times 10^4$ ($P_{elec} =$ 6 W). (a) Snapshot of filtered tracks obtained by *Shake-The-Box* (the purple cross locates the entry point of the beam), (b) parameters of *Shake-The-Box*, as prescribed in the *LaVision GmbH* DaVis 10 software. (c) Parameters of the "Range filter" used to remove spurious tracks: particles whose velocities or acceleration do not fit in the indicated bounds are removed. After filtering, 2 466 914 tracks are obtained, with a mean track length of 1.0 s (the maximum track length is 46.5 s for a particle track at the free surface). The mean number of tracks per time step is 2060.

Thèse accessible à l'adresse : https://theses.insa-lyon.fr/publication/2024ISAL0101/these.pdf © [B. Vincent], [2024], INSA Lyon, tous droits réservés

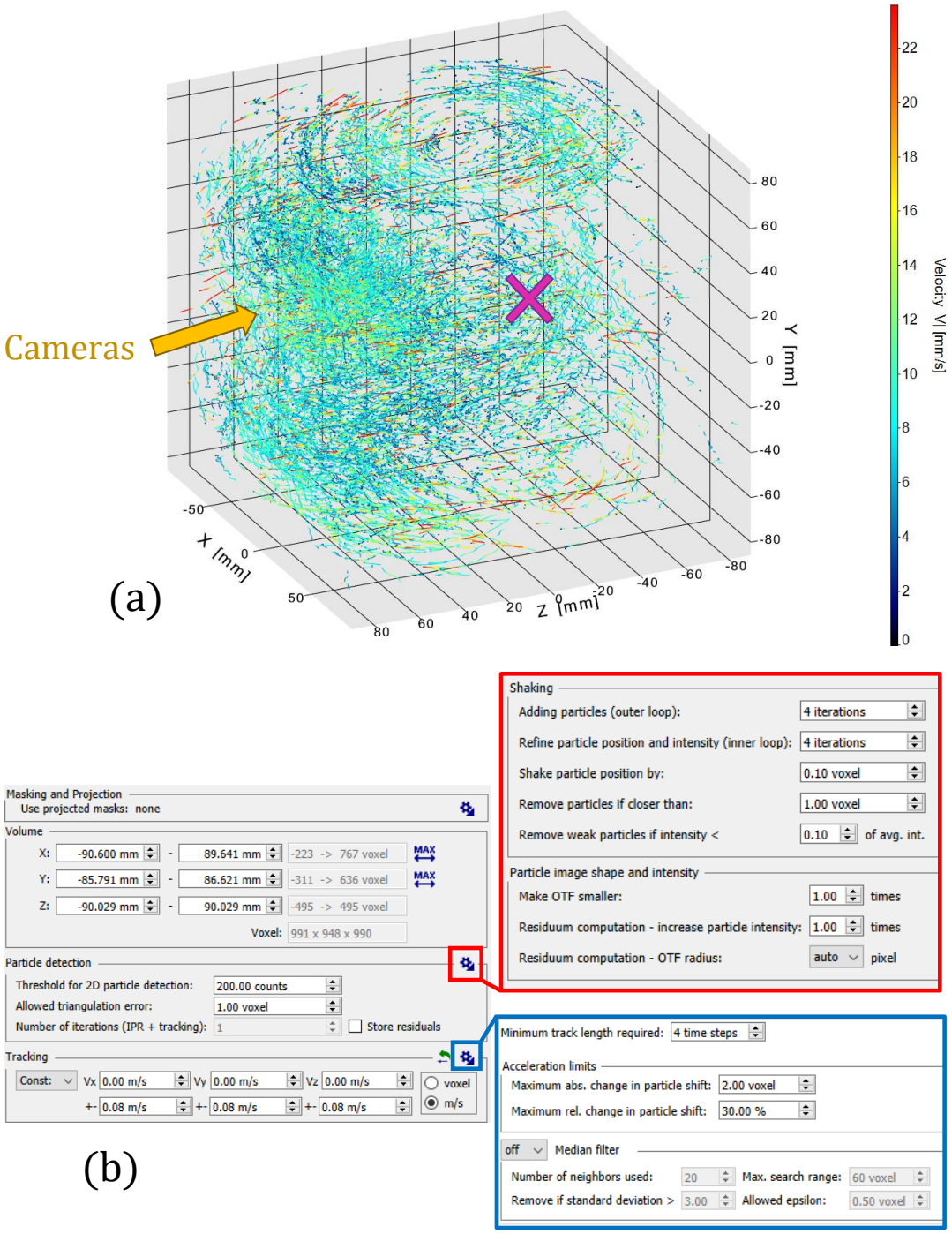


Figure E.10: Caption on next page.

Thèse accessible à l'adresse : https://theses.insa-lyon.fr/publication/2024ISAL0101/these.pdf © [B. Vincent], [2024], INSA Lyon, tous droits réservés

(c)

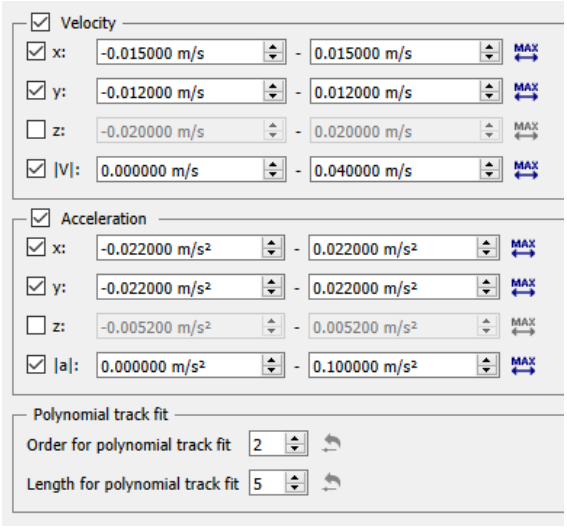
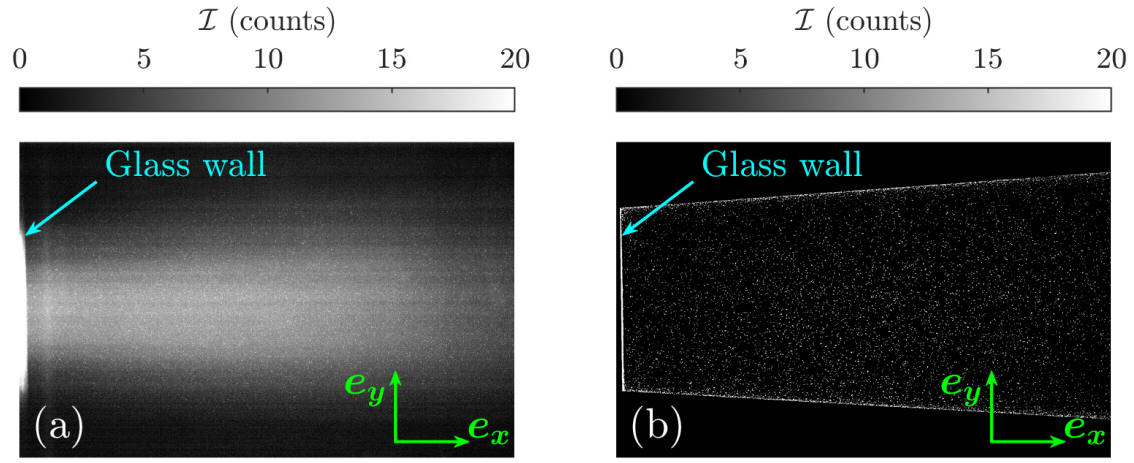
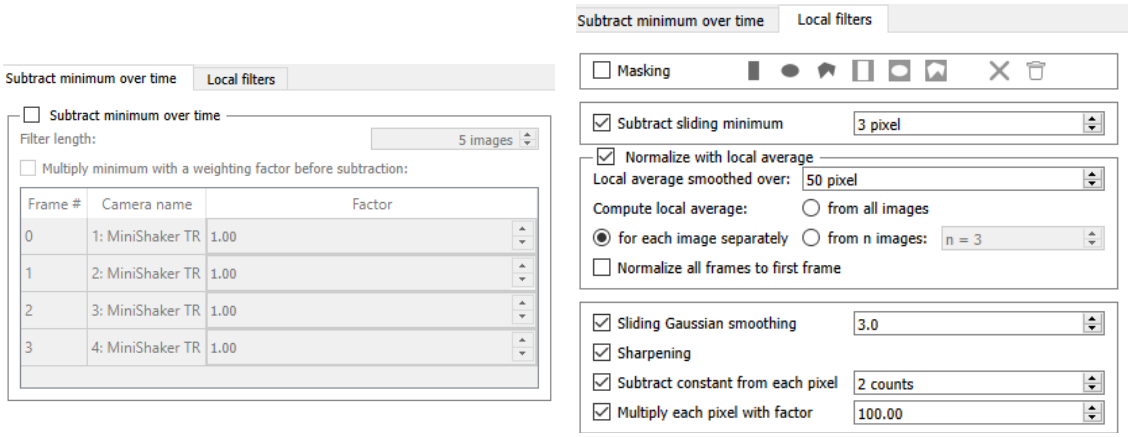


Figure E.10: Particle track detection by *Shake-The-Box* for $Gr_{ac} = 15.12 \times 10^4$ ($P_{elec} = 8$ W). (a) Snapshot of filtered tracks obtained by *Shake-The-Box* (the purple cross locates the entry point of the beam), (b) parameters of *Shake-The-Box*, as prescribed in the *LaVision GmbH* DaVis 10 software. (c) Parameters of the "Range filter" used to remove spurious tracks: particles whose velocities or acceleration do not fit in the indicated bounds are removed. After filtering, 2 196 447 tracks are obtained, with a mean track length of 0.94 s (the maximum track length is 51 s for a particle track at the free surface). The mean number of tracks per time step is 1744.

Thèse accessible à l'adresse : https://theses.insa-lyon.fr/publication/2024ISAL0101/these.pdf © [B. Vincent], [2024], INSA Lyon, tous droits réservés

Processing of the images used for the near-wall measurements





(c)

Figure E.11: Processing of the images recorded near the wall impinged by the first jet for $Gr_{ac} = 1.65 \times 10^4$ ($P_{elec} = 1$ W): (a) raw image, (b) processed image and (c) parameters of the "Image preprocessing" module of *LaVision GmbH* DaVis 10 to obtain (b) from (a).

Thèse accessible à l'adresse : https://theses.insa-lyon.fr/publication/2024ISAL0101/these.pdf © [B. Vincent], [2024], INSA Lyon, tous droits réservés

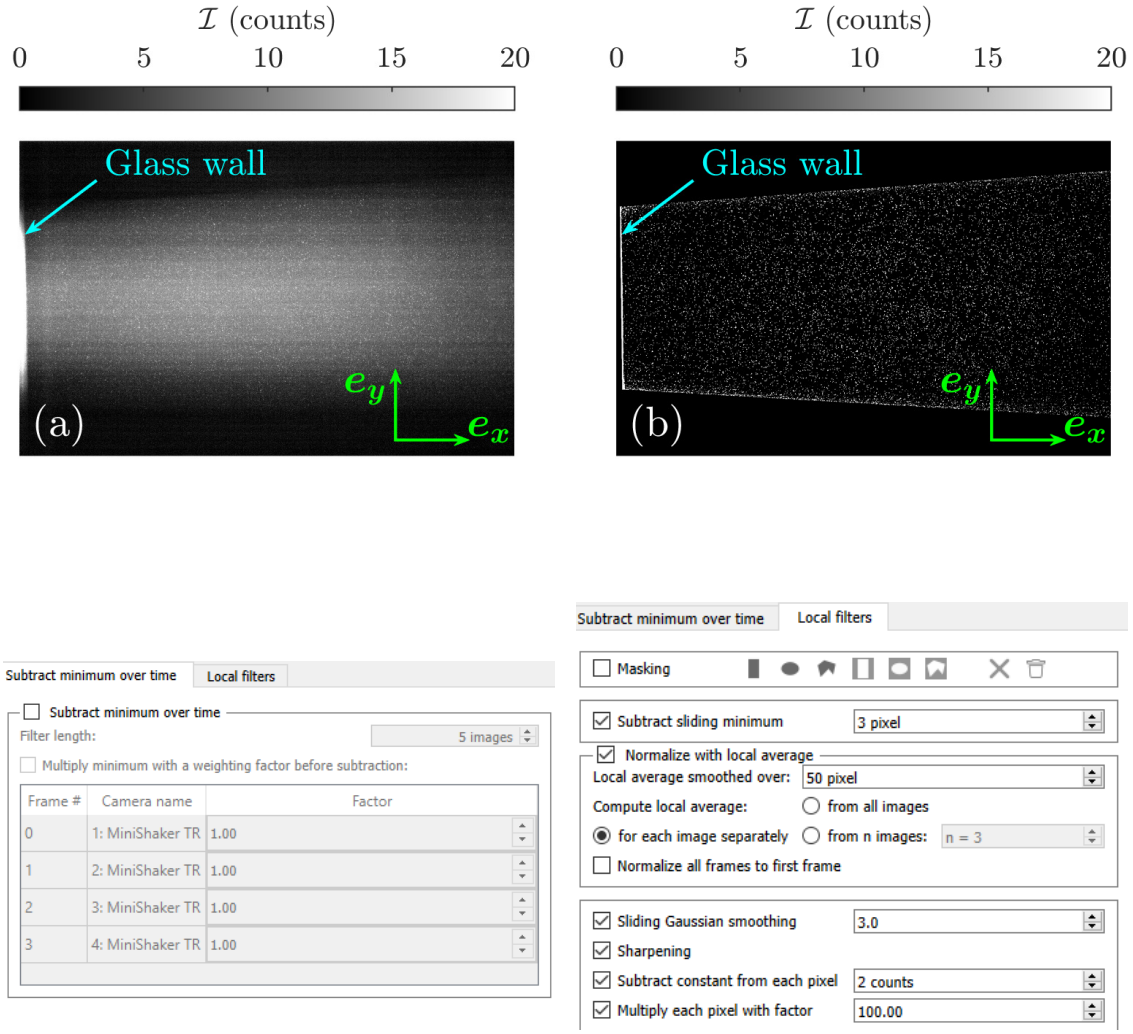


Figure E.12: Processing of the images recorded near the wall impinged by the first jet for $Gr_{ac} = 3.37 \times 10^4$ ($P_{elec} = 2$ W): (a) raw image, (b) processed image and (c) parameters of the "Image preprocessing" module of *LaVision GmbH* DaVis 10 to obtain (b) from (a).

Thèse accessible à l'adresse : https://theses.insa-lyon.fr/publication/2024ISAL0101/these.pdf © [B. Vincent], [2024], INSA Lyon, tous droits réservés

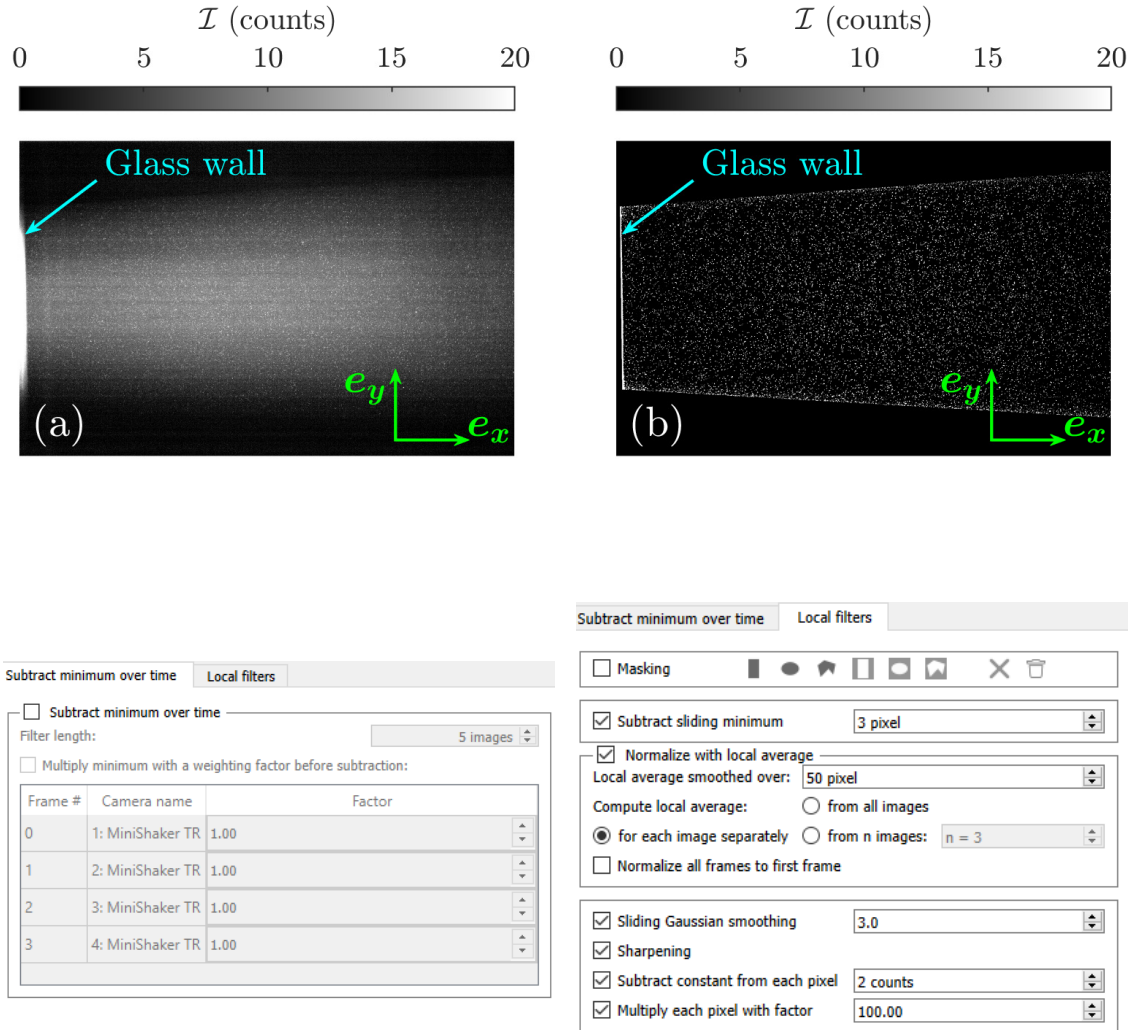
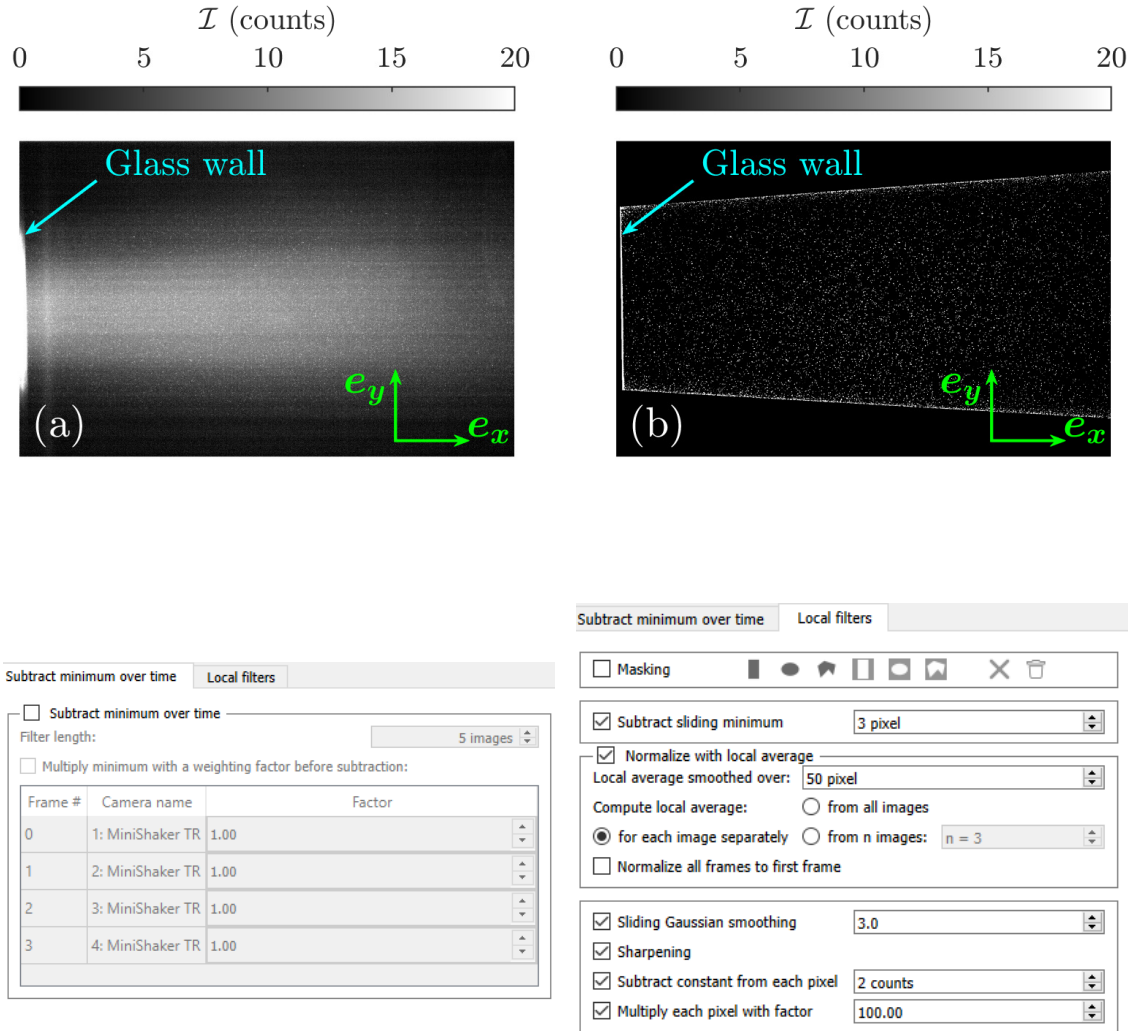


Figure E.13: Processing of the images recorded near the wall impinged by the first jet for $Gr_{ac} = 6.82 \times 10^4$ ($P_{elec} = 4$ W): (a) raw image, (b) processed image and (c) parameters of the "Image preprocessing" module of *LaVision GmbH* DaVis 10 to obtain (b) from (a).

Thèse accessible à l'adresse : https://theses.insa-lyon.fr/publication/2024ISAL0101/these.pdf © [B. Vincent], [2024], INSA Lyon, tous droits réservés



(c)

Figure E.14: Processing of the images recorded near the wall impinged by the first jet for $Gr_{ac} = 10.29 \times 10^4$ ($P_{elec} = 6$ W): (a) raw image, (b) processed image and (c) parameters of the "Image preprocessing" module of *LaVision GmbH* DaVis 10 to obtain (b) from (a).

Thèse accessible à l'adresse : https://theses.insa-lyon.fr/publication/2024ISAL0101/these.pdf © [B. Vincent], [2024], INSA Lyon, tous droits réservés

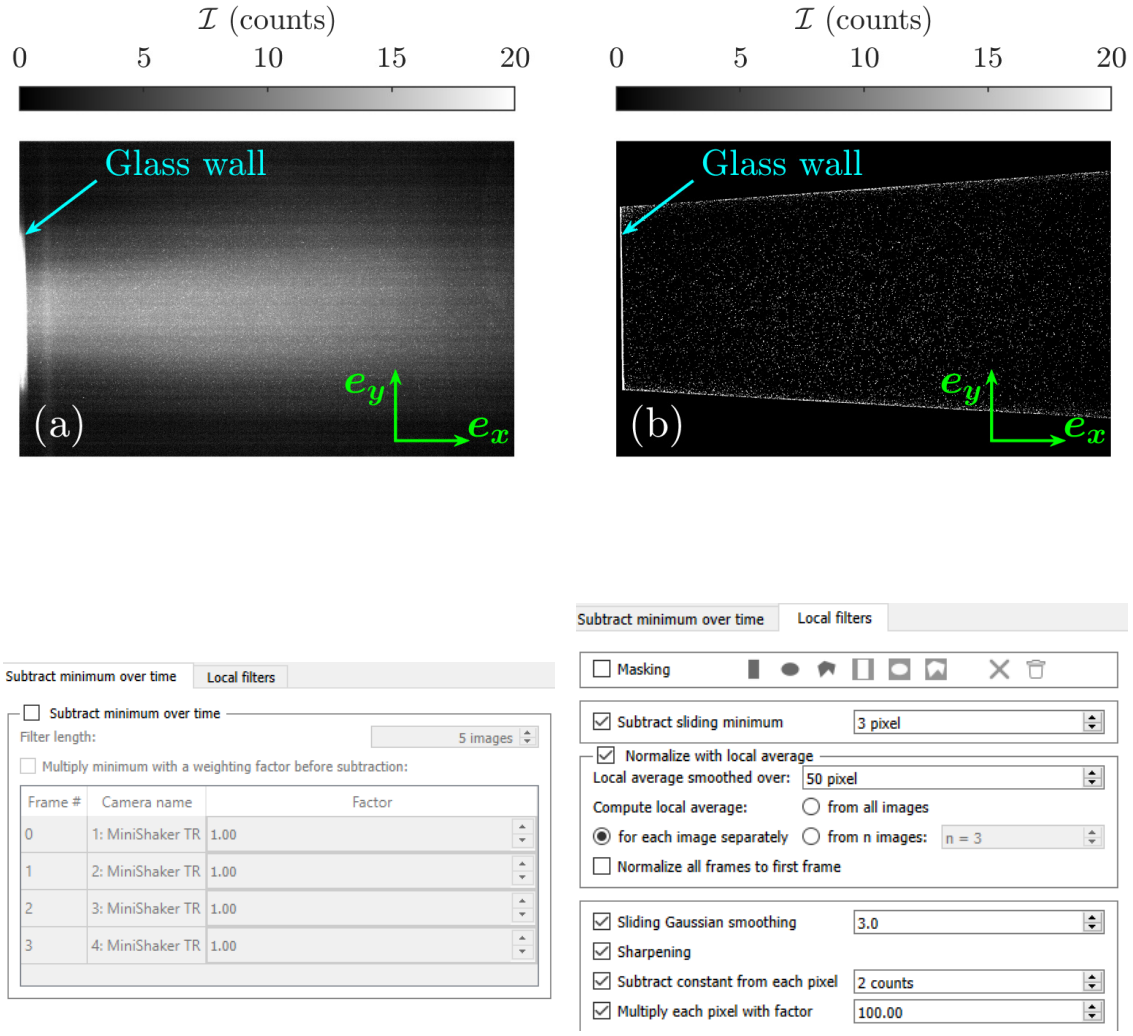


Figure E.15: Processing of the images recorded near the wall impinged by the first jet for $Gr_{ac} = 13.80 \times 10^4$ ($P_{elec} = 8$ W): (a) raw image, (b) processed image and (c) parameters of the "Image preprocessing" module of *LaVision GmbH* DaVis 10 to obtain (b) from (a).

Thèse accessible à l'adresse : https://theses.insa-lyon.fr/publication/2024ISAL0101/these.pdf © [B. Vincent], [2024], INSA Lyon, tous droits réservés

Shake-The-Box parameters and filtering the tracks measured near the wall impinged by the first jet

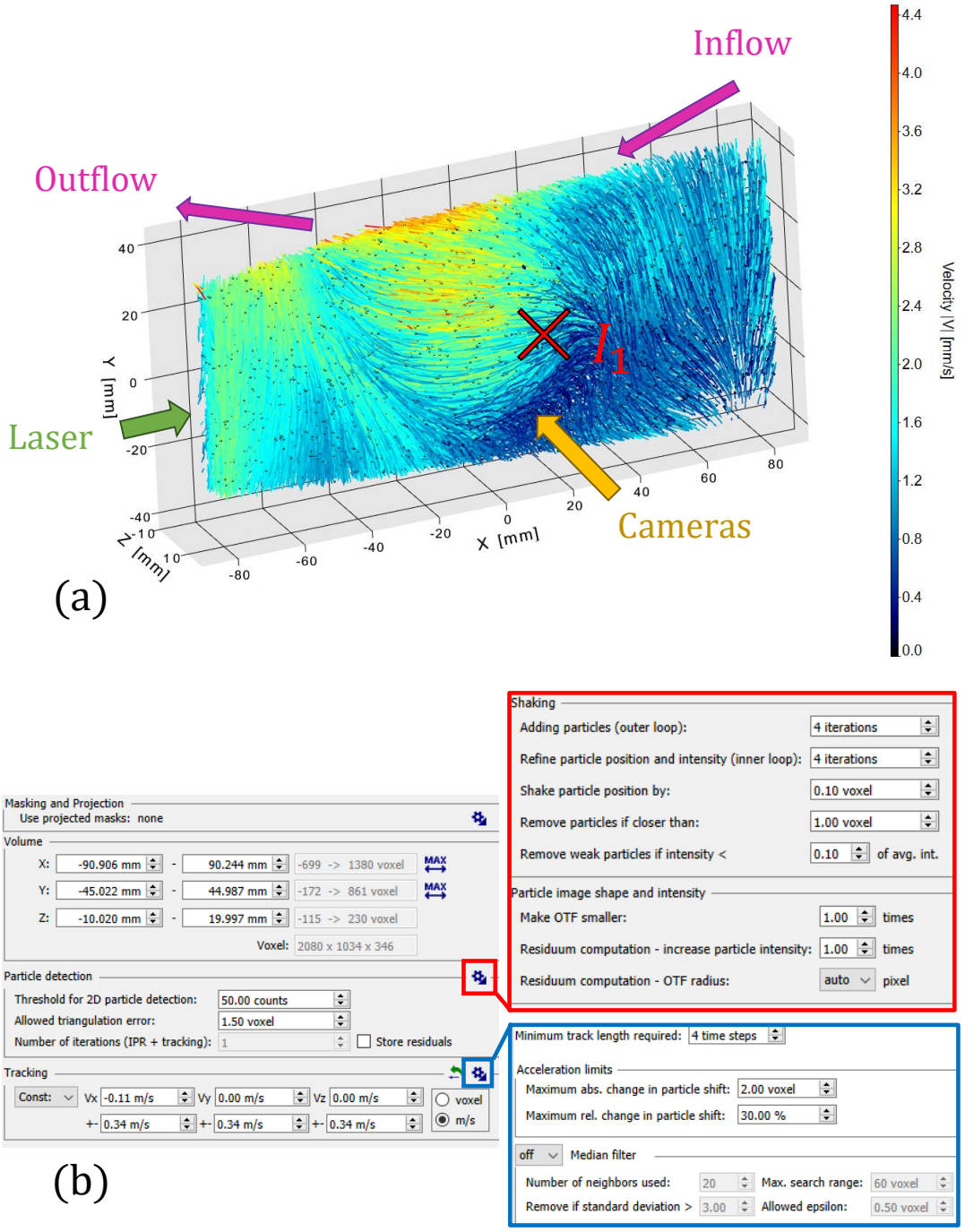
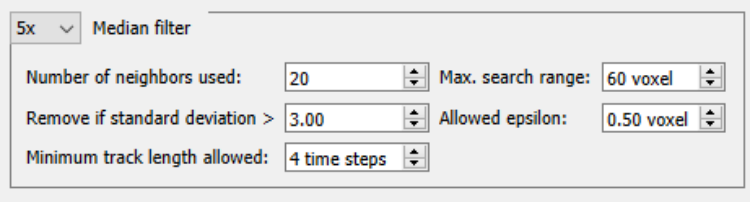


Figure E.16: See caption on the next page

Thèse accessible à l'adresse : https://theses.insa-lyon.fr/publication/2024ISAL0101/these.pdf © [B. Vincent], [2024], INSA Lyon, tous droits réservés



(c)

Figure E.17: Particle track detection by *Shake-The-Box* near the first jet impingement I_1. The case $Gr_{ac} = 1.65 \times 10^4$ ($P_{elec} = 1$ W) is shown. (a) Snapshot of filtered tracks obtained by *Shake-The-Box* (the red cross locates the first jet impingement I_1), (b) parameters of *Shake-The-Box*, as prescribed in the *LaVision GmbH* DaVis 10 software. (c) Parameters of the "Median filter", which removes spurious tracks after three main steps: (i) the neighbours of a given particle are looked for, then (ii) the median velocity of the particle group is computed together with the velocity deviation of each particle. Finally, (iii) the algorithm removes the particles for which the velocity deviation exceeds the prescribed threshold. After filtering, 1 528 214 tracks are obtained over the recording duration (29 minutes), with a mean track length of 4.8 s (the maximum track length is 45.33 s). The mean number of tracks per time step is 6 719.

Thèse accessible à l'adresse : https://theses.insa-lyon.fr/publication/2024ISAL0101/these.pdf © [B. Vincent], [2024], INSA Lyon, tous droits réservés

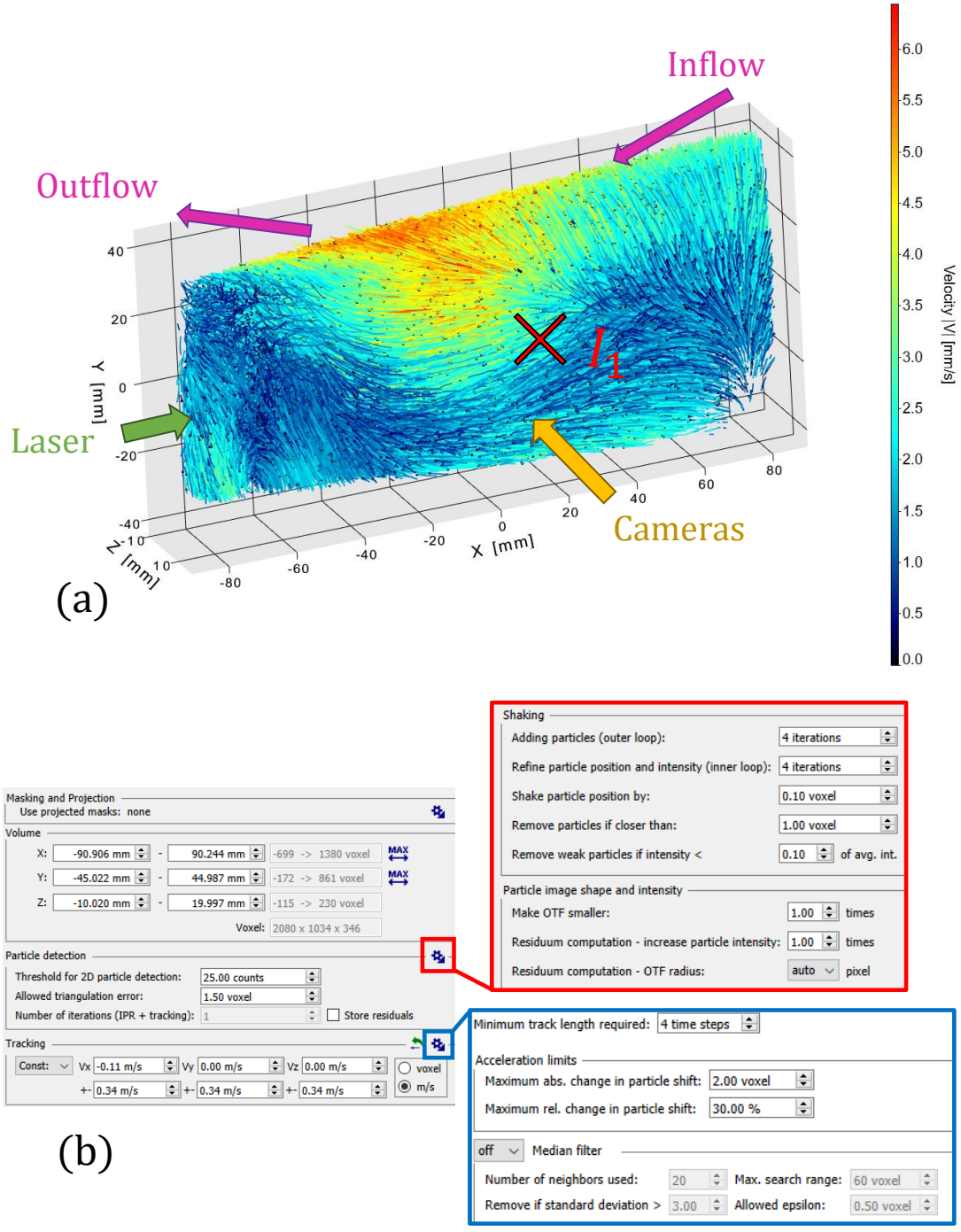
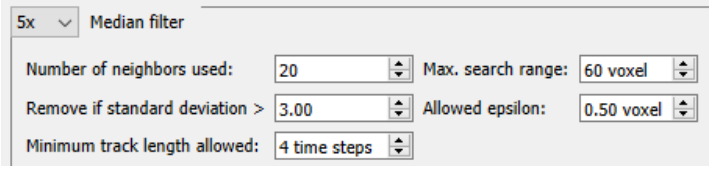


Figure E.18: See caption on the next page

Thèse accessible à l'adresse : https://theses.insa-lyon.fr/publication/2024ISAL0101/these.pdf © [B. Vincent], [2024], INSA Lyon, tous droits réservés



(c)

Figure E.19: Particle track detection by *Shake-The-Box* near the first jet impingement I_1. The case $Gr_{ac} = 3.37 \times 10^4$ ($P_{elec} = 2$ W) is shown. (a) Snapshot of filtered tracks obtained by *Shake-The-Box* (the red cross locates the first jet impingement I_1), (b) parameters of *Shake-The-Box*, as prescribed in the *LaVision GmbH* DaVis 10 software. (c) Parameters of the "Median filter", which removes spurious tracks after three main steps: (i) the neighbours of a given particle are looked for, then (ii) the median velocity of the particle group is computed together with the velocity deviation of each particle. Finally, (iii) the algorithm removes the particles for which the velocity deviation exceeds the prescribed threshold. After filtering, 3 525 753 tracks are obtained over the recording duration (20 minutes), with a mean track length of 3.6 s (the maximum track length is 39.6 s). The mean number of tracks per time step is 11 123.

Thèse accessible à l'adresse : https://theses.insa-lyon.fr/publication/2024ISAL0101/these.pdf © [B. Vincent], [2024], INSA Lyon, tous droits réservés

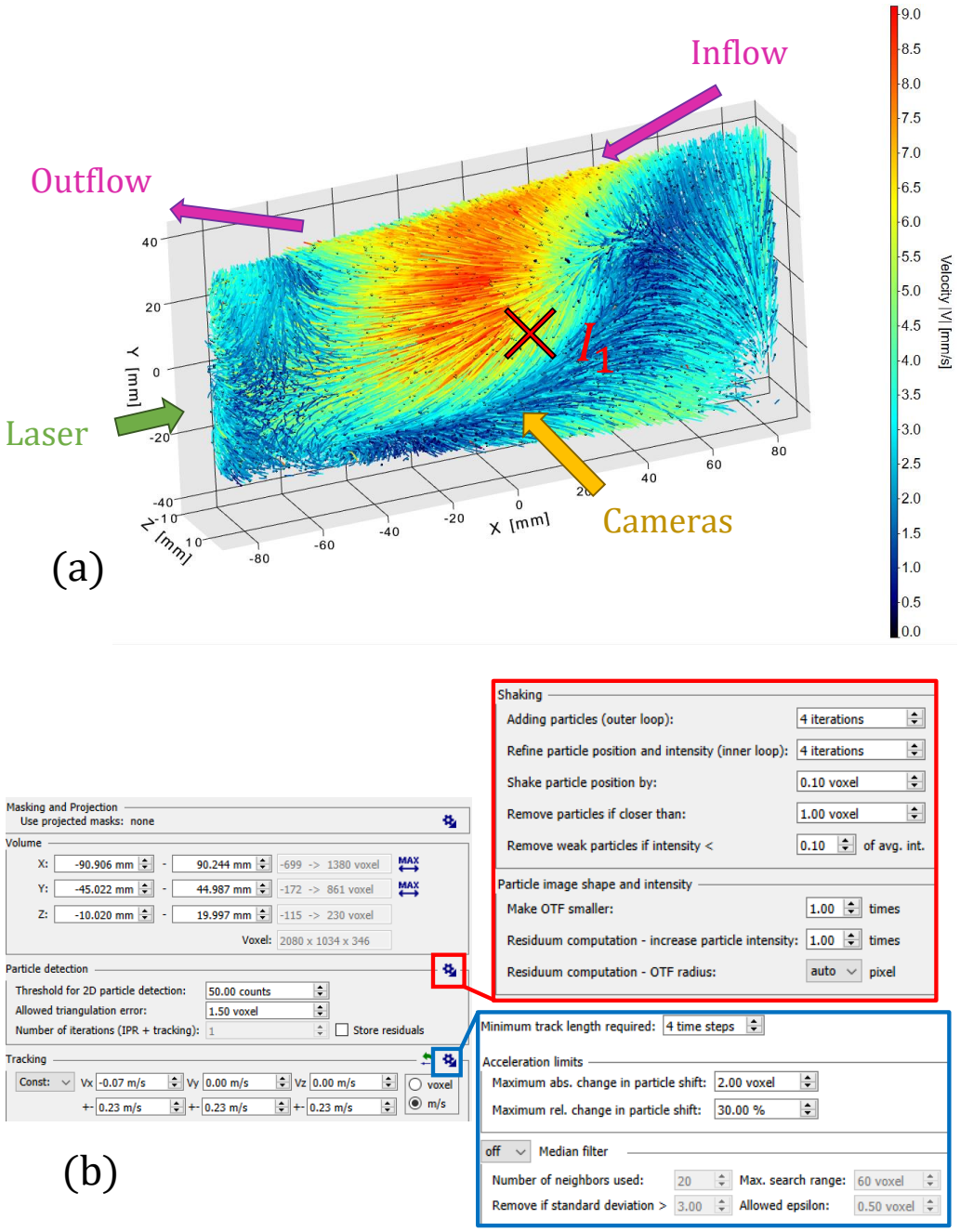


Figure E.20: Particle track detection by *Shake-The-Box* near the first jet impingement I_1. The case $Gr_{ac} = 6.82 \times 10^4$ ($P_{elec} = 4$ W) is shown. (a) Snapshot of filtered tracks obtained by *Shake-The-Box* (the red cross locates the first jet impingement I_1) and (b) parameters of *Shake-The-Box*, as prescribed in the *LaVision GmbH* DaVis 10 software. The obtained tracks did not require to be filtered. In total, 5 502 200 tracks are obtained over the recording duration (20 minutes), with a mean track length of 2.2 s (the maximum track length is 24 s). The mean number of tracks per time step is 10 551.

Thèse accessible à l'adresse : https://theses.insa-lyon.fr/publication/2024ISAL0101/these.pdf © [B. Vincent], [2024], INSA Lyon, tous droits réservés

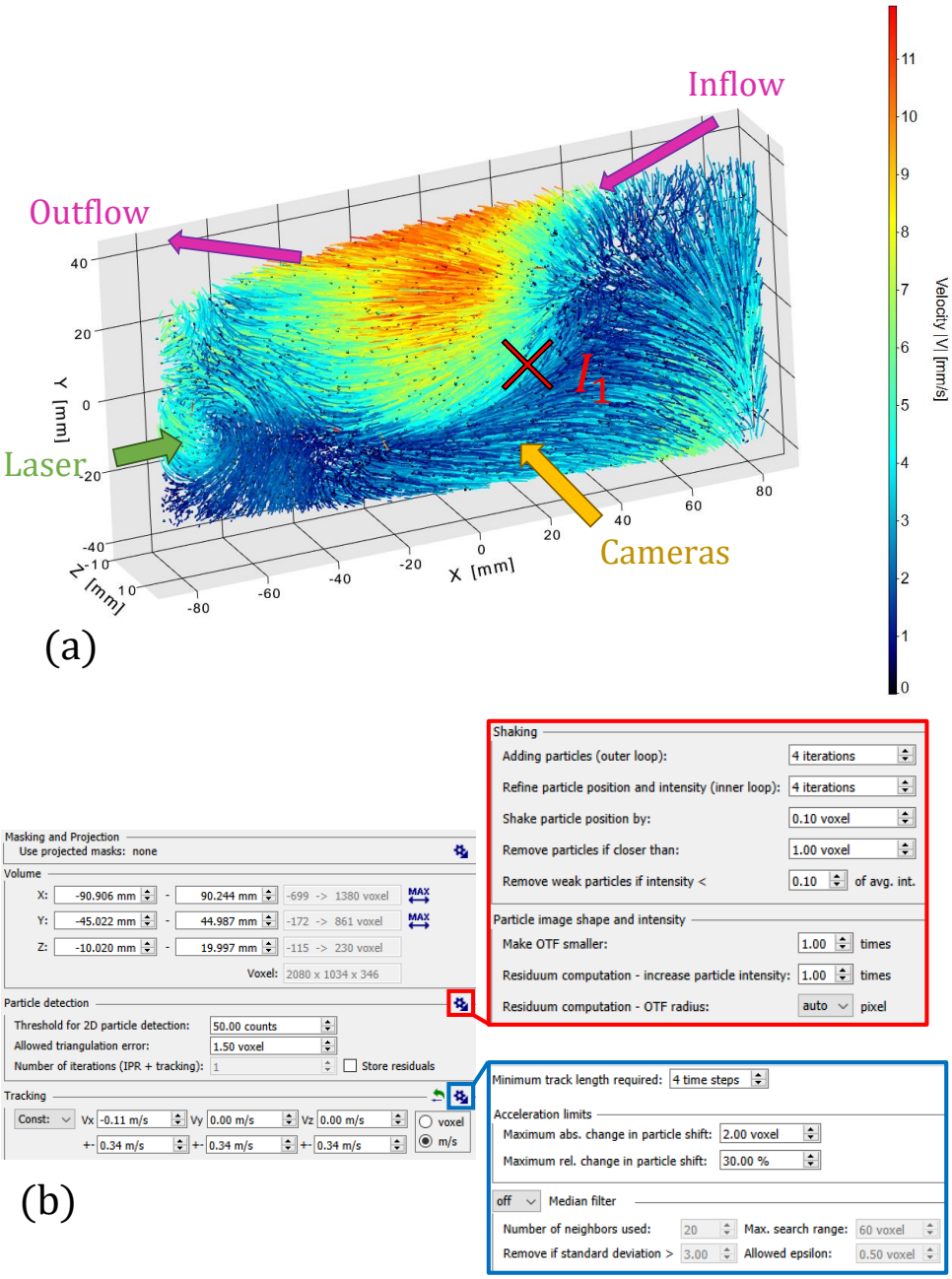
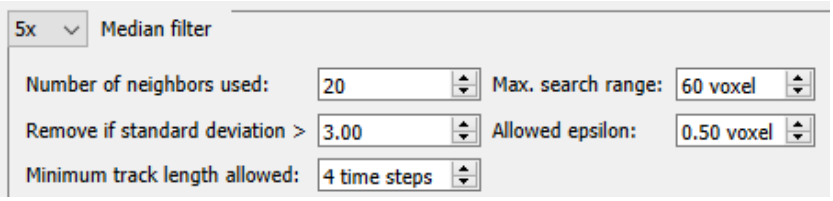


Figure E.21: See caption on the next page

Thèse accessible à l'adresse : https://theses.insa-lyon.fr/publication/2024ISAL0101/these.pdf © [B. Vincent], [2024], INSA Lyon, tous droits réservés



(c)

Figure E.22: Particle track detection by *Shake-The-Box* near the first jet impingement I_1. The case $Gr_{ac} = 10.29 \times 10^4$ ($P_{elec} = 6$ W) is shown. (a) Snapshot of filtered tracks obtained by *Shake-The-Box* (the red cross locates the first jet impingement I_1), (b) parameters of *Shake-The-Box*, as prescribed in the *LaVision GmbH* DaVis 10 software. (c) Parameters of the "Median filter", which removes spurious tracks after three main steps: (i) the neighbours of a given particle are looked for, then (ii) the median velocity of the particle group is computed together with the velocity deviation of each particle. Finally, (iii) the algorithm removes the particles for which the velocity deviation exceeds the prescribed threshold. After filtering, 3 837 350 tracks are obtained over the recording duration (20 minutes), with a mean track length of 1.8 s (the maximum track length is 18 s). The mean number of tracks per time step is 5 919.

Thèse accessible à l'adresse : https://theses.insa-lyon.fr/publication/2024ISAL0101/these.pdf © [B. Vincent], [2024], INSA Lyon, tous droits réservés

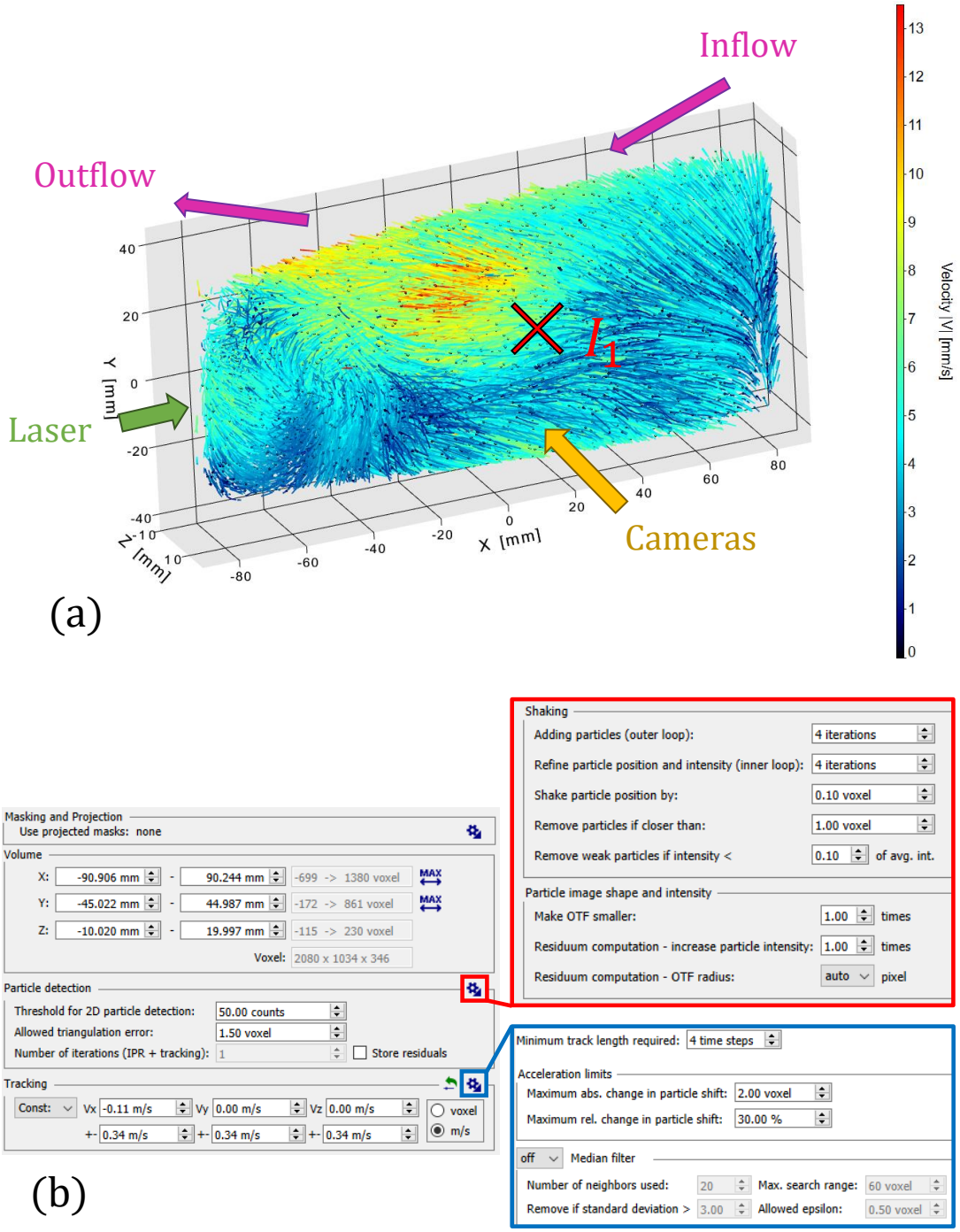
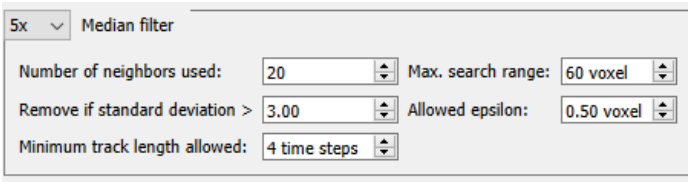


Figure E.23: See caption on the next page

Thèse accessible à l'adresse : https://theses.insa-lyon.fr/publication/2024ISAL0101/these.pdf © [B. Vincent], [2024], INSA Lyon, tous droits réservés



(c)

Figure E.24: Particle track detection by *Shake-The-Box* near the first jet impingement I_1. The case $Gr_{ac} = 13.80 \times 10^4$ ($P_{elec} = 8$ W) is shown. (a) Snapshot of filtered tracks obtained by *Shake-The-Box* (the red cross locates the first jet impingement I_1), (b) parameters of *Shake-The-Box*, as prescribed in the *LaVision GmbH* DaVis 10 software. (c) Parameters of the "Median filter", which removes spurious tracks after three main steps: (i) the neighbours of a given particle are looked for, then (ii) the median velocity of the particle group is computed together with the velocity deviation of each particle. Finally, (iii) the algorithm removes the particles for which the velocity deviation exceeds the prescribed threshold. After filtering, 3 892 465 tracks are obtained over the recording duration (20 minutes), with a mean track length of 1.6 s (the maximum track length is 20 s). The mean number of tracks per time step is 5 752.

Thèse accessible à l'adresse : https://theses.insa-lyon.fr/publication/2024ISAL0101/these.pdf © [B. Vincent], [2024], INSA Lyon, tous droits réservés

Thèse accessible à l'adresse : https://theses.insa-lyon.fr/publication/2024ISAL0101/these.pdf © [B. Vincent], [2024], INSA Lyon, tous droits réservés

FOLIO ADMINISTRATIF

THESE DE L'INSA LYON, MEMBRE DE L'UNIVERSITE DE LYON

NOM : **VINCENT** DATE de SOUTENANCE : **29/11/2024**
(avec précision du nom de jeune fille, le cas échéant)

Prénoms : **Bjarne**

TITRE : **Experimental and numerical study of three-dimensional flows generated by ultrasounds**

NATURE : **Doctorat** Numéro d'ordre : **2024ISAL0101**

École Doctorale : **Mécanique, Energétique, Génie civil et Acoustique (MEGA)**

Spécialité : **Mécanique des Fluides**

RÉSUMÉ :
The contactless nature of acoustic streaming (i.e., flows driven by the attenuation of progressive sound waves) makes it an attractive flow actuation solution whenever the access to the fluid is difficult, as it is regularly the case during the solidification of semiconductors, for instance. In particular, streaming flows can be beneficial to either stir the melt of to control hydrodynamic instabilities. This study aims precisely to gain a better understanding of streaming jets, and thus to pave the way for the design of complex streaming flows to optimise solidification processes.
First, I investigated the scaling of streaming jets flowing in a closed cavity and over distances larger than the sound attenuation length L_α. As such, this study covers regions in which the acoustic forcing is driving the flow (at distances $x < L_\alpha$ from the source) or nearly ineffective ($> L_\alpha$). Using numerical simulations, I derived scaling laws for the jet velocity in each of these regions, allowing to draw a complete phenomenological picture of a streaming jet.
Second, I studied numerically the stability of that flow for different cavity sizes. For each case, destabilisation is rooted in the downstream cavity end, near the jet impingement. Confining the flow greatly affects the nature of the primary instability: whilst non-oscillatory perturbations become unstable in weakly-confined settings, reducing the cavity radius causes the flow to become unstable through either supercritical or subcritical Hopf bifurcations. The change of the unstable perturbation topology is explained using critical point theory.
Third, I investigated experimentally a novel three-dimensional (3D) streaming flow for stirring purposes. I relied on a high-end Particle Tracking Velocimetry (PTV) method to capture the flow structures, their leading velocities, and to determine how these velocities scale with the forcing magnitude. The flow was driven by a helix-shaped forcing obtained from multiple reflections of a single sound beam in a closed water cavity. The main velocity levels are sustained by the beam-forced jets. Besides providing leading frequencies estimates as the forcing magnitude is increased, I showed that the scaling laws derived for a single jet can be used to design this 3D streaming flow.

MOTS-CLÉS : **acoustic streaming, stability, Particle Tracking Velocimetry**

Laboratoire(s) de recherche : **Laboratoire de Mécanique des Fluides et d'Acoustique - UMR5509**
Fluid and Complex Systems Research Centre

Directeurs de thèse : **Pr. Valéry BOTTON, Pr. Alban POTHÉRAT**
Co-encadrante de thèse : **Dr. Sophie MIRALLES**

Président du Jury : **Pr. Régis MARCHIANO**

Composition du Jury :
Pr. Régis MARCHIANO, Pr. Dwight BARKLEY, Pr. Anne JUEL, Pr. Valéry BOTTON, Pr. Alban POTHÉRAT, Dr. Sophie MIRALLES (MdC), Dr. Abhishek KUMAR (MdC)

Thèse accessible à l'adresse : https://theses.insa-lyon.fr/publication/2024ISAL0101/these.pdf © [B. Vincent], [2024], INSA Lyon, tous droits réservés